COMPUTER SIMULATION OF HOLLOWCORE CONCRETE FLOORING SYSTEMS EXPOSED TO FIRE

A thesis submitted in partial fulfilment

of the requirements for the

Degree of Doctor of Philosophy**.**

By

Jeremy J. Chang

Supervised by

Professor Andrew H. Buchanan

Dr. Rajesh P. Dhakal

Associate Professor Peter J. Moss

Department of Civil Engineering

University of Canterbury

Christchurch, New Zealand.

April, 2007

Abstract

Multi-storey buildings with precast hollowcore concrete floor systems are very common in New Zealand and in many other countries, but the structural behaviour of such systems under fire exposure is not easy to predict because of the complex geometry, composite construction, and a wide range of possible support conditions. The 2006 version of the New Zealand Concrete Standard NZS3101 introduces new details for connection of hollowcore floor units to reinforced concrete supporting beams to improve seismic performance, but the fire performance of the new connection systems is unknown. Currently available methods for simulating fire performance of hollowcore slabs are not suitable for design purposes. Therefore, a simple yet sufficiently accurate simulation method needs to be developed.

This study was carried out using a proposed simulation method to investigate the fire performance of hollowcore floor slabs with different connection details between the hollowcore units and their reinforced concrete supporting beams conforming to NZS3101. The proposed simulation method is examined on the platform of SAFIR, a non-linear finite element program that includes both thermal and structural analysis. The proposed simulation method was validated using available experimental results from a limited number of tests. It does not take account of shear and anchorage failures or spalling effects, so designers should consult other studies for this behaviour of hollowcore concrete flooring systems.

By using the proposed simulation scheme in SAFIR, it is investigated whether the tensile membrane action established through beams parallel to the hollowcore units and different floor aspect ratios will enhance the fire resistance of hollowcore concrete flooring systems. From the simulation results it is concluded that rigid connections at both the ends and the sides of the hollowcore flooring systems to the supporting beams provide better fire resistance than rotationally flexible connections, and the fire resistance of hollowcore flooring systems can be increased by using stiffer supporting beams at the end of the slabs and also by decreasing the spacing between the beams parallel to the hollowcore units.

Acknowledgements

I would like to express my gratitude to the following people who have helped me throughout my research:

- My supervisors, Professor Andy Buchanan, Dr. Rajesh Dhakal and Associate Professor Peter Moss, for their invaluable guidance and constant supports over the years.
- Professor Jean-Marc Franssen of the Univerisity of Liège for his invaluable help and advice with the SAFIR program throughout the project.
- Dr. Linus Lim for his help with the SAFIR program and his guidance in my study.
- Professor John Mander of the Future Building Systems project and FRST for the financial support.
- Professor Roger Plank of the University of Sheffield for his insightful advice and suggestions.
- Professor Des Bull and Professor Athol Carr for their generous help.
- Professor Luigi Materazzi and Dr. Marco Breccolotti of the University of Perugia for generously sharing information of their research.
- David Barber, Darin Millar and Bill Gordon for their help and encouragements.
- The Civil Engineering Department and everyone I have encountered during my study at Canterbury, especially Dr Mike Spearpoint, Dr. Charley Fleishmann, Dr. Massimo Fragiacomo and Paola Bulian, Dr. Stefano Pampanin and Dr. Sonia Giovinazzi, Roger Harrison, Pauline Anderson, Keryn Goble, Hadley Cave, Shannon Page, Kerry Mulligan, Didier Pettinga, Michele Palmieri, Gabriele Attanasi and Laurent Pasticier, for all the help and encouragements.
- Finally, Mum, Dad and my brother Thomas, for their unwavering supports.

Table of Contents

1. INTRODUCTION 1

1.1. Background 1

1.2. Objectives 2

1.3. Scope of Research 3

1.3.1. Development of a model to simulate buildings with hollowcore concrete flooring systems in fire 3

1.3.2. Investigate the performance in fire of buildings with hollowcore concrete flooring designed according to NZS3101 3

1.3.3. Assessing tensile membrane action in hollowcore concrete flooring systems 3

1.4. Outline of Thesis 4

2. REVIEW OF FIRE DESIGN FOR HOLLOWCORE SLABS 5

2.1. Introduction 5

2.2. Description of Hollowcore Slabs 5

2.3. Requirements and Recommendations for Fire Design of Concrete Slabs 6

2.3.1. Requirements for fire design of concrete slabs 6

2.3.2. Recommendations from New Zealand Standards 7

2.3.3. Recommendations from Eurocode 7

2.3.4. Recommendations from ASTM E119 9

2.3.5. Recommendations from other sources 10

2.4. Engineering Design Method 14

2.5. Proprietary Fire Rating of Hollowcore Units 14

3. MATERIAL PROPERTIES OF CONCRETE AND STEEL 17

3.1. Thermal Properties of Concrete 17

3.1.1. Thermal conductivity 17

3.1.2. Thermal diffusivity 19

3.1.3. Specific heat 21

3.1.4. Thermal expansion 23

3.1.5. Spalling 27

3.2. Thermal Properties of Steel 30

3.2.1. Thermal conductivity 30

3.2.2. Specific heat 30

3.2.3. Thermal expansion 31

3.3. Mechanical Properties of Concrete 33

3.3.1. Compressive strength 33

3.3.2. Tensile strength 39

3.3.3. Modulus of elasticity *41*
3.3.4. Elastic shear modulus and Poisson's ratio *42*
3.3.5. Constitutive law *43*
3.3.6. Creep Strain *47*
3.3.7. Transient strain *48*
3.4. Mechanical Properties of Steel 49
3.4.1. Ultimate and yield strengths *49*
3.4.2. Modulus of elasticity *51*
3.4.3. Components of strain *52*

4. REVIEW OF FIRE BEHAVIOUR OF HOLLOWCORE CONCRETE SLABS 55
4.1. Structural Behaviour of Hollowcore Concrete Slabs in Ambient Conditions 55
4.1.1. Flexure *55*
4.1.2. Floor diaphragm action *56*
4.1.3. Shear compression *57*
4.1.4. Shear tension *59*
4.1.5. Anchorage failure *61*
4.2. Structural Behaviour of Hollowcore Concrete Slabs in Fire Tests 62
4.2.1. DIFT [Andersen et al. 1999] *62*
4.2.2. University of Ghent [FeBe Studiecommissie SSTC 1998] *64*
4.2.3. BRE [Lennon 2003] *68*
4.2.4. Danish Prefab Concrete Association [BEF 2005] *69*
4.2.5. Delft University of Technology [Fellinger 2004] *72*
4.3. Shear and Anchorage Behaviour of Hollowcore Concrete Slabs in Fire 76
4.3.1. Incompatible thermal strains *76*
4.3.2. Thermal cracks *77*
4.3.3. Deterioration of mechanical properties *77*
4.3.4. Anchorage failure *78*
4.3.5. Effect of support conditions *78*
4.4. Summary from the Fire Test Results 79
4.4.1. Spalling *79*
4.4.2. Shear and anchorage failure *80*
4.4.3. Load level *80*
4.4.4. Axial restraint *80*
4.4.5. Core filling *80*
4.4.6. Other observed effects of hollowcore slabs in fires *81*

5. THE SAFIR FINITE ELEMENT PROGRAM 83
5.1. Introduction 83
5.2. Compatibilities of SAFIR 83
5.3. Analysis Procedure 83
5.3.1. Thermal analysis 84
5.3.2. Torsional analysis 84
5.3.3. Structural analysis 85
5.4. Structural Elements 86
5.4.1. SAFIR beam element 87
5.4.2. The SAFIR shell element 88
5.5. Limitations of SAFIR 92

6. MODEL DEVELOPMENT 95
6.1. Introduction 95
6.2. Existing Methods for Simulating Hollowcore Concrete Slabs 95
6.2.1. Finite element analysis for thermal analysis only 95
6.2.2. Finite element analysis for thermal and mechanical analyses 96
6.2.3. Finite element analysis including shear and anchorage failures 98
6.3. Development of a New Model 99
6.3.1. Concerns related to shell elements 100
6.3.2. Concerns related to beam elements 103
6.4. Proposed Model 103
6.4.1. Grillage analogy 104
6.4.2. Assumption made with transverse beams 114
6.4.3. Other assumptions regarding the overall model 115
6.5. Summary 116
6.5.1. Model description 116
6.5.2. Advantages of the model 116
6.5.3. Disadvantages of the model 117

7. MODEL VALIDATION 119
7.1. Stage One: Background comparisons 120
7.2. Stage Two: Comparing 3D beams to shell elements in modelling an one-way reinforced concrete slab 126
7.3. Stage Three: Comparing beam grillage to shell elements in modelling a one-way reinforced concrete slab 131
7.4. Stage Four: Comparing results from a beam grillage model to experimental

results of a one-way prestressed hollowcore concrete slab 138
7.4.1. DIFT *138*
7.4.2. University of Ghent *142*
7.4.3. BEF *148*
7.4.4. Summary from Stage 4 *150*
7.5. Stage Five: Comparing shell elements to beam grillage in modelling the topping of a one-way prestressed hollowcore concrete slab 150
7.6. Conclusions from Model Validation 156

8. FIRE PERFORMANCE OF HOLLOWCORE CONCRETE FLOORING SYSTEMS WITH VARIOUS SUPPORT CONDITIONS 159
8.1. Introduction 159
8.2. Simulation Model 159
8.2.1. Sensitivity studies *160*
8.3. Floor Slabs with Ideal Support Conditions without End Beams 164
8.3.1. Pin-pin end supports *164*
8.3.2. Pin-roller end supports *167*
8.3.3. Fix-fix end supports *169*
8.3.4. Fix-slide end supports *173*
8.3.5. Summary *179*
8.4. Effect of Core-filling on the Structural Performance of Floor Slab in Fire 181
8.5. Floor Slabs with Ideal Support Conditions with End Beams 186
8.5.1. Pin-pin supports *188*
8.5.2. Pin-roller supports *189*
8.5.3. Fix-fix supports *191*
8.5.4. Fix-slide supports *194*
8.6. Summary and Discussion 196
8.6.1. Effect of end beams *196*
8.6.2. Effect of core-filling *198*
8.6.3. Effect of support conditions *199*

9. FIRE PERFORMANCE OF HOLLOWCORE CONCRETE FLOORING SYSTEMS WITH END CONNECTIONS FROM NZS3101 201
9.1. Introduction 201
9.2. Design Details of Studied Subassemblies 202
9.2.1. Subassembly from Matthews [2004] *202*
9.2.2. Subassembly from Lindsay [2004] *203*
9.2.3. Subassembly from MacPherson [2005] *204*

9.3. Modelling the End Connections from the Subassemblies 206
9.3.1. Modelling Matthews's end connections 206
9.3.2. Modelling Lindsay's end connection 207
9.3.3. Modelling MacPherson's end connections 208
9.3.4. Simplifications made by using these models 208
9.4. Study on Slabs with Different End Connections and Different Supporting Conditions at the Ends of the End Beams 209
9.4.1. Slabs with Matthews's end connection 210
9.4.2. Slabs with Lindsay's end connection 210
9.4.3. Slabs with MacPherson's end connection 210
9.4.4. Rigid end connection 211
9.4.5. Analyses and discussions – slabs with fix-fix supports 211
9.4.6. Analyses and discussions – slabs with fix-slide supports 214
9.4.7. Overall discussion 217
9.5. Attempt to Simulate the Closing of Gap in Lindsay's Connection in SAFIR 218
9.6. Subassemblies with Different End connections 221
9.7. Summaries 226

10. EFFECT OF MEMBRANE ACTION ON THE FIRE PERFORMANCE OF HOLLOWCORE CONCRETE FLOORING SYSTEMS WITH SIDE BEAMS 229
10.1. Introduction 229
10.2. Floor and Beam Geometry 230
10.3. Subassemblies with Side Beams 5.1m Apart and No Infill Slab 231
10.3.1. Comparisons among the subassemblies with side beams 233
10.3.2. Comparisons between the subassemblies with and without side beams 237
10.3.3. Summary 240
10.4. Subassemblies with Side Beams 10m Apart and Different Side Connections 241
10.4.1. Subassemblies with the no-infill side connection and various end connections 241
10.4.2. Subassemblies with the infill side connection and various end connections 244
10.4.3. Comparison of subassemblies with and without in-situ infill at the side 246
10.4.4. Summary 248
10.5. Effect of Aspect Ratio of the Floor 249
10.5.1. Change of the impact from the side supports with the span length 250
10.5.2. Change of fire resistance with the floor aspect ratio 252
10.6. Summary 255
10.6.1. Side connections 255
10.6.2. Membrane action in hollowcore concrete flooring systems 255

10.6.3. Future research *256*

11. FIRE PERFORMANCE OF HOLLOWCORE FLOORING SYSTEMS IN PARAMETRIC FIRES 257

11.1. Introduction 257

11.2. Model Description 257

11.3. Studied Parametric Fires 258

11.4. Equivalent Fire Severity 260

11.4.1.Equivalent fire severity in Eurocode formula *260*

11.4.2.Equivalent fire severity in maximum temperature concept *261*

11.5. Fire Performance of the Subassemblies in Parametric Fires 262

11.5.1.Subassembly with Matthews's end connection *262*

11.5.2.Subassembly with Lindsay's end connection *264*

11.5.3.Discussion *265*

11.6. Summaries and Conclusions 268

12. CONCLUSIONS AND RECOMMENDATIONS 269

12.1. Introduction 269

12.2. New Model to Simulate Buildings with Hollowcore Concrete Flooring Systems in Fire 269

12.2.1. Features of the new model *269*

12.2.2. Disadvantages of the new model *270*

12.3. Structural Fire Performance of Hollowcore Concrete Flooring Systems with Various End Supports 270

12.4. Structural Fire Performance of Hollowcore Concrete Flooring Systems Designed According to NZS3101 271

12.5. Membrane Action in Hollowcore Concrete Flooring Systems 272

12.6. Hollowcore Concrete Flooring Systems Exposed to Parametric Fires 272

12.7. Recommendations to Avoid Shear and Anchorage Failure 272

12.8. Recommendations for Future Research 273

13. REFERENCES 275

APPENDIX A SAFIR INPUT FILES A-1

A.1. Sample Thermal Analysis Input File for Beam Elements A-1

A.2. Sample Thermal Analysis Input File for Shell Elements A-8

A.3. Sample 3D Structural Analysis Input File A-10

APPENDIX B MATERIAL PROPERTIES B-1

B.1. Stress-Strain Relationship of Normal Weight Concrete in Fire under Compression B-1

APPENDIX C TEST INFORMATION C-1

C.1. DIFT [Andersen et al. 1999] C-1

C.1.1. Hollowcore units C-1

C.1.2. Experimental setup C-2

C.2. University of Ghent [FeBe Studiecommissie SSTC 1998] C-3

C.2.1. Hollowcore units C-3

C.2.2. Experimental set-up C-5

C.3. Danish Prefab Concrete Association (BEF) [BEF 2005] C-9

C.3.1. Hollowcore units C-9

C.3.2. Experimental Set-up C-10

APPENDIX D CALCULATION OF MAXIMUM UDL ON THE 100mm THICK SLAB D-1

D.1. Calculation – Supported at the short side D-1

D.2. Calculation – Supported at the long side D-2

List of Figures

Figure 2-1 ISO 834 standard temperature-time curve 6
Figure 2-2 Design methods for standard fire [Hietanen 2005] 8
Figure 2-3 Definition of restraint by ASTM E119 for precast systems [Gustaferro et al., 1989] 9
Figure 2-4 Standard fire temperature curves 10
Figure 2-5 Schematic drawing of a continuous slab; the bending moment diagram at cold condition and after 3 hours of the ASTM E119 standard fire [Gustaferro et al. 1989] 12
Figure 3-1 Thermal conductivity of different structural concretes [Schneider 1982] . 18
Figure 3-2 Thermal conductivity of concrete according to EC2 [EC2 1995, EC2 2002] 19
Figure 3-3 Thermal diffusivity of concrete [Schneider 1982] 20
Figure 3-4 Change of specific heat with temperature of cement paste [Harmathy 1970] 21
Figure 3-5 Specific heat of different concretes [Schneider, 1985] 22
Figure 3-6 Specific heat of siliceous concrete according to EC2 [1995, 2002] 23
Figure 3-7 Thermal expansion of different type of concrete [Schneider 1982] 24
Figure 3-8 Temperature at the centre of the specimen versus heating time for Anderberg's tests [Thelandresson 1987] 25
Figure 3-9 Measured total deformation of the heated concrete specimens (applied compressive loading = 0.45 fc20) 26
Figure 3-10 Thermal elongation of siliceous aggregate concrete according to Eurocode 2 [1995, 2002] 26
Figure 3-11 Thermal conductivity of steel according to Eurocode 3 [EC3 2002] 30
Figure 3-12 Specific heat of steel according to Eurocode 3 [EC3 2002] 31
Figure 3-13 Thermal elongation of different steel from experiments and according to Eurocode 3 [FIP 1978, EC3 2002] 32
Figure 3-14 Stress-strain relationship of concrete under different temperatures in uniaxial tests [Schneider 1988] 33
Figure 3-15 Variation of concrete compressive strength for different aggregates [Schneider 1985] 34
Figure 3-16 Strength ratio of calcareous aggregate concrete under various conditions [Bažant 1996] 35
Figure 3-17 Reduction coefficient from Eurocode 2 for decrease of characteristic strength of concrete with siliceous aggregate 36
Figure 3-18 Biaxial ultimate strength envelope [Ehm et al. 1985] 37

Figure 3-19 Concrete stress-strain relationships at high temperatures with biaxial stress ratios of zero [Ehm et al. 1985]....38
Figure 3-20 Concrete stress-strain relationships at high temperatures with biaxial stress ratios at unity [Ehm et al. 1985]....38
Figure 3-21 Example of stres-strain relationship of concrete in direction tension test [Terrin 1980]....39
Figure 3-22 Various measurements of the splitting tensile strength of concrete at elevated temperature [Fellinger 2004]....40
Figure 3-23 Modulus of elasticity according from Schneider [1988]....41
Figure 3-24 Modulus of elasticity from Cruz [1966]....42
Figure 3-25 Regression of Poisson's ratio of Portland cement/quartzite aggregate concrete with temperature [Maréchal 1972]....42
Figure 3-26 Typical plot of compressive stress against axial, lateral and volumetric strain [Chen 1982, fig 2-1]....44
Figure 3-27 Stress-strain relations for different temperatures [Anderberg et al. 1976, fig 20]....44
Figure 3-28 Compressive strains at failure of concrete specimens subjected to different load levels during heating [Schneider 1976]....45
Figure 3-29 Model for compression stress-strain relationships for siliceous and calcareous concrete at elevated temperatures [EC2 2002] 46
Figure 3-30 Graphical representation of the calculation of thermal stresses in a simply supported slab [Fellinger 2004] 46
Figure 3-31 The principle of strain hardening for creep [Anderberg et al. 1976] 47
Figure 3-32 Component of total strain [Anderberg et al. 1976] 48
Figure 3-33 Stress-strain curves for steel illustrating yield strength and proof strength [Buchanan, 2001]....49
Figure 3-34 Ultimate and yield strength of cold-worked steel [Harmathy 1993]....50
Figure 3-35 Strength reduction factor for reinforcing steel [EC2 2002] 50
Figure 3-36 Strength reduction factor for cold formed prestressing steel [EC2 2002]51
Figure 3-37 Variation of modulus of elasticity of steel with temperature (1) Structural steel (2) Prestressing steel (3) Reinforcing steel [Harmathy 1993] 51
Figure 3-38 Variation of E-modulus with temperature for cold worked reinforcing steel and prestressing steel according to EC2 [EC2 2002] 52
Figure 3-39 Typical stress-strain curves for prestressing steel at elevated temperature [Harmathy 1993]....53
Figure 3-40 Stress strain relationships of steel at elevated temperatures [EC2 1995].53
Figure 3-41 Creep of steel tested in tension [Kirby et al. 1988]....54

Figure 4-1 Linear elastic stress distribution over the height of the cross section due to prestressing and bending moments and non-linear stress distribution in the crack close to flexural failure [Fellinger 2004].....56
Figure 4-2 Development of flexural cracks and shear cracks and axial stress in bottom fibre of the concrete cross section and in the steel strands [Fellinger 2004] 57
Figure 4-3 Analytical comb-teeth model from Kani [1964] 58
Figure 4-4 Schematic bending stress distribution (including prestress) and shear stress distribution over the depth of a hollowcore concrete slab [Fellinger 2004] 59
Figure 4-5 Location of critical point in arch analogy [Fellinger 2004] 60
Figure 4-6 Location of the compressive thrust [Fellinger 2004] 61
Figure 4-7 Experiment set-up in the 1998 DIFT tests 63
Figure 4-8 Cross sections of the tested elements in 1998 by SSTC 64
Figure 4-9 Detailing of Test 1 in 1998 SSTC tests [Detroppe et al. 2002].....65
Figure 4-10 Peripheral tie beams for diaphragm action [FeBe Studiecommissie SSTC 1998, Fig 1.10].....66
Figure 4-11 T-shaped ending of the transverse tie beams.....66
Figure 4-12 Comparison of furnace temperatures from 2003 BRE tests to ISO fire curve.....68
Figure 4-13 Layout of the DIFT test carried out in 2004 [BEF 2004] 70
Figure 4-14 Cross section of the HC unit used in BEF 2005 and 2004 tests [BEF 2004] 70
Figure 4-15 Layout of the BEF test carried out in 2005 [BEF 2005].....72
Figure 4-16 Test set-up from Delft of the double ribs sawn from hollowcore slabs [Fellinger 2004] 73
Figure 4-17 Cross section of the test specimens used for the tests by Fellinger [2004] 73
Figure 4-18 Different thrust line position [Carlson et al. 1965] 81
Figure 5-1 Convergence iterations for the SAFIR structural analysis [Franssen et al. 2002b] 85
Figure 5-2 In Beam element (a) local axis (b) degrees of freedom at nodes (c) cross section [Franssen et al. 2002b].....87
Figure 5-3 Geometry of the shell element [Franssen et al. 2002b].....89
Figure 5-4 Rankine criterion for tension and Von Mises for compression [Doneux et al. 2003] 91
Figure 6-1 Discretisation used for thermal analysis of a hollowcore unit [Micelli 2000b] 96

Figure 6-2 Discretisation of the HC unit used in by Detroppe et al. [2004].....97
Figure 6-3 Overview of the modelling approach by Fellinger [2004].....98
Figure 6-4 Sample box of shell elements.....101
Figure 6-5 Integration points in the shell elements.....102
Figure 6-6 Disintegration of the cross section of hollowcore unit.....104
Figure 6-7 Model scheme of hollowcore units 104
Figure 6-8 Grillage idealisation of a slab (a) original slab (b) corresponding grillage mesh (c) segment of grillage mesh [O'Brien et al, 1999].....105
Figure 6-9 Grillage used for SAFIR simulation of the DIFT 1999 test.....108
Figure 6-10 Results for simulation of DIFT 1999 test with SP18 hollowcore section 109
Figure 6-11 Comparison between simulation results of grillage models with sharing rotations in each intersections or not for DIFT 1999 test with SP18 hollowcore.....110
Figure 6-12 Comparison scheme between shell and grillage models.....112
Figure 6-13 Comparison of vertical displacement at the centre of the slab in (a) Scenario A (b) Scenario B (c) Scenario C (d) Scenario D 113
Figure 7-1 Layout of grillage model in Stage One comparison.....120
Figure 7-2 Comparison of vertical displacement at the centre of the slab in (a) Scenario A (b) Scenario B (c) Scenario C (d) Scenario D 122
Figure 7-3 Comparison of horizontal displacement along the length at the corner in (a) Scenario A (b) Scenario B (c) Scenario C (d) Scenario D 123
Figure 7-4 Comparison of horizontal displacement along the width at the corner in (a) Scenario A (b) Scenario B (c) Scenario C (d) Scenario D 123
Figure 7-5 Axial forces at the centre of the slab in (a) Scenario A (b) Scenario B (c) Scenario C (d) Scenario D 125
Figure 7-6 Stage Two comparison scheme 127
Figure 7-7 Midspan vertical displacement at the centre of the slab in (a) Scenario A (b) Scenario B.....128
Figure 7-8 Membrane stress distribution right before failure time in (a) Scenario A (b) Scenario B.....129
Figure 7-9 Horizontal displacement at the centre of the roller end in (a) Scenario A (b) Scenario B.....129
Figure 7-10 Stage 2 comparison scheme 131
Figure 7-11 Results of Midspan vertical displacement from (a) Scenario A (b) Scenario B.....132
Figure 7-12 Results of Midspan lateral displacement at the side from (a) Scenario A (b) Scenario B.....133

Figure 7-13 Comparison of membrane/axial force distribution from the (a) shell model (b) beam model in Scenario B after 60min. of ISO fire exposure 133
Figure 7-14 Results of Midspan displacement in Scenario C: (a) vertical displacement; (b) side horizontal displacement with negative means inward 134
Figure 7-15 Membrane force distribution at 34min. and Membrane force trends in shell element models from Scenario A & C 135
Figure 7-16 Results of Midspan displacement in Scenario D: (a) vertical displacement; (b) side horizontal displacement 136
Figure 7-17 Comparison of results when sharing the rotations at the intersections in the four scenarios 137
Figure 7-18 Grillage model for tests in DIFT 1999 139
Figure 7-19 (a) Discretisation of the web of SP18 for the longitudinal beams (b) Discretisation of the transverse beams 139
Figure 7-20 Comparison of midspan vertical displacements at the centre of the slabs with (a) SP18 (b) SP22 (c) SP27 units 140
Figure 7-21 Comparison of midspan lateral displacements at the side of the slabs with (a) SP18 (b) SP22 (c) SP27 units 141
Figure 7-22 Comparison of horizontal displacements at the end of the slabs with (a) SP18 (b) SP22 (c) SP27 units 142
Figure 7-23 Illustration of the simulation model for the Test 1 from University of Ghent 143
Figure 7-24 Divided hollowcore sections for the Test 4 model 144
Figure 7-25 Comparison of vertical displacements of the model with and without transverse beams 144
Figure 7-26 Sensitivity study on prestressing levels 145
Figure 7-27 Comparison of vertical displacements between cases with different rebar strengths 146
Figure 7-28 Simulation results with different end conditions for slabs from (a) Test 1 (b) Test 4 147
Figure 7-29 Illustration of the model used for BEF tests 148
Figure 7-30 Comparison between the vertical displacements at midspan (ctre) or at the location of the point load (qtre) from simulation (sim) and BEF test (test) results with different level of loading 149
Figure 7-31 Cross section of a DYCORE 300 unit [Firth Stresscrete et al. 2007] 151
Figure 7-32 Illustrations of the models used in Stage Five 152
Figure 7-33 Comparison of midspan vertical displacements between the models with the topping simulated as part of the grillage or not of the slab with pin-pin support conditions 152

Figure 7-34 Comparison of midspan vertical displacements between the models with the topping simulated as part of the grillage or not of the slab with fix-fix support conditions 153
Figure 7-35 Comparison of midspan vertical displacements between the models with the topping simulated as part of the grillage or not of the slab with pin-roller support conditions 154
Figure 7-36 Comparison of roller end horizontal displacements between the models with the topping simulated as part of the grillage or not of the slab with pin-roller support conditions 154
Figure 7-37 Comparison of midspan vertical displacements between the models with the topping simulated as part of the grillage or not of the slab with fix-slide support conditions 155
Figure 7-38 Comparison of roller end horizontal displacements between the models with the topping simulated as part of the grillage or not of the slab with fix-slide support conditions 155
Figure 8-1 Model layout for the basic connection type studies 160
Figure 8-2 Comparison of midspan vertical displacement from the crude model to that from (a) fine model (b) no-shell model with pin-pin connections 161
Figure 8-3 Comparison of midspan vertical displacement from the crude model to that from (a) fine model (b) no-shell model with pin-roller connections 161
Figure 8-4 Comparison of horizontal displacement at the roller end from the crude model to that from the fine model and the no-shell model with pin-roller connections 161
Figure 8-5 Comparison of midspan vertical displacement from the crude and fine models with fix-fix connections 162
Figure 8-6 Comparison of midspan vertical displacement from the crude model to that from the fine model with fix-slide connections 163
Figure 8-7 Comparison of horizontal displacement at the roller end from the crude model to that from the fine model with fix-slide connections (+: outward) 163
Figure 8-8 Layout of the hollowcore slab without end beams 164
Figure 8-9 Pin-pin supported slab without end beams 165
Figure 8-10 Midspan vertical displacements in hollowcore slab with pin-pin supports 165
Figure 8-11 Deformation in the profile of the floor with pin-pin supports at 2 hour 165
Figure 8-12 Membrane force distribution in the topping slab with pin-pin supports at 4 hr. 166

Figure 8-13 Strand stress at the centre of Units 1 & 2 in the slab with pin-pin supports 166
Figure 8-14 Pin-roller supported slab without end beams 167
Figure 8-15 Midspan vertical displacements in hollowcore slab with pin-roller supports 168
Figure 8-16 Roller end horizontal displacements in hollowcore slab with pin-roller supports 168
Figure 8-17 Membrane force distribution in the topping slab with pin-roller supports at 63 minutes 168
Figure 8-18 Fix-fix supported slab without end beams 169
Figure 8-19 Membrane force distribution in the topping slab with fix-fix supports at 106 minutes 170
Figure 8-20 Midspan vertical displacements in hollowcore slab with fix-fix supports 170
Figure 8-21 Axial force diagram within all the beam elements at 106 minutes 171
Figure 8-22 Strand stress at the centre of Unit 2 at the midspan of the slab with fix-fix supports 171
Figure 8-23 Strand stress at the centre of Unit 2 near the supports of the slab with fix-fix supports 172
Figure 8-24 Stress distribution in the cross section near the end supports at the central web of Unit 2 near the supports at different times 173
Figure 8-25 Fix-slide supported slab without end beams 174
Figure 8-26 Midspan vertical displacements in hollowcore slab with fix-slide supports 174
Figure 8-27 Slide end horizontal displacements in the slab with fix-slide supports . 175
Figure 8 28 Axial force diagram within all the beam elements at 92 minutes..... 175
Figure 8-29 Axial force history in different beams in the slab with fix-slide supports 176
Figure 8-30 Stress of the strands in Unit 2 in the slab with fix-slide supports 177
Figure 8-31 Stress distribution in the concrete along the sides of Unit 2 near the supports with different lengths of ISO fire exposure 178
Figure 8-32 Vertical displacements of the slabs with and without core-filling with (a) pin-pin (b) pin-roller (c) fix-fix (d) fix-slide supports 182
Figure 8-33 Strand stress at the centre of Unit 2 near the supports from the fix-fix supported slab with and without core-filling 183
Figure 8-34 Strand stress in Unit 2 at the midspan of the slab with fix-side supports with and without core-filling 184

Figure 8-35 Stress distribution in the flange near the side of Unit 2 in the fix-slide supported slab at the midspan at (a) 15min. (b) 30min. (c) 45 min. 184
Figure 8-36 Membrane force in the topping concrete between Units 1 and 2 and Units 2 and 3 in the fix-slide supported slab 185
Figure 8-37 Layout of the hollowcore slab with end beams 187
Figure 8-38 Discretised end beam in SAFIR 187
Figure 8-39 Pin-pin supported slab with end beams 188
Figure 8-40 Midspan vertical displacement of the pin-pin supported slabs with and without end beams 188
Figure 8-41 Pin-roller supported slab with end beams 189
Figure 8-42 Midspan vertical displacement of the pin-roller supported slabs with and without end beams 190
Figure 8-43 Horizontal displacements at the roller end from the pin-roller supported slabs with and without end beams 190
Figure 8-44 Stress distributions along the height of the central web of Unit 2 at the midspan of the pin-roller supported slabs with and without end beams at different times 191
Figure 8-45 Fix-fix supported slab with end beams 191
Figure 8-46 Midspan vertical displacements of the fix-fix supported slabs with and without end beams 192
Figure 8-47 Membrane stress distribution at the topping of the fix-fix supported slabs with end beams at 106 minutes 193
Figure 8-48 Stress distributions in the cross section near the end supports at the central web of Unit 2 at different times from the fix-fix supported slab with and without end beams 194
Figure 8-49 Fix-slide supported slab with end beams 194
Figure 8-50 Midspan vertical displacements of the fix-slide supported slabs with and without end beams 195
Figure 8-51 Horizontal displacements at the roller end from the fix-slide supported slab with and without end beams 196
Figure 8-52 Rotation about the width of the slab at the centre of Unit 2 at the end of the fix-slide supported slab with end beams 196
Figure 8-53 Fire exposure time versus the height of the HC slabs [Fellinger 2004] 200
Figure 9-1 Dimensions and layout of the subassembly from Matthews [2004] 203
Figure 9-2 (a) End connection details (b) lateral beam-to-hollowcore connection from Matthews [2004] 203
Figure 9-3 Floor plan of the specimen in the research by Lindsay [2004] 204

Figure 9-4 (a) End connection details (b) lateral beam-to-hollowcore connection from Lindsay [2004] 204
Figure 9-5 (a) End connection (b) lateral beam-to-hollowcore connection from MacPherson [2005] 205
Figure 9-6 Modelling Matthews' end connection details (a) original detail (b) node-line of the model in SAFIR and force paths in the connection (c) Simulation scheme in SAFIR (d) deformed shape of the connection 206
Figure 9-7 Modelling Lindsay's end connection details (a) original detail (b) node-line of the model in SAFIR and force paths in the connection (c) Simulation scheme in SAFIR (d) deformed shape of the connection 208
Figure 9-8 Sharing of rotation in vertical axis and displacement along span length at the corners 209
Figure 9-9 Locations of the recorded displacements and stresses of the fix-fix supported slab 212
Figure 9-10 Midspan vertical displacements from fix-fix supported slabs with various end connections 212
Figure 9-11 Strand stress histories of fix-fix supported slabs with various end connection details 213
Figure 9-12 Membrane stress distributions in the topping of the fix-fix supported slabs with various end connections after 50 minutes of ISO fire exposure 214
Figure 9-13 Locations of the recorded displacements and stresses of the fix-slide supported slab 215
Figure 9-14 Midspan vertical displacements from fix-slide supported slabs with various end connections 215
Figure 9-15 Strand stress histories of fix-slide supported slabs with various end connection details 216
Figure 9-16 Membrane stress distributions in the topping of the fix-slide supported slabs with various end connections after 48 minutes 216
Figure 9-17 Method to simulate Lindsay's connection (a) original method (b) including restraints at the base of the face of the HC units 219
Figure 9-18 Relative movement at the bottom of the hollowcore unit and the end beam in Case C 219
Figure 9-19 Bending moments along the span length at the centre of the end beam from the case with and without restraints on the movement at the bottom of the face of the hollowcore units 221
Figure 9-20 Cross section of the column [Matthews 2004] 222
Figure 9-21 Sample subassembly model 222

Figure 9-22 Midspan vertical displacements from the subassemblies with various end connections 224
Figure 9-23 Strand stress histories of the subassemblies with various end connections 225
Figure 9-24 Membrane stress distributions in the topping of the subassemblies after 50 minutes of ISO fire exposure 225
Figure 10-1 Simulation model for a 10 by 12.2m subassembly with infill slab at the side and MacPherson's end connection 231
Figure 10-2 Sample floor slab 232
Figure 10-3 Layout of the subassemblies (a) without side beams as analysed in Chapter 9 (b) with side beams as analysed in this chapter 233
Figure 10-4 Midspan vertical displacement at the centre of the slab with side beams and different end connections 234
Figure 10-5 Axial force distribution within the subassembly with Matthews' end connection and side beams after 2 hours of ISO fire exposure 235
Figure 10-6 Axial force within the web at the corner of the slabs with side beams and different end connections 235
Figure 10-7 Strand stress history at the centre of the web in the centre unit of the slabs with side beams and different end connections 236
Figure 10-8 Membrane force within the topping at the corner of the slabs with side beams and different end connections 237
Figure 10-9 Comparison of midspan vertical displacements of the subassemblies with and without side beams and with (a) rigid end connection (b) Matthews' (c) Lindsay's (d) MacPherson's end connection 238
Figure 10-10 Location of the axial forces shown in Figure 10-10 239
Figure 10-11 Axial force within the web at different location in the subassemblies with and without side beams with (a) rigid (b) Matthews' (c) Lindsay's (d) and MacPherson's end connection 240
Figure 10-12 Simulation models used to study the effect of lateral connections (a) no-infill side connection (b) infill side connection 241
Figure 10-13 Location of the extracted data for Figures 10-14 and 10-15 242
Figure 10-14 Maximum midspan vertical displacement of the 10.1m wide 12.2m long slab in the subassemblies with the no-infill side connection and different end connections 243
Figure 10-15 Axial force within the web at the corner of the 10.1m wide 12.2m long slab in the subassemblies with the no-infill side connection and different end connections 243
Figure 10-16 Location of the extracted data for Figures 10-17 and 10-18 245

Figure 10-17 Maximum midspan vertical displacement of the slab with the infill side connection and different end connections....245
Figure 10-18 Maximum compressive axial force within the web in the subassemblies with the infill side connection and different end connections 246
Figure 10-19 Location of the observed displacements 247
Figure 10-20 Comparison of midspan vertical displacements of the subassemblies with and without in-situ infill at the side and with (a) rigid end connection (b) Matthews' (c) Lindsay's (d) MacPherson's end connection 248
Figure 10-21 Simulated model for investigating the effect of floor aspect ratio....249
Figure 10-22 Typical floor aspect ratios investigated....250
Figure 10-23 Maximum displacement at the midspan of the slab with span length of (a) 9.2m (b) 12.2m (c) 15.2m (d) 18.2m 252
Figure 10-24 Maximum midspan vertical displacement of the slab with different span length (a) 6.2m (b) 9.2m (c) 12.2m (d) 15.2m (e) 18.2m. 254
Figure 11-1 Simulated model for investigating the fire performance in parametric fires 257
Figure 11-2 Studied parametric fires....259
Figure 11-3 Equivalent fire severity using maximum temperature concept....261
Figure 11-4 Vertical displacements at the centre of the slab with Matthews' end connection exposed to the ISO fire and parametric fires....262
Figure 11-5 Axial force in the of the centre unit of the slab with Matthews' end connection....263
Figure 11-6 Location of the observed axial force....264
Figure 11 7 Vertical displacements at the centre of the slab with Lindsay's end connection exposed to the ISO fire and parametric fires....265
Figure 11 8 Axial force at the central web of the centre unit of the slab with Lindsay's end connection....265
Figure A-1 Mesh of the web in 300DYCORE....A-1
Figure A-2 Cross section of the shell element used for the 75mm topping....A-8
Figure A-3 Layout of the structural analysis for the subassembly from MacPherson [2005]....A-10
Figure C-1 Types of hollowcore concrete used in the 1998 DIFT tests....C-1
Figure C-2 Experiment set-up in the 1998 DIFT tests [Andersen 1999]....C-2
Figure C-3 Cross section of SP200 [FeBe Studiecommissie SSTC 1998]....C-4
Figure C-4 Cross section of VS20/60 [FeBe Studiecommissie SSTC 1998] C-5
Figure C-5 Cross section of SP265 [FeBe Studiecommissie SSTC 1998]....C-6
Figure C-6 Layout of Test 1 carried out at University of Ghant in 1998 [FeBe Studiecommissie SSTC 1998] C-7

Figure C-7 Layout of Test 2 carried out at University of Ghant in 1998 [FeBe Studiecommissie SSTC 1998] C-8
Figure C-8 Layout of Test 3 carried out at University of Ghant in 1999 [FeBe Studiecommissie SSTC 1998] C-9
Figure C-9 Layout of Test 4 carried out at University of Ghant in 1999 [FeBe Studiecommissie SSTC 1998] C-10
Figure C-10 Cross section of the hollowcore unit used in the BEF 2005 tests [BEF 2005] C-11
Figure C-11 Test layout in the BEF 2005 tests [modified from BEF 2005] C-12
Figure C-12 Loading Arrangement on the load plate in the BEF 2005 tests [modified from BEF 2005] C-13

List of Tables

Table 4-1 Studied parameters in 1998 tests in University of Ghent 67
Table 6-1 Parameters used for SP18 in DIFT 1999 test [test no. X52650d, Andersen et al. 1999] 107
Table 6-2 Properties of the reinforcing steel at ambient conditions [Lim 2003] 111
Table 6-3 Key parameters used in the shell element model by Lim [2003] 111
Table 6-4 Key parameters of scenarios in comparison between shell and grillage models 112
Table 7-1 Key parameters of scenarios in Stage One validation 121
Table 7-2 Summary of key parameters of scenarios in comparison stage 1 126
Table 7-3 Summary of key parameters of scenarios in comparison stage 2 132
Table 8-1 Summary of the simulation results of the slabs without end beams 179
Table 8-2 Summary of the simulation results of the slabs without end beams and without core-filling 181
Table 8-3 Summary of the simulation results of the slabs with end beams 187
Table 8-4 Stopping time of the simulation of the slabs with and without end beams 197
Table 8-5 Stopping time of the simulation of the slabs with and without core-filling 198
Table 8-6 Stopping time of the simulation of the slabs with various support conditions 199
Table 9-1 Summary of the simulation results of the slabs with Matthews's end connection 210
Table 9-2 Summary of the simulation results of the slabs with Lindsay's end connection 210
Table 9-3 Summary of the simulation results of the slabs with MacPherson's end connection 211
Table 9-4 Summary of the simulation results of the slabs with rigid end connection 211
Table 9-5 Summary of the predicted fire resistance of the slab with various end connections 218
Table 9-6 Summary of the simulation results of the subassemblies with various end connections 223
Table 9-7 Summary of the predicted fire resistance of the subassemblies with various end connections 226
Table 9-8 Interpretation of the results from the predicted fire resistance of the slab with various end connections 227
Table 10-1 Summary of the simulation results of the subassemblies with various end connections and no side beams 232

Table 10-2 Summary of the simulation results of the subassemblies with various end connections and side beams 233
Table 10-3 Summary of the simulation results of the subassemblies with side beam at 10m spacing various end connections and no-infill side connection 242
Table 10-4 Summary of the simulation results of the subassemblies with various end connections and side beams with in-situ infill 244
Table 10-5 Comparison of midspan displacement with different side supports of the subassembly with Matthews's end connection after 120 minutes of ISO fire exposure 247
Table 10-6 Summary of the simulation results of 10.2m wide subassembly with various side supports and span length 251
Table 10-7 Summary of the simulation results of subassemblies with different floor aspect ratios 253
Table 11-1 Window sizes and burning periods for fuel load of 1000MJ/m2 260
Table 11-2 Equivalent fire severities obtained using different methods 266
Table 11-3 Available design methods for hollowcore concrete flooring systems 267
Table B-1 Values for the main parameters of the stress-strain relationships of normal weight concrete with siliceous or calcareous aggregates concrete at elevated temperatures [EC2 2002] B-1
Table C-1 Material properties of the strands in the 1998 DIFT tests [Andersen et al. 1999] C-2
Table C-2 Magnitude and locations of the load in the 1998 DIFT tests [Andersen 1999] C-3
Table C-3 Loading arrangements in the BEF 2005 tests C-13
Table D-1 Properties of the reinforcing steel at ambient conditions [Lim 2003] D-1

1. Introduction

1.1. Background

Multi-storey buildings with precast concrete floor systems are very common in New Zealand and in many other countries due to low onsite labour cost and high quality control. Among different precast flooring systems, prestressed hollowcore concrete slabs are the most popular because of their light weight and the economical use of concrete.

Hollowcore concrete slabs are precast and pre-tensioned concrete slabs. Each unit is 1.2m wide, the depths of available unit in New Zealand are 200, 300 or 400mm, and the span length can be up to 20m for 400mm deep units. The units span one-way, and the current practice in New Zealand requires a layer of cast in-situ topping concrete which increases the shear strength and connects the hollowcore concrete units together laterally. The topping concrete can give the completed floor some two-way spanning capability.

It is necessary to know the fire resistance of the floor slabs in multi-storey building design. If the provided fire resistance of the floor slabs is less than the worst foreseeable fire severity, the consequence can be catastrophic once the fire happens. While the trend in the world of fire engineering is shifting towards performance-based design, the current practice in determining the fire resistance of hollowcore concrete system is still using tabulated data from the concrete standards, which in many countries are based upon equivalent slab thickness and not actual experimental results. It is quick and easy for designers to use tabulated data for the fire design of hollowcore concrete slabs. Because tabulated data is not performance based, by using it the designers choose to ignore the structural behaviour of hollowcore flooring systems under fire.

The structural behaviour of a hollowcore flooring system under fire is complicated, and conducting fire experiments with large hollowcore floor slab subassemblies is almost impossible. Precise computer models for simulating the structural behaviour of hollowcore slabs under fires have been developed to improve the understanding of this behaviour [Fellinger 2004], however, such analyses are too time-consuming to apply in the day-to-day design process. At the other end of the spectrum, simplistic

approaches using simple code rules are insufficient to capture the thermal expansion across the units, the effects of the support conditions, or two-way behaviour. Therefore, it is necessary to develop a simple yet sufficiently accurate method for designers to model the structural fire behaviour of hollowcore slabs.

New details for connection of hollowcore floor units to reinforced concrete supporting beams were introduced in the New Zealand Concrete Standard NZS3101:2006 [SNZ 2006a] to improve seismic performance. The new details are based on the outcomes of several tests conducted in the University of Canterbury regarding the seismic performance of hollowcore flooring systems. These new connection details enhance the seismic performance, but there are doubts about their influence on the fire performance of the floor slabs.

Previous study carried out by Lim [2003] showed that the fire resistance of a two-way supported solid concrete slab is increased through tensile membrane action. Even though the hollowcore concrete slab units span one-way only, the topping concrete is supported in a two-way manner, so this research explores the possibility of establishing tensile membrane action in hollowcore concrete flooring system for various the length to width aspect ratios.

1.2. Objectives

There are four objectives in this research:

1. To develop a simple and accurate computer model to predict the behaviour of structures with hollowcore concrete flooring systems exposed to fire.

2. To investigate the structural performance of buildings with hollowcore concrete flooring systems exposed to fire, designed according to the past and current New Zealand Concrete Standard NZS3101.

3. To determine whether tensile membrane action will enhance the fire resistance of hollowcore concrete flooring systems.

4. To recommend qualitative fire design guidelines for hollowcore flooring systems.

1.3. Scope of Research

The scope of this research covers:

1.3.1. Development of a model to simulate buildings with hollowcore concrete flooring systems in fire

This part of the research aims to use commercially available software to develop a model to simulate the structural behaviour of subassemblies with hollowcore concrete flooring systems under fire. The software used in this study is the finite element analysis program SAFIR. The focus is on the global behaviour of the subassemblies rather than the structural behaviour of hollowcore concrete slabs at the micro scale. The developed model is then compared with several experimental results for validation. SAFIR is able to determine the fire resistance of the hollowcore concrete flooring systems based on the induced thermal stress and weakened mechanical material properties in fire that could cause flexural failure, but ignores the possibility of shear and anchorage failure. Fellinger [2004] stated that shear and anchorage failure can have more significant influence upon the fire resistance of hollowcore slabs than flexural failure, and because this type of failure is very brittle compared to flexural failure, it can occur very abruptly. Nevertheless, shear and anchorage failure of hollowcore slab has never been observed in practice. Computer simulation of shear and anchorage failure is not included in the scope of this research.

1.3.2. Investigate the performance in fire of buildings with hollowcore concrete flooring designed according to NZS3101

The frame-floor subassemblies subjected to seismic testing by Matthews [2004], Lindsay [2004] and MacPherson [2005] are simulated for fire exposure using the newly developed modelling method. These three subassemblies consists of the end and side connection details of hollowcore concrete flooring system recommended by the previous and current version of New Zealand Concrete Standard NZS 3101 [SNZ 1995, 2006]. The floors are loaded uniformly and exposed to the ISO834 standard fire from below.

1.3.3. Assessing tensile membrane action in hollowcore concrete flooring systems

Using the newly developed modelling method running under SAFIR, the above

subassemblies are simulated with different aspect ratios to compare the structural performance when being heated by the ISO fire from below.

This study is conducted using computational analysis only, and no experimental testing was carried out in the course of this research.

1.4. Outline of Thesis

Chapter 1 of this thesis gives an overview of the research and the objectives and scope of this project. Chapter 2 reviews the design criteria and recommendations of buildings with hollowcore concrete flooring systems in terms of fire. Chapter 3 outlines the material properties of concrete and steel under elevated temperature with some explanations. Chapter 4 provides a review of the structural behaviour of hollowcore concrete slabs in ambient conditions as well as the observed behaviour under fire from obtained fire test results. Chapter 5 describes the SAFIR program and its capacities.

Chapter 6 describes the new model and its development, and Chapter 7 describes the validation process of the new model.

Chapter 8 investigates the effect of the support conditions, and Chapter 9 studies the influence of end connections recommended by the current and previous New Zealand Concrete Standards. Chapter 10 explores the influence of different side connections used in the New Zealand Concrete Standard and determines the effect of the membrane action to the fire performance by changing the length to width aspect ratio of the floor. Chapter 11 studies the effect of realistic fire to the fire performance of the hollowcore concrete flooring system. And finally, Chapter 12 shows the conclusions and recommendations drawn from this research regarding preventing flexural failure of hollowcore concrete flooring system and from other researches regarding other types of failure modes such as shear and anchorage failure.

2. Review of Fire Design for Hollowcore Slabs

2.1. Introduction

This section describes the characteristics of hollowcore slabs, and the advantages and disadvantages of hollowcore flooring systems. This section also compares the requirements and recommendations to the fire design of concrete slabs from New Zealand, United States and Europe. These requirements form the framework of this research as this study focuses on providing a new method for the fire design of structures with hollowcore concrete flooring systems.

2.2. Description of Hollowcore Slabs

Hollowcore concrete slabs are precast, pre-tensioned concrete units. They are typically 1.2m wide with full length voids. The depths of the units vary according to demand. In New Zealand, the commonly produced depths are 200, 300 and 400mm deep.

Hollowcore flooring systems consist of adjacent hollowcore concrete slabs with or without a layer of in-situ reinforced concrete topping depending on the functional requirement and the design. All New Zealand applications use topping concrete because it helps to establish diaphragm behaviour and carry the lateral forces in earthquakes. Hollowcore flooring systems became increasingly popular in recent decades, and are common for large floor spans in commercial buildings. There are several advantages of using hollowcore concrete slabs. Precasting minimises the onsite labour cost and increases the speed of erection and controls the quality of the products; prestressing can fully utilise the strength of steel and use less steel. The voids in the slabs can save concrete and reduce the self-weight of the slabs. Compared to solid reinforced concrete slabs, hollowcore concrete slabs use 50% less steel and 30% less concrete [Fellinger 2004].

There are two different processes that can be used to create the voids within the hollowcore concrete units: extrusion or slip form; in New Zealand the extrusion process is used. In this process, “zero slump” concrete is pierced by an extrusion machine which creates the voids [Matthews 2004]. Due to the nature of this process, it is not possible to include reinforcement in the hollowcore concrete units. The

prestressing strands are placed in the casting bed and stressed before the concrete is cast. With pre-tensioned concrete, anchorages for the prestressing steel are not used and the prestressing force in the strands is transmitted to the concrete only by bond stresses [Fellinger 2004].

2.3. Requirements and Recommendations for Fire Design of Concrete Slabs

2.3.1. Requirements for fire design of concrete slabs

The New Zealand Building Code [BIA 1992] requires that, in terms of the structural stability and safeguard against fire spread, the structural members exposed to fire shall allow adequate time for people to evacuate safely and also allow fire service personnel to undertake rescue and fire fighting operations. This is achieved by providing structural members with a fire resistance rating in accordance with ISO834 [ISO834 1999] or AS/NZ 1530 Part 4 [Standards Australia 2005a]. Within the claimed duration of fire resistance under the ISO834 standard fire shown in Figure 2-1, the load capacity of the floor should be maintained, flames or hot gases should not penetrate the slabs, and the floor should prevent an average temperature rise of 140^{o}C or a local maximum of 180^{o}C on the unexposed face. These three requirements, in such order, are also known as the stability, integrity and insulation criteria for the structural members.

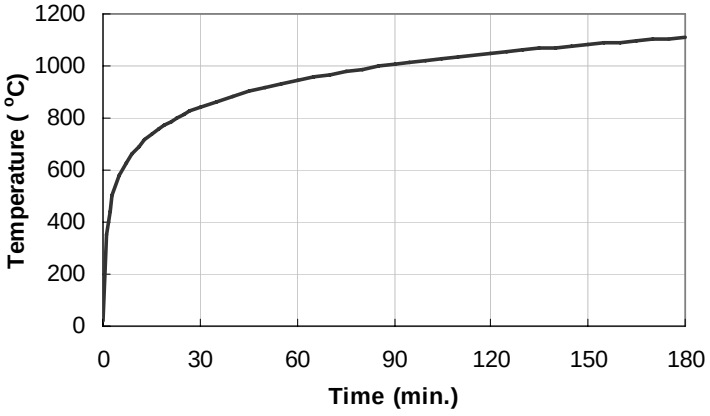

Figure 2-1 ISO 834 standard temperature-time curve

In Europe, The performance requirement of the structures in fire is defined in Eurocode 1 [EC1 2002], which is similar to the New Zealand Building Code and asks for an adequate level of load bearing ability, as well as integrity and insulation of the

structural members to allow the evacuation of the occupants and the rescue operation by the fire-fighters.

2.3.2. Recommendations from New Zealand Standards

The design requirements for fire resistance in the New Zealand Concrete Structures Standard NZS 3101 [SNZ 2006] are based upon the Australian Standard AS3600 [Standards Australia 2005b] and Eurocode 2 [EC2 2002]. NZS 3101 states that the structural member shall be designed to have the required fire resistance rating for stability, integrity and insulation as required by the New Zealand Building Code [BIA 1992], which has been explained previously.

Other than using engineering design, NZS 3101 also provides tabulated data for concrete slabs to fulfil these criteria:

Stability – the standard specifies a minimum concrete cover to the tendons to achieve a particular fire resistance rating. This is also affected by the rotational restraints at the supports. Hence the fire resistance of continuous slabs are considered separately, and the two-way supported slabs are considered separately from one-way supported slabs and have different fire resistance based on the aspect ratio.

Integrity – the standard states that a slab has a fire resistance rating for integrity if it meets the requirements for both insulation and stability for that rating.

Insulation – this criterion depends on the effective thickness of the slabs and the type of aggregate of the concrete. The effective thickness of hollowcore slabs is the net cross-sectional area divided by the width of the cross section.

2.3.3. Recommendations from Eurocodes

Eurocode 2 [EC2 2002] for the design of concrete structures re-states the idea of retaining stability, integrity and insulation of the structural members as stated in Eurocode 1, but with much more detail. In Eurocode 2 the criterion on insulation is quantified. The requirements to meet the three criteria are as those from Eurocode 2.

Eurocode 2 provides three alternative design methods for calculating the fire resistance:

Simplified calculation methods – Eurocode 2 suggests two simplified calculation methods for assessing the ultimate load-bearing capacity of heated concrete members: 500^{o}C isotherm method and zone method. The first method disregards the part of the cross section with concrete heated above 500^{o}C and full strength is used for the remaining cross-section. In the second method the cross section of the element is divided into zones, each with a different amount of strength.

Advanced calculation methods - Advanced calculation methods are based upon the fundamental physical behaviour aiming to provide a reliable approximation of the expected structural behaviour under fire. Both thermal and mechanical analysis should consider the temperature dependent properties of the materials. The result should be verified against relevant test results.

Tabulated data – The previously described tabulated data for the fire resistance rating of prestressed concrete slabs in NZS3101 are originally from Eurocode 2. This tabulated data gives standard fire resistance based on minimum slab thickness and cover to the reinforcement.

These design methods from Eurocode 2 are illustrated in Figure 2-2.

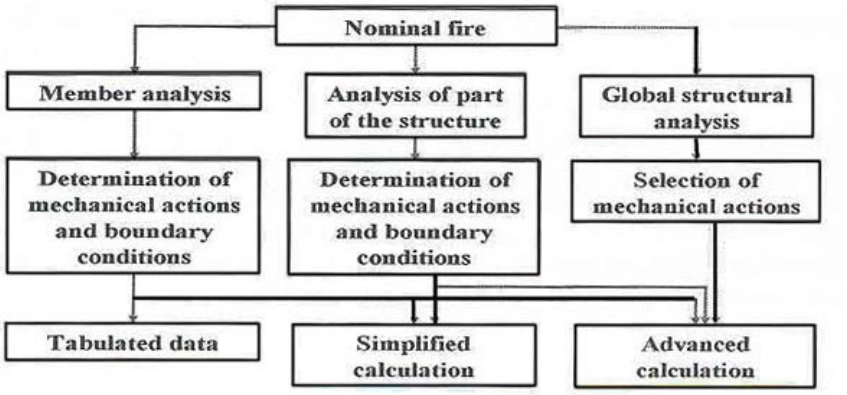

Figure 2-2 Design methods for standard fire [Hietanen 2005]

Eurocode 2 also provides details of the temperature dependent thermal and mechanical properties of concrete, reinforcing and prestressing steel. These properties will be explained in detail in Chapter 3.

2.3.4. Recommendations from ASTM E119

In the USA, ASTM E119 [ASTM 1999] specifies laboratory procedures and criteria for determining fire resistance ratings of different proprietary floor systems. Fire testing of concrete members or assemblies according to ASTM E119 is often decided on the following two criteria [Phan 2005]:

Heat transmission – This criterion limits the temperature rise of the unexposed surface. To meet this criterion, the walls, floors or roofs are required to have a sufficient thickness. This is equivalent to the insulation criteria in the previous sections.

Load carrying ability – This criterion limits the thermally reduced yield strength of steel reinforcement be at least 50% of the yield strength at ambient temperature. This is achieved by providing sufficient thickness of concrete cover.

ASTME119 also recognises the difference in the fire resistance of concrete floor slabs caused by the restraint conditions at the supports. For a precast flooring system to be qualified as restrained, ASTM119 states the requirement as:

> *"The space between the ends of precast units and the vertical faces of the supports, or between the ends of solid or hollow-core slab units does not exceed 0.25 percent of the length for normal weight concrete members or 0.1 percent of the length for structural lightweight concrete members."*

This definition is schematically illustrated in Figure 2-3.

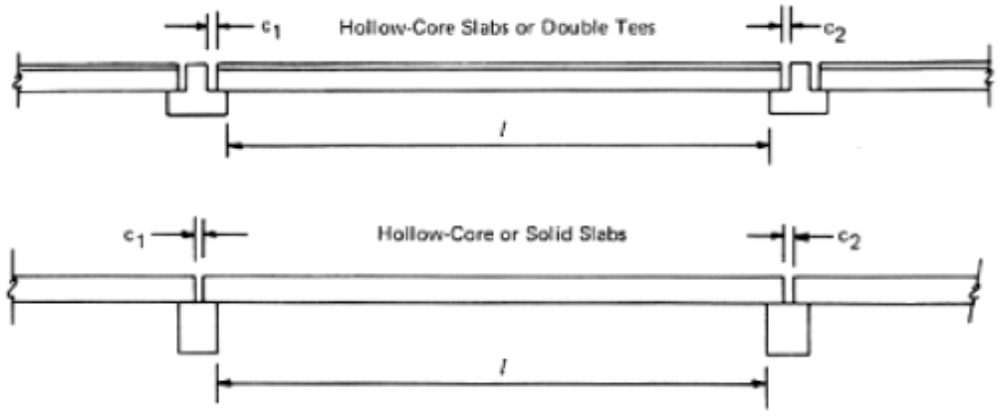

To be considered as restrained:

$c_1 + c_2 \leq 0.0025l$ for normal weight concrete

$c_1 + c_2 \leq 0.0010l$ for lightweight concrete

Example: Determine maximum value of $c_1 + c_2$ for normal weight hollow-core slabs with a clear span of 30 ft.

Solution: $c_1 + c_2 = 0.0025(30 \times 12) = 0.90$ in.

Figure 2-3 Definition of restraint by ASTM E119 for precast systems [Gustaferro et al. 1989]

2.3.5. Recommendations from other sources

Even though the following organisations are not national or international standardisation bodies, their recommendations form the foundation of some of the codes and standards mentioned before, and it is essential to acknowledge their importance.

Prestressed Concrete Institute (PCI)

The 1989 design manual from PCI Fire Committee provided some calculation methods to evaluate the fire resistance of structures with precast and prestressed concrete but not specifically for hollowcore slabs [Gustaferro et al. 1989]. The standard fire follows ASTM E119, in which the time-temperature curve is shown along with the ISO834 standard fire in Figure 2-4.

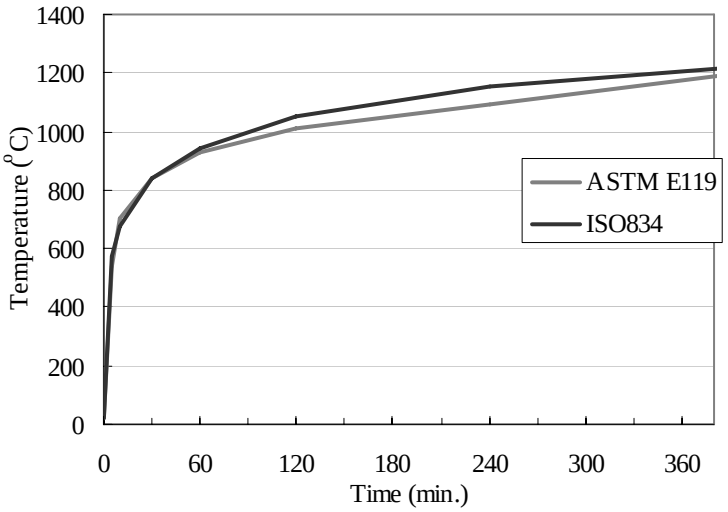

Figure 2-4 Standard fire temperature curves

The manual considers different restraint conditions on the slabs. In simply supported slabs the ends of the slab are free to rotate and move. The recommended calculation method focuses on the flexural failure mode; this is reflecting the fact that in all the fire tests none of the simply supported prestressed slabs designed according to ACI 318 has failed in shear. This flexure calculation method considers the loss of moment capacity during fire, resulting from the reduction of tensile strength in the prestressed strands and not by the loss of compressive strength in concrete. This is because the compression zone, which is near the top of the slab, remains at low temperatures during fires. The steel or concrete temperature with different cover thickness or depth after different time of exposure is obtained from experimental

results and given as graphs in the manual.

The continuous slab is taken as having an intermediate support in the simply supported slab, therefore both ends of the slab can still rotate and displace freely, but the bending moment diagram is different due to the presence of the intermediate support. The schematic drawing of a continuous slab, as well as the bending moment diagrams before and after the exposure of fire are shown in Figure 2-5. In the continuous slab the topping is used to provide continuity across the support, but it has been observed that the reinforcing bars in the topping around the support, which are the negative moment reinforcement, yield early during the fire tests and cause the redistribution of bending moments [Gustaferro 1970]. The behaviour of continuous beams and slabs in fire was tested on a series of 300mm by 350mm deep beams. At the support there are six no.6 (20mm diameter) reinforcement bars at the top and two at the bottom, at the midspan there are two bars at the top and four bars at the bottom. During the fire test the bottom of the beams was hotter than the top, therefore it expanded more and created thermal bowing. The thermal bowing caused the ends of the beam to lift from their supports and consequently increased the reaction at the interior supports causing a redistribution of moments. In summary, thermal bowing increases the negative moment along the length of the beam.

When the negative moment reinforcement yields, the negative bending moment capacity is reached, hence the amount of moment redistribution depends upon the amount of negative moment reinforcement. It is important to limit the negative moment reinforcement so that compression failure in the negative moment region does not occur. Furthermore, the length of the negative moment reinforcement must be long enough to accommodate the complete redistributed moment and change in the inflection points. Therefore it is recommended that at least 20% of the maximum negative moment reinforcement is extended throughout the span.

This design method indicates that the positive bending moment capacity can be designed as for simply supported slab, and the negative bending moment capacity should be designed as the total bending moment minus the positive bending moment. The total moment is the maximum bending moment the beam or slab would encounter if it is simply supported, for uniformly distributed load that means $wL^2/8$, where w is the uniformly distributed load and L is the length of the span; the positive bending

moment can be obtained from the figures in the appendix of PCI Design for Fire Resistance of Precast Prestressed Concrete [Gustaferro et al. 1989] or tables in Chapter 5 of PCI Design Handbook [Martin et al. 2004]. Gustaferro et al. [1989] also provides the calculation method for the minimum length of the negative moment reinforcement. The manual also provides the calculation method for the minimum length of the negative moment reinforcement.

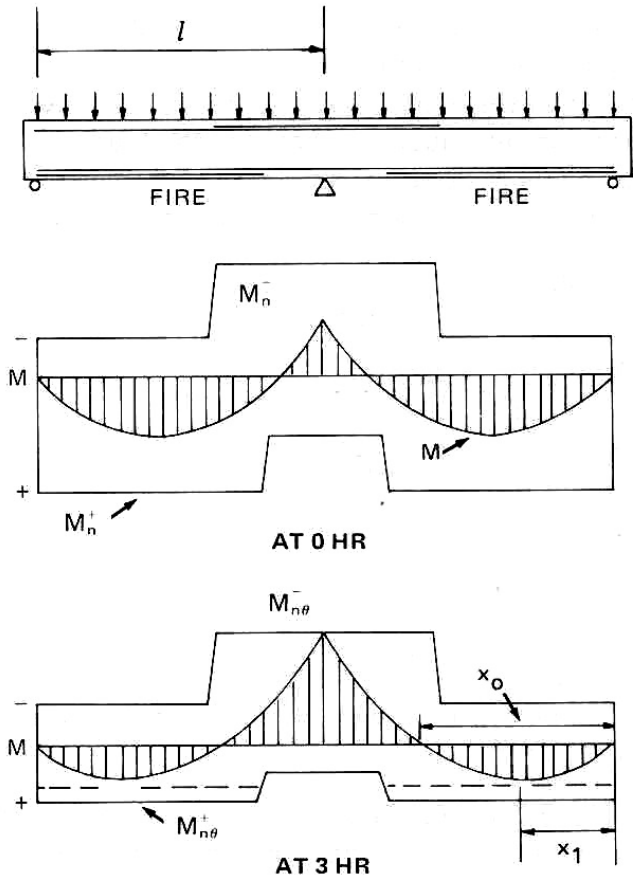

Figure 2-5 Schematic drawing of a continuous slab; the bending moment diagram at cold condition and after 3 hours of the ASTM E119 standard fire [Gustaferro et al. 1989]

Because of the redistribution of bending moments, continuous slabs have more fire resistance than simply supported slabs with the same cross-sectional dimensions and under the same loadings.

The restraint to thermal expansion usually happens when the expansion of a heated floor is limited by the unheated surrounding structural members. This limitation of thermal expansion acts as “fictitious reinforcement” located along the thrust line and can increase the bending moment capacity [Salse et al. 1971]. It is assumed that this fictitious reinforcement has the same yield strength as the thrust.

Therefore it is possible to determine the magnitude and location of the thrust, as well as the increased moment capacity caused by this thrust force.

The proposed design procedure for this situation is first to determine the remaining moment capacity as if the slab is simply supported, and calculate the deflection if the applied moment is greater than the remaining moment. The position of the thrust line is determined at the support and the magnitude of the required thrust is calculated, which will be compared with the load capacity of the supporting structure. It also provides the calculation method to consider the moment caused by the thrust, which in combination with the remaining moment capacity should be greater than the applied moment.

International Federation for Structural Concrete (fib)

The Commission on Prefabrication under fib published a guideline for design of hollowcore concrete slabs in 1987 [FIP 1987] and a revised version in 2000 [Fib 2000]. However, even though the flexural and shear design has been discussed thoroughly in the later recommendation, the design for fire resistance has been omitted.

The 1987 recommendations [FIP 1987] provide two methods to determine the fire resistance, either by carrying out fire tests in accordance with the ISO 834 standard criteria, or by calculation of the residual flexural resistance. In the calculation method, the applied bending moment is checked against the remaining ultimate moment capacity contributed by the reinforcing steel and prestressing strands. This approach is the same as that from PCI. The shear capacity is considered but no calculation method is given. It is recommended to provide complementary reinforcement around the neutral axis to prevent cracking of the webs caused by shear forces.

Other recommendations from FIP [1987] or Fib [2000] given to improve the flexural and shear capacity of hollowcore concrete slabs under ambient conditions, such as to fill half of the voids of the hollowcore units near the connections to avoid shear failure, may be beneficial under the fire conditions as well and should be incorporated into the design for improving the fire performance.

2.4. Engineering Design Method

All the standards mentioned above allow for using an engineering design method to calculate the required dimensions for structural members to meet the desired fire resistance. The latest version of NZS3101 adheres to Eurocode 2 in terms of assessing fire resistance rating by calculation, so that using computer analyses based on fundamental physical behaviour for both thermal analysis and mechanical behaviour is allowed and falls into the "advanced calculation methods" category. There are several computer programs available to analyse the behaviour of concrete structures under fire conditions, in both micro and macro scale. Due to the advancing of computational power, finite element programs such as Vulcan (Huang et al. 2006) and SAFIR (Franssen 2002a) are used not only for research or forensic analysis purposes but also for design by industry. Nevertheless, in terms of fire design of hollowcore concrete slabs, to the author's knowledge there is no ideal computer model for such purpose so far, hence one of the aims of this research is to create such a model. The computer simulations of the behaviour of hollowcore concrete slabs under fire conditions are discussed later in Chapter 6.

2.5. Proprietary Fire Rating of Hollowcore Units

Proprietary fire rating is the fire resistance rating of proprietary products made by specific manufacturers. These ratings are obtained by either testing or by calculation depending on the manufacturers, and the engineer should consult the manufacturer to confirm the accuracy of the fire rating. In the United States, Underwriters Laboratories has conducted more than 30 standard fire tests on hollowcore floor assemblies and published the results for more than 50 designs of hollowcore slabs which qualify for ratings of 1 to 4 hours. For hollowcore units not found in the Underwriters Laboratories ratings, the fire resistance rating can be obtained by conducting standard fire tests in accordance with ASTM E119 [ASTM 1999] as mentioned before or by using the effective thickness method described in the PCI Manual [Gustaferro et al. 1989]. Similarly in Canada, the fire resistance can be determined by conducting fire tests in accordance with CAN/ULC-S101-M [ULC 1989] or using the effective thickness method in Appendix D of National Building Code of Canada [CCBFC 2005]. Engineers should give different levels of caution to the prescribed fire ratings depending on the methods used.

The studied hollowcore units in this research are manufactured by Stresscrete, and their fire ratings were obtained using effective thickness method as specified in NZS 3101 [Firth Stresscrete 2007], therefore engineers should give this rating the same level of caution as the effective thickness method.

3. Material Properties of Concrete and Steel

This chapter describes the thermal and mechanical properties of concrete and steel. It also briefly explains the reasons for the change of these properties during heating, and provides references for further understanding these changes.

The properties from both 1995 and 2002 versions of Eurocodes are described in this chapter. The Eurocode formulation is a well accepted approach giving a reasonable representation for parameters which in reality show a degree of variation and complexity as found out in various studies shown in this chapter. The equations from both versions of Eurocode are presented because the thermal analyses in this research were conducted using the finite element program SAFIR2004 which follows the 2002 version of Eurocode, whereas the structural analyses were conducted using SAFIR2002 which follows the 1995 version. The reason behind this was that the corrected concrete model in SAFIR2004 was introduced after the completion of much of this research.

3.1. Thermal Properties of Concrete

3.1.1. Thermal conductivity

Thermal conductivity determines the ability of a material to conduct heat. It is expressed as the ratio of heat flux to temperature gradient ($Wm^{-1} K^{-1}$). The thermal conductivity in concrete represents the uniform flow of heat through a unit thickness of concrete over a unit area subjected to a unit temperature difference between the opposite faces [Bažant et al. 1996].

Under the ambient condition, the thermal conductivity of concrete depends on factors such as the thermal conductivity of aggregate and moisture content. At ambient temperature the thermal conductivity of concrete with siliceous aggregates is higher than that with limestone [Blundell et al. 1976]. In terms of moisture content, because the thermal conductivity of air is very much less than that of water, the dehydration of concrete will reduce the thermal conductivity, and concrete with 50% less moisture content than saturated concrete could have a 25% reduction in conductivity [Zoldners 1971].

Under elevated temperatures, the thermal conductivity decreases as the

temperature increases. The cement-water ratio and the mix portions of aggregate are still very important to the thermal conductivity of concrete in elevated temperatures. Because loss of moisture during heating reduces the thermal conductivity, concrete with higher initial moisture content will experience a more rapid loss of conductivity. The thermal conductivity of concrete differs with aggregate type also under elevated temperatures as shown in Figure 3-1. The thermal conductivity of aggregates in normal concrete is higher than that of the cement paste, and is lower in lightweight concrete [Schneider 1982].

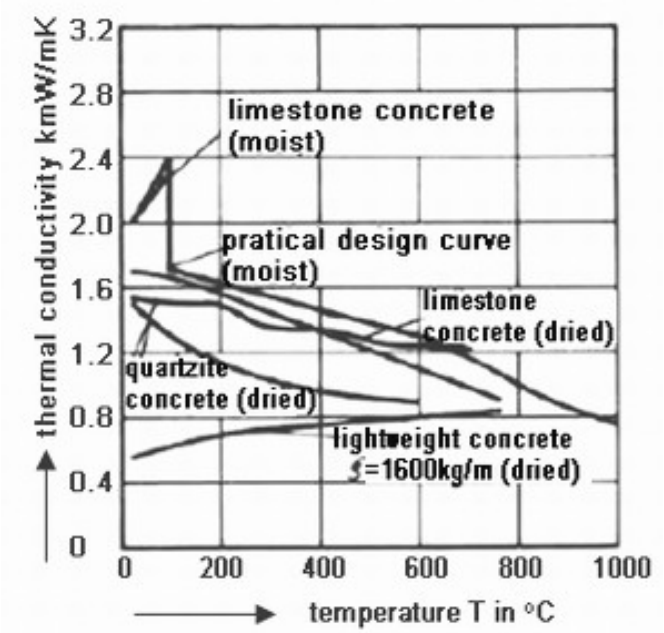

Figure 3-1 Thermal conductivity of different structural concretes [Schneider 1982]

All concrete products manufactured in New Zealand are with siliceous aggregates. Thermal conductivity of siliceous aggregate concrete from the 1995 version of Eurocode 2 [EC2 1995] is defined as:

$$\lambda = 2 - 0.24\theta_c/120 + 0.012(\theta_c/120)^2 \qquad \text{For } 20^oC < \theta_c < 1200^oC \quad \text{Eq. 3-1}$$

where λ is the thermal conductivity in W/mK, and θ_c is the concrete temperature in Celsius degrees.

The temperature- thermal conductivity relationship has been updated in the 2002 version [EC2 2002] and is given as a range of values, with the upper limit being defined as:

$$\lambda = 2 - 0.2451(\theta_c/100) + 0.0107(\theta_c/100)^2 \qquad \text{Eq. 3-2}$$

and the lower limit being defined as:

$$\lambda = 1.36 - 0.136(\theta_c/100) + 0.0057(\theta_c/100)^2 \qquad \text{Eq. 3-3}$$

The lower limit was derived from test results of different types of concrete structures, and the upper limit was from steel/composite structures.

Figure 3-2 shows the thermal conductivity curves from both versions of Eurocode 2. It is apparent that the 1995 version gives a higher conductivity. However, the trend of the curve in the 1995 version is similar to that of the lower limit in the 2002 version.

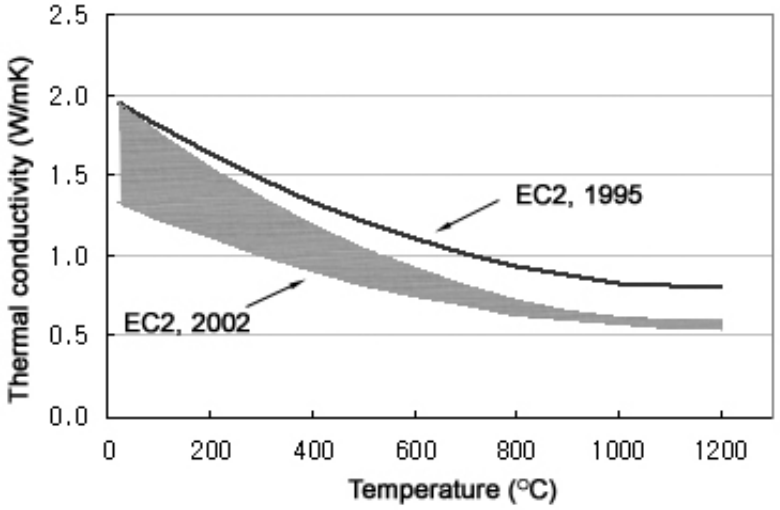

Figure 3-2 Thermal conductivity of concrete according to EC2 [EC2 1995, EC2 2002]

3.1.2. Thermal diffusivity

Thermal diffusivity indicates the rate of temperature change in a material and is used for calculating temperature distribution under transient conditions. Thermal diffusivity can be calculated from the following equation:

$$D = \lambda / c\rho \qquad \text{Eq. 3-4}$$

where D is thermal diffusivity in m^2s^{-1}, λ is thermal conductivity in W/mK, c is specific heat in $Jkg^{-1}K^{-1}$ and ρ is the density of the material in kgm^{-3}. Thermal diffusivity can also be determined by direct measurement [US Army Corps of Engineers, 1988].

Under ambient conditions the thermal diffusivity of concrete is influenced by the aggregate types and the aggregate-cement ratio. The thermal diffusivity of hardened

cement paste is generally less than that of ordinary aggregates; hence, the values for ordinary concrete are less than those for the aggregate [Bažant et al. 1996].

At elevated temperatures, the aggregate types, cement ratio and moisture content have the same effect on thermal diffusivity as on the thermal conductivity [Schneider 1982]. The thermal diffusivity of siliceous concrete from different researches collected by Schneider is shown in Figure 3-3. The difference at low temperatures (below 200^{o}C) was caused by different levels of moisture content; this explains the rather similar values from different researches at the high temperatures when the moisture diminishes.

In the Eurocode 2 [EC2 1995], the thermal diffusivity of siliceous concrete is considered to be independent of the concrete temperature and equals to 0.69 x 10^{-6} m^2/s.

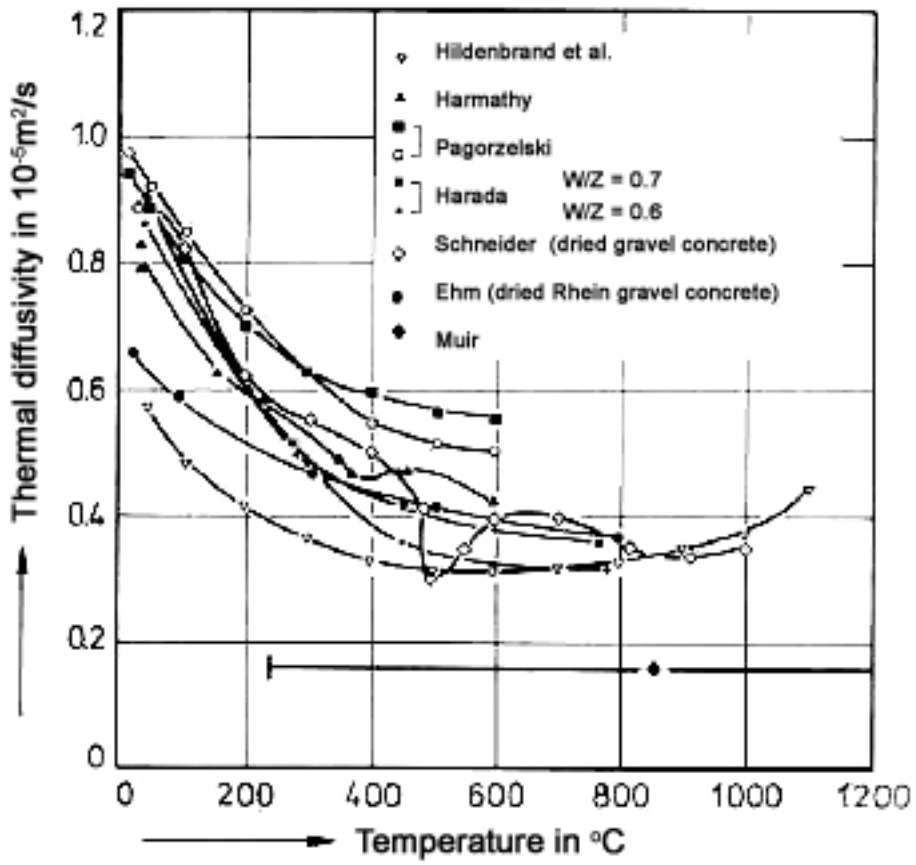

Figure 3-3 Thermal diffusivity of concrete [Schneider 1982]

3.1.3. Specific heat

The specific heat is the amount of heat energy per unit mass required to change the temperature of the material by one degree. At constant pressure, the specific heat, c_p ($Jkg^{-1}K^{-1}$), is defined as

$$c_p = \left(\frac{\partial H}{\partial T_p} \right) \qquad \text{Eq. 3-5}$$

where H is enthalpy in J, T is temperature in K, and $_P$ means pressure.

Compared to the thermal conductivity or diffusivity, this thermal property does not vary much with the temperature [Neville 1990]. Figure 3-4 shows the variation of specific heat of cement paste with temperature [Harmathy 1970]. There is a big increase of the specific heat between 100°C and 800°C which is due to the latent heat induced by the dehydration of cement. The peak showing at 500°C is caused by the dehydration of the compounds.

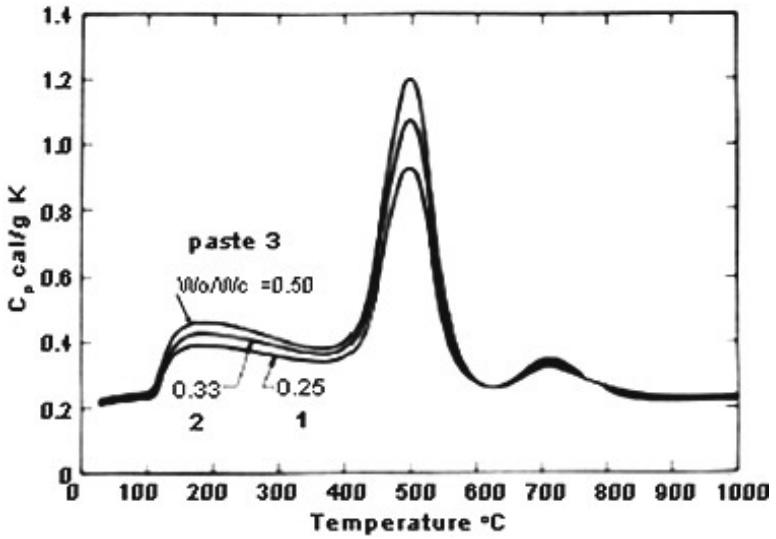

Figure 3-4 Change of specific heat with temperature of cement paste [Harmathy 1970]

It has been found that that aggregate type, mix proportions or age do not have great effect on the specific heat of ordinary concretes [Carman et al. 1921]. The main factor affecting the specific heat of concrete is the moisture content at the time of heating as water has relatively high specific heat. The specific heat of saturated concrete is almost twice the value as that of dry concrete [Franssen 1987]. The effect of the moisture content along with the types of aggregate to the specific heat under elevated temperature is shown in Figure 3-5.

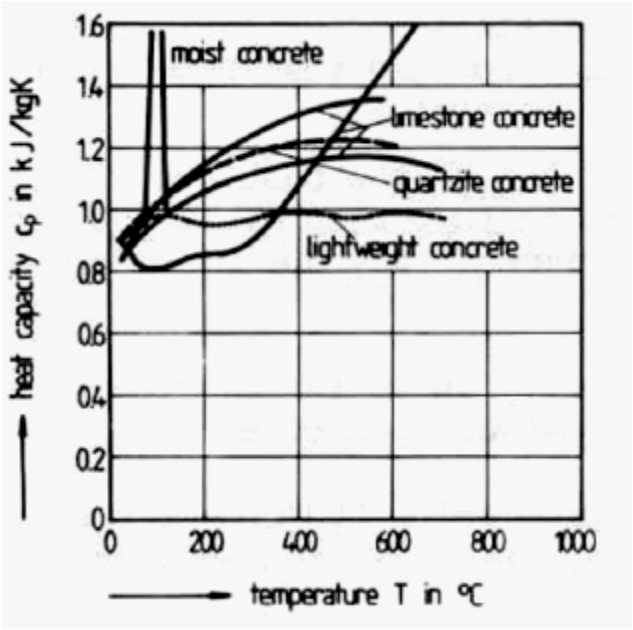

Figure 3-5 Specific heat of different concretes [Schneider, 1985]

As for the thermal conductivity, the specific heat in Eurocode 2 has been significantly updated. In the 1995 version, the specific heat of concrete with siliceous aggregates is expressed as a function of temperature in one single equation:

$$c_p = 900 + 80\theta_c/120 - 4(\theta_c/120)^2 \ \text{(J/kgK)} \qquad \text{For } 20^oC < \theta_c < 1200^oC \qquad \text{Eq. 3-6}$$

where c_p is the specific heat, θ is the concrete temperature in ^oC.

In the 2002 version the specific heat of dry siliceous or calcareous concrete is expressed by the following equations:

$$\begin{aligned} c_p &= 900 \ \text{(J/kgK)} && \text{For } 20^oC < \theta_c \le 100^oC \\ c_p &= 900 + (\theta_c - 100) \ \text{(J/kgK)} && \text{For } 100^oC < \theta_c \le 200^oC \\ c_p &= 100 + (\theta_c/100)/2 \ \text{(J/kgK)} && \text{For } 200^oC < \theta_c \le 400^oC \\ c_p &= 1100 \ \text{(J/kgK)} && \text{For } 400^oC < \theta_c \le 1200^oC \end{aligned} \qquad \text{Eq. 3-7}$$

When the moisture content is not considered explicitly, the function given for the specific heat may be assumed as a constant value when the temperature is below 100^oC, or 115^oC depending on the moisture content. Figure 3-6 shows the variation of the specific heat with temperature from both versions of Eurocode 2. It is apparent that the specific heat calculated using the older version is close to that from the new version when the concrete temperature is under 400^oC. Above 400^oC, the 2002 version restrains the specific heat as 1100J/kgK, the difference of the value obtained using different versions increases with temperature.

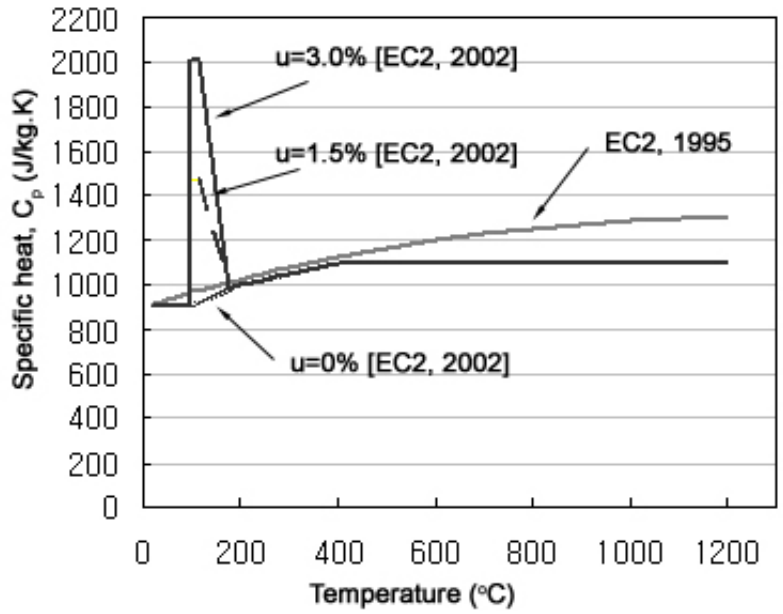

Figure 3-6 Specific heat of siliceous concrete according to EC2 [1995, 2002]

3.1.4. Thermal expansion

Like most materials, concrete undergoes thermal expansion when it is subjected to a temperature change. Because concrete is an isotropic material, the thermal strain is the same in all directions. As heat propagates through concrete, thermal gradients will produce non-uniform deformations across the concrete. Non-uniform thermal expansion in concrete can induce mechanical stress which can lead to cracking or large scale spalling [Bažant et al. 1996]. The total thermal expansion has several components; each is discussed separately below.

Thermal expansion of aggregates

Thermal expansion of aggregate contributes to between 65% and 80% of the total thermal expansion [Bažant et al. 1996]. The types of aggregate containing a high amount of silica, such as quartzite and sandstone, have a high coefficient of thermal expansion [Browne 1972]. The differences in thermal expansion caused by the aggregate type are shown in Figure 3-7.

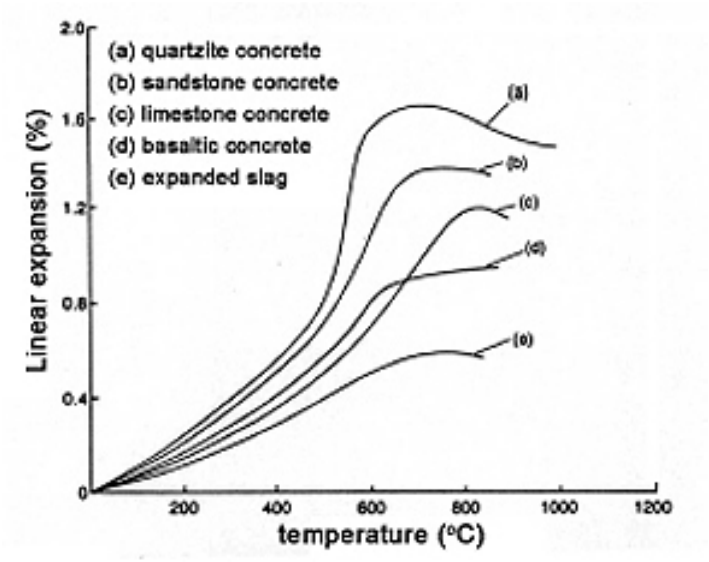

Figure 3-7 Thermal expansion of different type of concrete [Schneider 1982]

Thermal expansion of hardened cement paste

During heating, cement paste initially experiences thermal expansion and then shrinkage. When the hardened cement paste is heated up to 150^{o}C, the paste expands by up to 0.2% of the initial volume. The thermal expansion reaches a plateau in the temperature range 150^{o}C to 300^{o}C. In between 300^{o}C and 800^{o}C, the paste shrinks in the order of 1.6% to 2.2% caused by loss of moisture from the cement paste [Bažant et al. 1996]. When the cement paste is heated, the free pore water is driven out, and when the temperatures are well above 100^{o}C for some time, the solid paste matrix will be dehydrated [Cruz et al. 1980].

Transitional thermal creep

Unlike steel, thermal expansion in concrete can be influenced significantly by the presence of compressive loads during heating. Khoury et al. [1985a, 1985b, and 1986] demonstrated that there is considerable contraction for concrete compared with the free thermal strains. These contractions are called “load-induced thermal strain”, “transitional thermal creep” or “transient strain”. The total thermal strain equals the difference between the free thermal strains and the load-induced thermal strain. The load-induced thermal strain significantly exceeds that expected from any increase with temperature of basic creep and elastic strains.

Transient strain is caused by expansion of cement paste when it is heated for the first time under load. Khoury et al. [1985a] found that for the case of the loaded specimen under cycles of heating and cooling, the effect of transient strain does not

appear during the material cooling phase and is significantly reduced during the thermal cycles.

Khoury et al. [1985a] showed that these load-induced thermal strains occur only in compression, and they are much influenced by the moisture content and the heating rate. The load-induced thermal strains accommodate the incompatibilities of thermal strain between aggregates and cement paste. They provide a significant relaxation and redistribution of thermal stresses, so that they help to avoid excessive damage to the concrete especially when the temperatures are above 100^{o}C.

Path dependence

The thermal expansion in concrete is also affected by the stress path. Tests carried out by Anderberg et al [1973] showed that by applying stresses before and throughout heating, the thermal expansion can be much less than when applying stresses only after the fire temperature becomes constant. Thelandresson [1987] studied this area further and introduced the concept of the thermal-mechanical interaction, which indicates that the thermal expansion of concrete is not only a function of temperature but also depends on the applied level of stress during heating.

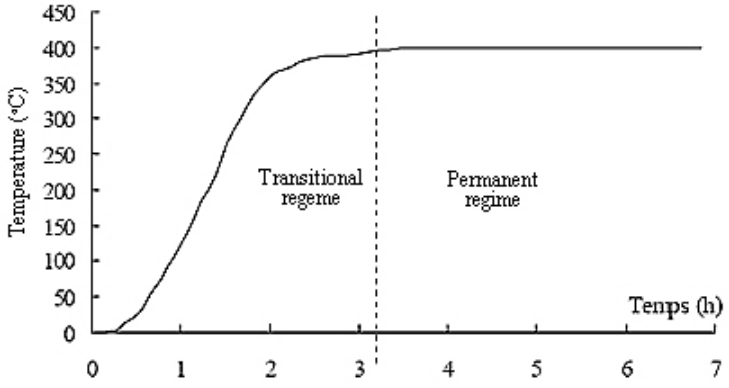

Figure 3-8 Temperature at the centre of the specimen versus heating time for Anderberg's tests [Thelandresson 1987]

The influences of path dependence within concrete are best shown by the tests in Anderberg et al. [1973]. In these tests two concrete specimens were exposed to fires and the temperature at the centre of the specimens was as shown in Figure 3-8. Figure 3-9 shows the uniaxial deformation from these tests. In Case 1 a uniaxial compressive stress was applied to the specimen once the fire temperature becomes constant. In Case 2 the load was applied from the beginning until the end of the experiment, so the free expansion is completely restrained.

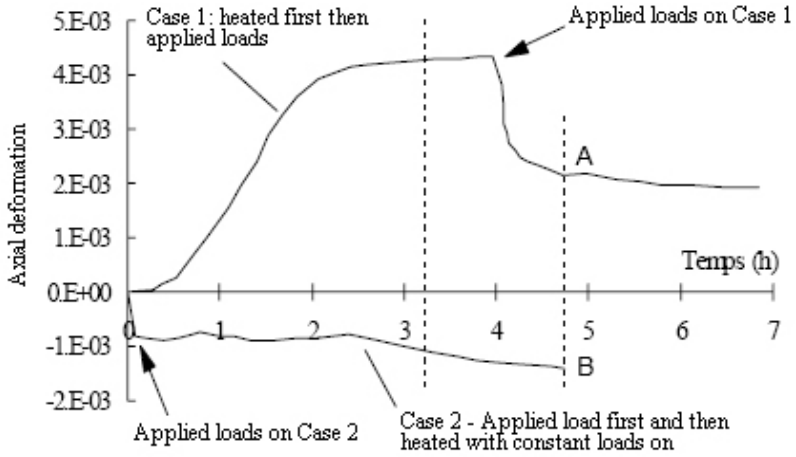

Figure 3-9 Measured total deformation of the heated concrete specimens (applied compressive loading = 0.45 f_{c20})

However, in Eurocode 2 [EC2 1995 and 2002] the thermal elongation of concrete is considered only as a function of temperature, and the coefficient of thermal elongation of siliceous concrete as shown in Figure 3-10 is expressed as

$$\varepsilon_c(\theta_c) = -1.8\times10^{-4} + 9\times10^{-6}\,\theta_c + 2.3\times10^{-11}\,\theta_c^3 \qquad \text{For } 20^\circ\text{C} < \theta_c \le 700^\circ\text{C}$$
$$\varepsilon_c(\theta_c) = 14\times10^{-3} \qquad \text{For } 700^\circ\text{C} < \theta_c \le 1200^\circ\text{C} \qquad \text{Eq. 3-8}$$

where θ is the concrete temperature in Celsius degrees.

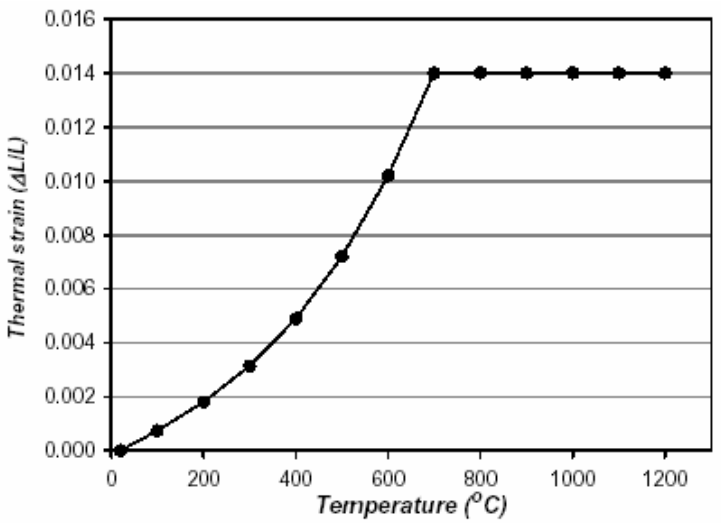

Figure 3-10 Thermal elongation of siliceous aggregate concrete according to Eurocode 2 [1995, 2002]

3.1.5. Spalling

Overall

Spalling is the separation of concrete from the surface of a concrete element when heated. It can seriously reduce fire resistance. Spalling has been classified into the following categories [Institution of Structural Engineers, 1975]:

1. General or destructive spalling – This is a violent spalling form which occurs at the early stage of heating and may cause extensive damage or complete destruction of the concrete element

2. Local spalling – This consists of sometimes violent surface spalling, aggregate splitting or corner break-off.

3. Sloughing off – This is a progressive form of breakdown of the concrete element after prolonged heating. The breakdown process may continue slowly through the later stages of heating.

These three categories in other studies, such as in Ali [2002], Ali et al. [2001] and Connolly [1997], are also known as “explosive spalling”, “aggregate spalling” and “corner spalling” respectively.

Spalling is affected by the moisture content of the concrete because the elevated temperatures cause vaporisation of free water and combined water within the concrete and cause large chunks of concrete to split off, therefore spalling is less likely to happen in concrete with low moisture content. Tests carried out by Meyer-Ottens [1974a and 1974b] showed that no spalling occurred in concrete which has less than 2% of moisture by weight.

High pore pressure can be caused by high moisture content, low permeability [Zhukov 1976], small pore size, low porosity or high concrete density. High pore pressure increases the risk of explosive spalling. The build-up of pore pressure induces stresses within the gel structure [Ali 2002]. Petrov-Denisov et al [1972] stated that the pores of the material can be classified as either open or closed; and the closed pores in the zone just behind the progressing evaporation front still contain water and steam, which raise the pressure within the pores with the increasing temperature. The thermal stress and pore pressure increase the strain energy. When the pressure difference is big enough across the walls that separate the open and closed pores, the

walls would break down and initiate spalling. However, if the gel structure is strong and impermeable, the strain energy can accumulate to a very high level, and the sudden release of this energy can take form of the explosive spalling.

Explosive spalling can also be caused from thermal stress. Restrained thermal dilatation around the heated surface can induce compressive stresses, which are then released via brittle fracture of concrete, i.e. spalling [Bažant 1997]. Experiments from Connolly [1995] showed that concrete subjected to a high level of net effective stress, which is the sum of the load stress and thermally induced stresses minus pore pressure stress, is more vulnerable to explosive spalling.

The probability of explosive spalling is also increased under the following situation: higher heating rate, low water-cement ratio, large aggregate size, high free moisture content or the specimen being young [Connolly 1997].

Other factors to increase the likelihood of concrete spalling in general according to Hertz [2003] are:

- Low tensile strength of concrete– low tensile strength of concrete increases the risk of spalling because it decreases the energy and the pressure necessary to explode the material.
- Dense reinforcement and large aggregates – dense reinforcement and large aggregates can increase the tensile stress in the cement matrix due to its thermal expansion, and therefore may contribute to spalling.
- Non-uniform thickness of the member– Non-uniform concrete thickness may induce thermal stresses and consequently causes spalling.
- Prestressing – prestressing and compression stresses may increase the risk of spalling in the same manner as thermal stresses.

Spalling in high strength concrete

Sometimes hollowcore units are made with high strength concrete. High strength concrete, or “dense concrete” as referred to by Hertz [2003], may be different to traditional concrete in terms of the likelihood of spalling. Tests have shown that spalling occurs often near the critical point of temperature at 374^{o}C, beyond this temperature a pore cannot contain both liquid and vapour at the same time. If the

material is dense enough, experiments have shown that even crystal water, which is the water that is contained in minerals, is sufficient to cause explosive spalling. This has not been found in traditional concrete. However, most of the factors influencing the spalling of traditional concrete also influence the spalling of dense concrete [Messerschmidt 1994], and without axial restraint, normal and high strength concrete members showed similar vulnerability to explosive spalling under loading only [Ali 2002].

Even though the low permeability makes dense concrete susceptible to spalling, the effect of high splitting tensile strength can overcome the problem [Ali 2002]. Further tests even showed that under axial restraint, normal strength concrete members have higher degrees of spalling than high strength concrete. Eurocode 2 [EC2 2002] suggests four methods to prevent spalling in high strength concrete: using surface reinforcement mesh, using tested types of concrete, having protective layers, or using polypropylene fibres in the concrete mix.

3.2. Thermal Properties of Steel

3.2.1. Thermal conductivity

The thermal conductivity of steel depends mainly on the composition of the material and the heat treatment. Similarly to the thermal conductivity of concrete, the thermal conductivity of steel also decreases with increasing temperature.

The thermal conductivity according to Eurocode 3 [EC3 2002] has the following relationship with the steel temperature

$$\begin{aligned} \lambda_a &= 54 - 3.33 \cdot 10^{-2}\,\theta \,(\text{W/mK}) && \text{for } 20^o C \le \theta \le 800^o C \\ \lambda_a &= 27.3\,(\text{W/mK}) && \text{for } 800^o C < \theta \le 1200^o C \end{aligned} \qquad \text{Eq. 3-9}$$

where λ_a is the thermal conductivity of steel, and θ is the temperature of steel. This relationship is plotted in Figure 3-11.

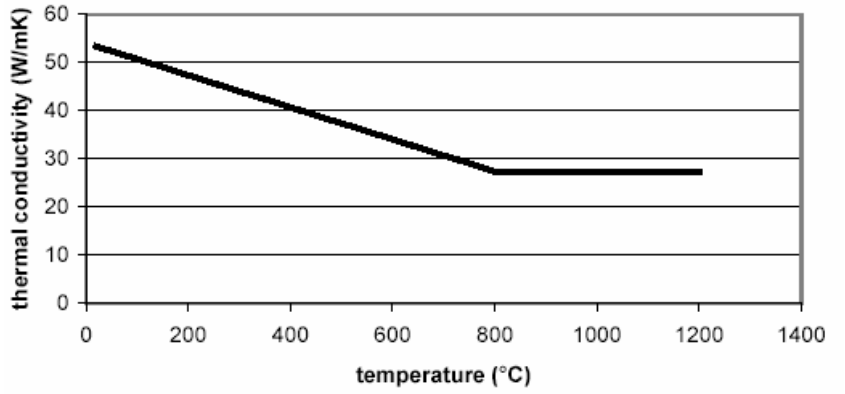

Figure 3-11 Thermal conductivity of steel according to Eurocode 3 [EC3 2002]

3.2.2. Specific heat

Unlike the conductivity, the specific heat of steel is independent of the steel composition. Eurocode 3 [EC3 2002] expresses the relationship between the specific heat of steel and temperature using the following equations

$$\begin{aligned} c_p &= 425 + 0.773\theta - 1.69 \cdot 10^{-3}\theta^2 + 2.22 \cdot 10^{-6}\theta^3 && \text{for } 20^o C \le \theta \le 600^o C \\ c_p &= 666 + 13002/(738 - \theta) && \text{for } 600^o C < \theta \le 735^o C \\ c_p &= 545 + 17820/(\theta - 731) && \text{for } 730^o C < \theta \le 900^o C \\ c_p &= 650 && \text{for } 900^o C < \theta \le 1200^o C \end{aligned} \qquad \text{Eq. 3-10}$$

Figure 3-12 shows the relationship between the specific heat of steel and temperature according to the Eurocode 3. The peak at around 730°C is caused by a

metallurgical change in the steel.

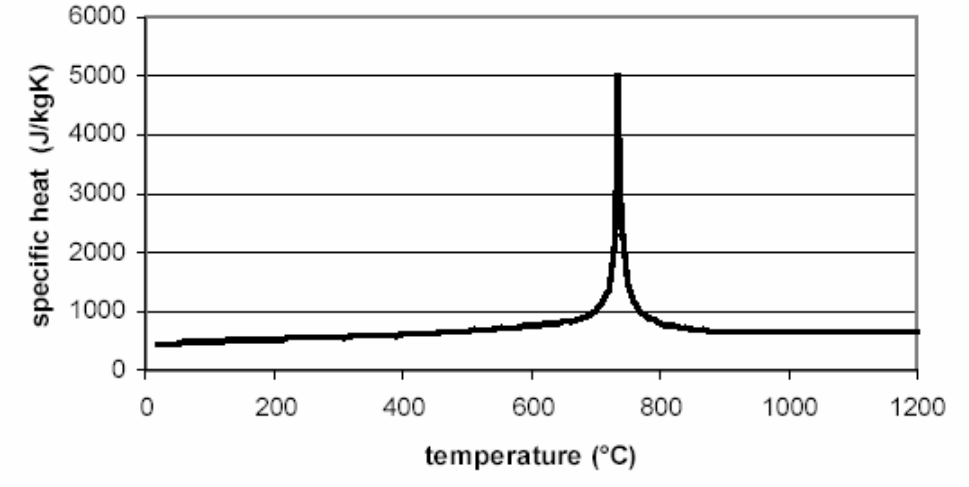

Figure 3-12 Specific heat of steel according to Eurocode 3 [EC3 2002]

3.2.3. Thermal expansion

Thermal expansion of steel can be obtained directly from conventional thermal expansion tests. The coefficient of thermal expansion of steel at room temperatures is about $11.4\times10^{-6}m^{-1}K^{-1}$ [Harmathy 1993].

The thermal expansion of steel depends on the carbon content and the heat treatment. Figure 3-13 shows the different relationships between the thermal expansion and the temperature for reinforcing steels which had different heat treatment in the manufacturing process [FIP 1978]. The coefficient of thermal expansion is not constant but rises with the increasing temperature. This relationship is expressed by the following equations from Eurocode 3 and is also shown in Figure 3-13.

$$\begin{aligned} \Delta L / L_s &= -2.416\cdot10^{-4} + 1.2\cdot10^{-5}\theta + 0.4\cdot10^{-8}\theta^2 && \text{for } 20^oC < \theta \le 750^oC \\ \Delta L / L_s &= 11\cdot10^{-3} && \text{for } 750^oC < \theta \le 860^oC \\ \Delta L / L_s &= -6.2\cdot10^{-3} + 2\cdot10^{-5}\theta && \text{for } 860^oC < \theta \end{aligned} \quad \text{Eq. 3-11}$$

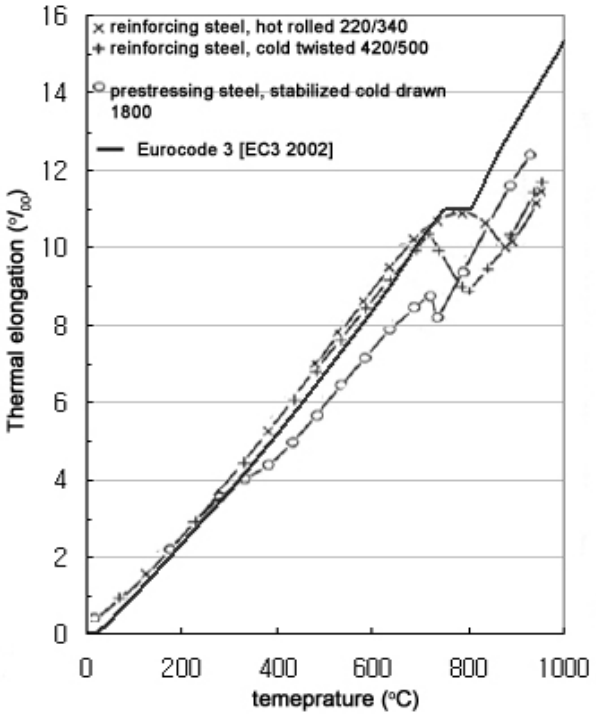

Figure 3-13 Thermal elongation of different steel from experiments and according to Eurocode 3 [FIP 1978, EC3 2002]

3.3. Mechanical Properties of Concrete

3.3.1. Compressive strength

Uniaxial stress behaviour

The compressive strength of concrete is generally obtained by using uniaxial compressive tests, and it reduces under high temperatures. Figure 3-14 shows the stress-strain relationship of concrete at different temperatures obtained from compressive uniaxial tests. This figure shows an irreversible rigidity loss caused by the thermal damage and also an irreversible loss of compressive strength caused by the loss of cohesion between particles at high temperatures, or according to Schneider [1988], thermal decohesion.

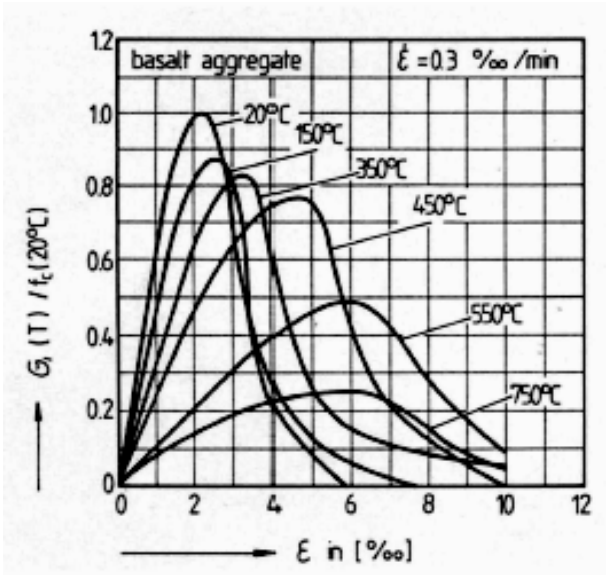

Figure 3-14 Stress-strain relationship of concrete under different temperatures in uniaxial tests [Schneider 1988]

Many factors can influence the strength of concrete under high temperatures; the more significant ones are the initial moisture content and the type of aggregates used [Schneider 1988]. Figure 3-15 shows the strength reduction of unloaded concrete during heating. It also shows that the strength reduction at high temperatures depends on the aggregate types. From 450^{o}C, the concrete with siliceous aggregates has greater strength reduction compared to those with calcareous or lightweight aggregates [Schneider 1985]. This effect is caused by the thermal instability of the aggregates, which is related to the aggregate itself, and by the incompatibility between the shrinking cement paste and the expanding aggregate particles, which is related to

the bonding between aggregates and cement.

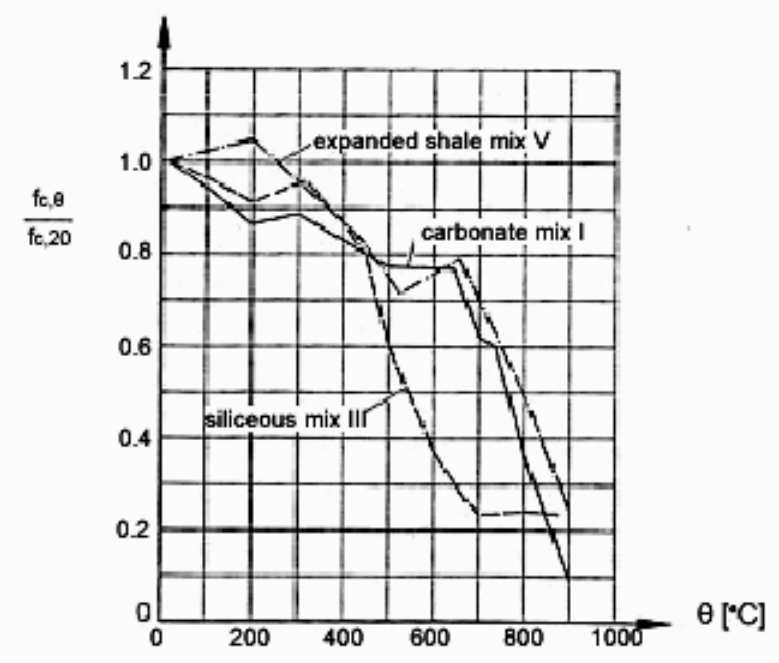

Figure 3-15 Variation of concrete compressive strength for different aggregates [Schneider 1985]

The concrete compressive strength at high temperatures also depends on the loading condition. Applying high stress level during heating can increase the concrete compressive strength [Schneider 1976]. The strength reduction with different loading conditions under high temperatures from the test results obtained by Bažant [1996] is shown in Figure 3-16. These loading conditions are:

1. Unstressed – The unloaded specimen was heated to the required temperature and then loaded to failure while hot.

2. Stressed – the specimen was loaded in compression and then heated to the required temperature. The load was then increased until reaching failure.

3. Unstressed residual – the unloaded specimen was heated to the required temperature and then allowed to cool slowly to room temperature. After seven days the specimen was loaded to failure in compression.

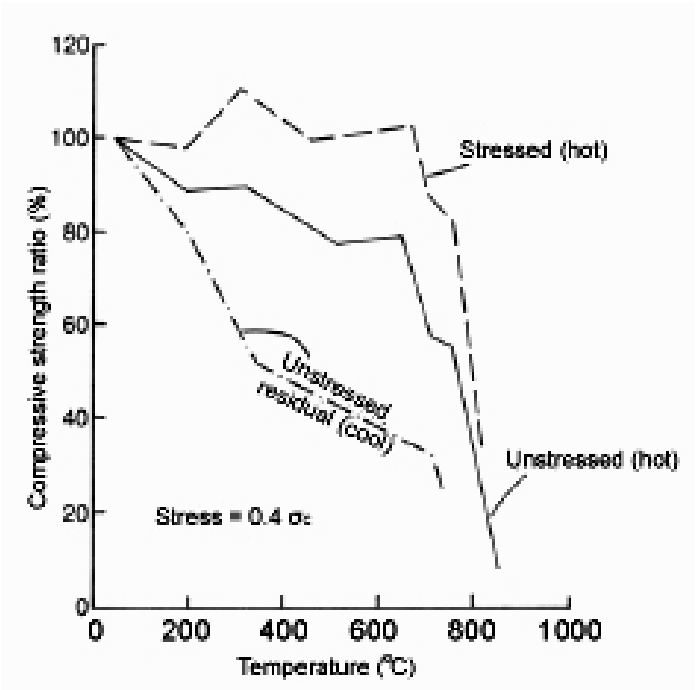

Figure 3-16 Strength ratio of calcareous aggregate concrete under various conditions [Bažant 1996]

In Figure 3-16 the stressed specimens were tested with a stress level of 40% of the concrete compressive strength in ambient conditions. The gaining of around 10% of strength was found at 300^{o}C in the stressed specimens. It is further found that the applied stress level itself has little effect on the ultimate strength of concrete as long as this stress is greater than 20% of the uniaxial compressive strength under ambient conditions.

It is known that high strength concretes are more sensitive to high temperatures because their reduced porosity favours pore-pressure built-up and decreased thermal diffusivity [Felicetti et al. 1998]. According to CEB-FIP [1994], high-strength concrete has a compressive strength of 60 to 120MPa. Diderichs et al. [1988, 1989] point out that high strength concretes lose their compressive strength and stiffness more rapidly because they have denser cement paste which dries slower and less “drying hardening”, and their cement paste has greater thermal expansion up to 200^{o}C. Besides, high strength concrete has a more homogeneous microstructure which makes it be more vulnerable to thermally-induced defects.

Eurocode 2 [1995, 2002] uses a reduction coefficient $k_c(\theta)$ to express the diminishing characteristic concrete compressive strength under elevated temperatures, i.e.:

$$f_c(\theta) = k_c(\theta) \cdot f_c(20^o C) \qquad \text{Eq. 3-12}$$

where $f_c(\theta)$ is the reduced concrete strength at temperature θ. The reduction coefficient from the 2002 version of Eurocode 2 is slightly different from the 1995 version as shown in Figure 3-17. In the version of SAFIR used in this study, the reduction coefficient from EC2 [1995] was used.

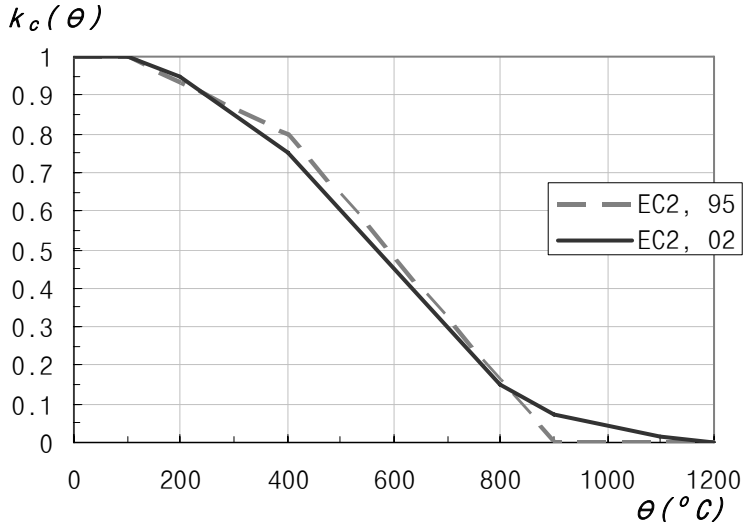

Figure 3-17 Reduction coefficient from Eurocode 2 for decrease of characteristic strength of concrete with siliceous aggregate

Biaxial stress behaviour

The test results from Kordina et al. [1985] as well as Ehm et al.[1985] show that the biaxial compressive strength is higher than that under the uniaxial condition. This is shown in Figure 3-18 which displays the ultimate strength of normal concrete at different temperatures and at different stress ratios. The relationship is between the principal stresses at failure σ_1: f'$_o$ and σ_2: f'$_o$. The figure shows that even if the load levels in the second axis are small, the ultimate strength increases compared to the uniaxial strength. It is also observed that the stress ratio σ_1: σ_2, which gives the highest biaxial strength, increases with the temperature [Ehm et al. 1985]. In addition, these curves show that under high temperatures concrete is more sensitive to the stress ratio due to the degradation of concrete in the micro-structural level and the increase of porosity with temperature in concrete [Nechnech 2000].

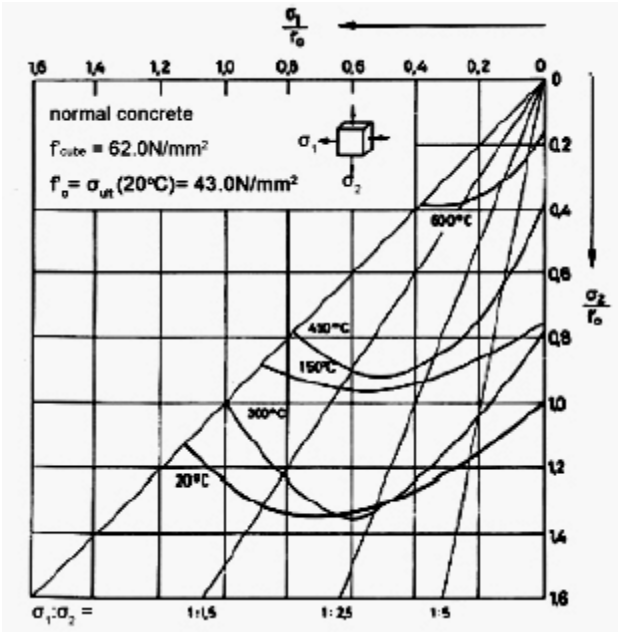

Figure 3-18 Biaxial ultimate strength envelope [Ehm et al. 1985]

Ehm et al. [1985] found out in the tests that explosive fractures and brittle failure occurred at room temperature and at 300°C, which indicates that the highest strength of the concrete specimens was reached at these temperatures. At 150°C, 450°C and at higher temperatures, the specimens failed in a moderate manner and demonstrated a plastic-like stress-strain behaviour. Kordina et al. [1985] noticed that in these tests the compressive strength at 300°C was higher than at 150°C. This increase of the compressive strength is caused by the evaporation of the water trapped inside the concrete. The evaporation of water increases the Van Der Waals force at the surface between the calcium silicate hydrate compound particles which strengthens the cement paste. Van der Waals force is the electrostatic attraction force between molecules [Shellers et al. 1984]. It is known that the Van Der Waals force is less important than the chemical bonding force which decreases at high temperatures, but at such temperatures the chemical bonding of the paste is not yet affected. In high strength concretes the drying hardening effects are smaller as they have a denser paste which is more difficult to dry [Felicetti et al. 1998].

The deformation behaviour of concrete at high temperature under biaxial stress is shown in Figure 3-19 and Figure 3-20, where Figure 3-19 shows the stress-strain relationship with biaxial stress ratio of zero (σ_1: σ_2 = 1:0), and Figure 3-19 of unity (σ_1: σ_2 = 1:1). The graphs indicate that the strains depend significantly on the temperature and stress ratio. The strains, ε_1 and ε_2, which correspond to the ultimate strength,

increase considerably with increasing temperatures. The principal strain ε_2 at failure varies from positive under uniaxial loading to negative under symmetric biaxial loading [Ehm et al 1985].

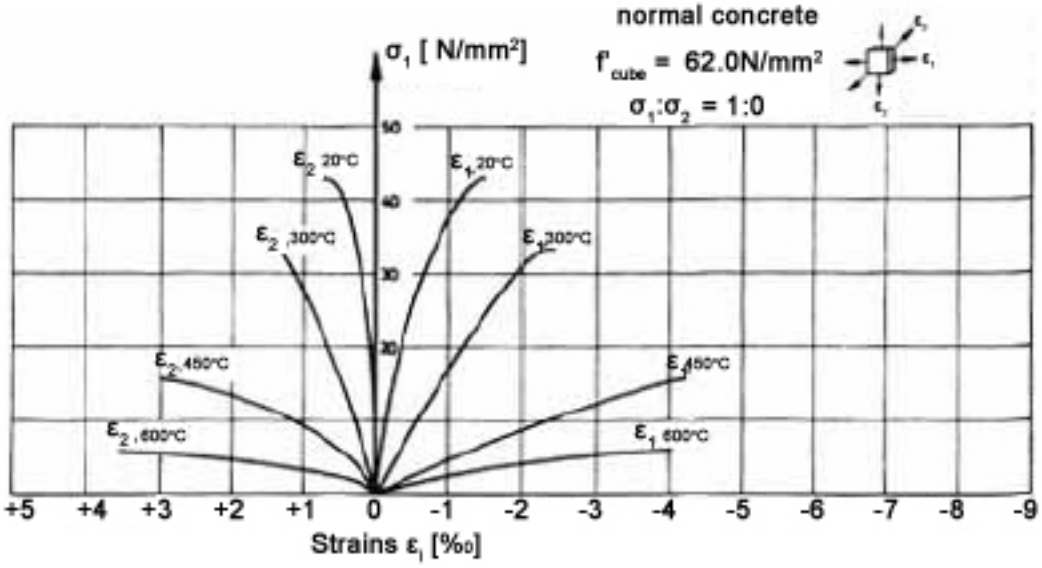

Figure 3-19 Concrete stress-strain relationships at high temperatures with biaxial stress ratios of zero [Ehm et al. 1985]

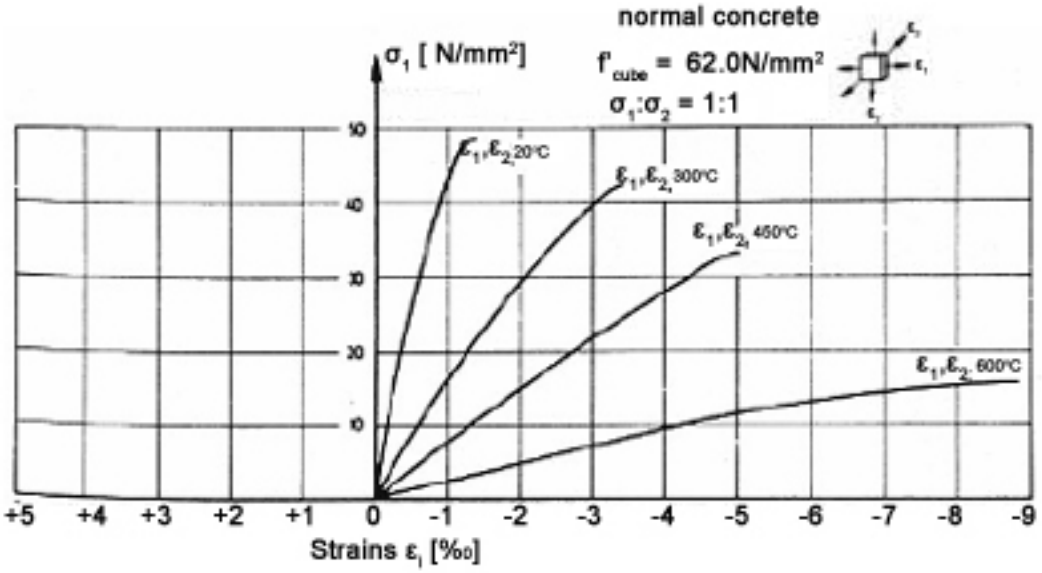

Figure 3-20 Concrete stress-strain relationships at high temperatures with biaxial stress ratios at unity [Ehm et al. 1985]

3.3.2. Tensile strength

The tensile strength of concrete can be measured using a direct tension test and has a stress-strain relationship similar to that shown in Figure 3-21. There are two important phases shown in this figure: in the first phase the behaviour of concrete is almost linearly elastic up to $0.8f_t$, and followed by a non-linear increase up to the peak $1.0f_t$ which corresponds to the equivalent strain of $\varepsilon_{t,1}$. Beyond this phase, micro-cracks in the cement paste propagate and eventually form cracks perpendicular to the principal loading direction.

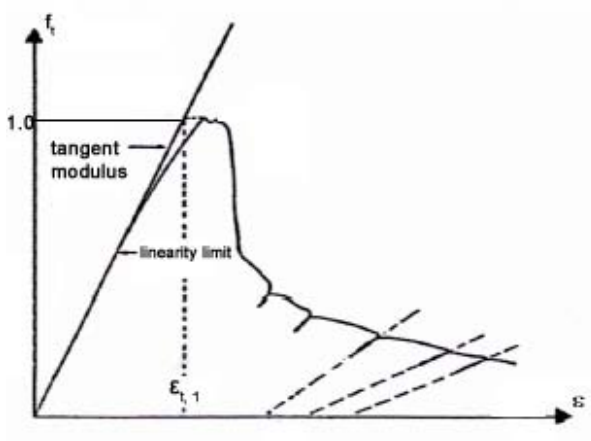

Figure 3-21 Example of stres-strain relationship of concrete in direction tension test [Terrin 1980]

Under the cold condition, the tensile strength of concrete is generally less than 20% of the compressive strength [Park et al. 1975]. Eurocode [EC2 2002], and FIB Bulletin 1 [FIB 1999] provide a method to calculate the mean splitting tensile strength f_{ctm} as a function of the characteristic compressive strength f_{ck} (MPa) as

$$\begin{aligned} f_{cm} &= 0.30\, f_{ck}^{2/3} && f_{ck} \le 50[\text{MPa}] \\ f_{cm} &= 2.12 \ln\left[1 + \frac{f_{ck}+8}{10}\right] && f_{ck} > 50[\text{MPa}] \end{aligned} \qquad \text{Eq. 3-13}$$

and the characteristic tensile strength f_{ctk} is calculated as

$$f_{ctk} = 0.7\, f_{ctm} \qquad \text{Eq. 3-14}$$

Other recommended values for the tensile strength are $0.33\sqrt{f'_c}$ from Bažant et al. [1982] or $0.62\sqrt{f'_c}$ from ACI [Mindess et al. 1981]. However, Lim [2003] found out that using $0.25\sqrt{f'_c}$ (1.5MPa for f'_c of 36MPa) works well in SAFIR for simulating reinforced concrete slabs.

There are a few test results available regarding the tensile strength of concrete at elevated temperatures. Figure 3-22 shows the results from Blundell et al. [1976], Bažant et al[1986], Sager [1985] and Schneider [1985], as well as the Eurocode suggested curve, summarised by Fellinger [2004]. The figure shows that a drop in strength between 80-200^{o}C was found in several studies. The drop is typical for short term heating and is not observed when the specimen is kept at high temperature for a long time before testing. [Diederich et al. 1987; Harmathy et al. 1966].

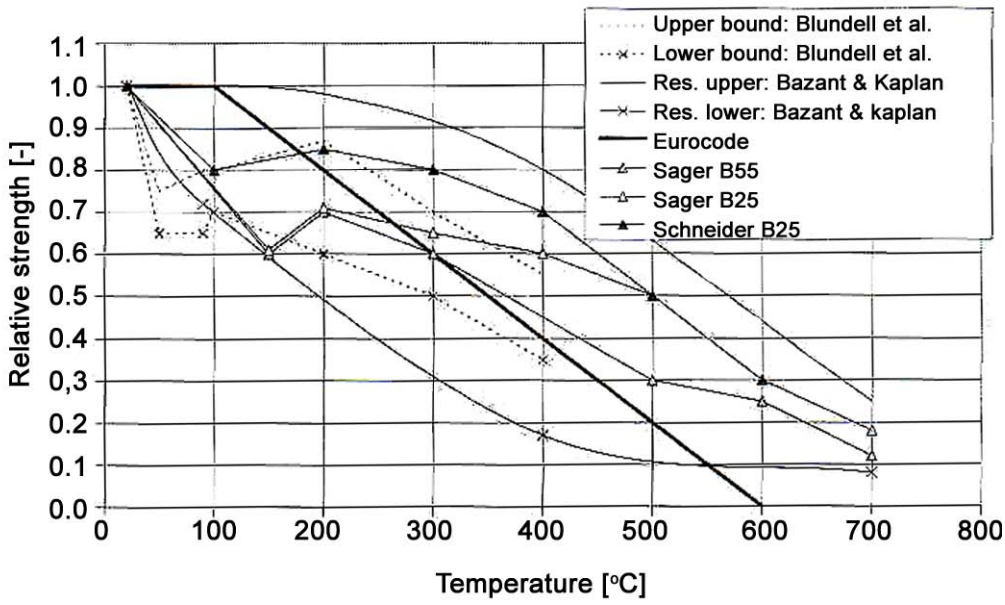

Figure 3-22 Various measurements of the splitting tensile strength of concrete at elevated temperature [Fellinger 2004]

No conclusive explanation has been given about the decrease of tensile strength and stiffness at elevated temperatures. Khoury [1992] explained this phenomenon as the warm evaporable water reducing the surface energy of the gel and the cohesive forces between the calcium-silicate-hydrate layers. Rostásy et al. [1986] found out that the tensile strength and stiffness decreases with the moisture content, but the compressive strength and stiffness may increase for a while when the moisture content decreases as explained in the previous section.

In Eurocode 2 [1995, 2002], the relative strength is estimated as having a linear decrease between 100 to 600^{o}C, and drops to zero when the temperature is higher.

3.3.3. Modulus of elasticity

The modulus of elasticity decreases when the temperature increases; this is due to the bond breakage in the cement paste under high temperatures. The rapid short-time creep can also reduce the modulus of elasticity [Bažant et al. 1996].

The moisture content and the type of aggregates can affect the rate of reduction of the modulus of elasticity in concrete. Figure 3-23 and Figure 3-24 show the influence of using different aggregates on the modulus of elasticity at elevated temperatures. The different values obtained from these two figures might be due to the different levels of moisture content in the specimens. It has been found that aggregates which are more stable chemically, such as limestone, have a lower reduction of stiffness under high temperature; Figure 3-24 shows that siliceous aggregates has a sudden drop of elastic modulus when the temperature exceeds 500^{o}C.

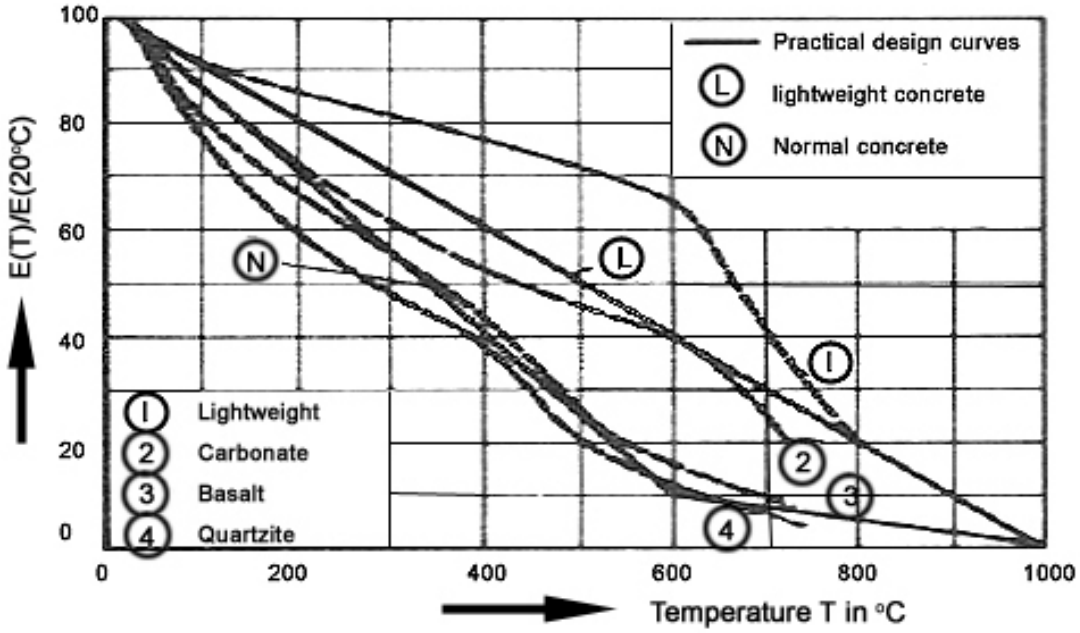

Figure 3-23 Modulus of elasticity according from Schneider [1988]

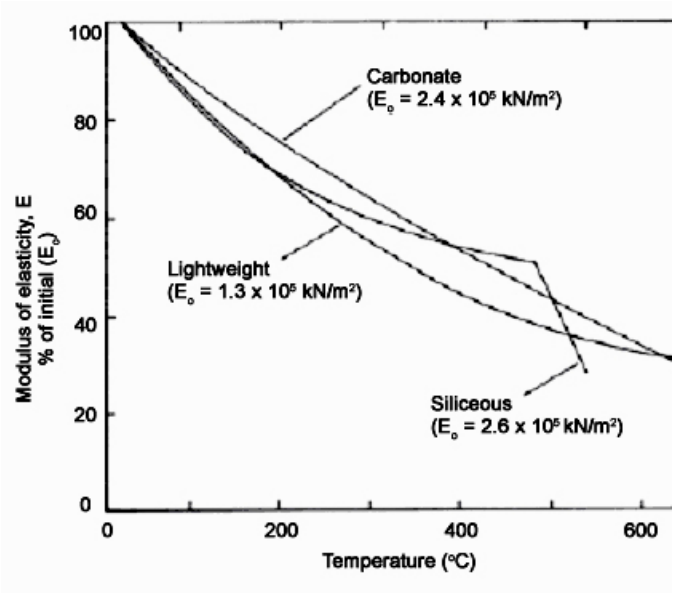

Figure 3-24 Modulus of elasticity from Cruz [1966]

3.3.4. Elastic shear modulus and Poisson's ratio

The shear modulus of elasticity of concrete, G, changes with temperature in a similar manner to the modulus of elasticity, E [Anderberg et al. 1976].

Poisson's ratio of concrete, ν, is around 0.2 at room temperature, and drops to 0.1 when the temperature is raised to 400°C [Maréchal 1972]. This relationship has been shown in Figure 3-25. The regression of Poisson's ratio with increasing temperature is caused by the weakening of microstructure resulting from rupture of bonds at heating. Another possible reason for the reduction is cracking, which can be limited when the heated concrete is restrained or subjected to confined pressure.

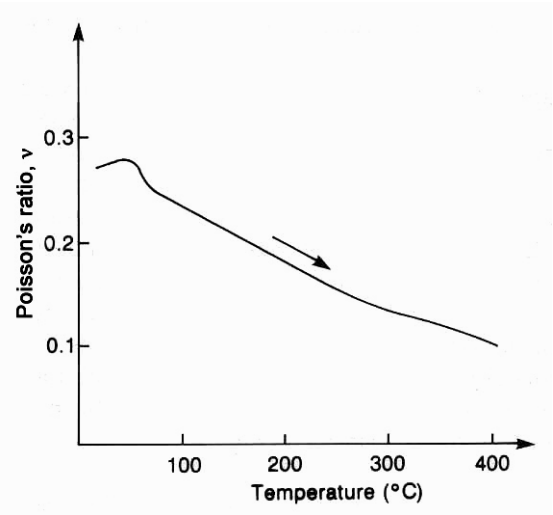

Figure 3-25 Regression of Poisson's ratio of Portland cement/quartzite aggregate concrete with temperature [Maréchal 1972]

3.3.5. Constitutive law

The material in this section is based on the constitutive law for concrete under transient high temperature conditions by Anderberg et al. [1976]. The equations are extracted from Anderberg et al. [1976] unless otherwise stated.

When a concrete structure member is exposed to fire, the total strain within such member, ε_T , can be break down into four parts as:

$$\varepsilon_T = \varepsilon_{th}(\theta) + \varepsilon_{\sigma}(\tilde{\sigma}, \sigma, \theta) + \varepsilon_{cr}(\sigma, \theta, t) + \varepsilon_{tr}(\sigma, \theta) \qquad \text{Eq. 3-15}$$

where $\varepsilon_{th}(\theta)$ is the thermal strain and depends only upon the temperature within the structure, $\varepsilon_{\sigma}(\tilde{\sigma}, \sigma, \theta)$ is the mechanical strain being a function of stress history $\tilde{\sigma}$, applied stress σ, and of temperature θ; $\varepsilon_{cr}(\sigma, T, t)$ is the creep strain which is a function of applied stress, and temperature as well as time t; and $\varepsilon_{tr}(\sigma, \theta)$ is the transient strain which is a function of applied stress and time.

Thermal Strain, $\varepsilon_{th}(\theta)$

Thermal strain is the unrestrained thermal expansion of concrete. This is a function of temperature and follows the measured thermal expansion curve. Thermal strain includes shrinkage which depends on the initial thermal content. Details of thermal expansion of concrete were given in Section 3.1.4.

Mechanical strain, $\varepsilon_{\sigma}(\tilde{\sigma}, \sigma, \theta)$

Mechanical strain, or stress-related strain, is the strain which induces stresses in the structural members following the stress-strain relations of concrete.

Figure 3-26 shows a typical stress-strain relationship in cold conditions. Figure 3-26(a) shows that the stress-strain relationship is almost linear until reaching 30% of the maximum compressive strength f_c'. After this point, the curvature of the line increases slowly until around 0.75 f_c' to 0.90 f_c' due to progressive microcracking in concrete, and then the curvature increases rapidly until reaching the peak point f_c'. After this point, the curve starts descending until reaching the ultimate strain ε_u where crushing failure would occur. The post-peak descending branch is associated with the lateral expansion and reverses the direction of the volume change, which is shown in the stress and volumetric strain relation in Figure 3-26(b).

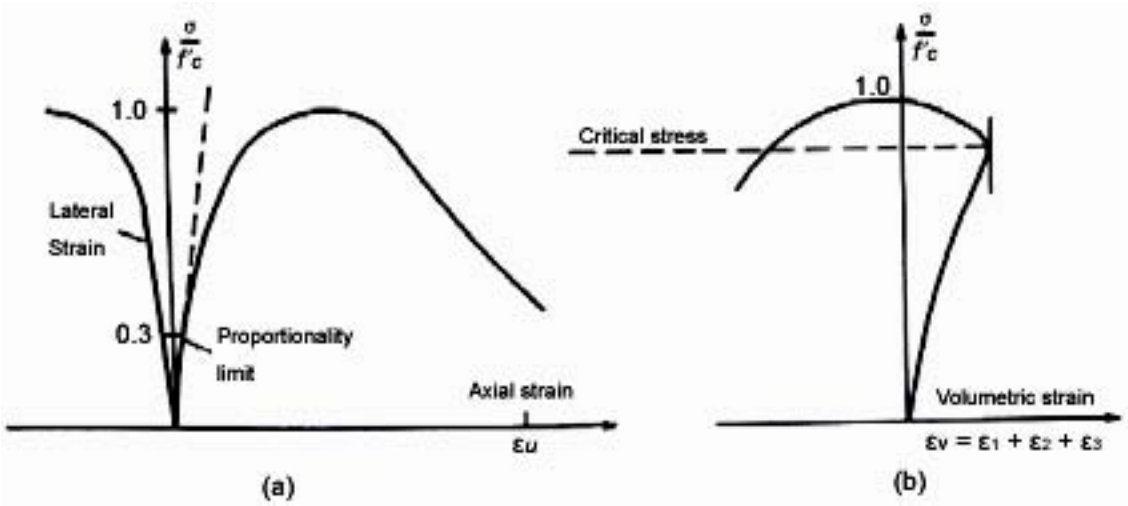

Figure 3-26 Typical plot of compressive stress against axial, lateral and volumetric strain [Chen 1982, fig 2-1]

Anderberg et al. [1976] found out that the stress-strain relations change with the current temperature and the pre-history of stress. The stress-strain relationships of concrete without bearing loads for different temperatures are shown in Figure 3-27. The figure shows that the ultimate strain increases with increasing temperature while the ultimate stress decreases. Weigler et al. [1967] found out that for the same temperature range, preloaded specimens give higher strength and smaller strains than those shown here. The test results from Schneider [1976] are shown in Figure 3-28 and confirm the same finding. The details of this phenomenon were described in Section 3.3.1.

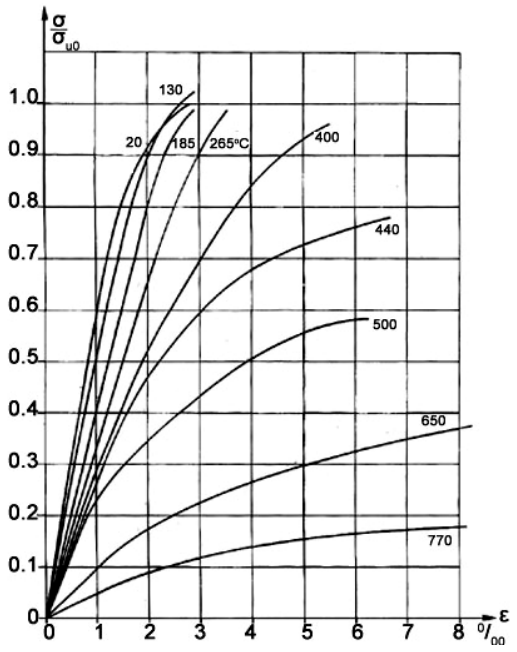

Figure 3-27 Stress-strain relations for different temperatures [Anderberg et al. 1976, fig 20]

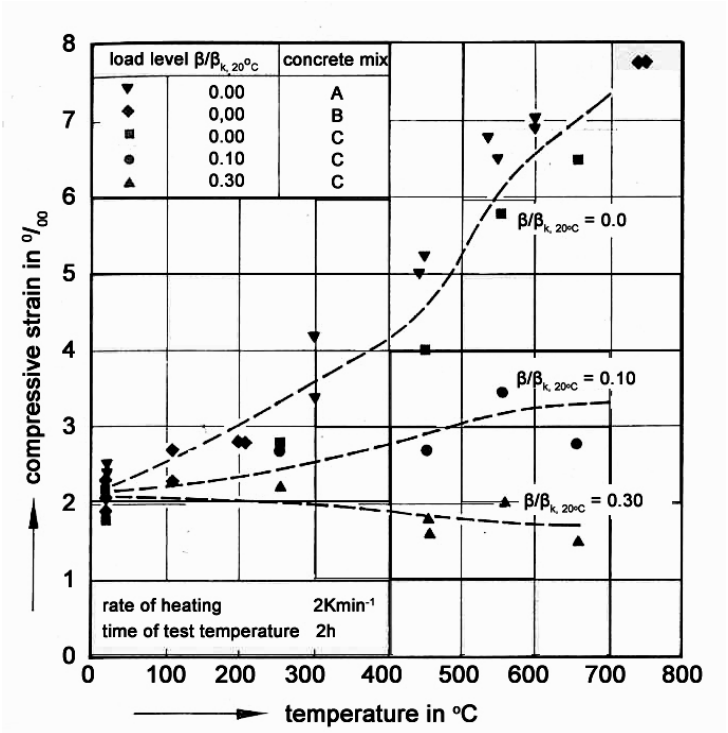

Figure 3-28 Compressive strains at failure of concrete specimens subjected to different load levels during heating [Schneider 1976]

Eurocode 2 [2002] specifies the strength and deformation relationship of uniaxial stressed concrete with a shape shown in Figure 3-29. Range I of the model is expressed as

$$\sigma(\theta) = \frac{3\varepsilon \cdot f_{c,\theta}}{\varepsilon_{c1,\theta}\left(2 + \left(\frac{\varepsilon}{\varepsilon_{c1,\theta}}\right)^3\right)} \qquad \text{for } \varepsilon < \varepsilon_{c1,\theta} \qquad \text{Eq. 3-16}$$

and the values for $f_{c1,\theta}$ and $\varepsilon_{c1,\theta}$ are shown in Table B-1 in Appendix B. In Range II, the descending branch, both linear and non-linear models shown here are permitted to be used in design.

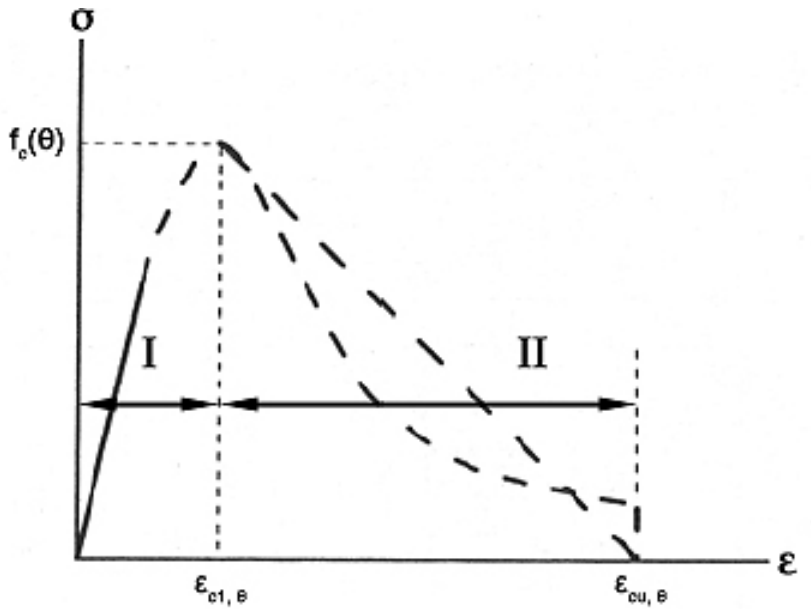

Figure 3-29 Model for compression stress-strain relationships for siliceous and calcareous concrete at elevated temperatures [EC2 2002]

Following the same trend of thought, the constitutive laws can be used to trace back the thermal stress, as in most situations the thermal strain and total strain can be obtained easily, and the thermally induced mechanical strains or the thermal stresses are calculated later based upon equilibrium. The graphical representation of this method in a simply supported slab is shown in Figure 3-30.

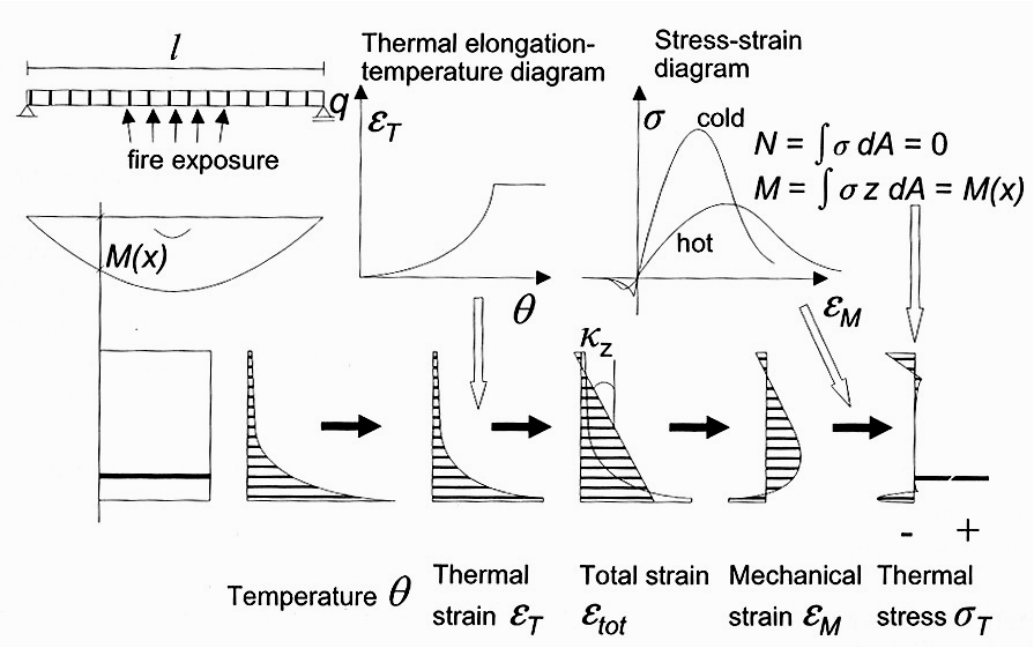

Figure 3-30 Graphical representation of the calculation of thermal stresses in a simply supported slab [Fellinger 2004]

3.3.6. Creep Strain, $\varepsilon_{cr}(\sigma,\theta,t)$

Creep strain is the long-term deformation of materials under constant load. In most conditions under ambient temperature, creep only becomes a problem when the applied permanent loads are high [Buchanan 2001]. The basic creep ε_{cr} at constant temperature and constant stress has the following relationship: [Anderberg et al. 1976]

$$\varepsilon_{cr} = \beta \frac{\sigma}{\sigma_u(\theta)} \left(\frac{t}{t_r} \right)^P e^{k_1(\theta-20)} \qquad \text{Eq. 3-17}$$

where

$\beta = -0.53 \cdot 10^{-3}$
$\sigma_u(\theta)$ = ultimate stress at temperature θ
t = time
t_r = 3 hours
P = 0.5
$k_1 = 3.04 \cdot 10^{-3}\ ^oC^{-1}$

Figure 3-31 shows the change of creep strain with time. It shows that when the temperature and the stress vary with time, the basic creep follows the strain hardening principle, which means the stiffness and strength of the material increase with plastic deformation, and further plastic deformation would happen only when the previous maximum stress is reached. The effects of creep are implicitly allowed in the stress-strain relationships and not explicitly defined in the Eurocode.

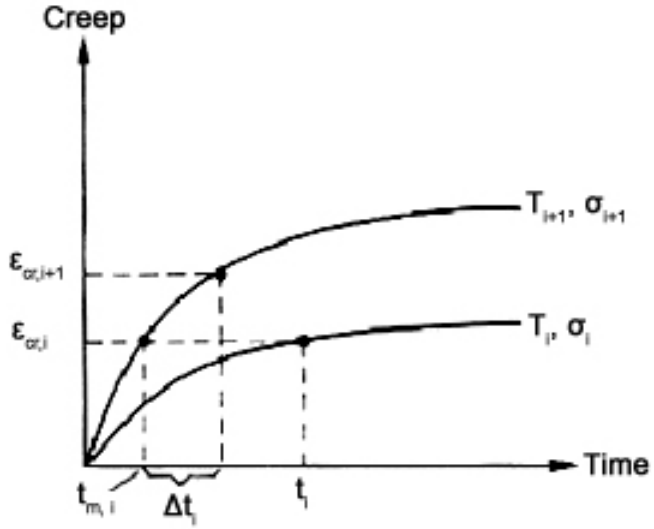

Figure 3-31 The principle of strain hardening for creep [Anderberg et al. 1976]

3.3.7. Transient strain, $\varepsilon_{tr}(\sigma,\theta)$

Transient strain is caused by expansion of cement paste when it is heated for the first time under load. This has been named differently in different researches and has been discussed in detail in Section 3.1.4 “Transitional thermal creep”. Transient strain cannot be measured directly and must be calculated from the remaining four strain components as the equation shown below [Anderberg et al. 1976].

$$\varepsilon_{tr} = \varepsilon_T - \varepsilon_{th} - \varepsilon_\sigma - \varepsilon_{cr} \qquad \text{Eq. 3-18}$$

The relative magnitude of each component of strain is shown in Figure 3-32. It has been found that for siliceous aggregate concrete, when the temperature is below 500^{o}C the transient strain is of opposite sign to the thermal strain. The graph also shows that the transient strain significantly affects the total strain, which is the measured local deflection.

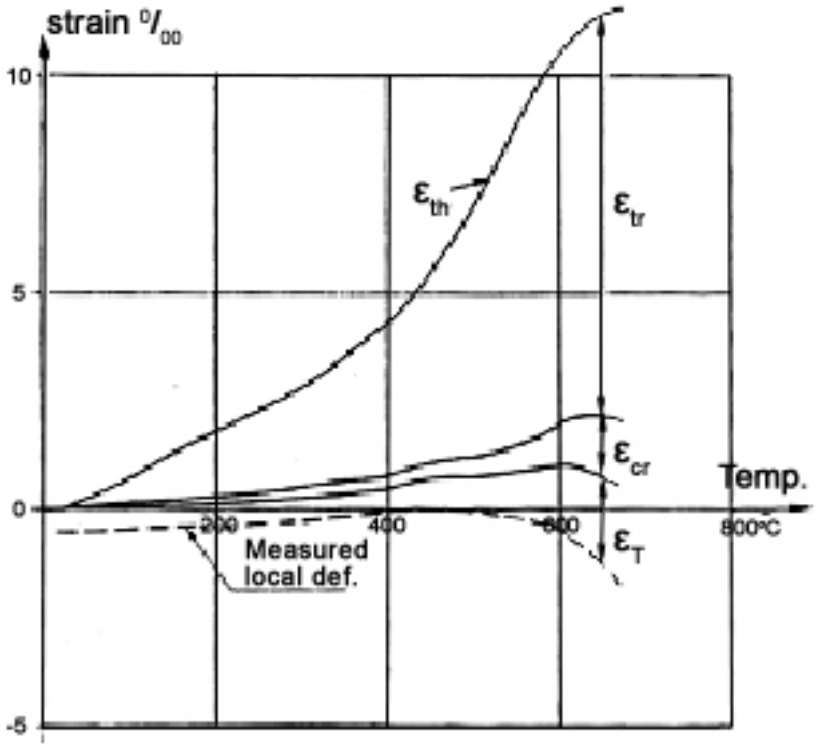

Figure 3-32 Component of total strain [Anderberg et al. 1976]

3.4. Mechanical Properties of Steel

3.4.1. Ultimate and yield strengths

Most normal construction steels have a well-defined yield strength at normal temperature, but this disappears at elevated temperatures as shown in Figure 3-33. Figure 3-34 shows the test results on the ultimate and yield strength of cold-formed steel from various researches collected by Harmathy [1993], which are based on a multitude of data gathered from Simmons & Cross [1955], Brockenbrough & Johnson [1968], Bobrowski [1978], Harmathy & Stanzak [1970], Bennetts [1981], Holmes et al. [1982] and Anderberg [1983]. The yield strength is well-defined in the test results until reaching 300^{o}C due to partial coalescence of dislocations due to their greater mobility [Harmathy 1993]. At higher temperatures, the effective yield strength is recommended by Kirby & Preston [1988] to be the 1% proof strength as illustrated in Figure 3-33. The 1% proof strength was chosen because the experimental results by Kirby & Preston [1988] showed that once the strain exceeds 1%, the specimen starts to have a "runaway" situation.

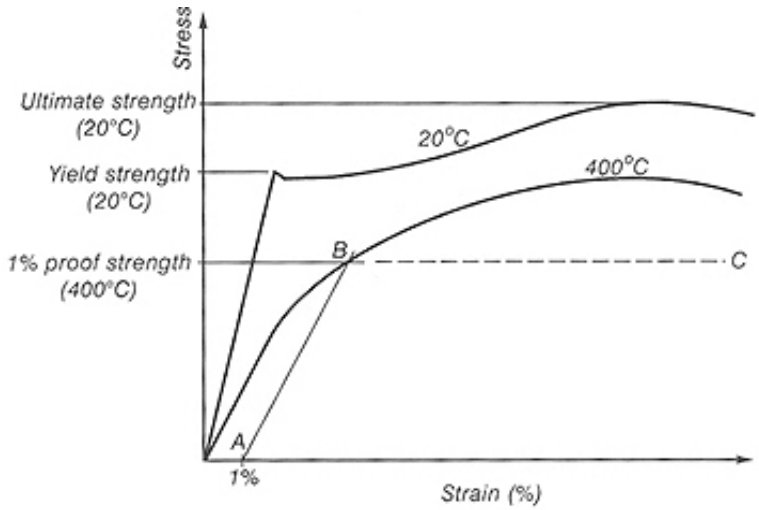

Figure 3-33 Stress-strain curves for steel illustrating yield strength and proof strength [Buchanan, 2001]

Figure 3-34 shows that there is a significant scatter in the yield and ultimate strengths from the different tests. The dotted curve shows the recommended relationship by The Institution of Structural Engineers [1975] for both yield and ultimate strength.

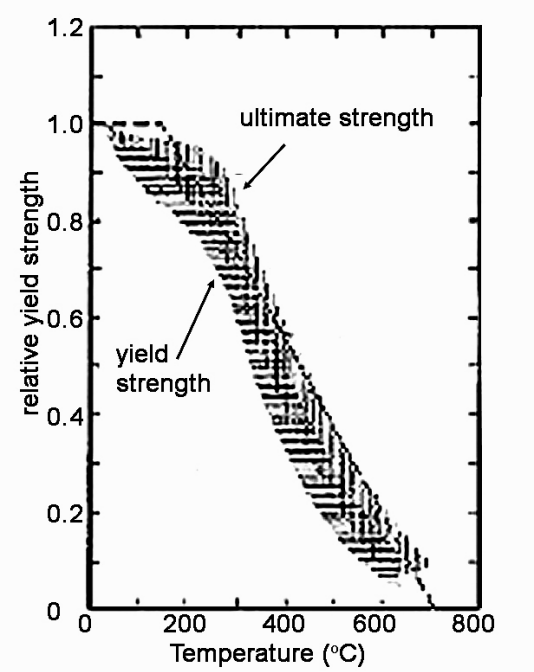

Figure 3-34 Ultimate and yield strength of cold-worked steel [Harmathy 1993]

Even though reinforcing steel and prestressing steel are both cold formed, they are given different strength reduction relationships in Eurocode 2 [EC2 2002]. Figure 3-35 and Figure 3-36 show the strength reduction factors for reinforcing and prestressing steel respectively. The stress strain relationship includes, in an approximate manner, the effect of high temperature creep. The material model is applicable only for heating rates similar to those under the standard fire conditions.

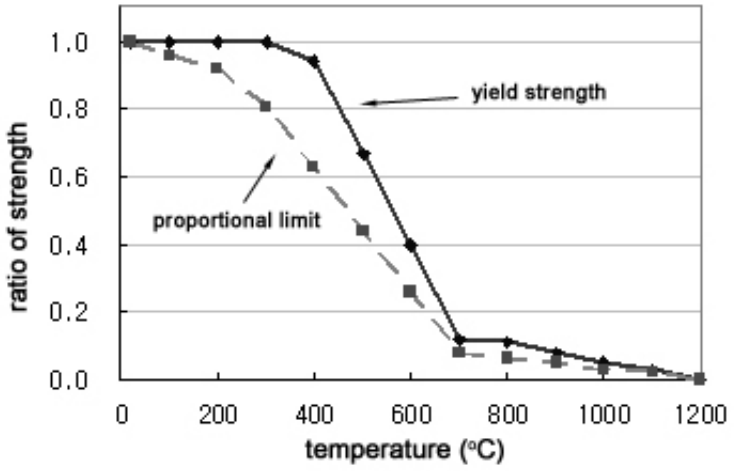

Figure 3-35 Strength reduction factor for reinforcing steel [EC2 2002]

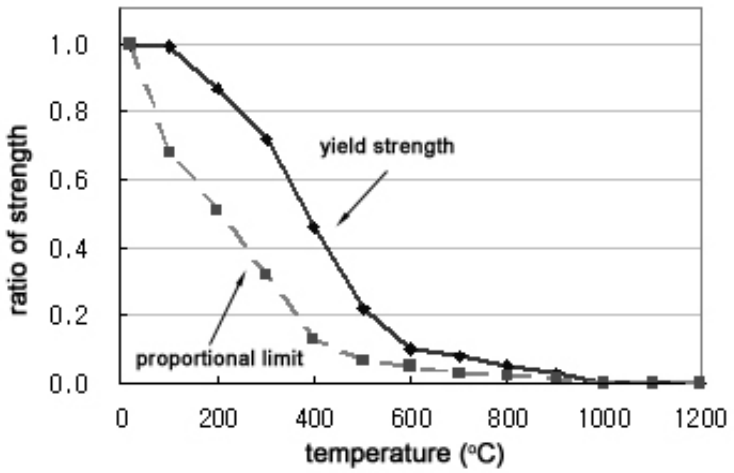

Figure 3-36 Strength reduction factor for cold formed prestressing steel [EC2 2002]

3.4.2. Modulus of elasticity

Modulus of elasticity in either ambient or elevated temperatures is defined as the tangent-stiffness following the gradient of linear-elastic portion as shown in Figure 3-33. Under increasing temperature, the modulus of elasticity of steel reduces in a similar fashion to the yield strength. Harmathy [1993] compared the effect of temperature on the elasticity of steel and the results are shown in Figure 3-37.

Eurocode 2 [EC2 2002] acknowledges that the modulus of elasticity in reinforcing steel reduces faster than in prestressing steel with increasing temperature, and the relationships of modulus of elasticity from Eurocode 2 are shown in Figure 3-38. The red and green lines are from Figure 3-37. It is apparent that the Eurocode 2 gives a greater reduction on the modulus of elasticity in elevated temperatures than that observed by Harmathy [1993].

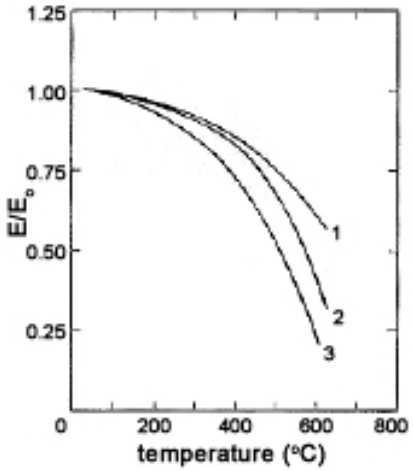

Figure 3-37 Variation of modulus of elasticity of steel with temperature (1) Structural steel (2) Prestressing steel (3) Reinforcing steel [Harmathy 1993]

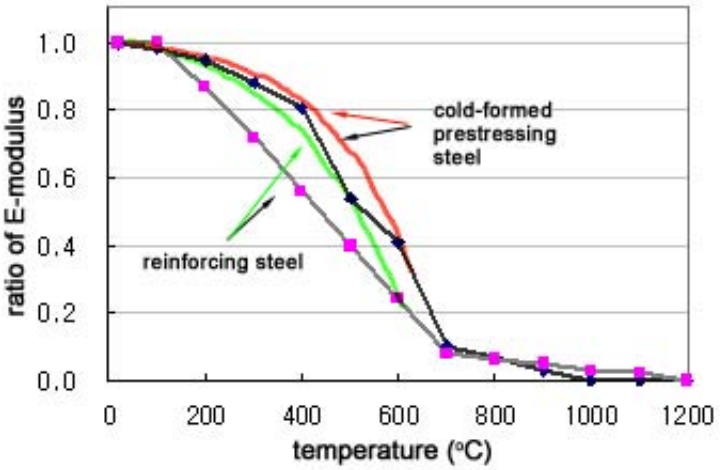

Figure 3-38 Variation of E-modulus with temperature for cold worked reinforcing steel and prestressing steel according to EC2 [EC2 2002]

3.4.3. Components of strain

The total strain of steel at elevated temperature is expressed by the following equation. The transient strain does not exist in steel.

$$\varepsilon_T = \varepsilon_{th}(\theta) + \varepsilon_\sigma(\tilde{\sigma}, \sigma, \theta) + \varepsilon_{cr}(\sigma, \theta, t) \qquad \text{Eq. 3-19}$$

where

ε_T = total strain
θ = temperature
$\tilde{\sigma}$ = stress history
σ = stress
t = time
$\varepsilon_{th}(\theta)$ = thermal strain
$\varepsilon_\sigma(\tilde{\sigma}, \sigma, \theta)$ = mechanical strain
$\varepsilon_{cr}(\sigma, \theta, t)$ = creep strain

Thermal strain, $\varepsilon_{th}(\theta)$

The thermal strain of steel is the thermal expansion that occurs when steel is heated. Details of the thermal expansion of steel have been discussed in Section 3.2.3.

Mechanical strain, $\varepsilon_\sigma(\tilde{\sigma}, \sigma, \theta)$

Mechanical strain of steel, or stress-related strain of steel, can be measured directly from steady-state tests. Typical stress-strain relationships of steel at various temperatures are shown in Figure 3-39. This curve shows both the yield strength and modulus of elasticity decrease with increasing temperature.

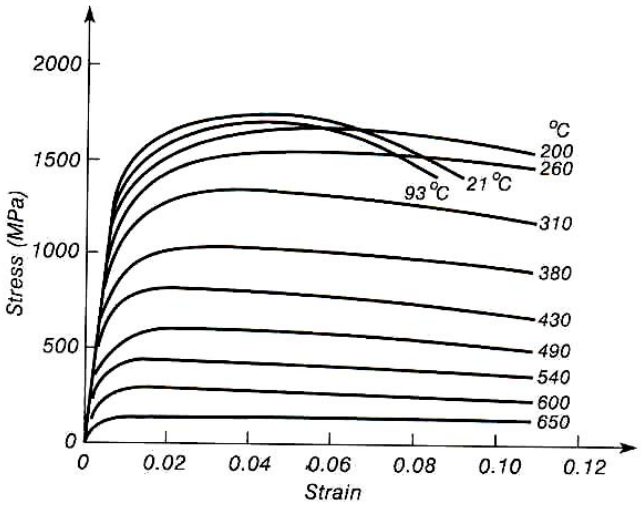

Figure 3-39 Typical stress-strain curves for prestressing steel at elevated temperature [Harmathy 1993]

In Eurocode 2, the stress-strain relationship of steel is defined by three parameters:

1. the slope of the linear elastic range $E_{s,\theta}$
2. the proportional limit $f_{sp,\theta}$
3. the maximum stress level $f_{sy,\theta}$

Figure 3-40 shows the stress-strain relationships of hot-rolled structural and reinforcing steels at elevated temperatures according to Eurocode 2 [EC2 1995].

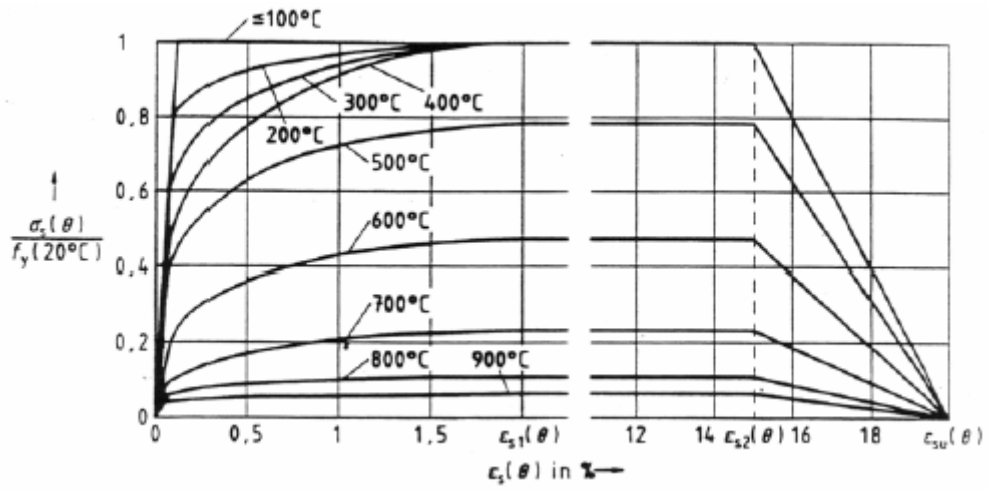

Figure 3-40 Stress strain relationships of steel at elevated temperatures [EC2 1995]

Creep strain, $\varepsilon_{cr}(\sigma,\theta,t)$

Creep strain is relatively unimportant in structural steel at normal temperatures, but it becomes very significant in temperatures over 400 or 500^{o}C. Figure 3-41 shows the tests results of steel creep from Kirby et al. [1988]. It shows that the creep strain is highly dependent on the temperature and stress level of the steel. When a steel member of a particular stress level reaches a critical temperature, the member becomes plastic and the runaway failure occurs as a result of rapid increase in creep strain.

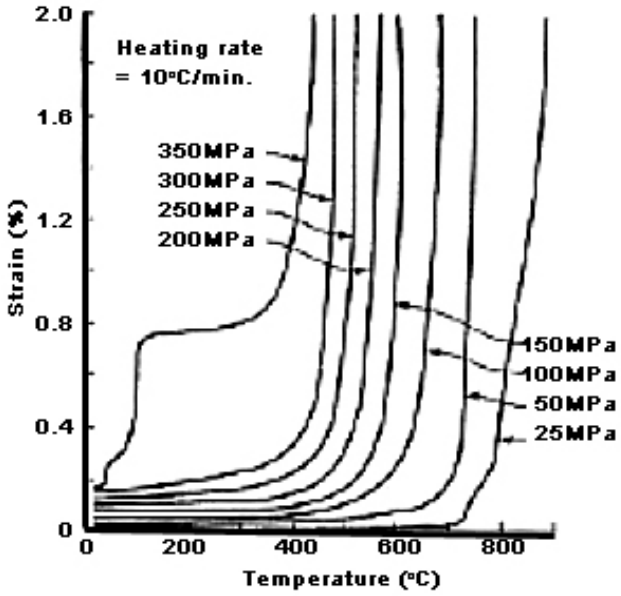

Figure 3-41 Creep of steel tested in tension [Kirby et al. 1988]

4. Review of Fire Behaviour of Hollowcore Concrete Slabs

This chapter presents the structural behaviour of hollowcore concrete slabs in ambient conditions and in fire gathered from the literature. The first part of this chapter will outline the structural behaviour of hollowcore concrete slabs under ambient conditions. The second part will describe the structural behaviour of these slabs in fire tests. The third part presents the shear and anchorage behaviour of hollowcore concrete slabs. The shear and anchorage failure mechanism is presented in more detail than that for flexural failure in this chapter because it is ignored in the simulations presented later which focus solely on the flexural failure mechanism, and recommendations on overcoming the shear and anchorage failure in Chapter 12 are based upon Fellinger [2004] which is summarised here.

4.1. Structural Behaviour of Hollowcore Concrete Slabs in Ambient Conditions

This section outlines the basic structural behaviour of hollowcore concrete slabs under gravity load at ambient temperatures.

4.1.1. Flexure

Figure 4-1 shows the breakdown of the stress distribution within a prestressed concrete member, where β_1 and β_2 are shape factors for the concrete section, d is the total height of the element, h_x is the height of the compressive zone, and f_c is the compressive strength of the concrete. Before applying loads, the prestressed strands are in tension, and through equilibrium the concrete is in compression as shown in Figure 4-1(a). Figure 4-1(c) shows the bending moment caused by mechanical loading, which reduces the compressive stresses at the bottom of the concrete. Afterwards the load becomes large enough, the tensile stresses at the bottom of the concrete reach the tensile strength limit of concrete and cause flexural cracks which grow upwards from the bottom of the slab, and the tensile stresses are consequentially released in the crack and taken over by the strands, causing a local stress increase in the strands. The stress distribution at this stage is shown in Figure 4-1(d). Loads added after the formation of cracks increase both the tensile stress in the strand and the compressive stress in the compression zone of concrete as shown Figure 4-1(e). In design the number of strands in the slabs has to be sufficient so that the localised stress increase

does not cause the strands to yield, but the strands should reach the yield limit before the induced compressive stress causes crushing in the concrete compression zone. In cold conditions, rupture of the strands will occur after significant yielding and large deflection [Fellinger 2004].

As the hollowcore concrete slabs have a known ultimate limit state flexural strength, the occurrence of a flexural failure depends on strands becoming plastic under tension or concrete crushing under compression, but the latter case is less likely to happen [FeBe Studiecommissie SSTC 1998].

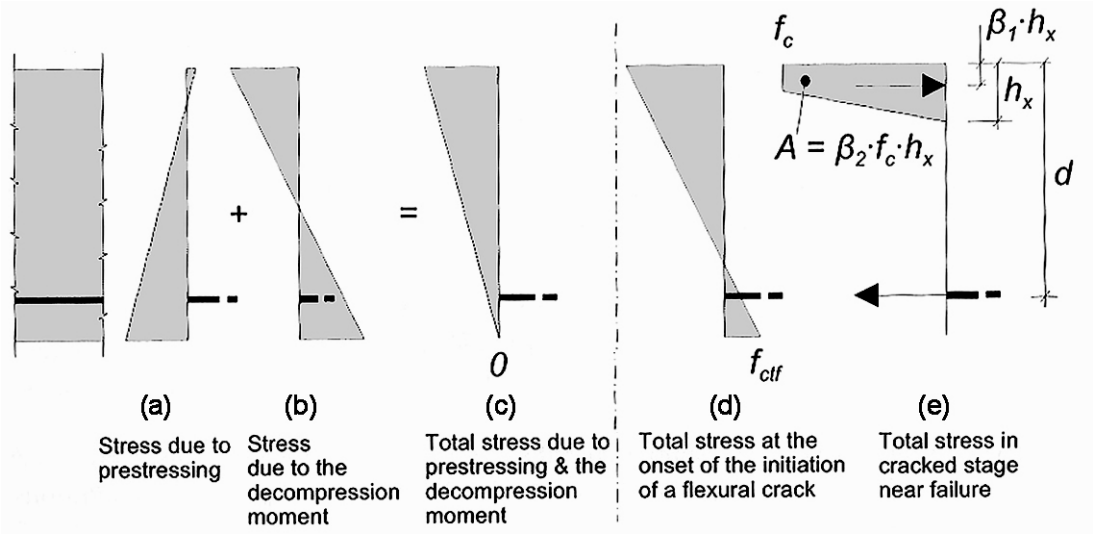

Figure 4-1 Linear elastic stress distribution over the height of the cross section due to prestressing and bending moments and non-linear stress distribution in the crack close to flexural failure [Fellinger 2004]

4.1.2. Floor diaphragm action

Hollowcore concrete slabs can function as floor diaphragms to transfer lateral loads. The lateral loads are transferred as shear forces between adjacent members and eventually to the supporting elements [Fellinger 2004]. Whether the transfer can happen or not relies on the stiffness, strength and ductility of the joints between each hollowcore unit and of the topping. However, the study by Davies et al. [1990] showed that the hollowcore concrete slabs are able to establish floor diaphragm action through the joints alone. The shear capacity can be increased by increasing the concrete strength or increasing compressive stress which can be achieved by using higher prestressing levels.

4.1.3. Shear compression

Shear compression failure starts with flexural cracks, so it is also referred to as "flexural shear failure". The information in this section is from Fellinger [2004] unless stated otherwise. As with all typical reinforced concrete beams, inclined shear cracks are developed from flexural cracks in areas where there are both the bending moment and shear forces. After the flexural crack occurs, the tensile forces are carried by the strand, and the stress in concrete is released at the crack area and helps the crack growth. The flexural cracks are vertical near the centre of beam, but they are more inclined near the supports where shear forces are higher. The concrete behind the crack is unloaded of tensile stress as shown in Figure 4-2. With the increase in the crack length, the unloaded concrete zone increases, and as a result, it requires lower loads to enlarge the cracks than to develop new smaller cracks.

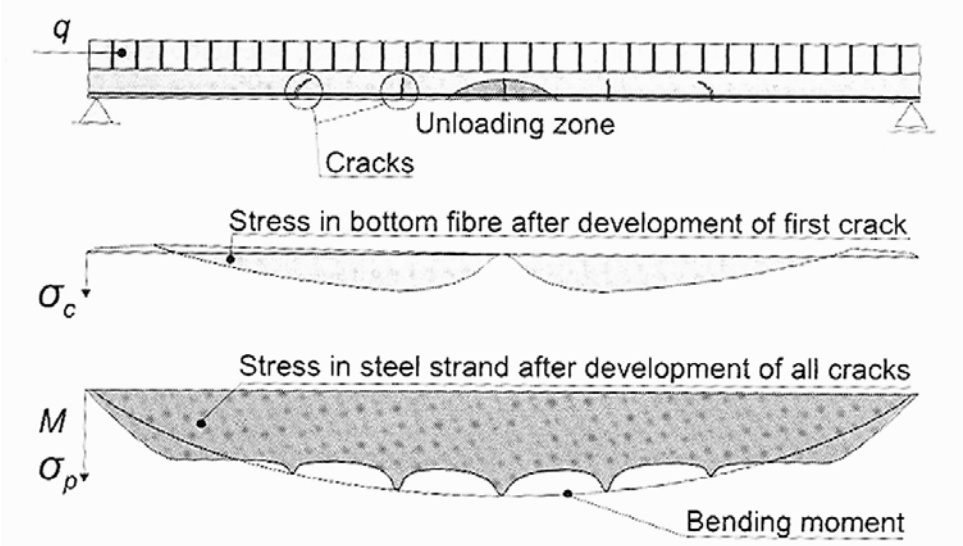

Figure 4-2 Development of flexural cracks and shear cracks and axial stress in bottom fibre of the concrete cross section and in the steel strands [Fellinger 2004]

A new state of equilibrium is found after the flexural crack is developed. Kani [1964] stated that the concrete beam transformed into a comb-teeth like structure because of the flexural cracks, as the compression zone of the beam being the backbone of the comb, and the tensile zone being the teeth separated from each other by flexural cracks as shown in Figure 4-3. The teeth of the structure are linked by the compressive zone and loaded by the bond stresses between the reinforcement and the confining concrete as cantilever beams.

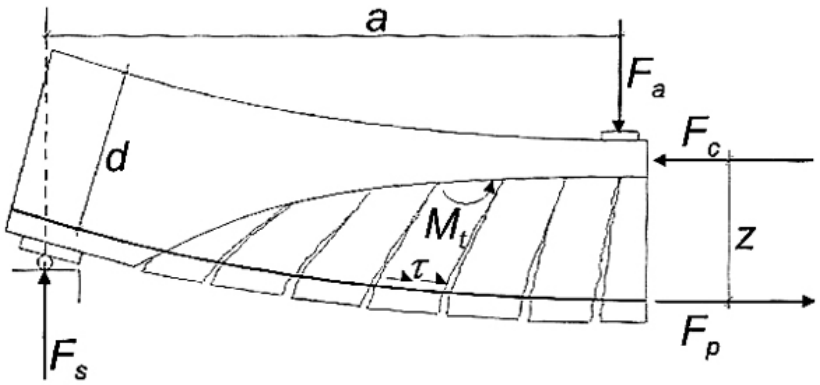

Figure 4-3 Analytical comb-teeth model from Kani [1964]

Even after cracking, concrete sections will still have some remaining shear capacity, as the shear force is transmitted by aggregate interlock in the crack, the dowel action of the strand and by the uncracked concrete in the compression zone. In normal reinforced concrete, shear is resisted by vertical stirrups. Hollowcore concrete slabs have no shear reinforcement, so the mechanism of shear transfer across cracks in concrete is the combination of aggregate interlock and dowel action [Elliott et al. 1992].

If the cracks are not opened, the shear force can be transmitted via the friction of the rough crack surface. This is called “interlocking effect”, and has been studied thoroughly by Davies et al. [1990] and Elliott et al. [1992]. The shear transfer capacity between hollowcore concrete units also relies on the interlocking effect. This effect can be found in both ambient and heated conditions [FeBe Studiecommissie SSTC 1998].

Dowel action uses the shearing and flexure of the bars which pass through the crack to transfer the shear force. This action can be either the clamping action which uses tie steel to generate the stress normal to the shear plane, or dowel kinking which includes the shear resistance of the tie steel itself [Elliott et al 1992]. In hollowcore concrete slabs the only dowel action available is from the prestressing tendons. Maintaining shear capacity across the cracks is also important for the slabs exposed in fires as observed in the fire tests from Universities of Ghent and Liège [FeBe Studiecommissie SSTC 1998]. After the initiation of the crack, the capacity of all contributions gradually decreases until failure is reached.

4.1.4. Shear tension

Another type of shear failure which may occur under loading in hollowcore concrete units is called shear tension failure. The information in this section is from Fellinger [2004] unless stated otherwise. Shear tension failure is induced by the cracking in the web near the supports due to shear stresses. This is different from the shear compression which is caused by flexural tensile stress in the lower flange. Because there is no reinforcement in the web to take over the tensile forces, and no load distribution could be established once the shear tensile cracks are formed which causes the shear tension capacity of the web to diminish immediately, the mode of shear tension failure in hollowcore concrete units is brittle. This also shows that the shear capacity of hollowcore slab relies entirely on the tensile strength of the concrete section in the hollowcore units.

The concentration of shear stress in the web is caused by the cross-sectional shape of the hollowcore slabs. The schematic drawing of the shear stress distribution along the thickness is shown in Figure 4-4. Based on the theory of elasticity and Bernoulli's hypothesis that a normal cross-sectional plane remains plane, the bending stresses are distributed linearly along the depth. The principal tensile stress is the combination of shear stress, which is T_{xz} in Figure 4-4, and axial stress, which is σ_{xx}, and has an inclination of approximately 45 degrees.

The maximum principal tensile stress is found in the thinnest part of the web near the supports. This is because the maximum shear stress occurs at the supports, and the prestress, which can reduce the principal tensile stress, is not fully developed at the ends of the slab.

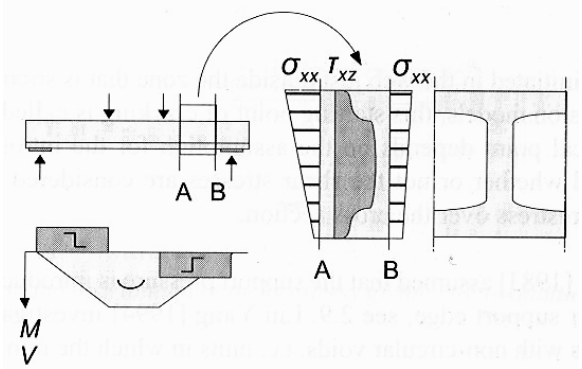

Figure 4-4 Schematic bending stress distribution (including prestress) and shear stress distribution over the depth of a hollowcore concrete slab [Fellinger 2004]

The cracks will be initiated in the web in a zone close to, but not exactly at, the supports. This is because the stress distribution in that area is influenced by the vertical support pressure. As shown in Figure 4-5, near the supports the compression force in the upper flange is transformed into a vertical pressure. Because of this local compressive stress which is found only near the supports, the principal tensile stress at the supports is reduced. In the close vicinity of the support, the slab can even act as a tied arch, which means in hollowcore concrete units the support pressure is directly transferred through a concrete arch tied by the strands to the point load, and the cracks in the webs caused by the principal tensile stress will occur outside the area that is strengthened by the support pressure.

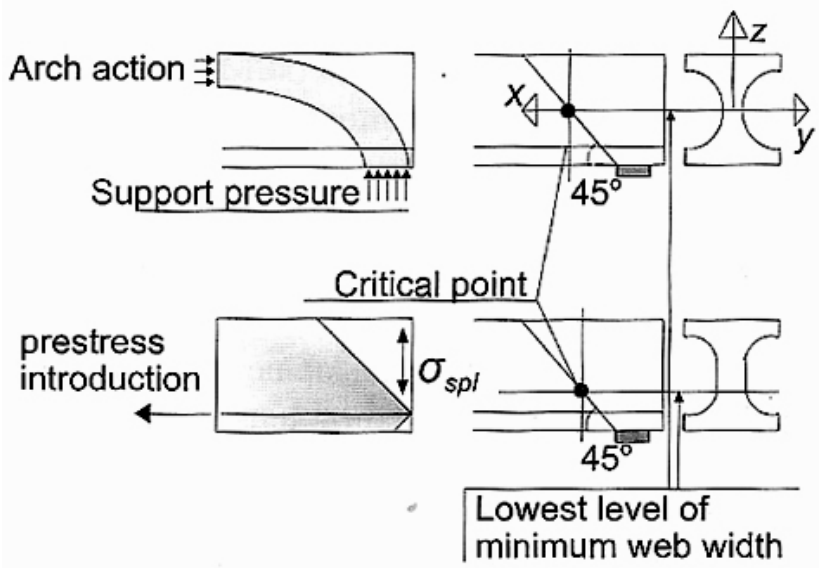

Figure 4-5 Location of critical point in arch analogy [Fellinger 2004]

The discussions so far focused on the principal tensile stresses calculated based upon the theory of elasticity with Bernoulli's hypothesis, i.e. the beam theory. However, the beam can also act like a tied arch. In the beam theory, the compressive thrust line is located at the top of the cross section, and the principal tensile stress that caused shear tension failure are induced by the curvature of the compressive thrust. In the arch analogy, the compressive thrust is fully tied at the supports. The horizontal component of the compressive force is constant in the arch and transfers completely to the tie at the supports. The tensile stresses are perpendicular to the curved thrust line, and no shear stresses arise in the arch. The minimum size of the tensile stresses in the arch to maintain equilibrium decreases with increasing anchorage. Figure 4-6 shows the thrust lines defined by the beam theory (a), arch analogy (b) and by the

ultimate steel stress limited by bond of the strands (c). The actual thrust line lies between a and b. Both the actual location of the thrust line and the size of the tensile stress depend on the constitutive and kinematic relations.

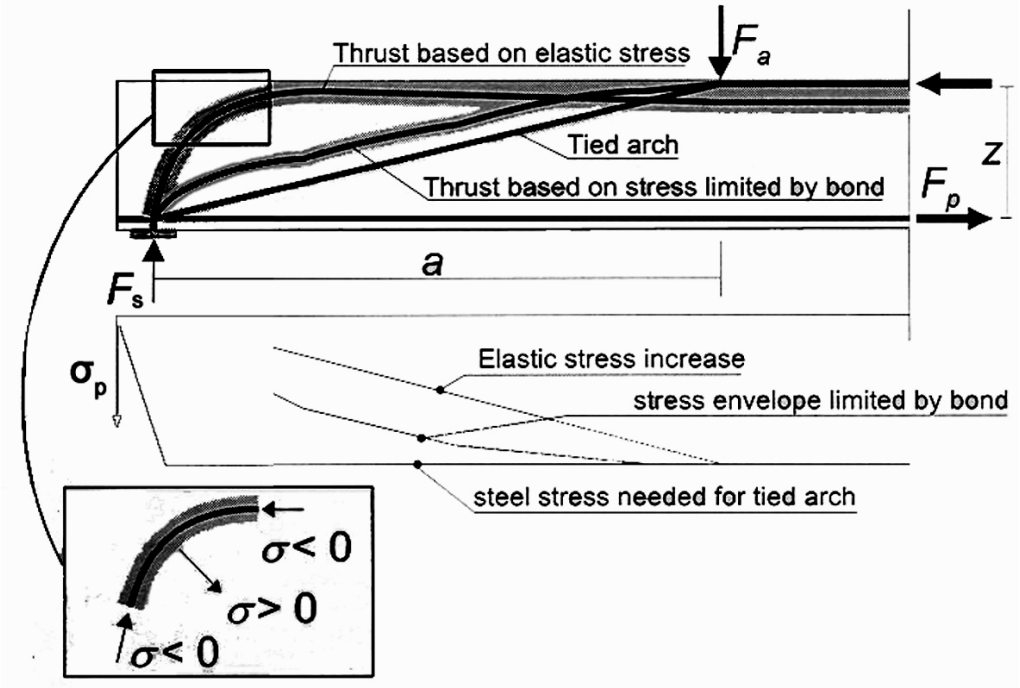

Figure 4-6 Location of the compressive thrust [Fellinger 2004]

More information on the tensile shear stresses can be found in Kani [1964] about the formation of tied arch in general, and Fellinger [2004] regarding specifically on hollowcore concrete units.

4.1.5. Anchorage failure

Anchorage of the strands causes splitting stresses in the plain concrete. The anchorage capacity drastically decreases once a splitting crack is developed. In ambient conditions, anchorage failure can be either brittle or ductile, depending on the loading configuration and the location of the flexural crack. Brittle anchorage failure occurs if the flexural crack is near the ends of the slab. Because close to the ends of the slab the tensile stress released from the cracked concrete can not be translated in the strand, the strand is pulled out immediately, and the anchorage capacity equals the cracking moment resistance. Ductile anchorage failure occurs if the initial stress increment due to cracking can be sustained by the strand, but the later added load increases the stress within the strands and causes the strand to pull out before it yields [Fellinger 2004].

4.2. Structural Behaviour of Hollowcore Concrete Slabs in Fire Tests

To the author's knowledge, there have been no known structural failures in buildings constructed using hollowcore concrete floor system that have occurred during fire. One of the reasons is the good fire resistance of the concrete structures in general, and another reason is that the connections and the restraints provided from the surrounding structure members reduce the likelihood of premature failures. On the other hand, failures with hollowcore concrete slabs in experiments have been observed; and each study provides a different view on the fire performance of hollowcore concrete slabs. This section reviews some studies carried out previously and points out the differences between each study which lead to different conclusions.

4.2.1. DIFT [Andersen et al. 1999]

The Danish Institute of Fire Technology (DIFT) in Denmark conducted three tests on precast prestressed hollowcore concrete slabs in 1998. The aim of these experiments was to investigate the spalling effect of high strength concrete and the practical aspects of fire protection in hollowcore concrete slabs by carrying out fire resistance testing following the standard fire testing conditions according to ISO834, and the fire temperature-time curve as shown in Figure 2-1.

Three types of hollowcore slab sections were used in the test: 185mm (SP18), 220mm (SP22) and 270mm (SP27) deep. The one way slabs were simply supported and spanned 6.2m long with a 6.0m exposed length to fire. There were four equal line loads used to give a total external load of 135kN, 135kN and 112kN for each type of hollowcore slab respectively, which equals 85% of the maximum design load for each case. The mechanical properties of the hollowcore units and of the prestressing strands are shown in Section C.1 of Appendix C. The temperature curve used in the experiment followed the ISO834 standard fire. There was no topping used in the specimens as shown in Figure 4-7, a schematic drawing of the experimental set-up.

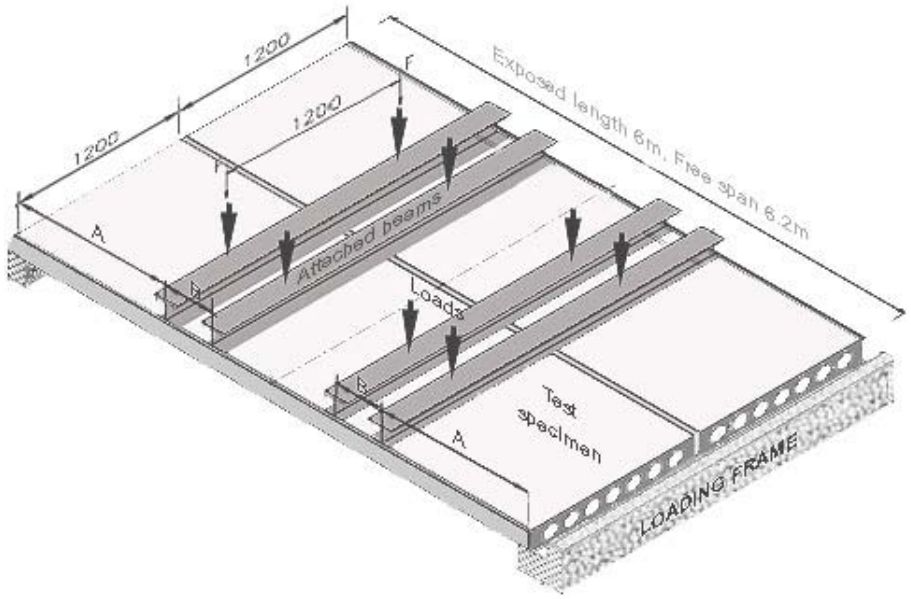

Figure 4-7 Experiment set-up in the 1998 DIFT tests

The experimental results were alarming. In all three tests the specimens did not last for longer than 30 minutes under the ISO fire, and the failure mechanism for all of them was shear and anchorage failure, or tensile shear failure as described in the previous section. In the SP18 and SP22 case, the location of the shear failures was around 1m from the support. In the SP27 case, the shear failure occurred at the support as the supporting concrete snapped off.

Prior to the test, DIFT carried out calculations to predict the time of failure, but premature failure made the predicted failure time inaccurate. To predict the failure time, DIFT used two computer programs, FIRE-2D and Super Tempcalc + Fire Design, as well as hand calculation carried out by using Danish Design Code for Concrete Structures DS411 with two different assumptions. All of these methods could predict the time of flexural failure but not shear or anchorage failure. As no moment capacity failure occurred in these three tests, the predicted times from the computer models were of no use. Further analysis also indicated that at the time of failure the temperature of the reinforcement was not high enough for a reduction in the material properties to have occurred.

Andersen et al. [1999] provided a hypothesis to explain the premature failures. They suggested that the collapse was initiated by the bond failure between the strands and the surrounding concrete, and the shear capacity became insufficient due to the axial compressive forces at the end of the slabs being diminished. It also states that as

the strands were relatively cool, moisture would be likely to condense on the strands and reduce the friction between the strands and the concrete, leading to broken bond between them causing anchorage failure. Nevertheless, there is no experimental evidence yet to support this hypothesis.

The first argument could be interpreted as the reason that differentiates the standard test and the real situation in practice since no such poor fire performance has been found in hollowcore concrete floor systems yet. In practice axial restraints at the end of the slabs are usually provided by the peripheral beams or surrounding floor slabs.

4.2.2. University of Ghent [FeBe Studiecommissie SSTC 1998]

Four tests on fire performance of hollowcore slabs were carried out in University of Ghent in Belgium in 1998, focusing on the influence of detailing and of restraint conditions on the shear capacity. Three types of hollowcore unit cross-sections were used, and these are shown in Figure 4-8. Each of the four tests consisted of two slabs.

Each test had two floor spans of 3m supported on three beams, and the width of the floor was 2.4m. The specimens were exposed to the ISO834 standard fire. Other than the self-weight, the floor experienced a line load of 100kN in the middle of each of the two spans. Figure 4-9 shows the representative layout of the slabs.

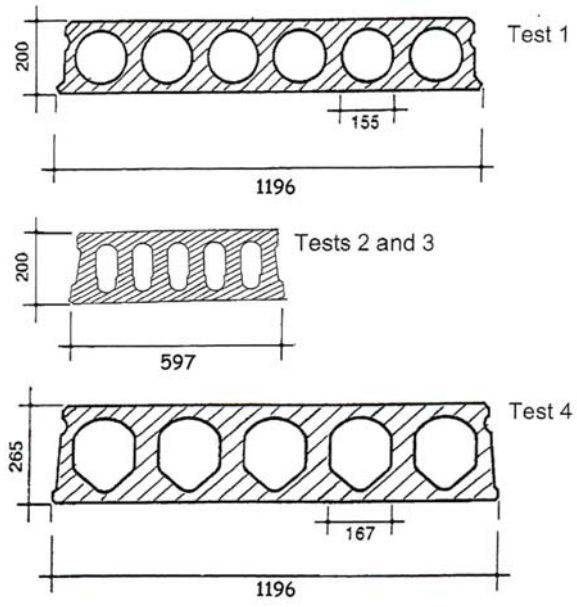

Figure 4-8 Cross sections of the tested elements in 1998 by SSTC

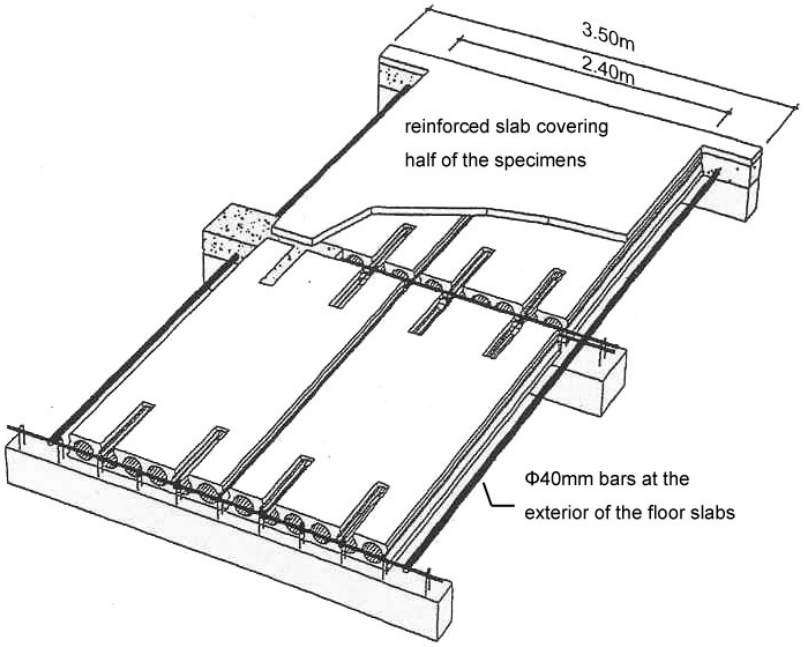

Figure 4-9 Detailing of Test 1 in 1998 SSTC tests [Detroppe et al. 2002]

Four parameters were studied [Dotreppe et al. 2002], and these parameters are also tabulated in Table 4-1:

- Longitudinal tie-reinforcement: in Tests 1 and 4, four bars were cast in opened cores and anchored into the supporting beams; in the other two tests the bars were placed in the longitudinal joints between the units. In theory these bars could reduce the width of the thermal cracks and assure the interlocking effect which decreases the possibility of shear failures.

- Peripheral ties: The peripheral ties are used to transfer the vertical and horizontal forces of precast floors. In Tests 2 and 3, a small edge beam of 100mm width, reinforced with two bars of 12mm diameter was at one end of the floor as shown in the right figure of Figure 4-10. Lapping of the tie was at the support with the prestressing tendons at the other end. Using this layout ensures that the shear capacity of the floor under the cold condition is not increased, and in Tests 1 and 4 did not have these ties. The left figure of Figure 4-10 shows an example of how peripheral tie beams are used in buildings, at the support area, the tie beam is normally located in the joint at the floor ends [Van Acker 2003].

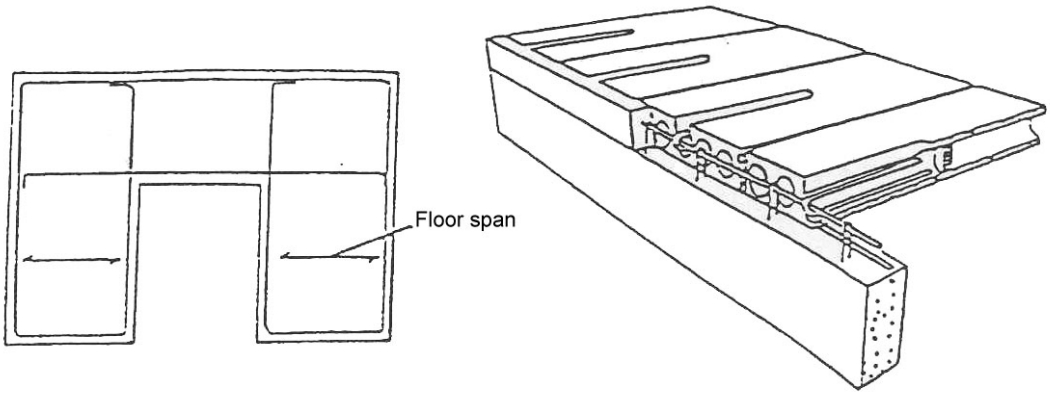

Figure 4-10 Peripheral tie beams for diaphragm action [FeBe Studiecommissie SSTC 1998, Fig 1.10]

- **Reinforced topping**: Tests 1 and 4 had a layer of reinforced concrete topping covering one of the two slabs, and the other two tests had none. Through the bond between the topping and the hollowcore units, the reinforced topping increases the thickness of the floor slab and provides more area to take the compressive stress, and it should consequently reduce the possibility of developing thermal cracks in the web between the voids in the hollowcore units under fire, and it should also increase the shear capacity of the slab.

- **Surrounding structure**: the effect of surrounding structure was replicated by a longitudinal bar at both sides of the floor, and a T-shaped ending of the transverse tie beams on top of the three supporting beams as shown in Figure 4-11. In Tests 1 and 2 φ40mm longitudinal bars were used, in Test 3 φ25mm bars were used, and in Test 4 no longitudinal bars were used. The unheated surrounding structural members could provide restraint to the thermal expansion of the heated floors.

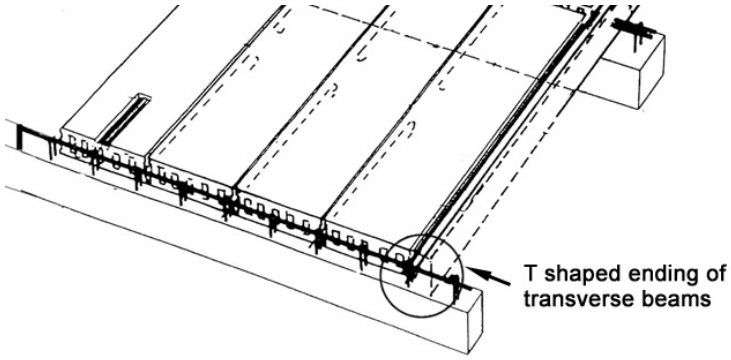

Figure 4-11 T-shaped ending of the transverse tie beams

Table 4-1 Studied parameters in 1998 tests in University of Ghent

Parameters	Test 1	Test 2	Test 3	Test 4
Longitudinal tie-reinforcement	4 bars cast in opened cores and anchored in the supporting beam	4 bars placed in the longitudinal joints between the units	4 bars placed in the longitudinal joints between the units	4 bars cast in opened cores and anchored in the supporting beam
Peripheral ties	none	a reinforced edge beam at one side; lapping of the reinforcement at the support with prestressing tendons at the other side	a reinforced edge beam at one side; lapping of the reinforcement at the support with prestressing tendons at the other side	none
Reinforced topping	50mm topping	none	none	30mm topping
Surrounding structure	Φ40mm cold longitudinal bar at both sides; a T-shaped ending of the transverse tie-beams above three beams	Φ40mm cold longitudinal bar at both sides; a T-shaped ending of the transversal tie-beams above three beams	a T-shaped ending of the transversal tie-beams above three beams	Φ25mm cold longitudinal bar at both sides; a T-shaped ending of the transverse tie-beams above thee beams

The experimental results were very positive. Test 1 was terminated after 83 minutes as spalling was found on the horizontal face. Other tests could reach the final time of simulation which was 120 minutes. After testing, the external load was increased until failure was reached to check the remaining capacity of the slab after heating. Both Tests 2 and 3 had flexural failure when checking the remaining capacity, while Test 4 failed in shear. The results showed that the slabs were still able to sustain a very high load after exposure to fire, therefore the hollowcore units still had large remaining bending and shear resistance capacities. Also, the temperature readings during the tests showed that the temperatures measured using thermocouples placed on the strands matched the data in Eurocode 2-1.2.

The tests showed that all four parameters have favourable effects on the fire performance of the hollowcore slabs. However, in Tests 1 and 4, longitudinal cracks at the mid depth of the lateral floor face were induced due to the thermal bowing caused by the cold topping, as the reinforcement in the topping limited the thermally induced strains. Because the type of hollowcore units used in Tests 1 and 4 had a small number of big voids, which means the concrete section is small, the report suggested that the shape and area of the cross-section were the reason behind the occurrence of spalling and cracking in the fire tests. Nevertheless, these cracks were not significant enough

to cause structural failures as their size was limited by the axial restraints. The report suggested that the interlocking effect at these small cracks, which was described in Section 4.1.3, provided a positive influence on the overall structural performance.

4.2.3. BRE [Lennon 2003]

Building Research Establishment (BRE) in UK has carried out four tests regarding precast concrete hollowcore slabs. In the first two tests, conducted in 1999 in the Cardington facilities, extensive cracking and explosive spalling were observed. Lennon [2003] concluded that these phenomena were caused by inadequate curing periods and improper storage which incurred high moisture content, and the moisture content in the hollowcore slabs in practice should be lower than in those specimens.

BRE later carried out two new tests with different designs to the previous ones. The aim of these new tests was to investigate whether premature failures observed in some standard tests can be avoided through using continuity in the floor. One slab had a reinforced concrete topping, and the other slab did not have the concrete topping but there were hooked bars in the joints between the units to provide continuity within the floor. Both slabs had all joints filled. Both designs took account of the recommendations from the European Commission on Prefabrication [FIB 2001].

The temperature curve in the furnace was different from the ISO 834 standard fire and the comparison is shown in Figure 4-12. The increment of temperature in the furnace in the growth phase is larger than that in the ISO834 standard fire curve, and the maximum temperature experienced by the slabs was higher than that at 60 minutes of the ISO834 standard fire.

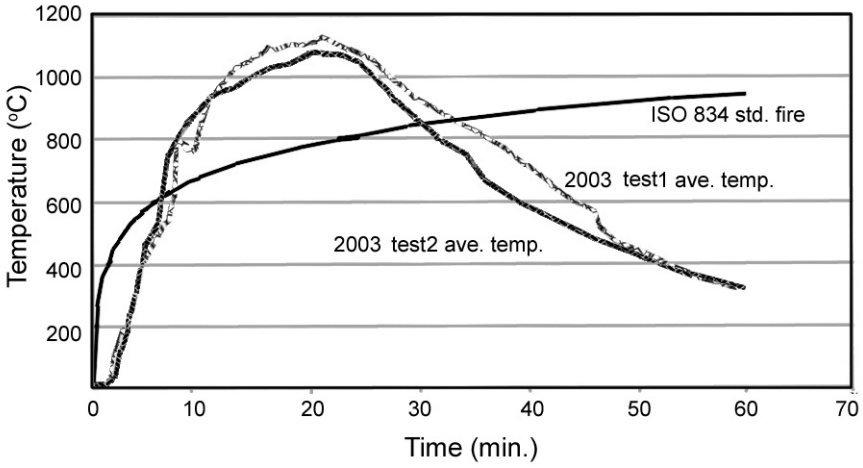

Figure 4-12 Comparison of furnace temperatures from 2003 BRE tests to ISO fire curve

In the later tests no significant spalling was observed, and no premature shear failure occurred. There was no sign of integrity failure or loss of load bearing capacity after the experiment. The vertical displacements induced during the fire recovered a limited amount afterwards; and the floors could sustain the applied load for a long time after testing. The downwards displacement has been observed to be larger in the slab without the concrete topping than that in the slab with the topping.

Other than the above observations, this report also responded to the problem of anchorage failure observed in DIFT [Andersen et al. 1999]. Lennon is in favour of the idea that the anchorage failure is caused by the nature of the standard test; as long as the continuity between the slabs is provided, either by reinforcement or structural topping, the anchorage failure would unlikely to happen. This is why it is not observed in practice or in the second BRE test described above.

4.2.4. Danish Prefab Concrete Association [BEF 2005]

Three tests were carried out in 2005 by the Danish Prefab Concrete Association (Betonelement-Foreiningen, BEF) to study the feasibility of using only structural codes, which calculate only the flexural capacity under fire conditions, to predict the fire resistance of hollowcore slabs. The 2005 tests were conducted following a set of unsuccessful tests carried out by DIFT in 2004, which will be described later. The purpose of the 2005 tests is to confirm that after exposure to 60 minutes of the ISO834 standard fire, the hollowcore slabs can resist at least 65% of the slab's ultimate design shear capacity in cold conditions as derived from the Danish Standard DS411.

In these tests the fire followed the first 60 minutes of the ISO834 standard fire and was then extinguished, and were similar to the tests done in University of Ghent mentioned earlier. This set of tests from BEF in 2005 looked at the structural performance during the cooling phase, and the tests continued for a further 60 to 90 minutes after the fire stopped with the load still applied.

BEF Tests 2004

In 2004 DIFT did some tests on hollowcore slabs exposed to fires [DIFT 2004], the specimens consisted of two prestressed hollowcore concrete units and were 3m wide spanning 6m. The layout and the loading conditions are shown in Figure 4-13. The test consisted of two hollowcore slabs with cast longitudinal joint, transverse

joints at the ends and longitudinal edge joints [BEF 2005]. Each hollowcore unit was 1.20m wide and 6.13m long and 265mm thick without the concrete topping. The cross section of the hollowcore unit is as shown in Figure 4-14. A separation between the hollowcore units and the edge joints was built in to prevent transfer of loads between them [BEF 2005].

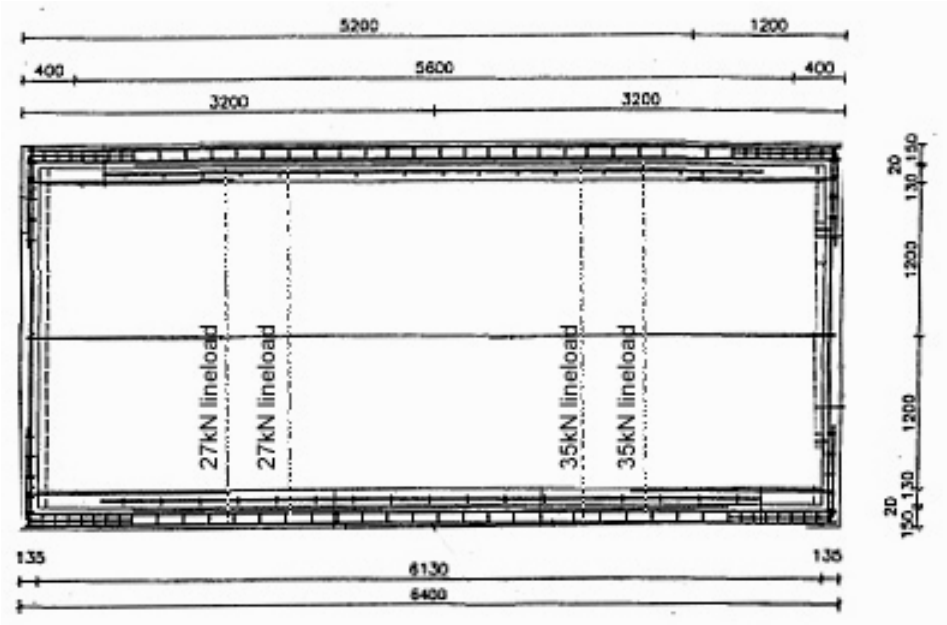

Figure 4-13 Layout of the DIFT test carried out in 2004 [BEF 2004]

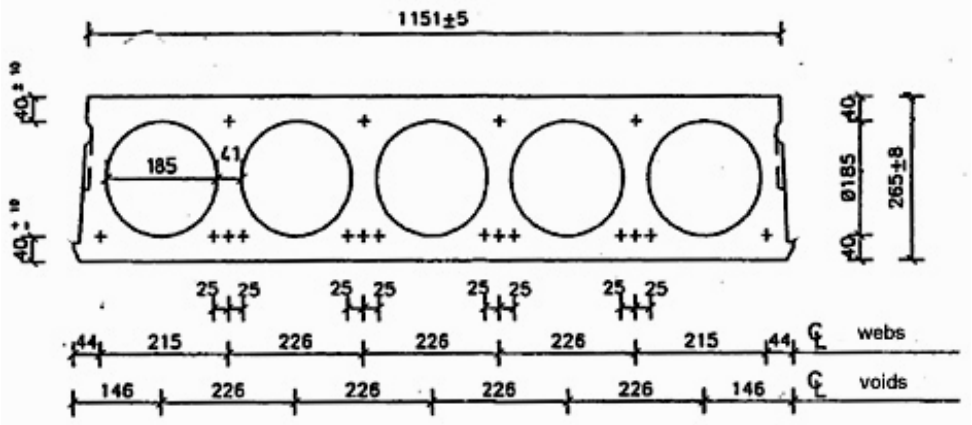

Figure 4-14 Cross section of the HC unit used in BEF 2005 and 2004 tests [BEF 2004]

The testing procedure followed EN1365-2. The load bearing capacity of the slabs was lost after being exposed to only 25 minutes of ISO834 fire. This was due to the cracks in the longitudinal direction in the specimen. The cracks at the end of the slabs were explained by BEF [2005] as developing from a small crack at the slab ends due to thermal bowing which then grew to the transverse joint and finally caused anchorage failure and also let the cracks propagate away from the support. Also,

during the test because the edge beams deformed much less than the hollowcore slabs, a noticeable torsion was observed in the slabs and might have contributed to this early failure.

The report stated that the accuracy of the results was in doubt due to the nature of fire resistance testing and the consequent difficulty in quantifying the uncertainty of measurement of fire resistance [BEF 2004]. The standard fire testing procedure defines the fire resistance of the slab for meeting the stability criteria as the time when the structure collapses or the maximum deformation exceeds 1/30 of the span length [ISO834, 1999]. The report states that the structure could last in fire for a much longer duration if there was no interference from the edge beams.

BEF Tests 2005

The arrangement of the hollowcore units in the 2005 tests was different to the 2004 tests to avoid the torsion observed before. The span length in the 2005 test was 3.2m, and there was a 1.775m wide buffer zone at each side of the test zone to reduce the torsion as shown in Figure 4-15. The hollowcore units were the same as those used in the 2004 test and are as shown in Figure 4-14. Transverse reinforcements of the joints designed in accordance to the Danish Prefab Concrete Association's Guidelines [BEF 2003] were used at the ends of the slabs. The ultimate shear capacity in the cold condition was 91.6kN/m. Three load levels were used in the tests, which were 65%, 75% and 80% of the ultimate shear capacity. The line load was located at 523mm from the end. This location was determined in accordance with the Eurocode rules for testing of the shear capacity in cold conditions [CEN/TC229 2005].

The test results show that the hollowcore units have good shear capacity in fire when they are mounted correctly. The test report concluded that the tested hollowcore units, being correctly mounted, can sustain 60 minutes of ISO fire when the shear load is less than 75% of the ultimate shear capacity. The slab loaded to 80% of its ultimate shear capacity ruptured after being exposed to 45 minutes of the ISO standard fire, and the slab loaded to less than 75% of the ultimate shear capacity could withstand 60 minutes of the ISO fire and stood until the end of the testing time without any rupturing or spalling.

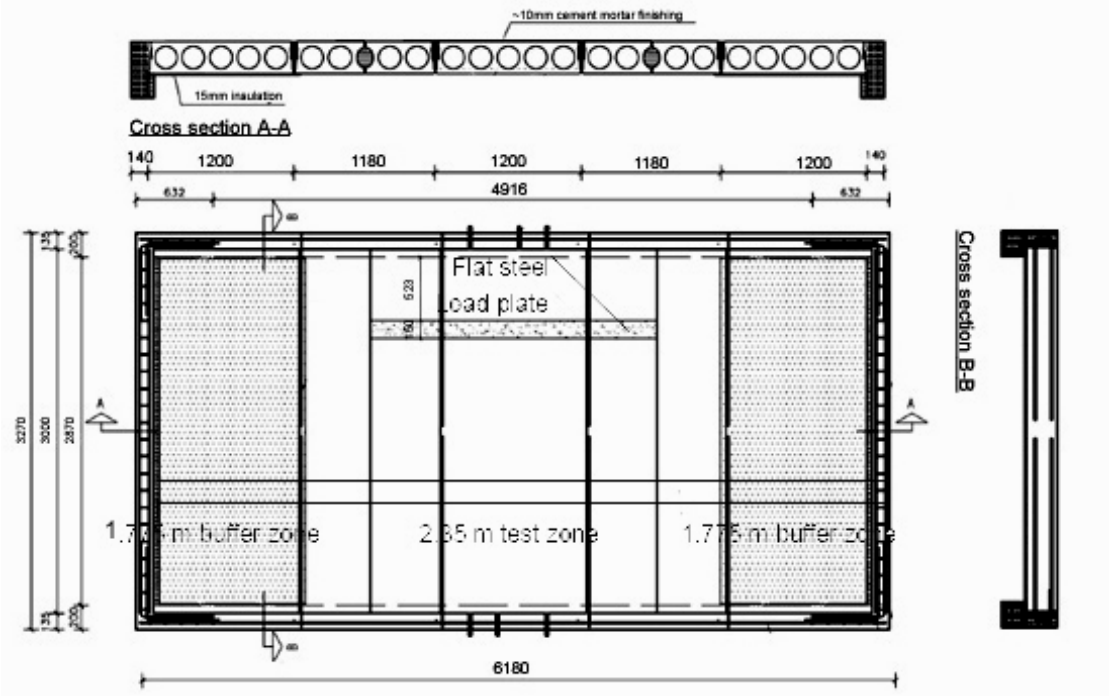

Figure 4-15 Layout of the BEF test carried out in 2005 [BEF 2005]

Furthermore, the results in the 2005 tests showed that the transverse reinforcements of the joints at the end of the specimen are very important to prevent the vertical cleavage of the element edges in fire. After the tests, many densely distributed cracks were found in the transverse joints at the end of the elements and it was noted that the prestressed wires had retracted into the slab. If these cracks were not controlled by the transverse reinforcements, there was a risk of anchorage failure as the cracks might propagate away from the support at the underside of the slab [BEF2005].

4.2.5. Delft University of Technology [Fellinger 2004]

The objective of this set of tests was to identify the mechanisms for shear and anchorage failure of hollowcore concrete slab during fire exposure by determining the crack propagation and slip development.

25 fire tests in total were carried out. To ensure that shear and anchorage failure would occur within 30-120 minutes and avoid flexural failure occurring, a single line load was imposed at a distance of 2.5 times the thickness of the specimen from the support in accordance to prEN1168-1:1997, which is the same as in the standard shear tests at ambient conditions. This can ensure the load level is not enough to create flexural failure but sufficient to cause shear and anchorage failure. The schematic

drawing of the test layout is shown in Figure 4-16.

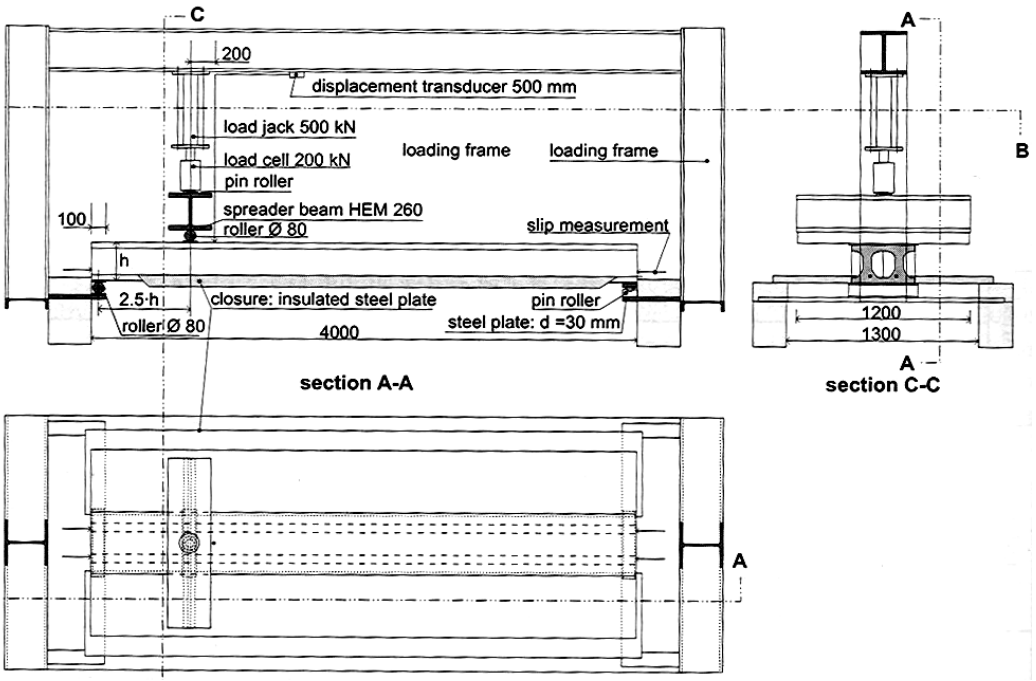

Figure 4-16 Test set-up from Delft of the double ribs sawn from hollowcore slabs [Fellinger 2004]

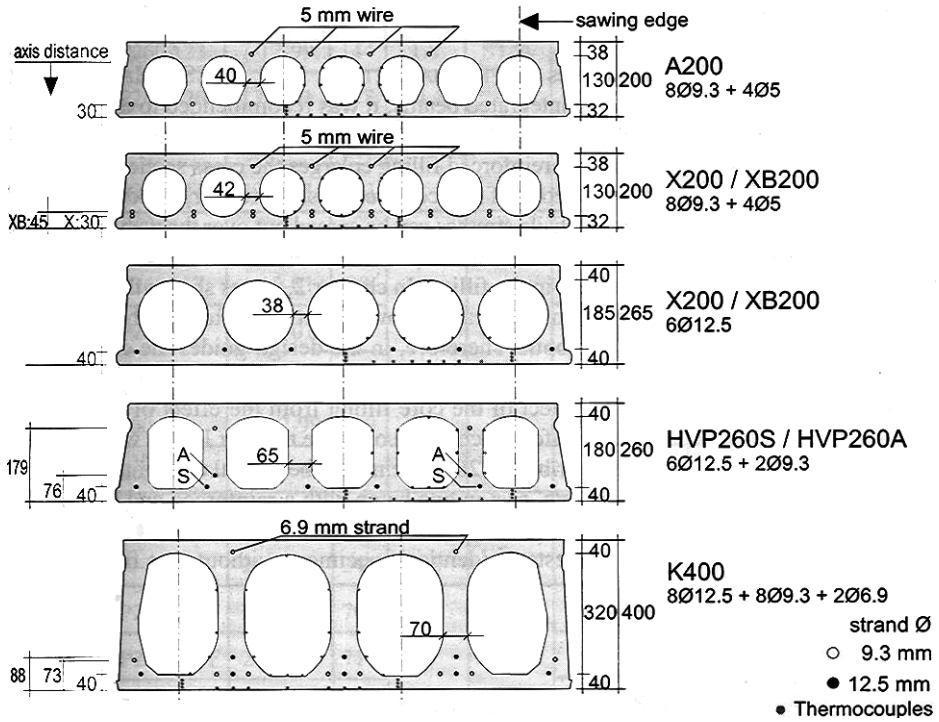

Figure 4-17 Cross section of the test specimens used for the tests by Fellinger [2004]

Among the 25 fire tests, 6 specimens were with the entire unit widths (hollowcore units tests), and the rests were double ribs (double rib tests), i.e. a section extracted between the middle of hollowcores, consisting of two webs. The first series of double rib tests were carried out on slabs with five different cross sections as shown in Figure

4-17, ranging from 200mm to 400mm thick. Among the five cross sections, X200 and XB200 are identical except the cover thickness is different, where in X200 the distance from the bottom surface to the centre of the strand was 30mm, and in XB200 was 45mm. The loading was varied according to the desired value relative to the design anchorage capacity or the actual capacity at ambient conditions.

In the second part of the double rib tests, the effect of the load level was explored, where the level of loading becomes the varying parameter, and the cross section of the HC slab remains the same using the HVP260 units. In total, 7 test results are related to this part of the tests. The results showed that the crack pattern and the slip formation in fire are barely influenced by the load level, but the failure time is very sensitive to the load level. In all the tests the load bearing capacity with respect to shear and anchorage failure decreases rapidly in the first 30-60 minutes under fire due to the damage caused by the incompatible thermal strain, but the influence from the thermal strain becomes less important than the load level in the later stages. In the cases where failure occurs within 60 minutes, the failure was induced by the increasing damage from the incompatible thermal strains and the mechanical loading. The report also stated that if the load was not high enough to cause failure within 60 minutes, the failure was postponed to after 90 minutes. Between 60 to 90 minutes, the remaining thermal stresses after the formation of thermal cracks decreased further due to a decreasing incompatibility of the thermal strains. Failure occurring beyond 90 minutes was caused by the decreasing strength properties and the mechanical loading.

The test results showed that if the strands are positioned high in the web, a horizontal splitting crack through the web could develop and shear failure may occur, and in situations where no horizontal crack through the web is developed, anchorage failure may occur.

In the cases where no horizontal crack through the webs is developed, the slab cannot have shear failure but is still susceptible to the anchorage failure. It was found that incompatible thermal elongations cause vertical cracks to develop over the entire length of the specimen, and the applied bending moment and a decreasing prestressing cause the vertical crack near the maximum bending moment to grow through the lower flange. This decreasing prestressing was caused by the slip, the splitting cracks along the strand and the decreasing stiffness of the strands and of the

concrete over the cross section at elevated temperatures. Eventually the governing flexural crack opened and the strand was pulled out and the failure mechanism was completed.

Shear failure occurs in slabs with horizontal cracks though the webs. The horizontal cracks developed in an early stage of fire exposure. The horizontal cracks were found at the smallest web width at mid depth along the entire length of the specimen, or developed as a splitting crack along a strand. During fire, the horizontal cracks grew into one crack accompanied by some vertical cracks. The splitting crack either grew only horizontally along the strands which are positioned quite high in the web or from the strand to the nearest void and then down to the exposed soffit. At failure, a combined horizontal and vertical crack opened, and the strands were pulled out.

The study also explored the effect of core filling and of providing restraints at the ends. This is because international guidelines recommend filling the cores with reinforced concrete over some length to increase the cross sectional area to bear the shear force near the ends and consequently to increase the fire resistance. As core filling is often combined with some restraint, such as axial restraint, transverse restraint or both, the effect of core filling and the effect of having restraints at the ends are studied separately in double ribs tests. Contrary to expectations, the results show that having core filling alone did not prevent or reduce the crack development in the webs, nor did it affect the slip development. It was found that the fire resistance was slightly lower than in the comparative tests without core filling, which was because there was no bond between the hollowcore slab and the filling. The thermal stress was not spread over the composite cross section but stays in the hollowcore unit section alone due to the lack of bonding between the units and core filling. This makes the core filling become ineffective in terms of increasing shear resistance. The lack of bond could be caused by the differences in shrinkage of the core filling and of the hollowcore units as the concrete matures.

In terms of the effect of axial restraint, in one of the tests the axial restraint could not prevent the development of the horizontal crack through the thinnest part of the web, so that the horizontal crack is not driven by the axial thermal elongations, and having the axial restraint did not increase the fire resistance. However, in a

comparison between having an axial restraint or not in a 200mm thick hollowcore unit, it has been found that axial restraint limited the growth of the vertical cracks to a certain extent, and it strongly reduced the slip development. With axial restraint the slab could sustain a slightly greater shear load and a much longer fire exposure.

In the six hollowcore unit tests, four types of cross sections were used, and three tests were identical except for the slight difference in the concrete age. The loading setup also followed the standard shear test setup in prEN1168-1:1997. All tests were simply supported [Fellinger 2000]. The result showed that the test with the smallest depth unit (XB200) failed in flexure with a combination of anchorage failure, while all the rest experienced failure caused by shear tension. [Fellinger 2000]

4.3. Shear and Anchorage Behaviour of Hollowcore Concrete Slabs in Fire

The information in this section is from Fellinger [2004] unless stated otherwise. Other than the flexural failure mode, shear and anchorage failure can also dominate the structural behaviour of hollowcore slabs in fire. Besides, as shear and anchorage failure is very brittle compared to bending failure, failure can occur very suddenly. From the test results gathered by Fellinger [2004], one out of every four tests failed in relation to the shear and anchorage mechanism, and this shows that it is important to consider this type of failure. However, this type of failure in hollowcore slabs has never been found in real fires.

4.3.1. Incompatible thermal strains

The effect of incompatible thermal strains on the load bearing capacity is a very important part in the shear and anchorage behaviour of hollowcore slabs. This effect can cause shear and anchorage failure in the early stage of fire. The transient heat flow creates a large non-linearly distributed temperature gradient over the depth of the cross section. This non-linear temperature gradient induces non-linearly distributed thermal strains as described in Section 3.3.5. The thermal strains do not depend on the mechanical loading and can be calculated directly from the thermal gradient, and they do not comply with the compatibility requirements. In order to meet the compatibility requirements, mechanical strains have to develop to counteract the thermal strains, which result in thermal stresses. Compressive thermal stresses are developed in both

the lower flange and upper flanges of the hollowcore slab, and tensile thermal stresses are developed in the web which is likely to lead to vertical cracks in hollowcore slabs due to the reduced thickness of the web, and the size of the vertical cracks in the webs increases with the slab depth. The constitution of thermal stresses has been shown in Figure 3-30. More details on thermal stress can be found in Section 3.3.5 Constitutive law.

The incompatible thermal strains can cause splitting cracks along the strands and reduce the anchorage capacity of the hollowcore slab. The splitting cracks along the strands, i.e. diminishing of bond, causes large slippage of the strands.

To counteract the incompatible thermal strains, mechanical strains are developed in the hollowcore units, which can easily exceed the elastic limit of concrete in the early stage of fire and becomes irreversible. The irreversible mechanical strains take the form of the cracking of the webs or slip of the strands, and dramatically reduce the shear capacity of the hollowcore concrete slab.

4.3.2. Thermal cracks

The shear capacity is reduced by thermal cracks. Once the crack occurs, the imposed mechanical strains are localised in the cracks. If the bond of the strand decreases in fire, the cracks will propagate and further reduce the shear capacity. This is the reason the shear and anchorage failure under fire condition are related and usually happen together. Because the calculation model for shear compression failure at ambient conditions is valid for the cracked part of the hollowcore slab with thermal cracks, shear failure of hollowcore concrete slabs in fire is more similar to shear compression failure described in Section 4.1.3 than shear tension failure described in Section 4.1.4.

4.3.3. Deterioration of mechanical properties

In the early stage of fire the shear and anchorage capacity is reduced by the thermal stresses, but in the later stage of the fire it is determined by the deterioration of the mechanical properties. The thermal stresses are related to the thermal gradient, and after some time of fire exposure the temperature within the hollowcore slabs start to become uniform which reduces the thermal stresses. Consequently, after the early stage of fire, the shear and anchorage capacity is not further reduced by the thermal stresses but is governed by the thermal-dependent mechanical properties. This is

reflected in tests carried out in Delft University of Technology in Section 4.2.5, in which case once the shear and anchorage failure does not happen within 60 minutes of ISO fire exposure, which means the incompatible thermal strains have not caused the failure, it will not happen until after 90 minutes of fire exposure, which is caused by the deterioration of mechanical strength.

4.3.4. Anchorage failure

Under fire conditions, splitting cracks along the strands in fire due to wedge action of the strand drawing in are most likely to occur over the transfer length, which is the length needed to fully develop the prestress along the length of the member. This is because of a combination of differential thermal elongations over the concrete cover around the strand and the wedge action of the strand. The transfer length is a function of the concrete strength, prestressing level and the diameter of the strands [Mitchell et al. 1993], and usually is less than 1.4m according to the results of Oh et al. [2006].

The study of Hertz [1982] distinguished between splitting and bond failure for ribbed bar. Hertz found out that splitting failure might be affected by thermal stresses over the concrete cover which results from the thermal gradients. Early fire tests in Finland [Hietanen 1992] confirmed the idea and showed that protecting the slab from heating over the transfer length of the prestress can increase the fire resistance of the specimen.

In terms of anchorage failure, Hertz [1982] stated that anchorage failure during fire happens when the reinforcing bar is the warmest and the effect of thermal gradients is negligible at this time. This statement is not valid for prestressing strands, in which case anchorage failure can occur much earlier than for the temperature in the concrete around the strands to rise, even though there is a slight tendency for shear and anchorage failure to increase with increasing axis distance of the strand, which is completely opposite to the flexural behaviour. The effectiveness of the cold support observed by Hietanen [1992] cannot be attributed to the low temperature in the strand, as the strand temperature does not affect the failure type.

4.3.5. Effect of support conditions

The distribution of the mechanical strands over the cross section that counteract the incompatible thermal strains depends on the shape of the hollow cores and on the support conditions.

In simply supported slabs, there are no axial stresses at the ends. Therefore, the thermal stresses have to build up over a certain development length. Over this length, the kinematic requirement in Bernoulli's hypothesis that plane section remains plane is not fulfilled and the end surface will be warped to some extent. The development length depends upon the ratio between shear deformation and axial deformation. For concrete structures, the development length is determined to be half the slab depth based on some limited investigations using finite element analysis. However a perfectly stress free simply supported slab does not exist in practice. The hollowcore slab must always be connected to the support with reinforced concrete for overall structural integrity, and to provide redundancy in the structural system the forces within the hollowcore units will change due to thermal stresses, and additional forces will develop at the supports depending on the boundary conditions.

There are benefits in having axial restraints at the supports. Because the axial restraints reduce the thermally induced tensile strains and cracking in the web, which are some major factors to trigger shear and anchorage failure, the shear capacity can of the slab can be enhanced by the presence of the axial restraints. However, since there is no knowledge so far about the amount of restraint which is sufficient to avoid premature shear and anchorage failure, it is recommended not to rely on axial restraints to eliminate the possibility of having shear and anchorage failure.

The flexibility of the support reduces the shear capacity of the hollowcore slabs. The full scale tests done by Pajari & Koukkari [1998] showed that the shear tension capacity in hollowcore slabs with non rigid supports, in this case supported on beams, is significantly lower than that in hollowcore slabs with rigid supports. However, this can be overcome by filling the hollowcore beyond the critical point where the principal tensile stress is at its maximum.

4.4. Summary from the Fire Test Results

The findings from the fire test results reported here are summarised below thematically.

4.4.1. Spalling

Spalling has been reported in the BRE tests [Lennon 2003] and one test from University of Ghent [Febe Studiecommissie SSTC 1998]. However, Lennon [2003]

noticed that by providing adequate storage and curing period, this phenomenon can be avoided.

4.4.2. Shear and anchorage failure

The study from Fellinger [2004] shows that mechanical strains induced by thermal stress can cause splitting cracks along the strands and vertical cracks in the web. Splitting cracks along the strands reduce the anchorage capacity, and vertical cracks in the web reduce the shear capacity. These two types of cracks can cause shear and anchorage failure in the early stage of fire. If shear and anchorage failure in the hollowcore slab does not happen in the early stage of fire, it might still happen in the later stage of fire when the mechanical properties of concrete and steel decrease and the shear capacity is reduced.

Because shear failure can be caused by splitting cracks growing horizontally through the web if the strands are positioned too high, it is recommended to position the strand sufficiently low to avoid splitting cracks and consequently reduce the likelihood of having shear failure.

4.4.3. Load level

Both the BEF [2005] and Fellinger [2004] test results show that higher load levels speed up the time of failure. Fellinger further pointed out that the load level is more important than the thermal stresses to the failure time if the failure occurs after exposure to 60 minutes of the ISO fire.

4.4.4. Axial restraint

The studies from University of Ghent [Febe Studiecommissie SSTC 1998] and Fellinger [2004] have demonstrated that axial restraints influence the overall structural performance of hollowcore concrete slabs in fire positively. Tests from University of Ghent showed that axial restraints limit the gap in the cracks to allow interlocking effects which prolonged the failure time, and Fellinger [2004] found that because axial restraints limited the growth of vertical cracks and reduce slip development, the slab can sustain a higher shear load or a longer fire exposure.

4.4.5. Core filling

Fellinger [2004] did some comparison tests on having core filling alone and not in combination with axial restraints, and the test results showed that core filling by itself

does not increase the fire resistance, but to the contrary may cause damage to the hollowcore during fire due to the difference in shrinkage between the core filling and of the unit itself. However, studies by Pajari & Koukkari [1998] showed that having core filling can increase the shear capacity of the hollowcore units.

4.4.6. Other observed effects of hollowcore slabs in fires

The effect on the structural behaviour of precast prestressed slabs under fire caused by the restraints to thermal expansion has been recognised by the PCI design manual [Gustaferro et al. 1989] and several other studies, and as early as in 1965, Carlson et al. [1965] found out after comparison of fire tests on hollowcore slabs carried out in the USA with those in Europe that the effect of restraint often surpasses that of other factors, such as steel cover, size and shape of the member, aggregate type, reinforcement type and load intensity.

The restraints to thermal expansion act as an axial force on the line of thrust, which can have either positive or negative effect to the structural performance depending on its location. Figure 4-18 shows these different effects. Once the position of the thrust line is at the same level or higher than the centroidal axis of the slab, the thrust will increase the deflection of the member in fire and consequently reduce the fire endurance.

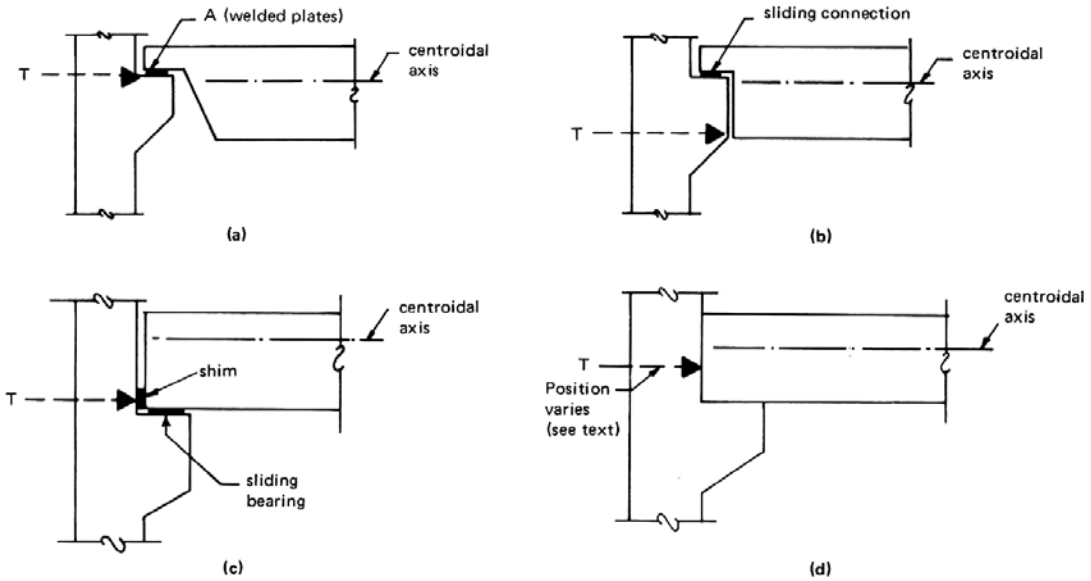

Figure 4-18 Different thrust line position [Carlson et al. 1965]

It is also possible that the thrust position changes during the course of fire as shown in Figure 4-18(d). From the fire tests it seems that when only minimal thrust

occurs, the thrust line is close to the bottom of the member throughout the duration of fire. If the thrust is greater than minimal, the thrust line will initially be at the bottom of the member but will rise in the course of the fire. For a maximum value of thrust, the thrust line will reach the level of the centroidal axis in less than 2 hours of fire exposure in normal weight concrete [Gustaferro et al. 1989].

In terms of the enhancement to the shear and anchorage behaviour, from the tests conducted by Fellinger [2004], it is concluded that axial restraint reduced the development of strand slippage and the propagation of vertical cracks perpendicular to the restrained direction, and it can consequently increase the fire resistance of the hollowcore concrete slabs.

5. The SAFIR Finite Element Program

5.1. Introduction

This chapter describes the computer program SAFIR which is used in this research. SAFIR is a non-linear finite element program. By breaking down the complex geometries of structural elements into several finite elements, the boundary conditions can be simplified and the structural elements can be analysed using a series of equilibrium equations [Franssen et al. 2002b].

SAFIR was developed by J.M. Franssen at the University of Liège, Belgium, and is developed based on a previous computer program named CEFICOSS (Computer Engineering of the Fire resistance of Composite and Steel Structures) which was written in the 1980's. Detailed descriptions of the SAFIR program can be found in Franssen et al. [2002a] and [2002b].

5.2. Compatibilities of SAFIR

SAFIR was originally written for analysing steel and composite structures exposed to fire. Other studies, such as that by Lim [2003], have explored the possibility of also using SAFIR to analyse concrete structures with satisfying results.

SAFIR is able to carry out thermal, torsional and structural analysis in two or three dimensions. The geometrical non-linearity caused by large displacement as well as the material non-linearity in the thermal and mechanical properties are considered in the analyses. Different types of elements, various calculation procedures as well as several material models are built into the program. Even though SAFIR was developed for analysing structural behaviour under fire conditions, it can also be used to analyse structures at ambient temperatures.

5.3. Analysis Procedure

SAFIR is able to run two types of analyses, which are the thermal analysis and structural analysis. The thermal analysis provides the temperature profile as a function of time which is subsequently used in the structural analysis. When using 3D beams in structural analysis, an additional torsional analysis is required to account for warping.

5.3.1. Thermal analysis

The thermal analysis in SAFIR needs to be performed before running the torsional or structural analysis. It is carried out to obtain the temperature distributions within the cross-section of the structural components. The parameters required for the thermal analysis are the cross-sectional geometry and the material properties. The temperature dependent reduction factors for the thermal properties of steel or concrete following the Eurocode 2 or 3 are written into the program already. Other materials, such as insulation or timber, can still be analysed in SAFIR with thermal properties at different temperatures defined by the users.

The thermal analyses in this study are two-dimensional because the results from the three-dimensional thermal analyses cannot be translated into to a suitable input format for the beam or shell elements in structural analysis in SAFIR. In the thermal analysis, the cross-section of beam, shell or truss elements is discretised into several “fibres”. Each fibre is simulated as a two-dimensional solid element, and each solid element is an isoparametric triangle or quadrilateral to minimise the complexity in the boundary conditions. Two-dimensional heat conduction is then calculated within each solid element to give an overall time-temperature profile, which is subsequently stored ready to be used by the structural analysis.

Convection at the boundaries and radiation in internal cavities of the cross section are considered in the thermal analysis. This important feature enables the users to run thermal analysis of hollowcore concrete slabs. The air inside the void is assumed to have a uniform temperature, and the specific heat of the air is neglected in the assumption. Detailed equations for heat transfer calculation can be found in Franssen et al. [2002b]. The validation of capturing the radiation in internal cavities is shown in FeBe Studiecommissie SSTC [1998].

5.3.2. Torsional analysis

The torsional analysis calculates the elastic torsional stiffness of the beam section at the room temperature. This analysis is required before performing the 3D structural analysis on beam elements. The input parameters for the torsional analysis are the geometry of the cross-section and the mechanical properties of the materials.

The torsional analysis carries out the calculations based on the given geometry of

structural member and ignores the effects such as cracking in concrete caused by loading or other structural influences; therefore, the value obtained form the torsional analysis is normally higher than that in reality. The elastic torsional stiffness decreases with increasing temperature as described in Section 3.3.4, but this is also overlooked in the torsional analysis to reduce the complexity. It is suggested that the calculated value can be further manipulated and halved to approximate the reduction of torsional stiffness in high temperatures [Franssen 2001].

The results obtained from the torsional analysis have to be inserted into the time-temperature profile obtained from the thermal analysis. The modified time-temperature profile can then be used in the structural analysis on 3D beams.

5.3.3. Structural analysis

Structural analysis is the last step in the series of analyses for determining the structural performance of a member or an assembly of members. Structural analysis can be performed in either two or three dimensions. Users can choose among different structural elements to construct the structural model, and the details of these elements will be discussed in Section 5.4.

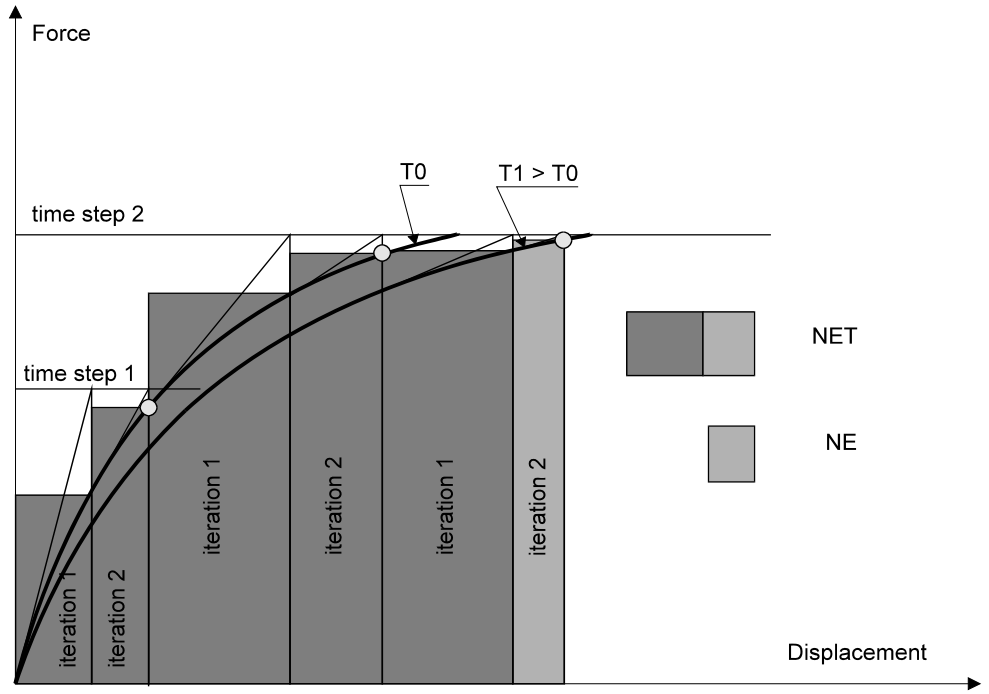

Figure 5-1 Convergence iterations for the SAFIR structural analysis [Franssen et al. 2002b]

The time-temperature profile generated from previous analyses forms part of the

input of the structural analysis. With consideration of the non-linear temperature-dependent mechanical properties, the structural analysis calculates the equilibrium between external load and internal stress at each time step using an iterative technique which follows the Newton-Raphson method as shown in Figure 5-1, where NE is the norm of the energy calculated at each iteration and NET is the norm of the total energy calculated as the summation of all the previous NE. The iteration continues in each time step until convergence is reached.

After convergence, the structural analysis can generate the following information at each time step:

1. Displacement of each node within the structure.
2. Axial and bending moment at each Gauss integration point in each element.
3. Stresses, strains and tangent modulus in each fibre of the element and each longitudinal integration point within the beam element.
4. Stresses, strains, bending and membrane stiffness in the shell elements.

SAFIR uses the arclength technique, or modified Riks's method as described by Crisfield [1981], to prevent the local failure of a single structural member leading to an overall structural failure. This allows the analysis to predict a more realistic time of failure. SAFIR uses total corotational procedures to solve for the large displacements, so the simulation can tolerate some sudden increase in the displacements. More information on this technique can be found in Crisfield [1981].

Several assumptions are made in the structural analysis in SAFIR. These include assuming perfect bonds exist between two materials such that slippage and anchorage failure are not taken into account, not including spalling, and not considering shear failure.

5.4. Structural Elements

For two-dimensional analyses, users can choose to use truss or beam elements to represent the structural members; for three-dimensional analyses, users can choose among truss, beam or shell elements or a combination of them. As the hollowcore concrete slab will be constructed using beam and shell elements, these two element types are briefly described below. Information on the truss element can be found in

Franssen et al. [2002b].

5.4.1. SAFIR beam element

SAFIR beam element can be used in the senses of both two and three dimensions. The physical position of the beam element in the space is defined with two end nodes, N1 and N2. The additional node N3, which lies between the line formed by N1 and N2, is used to provide an extra degree of freedom which accounts for the non-linear longitudinal displacement. For a 3D beam element, a fourth node N4 is needed to define the position of the local y-axis of the beam as shown in Figure 5-2.

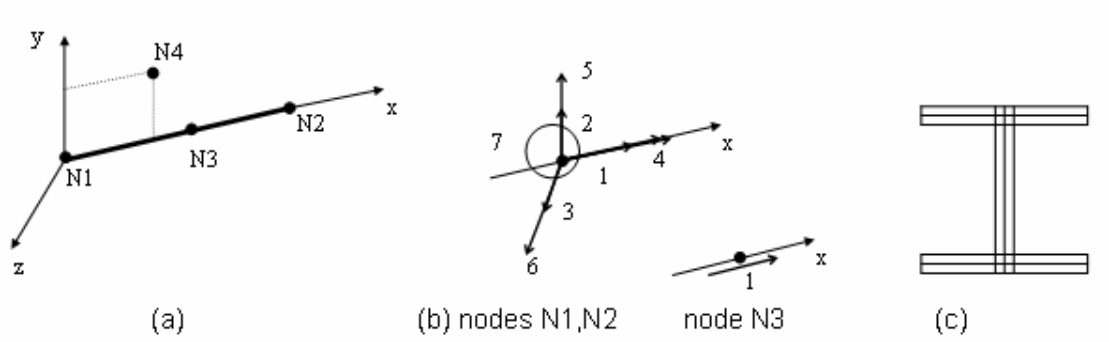

Figure 5-2 In Beam element (a) local axis (b) degrees of freedom at nodes (c) cross section [Franssen et al. 2002b]

Nodes at different locations have different degrees of freedom. In 2D analysis, the end nodes have three degrees of freedom to allow for two displacements and one rotation; in 3D analysis, the end nodes have seven degrees of freedom to allow for three displacements, three rotations and warping. N3 in either sense has only one degree of freedom. Being the node used to define orientation only, N4 has no degree of freedom.

The geometry of the cross-section of the beam element is defined by a fibre model, consisting quadrilateral and/or triangular elements. Each element, or “fibre”, consists of one single material, and composite section can be made by using fibres with different materials. The material behaviour is uniform within each fibre and calculated at the centre of the fibre.

Integration along the length of the beam is carried out using Gauss integration. Each beam can consist up to three Gauss integration points, but typically two are used. Stresses in the cross section are calculated at these integration points, and both

bending moment and axial stresses in the beam can be obtained from these stresses.

There are several assumptions made for the beam elements in SAFIR [Franssen et al. 2002b]:

1. The Bernoulli Hypothesis is adopted. This means that the plane section remains plane after bending. This allows for a linear strain distribution across the cross-section, and coincides with the assumption of general theory for the flexural strength of reinforced concrete sections. [Park et al. 1975]

2. Shear energy of the plane sections in the finite elements is ignored in accordance with the Bernoulli Hypothesis.

3. During unloading, the material behaves elastically with the modulus of elasticity equal to that at the origin of the stress-strain curve.

4. The plastic strain is not affected by the increasing temperature.

5. Plastifications are only considered in the longitudinal direction of beam elements, which means uniaxial constitutive models.

6. The non-linear portion of the strain is averaged on the length of the elements to avoid locking.

7. Non-uniform torsion is considered in the beam element.

8. Local buckling of steel fibres in the beam element is ignored.

5.4.2. The SAFIR shell element

Definition of configuration

The shell element in SAFIR is based on the element developed by Jetteur [1985] which was originally used in the non-linear finite element program FINELG [1984] [Talamona et al. 2002-2003]. It is more applicable for large displacements than the beam element in SAFIR.

A shell element is defined by four nodes and has a quadrilateral shape as shown in Figure 5-3, where a, b, c, d are the middle points of the edge of the element, and o is the intersection of line ac and bd. The z-axis is perpendicular to both ac and bd.

Each shell element has a constant thickness. There are four Gauss integration

points on the surface of the shell element. There are also two to ten Gauss integration points through the thickness as defined by the users, two if membrane behaviour is dominant, and ten if bending is dominant.

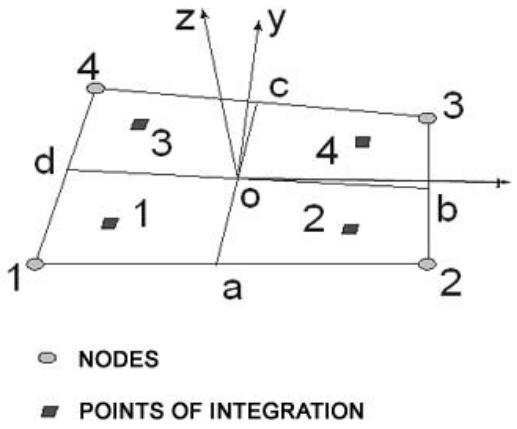

Figure 5-3 Geometry of the shell element [Franssen et al. 2002b]

Flexural behaviour

Detailed descriptions on the formulation of shell element are given in Talamona et al. [2005], and extracts from that study are shown in this section. The formulation for the flexural behaviour is based upon the Discrete Kirchhoff Quardrilateral (DKQ) which was originated by Batoz et al. [1982]. The features of DKQ include:

1. The out-of-plane displacement and the rotations are parabolic over each side.
2. The contribution of the shear strain energy is neglected.
3. The Kirchhoff constraints, i.e. zero transverse shear strain, are imposed along the edges rather than at every point in the element as in classical thin plate theory. The shear strain at each of the two Gauss integration points along the sides is set to be zero.
4. The rotation around the side is imposed to vary linearly.

Reinforcing bars

The reinforcing bars in the shell element are modelled based on a smeared model, which means they are modelled as a thin sheet of steel layer with an equivalent cross-sectional area to the actual bars in each shell element. Several layers of reinforcing bars can be used in one element. The smeared reinforcing bar runs parallel to the local x-y plane, it resists actions parallel to the direction of the reinforcement

but cannot resist shear forces directly. The assumption in using this model is that the temperature of the thin sheet of steel is the same as the concrete at such level, hence the reinforcing bars are not considered during the thermal analysis stage for shell elements.

Each smeared reinforcing bar, i.e. each thin sheet of steel layer, has its orientation. This is defined as being related to the local x axis. The layer of reinforcing bars develop stiffness and stress only in the direction of their axis, hence an elongation perpendicular to their axis or a shear strain in the element do not induce stresses in bars [Talamona et al. 2002-2003].

Concrete in shell element

It is important to understand that as the shell element can deform in both directions parallel to the element. The concrete model used for shell element is biaxial; this is different to the concrete model used for beam element which is uniaxial.

Based on the observed concrete behaviour under fire, several ideas have been considered and integrated into the program. The following considerations are extracted from Talamona et al. [2002-2003]:

1. The plane stress model is still valid. Even if thermal gradients appear in the thickness, no stress is generated perpendicular to the plane of the shell element.
2. Due to the poor behaviour of concrete in tension, a simple Rankine tension cut off as shown in Figure 5-4 has been implemented, which only limits the major principal stresses. This criterion means that concrete cracks under tension in one principal direction will induce a loss of strength in another principal direction, and eventually the strength is lost in all the directions. This criterion may seem as a crude approximation to the real behaviour, but is an acceptable practice as tensile strength should be provided not by concrete but by steel reinforcing bars.

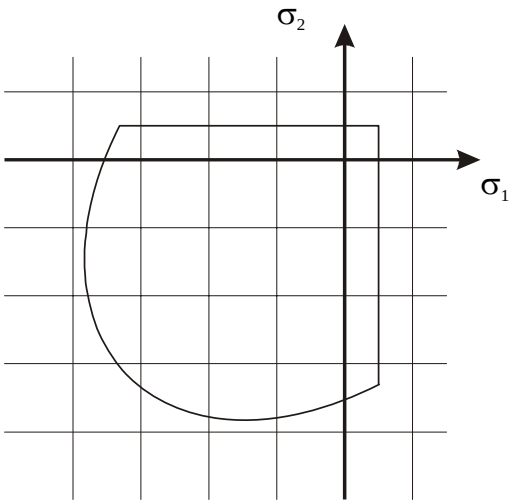

Figure 5-4 Rankine criterion for tension and Von Mises for compression [Doneux et al. 2003]

3. The closing of cracks are considered. This is necessary as many integration points in the structural usually experience stresses changing from tension to compression due to the transient nature of thermal strains in the concrete slab exposed to fire.

4. For modelling two-way slabs, the thermal strains needed to be taken into account. It has been observed from experimental results that the behaviour of two-way slabs under fire is significantly influenced by the large deflections that occur. The mode of load transmission may be changed from the bending mode at room temperature to tension membrane mode in fire. These large deflections are usually caused by thermal strains. Both Eurocode 2 [EC2 2002] and Eurocode 3 [EC3 2002] have recommendations on the non-linear temperature dependency of the thermal strain of concrete and steel.

5. Thermal elastic behaviour in compression is considered. The temperature dependent stiffness of concrete in compression influences the amplitude of the displacement and the stress distribution. This is especially important when the compression zone can reach high temperature, such as near the intermediate support in continuous slabs.

6. A Von Mises surface as shown in Figure 5-4 is used to limit the amount of compressive force that concrete can develop as it takes into account the reduced stiffness of concrete, especially in continuous slabs. A Von Mises surface is more conservative than the compression-compression behaviour of

concrete which was observed in tests, however, in fire the compression-compression behaviour is not likely to happen and this surface is considered sufficient for modelling concrete under fires.

7. Associated plasticity is used, which means the function of plastic potentials equals the yield function; hence the direction of the plastic deformation is perpendicular to the yield surface [Doneux et al. 2003].

8. Each surface of plasticity is subjected to an isotropic hardening, such that during hardening each surface undergoes a uniform contraction or expansion. [Doneux et al. 2003].

Details of the equations and theories used for shell element can be found in Talamona et al. [2002-2003] and Denoux et al. [2003], and validations of models with shell elements are in Talamona et al. [2003-2004].

5.5. Limitations of SAFIR

As stated in Section 5.3.3, SAFIR, like all the other programs using finite element analysis, calculates iteratively the equilibrium between external loads and internal stresses until reaching convergence at each time step. Therefore ideally the stopping of simulation is due to global structural failure, in such case the failure mode is definite and can be determined from the output files. However, it is also possible that the simulation be terminated due to numerical instability caused by local material failure, and in this situation the end time of the simulation is very likely unable to represent the time the structure collapses.

Another problem with SAFIR associates with the prestressing effect. In the structural analysis it is impossible to specify the sequence of applying the loads, therefore the prestressing is applied at the same time as the external loads during the first time step of the structural analysis, and the prestressing effect is influenced by the boundary condition at the supports. However, in reality, the prestressing is applied before the other mechanical loads, and the prestressing effect should be independent to the boundary condition.

It has been described in Section 5.4.1 that the Bernoulli's hypothesis is used in beam elements, which means plane section remains plane. As a consequence, shear

and anchorage failures, bond failures, spalling effects and stresses parallel to the cross-section of the beam elements cannot be captured.

Another limitation which is found in the 2002 version of SAFIR is the allowable size of the stiffness matrix. In this version analysing the entire floor of an actual building using the model proposed later in Chapter 7 is still not possible. However, the size of the stiffness matrix is increased in the later version of SAFIR, and it is recommended to use the later version of SAFIR once the concrete model of that version has been corrected.

6. Model Development

6.1. Introduction

This chapter describes the theories and concepts behind the proposed model for simulating hollowcore slabs exposed to fire; it also illustrates various alternatives considered in the process of the model development. The aim in this part of the research is to develop a model which can be modified easily to accommodate different cross sectional geometries without compromising the accuracy.

The focus of the proposed simulation model is to investigate the global behaviour of the structure and the interaction between the floor slabs and the surrounding structural members. The non-linear finite element program SAFIR is used for the analyses. The advantages and limitations of this program were discussed in Chapter 5.

The first part of this chapter describes the existing methods to predict the fire resistance of hollowcore concrete slabs. The second part explains the issues behind the development of the new model for SAFIR to process. Finally, the last part of this chapter presents the proposed model with discussions on its advantages and disadvantages.

6.2. Existing Methods for Simulating Hollowcore Concrete Slabs

Several researchers have carried out finite element analysis to predict the behaviour of hollowcore concrete slabs under fire. The results of these analyses help to design for fire resistance of these slabs. The adopted methods fall into three categories and are discussed separately below with examples.

6.2.1. Finite element analysis for thermal analysis only

The first type of models discussed here simulates only the thermal gradient within the hollowcore units. The idea behind this method is to model the temperature profiles very precisely, and then to predict the structural performance of hollowcore concrete slabs in fire by looking at the thermally reduced mechanical properties of the constituent materials and their interactions using other means of calculation. A study has been conducted in the University of Lecce using this practice. The finite element program FLUENT was used to model the temperature profiles of hollowcore concrete

sections under the ISO834 standard fire [Micelli 2000]. Figure 6-1 shows the discretisation of one hollowcore unit. These temperature profiles were then matched against the temperature dependent reduction factors from the Eurocode 2 manually to obtain the value of the thermal dependant material properties at different times under fire. From these material properties and the dimensions of the cross-section, the ultimate moment capacity was calculated at different times during fire.

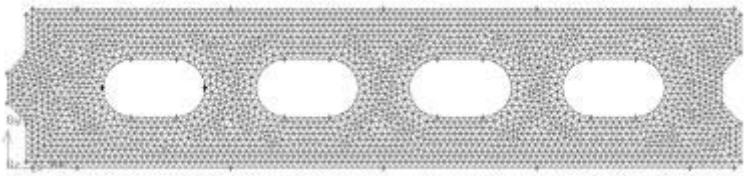

Figure 6-1 Discretisation used for thermal analysis of a hollowcore unit [Micelli 2000b]

This approach falls under Simple Calculation Method from the Eurocode 2, where temperature distribution in the cross-section is obtained through tests or calculations, and in this case through finite element analysis. The changes of mechanical properties with temperature were taken into account so that reduced strength with time was calculated. As the effects of thermal strains were not considered in this method, it does not fall into the category of the Advanced Calculation Method from Eurocode 2.

This method has the advantage of having the thermal profile being calculated in a sophisticated manner, so no fire tests were needed to obtain the temperature distribution in the section. However, by disregarding the thermal strains, it also overlooked the corresponding thermal stresses as well as the mechanical strains which are induced by the incompatible thermal strains. Even though this method saves time and computational power compared to using a full finite element analysis including simulation of the structural behaviour, the predicted fire resistance needs to be treated with great caution.

6.2.2. Finite element analysis for thermal and mechanical analyses

In this category both thermal and mechanical analyses are carried out using the finite element analysis method, but no change over the cross-section of the hollowcore unit is allowed, hence no shear or anchorage failure is considered, and no thermal expansion along the width of the unit is taken into account. The example of this case is a set of simulations carried out in the University of Liège using SAFIR on the hollowcore slabs tested in the University of Ghent [Dotreppe et al. 2004].

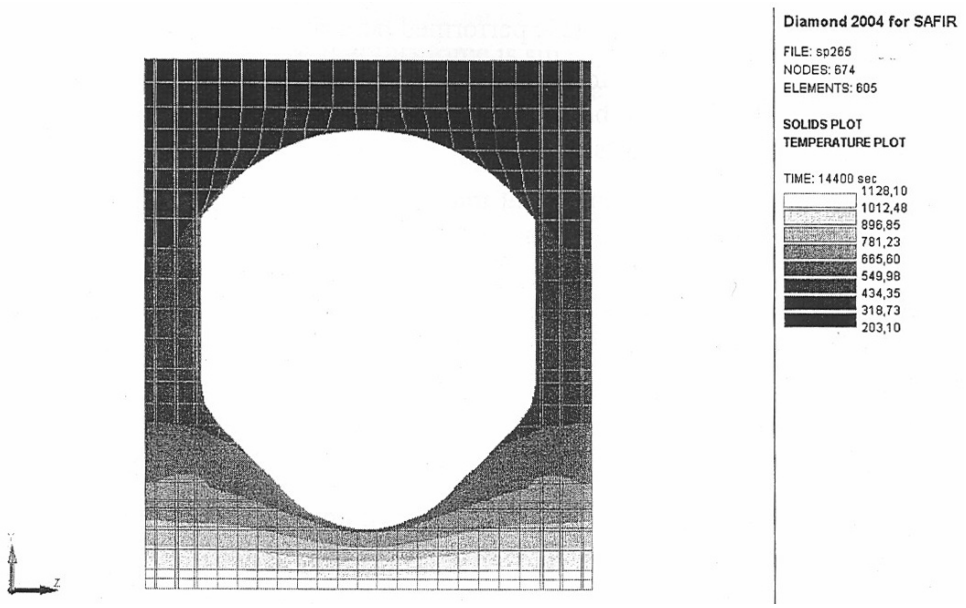

Figure 6-2 Discretisation of the HC unit used in by Detroppe et al. [2004]

In the thermal analysis, heat conduction and radiation as well as the effect from the moisture content of the concrete have been included to calculate the temperature profile. In the structural analysis, thermal strains and temperature-dependent mechanical properties were accounted for automatically by SAFIR. Beam elements were used in the structural analysis stage and they represent the cross section of the hollowcore units. Because of the nature of the finite element analysis, the cross section of the beam elements follows the Bernoulli's hypothesis that plain section remains plain and does not change during the simulation, and no effect from the side restraints was taken into account. The cross section of the beam element used in the analysis is shown in Figure 6-2. The temperature contours show the thermal profile of the hollowcore unit after being exposed to 2 hours of ISO fire.

The simulation results were satisfactory in certain ways. Judging from the comparison of results shown in the Annex of the test report [FeBe Studiecommissie SSTC 1998], the temperature profile was predicted accurately and an envelope of midspan deflection was created, where the actual data lies within the envelope. The simulation method was simple and took account of the stress induced by thermal strains and by the end supports, but no shear induced displacement was considered, and no interaction with the side restraints or interaction with parallel hollowcore units was taken into account. Hence, this method cannot be used to simulate the entire floor.

6.2.3. Finite element analysis including shear and anchorage failures

With proper planning and computational effort, it is possible to use finite element analysis to study the structural behaviour of hollowcore concrete units under fire with considerations of shear and anchorage failures. A sophisticated 2D model has been developed by Fellinger [2004]. This model is able to predict flexural capacity of the hollowcore unit as well as the shear and anchorage failures.

The model runs in DIANA and consists of three steps as shown in Figure 6-3. The first step calculates thermal response of the cross section to obtain the thermal profile, which will be averaged over the width of the cross section at different heights. The second step simulates the structural response of the cross section to capture the development of the splitting cracks, the transverse cracks at the mid-depth of the web, and the confining action of the concrete cover around the strands. The last step predicts the overall structural response of the entire web, which includes a bond model for simulating the concrete around the strand. The deformation and damage found in the structural response model does not feedback to the thermal response model, i.e. no feedback loop calculation.

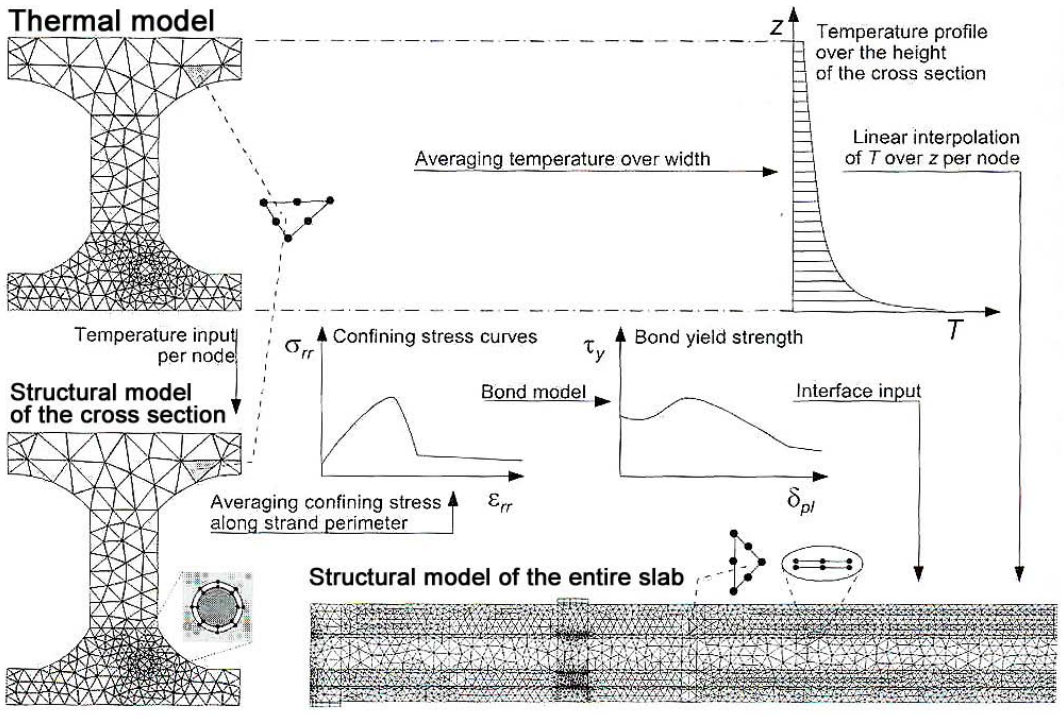

Figure 6-3 Overview of the modelling approach by Fellinger [2004]

This model has many advantages. The thermal and structural behaviour of the hollowcore units under fire can be simulated successfully in this model, the validation

is shown in the report [Fellinger 2004]. It takes account of the incompatible thermal strains, which cause cracks in the concrete web and slip of the strands; it can also predict the vertical cracks, the horizontal cracks through the smallest web width, and the splitting cracks around the strands.

A 3D model was attempted but was unsuccessful because the number of elements needed was too big; also the plasticity model was suitable only for 2D elements. However, as Fellinger [2004] points out, a 3D model is a more desirable option because the total shear force is contributed by the combination of splitting and transverse shear stresses in the cross section and the horizontal shear stresses along the slab from mechanical loading. This model is also needed to directly calculate the effect of slip and change in steel stress on the confinement action of the concrete around the strand, i.e. calculate the bond action.

This model provides a detailed understanding of the behaviour of hollowcore units exposed to fire, however, the computer effort required to run this analysis would be too great for design purposes. Besides, the integration of the hollowcore units with the surrounding structural members has not yet been attempted for this modelling method.

6.3. Development of a New Model

One of the aims of this study is to develop a model which can be used for simulating the behaviour of structures incorporating of hollowcore flooring systems for design purposes, and the results are expected to be reasonably accurate. The program SAFIR was chosen to carry out the analysis for several reasons. SAFIR uses finite element analysis and the calculations are carried out based on the fundamental theories as described in Chapter 5. The program is reliable in modelling structures with concrete floors, as the shell element used for simulating concrete floor slabs has been validated before by Lim [2003], and the combination of using shell and beam elements to simulate a concrete floor with non-uniform profile has been validated in Lim et al. [2004]. Most importantly, this program is commercially available and is already used by many fire engineers.

After it was decided to use SAFIR for the simulation, the next step was to identify which element type or combination of elements is better for modelling the floor slabs consisting of hollowcore units. There are three types of element in SAFIR for carrying

out structural analysis: truss, beam and shell elements. Details of the SAFIR program as well as of beam and shell elements were described in Chapter 5. The following paragraphs highlight the model development process and also illustrate some of the other attempted modelling methods and explain the reasons for not using them.

6.3.1. Concerns related to shell elements

The shell element in SAFIR has proven to be capable of modelling reinforced concrete slabs effectively [Lim 2003], and it is particularly useful for determining the membrane action in two-way slabs which cannot be captured by beam elements. Another advantage of using shell elements is that the needed number of fibres, i.e. discretised cells, within each shell element is much less than that in beam elements; therefore it is more economical in terms of both simulation time and computational effort.

Even though the shell element works well for solid slabs, the void in hollowcore slabs becomes too complicated for this element type. One of the possible solutions is to use the effective thickness of hollowcore concrete slabs based on the calculation method based on the New Zealand Concrete Structures Standard NZS3101 [SNZ 2006]. The method calculates the effective thickness of hollowcore slabs as the net cross-sectional area divided by the width of the cross section, which means the hollowcore slab is considered as a thinner solid concrete slab with the same cross sectional area of concrete. The problem of this option is that this would reduce the second moment of inertia of the slab and oversimplify the thermal gradient, this approach also does not allow for proper treatment of shear and other effects related to the actual thickness of the slab, so this method of modelling is not recommended.

It is possible to include air as a “user-defined material” at the centre of the shell element. SAFIR allows users to define alternative materials for both thermal and structural analyses by inputting the thermal and material properties into the program. In this case the properties of air, and consequently a layer of this user-defined material could be used in the shell element. However, there is a fundamental error in this method: by using air as a user-defined material at the centre of the slab, the program would treat air as a solid material, and in the thermal analysis only conduction is considered in solid materials. In practice, the dominant heat transfer mode through air within the voids is convection or radiation, and the conductivity of air is very small.

Therefore, the thermal profile obtained from simply replacing a section of concrete by air will be inaccurate.

The possibility of using shell elements vertically to model the webs in the hollow-core units has also been explored here, and it was concluded that this method was not to be recommended. Figure 6-4 shows the sample scheme of modelling one structural member with a shell element box.

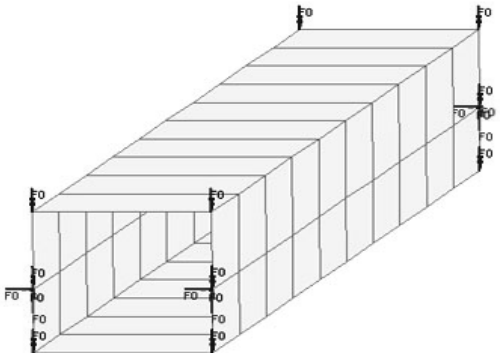

Figure 6-4 Sample box of shell elements

Even though this method preserves the actual height of the hollowcore unit and avoids the problem caused by the void in the thermal analysis, there are many weaknesses in this method. The most obvious flaw is the poor representation of thermal gradient in the webs. As the temperature is uniform across the shell elements, the thermal distribution along the web relies on the number of shell elements stacking up vertically. If the thermal distribution is modelled crudely, the temperature would jump from one discrete value to another along the web, and a triangular stress distribution induced by the unreal thermal differences would be found in each vertical shell element [Franssen 2004]. This might be able to be overcome by using as many shell elements as possible for modelling the web. However, as the shell element in SAFIR follows thin-shell theory with the thickness of the shell element being much less than the width and the length, one cannot use many shell elements stacking vertically to represent the web otherwise the width of the shell elements would very likely be less than the thickness of them.

Another problem in this method relates to the number of integration points within each shell element which derives from the formulation of the shell elements in SAFIR. As explained before in Section 5.4.2, the number of integration points through the

thickness can be defined by the user from two up to ten, but the integration across the surface is performed with a two by two points Gauss scheme as shown in Figure 6-5 [Talamona et al. 2002-2003]. Theoretically the stiffness at each integration point is integrated along the thickness of the shell element to give the membrane and bending stiffness, and consequently integrated in the plane to give the overall stiffness of the element. Therefore, by orientating the elements vertically and applying loads parallel to the shell plate, the lack of integration points may result in the results being too crude. Nevertheless, using more shell elements would increase the number of integration points along the web, and consequently overcomes the problem. Previous studies on simulating H-rolled steel columns from Talamona et al. [2003-2004] showed that putting a shell element vertically does work for steel structures.

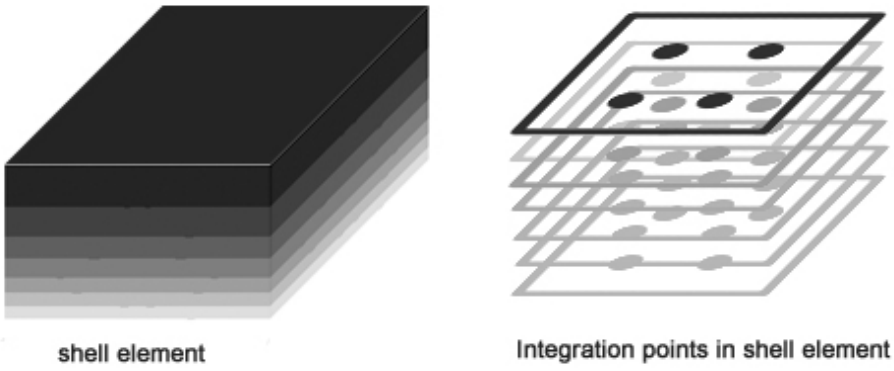

Figure 6-5 Integration points in the shell elements

One other problem with this method is related to the concrete behaviour within shell elements. Tensile force should be transferred via the smeared steel section in shell elements which represents the steel bars as concrete behaves poorly in tension [Talamona et al. 2002-2003]. Because the only steel sections in the hollowcore slab are the prestressed strands which are located close to the bottom of the units, the shell elements in the top flange or upper web area where there are no steel sections may behave strangely once the concrete starts to crack in tension.

Using solely shell elements cannot incorporate prestressed force from the strands into the model, and the prestressed forces affect the structural behaviour dramatically as shown later in Section 7.4.2. Based on all the above reasons, shell elements were used only for modelling the topping concrete layer but not for the hollowcore slabs.

6.3.2. Concerns related to beam elements

There are many advantages in using beam elements to model hollowcore units. The heat transfer can be properly modelled and a continuous thermal gradient can be maintained. Besides, the very important prestressing force can be considered in SAFIR only by using the beam elements. Furthermore, the fine fibres from discretisation in beam elements can help to identify the location of cracking or crushing in the slabs.

However, it is impractical to use the beam elements to model the entire floor slab because it would require one beam element consisting of the entire cross section of the floor, which means that this element will need a lot of discretised fibres or a very crude discretisation. Besides, using only beam elements cannot include the effect from the side supports or the continuity among the hollowcore units from the topping layer, as discussed in Section 6.2.2.

6.4. Proposed Model

In SAFIR it is possible to combine different types of element into one structure. Lim et al. [2004] have shown that an integrated SAFIR model with both shell and beam elements for high-bond slabs give similar yet slightly conservative results to the experimental outcomes. Therefore, a similar assemblage was used for the proposed model, with shell elements for the topping reinforced concrete slab, and 3D beam elements for the hollowcore units.

Figure 6-6 shows the discretisation of the cross-section of the proposed model. In the model for hollowcore concrete flooring systems with reinforced concrete topping, the beam and shell elements share common nodes to simulate the composite action between the beam and shell elements. The node-line of the beam element is offset to be in the same location as the mid-height of the topping concrete, while the centre of rotation is kept at the centroidal axis. This method of shifting the location of the node line was proven to work in SAFIR by Lim et al. [2004].

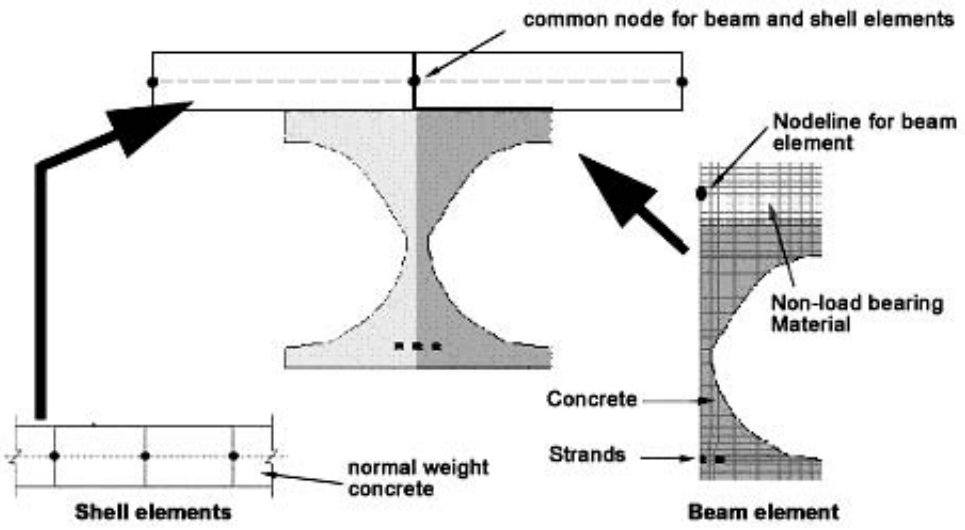

Figure 6-6 Disintegration of the cross section of hollowcore unit

6.4.1. Grillage analogy

In the proposed model, underneath the topping reinforced concrete slab modelled by shell elements, a grillage of beam elements as shown in Figure 6-7 is used to simulate the structural behaviour of each hollowcore concrete unit.

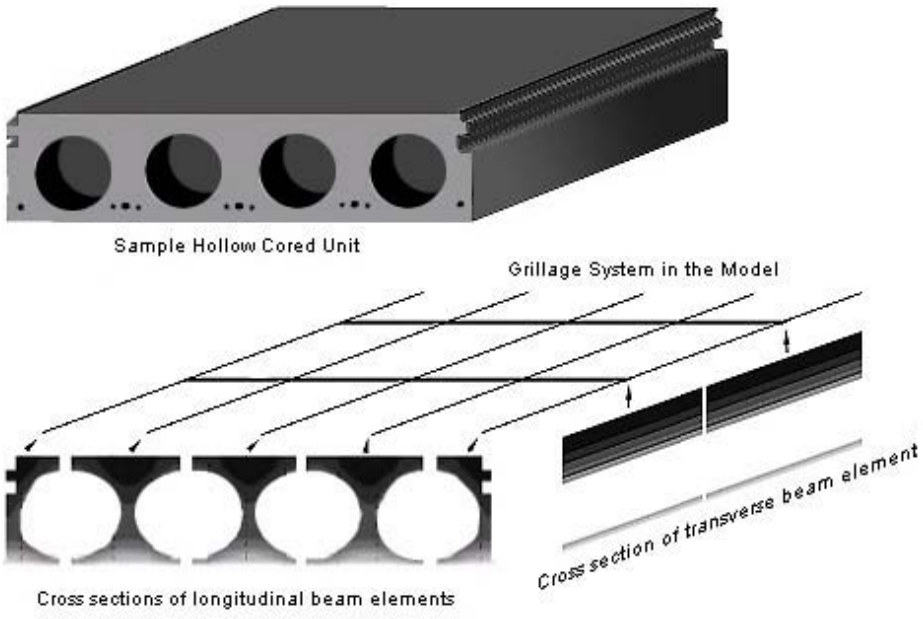

Figure 6-7 Model scheme of hollowcore units

From West [1973a] and Livesley [1964], a grillage is defined as a structure with straight longitudinal and transverse beams rigidly connected together, each beam with its own bending and torsional stiffness, and at each junction the deflection and slope

is calculated. This method translates a slab into a skeletal structure with a mesh of beams, where longitudinal beams provide the longitudinal stiffness, and transverse beams the transverse stiffness [O'Brien et al. 1999].

Using an equivalent grillage of beams to simulate the behaviour of bridge slabs has been practiced for a long time. A grillage analogy is easy to construct and quick to perform; the results are easy to interpret and are proved to be reliably accurate in bridge designs [Hambly 1991]. It was a popular method to simulate the slab behaviour under ambient conditions before the rapid advancement of computational powers, since then this method has been replaced by thin shell finite element analyses. However, Section 6.2 showed that using only finite element analysis is still too complicated for fire design purposes, and a grillage system becomes an ideal alternative.

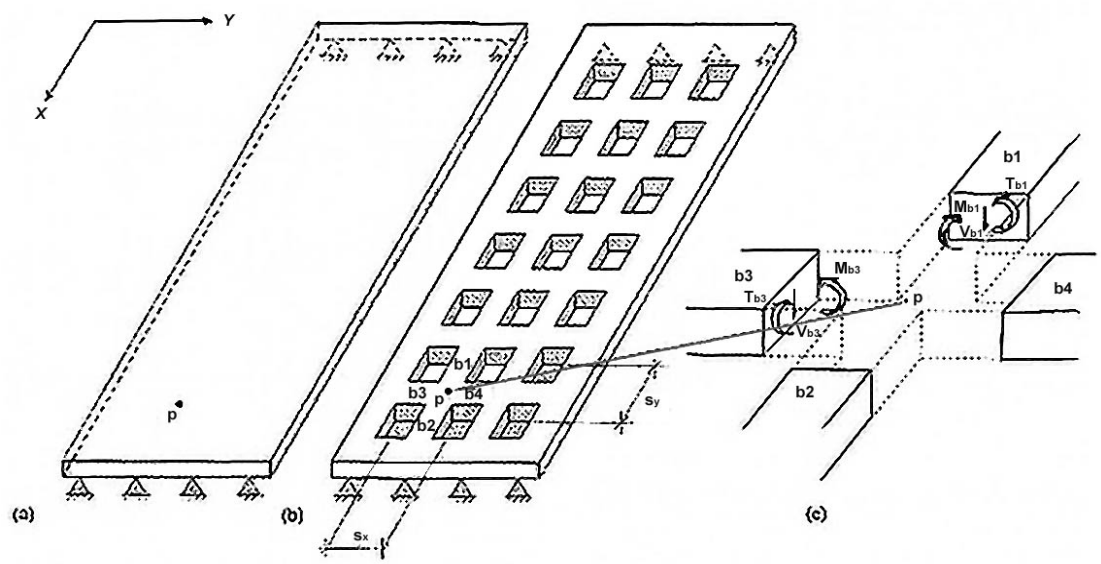

Figure 6-8 Grillage idealisation of a slab (a) original slab (b) corresponding grillage mesh (c) segment of grillage mesh [O'Brien et al, 1999]

Figure 6-8 illustrates the idea of using a grillage mesh to represent a slab. Figure 6-8(a) shows a pinned one-way supported slab. The initial concept of grillage meshes was developed with this support condition. Figure 6-8(b) shows the corresponding mesh as the input of the computer grillage analogy programs. Figure 6-8(c) shows the details at an intersecting point. The bending moment along the beams running in the X direction is contributed by b1 and b2, and in the Y direction by b3 and b4 [O'Brien et al., 1999].

There are many benefits in simulating the behaviour of hollowcore units in fire using a grillage system. If each hollowcore unit is modelled only as a beam or as a group of parallel beams in SAFIR, no transverse deformation of the cross section can occur. By splitting the width of the unit into several lines of longitudinal beam elements and connecting each line by transverse members in a grillage, the deformation across the width of the units is captured. The transverse beams in the grillage system have the same properties as the top and bottom flange of the hollowcore slabs, and for one hollowcore unit, the sum of the width of the transverse beams is equal to the length of the hollowcore unit, and the length of the beams is equal to the width of the hollowcore unit. Because the material behaviour in beam elements in SAFIR is one dimensional only, the expansion and deformation across the width of the cross section relies on the transverse beams in the grillage.

Parameters for grillage analogy

The parameters needed for carrying out the grillage analysis in SAFIR are either obtained from mechanical properties, such as the modulus of elasticity E and the Poisson ratio ν, or they are calculated automatically from the thermal and torsional analysis by SAFIR, such as the second moment of area I and the torsional stiffness J. As the shear modulus G is a function of E and ν, the value of G is determined automatically when E and ν are known. In the SAFIR torsional analysis output, the product of the shear modulus and the torsional stiffness, GJ, is calculated automatically.

It has been noticed that many studies neglect the torsional resistance from the beams while it is recommended to include this resistance in the analysis, especially for the slabs with cast in-situ concrete or prestressing [Bareš et al., 1968]. The twisting moments per unit breadth, mxy and myx, are calculated as

$$m_{xy} = \frac{T_{b1} + T_{b2}}{2s_x} \qquad \text{Eq. 6-1}$$

$$m_{yx} = \frac{T_{b3} + T_{b4}}{2s_y} \qquad \text{Eq. 6-2}$$

where T is the torque and is a function of G and J, s_x and s_y are widths of the longitudinal and transverse beams respectively. For materially orthotropic plates m_{xy} and m_{yx} are equal, but it is possible that the stiffness of the longitudinal and transverse

beams are drastically different, in which situation one should handle the torsion at the junction with care.

Further details about the theories behind grillage analogy can be found in Bareš et al. [1968], and the applications can be found in Hambly [1991] and West [1973a]. Several recommendations about the grillage layout are given by West [1973b]; however, in this research an appropriate grillage layout is decided based on the outcome of a sensitivity study.

Sharing rotations about the lateral axes at nodes where beams intersect in SAFIR

In SAFIR the degrees of freedom at each node may be shared or not in the intersecting elements. By sharing rotations, the rotation of the longitudinal beams is associated with an equivalent twist in the lateral beams. The problems of increasing stiffness may arise when sharing the rotations about the lateral axes, as the stiffness would be contributed by beams in both directions. Two examples are shown here to see the effect of sharing the rotations about the lateral axes at each node where beams intersect. The first case is based on the structure tested in DIFT in 1999 [Andersen et al. 1999]. Details of the test specimens and layout can be found in Appendix C. One 185mm thick hollowcore unit (SP18) without topping spans 6 metres and is exposed to the ISO fire.

Table 6-1 Parameters used for SP18 in DIFT 1999 test [test no. X52650d, Andersen et al. 1999]

Item	**Properties**
Concrete	siliceous, f'_c = 55MPa, f_t = 2MPa
Strands	φ 9.3mm, σ_u = 1.87GPa, mechanical prestressing = 62kN/strand
Self weight	2.75kN/m^2
applied load	4 line loads: one line load16.93kN 1084mm from both ends of the slab one line load 16.93kN 2284mm from both ends of the slab
Support condition	pin-roller (simply supported)

Table 6-1 shows the main parameters used in the simulation. The transverse beams had a spacing of 300mm as shown in Figure 6-9. The ratio of the transverse beam spacing to the longitudinal spacing is sufficiently fine in comparison to the value suggested by West [1973b].

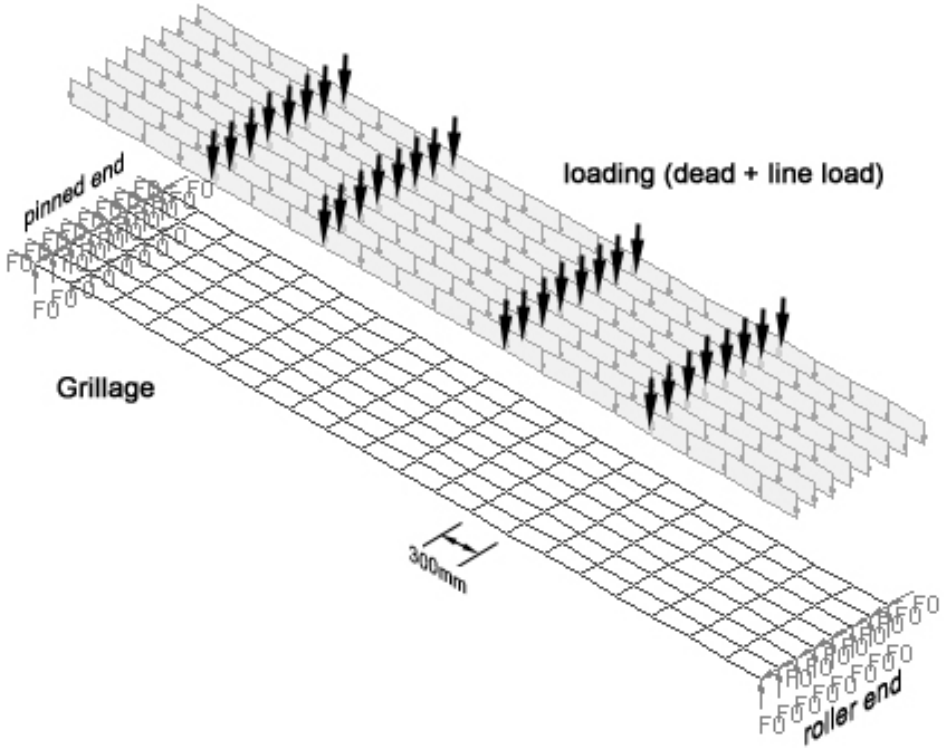

Figure 6-9 Grillage used for SAFIR simulation of the DIFT 1999 test

This case was simulated using two grillage models, one with sharing of bending in both the lateral axes at the nodal intersection points; and one without except for the nodes at the edge of the slab. The reason for sharing the rotation at the edge of the slab is to provide the necessary fixity on rotation of the transverse beam to carry out the calculation. Figure 6-10 shows the results from the simulation of all the displacements and rotations about the lateral direction at the centre and at the side of the slab. Figure 6-10(c) shows that the midspan vertical displacements at the centre or at the side of the slab were almost identical; this observation was also reflected in the rotations perpendicular to the span direction as shown in Figure 6-10(d).

Because of the midspan vertical displacements at the centre and at the side were the same, the horizontal displacement at the end along the span direction should also be the same, which is shown in Figure 6-10(b). Figure 6-10(a) shows that the midspan horizontal displacements along the width at the centre or at the side of the slab were different, which is understandable as the thermal expansion in the transverse direction would push the side outwards; this is reflected also in the rotations parallel to the span direction as shown in Figure 6-10(e).

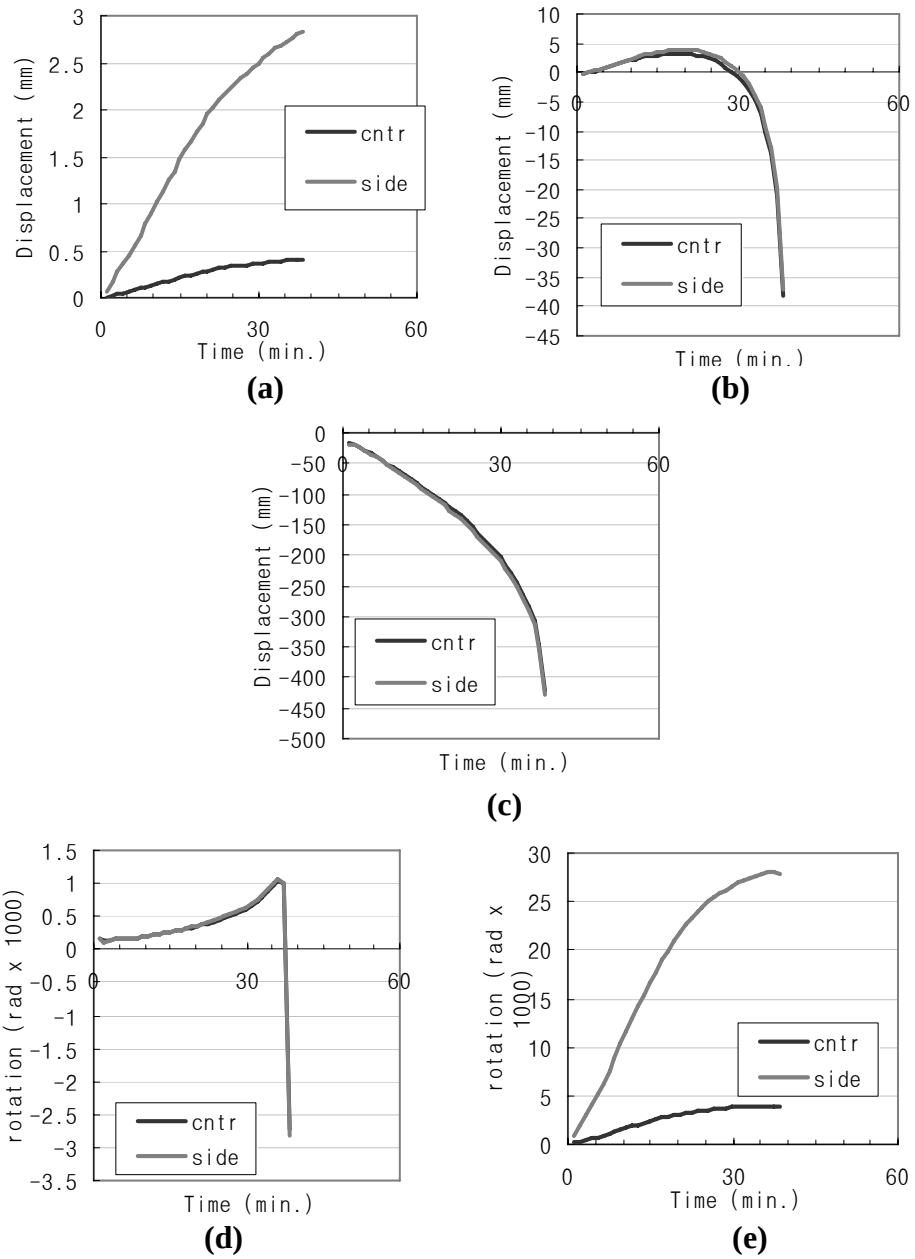

Figure 6-10 Results for simulation of DIFT 1999 test with SP18 hollowcore section: (a) lateral displacements along the width; (b) lateral displacements along the length; (c) vertical displacements; (d) bending perpendicular to the span direction (e) bending parallel to the span direction

Figure 6-11 shows the comparison between the cases with the rotations about the lateral axes at each node where beams intersect shared and the others not shared, where “rotation fixed” means the rotations were shared, and “rotation freed” means they were not shared. All the charts indicate that sharing the rotations about the lateral axes at each node where beams intersect did not make any difference in this case.

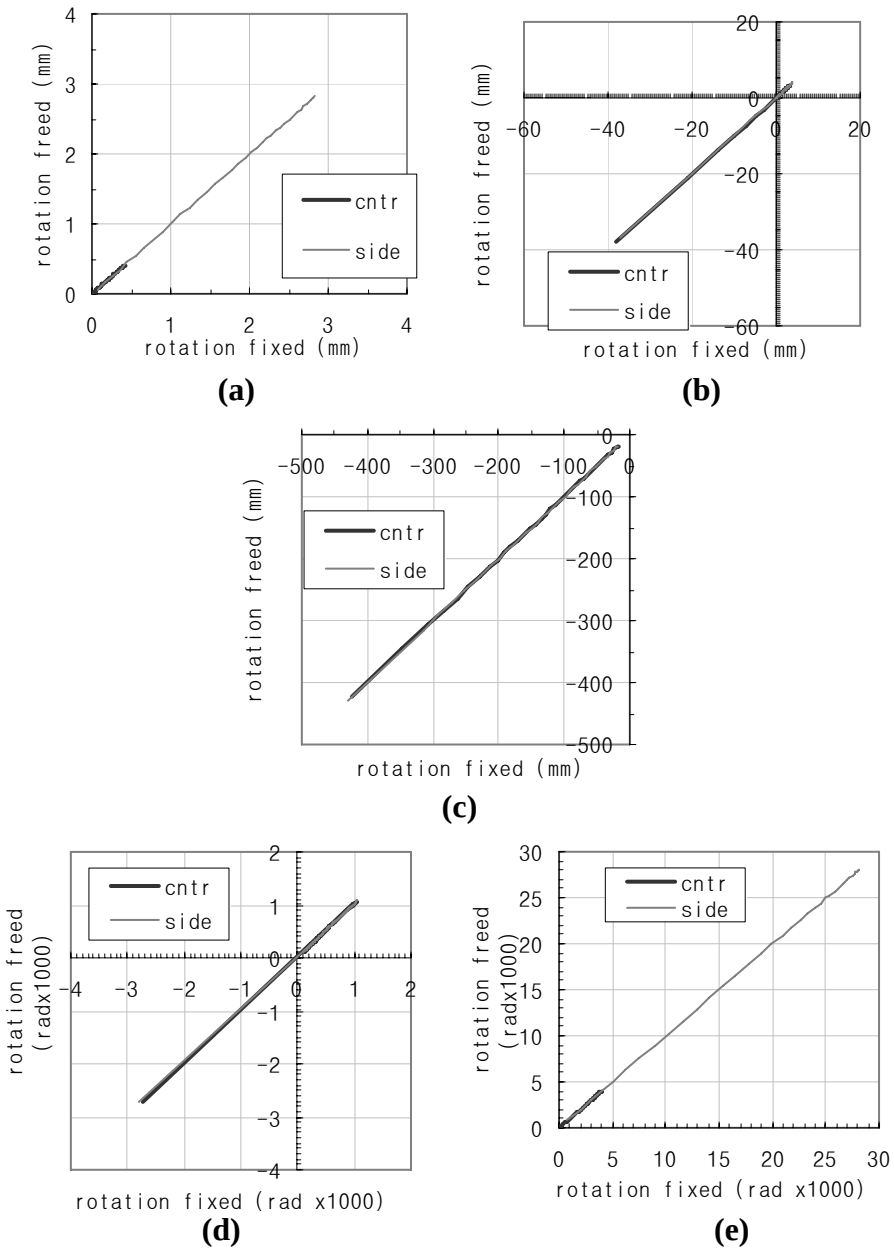

Figure 6-11 Comparison between simulation results of grillage models with sharing rotations in each intersections or not for DIFT 1999 test with SP18 hollowcore: (a) lateral displacements along the width; (b) lateral displacements along the length; (c) vertical displacements; (d) bending perpendicular to the span direction (e) bending parallel to the span direction

The second case is based on the fire tested slab from Lim [2003]. The tested solid reinforced concrete slab was 4.3m long, 3.3m wide and 100mm thick. Not including the area sitting on the supporting beams, the effective area was 4.16m by 3.16m. It had one layer of D147 mesh as reinforcement with the properties as shown in Table 6-2.

Table 6-2 Properties of the reinforcing steel at ambient conditions [Lim 2003]

Reinforced Steel	**Description**	**Bar diameter**	**Grid spacing**	**Yield stress**	**Steel content**	**Strain limit**
D147 mesh	Hot-rolled steel	8.7mm	300mm	565MPa	198mm^2/m	2.3%

Table 6-3 Key parameters used in the shell element model by Lim [2003]

Reinforcing Steel Properties	
Reinforcing mesh	198mm^2/m in both directions
Yield strength (ambient temperature), $f_{y,o}$:	565MPa
Steel model (thermal and mechanical)	Hot-rolled steel (EC2, 1995)
Concrete Properties	
Compressive strength (ambient temperature) f'_c:	36 MPa
Maximum concrete tensile strength, f_t:	1.5MPa
Concrete model (thermal and mechanical)	Siliceous aggregate (EC2, 1995)
Concrete cover, c_c:	25mm
Loads	
Self weight:	2.4 kPa
Live load:	3.0 kPa
Total applied load:	5.4 kPa

Lim [2003] simulated the slab using SAFIR with shell elements and showed good agreement with the experimental results. The experimental test had runaway failure, and the shell element model showed concrete crushing at the top surface of the slab causing failure. Twelve identical shell elements along each direction were used to model a quarter of the slab, and symmetric boundary conditions were used at the axes of symmetry. The key parameters used in the model are shown in Table 6-3. The tensile strength of the concrete was assumed to be 1.5MPa as Lim [2003] found out that this value gave the best fit between the experimental results and the SAFIR simulation. This was discussed before in Section 3.3.2.

Four scenarios with different floor widths and lengths were studied to investigate the relation between the grillage model and the floor aspect ratio. Each scenario was simulated again using a 3D beam grillage. Figure 6-12 shows the comparison scheme. In scenario A, both the length and the width of a quarter of the slab are modelled by ten identical beam elements. The reinforcing steel was at the middle of the element with cover thickness of 25mm. The material properties are the same as in the shell element model, other than the concrete material model is changed from being uniaxial to being biaxial.

Table 6-4 Key parameters of scenarios in comparison between shell and grillage models

Scenario	Boundary Condition	Length	Width
Scenario A [Lim 2003]	Pin-roller supports at four sides; symmetric rule applied in the models	4.160m	3.160m
Scenario B		4.160m	4.160m
Scenario C		4.160m	2.080m
Scenario D		4.160m	1.540m

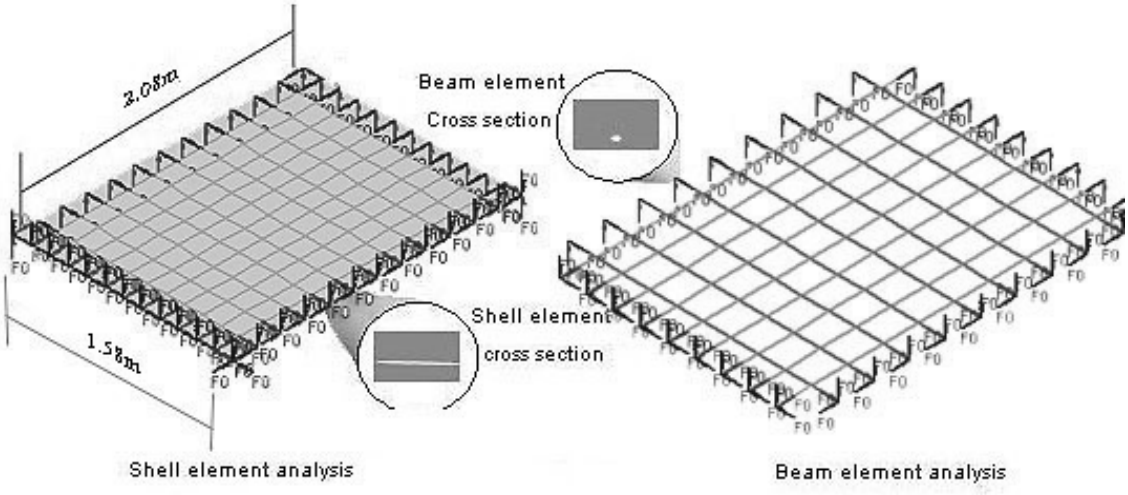

Figure 6-12 Comparison scheme between shell and grillage models

Because Lim [2003] showed a good agreement between the test results and the simulation results using shell elements in SAFIR, the simulations using shell element are deemed to give more accurate results. Hence, the grillage analogy will be justified if the grillage system could provide a result identical to the results from using shell element. Nevertheless, as Chapter 5 pointed out, the concrete model used for the shell and beam elements in SAFIR are different, one should expect some difference generated from the two modelling methods.

Figure 6-13 shows the results from the four scenarios. It is shown that the grillage models in Scenarios A, B and C not sharing the rotations about the lateral axes at each beam intersection gave a similar failure time to that from the shell element models.

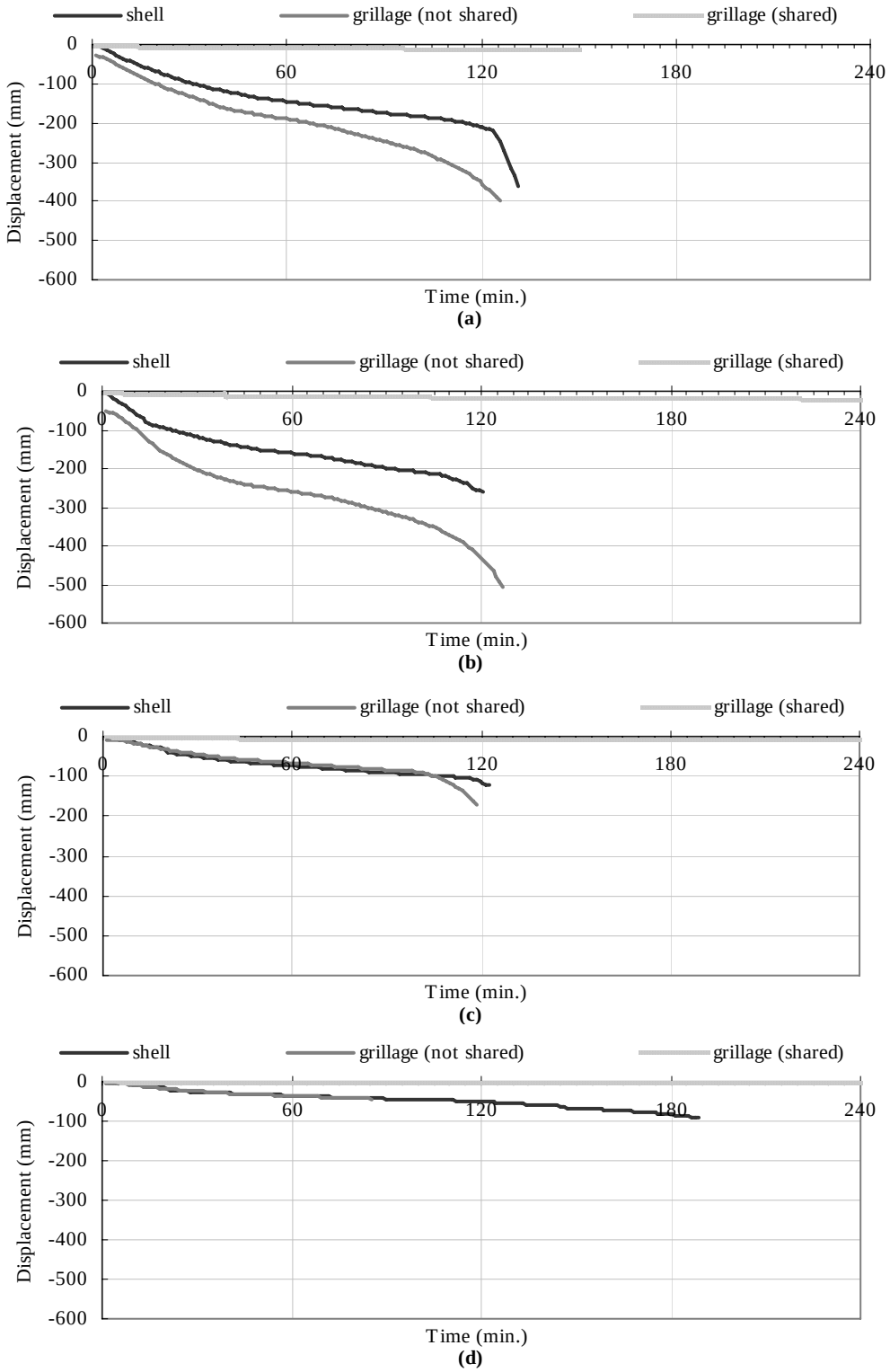

Figure 6-13 Comparison of vertical displacement at the centre of the slab in (a) Scenario A (b) Scenario B (c) Scenario C (d) Scenario D

The shell element models in all the scenarios determined the structure failed due to the crushing of concrete near the support of the slab, and in Scenarios B, C and D cracking of concrete at the centre also happened when failure was reached. The grillage models not sharing the rotations about the lateral axes at each beam intersection failed due to yielding of the reinforcing mesh. Figure 6-13 (d) shows that the grillage model sharing the rotations about the lateral axes at each beam intersection in Scenario D failed earlier than the shell element model of the same scenario, but the vertical displacements from these two models were almost identical.

In all four cases whether the rotations about the lateral axes at each beam intersection are shared or not made a big difference. The “grillage (not shared)” situation in Figure 6-13 means at the beam intersection each beam only shares the displacements in all directions and the rotation to the vertical axis; the “grillage (shared)” means the beams share both the displacements and rotations in all axis at the nodes where beams intersect. The figures show that the slabs would be too stiff in the cases where the rotations about the lateral axes at each node were controlled by the beams at both directions, and the results from the “grillage (not shared)” situation are always closer to the results from using shell elements. Ideally the rotational stiffness in different direction at a single point would be contributed separately by the beams in the grillage, i.e. the bending stiffness in the global X direction should be contributed from the beams running along the X direction. However, SAFIR can not achieve this kind of detail.

Judging from the two cases shown before, it was found that for two-way supported slabs sharing the rotations about the lateral axes in SAFIR will make the grillage too stiff. In one-way supported structure the sharing of rotation does not make much difference as shown in the first example. Because all the hollowcore concrete units are one-way supported only, and the reaction forces from the vertical support at the sides are transferred via the topping elements, whether rotation is shared or not does not pose a problem when studying the behaviour of hollowcore concrete flooring systems.

6.4.2. Assumption made with transverse beams

At the very beginning of the simulation, a computational problem arose because the transverse beams lacked tensile resistance. In the areas where the beams

experience sagging bending moment, the bottom of the beam would crack in tension while the top of the beam would crush in compression, and in the reverse direction where the beams experience hogging bending moment, the transverse beams would fail before reaching the first time step and stop the simulation. To allow for the finite element analysis to continue, it is necessary to maintain stress equilibrium over the cross-section of the beam element, therefore one part of the beam element is required to take the tensile force. To solve this problem, one fibre in the transverse beam element has been replaced by some material, behaving like steel in the simulation but with the same strength and stiffness as concrete. It is expected that the vertical cracks in the transverse direction should not cause overall failure of the floor; therefore, the end time of the simulation should not depend on the cracking of the transverse beams but on the overall behaviour of the structure.

6.4.3. Other assumptions regarding the overall model

Some details need to be overlooked to reduce the complexity of the model. This is necessary in order to reduce the effort of model construction as well as the computational power, especially when analysing the entire structure. In the proposed model, the failure mode is predominantly flexural. Although shear and anchorage failures as well as bond failures have been successfully modelled for single hollowcore units [Fellinger 2004], they are not incorporated into this model due to the complexity and the computational effort needed when applied throughout the entire structure. Besides, in practice shear failure in hollowcore concrete slabs is not likely to happen and has not been observed before. However, recommendations on the final design will consider the effect of shear and anchorage failure and suggestions by Fellinger [2004] will be taken into account.

Spalling effects may also create problems for the structural behaviour in fires. Spalling in hollowcore units has been observed by Lennon [2003] and has been described in Section 4.2.3. Detailed descriptions of the spalling phenomenon can be found in Section 3.1.5.

Even though spalling may cause premature failure of structures, it is not considered in this research, as many of the factors are too difficult to predict, such as the age of the floor when the fire occurs. Besides, introducing different times of spalling to the research will bring in one more parameter to the simulation, and even

though this is achievable in SAFIR by incorporating the change of cross section during the analysis, the results would be too specific and could not be representative.

6.5. Summary

A model to simulate the structural behaviour of hollowcore concrete flooring system has been proposed. This model is easy to construct and to process, and it is aimed to be used as a rather sophisticated design tool than for forensic engineering purposes, as the model does not take account of all the possible failure modes.

6.5.1. Model description

The program used to carry out the simulation is SAFIR. The proposed model is uses 3D beam grillage to simulate the hollowcore units, with longitudinal beams representing the webs and the flanges, and transverse beams representing the top and bottom flanges. In 3D beam grillages for simulating hollowcore units, the rotations about the beams in each direction are shared at the nodes of beam intersection. The reinforced concrete slab used as topping is simulated using shell elements. The model is illustrated in Figure 6-6.

6.5.2. Advantages of the model

- The model is easy to construct and process. The output file is easy to interpret.
- The model is able to capture the thermal gradient in the hollowcore units accurately.
- Continuity between the hollowcore units can be established by the shell elements which simulate the topping concrete
- The thermal strains and the thermal-reduced mechanical properties from Eurocode 2 are incorporated into the model. By including the thermal strains, the thermal stress and mechanical strains induced by incompatible thermal strains are included in the structural analysis.
- The transverse beam elements running across the width of the hollowcore units simulate the thermal expansion and thermal bowing across each unit.
- The model can take account of the prestressing effect.
- The model is designed to capture the flexural failure in the floor slab.

6.5.3. Disadvantages of the model

- The model assumes a perfect bond between different materials, and no anchorage failure can be captured.
- The model follows Bernoulli's hypothesis that plane section remains plane, so splitting cracks or horizontal cracks are not taken into account, and spalling is also ignored.
- The model cannot predict shear failure, which is similar to many other models in finite element analysis.
- As a default of SAFIR, the prestressing is applied at the same time as the loading in the structural analysis model and this effect is also influenced by the boundary condition at the supports, hence the stress distribution within the cross section at the first time step which is in ambient temperatures is different from the reality.

7. Model Validation

This chapter describes the validation process for the proposed model. There are five stages in the validation process. In each stage, either experimental results or reliable simulation data are available for comparison. Starting from the currently known capability of SAFIR, which is to simulate solid reinforced concrete slabs using shell elements, and then by introducing alterations to the model in each stage, the proposed model is validated in the final stage.

The five stages in the model validation process are:

1. Background comparisons (Section 7.1)
2. Comparing 3D beams to shell elements in modelling one-way reinforced concrete slabs (Section 7.2)
3. Comparing beam grillage to shell elements in modelling one-way reinforced concrete slabs (Section 7.3)
4. Comparing results from a beam grillage model to experimental results of one-way prestressed hollowcore concrete slabs (Section 7.4)
5. Comparing shell elements to beam grillage in modelling the topping of one-way prestressed hollowcore concrete slabs (Section 7.5)

The reinforced concrete slab used in the validation process is based on the slab tested by Lim [2003], as Lim used such a slab to show the good agreement between the simulation results using SAFIR shell elements and his fire test results. The validation process is built upon the premise that if the shell elements and the 3D beam grillage can provide similar if not identical results, one can give the same level of confidence to modelling slabs using grillage systems as to using shell elements. The results from each validation stage are discussed separately in the following sections. The information provided herein will be sufficient to construct the SAFIR input files; further details about the existing data can be found in the references in each section.

7.1. Stage One: Background comparisons

Stage One of the validation process compares a 3D beam grillage to shell elements in modelling two-way supported reinforced concrete slabs. The comparisons were presented briefly in Section 6.4.1 as the second example of checking the influence from sharing the rotations about the lateral axes at each node where the beams intersect.

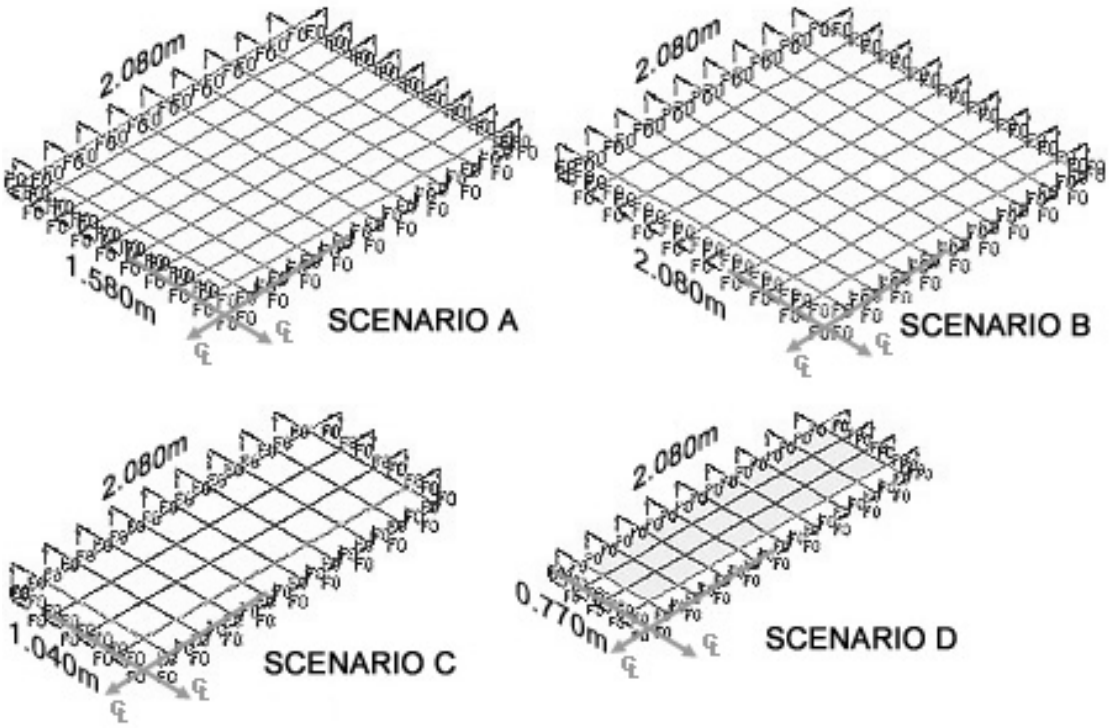

Figure 7-1 Layout of grillage model in Stage One comparison

The four cases studied are listed in Table 7-1. The model layout and more detailed information were described in Section 6.4.1. The slabs were exposed to the ISO834 standard fire from underneath, and the times stated from now on refer to the durations of fire exposure. The layout of the grillage systems is shown in Figure 7-1. Two beam elements with different width were used; one was 0.208m wide, and the other 0.158m wide. Scenarios A and D used a combination of two beam elements, with 0.158m ones running along the length and 0.208m ones the width. Scenarios B and C used only the 0.208m wide ones for the grillage. The grillage in both Scenarios A and B had 9 rows of beam elements in each direction, while the grillage in Scenarios C and D had 9 rows of beam elements along the width but 4 rows along the length. The total applied load onto the slab was 5.4kPa, beams in each direction took half of this load.

Table 7-1 Key parameters of scenarios in Stage One validation

Scenario	Boundary Condition	Length	Width
Scenario A [Lim 2003]	Pin-roller supports at four sides; symmetric rule applied in the models	4.160m	3.160m
Scenario B		4.160m	4.160m
Scenario C		4.160m	2.080m
Scenario D		4.160m	1.540m

Section 6.4.1 showed that sharing rotations about the lateral axes at each beam intersection is not suitable in two-way supported slabs and would make the model too stiff. It has also been observed that the 3D grillage model without sharing the rotations about the lateral axes at each node where the beams intersect can give an almost identical vertical displacement at the centre of the slab as the shell element model. Figure 7-2 shows the vertical displacement at the centre of the slabs predicted by the 3D grillages and the shell element models. The same figure has been shown before in Chapter 6 as Figure 6-13.

The simulations with shell elements model in all four scenarios at the predicted failure time stopped because of the crushing of the concrete near the side. The grillage models not sharing the rotation about the lateral axes at the intersections failed due to yielding of the reinforcing mesh. The grillage model sharing all the rotations at the node where the beams intersects did not fail until reaching the end time of the simulation except in Scenario A where the reinforcing steel at the midspan yielded at 150 minutes.

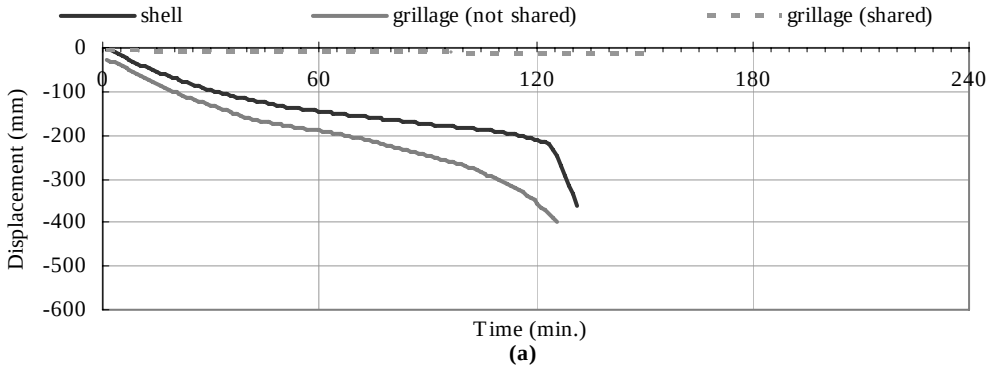

(a)

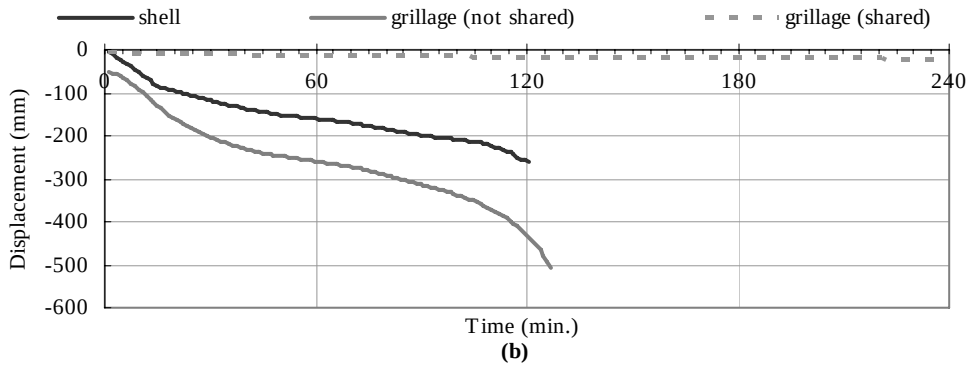

(b)

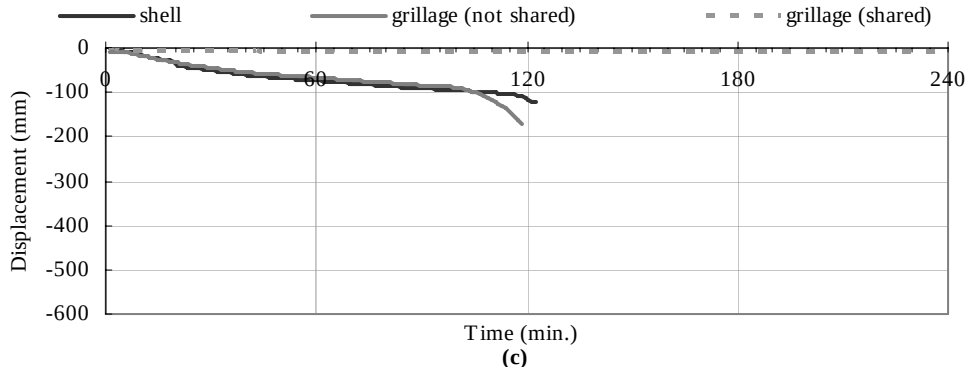

(c)

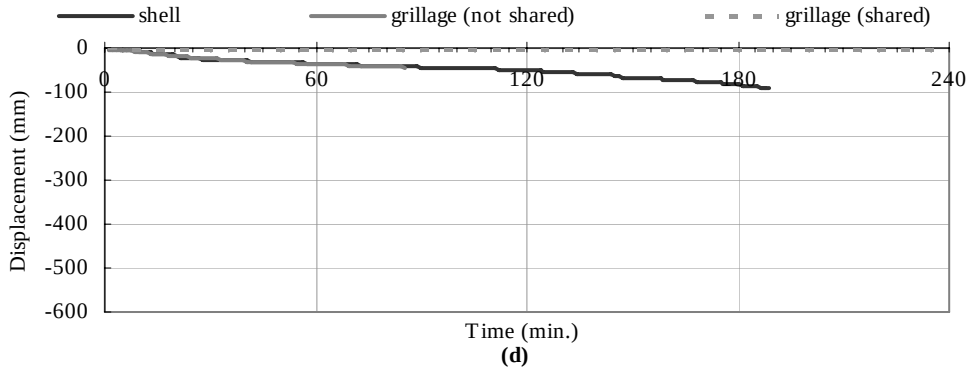

(d)

Figure 7-2 Comparison of vertical displacement at the centre of the slab in (a) Scenario A (b) Scenario B (c) Scenario C (d) Scenario D (notice the difference in the vertical scale)

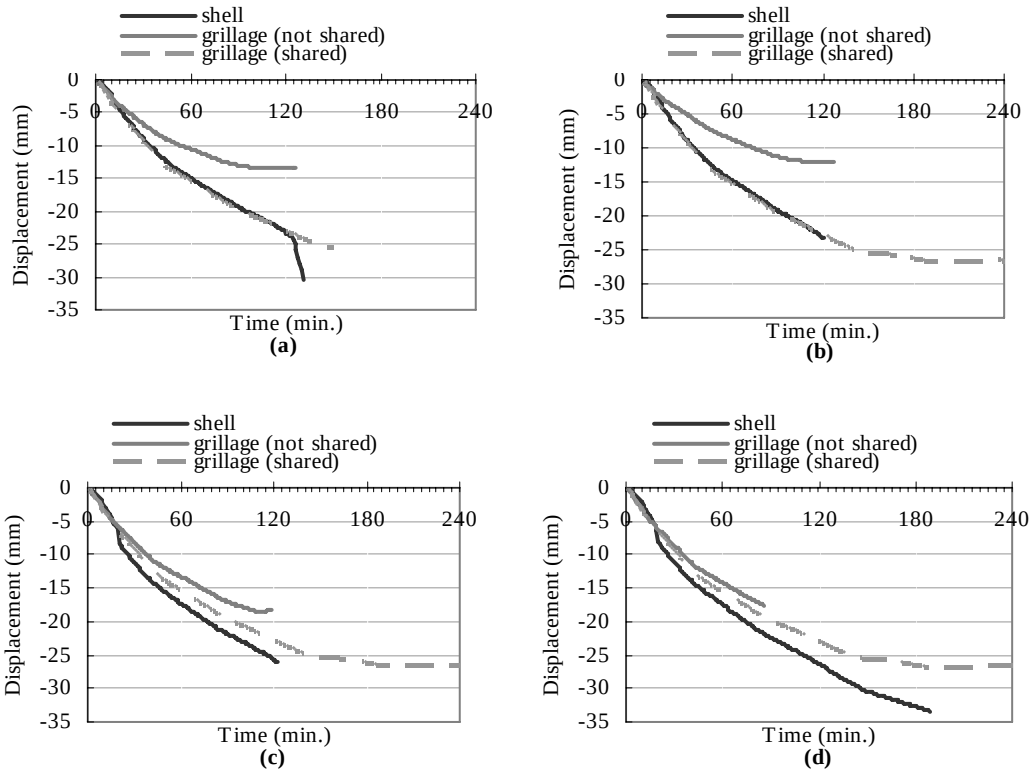

Figure 7-3 Comparison of horizontal displacement along the length at the corner in (a) Scenario A (b) Scenario B (c) Scenario C (d) Scenario D

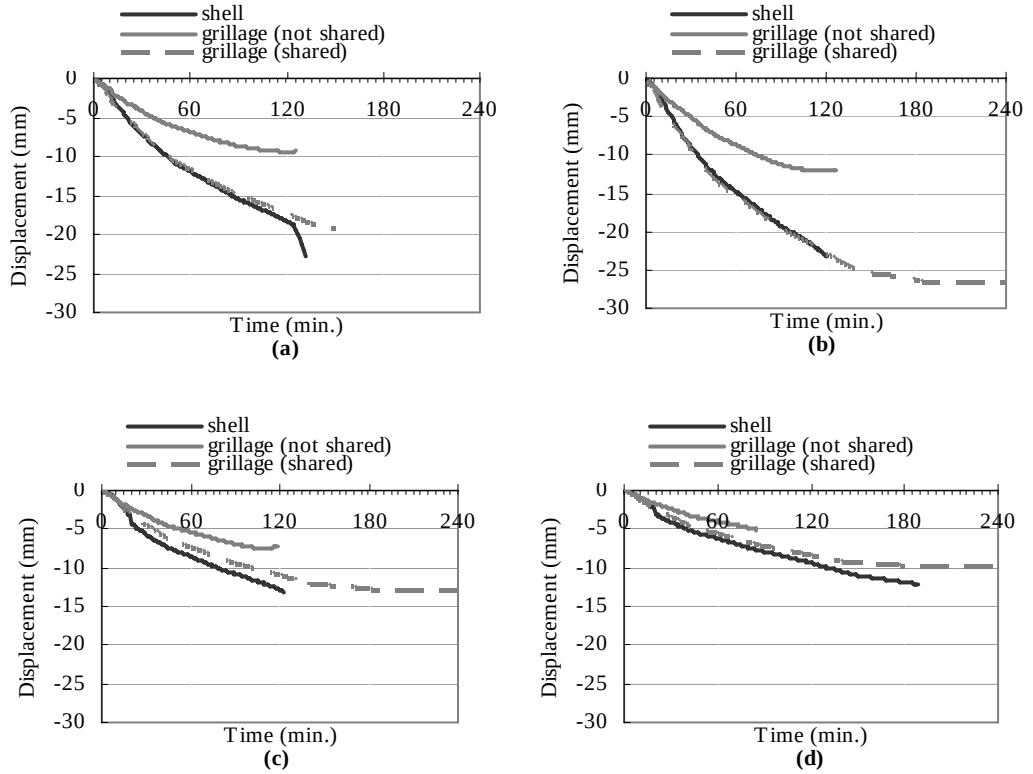

Figure 7-4 Comparison of horizontal displacement along the width at the corner in (a) Scenario A (b) Scenario B (c) Scenario C (d) Scenario D

The horizontal displacements at the corner of the slab along the length and along the width are shown in Figures 7-3 and 7-4 respectively, where negative values mean outward movements. The horizontal displacements from the grillage models with all rotations shared at the intersections are very close to that from the shell element models. This might be due to the stresses and thermal expansions in both directions being correlated in the two dimensional concrete model used in the shell element, and this behaviour could be reproduced by sharing the rotations at the intersecting points of the beam element grillages where the concrete model used is one dimensional. In the next stage of validation the two concrete models are compared against each other to see whether choosing different element types in SAFIR would affect the outcome.

Figure 7-5 shows the axial forces along the global axes at the centre of the slab in the four scenarios, where Y means along the width of the slab, and X the length. The axial force from the shell element model is calculated using the membrane force given in the output file multiplying the length or width of the corresponding shell element. The factors which influence the axial forces at any point in the slab are the deformation, the cracking and crushing of concrete at that point, and the induced mechanical stresses as explained previously in Section 3.4.3. It is expected that for a square slab such as in Scenario B, the axial forces along the length and the width are the same, which is shown in the figure. To summarise from the results shown in the figure, even though the trends demonstrated by the shell element and grillage models were different, from the maximum values in each case it showed that the grillage systems not sharing the rotations about the lateral axes at each node where the beams intersect gave a closer value to the axial force obtained from the shell element model, and the axial forces predicted by the grillage systems with all rotations shared were significantly smaller.

The overall results from this stage were somewhat satisfactory. For two-way supported reinforced concrete slabs, the vertical displacements predicted by the shell element and grillage models are closer if the rotations about the lateral axes at each node where the beams intersects are not shared, and the horizontal displacement predicted by these two methods are more similar if the rotations about the lateral axes are shared, or if the width-length ratio of the slab is small.

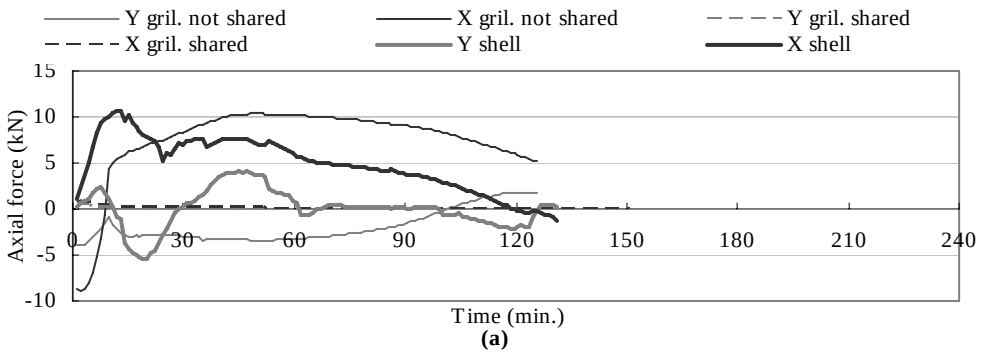

Figure 7-5 Axial forces at the centre of the slab in (a) Scenario A (b) Scenario B (c) Scenario C (d) Scenario D (+: tension, -: compression)

Judging from the vertical displacement as well as the axial forces at the centre of the slab, it is recommended that when using a beam grillage system to model a two-way reinforced concrete slab, the rotations about the lateral axes should not be

shared at each node where the beams intersect. In general the predicted deflected shapes for the grillage are closest to those for the shell elements if the rotations are not shared in the grillage.

7.2. Stage Two: Comparing 3D beams to shell elements in modelling a one-way reinforced concrete slab

The slabs from this stage onwards are one-way supported. This is because in the final proposed model each grillage system would be used to represent a single hollowcore unit, which is most commonly supported only at the ends. Besides comparing the structural behaviour obtained from using 3D beams and from using shell elements, the comparisons in this stage also verify whether the two dimensional concrete model used in the shell elements gives a different result to the one dimensional model used in the beam elements.

The modelled slab is 4.16m long and 3.16m wide. The slab thickness, reinforcement layout and the properties of the materials were the same as in Stage One. The end connections of the slab were roller supports. The modelled slab was exposed to an ISO834 standard fire from underneath.

Two scenarios were studied in this stage: the slab with the vertical supports at the short sides only or at the long sides only; and they are named as Scenarios A and B respectively. The key parameters used in these two scenarios are summarised in Table 7-2.

Table 7-2 Summary of key parameters of scenarios in comparison stage 1

Scenario	**Supported at the short sides only (A)**	**Supported at the long sides only (B)**
Span length	4.16m	3.16m
Boundary condition	Pin-roller supports along the width only; symmetric rule applied in the models	
Applied load	3188.6N/m2	5400N/m2
Beam element width	158mm	208mm

The load used in Stage One (5400N/m^2) was too large for Scenario A, as in this scenario the slab had a long span and could not sustain such a heavy load. The calculation of the flexural capacity of the structure in Scenario A in Appendix D shows that the maximum uniformly distributed load is 3542.9N/m^2. In this scenario

90% of the maximum load was used (3188.6N/m^2), so that the slab would not fail under the ambient condition. For Scenario B, the calculation shows that the maximum uniformly distributed load capacity is higher than 5400N/m^2, hence 5400N/m^2 was used for this case to be consistent with the rest of the validation process.

In the shell element models, twelve identical shell elements were used to represent a quarter of the slab, and the symmetric boundary conditions were used at the axes of symmetry. The results from the shell element model were compared to the results from the 3D beam element model as shown in Figure 7-6. In Scenario A, the width of each element was 1/20 of the width of the slab (158mm), and in Scenario B the width of the beam element in this case was 1/20 of the length of the slab (208mm). The length of the beam equalled half of the distance of the slab span, and symmetric boundary conditions were used at one end.

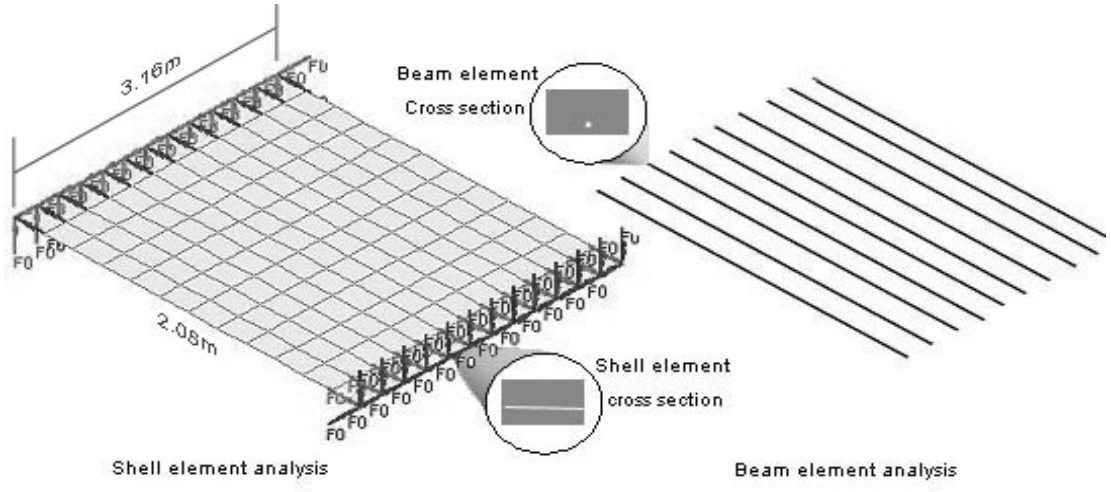

Figure 7-6 Stage Two comparison scheme

Since the cross section remain unchanged during the simulation following the Bernoulli's Hypothesis, and also because of no lateral loading was considered, no horizontal movement in the transverse direction was expected nor observed in the model using beam elements.

Figure 7-7 shows the vertical displacements at the midspan of the slab. The grey lines are from the simulations without any applied loads or self-weight. These simulations could last for much longer than 90 minutes in the ISO fire, and the deflections in these cases are only from thermal bowing. The results from the shell and beam element models for these cases are very similar, and they are closer to each

other in the slab with a shorter span.

Figure 7-7 also shows that to simulate the slabs with applied loads, the results from the two different methods matched each other well, except the shell element model had an earlier failure time due to crushing of concrete at the top surface near the supports. This can be explained as the support at the end does not allow for horizontal movement along the width, which induces high compression at the centre of the supported area of the slab as shown in Figure 7-8, and this is not found in using beams running parallel to each other. The compressive force near the edge and the tensile force at the centre region of the slab in Figure 7-8 indicate that thermal bowing happened not only along the span but also in the transverse direction.

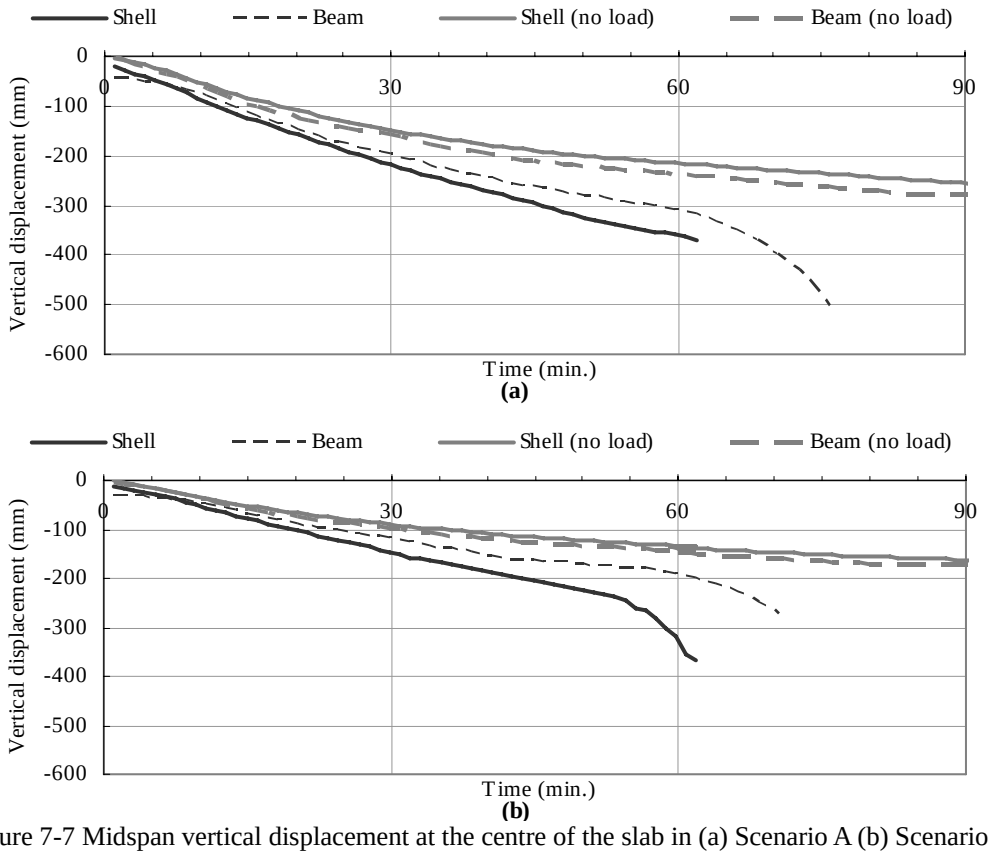

Figure 7-7 Midspan vertical displacement at the centre of the slab in (a) Scenario A (b) Scenario B

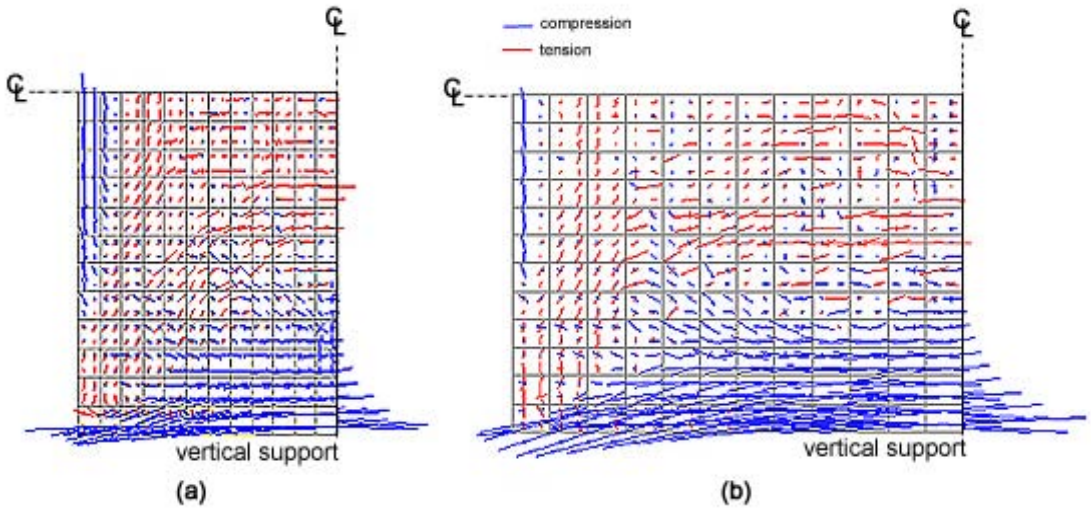

Figure 7-8 Membrane stress distribution right before failure time in (a) Scenario A (b) Scenario B (red: tension; blue: compression)

Figure 7-9 shows the horizontal displacement at the centre of the roller end of the slab, where positive values indicate inwards movements. The run away failure in the 3D beam models can be easily observed from this figure. The figure also shows that the horizontal displacements predicted by the 3D beam models are very similar to that by the shell element models.

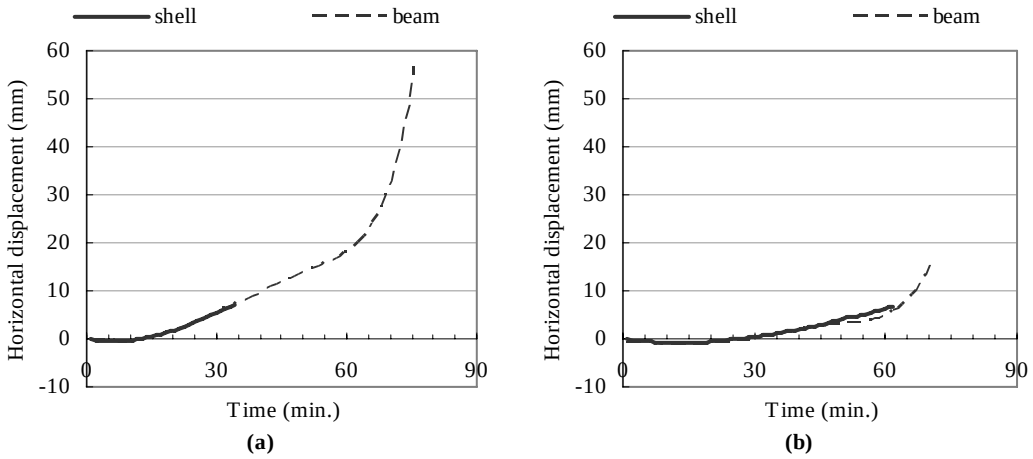

Figure 7-9 Horizontal displacement at the centre of the roller end in (a) Scenario A (b) Scenario B (+: inward)

The concrete models in the beam and shell element are different as described in Section 5.4. Comparisons with similar layouts to the slabs in this stage have been carried out by Wang [2004] who concluded that the two concrete models give drastically different outcomes. The results shown here contradict Wang's findings.

Further investigation showed that the comparison by Wang [2004] used the incorrect concrete model for the shell elements, and the corrected model agrees with the findings here.

To summarise from the comparisons in Stage Two, the vertical displacements obtained from using beam elements or shell elements were similar, and it is acceptable to use beam elements to replace shell elements to model one-way supported slabs, even though the shell element model might predict a more conservative time of failure.

7.3. Stage Three: Comparing beam grillage to shell elements in modelling a one-way reinforced concrete slab

The modelled slabs in this stage were the same as those in Stage Two, and so are the applied loads, the support conditions, and the layout of the shell element model. The difference between this and the previous stages is the model with beam elements, which is shown in Figure 7-10. In this stage, the transverse beams are introduced into the beam model to form the grillage. Having these transverse beams in the one-way supported slabs is aimed at allowing for the thermal bowing in the transverse direction but not to have any load bearing purpose; hence no load was applied directly onto the transverse beams.

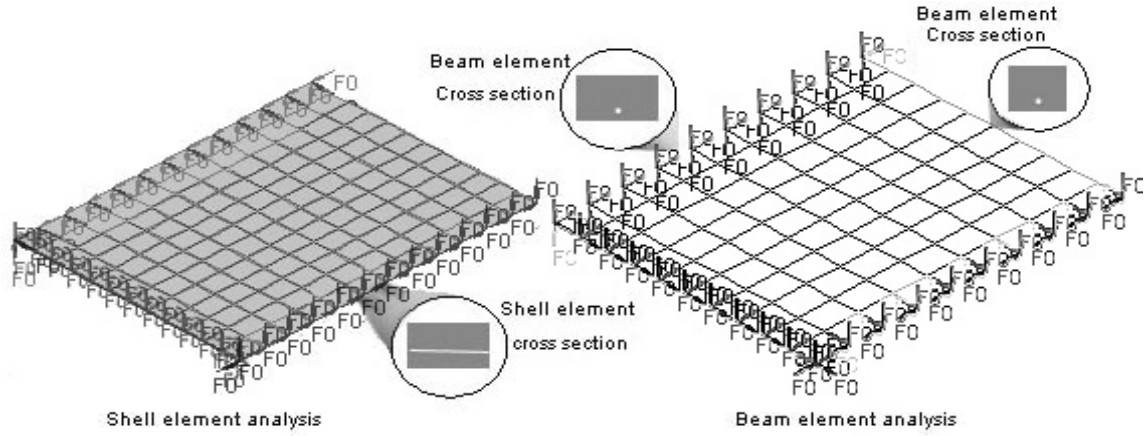

Figure 7-10 Stage 2 comparison scheme

Four scenarios were simulated in this stage. A summary of the key parameters of these scenarios is shown in Table 7-3. The slabs in the first two scenarios are the same as the slab of Scenario A in Stage One; and the slabs in Scenarios C and D have half of the slab width of those in Scenarios A and B respectively. These halved width slabs were used for observing the expansions in the transverse direction.

Since the slabs are one way supported like those in Stage Two, the uniformly distributed load used in each scenario is adjusted as in the previous stage. In the grillage model all the applied loads are only on the longitudinal beams and are adjusted in accordance to the width of the beam elements to represent a uniformly distributed load on the slab.

Table 7-3 Summary of key parameters of scenarios in comparison stage 2

Scenario	A	B	C	D
Boundary condition	Pin-roller supports along the slab width only; symmetric rule applied in the models			
Span length	4.16m	3.16m	4.16m	3.16m
Slab width	3.16m	4.16m	1.58m	2.08m
Applied load	3190N/m^2	5400N/m^2	3190N/m^2	5400N/m^2
Width of longitudinal beam elements	158mm	208mm	158mm	208mm
Width of transverse beam elements	208mm	158mm	208mm	158mm

Figure 7-11 (a) shows the comparison of the midspan vertical displacements from Scenario A. It is known that the vertical displacement at the side of the slab is expected to be different to the centre from the shell element model. With the contribution from the transverse beams, this behaviour can also be found in the grillage model. The figure shows that the vertical displacements from two different modelling methods matched against each other well until 45 minutes, and the difference in the vertical displacement between the two methods was larger at the centre than that at the side of the midspan. The grillage model predicted a run-away failure occurred at the time the simulation stopped. The simulation with the shell element model in this case stopped due to the high compression near the centre of supports and high tension near the middle of the slab. These high stresses within the shell element caused the finite element analysis not able to reach convergence and therefore the simulation was not able to continue beyond the stopping time.

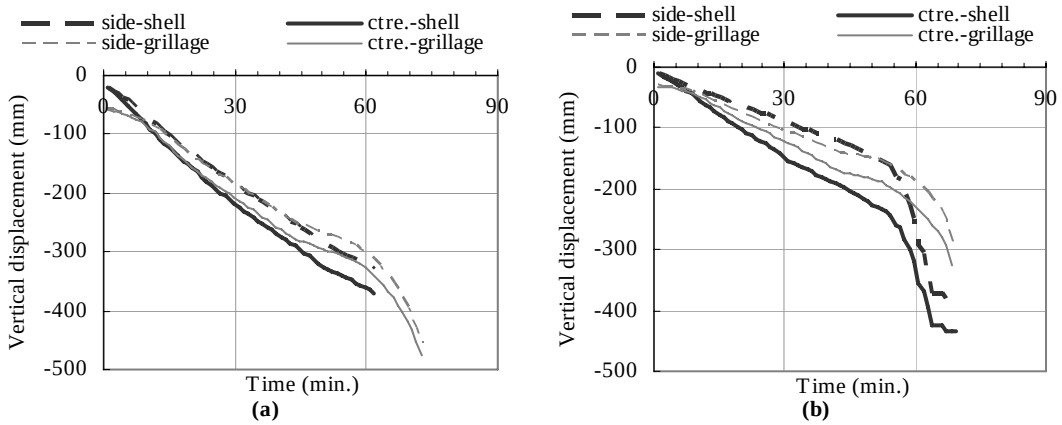

Figure 7-11 Results of Midspan vertical displacement from (a) Scenario A (b) Scenario B

Figure 7-12 (a) shows the midspan horizontal displacement in the transverse direction at the side of the slab in Scenario A. This horizontal displacement is a balance between the inward movement, which was caused by the loading and thermal bowing, and the outward movement, which was caused by the thermal expansion. The graph shows that both modelling methods gave very similar results.

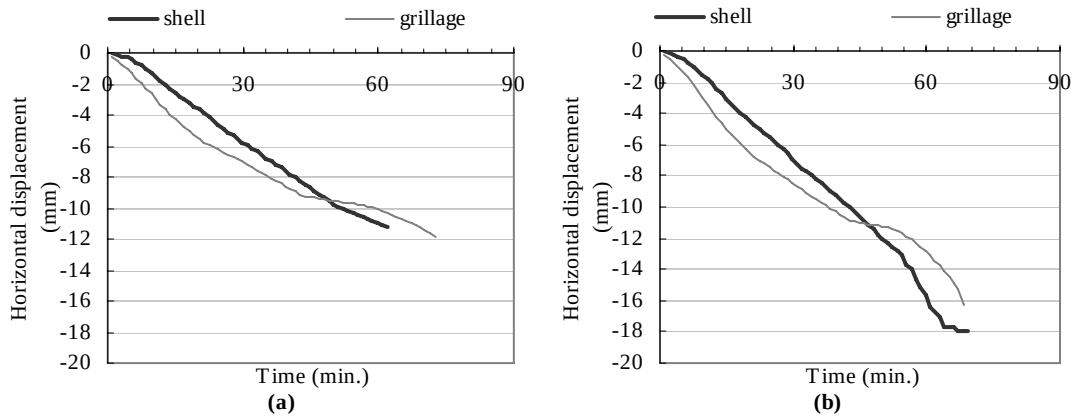

Figure 7-12 Results of Midspan lateral displacement at the side from (a) Scenario A (b) Scenario B (-: inward)

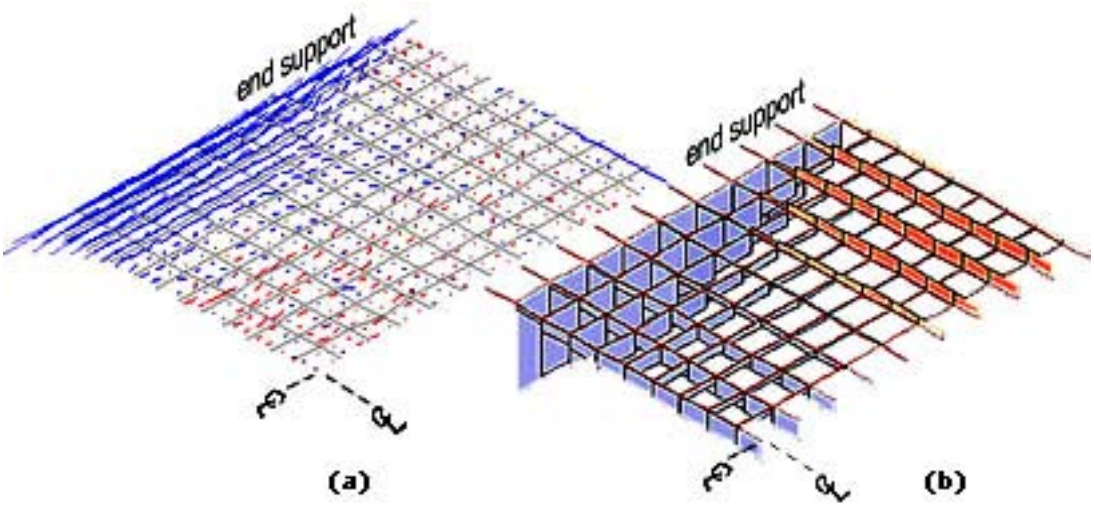

Figure 7-13 Comparison of membrane/axial force distribution from the (a) shell model (b) beam model in Scenario B after 60min. of ISO fire exposure (red: tension; blue: compression)

Figure 7-11 (b) and Figure 7-12 (b) showed the results from Scenario B. Although the horizontal displacements obtained from the shell element and grillage models matched well with each other, the midspan vertical displacements from the two models were slightly different. This might be due to the width of the slab being too wide and some membrane behaviour was established, i.e. a compressive ring forming around the edges surrounding a tensile region at the centre of the slab; the grillage model here could not pick up this behaviour as the loads were allocated solely onto

the longitudinal beams. This idea is further illustrated in Figure 7-13, where the tension in the transverse direction at the midspan was not found in the grillage model, and a higher compressive force at the centre of the slab was predicted in the grillage model than in the shell element model.

Scenarios C and D can be used to verify the previous argument. Scenarios C and D had half the slab width compared to that in Scenarios A and B respectively. Figure 7-14 shows the results from Scenario C, and it can be seen that the vertical displacements from the two simulation methods in this scenario were closer to each other than in Scenario A, and the difference in the horizontal displacements from the two methods was neither improved nor worsened.

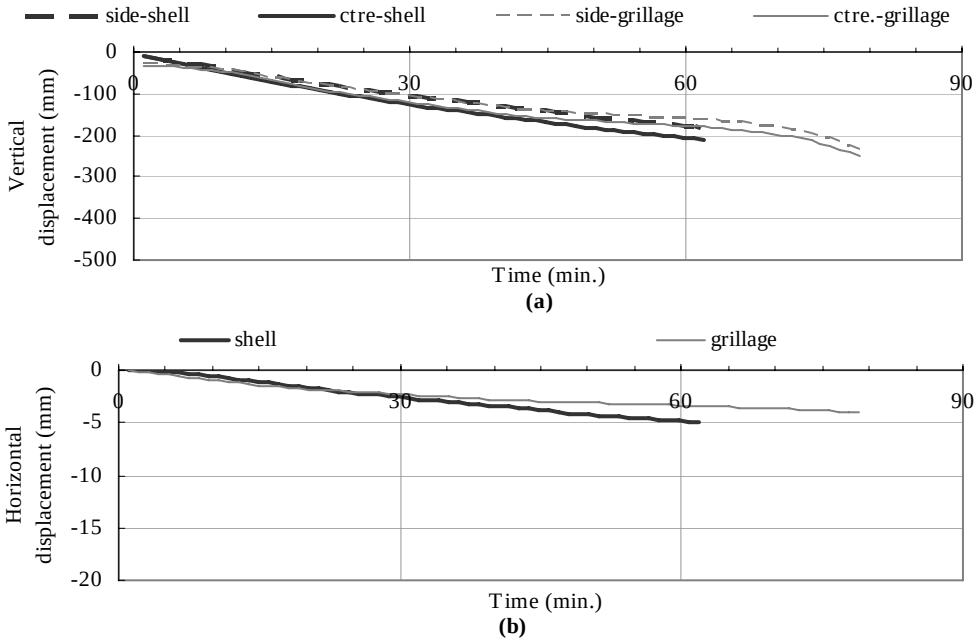

Figure 7-14 Results of Midspan displacement in Scenario C: (a) vertical displacement; (b) side horizontal displacement with negative means inward

Even though the slab has the same span, the shell element model in Scenario A lasted longer than in Scenario C. The failure of the shell element model in both scenarios A and C was caused by the crushing of concrete near the support, and the beam element model experienced runaway failure in both cases. Figure 7-15 shows the comparison of membrane force distributions between slabs in Scenarios A and C. It indicates that the highest compressive stress occurred near, but not at, the centre of the supporting edges, and the slab in Scenario C experienced a higher compressive stress than in Scenario A from 15 minutes onward, which explains the earlier failure

time in Scenario C.

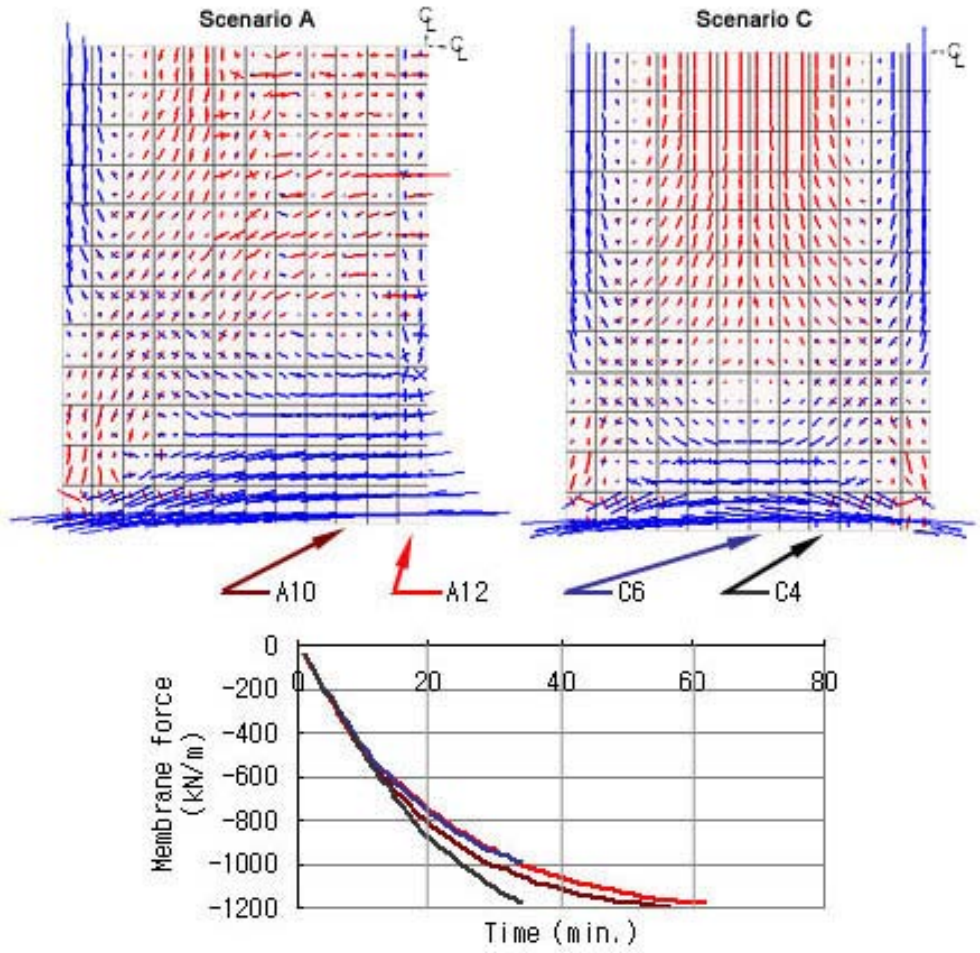

Figure 7-15 Membrane force distribution at 34min. and Membrane force trends in shell element models from Scenario A & C (red, +: tension; blue, -: compression)

Figure 7-16 shows the results from Scenario D, where the slab width was half of that in Scenario B. Unlike Scenario B, the shell element and grillage models in Scenario D gave very similar results in terms of both vertical and horizontal displacements. Comparing the results from Scenarios C and D to Scenarios A and B confirms that the membrane behaviour found in wider slabs could not be captured by the grillage model, therefore the grillage model predicted a smaller vertical displacement compared to that from the shell element model, especially at the sides of the slab.

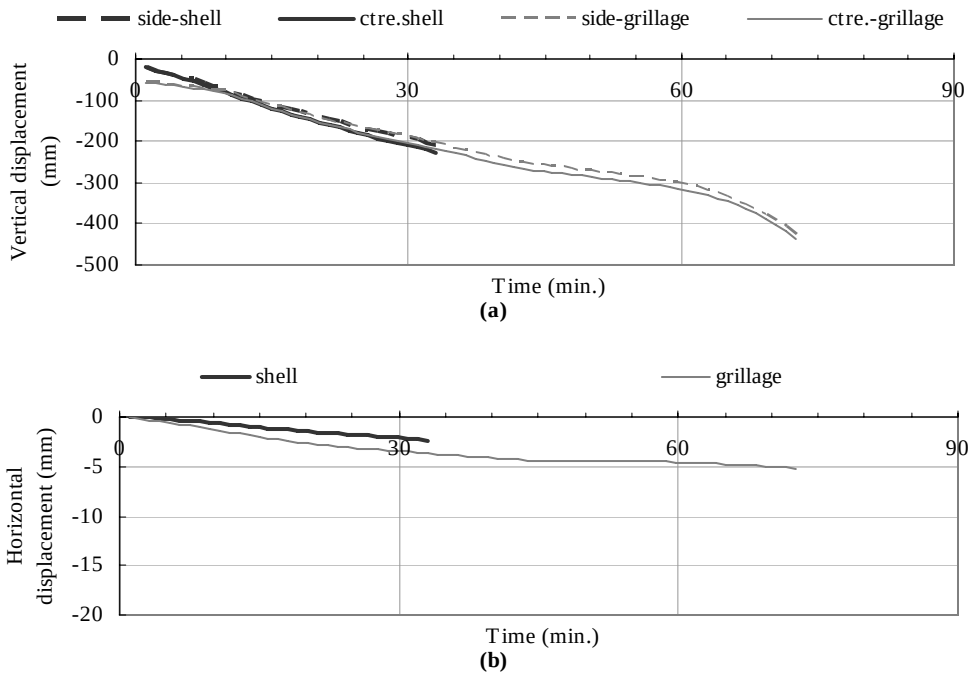

Figure 7-16 Results of Midspan displacement in Scenario D: (a) vertical displacement; (b) side horizontal displacement

The results of the grillage model shown before in this stage were from the models sharing rotations about the lateral axes at each node where the beams intersect. Another set of data from the model not sharing the rotations is shown for comparison in Figure 7-17. In this alternative model, the rotations were only shared at the node where the beams intersects near the end of the beams to allow the structure to be statically determinate. In all four scenarios, the midspan displacements at the centre or at the side of the slab from the two different models were nearly identical, with a maximum of 1.5% difference. This indicates that when using a beam grillage system to simulate an one-way supported slab in SAFIR, whether the rotations of the beams are shared or not at the node where the beams intersects does not change the results. Because sharing of rotations is closer to the original concept of grillage analogy, in the later analysis all rotations are shared at the nodes where the beams intersect.

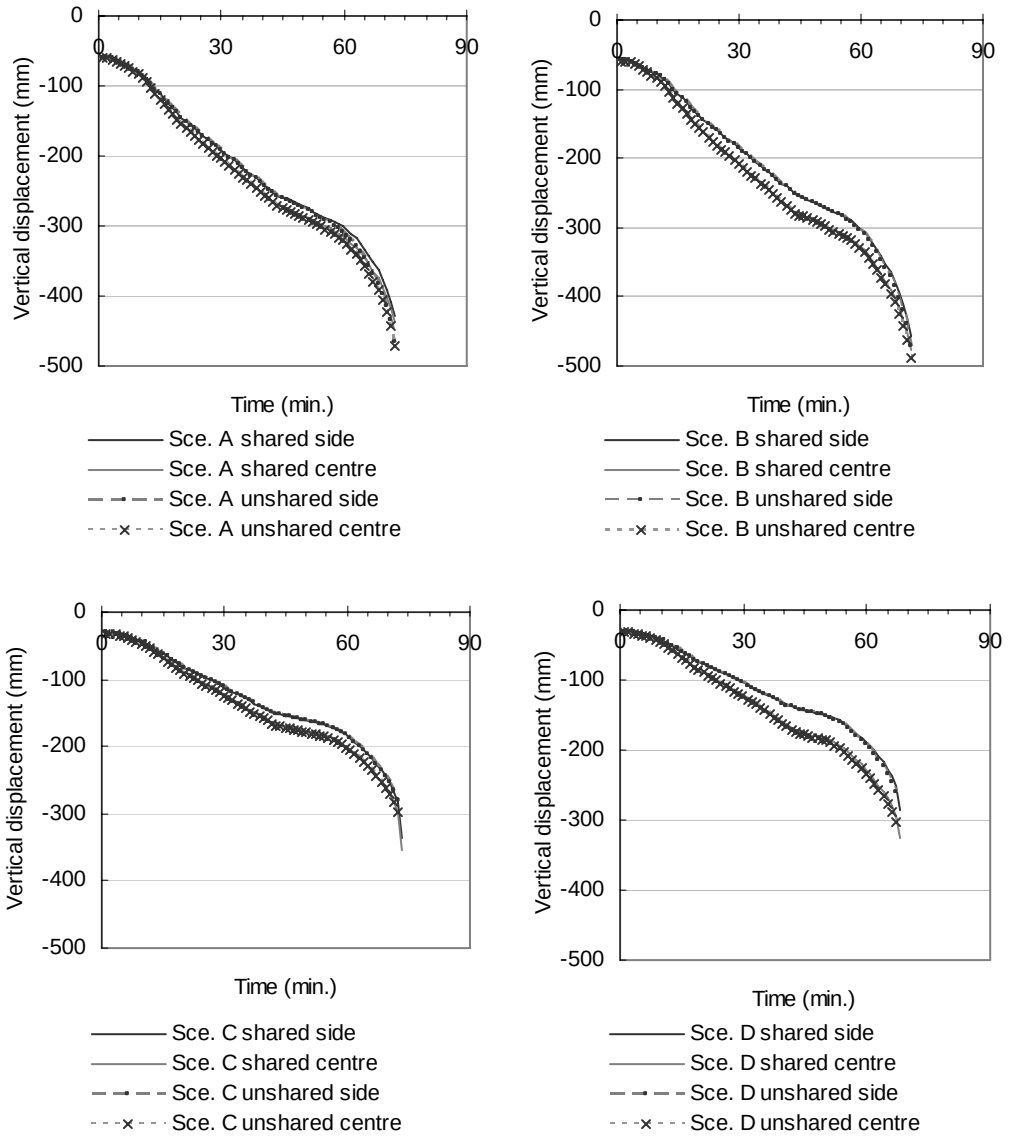

Figure 7-17 Comparison of results when sharing the rotations at the intersections in the four scenarios

The comparison in this stage showed that grillage beam systems can be used to replace shell elements to model one-way slabs and produce similar results. However, if the loads are only applied onto the longitudinal beams in the grillage beam system, the difference between the results produced from the two modelling methods would be larger when the slab width is greater. Since this research uses the grillage system only within the width of one hollowcore concrete unit, which is usually 1.2m, it is expected that the difference between these two modelling methods would be negligible.

7.4. Stage Four: Comparing results from a beam grillage model to experimental results of a one-way prestressed hollowcore concrete slab

Until this stage, the modelled structures were reinforced concrete slabs. In the previous stages it has been shown that the model with a grillage system made in beam elements can be used to simulate the reinforced concrete slabs with satisfying results in SAFIR, and in this stage the feasibility of using the grillage system to simulate floors made with hollowcore units will be explored by comparing the simulation results from the grillage models to experimental results from DIFT, University of Ghent, and BEF.

7.4.1. DIFT

The first set of experimental results used in this section is from the tests carried out by the Danish Institute of Fire Technology (DIFT) in 1998 [Andersen et al 1998]. Descriptions of this set of tests are in Chapter 4.2.1, and the technical details can be found in Section C.1 of Appendix C. Three different hollowcore slab sections were tested with 185mm (SP18), 220mm (SP22) and 270mm (SP27) thickness. The slabs were one way simply supported, with span length of 6.2m and no topping. Four equal line loads were applied to give a total load of 135.4kN, 135.4kN and 112.1kN respectively. The characteristic concrete strength of the HC unit was 2MPa in tension and 54MPa in compression.

In the simulation model, no symmetrical boundary was used at the midspan and the entire length of the specimen was modelled as shown in Figure 7-18 to take into account the prestressing effect. The discretised cross section of the beams used here are shown in Figure 7-19 where longitudinal beams were used to simulate the webs and the flanges of the hollowcore slab, and the transverse beams to take account of the thermal expansions in the top and bottom flanges along the width of the slab.

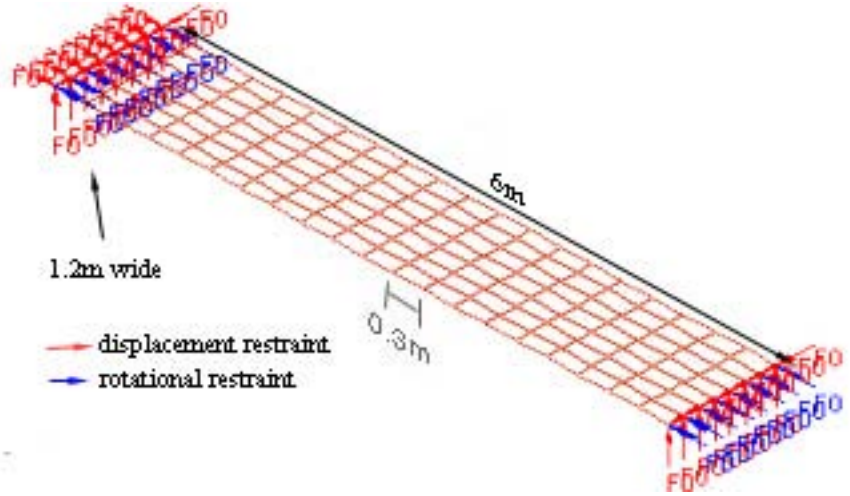

Figure 7-18 Grillage model for tests in DIFT 1999

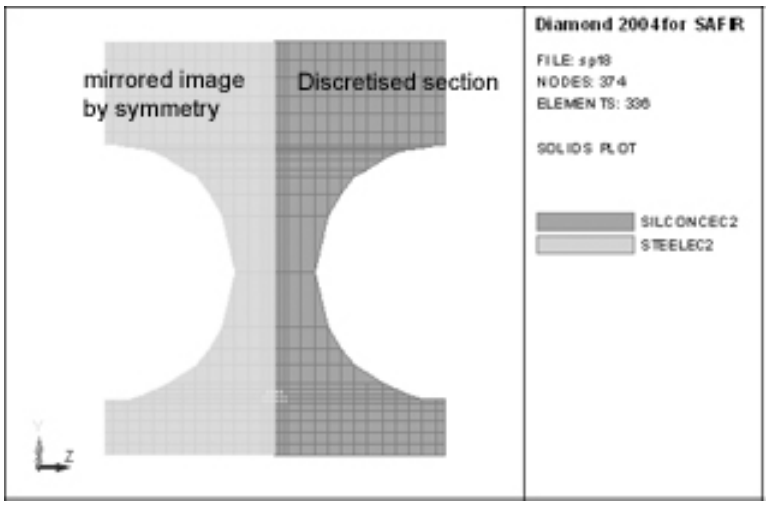

(a)

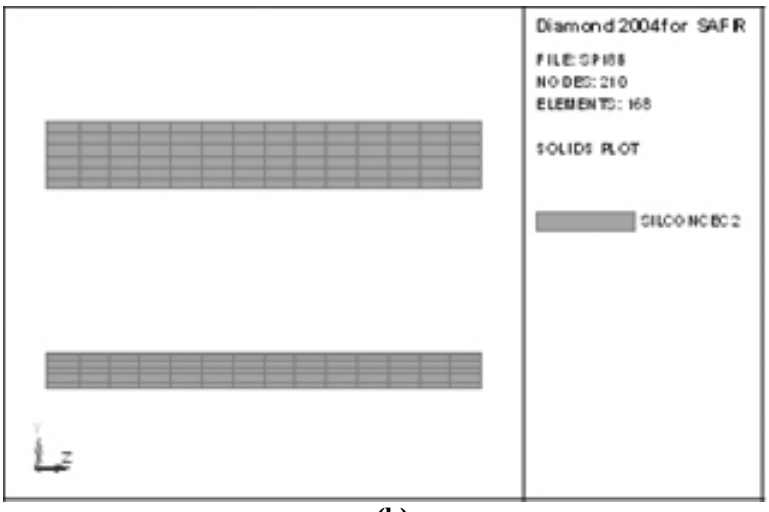

(b)

Figure 7-19 (a) Discretisation of the web of SP18 for the longitudinal beams (b) Discretisation of the transverse beams

Figure 7-20 shows the comparison of vertical displacements from the simulations and from the tests. Despite the difference in the failure times, the figures show that the simulation model could successfully predict the deformation of the slabs. The model predicted a later failure time than the recorded time from the test. The predicted failure in all three simulations was caused by yielding of prestressed strands at the midspan. The test specimens had shear and anchorage failure near the supports in less than 30 minutes of ISO fire exposure. Further explanations of the shear and anchorage failure can be found in Chapter 4.3. The results here show that the simulation model could not predict the shear failure, as expected.

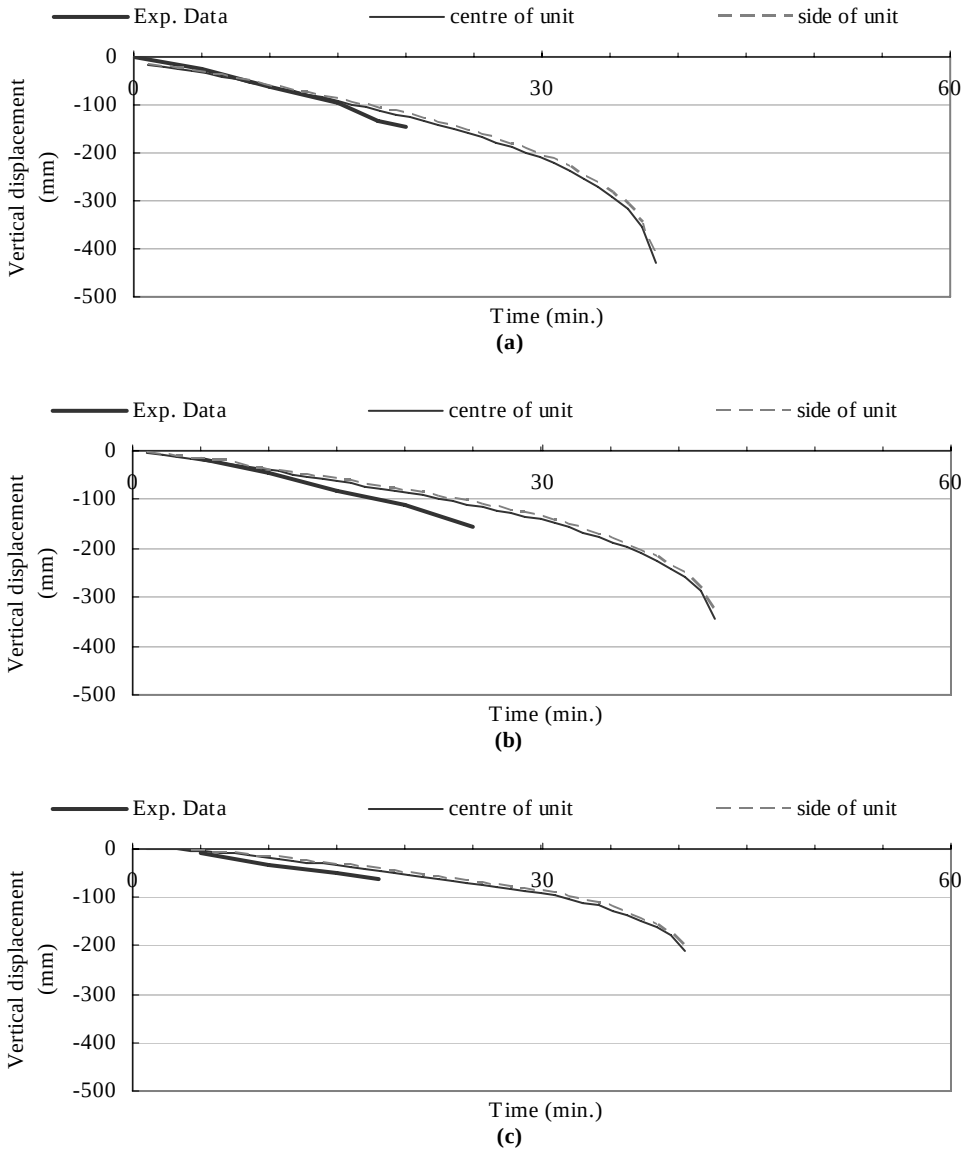

Figure 7-20 Comparison of midspan vertical displacements at the centre of the slabs with (a) SP18 (b) SP22 (c) SP27 units

The simulation model can calculate the lateral displacement at the sides as shown in Figure 7-21, where negative means outward movement. It shows that the lateral displacement was almost the same in all three cases since only the top and bottom flanges of the hollowcore slabs were considered for the transverse beams and the same concrete section was used in the three different units, therefore the predicted thermal expansions were almost the same. However, during the test this displacement was not measured and no comparison can be made.

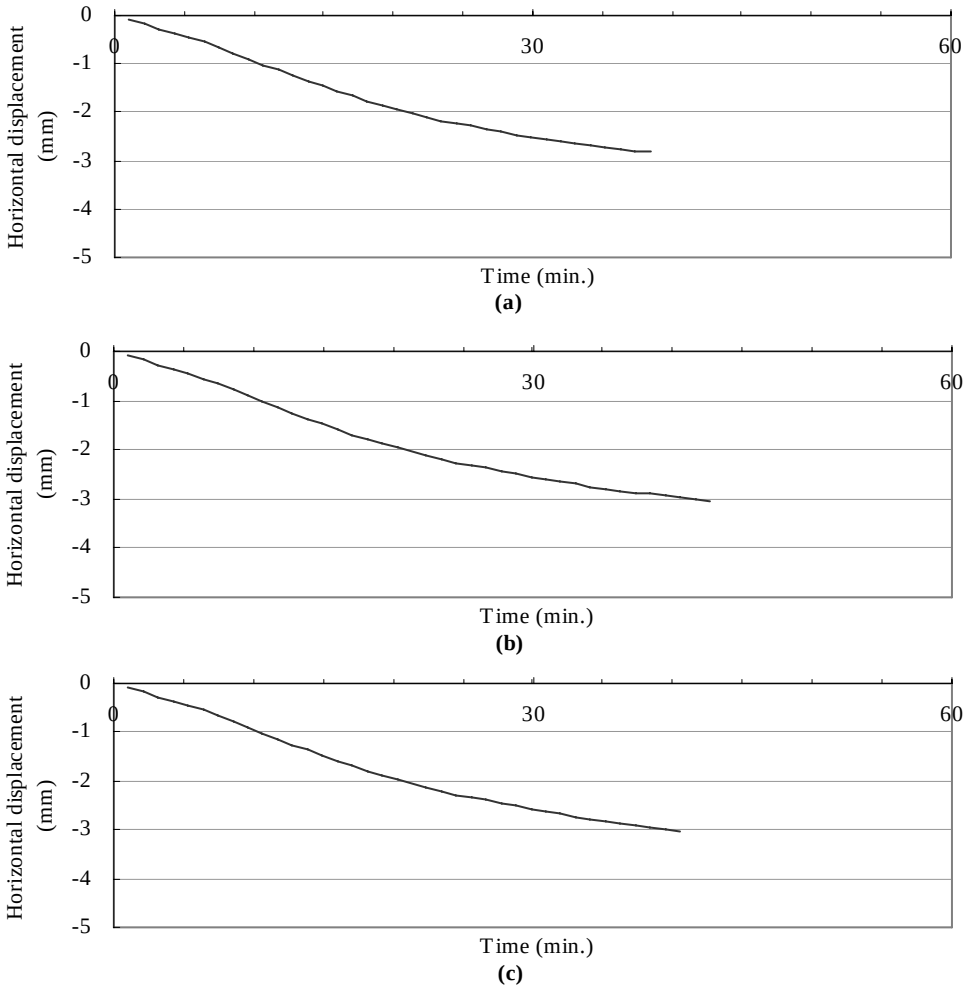

Figure 7-21 Comparison of midspan lateral displacements at the side of the slabs with (a) SP18 (b) SP22 (c) SP27 units

The slabs were simply supported, and Figure 7-22 shows the horizontal displacement at the roller end of the slab, where positive means outward movements. The horizontal displacement at the end is influenced by the thermal expansion of the slab along the span, and the bending of the slab which would pull the end inwards. The slab with more heated concrete area in the cross section would have more thermal

expansion, but because having more concrete area would make the slab stiffer, less bending would occur, more outward horizontal movement would be found in the deeper slab as shown in the figure below. There was no record on the horizontal displacement from the test, so no comparison could be made.

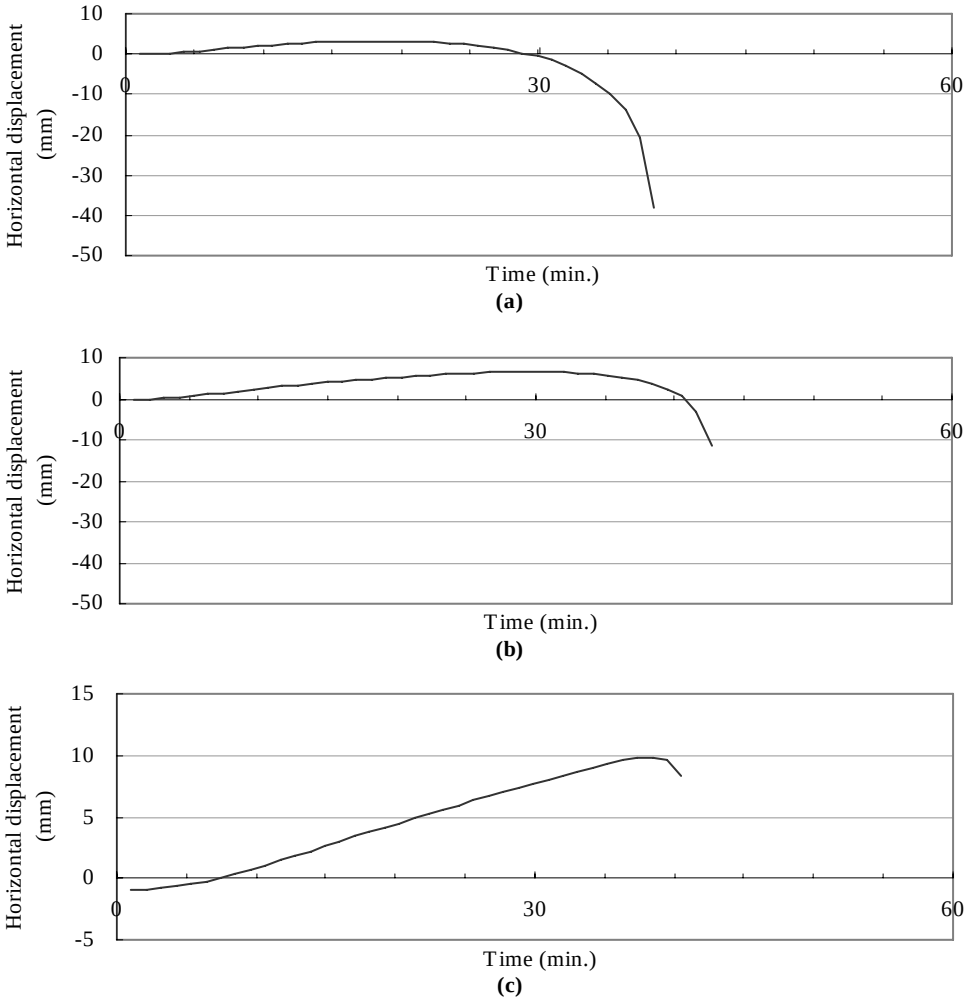

Figure 7-22 Comparison of horizontal displacements at the end of the slabs with (a) SP18 (b) SP22 (c) SP27 units

7.4.2. University of Ghent

The second set of experimental results is from University of Ghent [Febe Studiecommissie SSTC 1998]. The designs and findings of the tests were explained in Section 4.2.2, and the technical details are described in Section C.2 of Appendix C. The slabs with a layer of topping reinforced concrete were simulated here, these being the Tests 1 and 4. Each test consisted of two 2.4m wide floor consisting two hollowcore units, spanning 3m and supported on three beams as shown in Figure 4-9. Each floor was independent. The floors had a line load of 100kN in the middle of

each of the two spans, and were exposed to two hours of ISO fire. After two hours of fire exposure, extra load was applied to check the remaining load capacity. Only half of the floor was simulated, which was one 1.2m wide floor span of 3m; and the illustration of the simulation model is in Figure 7-23.

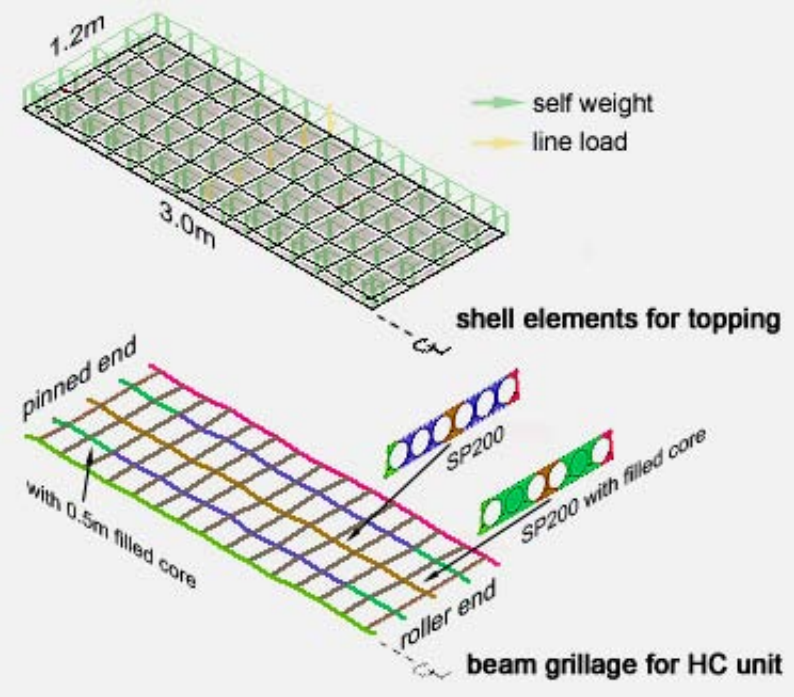

Figure 7-23 Illustration of the simulation model for the Test 1 from University of Ghent

In the simulation model, the filling of the cores at the ends was included but the peripheral ties or the detailed anchorage were not. The self-weight was applied as uniformly distributed load onto the shell elements. The shell elements were connected to the grillage underneath as demonstrated in Figure 6-6. Because the model was one unit wide, to simulate two units placed side by side to each other, symmetry was used at one side of the model.

In Test 1, the cross section of the hollowcore unit was divided into five parts, and in Test 5 was into four parts; each part was represented by one beam element in the longitudinal direction. Figure 7-23 shows the divided sections of SP200 which were used for Test 1 labelled in different colour; and Figure 7-24 shows the sections of SP265 which were used for Test 4.

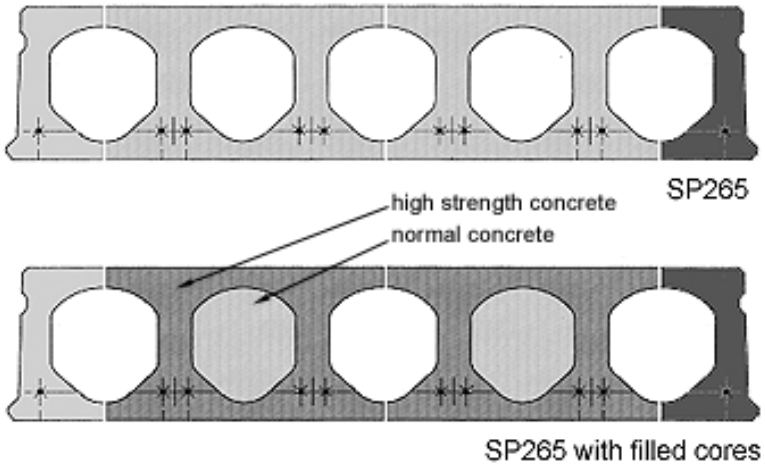

Figure 7-24 Divided hollowcore sections for the Test 4 model

In all of the tests, the compressive strength of the concrete in the HC units was 45MPa, and the strength of the strands was 1.85GPa. Because the values of some parameters were uncertain, a sensitivity study on these parameters was carried out first. In the sensitivity study the slab was assumed to be simply supported, and its dimensions were based on the slab from Test 1. The end time of each simulation was 240 minutes of ISO fire exposure.

The first sensitivity study was to ensure the transverse beams do not increase the stiffness of the slab. The simulation models with and without transverse beams failed at the same time reaching 170 minutes of fire exposure. Figure 7-25 shows the midspan vertical displacement of the slab, and it shows that the transverse beams had no influence on the vertical displacement. The result was as predicted since in this case the slab consisted of only two units, the effect from thermal bowing across the width should be negligible. The results confirmed the idea that the transverse beams should only contribute to the transverse displacement, or become effective when the slab consists of several units over the width.

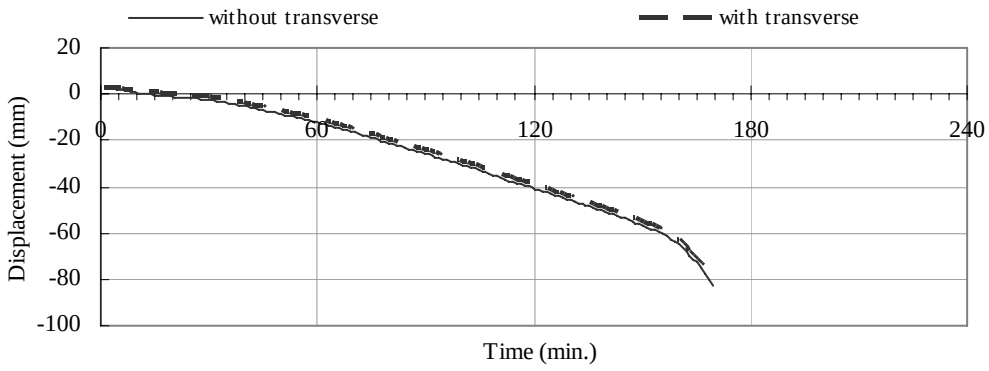

Figure 7-25 Comparison of vertical displacements of the model with and without transverse beams

The second sensitivity study was on the prestressing level. The prestressing level from the experiment was unknown from the test report and was assumed to equal 75% of the strand strength based on the normal practice in New Zealand. The comparison of the midspan vertical displacement from the models with different prestressing level is shown in Figure 7-26, which indicates the fire performance of the slab is affected by the level of prestressing to a limited extent, as the HC flooring system with prestressed level of 75% of the strand strength performed almost the same as the system with 80% of the strand strength in terms of vertical displacement at the midspan. The upward displacements at the midspan given in the very early stage of the fire from the models were caused by the eccentric prestressing force. The case with no prestressing had a larger vertical displacement from the beginning of the simulation as expected, and the simulation stopped within 10 minutes into the fire due to numerical instability. The conclusion drawn from here is that even if the assumed prestressing level (75% of the strand strength) was a little bit different from the value used in the test, the simulated results should be still very similar to the actual results.

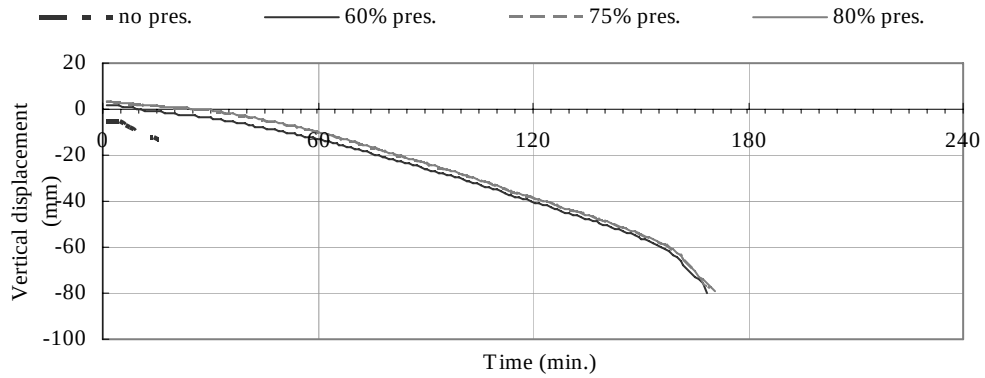

Figure 7-26 Sensitivity study on prestressing levels

The last sensitivity study was on the strength of the reinforcing bars in the topping concrete. The strength of the topping rebars was claimed to be 500MPa, however, no test was done to confirm the actual strength. Figure 7-27 shows the effect of different rebar strengths on the midspan vertical displacement, and the results indicate that even if the rebar strength was 100MPa smaller than the stated value, the difference to the overall performance was negligible.

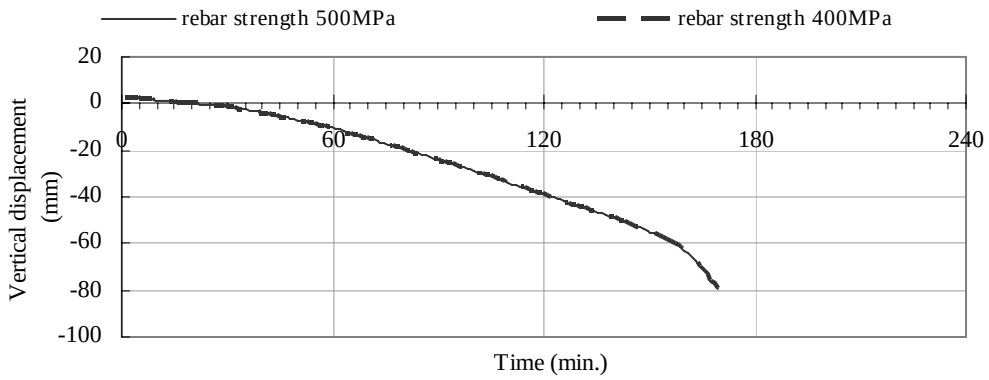

Figure 7-27 Comparison of vertical displacements between cases with different rebar strengths

The midspan vertical displacements from the simulations of Tests 1 and 4 are shown in Figure 7-28 (a) and (b), with the prestressing level assumed to be 75% of the strand strength and the rebar strength being 500MPa. In Test 1, the hollowcore unit was SP200 Ergon with circular voids. The simulation with no rotational restraints at the ends predicted that the slab had around 3 hours of fire resistance; the fire resistance reduces to 40 minutes if there are full rotational restraints. However, in reality the support condition is one of partial rotational restraint, and the slab withstood 83 minutes of the fire.

Figure 7-28 (a) shows that the simulation result was not very close to the experimental data from the test report [FeBe Studiecommissie SSTC 1998]. The maximum difference between the maximum deflections obtained from simulation and the test data was 15mm. During the experiment, shear cracking was observed 7 minutes from the start of the experiment, and vertical cracking was observed at 12 minutes. This explained the rapid increase in midspan deflection in the experiment at the early stage of the fire. Nevertheless, the simulation model could not predict the shear displacement or failure.

In Test 4, the hollowcore unit was changed to SP265 Ergon which had oval shaped voids, and the number of voids was changed from six to five, but the applied load and other mechanical values were the same as in Test 1. The experimental result in Figure 7-28 (b) shows that the slab could sustain up to 2 hours of ISO fire. The test specimen collapsed when the fire was stopped after 2 hours and more loading was added at the midspan to check the capacity. There was no shear failure or substantial shear displacement during the fire test, and the simulation result matches the test data

reasonably well. The model with pinned connections failed due to yielding in the prestressing strands, while the model with the fixed connection stopped due to crushing of the topping concrete in compression near the support. The maximum difference between the two deflections was around 10mm.

The predicted vertical displacements from the models with different connection types shown in the previous figures also reflected the method SAFIR calculates the prestressing effect. The prestressing effect was applied to the structure at the same time as the effect from the end connections, therefore the upward midspan displacement under the cold condition was found only in the situation with pinned connections.

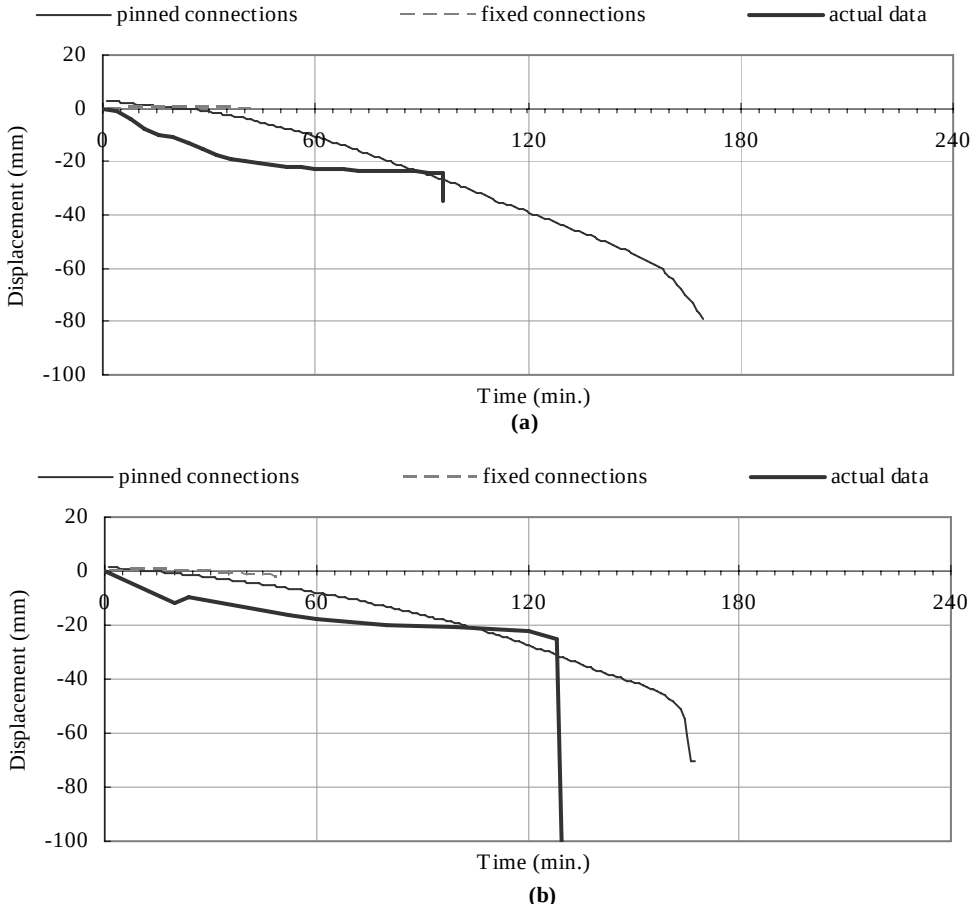

Figure 7-28 Simulation results with different end conditions for slabs from (a) Test 1 (b) Test 4

7.4.3. BEF

The last set of experimental results to be compared in this stage is from BEF [BEF 2005], the Danish Prefab Concrete Association. The designs and the findings of the tests were illustrated in Section 4.2.4, and the mechanical properties and dimensions of the specimen are shown in Section C.3 of Appendix C. In these tests the fire curve followed only 60 minutes of the ISO fire and then stopped, and the tests continued for a further 60 to 90 minutes with the constant applied load. The tested specimens were 265mm thick without topping and spanning 3.27m simply supported. Three load levels, 65%, 75% and 80% of the ultimate shear capacity of the slab under the ambient conditions (91.6kN/m) were used in the tests as line loads, which was located at 522.5mm from one end.

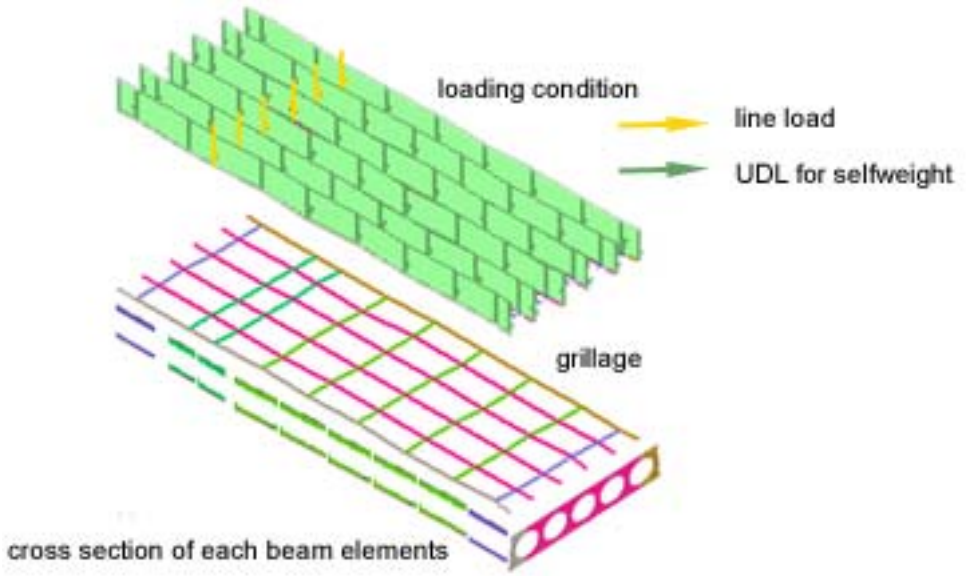

Figure 7-29 Illustration of the model used for BEF tests

Figure 7-29 illustrated the grillage model used here. The hollowcore unit was split into six parts in the model, where four identical parts are used to represent the four webs at the centre of the unit. The transverse beams connected the end nodes between each row of longitudinal beams. The interval between the transverse beams was varied to ensure that a transverse beam coincided with the exact location of the line load, and the loads could be applied onto the nodes where the longitudinal and transverse beams meet.

Figure 7-30 shows the comparisons of the vertical displacements between the analytical prediction and experimental results. The test results showed that the HC

slabs maintained a good resistance to shear stresses under elevated temperature. The simulation stopped after 140 minutes as the last recorded time in each test was 140 minutes from the beginning.

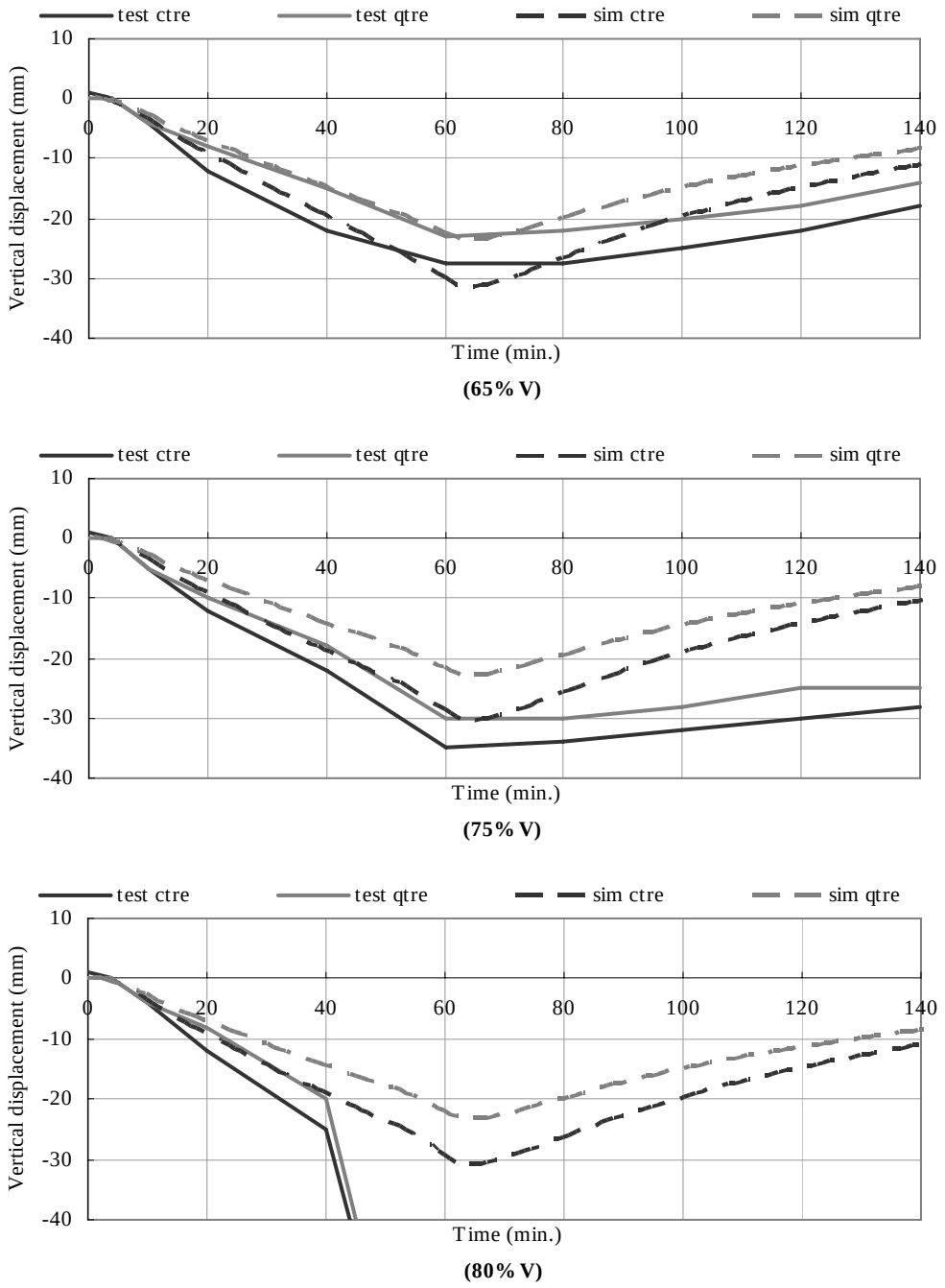

Figure 7-30 Comparison between the vertical displacements at midspan (ctre) or at the location of the point load (qtre) from simulation (sim) and BEF test (test) results with different level of loading

The results show that the vertical displacements calculated found from the simulation were very close to the test data. The difference between the vertical deflection at the centre and the side of the unit in the simulations is almost the same as

that from the tests. The difference between the predictions and the test data is presumed to be due to shear deformation. In the case with an applied load equal to 80% of the slab's shear capacity, the slab had a shear failure after exposure to 45 minutes of the ISO fire. Figure 7-30 (c) shows that the model could not foresee the shear failure and therefore it continued to provide results after this time. In the case loaded up to 80% of the slab's shear capacity, the large shear force was not captured in the analysis, and the model underestimated the deflection. Nevertheless, such high level of shear force is never designed for in normal practice.

7.4.4. Summary from Stage 4

The grillage model was used to check against three sets of experimental data. The results showed that the grillage model can predict the displacement caused by flexural bending very well, but cannot foresee the shear failure or take account of the shear deformations not caused by thermal stresses.

7.5. Stage Five: Comparing shell elements to beam grillage in modelling the topping of a one-way prestressed hollowcore concrete slab

The effect on the different methods of modelling the reinforced concrete topping slab is explored in the last stage of validation. When the topping exists as currently required in New Zealand, the continuity across the hollowcore units is established via the topping. In the proposed model, this continuity relies on shell elements. Nevertheless, to ensure that using a combination of two element types does not increase the stiffness of the model, it is necessary to check that within the hollowcore unit width, the models with topping represented by beam or shell elements give the same results.

The hollowcore unit used in this stage is DYCORE 300. The cross section of such unit is shown in Figure 7-31. The unit strength is 42MPa at 28 days; the self-weight of the unit is 3.20kPa. The strands are stress relieved 7-wire strand with properties based on BS5896, Specification for High Tensile Steel Wire and Strand for the Prestressing Concrete [BSI 1980], with strength of 1.87GPa, and area of 112mm^2.

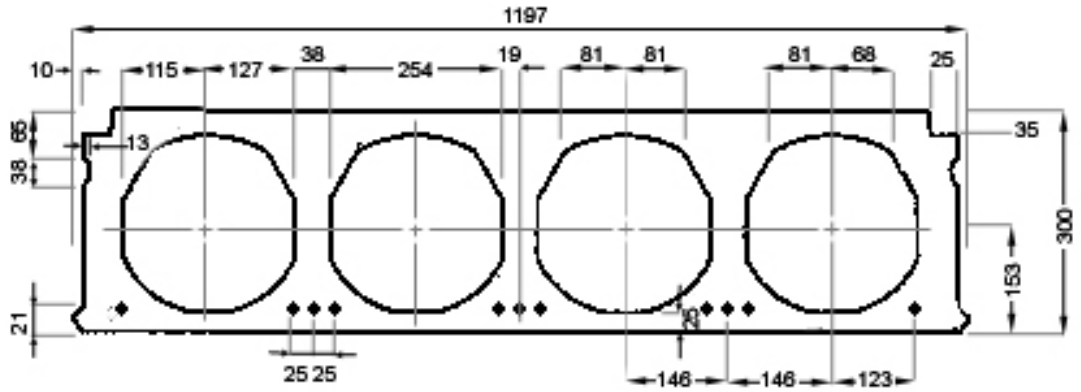

Figure 7-31 Cross section of a DYCORE 300 unit [Firth Stresscrete et al. 2007]

The span length of the slab was 12.2m. The load table from Firth Stresscrete et al. [2007] indicates that the slab with 12.2m span can sustain a live load of 7.8kPa under the ambient conditions where the weight of a 65mm ordinary concrete topping is considered but other superimposed dead loads are not. According to Loading Standard AS/NZS 1170 [Standards Australia et al. 2002], the load combination of ultimate limit state condition in ambient conditions is 1.2G + 1.5Q, where G is dead load and Q is live load. By assuming the unit weight of ordinary concrete being 24kN/m^3, the load capacity from this load combination would be 17.5kPa. The thickness of the concrete topping used in the simulation was 75mm instead of 65mm to coincide with the specimens tested by Matthews [2004], Lindsay [2004] and MacPherson [2005]. By making the adjustment on the weight of the topping, the allowable live load is reduced to 7.6kPa. The load combination of ultimate limit state condition in fire is 1.0G + 0.4Q, which would equal to 8.0kPa. Therefore, 8.0kPa was used as the total load applied onto the slab.

Figure 7-32 shows the models used in this stage. The hollowcore unit was split into five sections, where the three central sections were identical to represent the three webs in the middle. In one of the models the topping layer is modelled separately by a layer of shell elements, and in the other it is included in the beam elements.

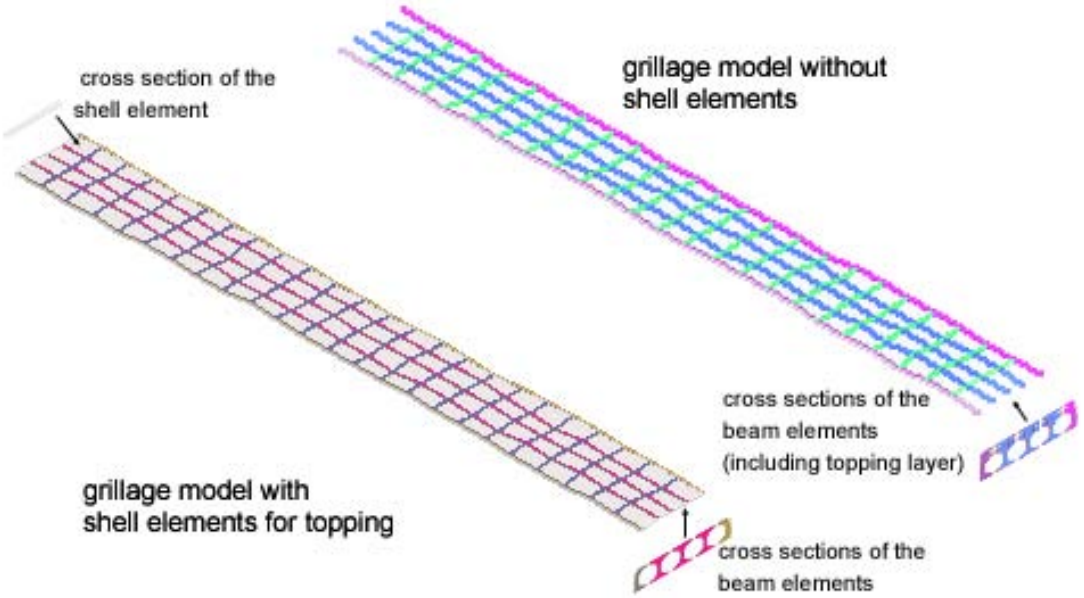

Figure 7-32 Illustrations of the models used in Stage Five

Other than the different methods of modelling the topping concrete, the effect from four end conditions was also investigated, which were pin-roller, pin-pin, fix-slide and fix-fix. Figures 7-33 and 7-34 show the midspan vertical displacements at the centre and at the side of the unit from the slabs with pin-pin and fix-fix connections. The overlapping of lines shows that the difference between the centre and side of the model using shell elements is minute, and the same for the model not using shell elements. The end time of the simulation was 120 minutes; therefore the figure shows that the model not using shell elements can last for longer than 120 minutes. The model using shell elements stopped after 60 minutes of ISO fire exposure.

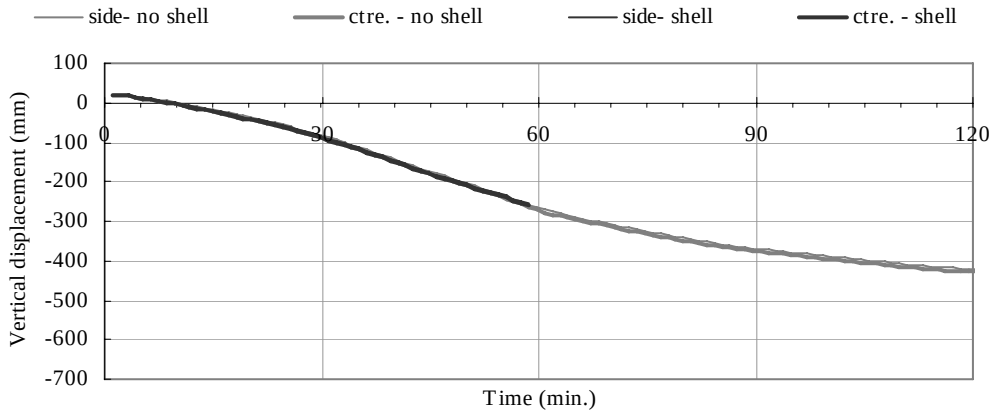

Figure 7-33 Comparison of midspan vertical displacements between the models with the topping simulated as part of the grillage or not of the slab with pin-pin support conditions

Figure 7-33 show that models with topping simulated separately using a layer of shell elements or together as part of the beam grillage gave almost identical midspan vertical displacements, and there is no difference between the displacement at the centre of the unit or at the side.

Figure 7-33 also shows that for the slab with pin-pin supports, the model with topping as part of the beam grillage did not fail before reaching the end time of the simulation, but the model with topping modelled separately using shell elements failed within 60 minutes of the ISO fire exposure. The output file showed that the failure was due to cracking of the topping concrete at the supports and crushing of the topping concrete near the midspan.

In the case with fix-fix supports, both models failed at around 90 minutes as shown in Figure 7-34. The failure in both cases was due to the large compression found in the concrete near the support, as well as the large increment of vertical displacement at the midspan in the last few time steps. The difference between the vertical displacements at the centre and at the side of the slab becomes noticeable in this case because of the overall deflections were small compared to the pin-pin case, and the thermal bowing effect across the width of the slab became more influential.

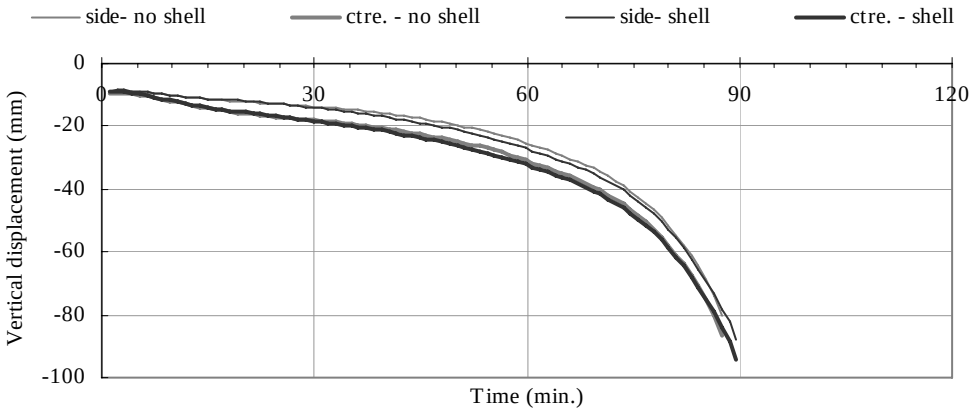

Figure 7-34 Comparison of midspan vertical displacements between the models with the topping simulated as part of the grillage or not of the slab with fix-fix support conditions

Figure 7-35 shows the comparison between the midspan vertical displacements of a hollowcore unit with pin-roller connections predicted by the two methods, where there is no difference between the displacement at the centre of the unit or at the side. Figure 7-36 shows the comparison between the horizontal displacements at the roller end, where negative means inward movement. These two figures also show that the

two modelling methods gave almost identical results. Even though the model with topping simulated as part of the beam grillage had a slightly later failure time, both models predicted a run-away failure after around 60 minutes of fire exposure.

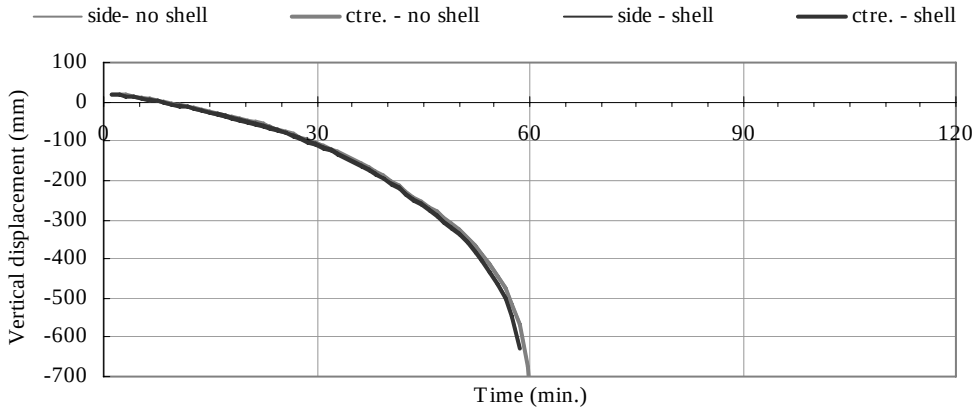

Figure 7-35 Comparison of midspan vertical displacements between the models with the topping simulated as part of the grillage or not of the slab with pin-roller support conditions

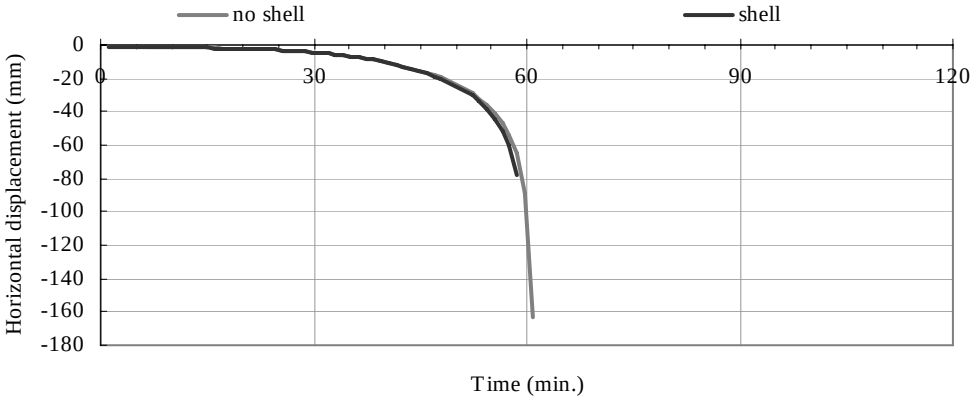

Figure 7-36 Comparison of roller end horizontal displacements between the models with the topping simulated as part of the grillage or not of the slab with pin-roller support conditions

Figure 7-37 shows the comparison between the midspan vertical displacements of a hollowcore unit with fix-slide connections predicted by the two methods. Figure 7-38 shows the comparison between the horizontal displacements at the slide end, where positive means outward movement. These two figures again showed that the two modelling methods gave very similar results except for the failure time. The model with topping simulated separately using shell elements failed due to crushing of topping concrete at the midspan and cracking of it near the support. The model not using shell elements had a run-away failure. The thermal bowing in the transverse direction is again noticeable as in the fix-fix case.

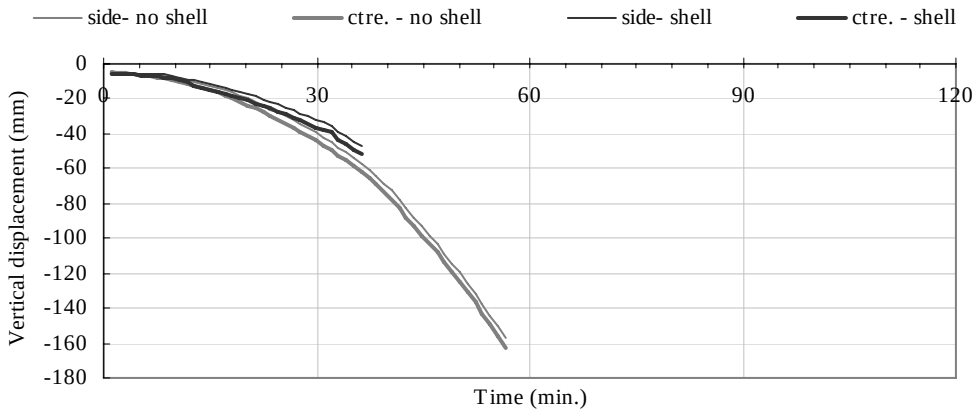

Figure 7-37 Comparison of midspan vertical displacements between the models with the topping simulated as part of the grillage or not of the slab with fix-slide support conditions

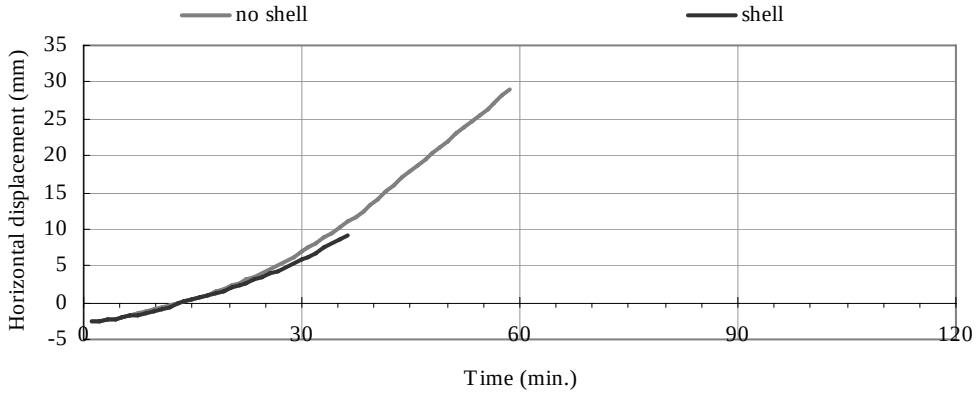

Figure 7-38 Comparison of roller end horizontal displacements between the models with the topping simulated as part of the grillage or not of the slab with fix-slide support conditions

Other than the failure time being different, it is found from the output file that the stress distribution within the cross section of the beam also differs with the modelling method. Because the compressive stress in concrete induced from the prestressing effect depends upon the cross section of the beam elements, by including the topping as part of the beam element, the topping also shares some compression to balance the prestressing effect, which in reality is not true. Therefore, even though the displacements from the two methods are almost identical, the internal stress given by the model where topping is modelled separately is more reliable.

To summarise the comparison in this stage, the models with topping concrete simulated using shell elements predicted the same displacement as the model with topping included in the beam grillage and did not make the structure stiffer. In some cases the model with topping simulated using shell elements stopped earlier due to the crushing or cracking of reinforced concrete in the topping layer and not because of the failure in the hollowcore unit, and users should pay special attention to this situation.

It is necessary for the users to confirm the failure mode from the output file.

7.6. Conclusions from Model Validation

This chapter described the process of model validation and compared the simulation results to the available experimental data. The findings from each step in the model validation process are summarised here.

- From the background comparison which compares beam grillage to shell elements in modelling two-way reinforced concrete slabs, it is found that sharing rotations of beams about the lateral axes at each beam intersection in two-way supported slabs is not recommended because it would make the model too stiff.

- From the comparison of 3D beams to shell elements in modelling one-way reinforced concrete slabs, it is found that it is acceptable to use beam elements to replace shell elements to model one-way supported slabs, even though the shell element model might predict an earlier failure time.

- From the comparison of beam grillage to shell elements in modelling one-way reinforced concrete slabs, it is found that grillage beam systems can be used to replace shell elements to model one-way slabs and produce similar results. Because sharing the rotations of beams about the lateral axes or not at each point where beams intersect does not make much difference in simulating one-way supported slabs, it is recommended to share them when modelling one-way supported slabs to follow the theory of grillage analogy more closely.

- By comparing the results from a beam grillage model to experimental results of one-way prestressed hollowcore concrete slabs, the results showed that the grillage model can predict the displacement caused by flexural bending very well, but cannot foresee the shear failure or take account of the shear deformations not caused by thermal stresses.

- From the comparison of shell elements to beam grillage in modelling the topping of one-way prestressed hollowcore concrete slabs, it is found that the models with topping concrete simulated using shell elements predicted the same displacement as the model with topping included in the beam grillage. However, in some cases the model with topping simulated using shell elements stopped earlier due to the

crushing or cracking of the shell elements rather than failure occurring in the hollowcore units. Therefore it is necessary for the users to verify the failure mode from the output file.

Throughout the comparison process the failure times predicted by shell and beam element models might be different, but the purpose of this section is to ensure that the beam grillage system can provide similar results to the shell element when modelling reinforced concrete slab, as only shell elements in SAFIR have been validated against experimental results before. Shell elements might predict earlier failure, but as explained previously in Chapter 6 it is impossible to include prestressing effect or voids in shell elements; therefore the idea of choosing the beam elements over shell elements is not a matter of failure time or being conservative, but rather about the ability to model hollowcore units.

8. Fire Performance of Hollowcore Concrete Flooring Systems with Various Support Conditions

8.1. Introduction

This chapter investigates the structural performance of hollowcore concrete flooring systems under fire with ideal support conditions, namely pin-pin, pin-roller, fix-fix and fix-slide supports. In practice all connections have a certain degree of restraint on rotations and displacements, and understanding the behaviour of the floor slabs in fire with ideal support conditions provides an envelope to the structural performance of such slabs in practice.

In this chapter, the fire performance of the floor slabs without end beams is studied first, followed by the investigation on the effect of core-filling on the structural fire performance to compare with the findings from Fellinger [2004]. The last part of the chapter investigates the fire performance of the floor slabs with end beams.

8.2. Simulation Model

The modelling scheme used in this section is 3D beam grillages for hollowcore units with a layer of shell elements for the topping concrete. The type of hollowcore unit used in this chapter is DYCORE300; the cross section of such units is shown in Figure 7-31, and the properties of it are described in Section 7.5. The floor is 12.2m long, 5.1m wide and has four hollowcore units across the slab as shown in Figure 8-1. This floor width coincides with the width of the subassemblies tested by Lindsay [2004] without the 0.75m wide cast in-situ concrete slab at the side. Two of the four cores of each hollowcore unit are filled with concrete and reinforced by 1.2m long Grade 300 R16 bars from the ends placed close to the bottom of the concrete infill. On top of the hollowcore units is a layer of 75mm cast in-situ concrete topping with a 665-mesh cold-drawn wire reinforcement at the mid-height of the topping. The reinforcing details of these structural members can be found in Matthews [2004]. The slab experiences a uniformly distributed load of 8.0kPa as calculated in Section 7.5. The floor slabs simulated in this chapter have no side supports and ideal end support conditions, namely pin-pin, pin-roller, fix-fix and fix-slide.

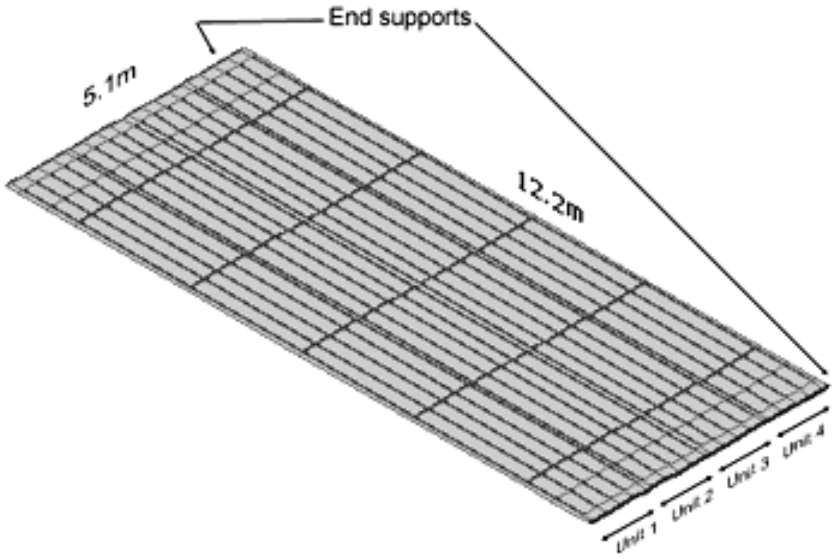

Figure 8-1 Model layout for the basic connection type studies

8.2.1. Sensitivity studies

The simulation models used in Section 7.5 used a mesh which was too fine to simulate floors with more than three hollowcore units in SAFIR2002. It was hence necessary to reduce the number of beam elements in the models without changing the results, so a sensitivity study with one hollowcore unit spanning 12.2m with different end support conditions was carried out. The fine layout used in Section 7.5 has a transverse beam spacing 0.5m as shown in Figure 7-32. The proposed crude layout has a spacing of 2.4m near the centre and 0.6m near the ends as shown in Figure 8-1. The width of the transverse beams and the length of the longitudinal beam elements vary with the spacing.

Simulating a hollowcore unit with pin-pin end supports, the results from the crude model, the fine model and the model not using shell elements for topping are almost identical. Figure 8-2 compares the midspan vertical displacement from the three models. The figure shows that there was negligible difference between the midspan vertical displacement at the side and at the centre of the unit. Figure 8-2 (a) shows that the crude model predicted a later failure time than the fine model. Further investigation indicates that the fine model failed within 60 minutes due to cracking and crushing in the topping layer. Figure 8-2 (b) shows that the crude model gave similar results to the model not using shell elements for topping. The vertical displacements predicted by these three models were almost identical.

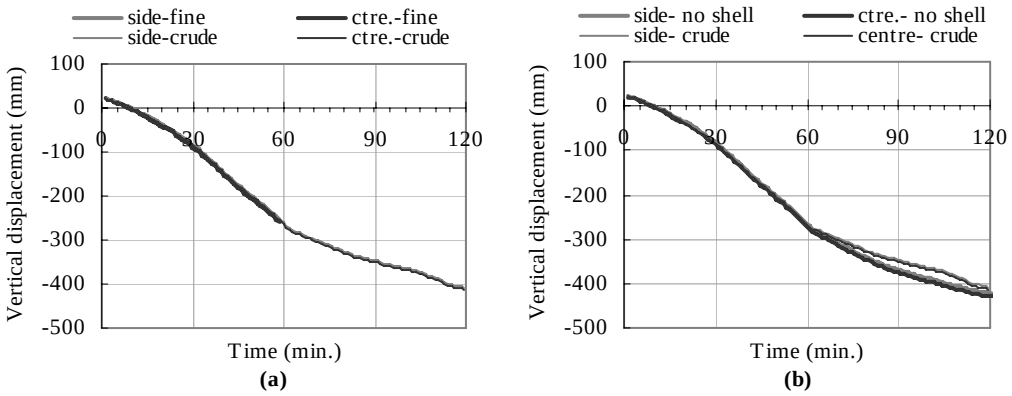

Figure 8-2 Comparison of midspan vertical displacement from the crude model to that from (a) fine model (b) no-shell model with pin-pin connections

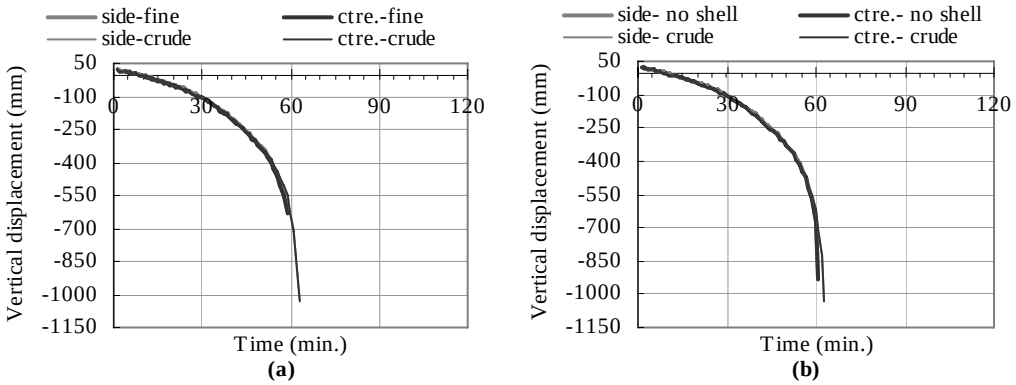

Figure 8-3 Comparison of midspan vertical displacement from the crude model to that from (a) fine model (b) no-shell model with pin-roller connections

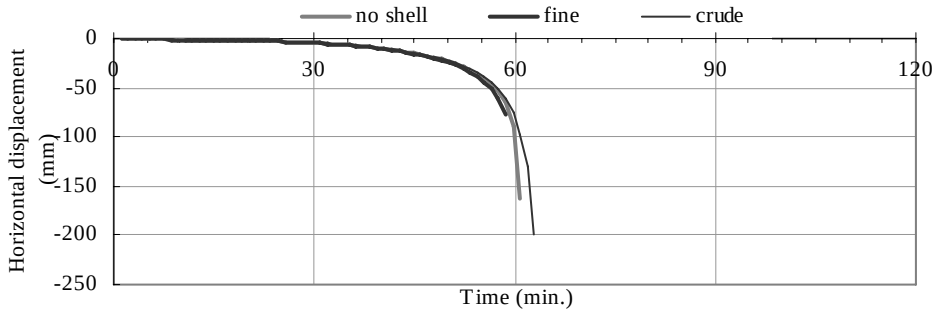

Figure 8-4 Comparison of horizontal displacement at the roller end from the crude model to that from the fine model and the no-shell model with pin-roller connections (-: inward)

In terms of simulating a hollowcore unit with pin-roller end supports, the results from the crude model, the fine model and the model not using shell elements for topping are again almost identical. Figure 8-3 shows the midspan vertical displacement from the three models. The results showed that the difference between the midspan vertical displacement at the side and at the centre of the unit was again

close to zero throughout the simulation. As in the cases with a pin-pin supported unit, Figure 8-3 (a) shows that the crude model again predicted a later failure time than the fine model which failed within 60 minutes, and Figure 8-3 (b) shows the results from the crude model and the model not using shell elements for topping were again almost identical. The models experienced runaway failure, i.e. a rapid and increasing rate of midspan deflection over a small increase of temperature, which causes the simulations to stop. The comparison of the horizontal displacements at the roller end predicted by the three models is shown in Figure 8-4, where inward movement is negative. From both Figures 8-3 and 8-4 it is concluded that the crude model gave very similar results to those from the other two models.

The results from the crude model and the fine model for a hollowcore unit with fix-fix end supports are still very similar. Figure 8-5 shows the midspan vertical displacements at the centre and the side of the slab. Due to the rotational restraints at the ends, the midspan vertical displacements at the centre and at the side of the unit were different. The two models gave very similar results in terms of both the failure time and the midspan vertical displacements, at the side or at the centre of the unit. Both the fine and crude models failed due to crushing of topping concrete near the supports.

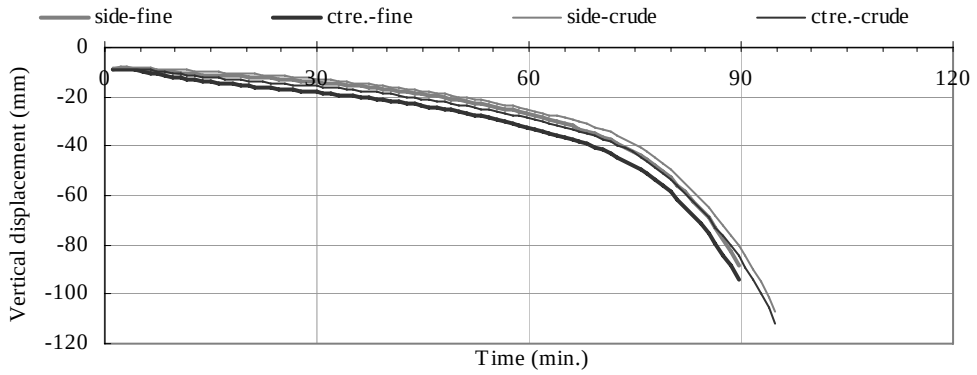

Figure 8-5 Comparison of midspan vertical displacement from the crude and fine models with fix-fix connections

The results from the crude model and the fine model to simulate a hollowcore unit with fix-fix end supports are again quite close. Figure 8-6 shows the midspan vertical displacements of the unit with fix-slide end supports predicted by the models; and Figure 8-7 shows the horizontal displacements at the slide end predicted by them, where the negative value means inward movement. The figures show that the vertical

displacements predicted by the two models were very similar, and the horizontal displacements from the two models were almost identical. In both cases the simulation stopped due to cracking of topping concrete near the supports.

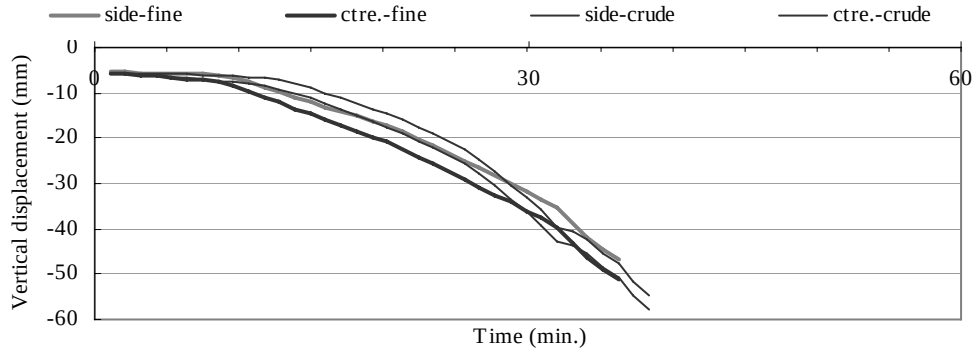

Figure 8-6 Comparison of midspan vertical displacement from the crude model to that from the fine model with fix-slide connections

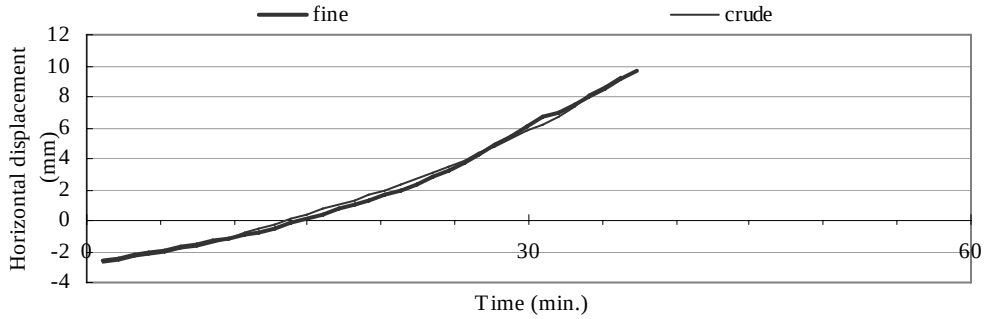

Figure 8-7 Comparison of horizontal displacement at the roller end from the crude model to that from the fine model with fix-slide connections (+: outward)

Based on the results shown above, it is concluded that the cruder model gave almost identical results to the fine model when modelling a single unit. This cruder model is then used to simulate larger structures.

8.3. Floor Slabs with Ideal Support Conditions without End Beams

This section investigates the behaviour of the slab without end beams or columns, i.e. the ends of the slabs remain at the same height. There are no supports at the sides of the slab. Figure 8-8 shows the layout of the slab and the label of each hollowcore unit. The length of the slab was 12m. Four DYCORE 300 units were modelled and the width of the slab was 5.1m as shown in Figure 8-1. Two of the four cores of each hollowcore unit are filled with concrete and reinforced by Grade 300 R16 bars placed close to the bottom 1.2m at the ends.

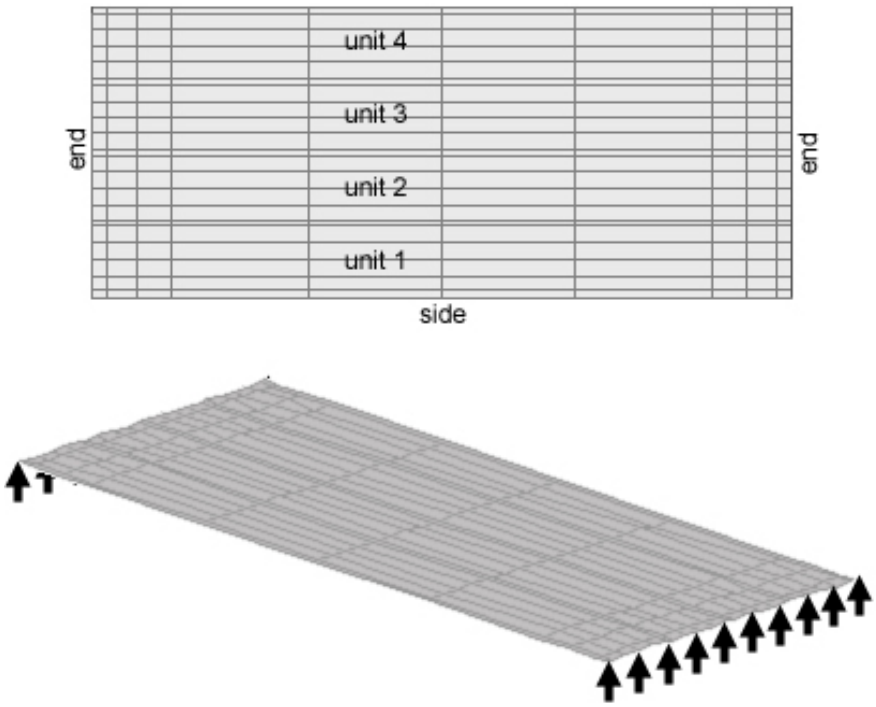

Figure 8-8 Layout of the hollowcore slab without end beams

8.3.1. Pin-pin end supports

The first case is the slab with pin-pin end supports as shown in Figure 8-9. Figure 8-10 shows the midspan vertical displacements from Unit 2 and from the side of Unit 1 referring to Figure 8-8. The difference between these vertical displacements shows that some bending in the transverse direction in the slab happened during the fire, this is shown more clearly in Figure 8-11. This difference increases with the time of fire exposure, which indicates that the bending in the transverse direction was dominated by thermal bowing and thermal expansion rather than from the loading.

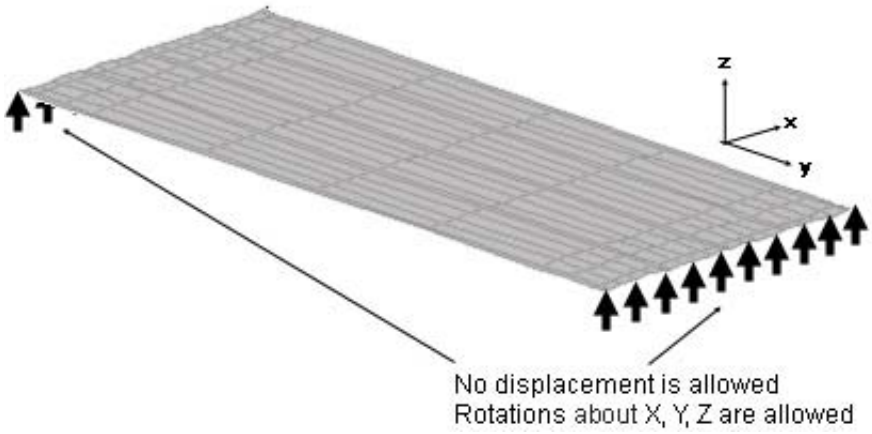

Figure 8-9 Pin-pin supported slab without end beams

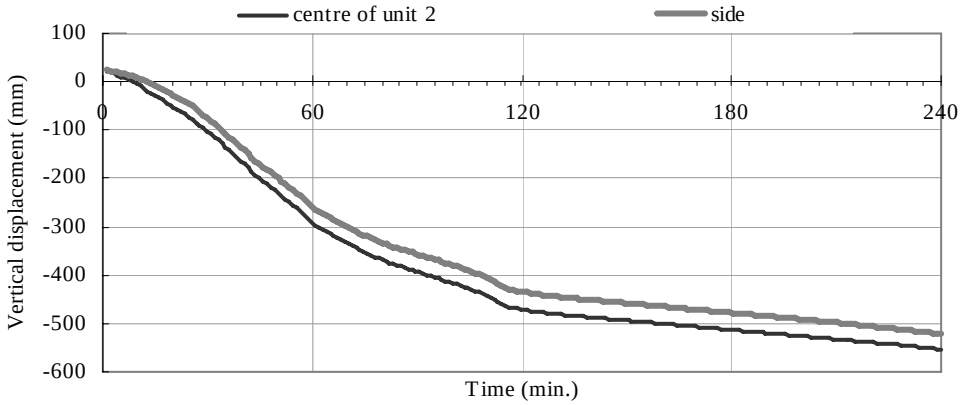

Figure 8-10 Midspan vertical displacements in hollowcore slab with pin-pin supports

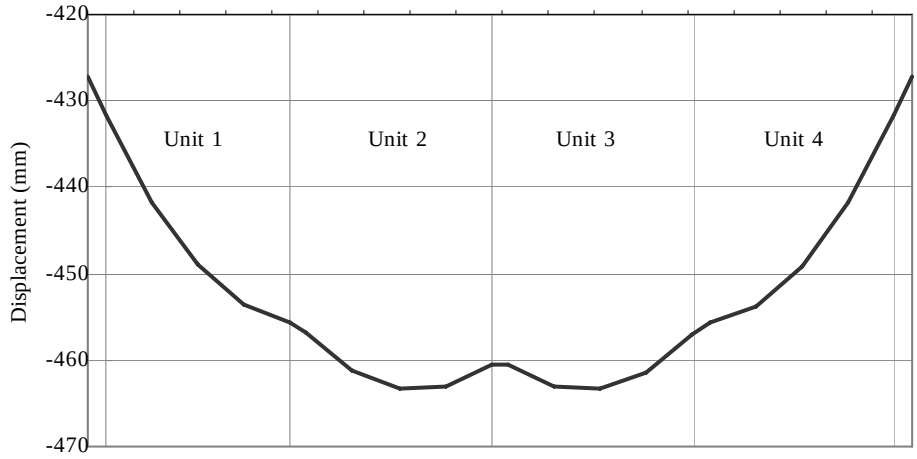

Figure 8-11 Deformation in the profile of the floor with pin-pin supports at 2 hour

Figure 8-12 shows the membrane force distribution within the topping after two hours of fire exposure, where blue is compression and red is tension. The corners of the slab at this time experienced a large compression. As the side of the slab was hanging freely, the centre part of the side units could be pushed outwards to accommodate the thermal bowing in the transverse direction and had less compressive

stress. The ends of the side units were restrained at the supports, so it experiences higher compressive force.

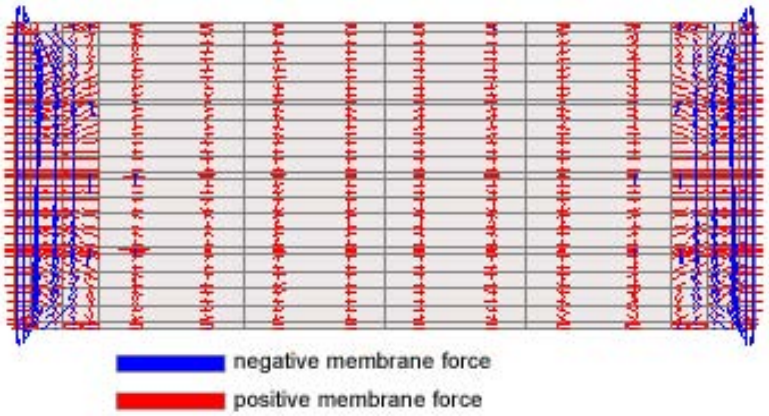

Figure 8-12 Membrane force distribution in the topping slab with pin-pin supports at 4 hr. (negative: compression)

The slab did not fail before reaching the end time of the simulation, which was 4 hours. Figure 8-13 shows the strand stress history within the strand at the centre of Units 1 and 2 compared to the thermally reduced yield and proportional limits of prestressed steel based on Eurocode 2 [EC2 2002]. The figure indicates that the strand stresses at midspan in Units 1 and 2 are the same, and they were at the level of proportional limit at the end time of the simulation. The stresses in the strands in both locations exceeded the proportional limit of prestressing steel at around 20 minutes, but at 115 minutes reduced back to the level of the proportional limit, which is also when the midspan deflection changed its rate of increase.

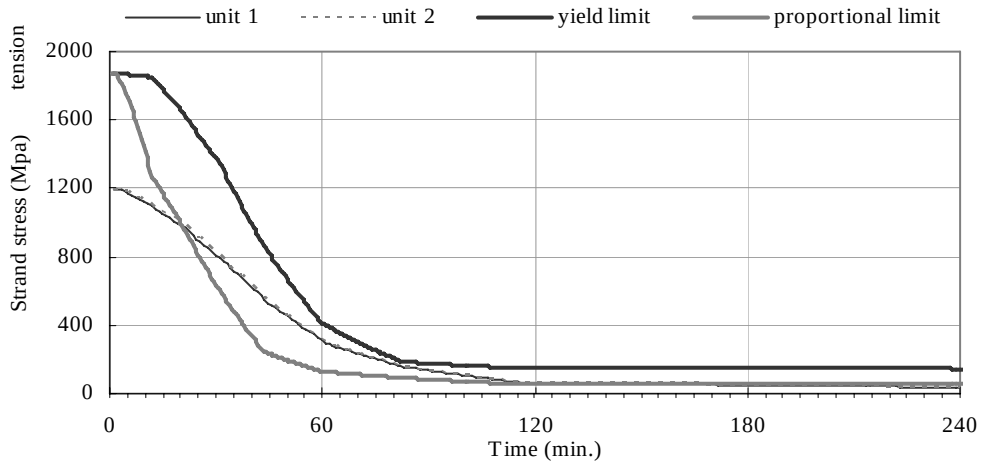

Figure 8-13 Strand stress at the centre of Units 1 & 2 in the slab with pin-pin supports

The results shows that a pin-pin supported slab without side supports and without end beams has at least 4 hours of fire resistance and no failure was observed from the simulation.

8.3.2. Pin-roller end supports

The support condition of the slab with pin-roller end supports is shown in Figure 8-14. The slab with pin-roller supports had runaway failure after 60 minutes of fire exposure as shown in Figures 8-15 and 8-16. Runaway failure occurs when plastic hinges form at the centre of the slab and cause rapid increase in the deflection. The output file indicates that at the time of failure the topping concrete at the midspan was crushed under compression which stopped the simulation. The large compression in the topping is illustrated in Figure 8-17 which shows the Membrane force distribution in the topping slab just before reaching failure. Judging from the horizontal displacement at the roller end as shown in Figure 8-16 it is obvious that run-away failure was occurring when the simulation stopped.

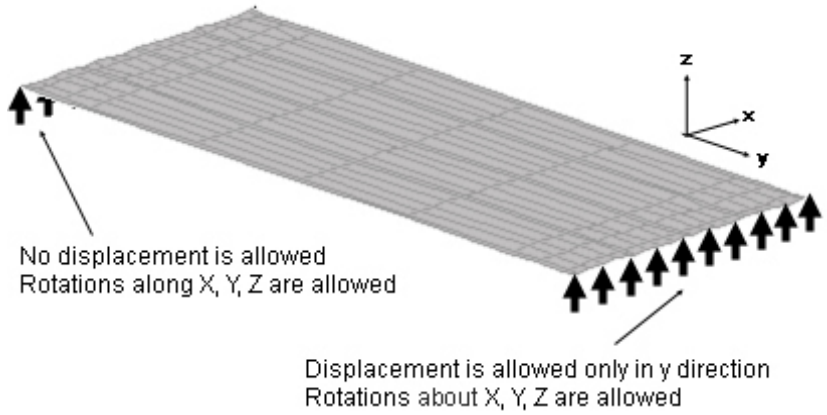

Figure 8-14 Pin-roller supported slab without end beams

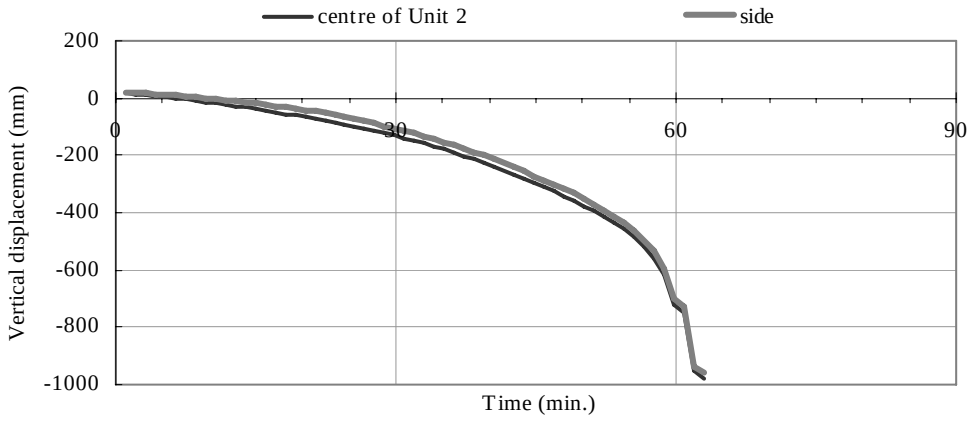

Figure 8-15 Midspan vertical displacements in hollowcore slab with pin-roller supports

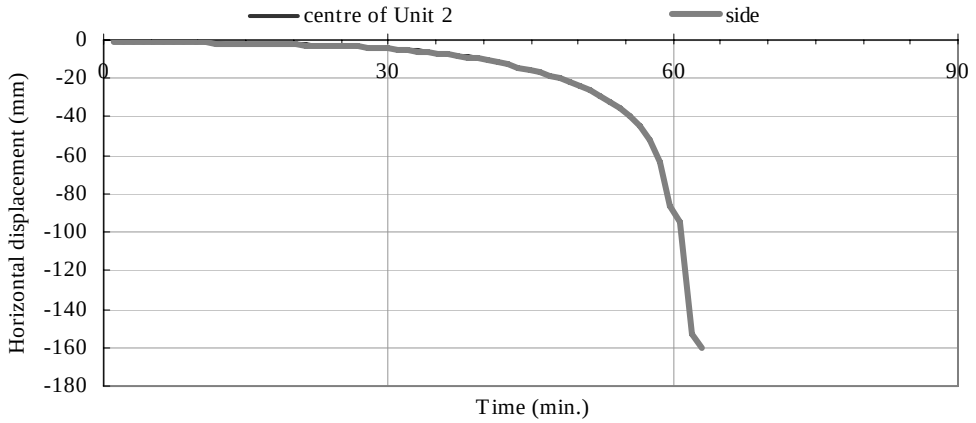

Figure 8-16 Roller end horizontal displacements in hollowcore slab with pin-roller supports (-: inward)

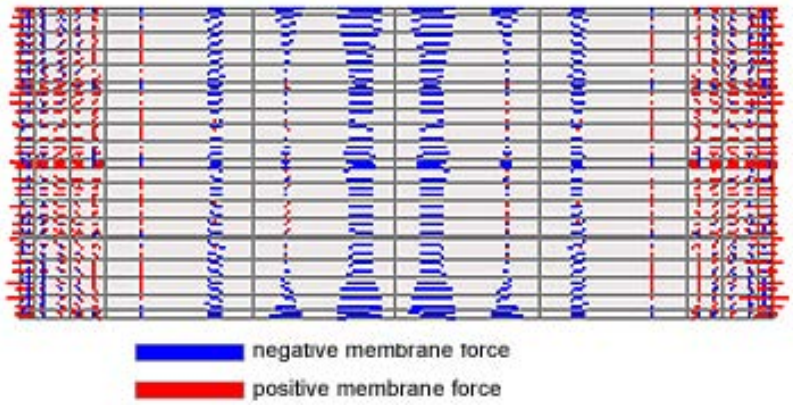

Figure 8-17 Membrane force distribution in the topping slab with pin-roller supports at 63 minutes (negative: compression)

8.3.3. Fix-fix end supports

The support condition of the slab with fix-fix end supports is shown in Figure 8-18. The simulation of the slab with fix-fix supports stopped after 106 minutes, and at the time the simulation stopped, the topping at the midspan was being crushed, the strands at the centre of Units 2 and 3 near the supports started to yield, the strands at the side of Units 2 and 3 at the midspan became inelastic, and the concrete near the supports at the centre of the hollowcore units was crushed at the bottom and cracked at the top.

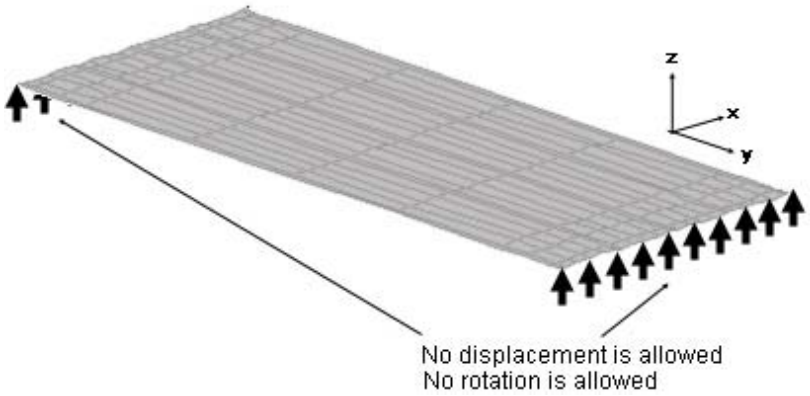

Figure 8-18 Fix-fix supported slab without end beams

The reason given by the output file that the simulation of the slab with fix-fix supports stopped after 106 minutes of fire exposure was due to crushing of the topping concrete at the midspan; this high compression can be seen in the membrane stress distribution shown in Figure 8-19. The forces shown in the figure are the membrane forces within the topping slab, which are the sum of stresses at the gauss points over the thickness of the slab.

The deflection of the slab caused a large compression at the centre and the high tension 1m from the supports. The compression nearer the supports was due to the reaction to bending from the supports as well as to the thermal expansion.

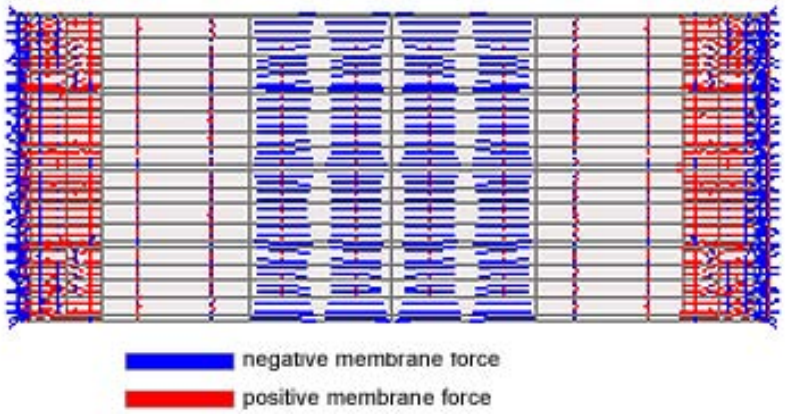

Figure 8-19 Membrane force distribution in the topping slab with fix-fix supports at 106 minutes (negative: compression)

Figure 8-20 shows the midspan vertical displacements at the centre of Unit 2 and at the side of the slab. The deflection started to increase more rapidly after 90 minutes indicating a progressive loss of stiffness at that time.

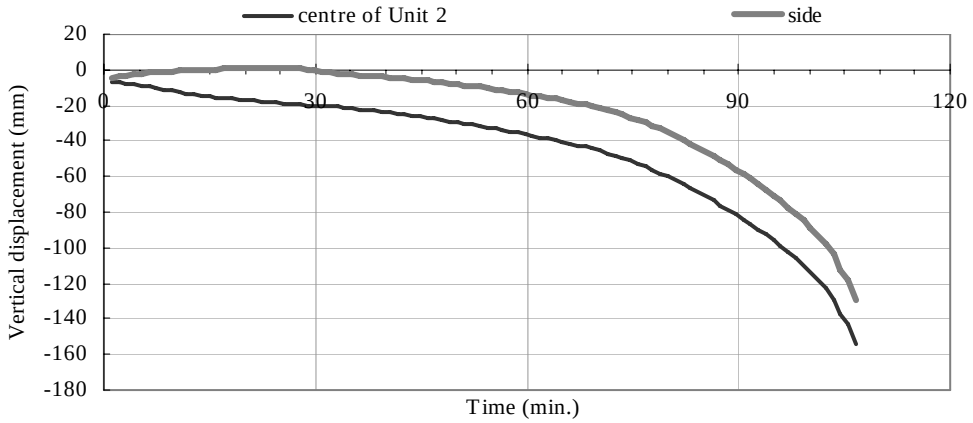

Figure 8-20 Midspan vertical displacements in hollowcore slab with fix-fix supports

To understand the behaviour within the hollowcore slabs at the time the simulation stopped, the axial force diagram at that time was used first to determine the locations of the extreme axial forces were as shown in Figure 8-21. The axial forces vary along the length because of the deflection of the slab, as the reaction from the supports is horizontal but the axial force is calculated along the beam as the sum of stress across the cross-section of the beam. The figure shows that at the time when the simulation stopped, all the hollowcore units were still under compression. The areas with the lowest compressive axial force were found at the midspan at the side of Units 2 and 3; and the areas with the highest compressive force were near the supports at the centre of each unit. These mean that the most likely locations for the steel strand to yield in

tension were at the midspan at the side of Units 2 and 3, and the most likely locations for the concrete to crush or the concrete to yield under compression were near the support at the centre of each unit.

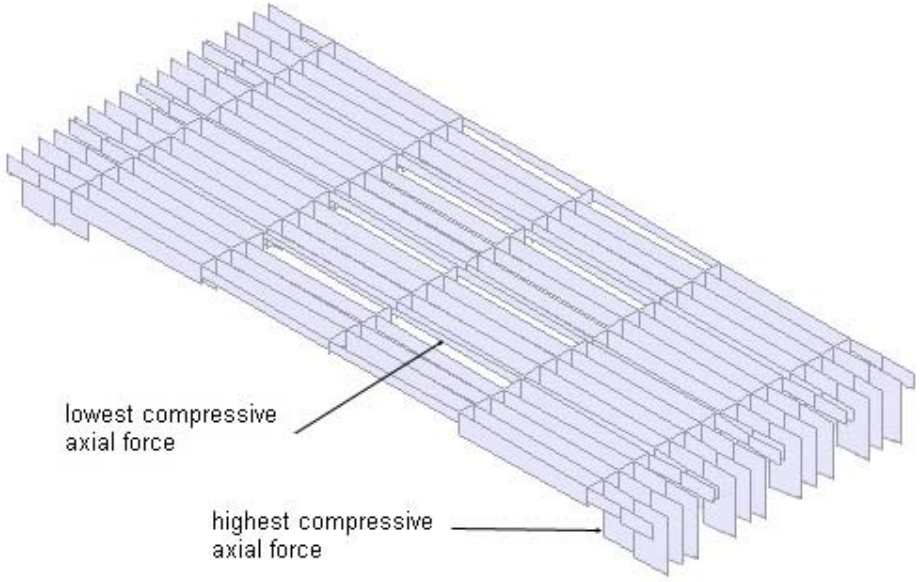

Figure 8-21 Axial force diagram within all the beam elements at 106 minutes (all in compression)

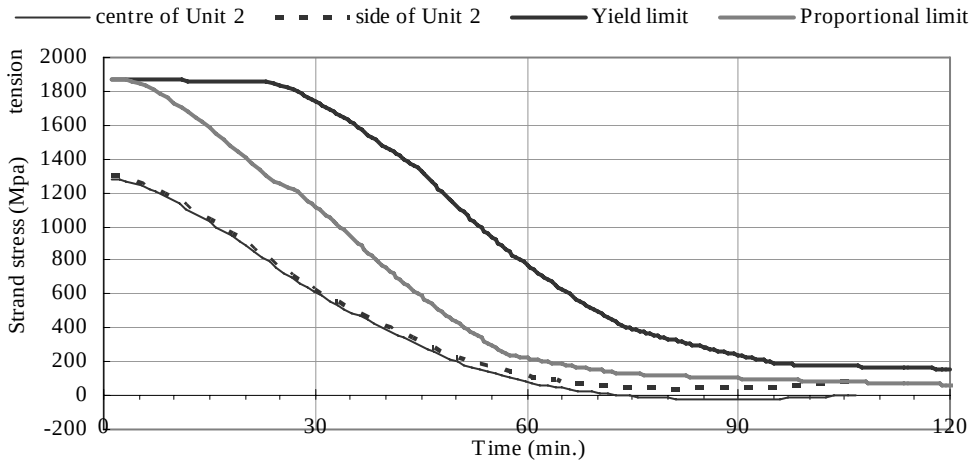

Figure 8-22 Strand stress at the centre of Unit 2 at the midspan of the slab with fix-fix supports

Figure 8-22 shows the stresses within the prestressing strand at the central web and at the side web of Unit 2 along with the thermally reduced prestressing steel strength based on Eurocode 2 [EC2 2002]. The difference between the stresses at these two locations increased with the fire exposure due to different deflections as well as the difference in equilibrium between each line of beams. When the simulation stopped, the strands at the side of Unit 2 at the midspan had reached the proportional limit and started to behave inelastically, while the strands at the centre of

Unit 2 at the midspan had zero stress.

Figure 8-23 shows the stress within the strand at the centre of Unit 2 near the supports. From 45 minutes onwards the compressive stress caused by the reaction to the thermal expansion from the supports became large enough to cause the strands to go into in compression, and this compressive stress became constant after 60 minutes. Because both the proportional and yield limit of the prestressing steel decrease with increasing temperatures, the yield limit eventually reduced to the level of the constant compressive stress causing the strands at this location to yield.

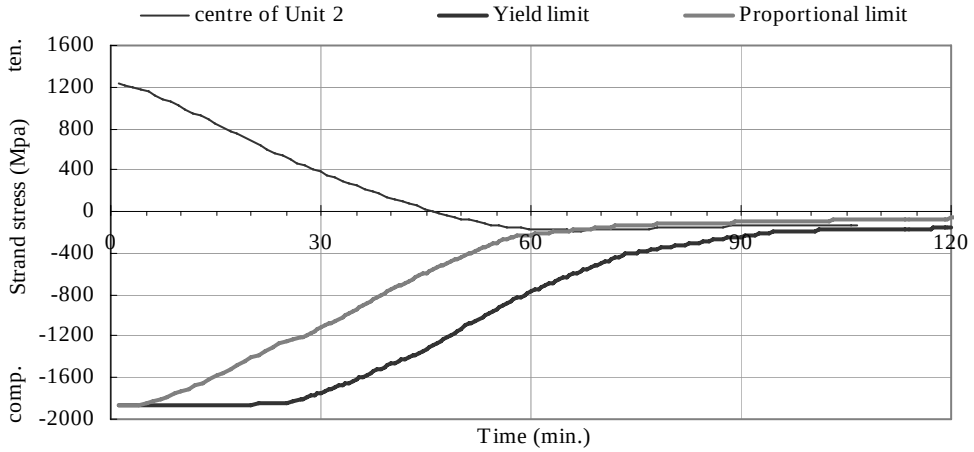

Figure 8-23 Strand stress at the centre of Unit 2 near the supports of the slab with fix-fix supports

Figure 8-24 shows the stress within the concrete section at the centre of Unit 2 near the support as well as the thermally reduced compressive strength of concrete following Eurocode 2. The background picture gives indication of the corresponding height of the stress. After 60 minutes the concrete below the strand level crushed in compression. Figure 8-24 also explains that the compression within the tendon observed in Figure 8-23 is related to loss of concrete at the top part of the hollowcore unit. At the time the simulation stopped, the concrete area below the midheight of the hollowcore unit was crushed in compression, and the top quarter of the unit cracked in tension.

In summary, in the slab with fix-fix end supports, at the time the simulation stopped, even though the reason for stopping given by the program was failure in the topping concrete, yielding of prestressing strands in compression was found near the supports along with crushing of concrete within the hollowcore unit in the same area,

therefore the stopping time was very close to the time of failure of the hollowcore units.

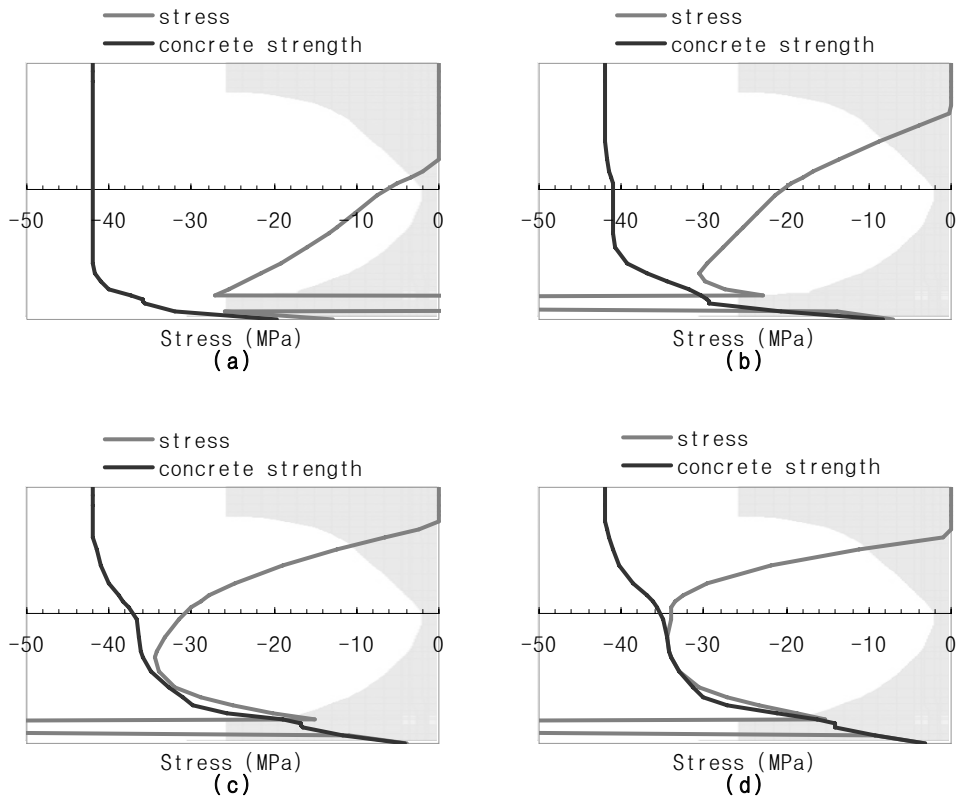

Figure 8-24 Stress distribution in the cross section near the end supports at the central web of Unit 2 near the supports at (a) 30 minutes, (b) 60 minutes (c) 92 minutes and (d) 106 minutes (-: compression)

8.3.4. Fix-slide end supports

The support condition of the slab with fix-slide end supports is shown in Figure 8-25. The simulation of a slab with fix-slide supports predicted that the slab would sustain 92 minutes of ISO fire exposure, and the simulation stopped due to yielding of prestressing strands 1m from the supports at the side of the Unit 2 and cracking of topping concrete at the same location.

Figure 8-26 shows the midspan vertical displacements at the centre of Unit 2 and at the side of the slab. Compared to the figures of the midspan vertical displacements of the slabs shown previously Figures 8-10, 8-15, and 8-20, Figure 8-26 shows that the differences found between the vertical displacements at the centre of Unit 2 and the side of the slab were consistent in the four cases with the ideal end supports. The difference between the vertical displacements at the centre of Unit 2 and the side of the slab was contributed by the bending in the transverse direction as explained

previously in the slab with pin-pin supports.

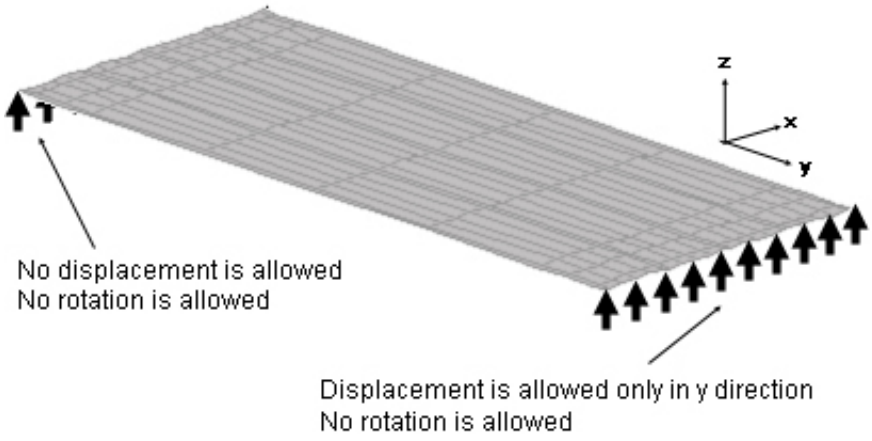

Figure 8-25 Fix-slide supported slab without end beams

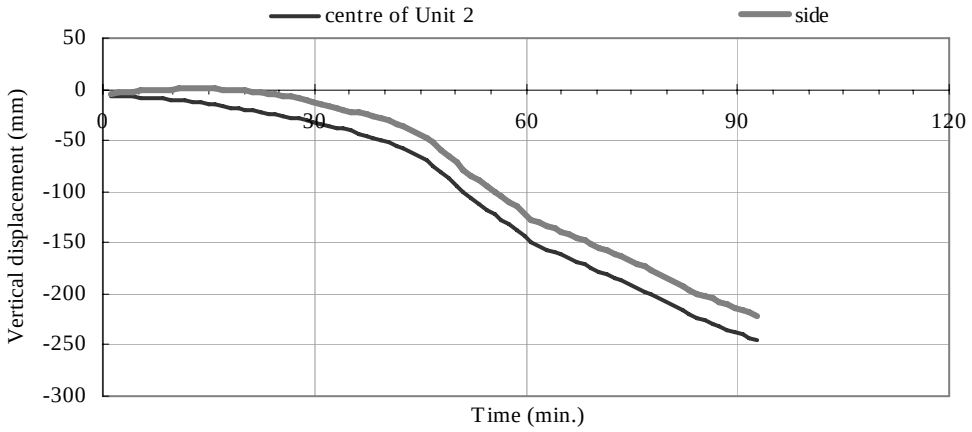

Figure 8-26 Midspan vertical displacements in hollowcore slab with fix-slide supports

The horizontal displacement at the slide end is shown in Figure 8-27, where positive means outward movement. The displacement history shown in this figure is very different from that in Figure 8-16. Figure 8-16 shows that in the pin-roller supported slab, the horizontal displacement at the roller end was dominated by the bending of the slab. Figure 8-27 shows that in the fix-slide supported slab, the slide end moved inwards under ambient conditions due to the applied loads, and the horizontal displacement was dominated by the thermal expansion of the slab in fire because of the rotational fixations at the end restricting the magnitude of bending in the longitudinal direction.

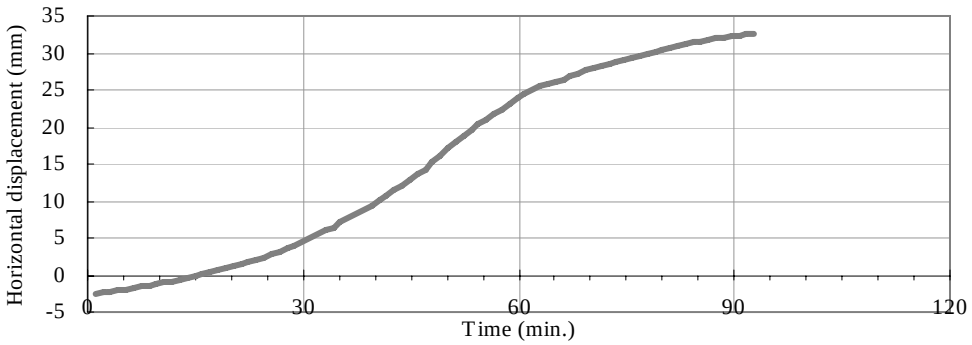

Figure 8-27 Slide end horizontal displacements in the slab with fix-slide supports (+: outward)

The simulation of the slab with fix-slide supports stopped because of yielding of prestressing strands 1m from the supports at the side of the Unit 2 and cracking of topping concrete at the same location. Figure 8-28 shows the axial force distribution within the beam elements just before the simulation stopped, where red means tension and blue means compression. The high compressive force in the central webs near the supports was caused by the reaction from the supports to both the thermal bowing and the mechanical deflection associated with the thermally reduced material strength.

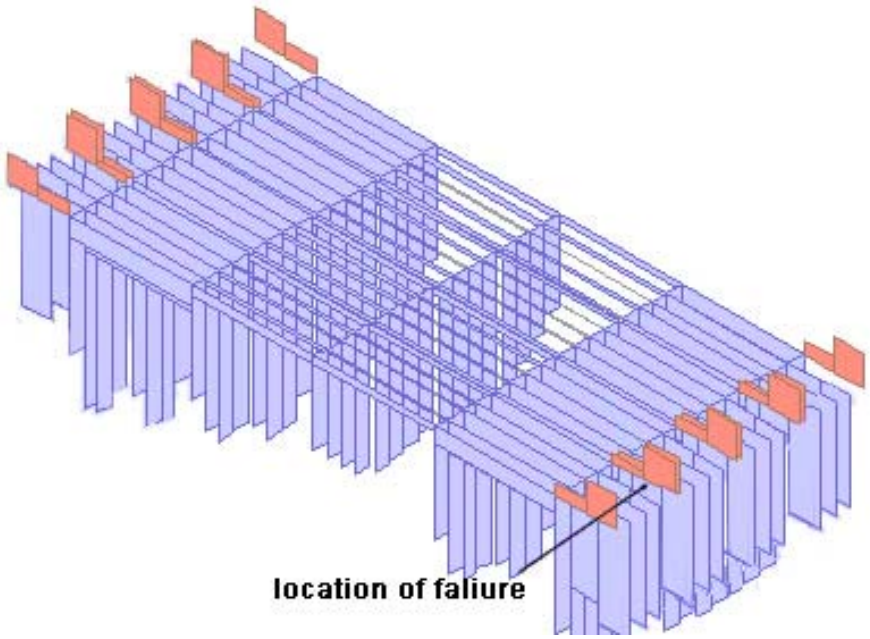

Figure 8-28 Axial force diagram within all the beam elements at 92 minutes (red: tension; blue: compression)

Figure 8-29 shows the history of axial forces near the fixed support and at the midspan from the central web as well as from the side of Unit 2, which also shows the high compressive force near the ends at the central web of Unit 2 at the time the

simulation stopped, and the high tensile force near the end at the side web of Unit 2 at that time.

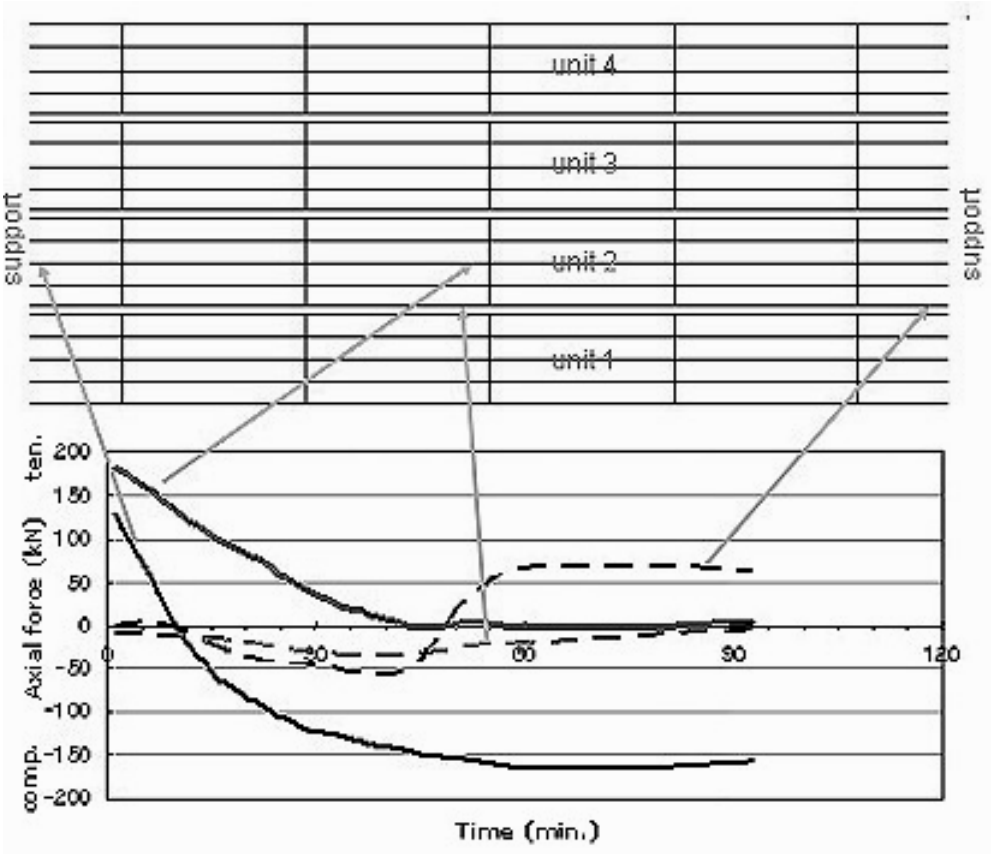

Figure 8-29 Axial force history in different beams in the slab with fix-slide supports

Figure 8-30 shows the stress within the strand at the midspan of the central web of Unit 2 as well as near the support at the side of Unit 2, which are the two of the locations with positive axial forces within the cross section as shown in Figure 8-29. Comparing Figures 8-39 and 8-30, at the side of Unit 2 near the supports, the axial force reached the maximum in compression at 45 minutes and then the compressive stress starts to become smaller, this time coincides with the time when the stress in the strand reached the proportional limit, hence the strands starts to behave inelastically after this time. A similar observation is found at the central web of Unit 2 at midspan where the compressive stress stopped developing at 50 minutes when the stress in the strand there reached the proportional limit. The difference is that the strand stress at the central web of the centre units at midspan follows the proportional limit of steel but the strand stress at the side of the centre units near the supports reached the yield limit at 92 minutes, which was when the slab collapsed.

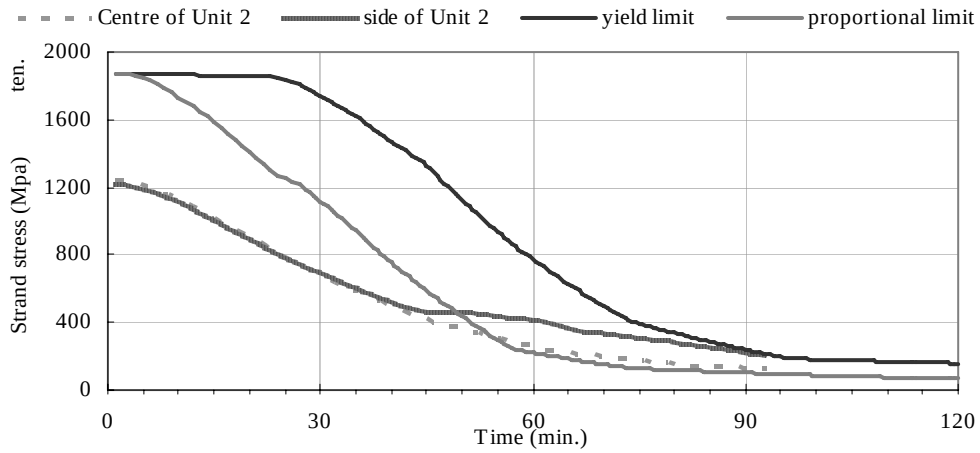

Figure 8-30 Stress of the strands in Unit 2 in the slab with fix-slide supports

Figures 8-29 and 8-30 also show that there were high tensile forces at the side of each unit near the support. It is necessary to check the stress within the concrete section to see how much concrete cracked in those regions. Figure 8-31 shows the stress distribution within the concrete along the side of Unit 2 at different times. At this location under the ambient condition, more than half of the concrete section was in compression reacting to the prestressing force in the strands. At 15 minutes, thermal expansion induced more compressive stress at the bottom of the concrete, which would be reduced when the deflection increases. It is noticeable that the area under compression dropped much below the mid-height of the hollowcore section when the floor was heated. The central region cracked in tension due to mechanical strains induced by incompatible thermal strains as illustrated before in Figure 3-30 in Section 3.3.5.

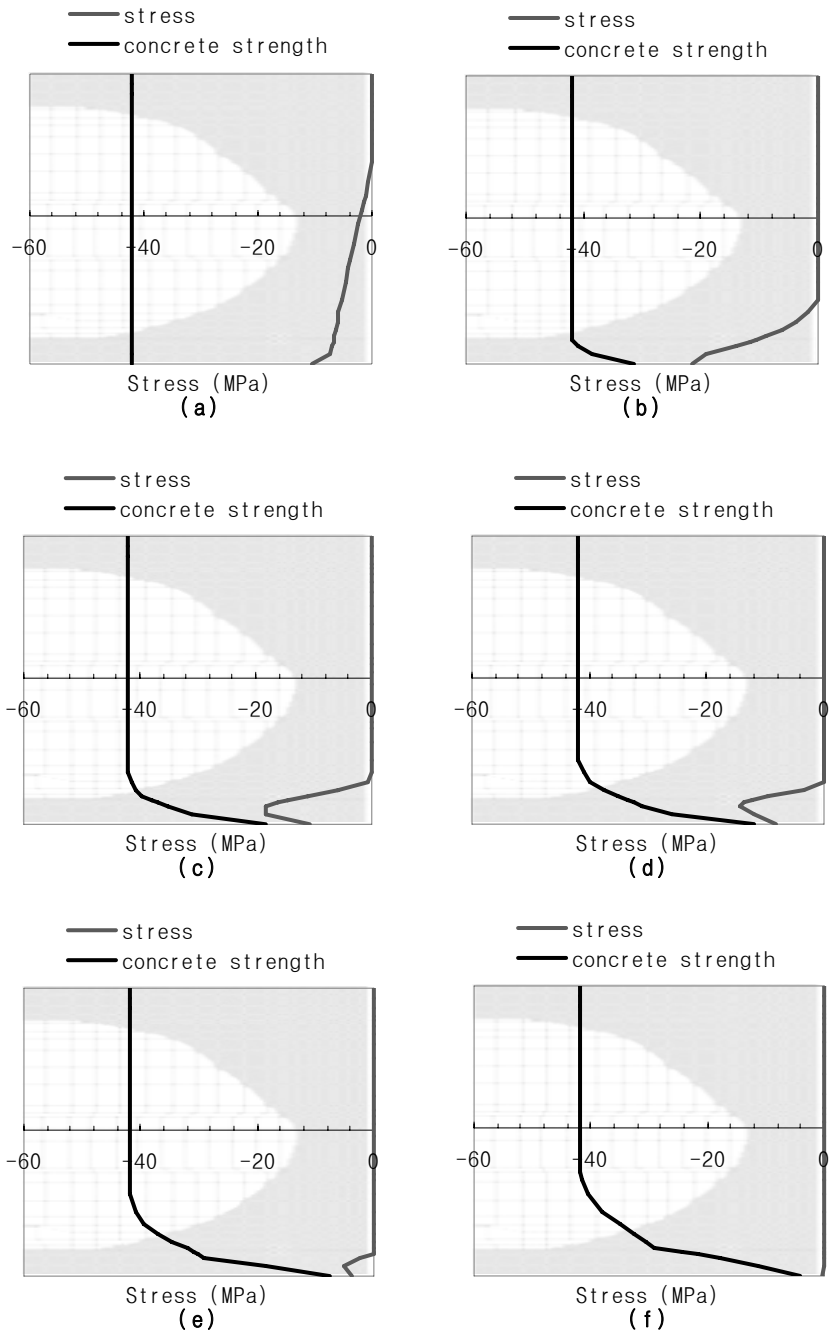

Figure 8-31 Stress distribution in the concrete along the sides of Unit 2 near the supports with (a) 1 min. (b) 15min. (c) 30min. (d) 45 min. (e) 60min. (f) 92 min. of ISO fire exposure (-: compression)

In the simulation, the interface between the prestressing strand and concrete was assumed to have a perfect bond by SAFIR; therefore the stress equilibrium forces the concrete around the prestressing strand to have high compressive stress. This was true until the strands started to behave inelastically. Afterwards when the compressive stress within the concrete diminished, the stress in concrete was dominated by the deflection of the slab rather than by the reaction force to the prestressing stress. This

is observed in Figure 8-31 (e) when the stress within the strand has already exceeded the proportional limit of the steel.

The entire cross section at the side of the unit cracked in tension close to the end time of the simulation as a result of the deflection; therefore this area relies on the prestressing strands to carry the load. When the prestressing strands reached the yield limit, the sides of the unit collapsed and caused failure.

In summary, the fix-slide supported slab lasted 92 minutes under the ISO fire before the cracking of topping concrete 1m from the supports stopped the simulation. At this time, yielding of prestressing strands at the sides of the centre units near the supports also happened.

8.3.5. Summary

The summary of the simulation results for the slabs without end beams is shown in Table 8-1. The slab with pin-pin supports has the highest fire resistance, and the slab with pin-roller supports would perform the worst with a runaway failure. Because the prestressing effect in SAFIR is applied at the same time as the imposed loads to the model, the internal stresses are different depending on the imposed load and the boundary conditions.

Table 8-1 Summary of the simulation results of the slabs without end beams

Support condition	Simulation stop time	Reason
Pin-pin	>240 minutes*	*designated end time of the simulation
Pin-roller	63 minutes	**Failure**: Runaway failure
Fix-fix	108 minutes	**Failure**: Yielding of prestressing strands near the ends of the slab. High compression in the topping near the midspan.
Fix-slide	92 minutes	**Failure:** Yielding of prestressing strands at the sides of the centre units near the supports. Cracking of topping concrete 1m from the support

The stated fire rating of hollowcore units by the manufacturer is 2 hours [CCANZ 1991]. It is an unrestrained rating based on minimum strand cover and equivalent concrete thickness requirements from MP9:SNZ1991 [SNZ 1991]. This tabulated data ignores the effect of the support conditions and applied loads, more importantly it also ignores the thermal stresses within the cross section, such as the web would experience a much higher stress than the top and bottom flanges. Judging from the

results especially the situation with pin-roller supports, the prescribed fire rating is less conservative and should be used with caution.

The simulations with slabs with rotationally fixed supports are likely to stop due to damage in the topping rather than in the hollowcore units, and more investigations into the output files were carried out to determine the damage caused by high temperatures to the units.

8.4. Effect of Core-filling on the Structural Performance of Floor Slab in Fire

This section explores the effect of core-filling to the structural performance of hollowcore concrete flooring systems in fire. In the previous section, the ends of the outer two cores of each hollowcore unit in each of the four slabs were filled with ordinary concrete. In this section the results from the slabs without core-filling are presented. The supporting conditions of the slabs in this section are the same as in the previous section.

Table 8-2 shows the summary of the results of the slabs without core-filling. Three out of the four slabs without core-filling behaved similarly to the slabs with core-filling. The slab with fix-slide failed much earlier when without core-filling. The reason for failure of each case without core-filling was very similar to that of the cases with core-filling. Like in the previous section, the results here again predict a much worse fire resistance of the structures than that stated by the manufacturer. Based on the simulation results, it is recommended not to use the prescribed fire resistance.

Table 8-2 Summary of the simulation results of the slabs without end beams and without core-filling

Support condition	Simulation stop time	Reason
Pin-pin	>240 minutes*	*designated end time of the simulation
Pin-roller	59 minutes	**Failure**: Runaway failure
Fix-fix	101 minutes	**Failure**: Yielding of prestressing strands near the ends. Cracking of topping concrete between the hollowcore units near the ends
Fix-slide	51 minutes	**Failure**: High compression in the topping near the supports. Cracking of topping concrete 1m from the supports

Figure 8-32 shows the midspan vertical displacements at the centre of the slab from the cases with different support conditions with and without core-filling. The figure shows that the displacements from the cases with pin-pin or pin-roller supports are almost identical.

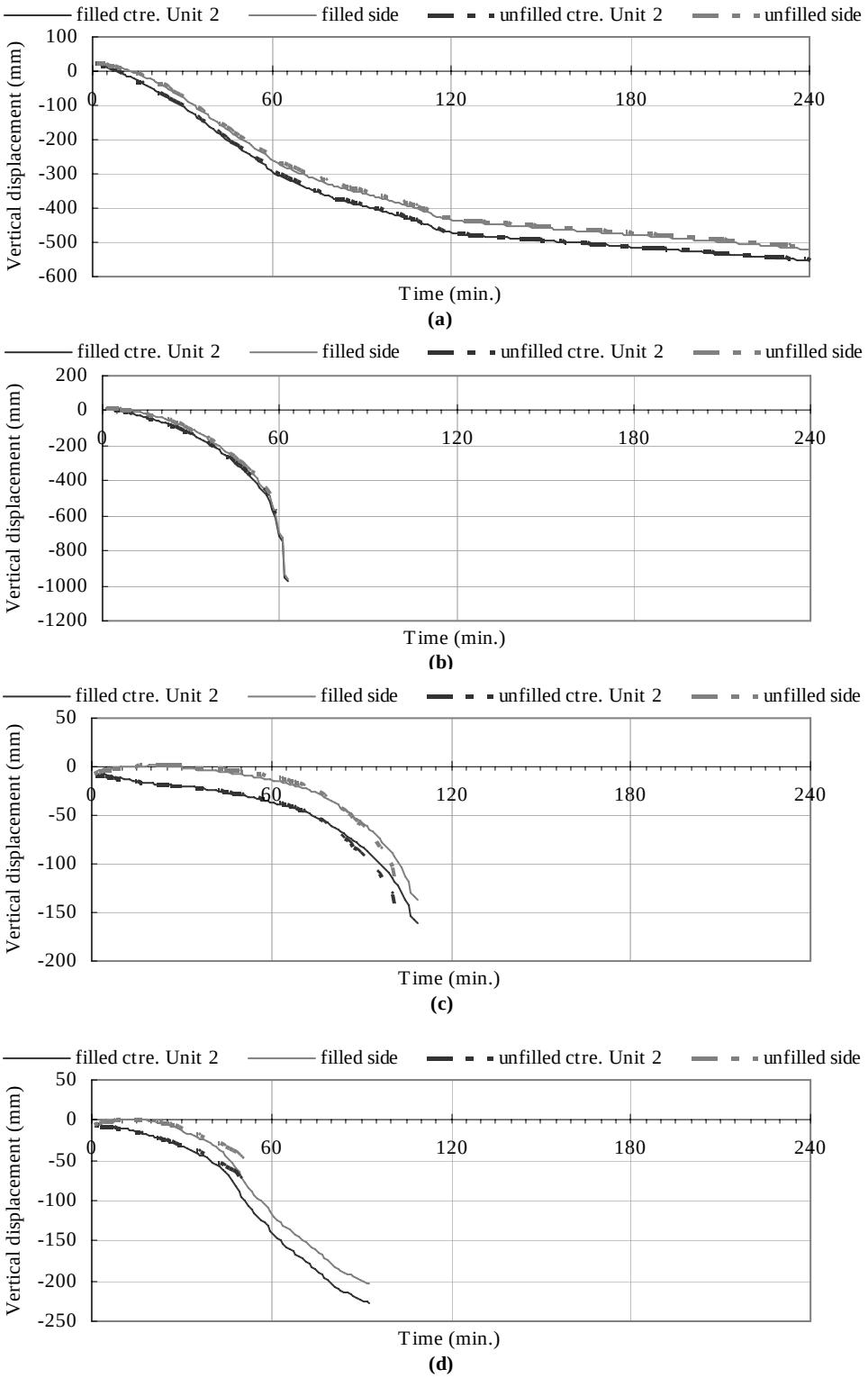

Figure 8-32 Vertical displacements of the slabs with and without core-filling with (a) pin-pin (b) pin-roller (c) fix-fix (d) fix-slide supports (notice the difference in scales)

The differences caused by core-filling are more noticeable in the cases with rotational restraints at the ends. Figure 8-32 (c) shows that the slab with fix-fix supports without core-filling had more deflection than the slab with core-filling close

to the time of failure. In the case with fix-slide supports, Figure 8-32 (d) shows that the vertical displacements from the slab with core-filling failed much earlier and had a smaller deflection.

Figure 8-33 shows the stresses within the strands at the centre of Unit 2 near the supports from the case with and without core-filling, where positive means tension. The compressive stress within the strand was larger in the case without core-filling because the smaller cross sectional area to share the compressive reaction force from the supports caused by the thermal expansion of the slab, consequently its strands reached the compressive yield limit earlier, and caused the slab to fail earlier.

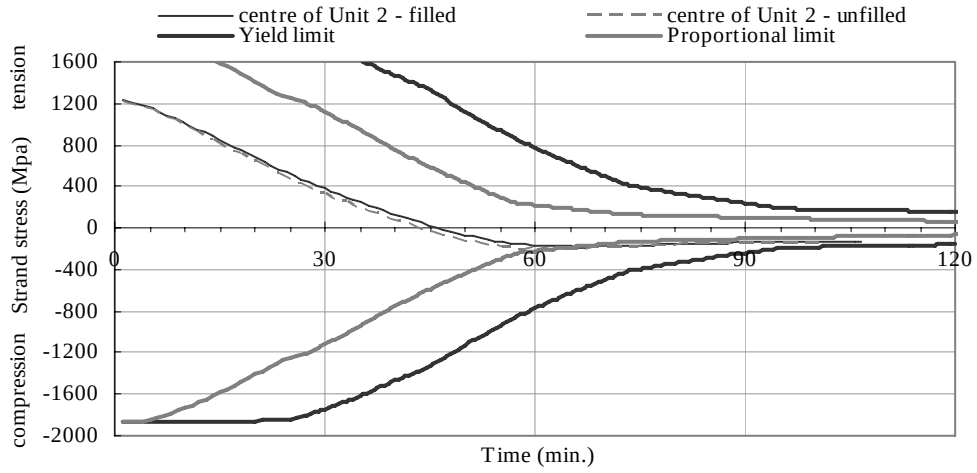

Figure 8-33 Strand stress at the centre of Unit 2 near the supports from the fix-fix supported slab with and without core-filling

Figure 8-34 shows the history of stress in the strands in the centre and at the side of Unit 2 at the midspan of the fix-slide supported slab. The beams representing the central web were the same in the two cases but not the ones representing the sides of the units, hence the influence from the core-filling was expected to be more obvious there. This is confirmed as the stresses from the two cases were found to be very similar at the central web of Unit 2, while the stresses at the sides of the unit were drastically different. The stress within the strand at the side of the unit without core-filling was lower as there was less concrete area to take the compressive force incurred from thermal expansion.

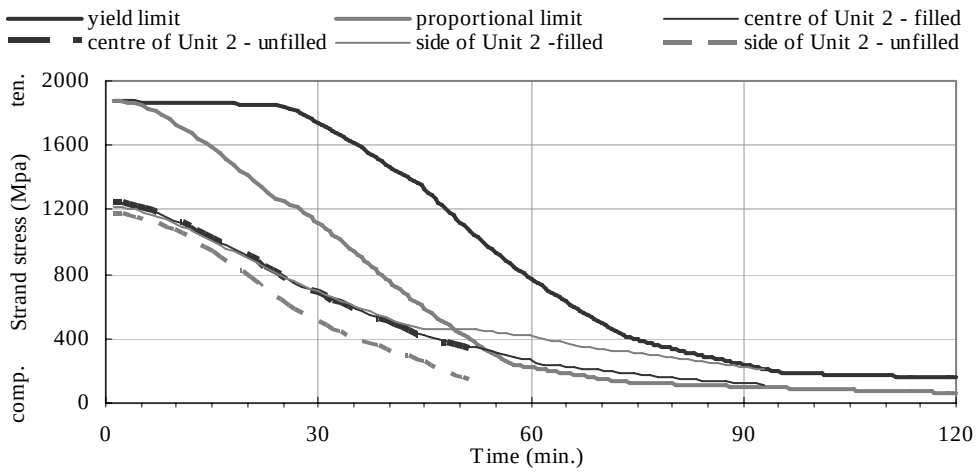

Figure 8-34 Strand stress in Unit 2 at the midspan of the slab with fix-side supports with and without core-filling

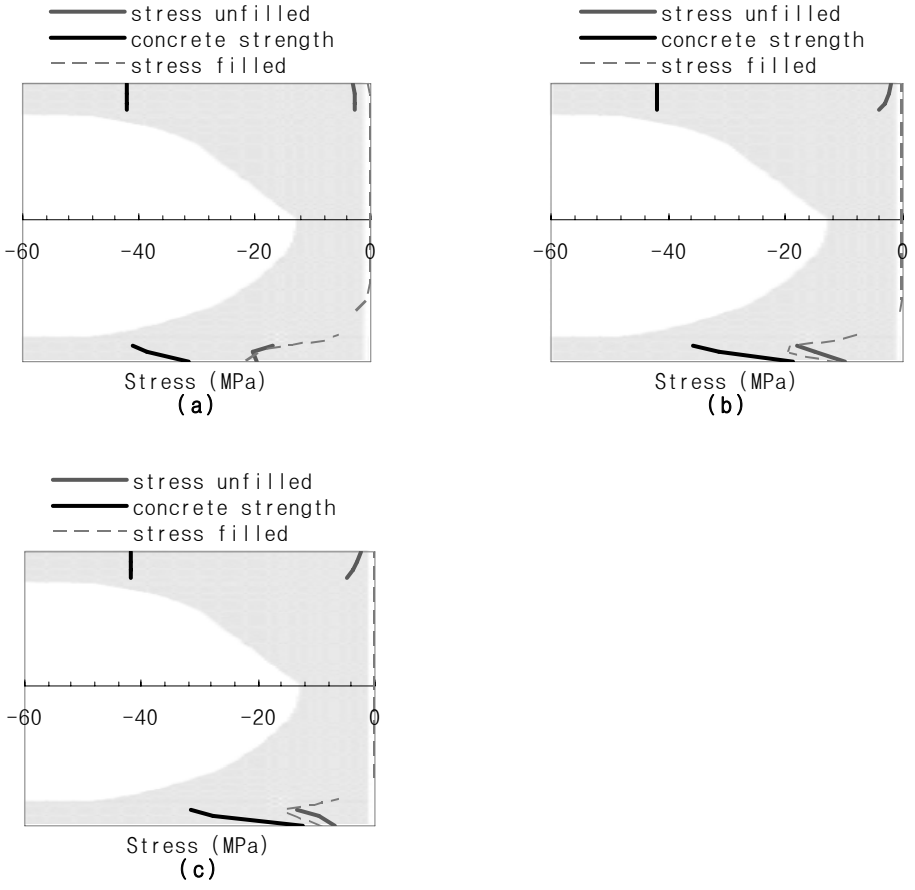

Figure 8-35 Stress distribution in the flange near the side of Unit 2 in the fix-slide supported slab at the midspan at (a) 15min. (b) 30min. (c) 45 min. (-: compression)

Figure 8-35 shows the stress distribution at the thinnest part of the flange at the side of Unit 2 at midspan at different times in the fix-slide supported slab. The vertical axis of Figure 8-35 is the thickness of the web, and the background picture shows the corresponding height. The solid grey lines are from the case without core-filling, and

the dashed thinner grey lines are from the case with core-filling. The figure shows that the compressive stress at the bottom of the flange in the case without core-filling was smaller than in the case with core-filling. However, it was found that the compressive stress existed at the top of the flange throughout the simulation in the case without core-filling, while there was no stress found at that area in the case with core-filling. This might be due to the lack of area to allocate the compressive force when there was no core-filling, therefore the entire cross section including the steel section had to share this force.

Figure 8-36 shows the membrane force within the topping shell elements in the fix-slide supported slab. The simulation was stopped by the SAFIR program due to very high tensile stresses in the topping concrete found between the units 1m from the supports. Figure 8-36 shows that, without the core-filling, the topping stress between the units was much higher than in the case with core-filling, and reached its maximum minutes before the program declared failure of the structure, and this confirms the reason given by SAFIR. However, the simulation results showed that the hollowcore units did not fail at the end time of the simulation.

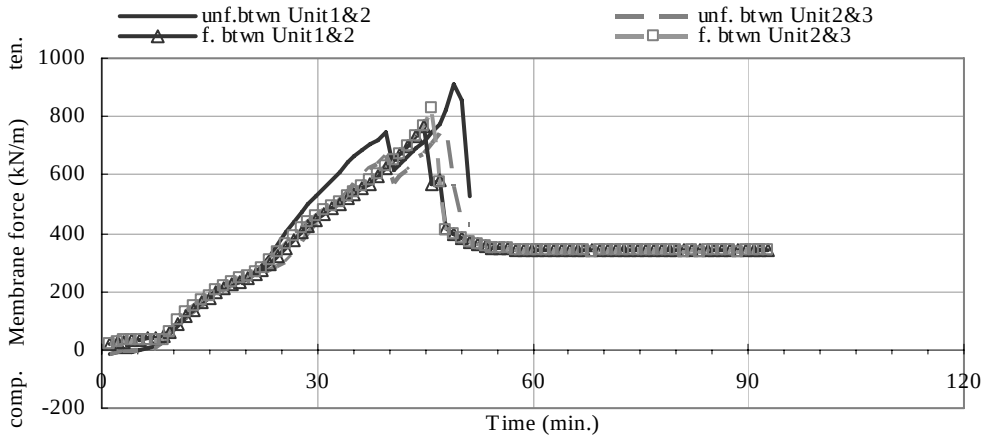

Figure 8-36 Membrane force in the topping concrete between Units 1 and 2 and Units 2 and 3 in the fix-slide supported slab

In the tests carried out in Delft University of Technology it was found that the core-filling by itself does not provide any benefit to the structural performance in fire and the filling concrete has to work in combination with the axial and rotational restraints to increase the fire resistance. Because of the incompatibility between the thermal expansion in the hollowcore units and the filling concrete, the units with core-filling might have even lower fire resistance than the ones without filling

[Fellinger 2004] as described in Section 4.2.5. However, this incompatibility could not be detected here as the simulation followed Bernoulli's hypothesis that plane section remains plane and assumed that there is a perfect bond between the core-filling and the hollowcore unit. Having core-filling in the simulation shown herein was simply translated as having stronger beam elements at the end of the slab and more area to bear the shear stress; therefore it was shown to be beneficial to the fire resistance by these simulations.

8.5. Floor Slabs with Ideal Support Conditions with End Beams

This section presents the results from the simulations of the floor slabs with end beams and ideal support conditions at the ends of the end beams, i.e. pin-pin, pin-roller, fix-fix and fix-slide supports. The hollowcore units had core-filling in the two outer cores using ordinary concrete as in Section 8.3.

Investigating the behaviour of the slab with these ideal supports at the corners not only forms part of the process in understanding a more complex structure, but it helps to establish the extreme scenarios when the slab becomes part of a larger subassembly. In practice all floor slabs are supported by columns at the corners, and the support conditions at the corner should be in between these four ideal support conditions. Which ideal support condition the real support is most similar to depends on the slenderness, strength and spacing of the columns.

Figure 8-37 shows the schematic drawing of the slab layout. In this model, the ends of the slab were connected rigidly to the beams directly and the seating was not considered. In later chapters this connection type is referred to as "rigid end connection". Compared to the support arrangement in the previous section shown in Figure 8-8, the supports of the slabs with end beams only existed at the four corners to allow for deflection of the end beam.

The end beams used in the model were 750mm deep by 450mm wide with 3-D25 bars at the top and bottom based on those used by MacPherson [2005]. The yield strength of the reinforcement was 450MPa. Figure 8-38(a) shows the discretised beam cross section used in SAFIR. The beam was subjected to three sided fire exposure up to the height covered by the hollowcore units, which is to the mid-depth of the beam. The ends of the floor slab are rigidly connected to the end beams, i.e. they shared the

same rotation as the end beams and no seating length was considered. The results of the simulations are summarised in Table 8-3. Notable observations in each case are discussed separately in this section.

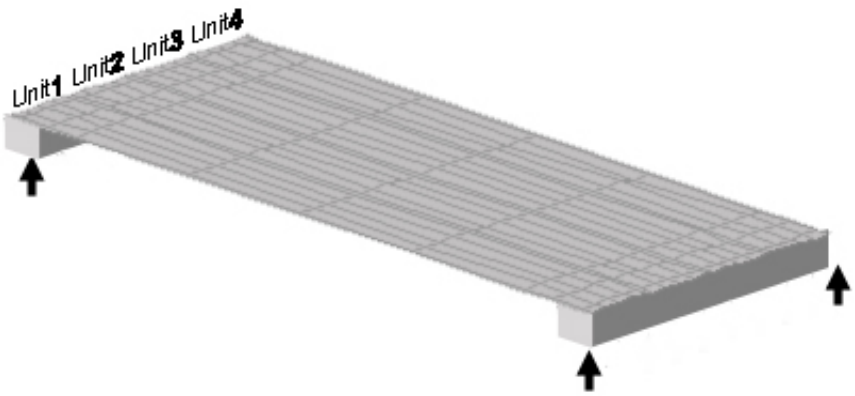

Figure 8-37 Layout of the hollowcore slab with end beams

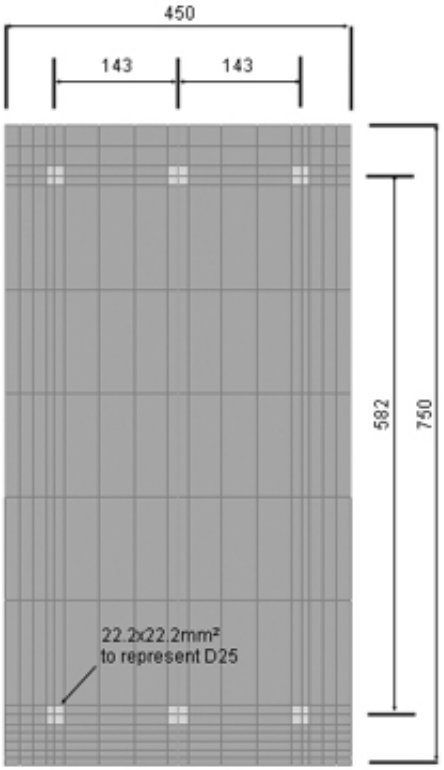

Figure 8-38 Discretised end beam in SAFIR

Table 8-3 Summary of the simulation results of the slabs with end beams

Support condition	Simulation stop time	Reason
Pin-pin	>240 minutes*	*designated end time of the simulation
Pin-roller	59 minutes	**Failure**: Runaway failure
Fix-fix	106 minutes	Terminated by SAFIR: Crushing of topping concrete near the corners
Fix-slide	>240 minutes*	*designated end time of the simulation

8.5.1. Pin-pin supports

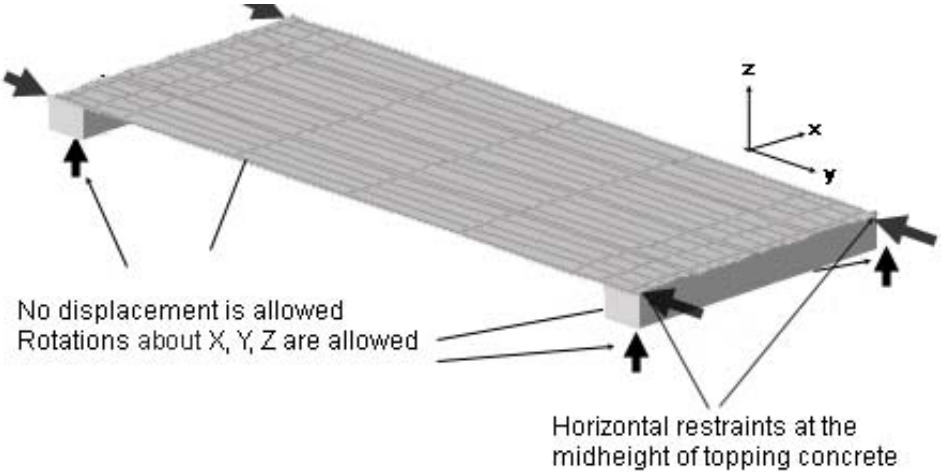

Figure 8-39 Pin-pin supported slab with end beams

The support condition for this case was shown in Figure 8-39. At the four corners, rotations about X, Y or Z axis are allowed, but displacement is not. The beam is hence free to twist if axial forces develop in the slabs. The simulation shows the slab could sustain more than 4 hours of ISO fire exposure.

Figure 8-40 shows the midspan vertical displacement at the centre of Unit 2 and at the side of the slab from the cases with and without end beams. The midspan vertical displacements at both locations were larger in the case with end beams than in the case without. The displacement at the centre of the slab increased in the case with end beams because of the slight deflection at the middle of the end beams.

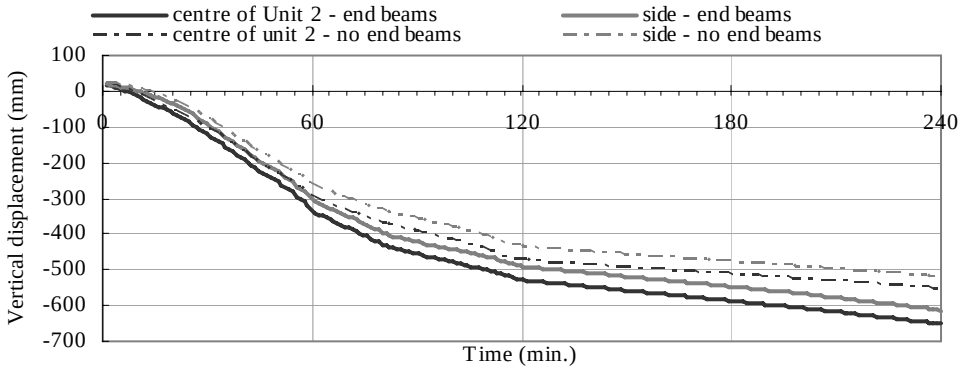

Figure 8-40 Midspan vertical displacement of the pin-pin supported slabs with and without end beams

The end beams were less likely to have torsion than rotation about the centre of the beam due to its large size; therefore when the floor slab deformed, the beams were forced to have a close to uniform rotation throughout the length of the beams rather than rotating differently at different locations, and at the corners of the slab this uniform rotation was greater than that of the slab without end beams, and the displacements at the sides of the slab here are greater than in the case without end beams because the rotation about the axis of the beam near the supports is greater.

8.5.2. Pin-roller supports

Figure 8-41 shows the support condition in this case, where two corners had pin supports and the other two had roller supports and can move along the span. This in practice would be close to a subassembly with very slender and weak columns. Both the pin-roller slabs with or without end beams collapsed due to runaway failure.

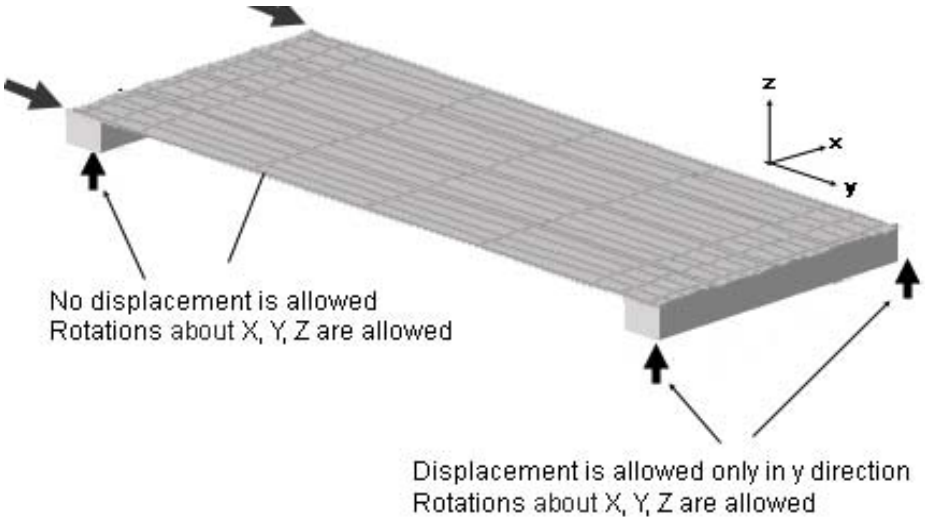

Figure 8-41 Pin-roller supported slab with end beams

Figure 8-42 shows the midspan vertical displacements at the centre of Unit 2 and at the side of the pin-roller supported slabs with and without end beams, and Figure 8-43 shows the horizontal displacements at the roller end at the centre of Unit 2. The slab with end beams failed earlier because of the greater deflection along the span as the end beams allowed the slab to deflect in the transverse direction.

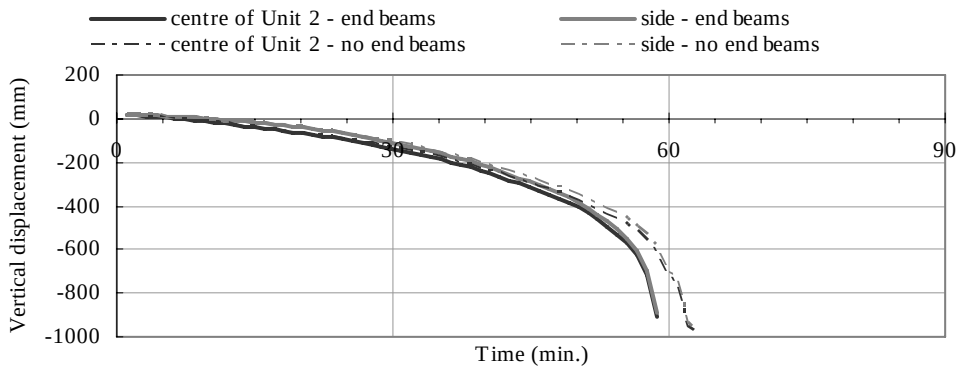

Figure 8-42 Midspan vertical displacement of the pin-roller supported slabs with and without end beams

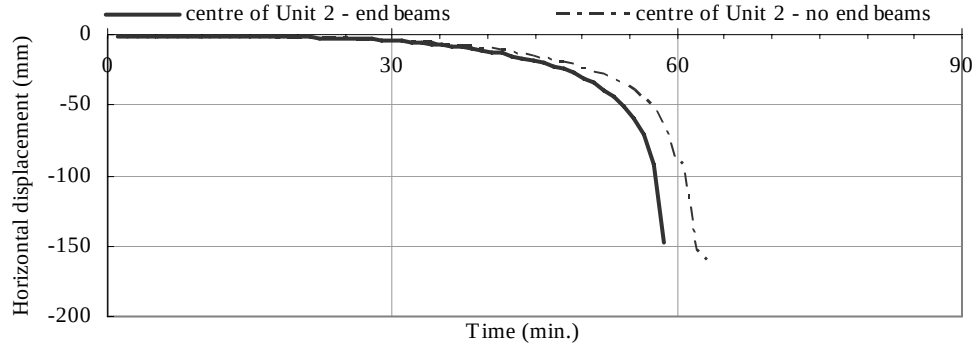

Figure 8-43 Horizontal displacements at the roller end from the pin-roller supported slabs with and without end beams (-: inward)

Figure 8-44 shows the stress distribution along the centreline of the central web in Unit 2 at the midspan of the slab at different times. The difference between the stress distributions of the slabs with and without end beams became noticeable after 54 minutes of fire exposure. In the slab with end beams, at the time when the slab failed the entire cross section of the central web was in tension, which means the deflection of the slab at this time was caused purely by the mechanical loading and not by thermal bowing. Since concrete loses its tensile strength in high temperature, the tensile force was taken entirely by the strands. In the case without end beams, at the same time of 54 minutes, the central web of Unit 2 still had some compressive stress at the bottom which indicates that the thermal bowing was still contributing to the deflection.

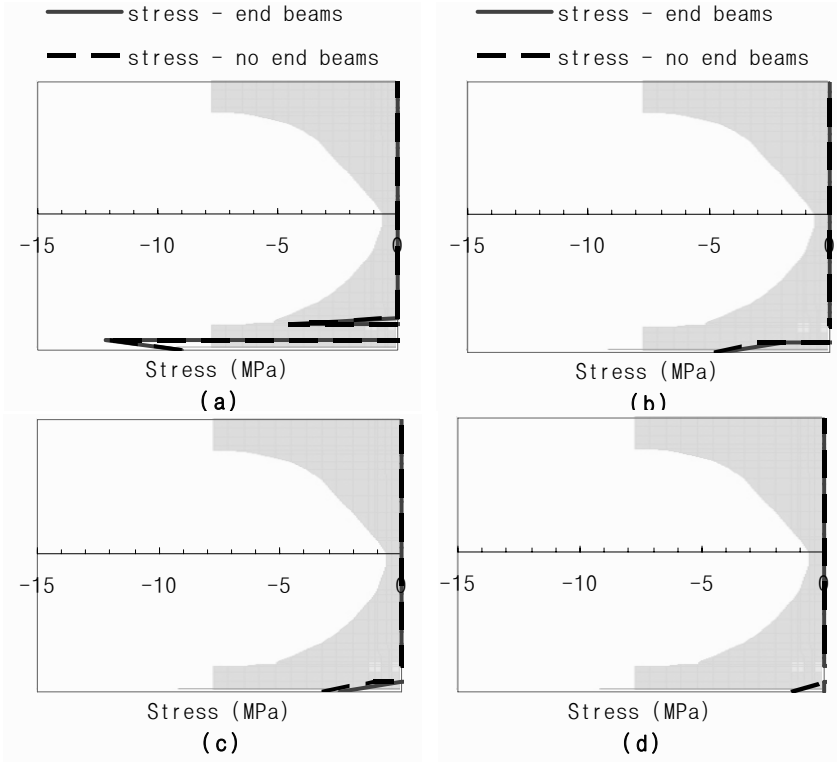

Figure 8-44 Stress distributions along the height of the central web of Unit 2 at the midspan of the pin-roller supported slabs with and without end beams at (a) 30min. (b) 50min. (c) 54min. (d) 58min. (-: compression)

8.5.3. Fix-fix supports

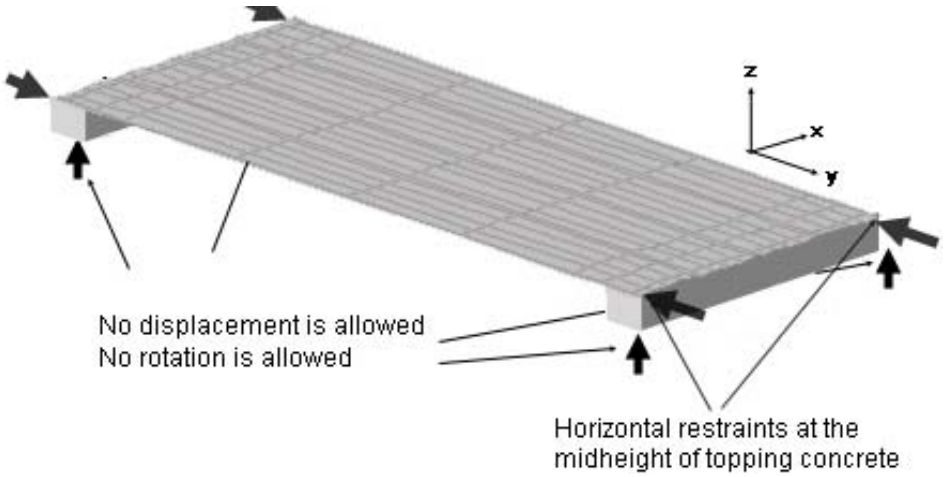

Figure 8-45 Fix-fix supported slab with end beams

Figure 8-45 is the schematic drawing of the support condition of this slab. The four corners were restrained to have no rotation or displacement. In practice this support condition is similar to having very stiff and strong columns at the four corners. The simulation was terminated by the program due to crushing of topping concrete

near the corners rather than failure occurring within the hollowcore units.

The end beams provided some degree of freedom for deflections at the ends of the slab in both lateral and vertical directions. This is different from the fix-fix case without end beams shown in Figure 8-18.

The structural performance of the fix-fix supported slab with end beams is in between that of the fix-fix supported slab without end beam and of the fix-slide supported slab without end beam. The midspan vertical displacements from the three cases are shown in Figure 8-46 and it is obvious that throughout the simulation the displacement curves from the fix-fix supported slab with end beams lay between those from the other two cases. The time the simulation stopped by SAFIR in the case with fix-fix supports and end beams was also in between those from the other two cases.

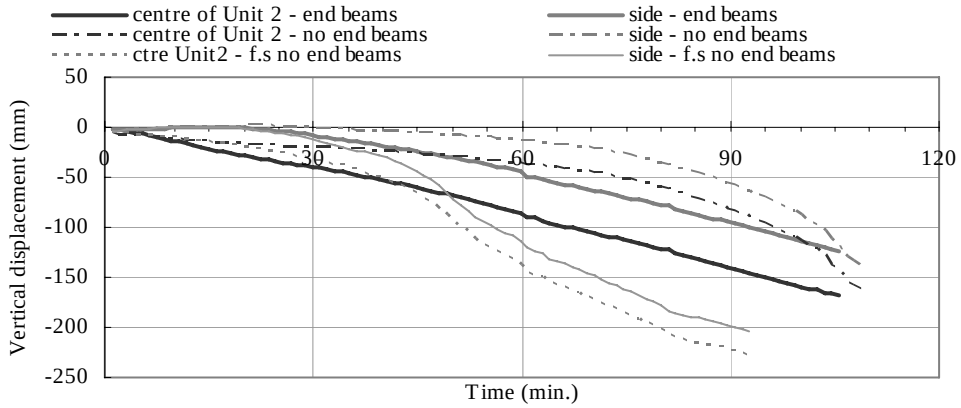

Figure 8-46 Midspan vertical displacements of the fix-fix supported slabs with and without end beams

Figure 8-46 also shows that the end beams not only provided freedom of the horizontal movement but also some freedom for the rotation at the end of the slab via the torsion of the end beams, and some freedom in the vertical displacement through the deflection of the end beams.

The Membrane force distributions in the topping slab between the fix-fix supported slabs with and without end beams are very different. The reason the simulation of the slab with end beam stopped was due to crushing of topping concrete near the corners. Figure 8-47 shows the membrane stress distribution at the topping of this case. The scale of this figure is the same as in Figures 8-17 and 8-19. This figure is very different from that of the case without end beams shown in Figure 8-19 even though both of them are of the slab with 106 minutes of ISO fire exposure. In the case

with end beams there were large compressive stresses concentrated around the supports. The central region of the slab with end beams had less compression compared to that of the slab without end beams. The stress distribution at the central region was even closer to the pin-roller supported case as shown in Figure 8-17. This indicates that there was less restraint on the horizontal and rotational movements at the ends of the slab other than at the four corners.

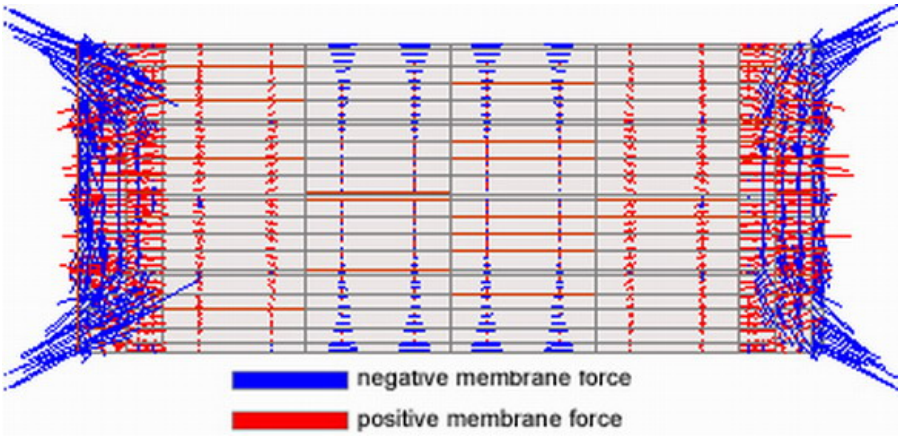

Figure 8-47 Membrane stress distribution at the topping of the fix-fix supported slabs with end beams at 106 minutes (negative: compression; positive: tension)

Figure 8-48 shows the stress distribution along the centreline of the central web of Unit 2 near the end supports of the slabs with and without end beams at different times. It is obvious that the stresses from the slab with end beams were different after 30 minutes of fire exposure, and the stress distributions in the case with end beams were closer to those from the cases without end beams and without restraints on the horizontal movements as shown in Figures 8-24 and 8-35, where the upper three quarters of the web were in tension. The stresses at the bottom quarter of the web from the slabs with and without end beams however were still very similar.

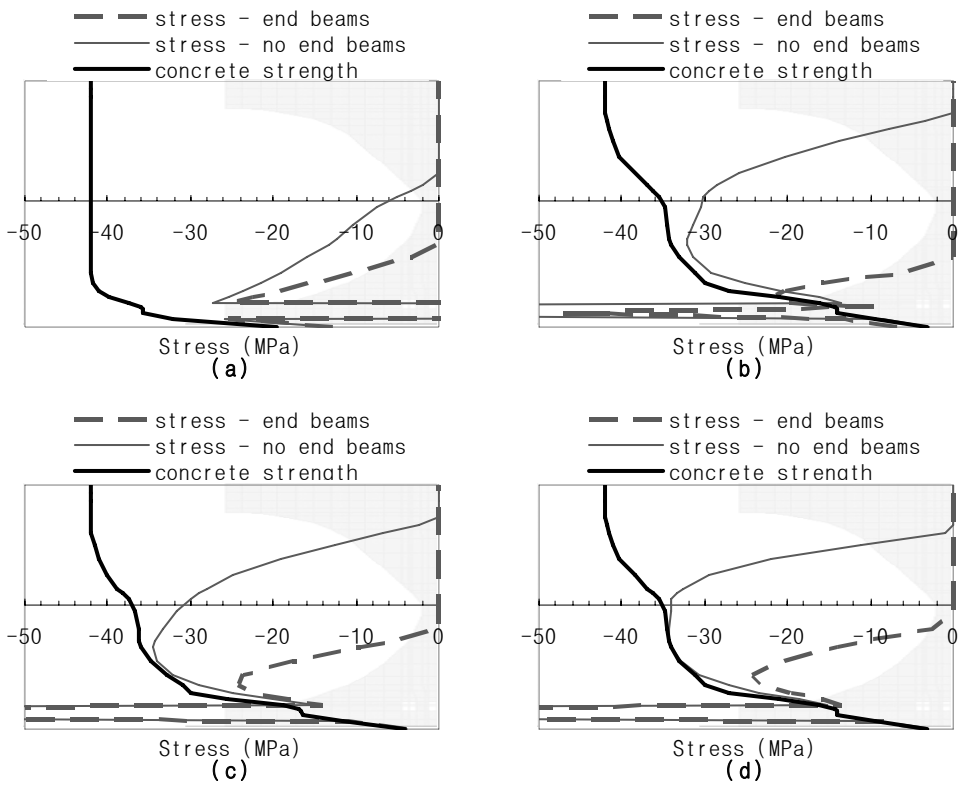

Figure 8-48 Stress distributions in the cross section near the end supports at the central web of Unit 2 at (a) 30min. (b) 60min. (c) 92min. (d) 106min. from the fix-fix supported slab with and without end beams (-: compression)

8.5.4. Fix-slide supports

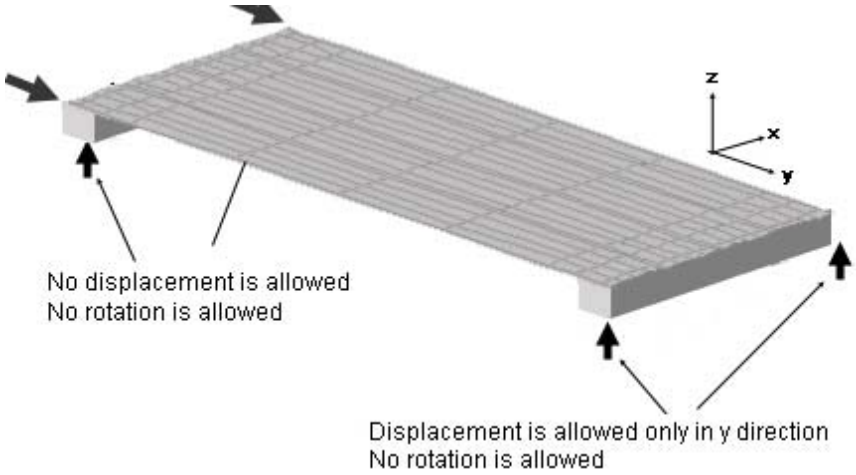

Figure 8-49 Fix-slide supported slab with end beams

The fix-slide supported slab with end beams is as shown in Figure 8-49, where two corners are restrained against rotations and displacements, and the other two corners are free to move along the span length but are also rotationally restrained. The

result shows the slab could sustain more than 4 hours of ISO fire exposure.

Figure 8-50 shows the midspan vertical displacements of the fix-slide supported slabs with end beams compared to those from the slab without end beams and from the fix-fix supported slab with end beams. The figure shows that the fix-slide supported slab with end beams had less deflection than the slab without.

Figure 8-51 shows the horizontal displacement at the slide end from the centre of Unit 2. The results indicate that the slide end of the slab from the case with end beams had less movement than from the case without after 30 minutes of fire exposure, which shows that by forcing the end horizontal movement to be closer to uniform across the slab, which was achieved by the end beams, the maximum end movement is subsequently restricted.

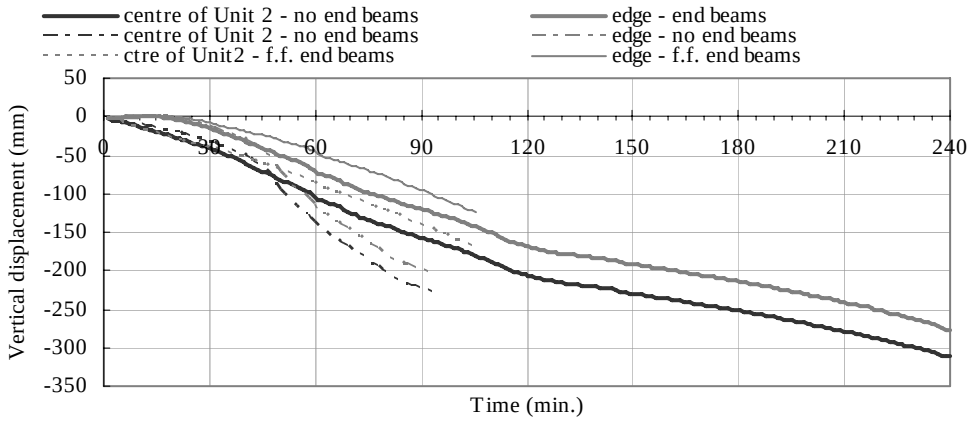

Figure 8-50 Midspan vertical displacements of the fix-slide supported slabs with and without end beams

Because the expanded length of the slab should be the same under the same duration of ISO fire exposure, Figures 8-51 and 8-52 together suggest that some rotation happened in the end beams which caused the slab near the supports to become convex upwards and shifted the midspan upwards under fire. This idea is proven in Figure 8-52; the rotation of the end beams where positive means to cause the slab bending upwards.

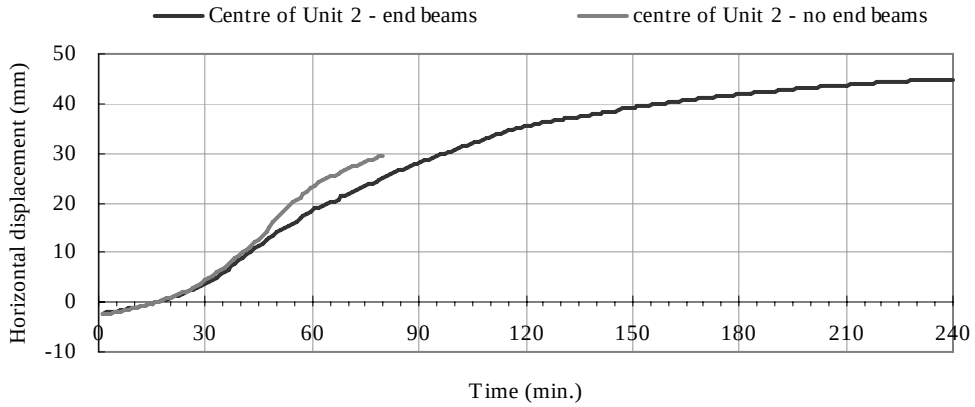

Figure 8-51 Horizontal displacements at the roller end from the fix-slide supported slab with and without end beams (+: outward)

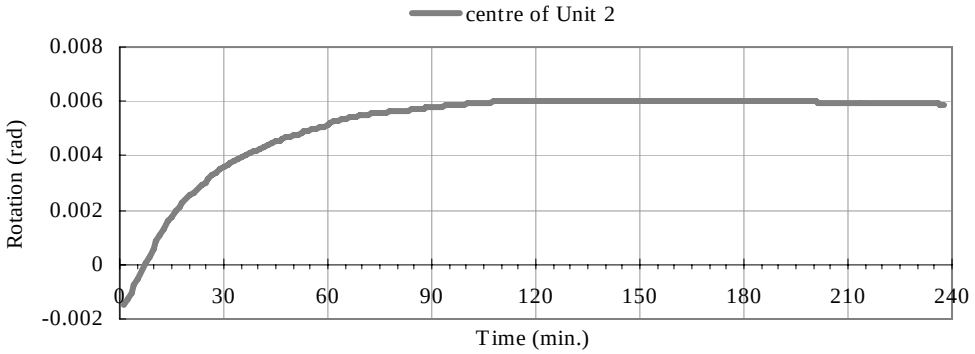

Figure 8-52 Rotation about the width of the slab at the centre of Unit 2 at the end of the fix-slide supported slab with end beams

8.6. Summary and Discussion

8.6.1. Effect of end beams

Table 8-4 shows the stopping time of the simulation of the slabs with and without end beams. The end beams in the models provided some freedom of rotation and vertical displacement at the centre of the slab near the ends; however, they also shifted the stresses to the corners of the slab around the supports. Whether the combination of these effects is beneficial depends on the support conditions. The increase in the vertical displacement at the centre of the slab made the runaway failure happen slightly earlier, the concentration of the stress at the corner made the topping of the fix-fix supported slab crush earlier, but the reduced restraint of the rotation at the end made the fix-slide case last much longer. In practice fully rigid supports cannot be achieved and the effect of reducing restraint by introducing end beams is apparent. Similarly, by fixing the points where the columns connect to the beams, very high

local stresses are induced and premature “failure” can result in the simulations.

The representation of each case in practice is also shown in Table 8-4. The models without end beams do not allow deflections at the ends of the slab but allow for the ends of each hollowcore units to rotate differently in the pin-pin and pin-roller supported cases. In application, the slab without end beams in reality is similar to a floor slab sitting on load bearing walls or very strong and stiff end beams which do not allow for bending, which provide vertical supports throughout the width of the slab at the ends. The support conditions without rotational restraints at the ends represent a very flexible connection between the floor slab and the load bearing wall; and the support conditions with rotational restraints represents a very rigid connection between them.

The models simulated with end beams represent the situation when the slab is supported by 450mm wide and 750mm thick gravity beams. These beams, even though they are certainly not small, are not strong enough to eliminate the occurrence of bending or twisting. In practice, whether the supports can have horizontal displacement or not depends on the stiffness of the columns, and the stiffness of the columns will also affect the degree of rotational restraints applied at the corners of the floor slab. Therefore, the boundary conditions from pin-roller supported case, which represents the slab with weak and slender columns, and the fix-fix supported case, which represents the slab with strong and stiff columns, are more likely to be found in reality.

Table 8-4 Stopping time of the simulation of the slabs with and without end beams

Support conditions	**Without end beams**		**With end beams**	
Pin-pin	>240 min.	Flexible connection on load bearing walls or very strong end beams	>240 min	Flexible connection on medium end beams
Pin-roller	63 min.		59 min.	
Fix-fix	108 min.	Rigid connection on load bearing walls or very strong end beams	106 min.	Rigid connection on medium end beams
Fix-slide	92 min.		>240 min.	

Based on the simulation results, the following three points can be made:

• Preventing end beams from deflecting can increase the fire resistance of the floor slab. This can be achieved by either protecting the end beams or using rigid or very stiff end beams.

• For floor slabs supported on beams and columns, it is recommended to use rigid connections between the slab and end beams.

• For floor slabs supported on load bearing walls, it is recommended to use rotationally flexible connections between the slab and the supporting walls.

8.6.2. Effect of core-filling

Table 8-5 shows the stopping time of the simulation of the slabs with and without core-filling. Fellinger [2004] tested the effect of core-filling and found out that having core-filling alone without the extra reinforcements does not improve the fire resistance of the slab, and the incompatibility between the thermal expansion of the drier hollowcore units and the later cast core-filling might even have negative effect on the performance of the slab in fire. Nevertheless, it is rare to find core-filling without extra reinforcement tied to the end beams. The core-filling in the simulation shown herein was treated as part of the beam elements with the assumption that there is a perfect bond between the core-filling and the hollowcore unit, i.e. the program considers that the beam elements at the end of the slab were stronger in the case with core-filling; therefore the results here showed that the core-filling has a beneficial effect to the fire resistance of the slab. The assumption on perfect bonding is realistic when there is no relative rotation or displacement between the hollowcore units and the end beams, as with those conditions a stronger tie between the hollowcore units, core-fillings and end beams can be achieved, and bond failure between the hollowcore units and core- fillings becomes less likely.

Table 8-5 Stopping time of the simulation of the slabs with and without core-filling

Support conditions	With core-filling	Without core-filling
Pin-pin	>240 min.	>240 min.
Pin-roller	63 min.	59 min.
Fix-fix	108 min.	101 min.
Fix-slide	92 min.	51 min.

8.6.3. Effect of support conditions

All of the results from this chapter are summarised in Table 8-6. In reality no supports or connections would behave the same as in the ideal situations but somewhat in between. In terms of applying the findings from the results shown here to practice, it can be concluded that providing good axial restraint has a beneficial effect on the structural performance in fire, and good rotational restraint at the slab supports is also beneficial. Therefore, for isolated floor system exposed completely to fire, the presence of strong and stiff columns will improve the fire resistance of the floor system.

Table 8-6 Stopping time of the simulation of the slabs with various support conditions

Support conditions	Without end beams, with core-filling	Without end beams, Without core-filling	With end beams, with core-filling
Pin-pin	>240 min.	>240 min.	>240 min
Pin-roller	63 min.	59 min.	59 min.
Fix-fix	108 min.	101 min.	106 min.
Fix-slide	92 min.	51 min.	>240 min.

Fellinger [2004] summarised 80 fire tests from various sources, which are shown in Figure 8-53, where small solid black diamond markers mean shear and anchorage failure has occurred, and small white diamond markers mean the test failed in other mechanisms. The figure shows that providing axial restraints increases the fire resistance and significantly reduces the likelihood of having shear and anchorage failure. The length of the cold support means a restriction to the rotations at the ends, and the results show that slabs with less rotational restraint at the ends are more likely to have shear and anchorage failure and fail within 1 hour of ISO fire exposure. Therefore, axial and rotational restraints at the ends are recommended.

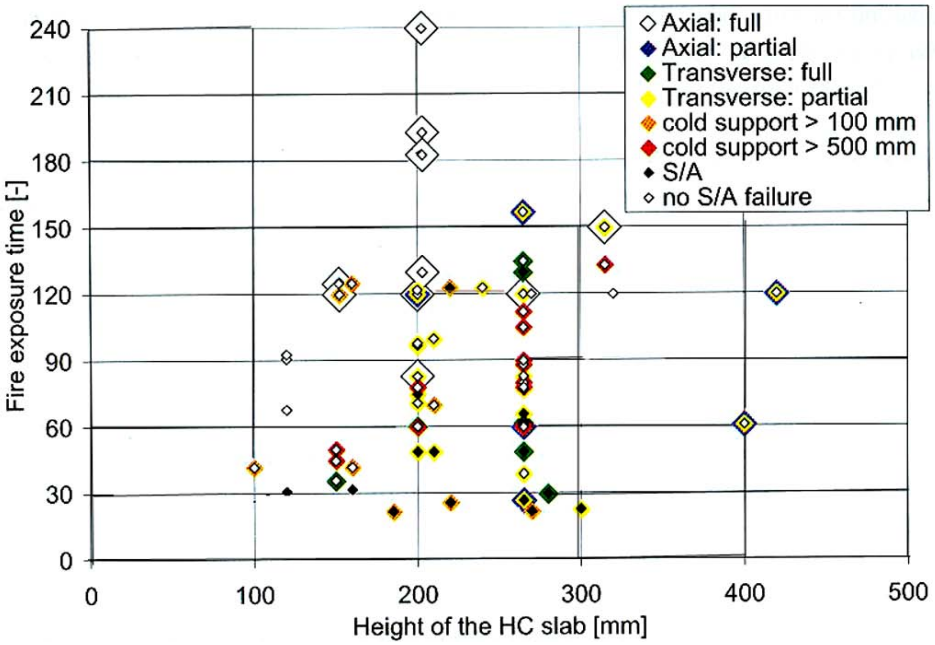

Figure 8-53 Fire exposure time versus the height of the HC slabs [Fellinger 2004]

9. Fire Performance of Hollowcore Concrete Flooring Systems with End Connections from NZS3101

9.1. Introduction

This chapter investigates the fire performance of hollowcore concrete flooring systems with end connections designed in accordance to both the 1995 and 2006 versions of the New Zealand Concrete Design Standards NZS3101 [SNZ 1995, 2006a].

New details for connection of hollowcore floor units to reinforced concrete supporting beams were introduced in the New Zealand Concrete Standard NZS3101:2006 [SNZ 2006a] to improve seismic performance. The problems of the connections of hollowcore concrete flooring systems from NZS3101:1995 [SNZ 1995] in earthquakes has been exposed by Matthews [2004]. Due to the high fixity of these connections, the rotation of the seating beam caused by the earthquakes transfers directly onto the hollowcore units and causes snapping of the floor slabs. With the excessive fixity in the end and side connections, incompatibility between the slab and the perimeter beams can also cause topping delamination and web splitting in the hollowcore units during earthquakes. Therefore, new seating details are proposed by Lindsay [2004] to reduce the fixity at both connections at the ends and the sides, and MacPherson [2005] proposed another end connection details to reduce the possibility of snapping action. The recommended seating connections for hollowcore flooring systems have been updated to the ones proposed by Lindsay and MacPherson in NZS3101:2006, but their influence on fire performance has yet to be determined. As the new recommendations appeared firstly in 2004 in Amendment 3 of the 1995 version of NZS3101 [SNZ 2004], there are already many buildings in New Zealand with hollowcore flooring system built before that, which have different end connection arrangements to the latest recommendations. This study also considers the influence from these old end connection designs to the fire resistances of the structures.

This chapter presents the structural behaviour under fire of three subassemblies based on those tested by Matthews [2004], Lindsay [2004] and MacPherson [2005], as Matthews' specimen is based on the older version of the Design Standards [SNZ

1995], and the other two follow the improved detailing recommended in the amendment [SNZ 2006]. The aim of this chapter is to study the effect of these end connections to the fire performance of the hollowcore concrete flooring systems. The first part in this chapter looks at the effect of the end connections and the support conditions, and the second part investigates the effect of the end connections in the subassembly.

The first part of this chapter describes the connection details of the studied subassemblies, and the second part describes how the end connections are modelled in the simulations. In terms of parametric analysis, Section 9.4 investigates the structural behaviour of the slabs in fire with these end connections mentioned before and ideal supporting conditions at the corners, namely pin-pin, pin-roller, fix-fix and fix-slide supports. Finally, in Section 9.6 the columns are included in the model to replace the ideal supporting conditions at the corners and complete the subassemblies, and the structural performance of these subassemblies in fire with different end connections is investigated.

9.2. Design Details of Studied Subassemblies

This section describes briefly the layouts and the connection details of the studied subassemblies. Specific details and explanations of these designs can be found in the referenced reports.

9.2.1. Subassembly from Matthews [2004]

The tested specimen by Matthews was two-bay by one-bay and had a bay width of 6.1m. The square columns were of 750mm x 750mm size and the perimeter beams were 750mm deep by 450mm wide for the end beams and 400mm wide for the side beams. The hollowcore units used were DYCORE300 and had a depth of 300mm. On top of the hollowcore units was a layer of 75mm cast in-situ concrete topping with a 665-mesh cold-drawn wire reinforcement at the mid-height of the topping. The reinforcing details of these structural members can be found in Matthews [2004]. The dimensions and layout of the subassembly are shown in Figure 9-1.

The connection used in Matthews specimen was the most common connection detail used in New Zealand from the mid 1980s until the introduction of Amendment 3 of NZS3101:1995 [SNZ 2005]. The ends of the hollowcore units were supported on

a mortar bed. The hooked starter bars were Grade 300 HD12 at 300mm centres and lapped with the non-ductile reinforcing mesh within the topping. The end connection detail in the end connection is shown in Figure 9-2(a). The same starter bar arrangement was used for the lateral connection as shown in Figure 9-2(b).

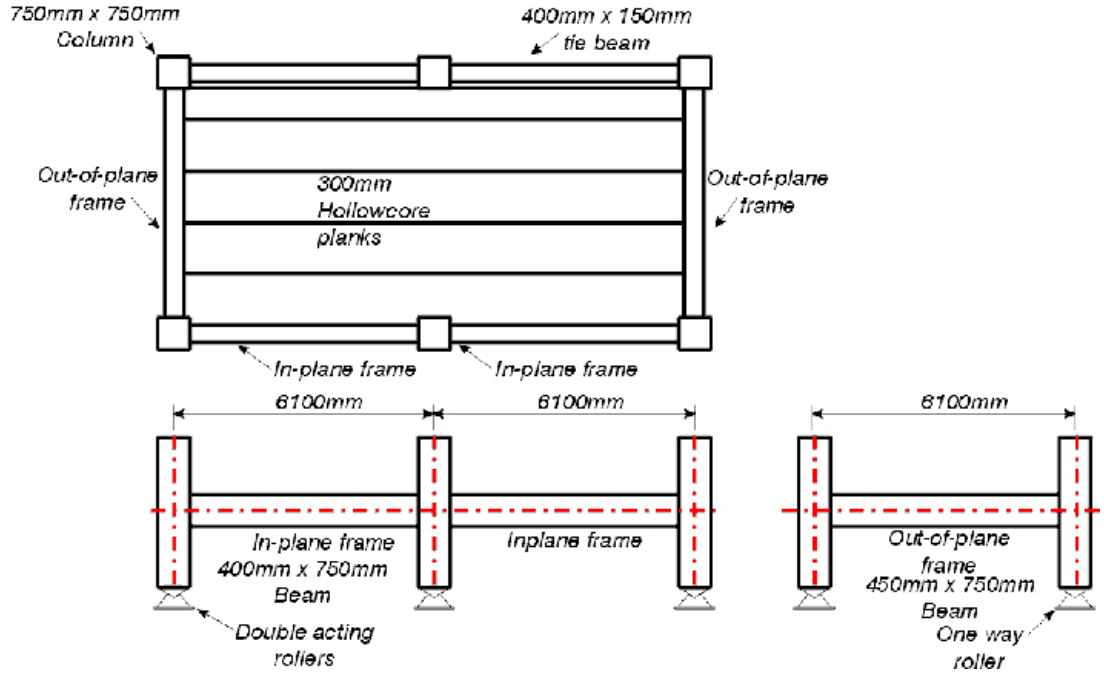

Figure 9-1 Dimensions and layout of the subassembly from Matthews [2004]

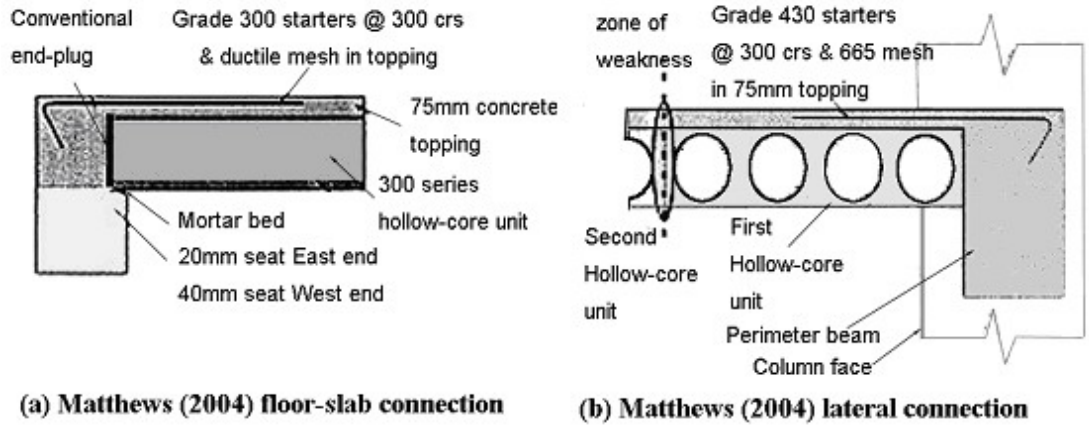

Figure 9-2 (a) End connection details (b) lateral beam-to-hollowcore connection from Matthews [2004]

9.2.2. Subassembly from Lindsay [2004]

The specimen layout from Lindsay [2004] is different to the layout from Matthews and is shown in Figure 9-3. The end connection in this case is the same as that in C.18.6.7 (a) of NZS3101:2006 [SNZ 2006], which consists of a soft packing behind the hollowcore units. Grade 300 hooked starter bars were used at 300mm

centres and lapped with the mesh within the topping.

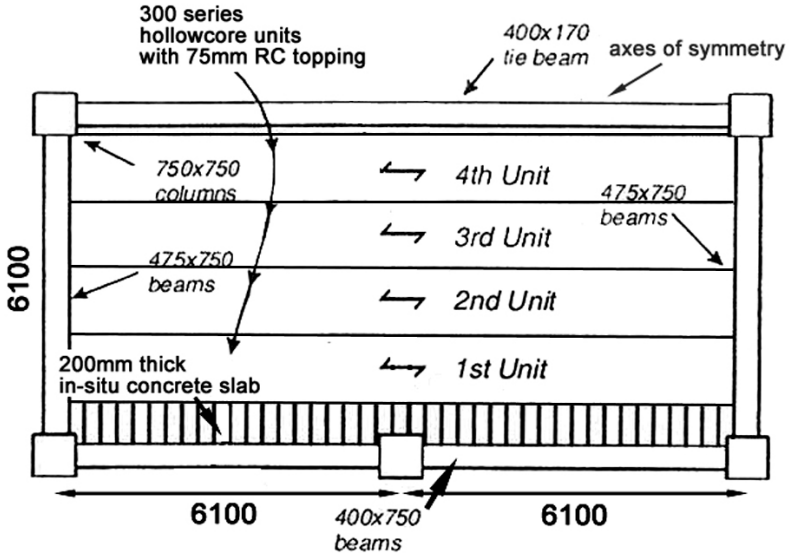

Figure 9-3 Floor plan of the specimen in the research by Lindsay [2004]

In the lateral connection, a 750mm timber infill was used between the first hollowcore unit and the perimeter beam as prescribed in NZS3101:2006 [SNZ 2006]. Grade 430 starters at 300 centres were used lapping the topping mesh in the area of timber infill. The details of the end and lateral connections are shown in Figures 9-4 (a) and (b) respectively.

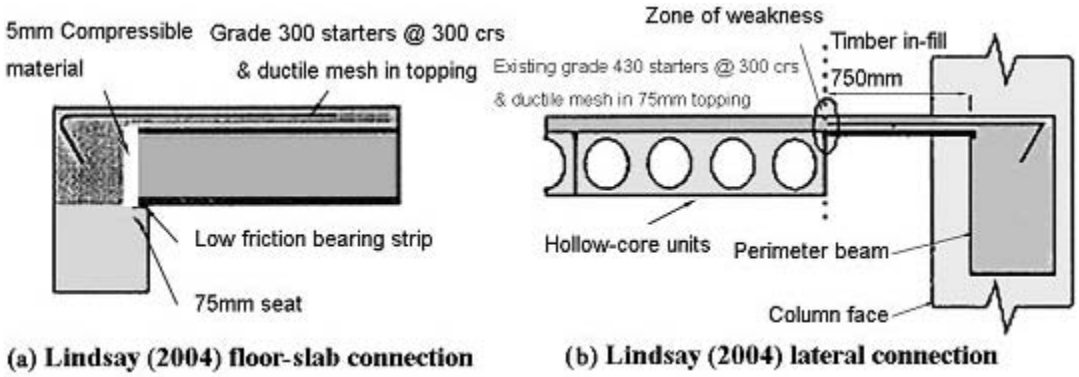

Figure 9-4 (a) End connection details (b) lateral beam-to-hollowcore connection from Lindsay [2004]

9.2.3. Subassembly from MacPherson [2005]

The overall layout of the subassembly from MacPherson [2005] is the same as the layout from Lindsay, which was shown in Figure 9-3. The end connection details from MacPherson are the same as those in C.18.6.7 (b) of NZS3101:2006 [SNZ 2006]. Two of the four cores of each hollowcore unit were reinforced by Grade 300 R16 bars

placed close to the bottom and filled with concrete, and Grade 300 D12 starter bars were used at 300mm centres and lapped with the topping mesh.

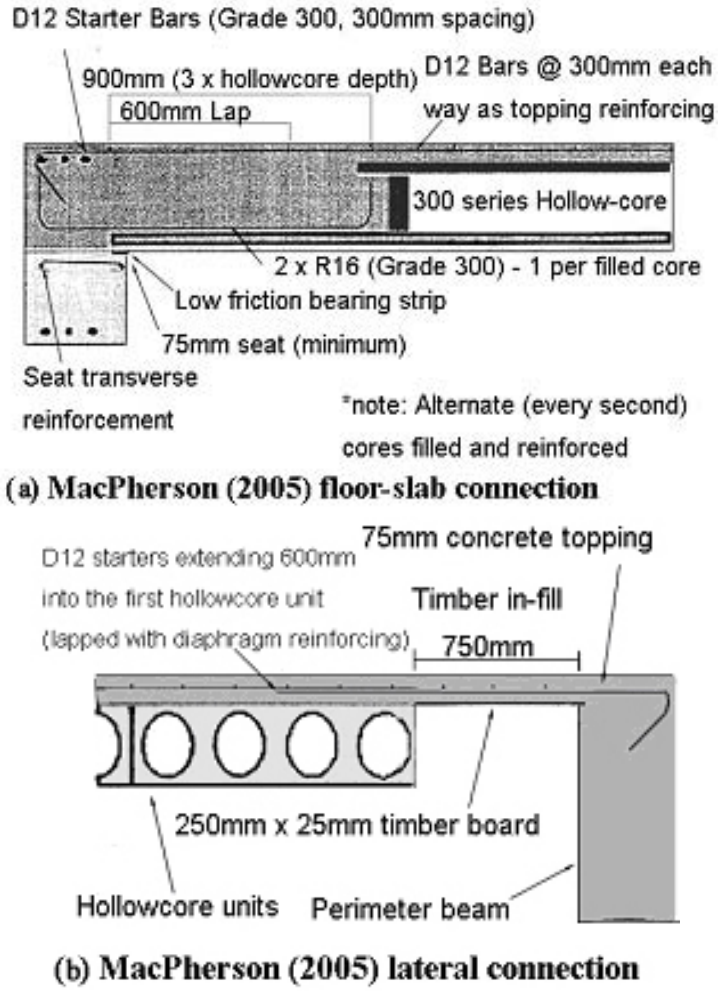

Figure 9-5 (a) End connection (b) lateral beam-to-hollowcore connection from MacPherson [2005]

The end connection detail of this case is shown in Figure 9-5(a). However, in the simulation model the core filling was extended to 1.2m long rather than the 900mm used by MacPherson to coincide with the extended length of the starter bar for the ease of modelling. The lateral connection in this case is the same as that from Lindsay except the starter bars were replaced from Grade 430 to Grade 300 D12 and extended 600mm into the topping of the first hollowcore units. The lateral connection detail is shown in Figure 9-5(b).

9.3. Modelling the End Connections from the Subassemblies

This section explains the method to translate the previously described end connections to the simulation model to be used in SAFIR.

9.3.1. Modelling Matthews' end connections

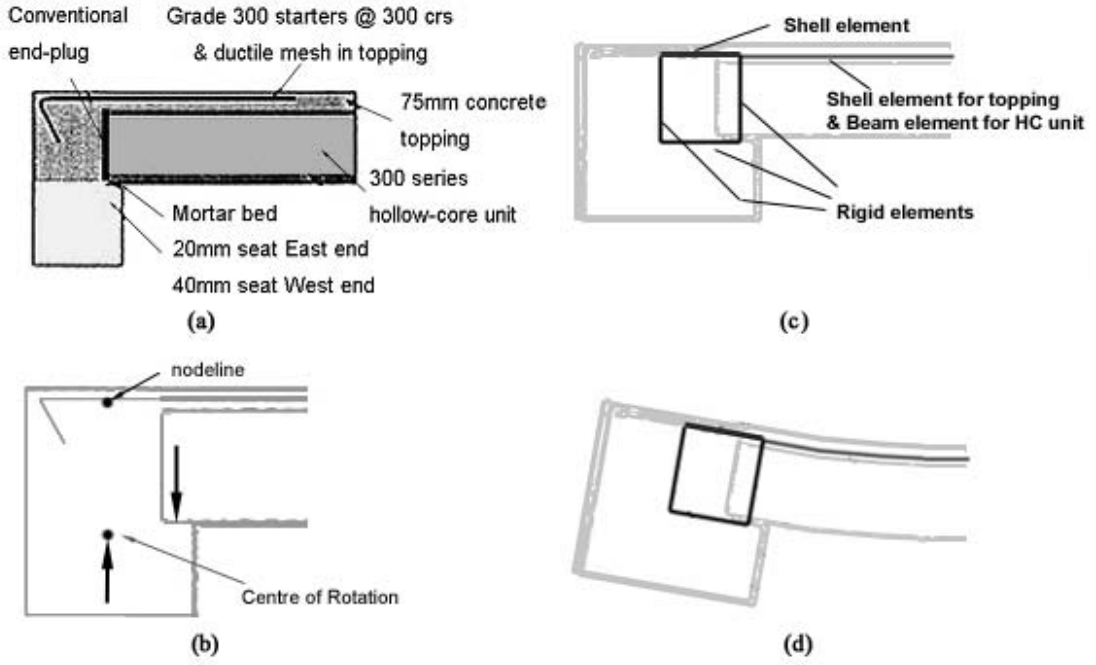

Figure 9-6 Modelling Matthews' end connection details (a) original detail (b) node-line of the model in SAFIR and force paths in the connection (c) Simulation scheme in SAFIR (d) deformed shape of the connection

Figure 9-6 shows how the end connection detail of Matthews' specimen was translated into the SAFIR model. Each hollowcore unit is modelled using a grillage of beam elements. The end beams are also modelled using beam elements. To model the end connection, three rigid elements are used connecting the end of each longitudinal beam in the beam grillage to the beam elements representing the end beam. In the end connection, many concerns were raised by the location of the node-line and the actual load paths as shown in Figure 9-6 (b). While the centres of gravity and torsion of the hollowcore units are at around the mid-height of the units, the hollowcore units and the topping have to share the same node-line in the model and are connected at the mid-height of the topping. To model the load path in the end connection correctly, a rigid element with a length equal to the distance between the bottom of the hollowcore unit and the mid-height of the topping was used to transfer the vertical load from the actual height of the seating to the slab as shown in Figure 9-6 (c).

Another rigid element was used in the model to represent the concrete section between the node-line of the end beam and the location of the seating. A third rigid element was used to connect vertically the shell elements that represent the area which has starter bars overlapping with reinforcing mesh in the topping to the beam element that represents the end beam.

In terms of the horizontal movement at the end connection along the span, Matthews' connection does not allow for relative displacement between the end of hollowcore units and the end beams, and at the points where the two rigid elements mentioned before meet together in the model, i.e. at the centre of the mortar bed in the experiment, the vertical and horizontal displacement are shared by the two rigid elements as shown in Figure 9-6 (c). This is further shown in the deformed shape of the connection during fire illustrated in Figure 9-6 (d). Lim [2003] and Bernhart [2004] have shown that with a rigid connection between the slab and the supporting beams, the tendency for the slab to expand is resisted by the beams which induces compression in the slab and a horizontal shear force in the beam.

9.3.2. Modelling Lindsay's end connection

The main difference between the model for the end connection details by Lindsay and Matthews is the presence of the soft packing behind the hollowcore units. The modelling scheme is shown in Figure 9-7. The connection is also modelled as three rigid elements at the ends of every line of beam elements representing the hollowcore units. The soft packing allows a relative displacement between the bottom of the hollowcore units and the end beam until these two surfaces press against each other, therefore the points representing the bottom of the hollowcore units and the seat do not share the horizontal displacement as shown in Figure 9-7 (c) but still share the vertical displacement. The horizontal displacement of the bottom of the hollowcore units in the model depends on the rotation of the concrete topping covering the gap as in the real situation. This is illustrated in Figure 9-7 (d), which is the deformed shape of the connection.

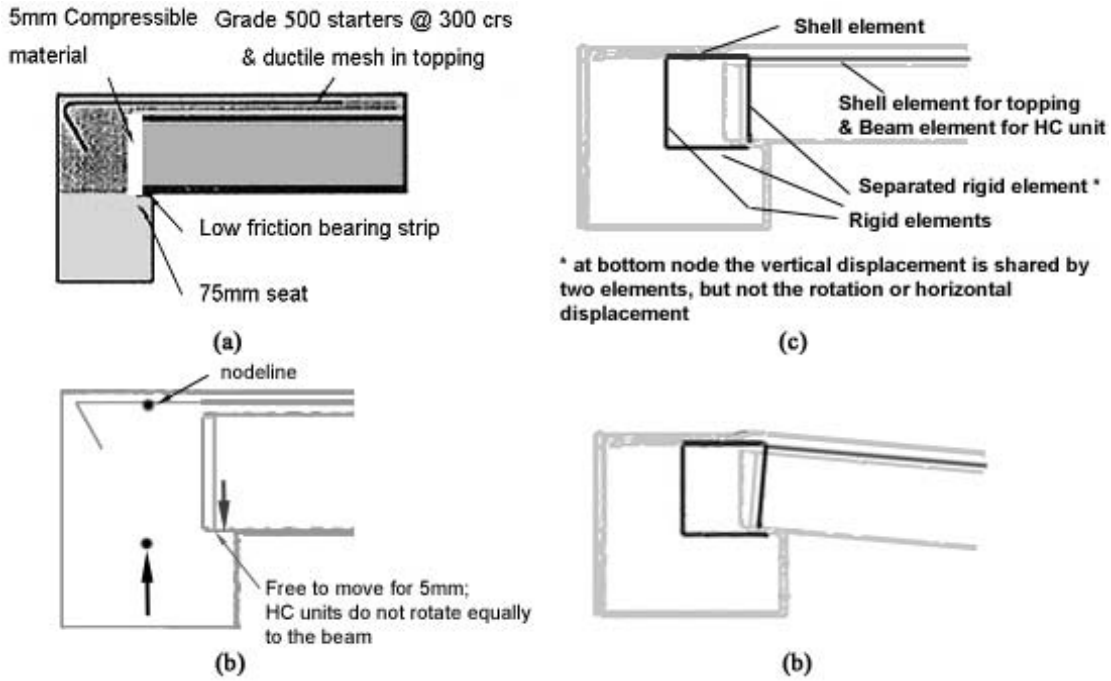

Figure 9-7 Modelling Lindsay's end connection details (a) original detail (b) node-line of the model in SAFIR and force paths in the connection (c) Simulation scheme in SAFIR (d) deformed shape of the connection

9.3.3. Modelling MacPherson's end connections

The layout of the rigid elements in the model for the end connection used by MacPherson's specimen is the same as the one used for simulating the end connection from Matthews' specimen and was shown in Figure 9-6. The difference between the two cases was the core filling. The core filling in MacPherson's specimen was modelled as part of the beam elements that represent the hollowcore units. The reinforcement within the core filling was not specifically modelled. This was because the rigid elements between the end face of the hollowcore units and the end beam in both models had a very high strength and stiffness, and it is assumed that the face of the end beam would not be separated from the end face of the hollowcore units in the connections used by Matthews or MacPherson.

9.3.4. Simplifications made by using these models

There are several simplifications made when translating these end connection details into the models. In the model for Matthews' end connection, the displacement of the bottom of the hollowcore slab moving away from the face of the end beam was not considered. This displacement could possibly occur while cooling but not during heating, and for the research reported here the fire follows the ISO834 standard fire

curve and has no cooling phase; therefore this simplification should not cause any concern to the results reported herein. In the model for Lindsay's test, the displacement of the bottom of the hollowcore units moving towards to the face of the end beams should be limited to 5mm, which was the size of the gap, but SAFIR could not manage this limitation well. This will be discussed further in the results section.

9.4. Study on Slabs with Different End Connections and Different Supporting Conditions at the Ends of the End Beams

This section studies the effect of having different end connections between the slab and the end beams, in combination to fix-fix or fix-slide supporting conditions at the ends of the end beams. The behaviour of the hollowcore concrete floor slab in a subassembly will be similar to one of these ideal supporting conditions depends on the slenderness of the columns at the corners. The aim of this section is to establish the envelope of the structural performance of the hollowcore concrete flooring systems in a subassembly in fire.

The support conditions are shown in Figures 8-45 and 8-49 respectively. The slabs consisted of four units spanning 12.2 metres with a total width of 5.1m as shown in Figure 8-1. The end beams as shown in Figure 8-38 were included in the model and were 750mm deep by 450mm wide with three D25 bars at both the top and bottom as used in Section 8.5.

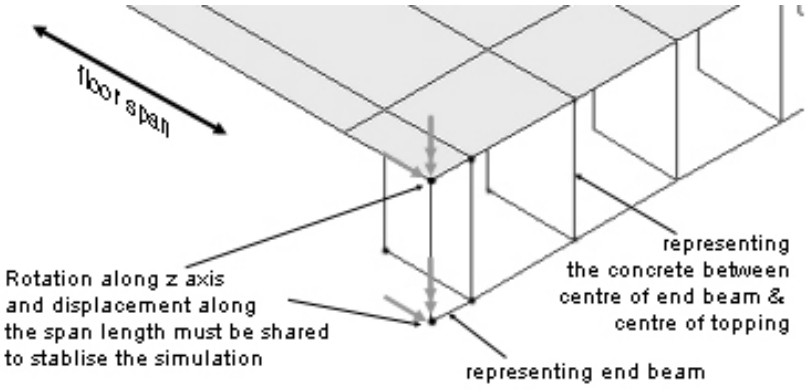

Figure 9-8 Sharing of rotation in vertical axis and displacement along span length at the corners

At the four corners of the slab in the model, the displacements along the span length of the slab and of the end beams must be shared to stabilise the simulation, and the rotation about the vertical axis has to be shared also as shown in Figure 9-8.

Because these sharing relationships restrained the rotation at the four corners, the pin-pin and pin-roller support conditions were not considered in this part of study.

9.4.1. Slabs with Matthews' end connection

The end connection used in Matthews [2004] is shown in Figure 9-2(a) and was modelled as shown in Figure 9-6, which was the most common end connection for hollowcore flooring system prior to the introduction of Amendment 3 of NZS3101:1005 [SNZ 2005]. In the simulated slab, the ideal supporting conditions, namely fix-fix and fix-slide supports, were used at the four ends of the end beams. These two cases are named as Case A and Case B respectively. The results of the simulations are shown in Table 9-1.

Table 9-1 Summary of the simulation results of the slabs with Matthews' end connection

Name	Support condition	Simulation stop time	Reason
Case A	**Fix-fix**	69 minutes	Terminated by SAFIR: Crushing of topping concrete near the corners
Case B	**Fix-slide**	>240 minutes*	*designated end time of the simulation

9.4.2. Slabs with Lindsay's end connection

The end connection from Lindsay [2004] was shown in Figure 9-4(a) and in the model was simulated as shown in Figure 9-7. This end connection is also the suggested end connection from C.18.6.7(a) of NZS3101:2006 [SNZ 2006b]. The simulation results of the floor slabs with Lindsay's end connection are shown in Table 9-2. The two cases are named as Cases C and D respectively as shown in the table.

Table 9-2 Summary of the simulation results of the slabs with Lindsay's end connection

Name	Support condition	Simulation stop time	Reason
Case C	**Fix-fix**	53 minutes	Terminated by SAFIR: No convergence after 20 iterations
Case D	**Fix-slide**	48 minutes	Terminated by SAFIR: No convergence after 20 iterations

9.4.3. Slabs with MacPherson's end connection

The end connection used in MacPherson [2005], i.e. the suggested end connection from C.18.6.7(b) of NZS3101:2006 [SNZ 2006b], has been shown in Figure 9-5(a). Table 9-3 shows the simulation results of the slabs with MacPherson's end connection

and ideal support conditions at the ends of the end beams. The two cases are named as Cases E and F respectively as shown in the table.

Table 9-3 Summary of the simulation results of the slabs with MacPherson's end connection

Name	Support condition	Simulation stop time	Reason
Case E	**Fix-fix**	66 minutes	Terminated by SAFIR: Crushing of topping concrete near the corners
Case F	**Fix-slide**	>240 minutes*	*designated end time of the simulation

9.4.4. Rigid end connection

The connection used in Section 8.5 assumed the slab is connected rigidly and directly to the end beams, therefore rotations and displacements are shared at the very end of the slab and do not consider the seating distance. From now onwards this ideal connection type is called "rigid end connection". The simulation results are shown in Table 9-4 which repeats the findings reported before in Table 8-3. The four types of support conditions are shown in Figures 8-39, 8-41, 8-45 and 8-49. Detailed discussions of the results shown in Table 9-4 can be found in Section 8.5. In this section each case is given a name as shown in the table.

Table 9-4 Summary of the simulation results of the slabs with rigid end connection

Name	Support condition	Simulation stop time	Reason
Case G	**Pin-pin**	>240 minutes*	*designated end time of the simulation
Case H	**Pin-roller**	59 minutes	**Failure**: Runaway failure
Case I	**Fix-fix**	106 minutes	Terminated by SAFIR: Crushing of topping concrete near the corners
Case J	**Fix-slide**	>240 minutes*	*designated end time of the simulation

9.4.5. Analyses and discussions – slabs with fix-fix supports

Both the end connections from Matthews and MacPherson fix the end of the slab to the end beams, while the end connection from Lindsay gives the end of the slab some freedom to rotate independently from the end beams.

Figure 9-10 shows the midspan vertical displacement at the centre and at the side of the fix-fix supported slabs with the three end connection arrangements, i.e. Cases A, C, and E. The locations of these points are shown in Figure 9-9. It also shows the displacements from Cases G and I, i.e. the slab was connected directly into the end

beams rigidly as shown previously in Section 8.4. The deflections at the side of Cases A and E are so close that they overlap with each other. The results show that the deflection of Cases A and E were closer to the one obtained from Case I as expected, but the deflection of Case C was closer to that from Case G. This was because the gap between the bottom of the slab and the end beam allowed the rotation at the end of the slabs to be different from that of the end beams, the slab would behave close to a pin-pin supported even though the ends of the end beams had rotational restraints as shown in Figure 8-45.

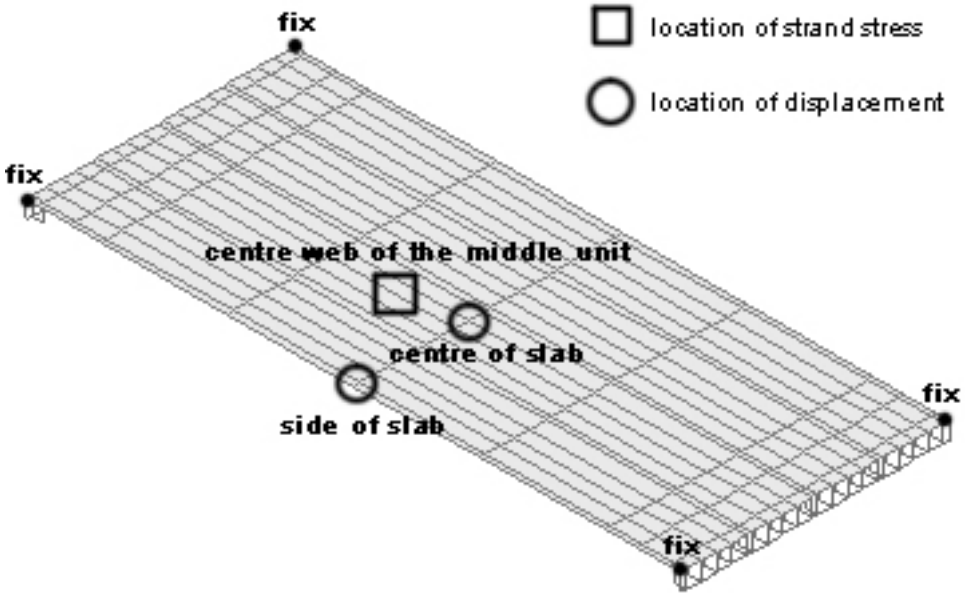

Figure 9-9 Locations of the recorded displacements and stresses of the fix-fix supported slab

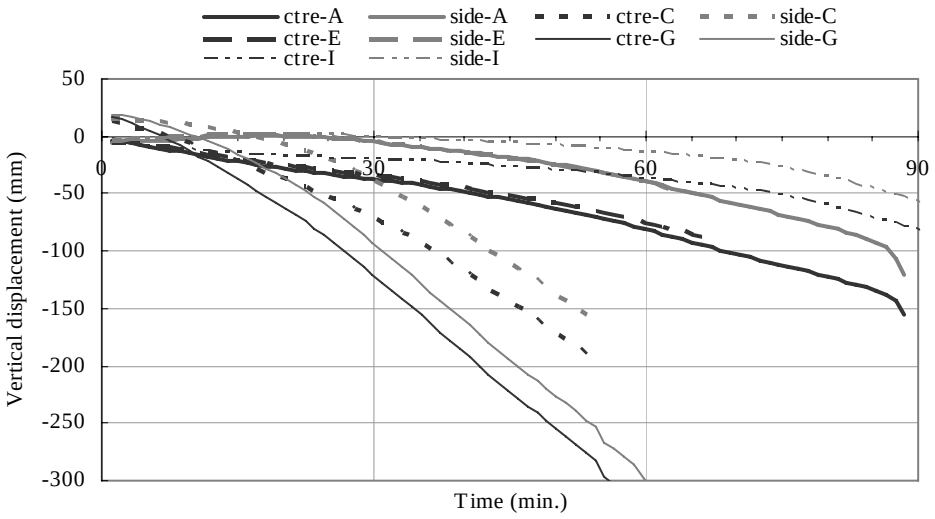

Figure 9-10 Midspan vertical displacements from fix-fix supported slabs with various end connections

Figure 9-11 shows the stress history of the strand at the midspan at the centre web of the middle units from the fix-fix supported slabs with different end connections, where the tensile force was the largest. The location of this point is shown in Figure 9-9. Figure 9-11 shows that the strand stresses from Cases A and E are very close that they overlapped each other, it also shows that the stress history of the strand from Case C was closer to that from Case G, but the strand stress from the slab with either Matthews' or MacPherson's end connection was very close to that from Case I.

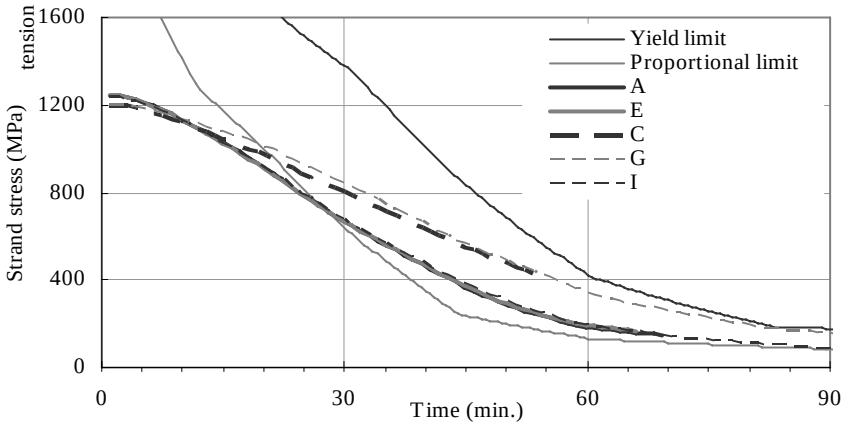

Figure 9-11 Strand stress histories of fix-fix supported slabs with various end connection details

Figure 9-12 shows the membrane stress distributions after 50 minutes of ISO fire exposure within the topping of the fix-fix supported slabs with different end connections, and those of the slabs with rigid end connections and with pin-pin and fix-fix supports. All the graphs are plotted using the same scale. The blue lines represent compressive forces, and the red ones mean tensile forces. In cases of the slab with Matthews' or MacPherson's end connections, as well as of the fix-fix supported slab with rigid end connections (Cases A, E and I), the simulation stopped due to crushing within the topping concrete near the corners. The figure shows the similarity between the stress distributions in the topping of these three cases. Even though the compression near the centre of the end beams in the topping of the slab with Lindsay's connection is greater than that of the pin-pin supported slab with rigid end connection, the figure shows the stress distributions in these two cases are very similar, which agrees with the finding from the plots of strain stress history as well as from of the midspan vertical displacements.

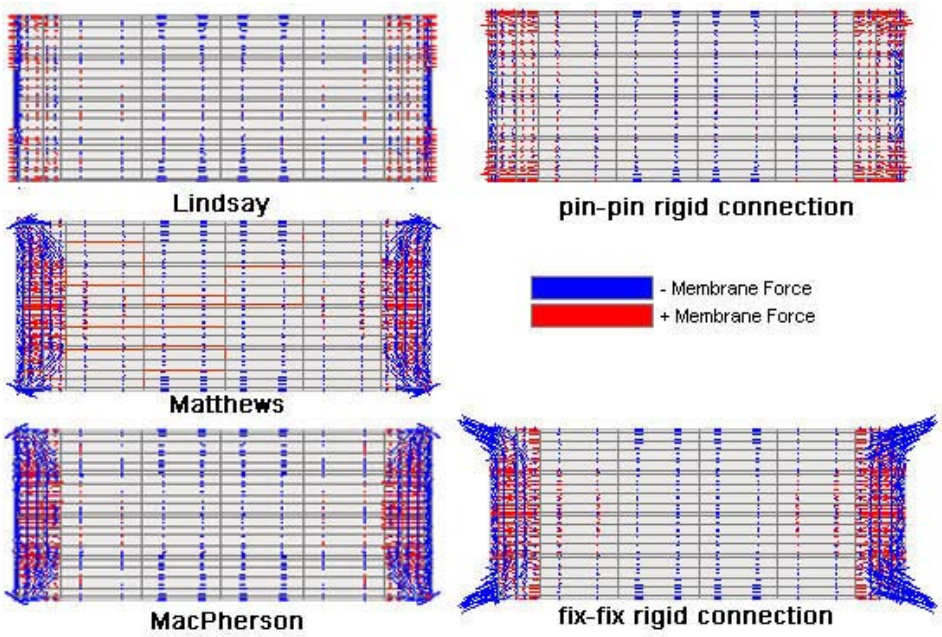

Figure 9-12 Membrane stress distributions in the topping of the fix-fix supported slabs with various end connections after 50 minutes of ISO fire exposure (negative: compression; positive: tension)

In summary, the results showed that the behaviour of the fix-fix supported slabs with Matthews' or MacPherson's end connections is very close to the fix-fix supported slab with rigid end connection, and the behaviour of the fix-fix supported slabs with Lindsay's end connections is very close to the pin-pin supported slab with rigid end connection.

9.4.6. Analyses and discussions – slabs with fix-slide supports

Figure 9-14 shows the midspan vertical displacement from the fix-slide supports slabs with different end connections. The locations of the observed displacements are shown in Figure 9-13. Figure 9-14 shows that the midspan deflections of the slabs with Matthews' or MacPherson's connections (Cases B and F) were in between those of the fix-fix or fix-slide supported slab with rigid end connection (Cases I and J). The midspan deflections of the slab with Lindsay's connections (Case D) were similar to those of the pin-roller supported slab with rigid end connections (Case H). This finding is similar to the one from the fix-fix supported slabs. However, in this case the displacements from the slab with Matthews' end connection (Case B) are not very close to those from the slab with MacPherson's end connection (Case F), which is different from the finding in the fix-fix supported slabs.

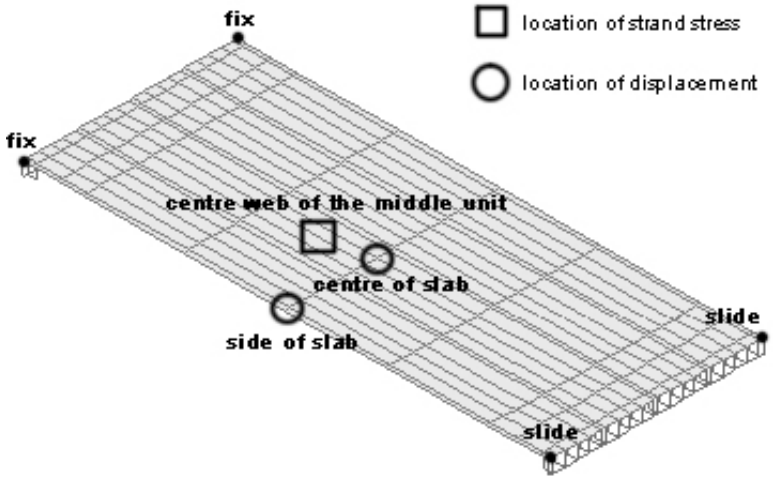

Figure 9-13 Locations of the recorded displacements and stresses of the fix-slide supported slab

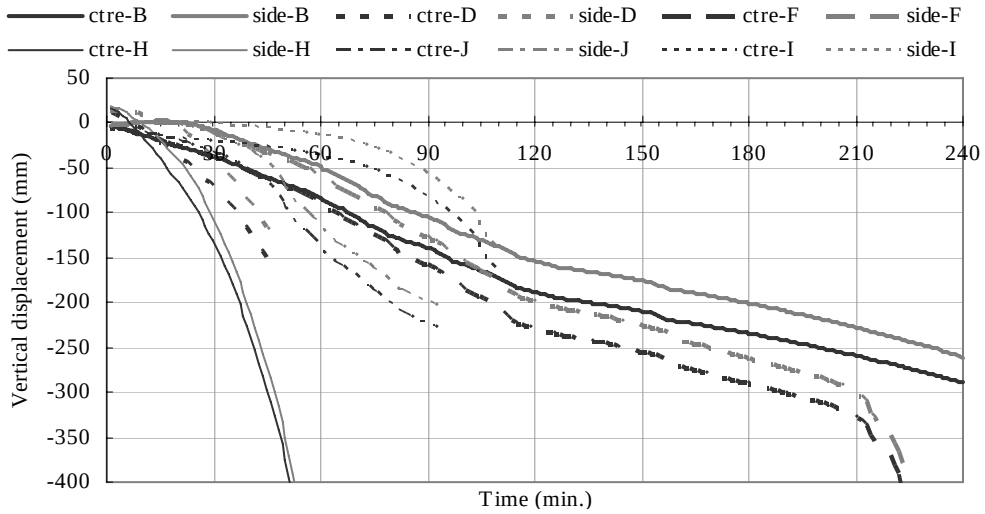

Figure 9-14 Midspan vertical displacements from fix-slide supported slabs with various end connections

Figure 9-15 shows the strand stresses at the midspan at the centre web of the middle units in the fix-slide supported slabs with various end connections. The location of extracted strand stresses is shown in Figure 9-13. Figure 9-15 gives the same conclusions to the ones drawn in the fix-fix supported slabs. The strand stress from the slab with Lindsay's end connection (Case D) was closer to that from the slab of pin-roller supported slab with rigid end connection (Case H) than to the others, but the strand stresses from the slabs with Matthews' and MacPherson's end connection (Cases B and F) are very close to that from the case of fix-slide supported slab with rigid end connection (Case J). The strand stress from the slab with Matthews' connection (Case B) is very close to that from the slab with MacPherson's end connection (Case F).

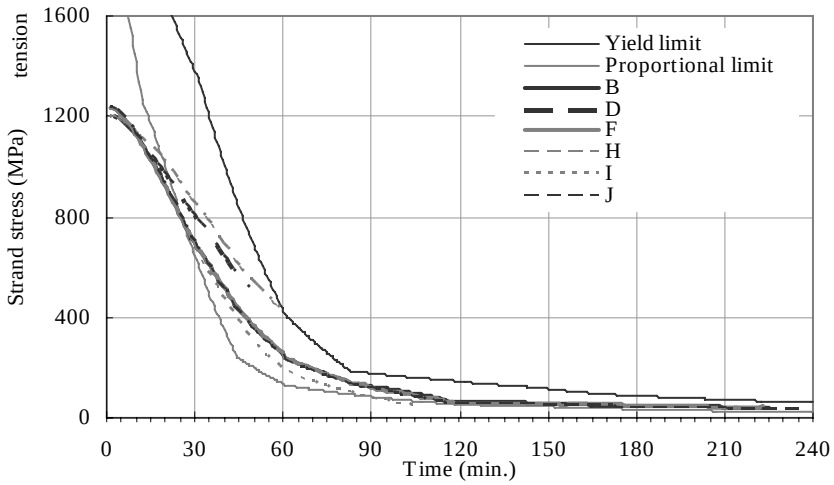

Figure 9-15 Strand stress histories of fix-slide supported slabs with various end connection details

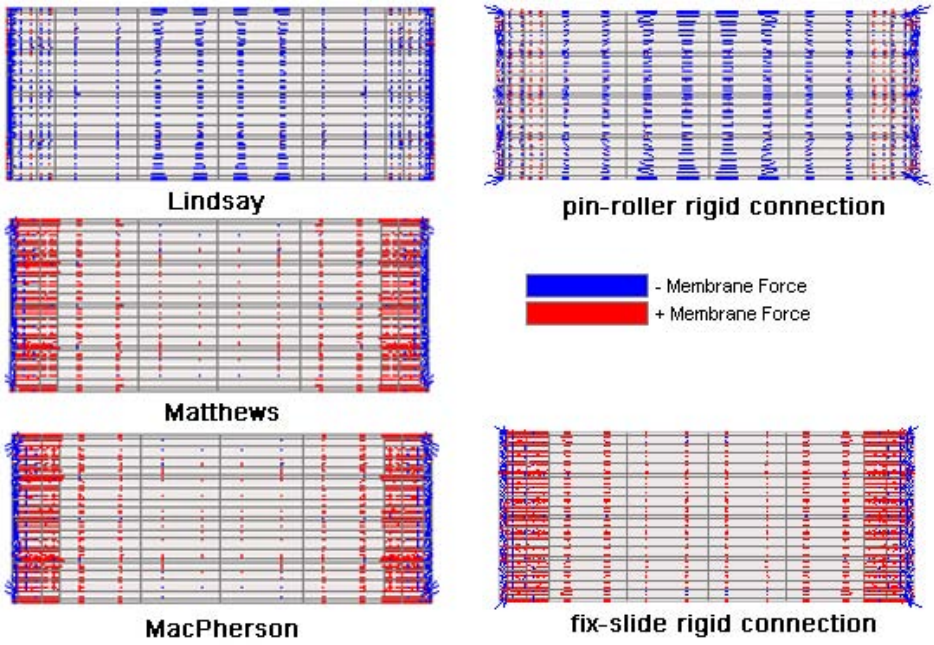

Figure 9-16 Membrane stress distributions in the topping of the fix-slide supported slabs with various end connections after 48 minutes (negative: compression; positive: tension)

Figure 9-16 shows the membrane stress distributions after 48 minutes of ISO fire exposure within the topping of the fix-slide supported slabs with different end connections (Cases B, D and F), and those of the slabs with rigid end connections and with pin-roller and fix-slide supports (Cases H and J) which were discussed in Section 8.5 and shown before in Figures 8-41 and 8-49 respectively. All the graphs are plotted using the same scale. The blue lines represent compressive forces, and the red ones mean tensile forces. The stress distributions here were taken after 48 minutes of ISO fire exposure and not 50 minutes as in Figure 9-12 because the simulation of Case D

lasted only 48 minutes. However, in Cases B, F, and J, the simulation lasted until reaching the designated end time. Figure 9-16 shows the stress distributions in the topping of Cases B, F, and J are very similar. Further investigation shows that they are similar throughout the simulation.

In terms of the slab with Lindsay's end connection, the stress distribution in the topping of Case D is very similar to that of the pin-roller supported slab with rigid end connection (Case H), which agrees with the finding from Figure 9-15 which is of the stress history within the strand as well as from Figure 9-14 which is of the midspan vertical displacements.

Even though the behaviour of the fix-slide supported slab with Lindsay's end connection (Case D) was shown before as being very similar to that of pin-roller supported slab with rigid end connection (Case H), in terms of the finish time of the simulation, Case H could last until reaching the designated end time of the simulation, but the simulation of Case D stopped after 48 minutes of ISO fire exposure due to no convergence in the iteration. Nevertheless, the difference is very likely to be caused by the numerical problem in the program and not from the actual failure happening within the slab.

In summary, other than for the finish time of the simulation, the findings from the simulation of the fix-slide supported slabs with Matthews' or MacPherson's end connections are very similar to those of a fix-slide supported slab with rigid end connection, and the findings from the simulation of the fix-slide supported slab with Lindsay's end connection are very similar to those of a pin-roller supported slab with rigid end connection.

9.4.7. Overall discussion

The simulations of the slabs with these three studied end connections all stopped for reasons other than failing of the hollowcore units. The behaviour of the slabs with these three studied end connections were close to that of the slabs with rigid end connection shown in Section 8.5 (Cases G, H, I and J), as the strand stress lied within the envelope formed by those of Cases G, H, I and J. However, the durations of simulation of Cases G, H, I and J were longer than that of the slabs with any of the three end connections. This shows that the end time of the simulation of the slab with end connections did not reflect the failure time of the slab.

From the figures shown in this section it is determined that the slabs with Matthews' and MacPherson's end connections would have a fire resistance lying between the envelope formed by the fix-fix and fix-slide supported slabs with rigid end connection (Cases I and J), and slabs with Lindsay's end connection would have at least the same fire resistance as the slab modelled with rigid end connection without rotational restraints at the supports, i.e. Cases G and H. The concluded fire resistances of the slabs with different end connections and support conditions are shown in Table 9-5.

Table 9-5 Summary of the predicted fire resistance of the slab with various end connections

Connection	Support condition	Predicted fire resistance	Reasons
Matthews/ MacPherson	fix-fix	69 minutes	Crushing of topping concrete near the corners
	fix-slide	>240 minutes*	Designated end time of the simulation
Linsday	fix-fix	>240 minutes*	Designated end time of the simulation
	fix-slide	59 minutes	**Failure:** runaway failure

The results here also indicate that to reduce the complexity of simulation, the study on the fire behaviour of slabs with Matthews' or MacPhersons's end connection can even be replaced by looking at the envelope of behaviour of slabs with rigid end connection with fix-fix and fix-slide supports at the corners. The study on the fire behaviour of slabs with Lindsay's end connection can even be replaced by looking at the envelope of behaviour of slabs with rigid end connection with pin-pin and pin-roller supports at the corners

9.5. Attempt to Simulate the Closing of Gap in Lindsay's Connection in SAFIR

In Section 9.2, Lindsay's end connection was modelled without considering the closing of gap between the bottom of the hollowcore units and the face of the end beam as illustrated in Figure 9-17 (a). The maximum and minimum observed relative movement between the end face of the hollowcore unit and the end beams in Case C is shown in Figure 9-18, which clearly indicates that the relative displacement is greater than the gap size and gap closing would have occurred if it was considered in the simulation. A more complicated method to model Lindsay's connection as shown

in Figure 9-17 (b) has been attempted and the results are presented here.

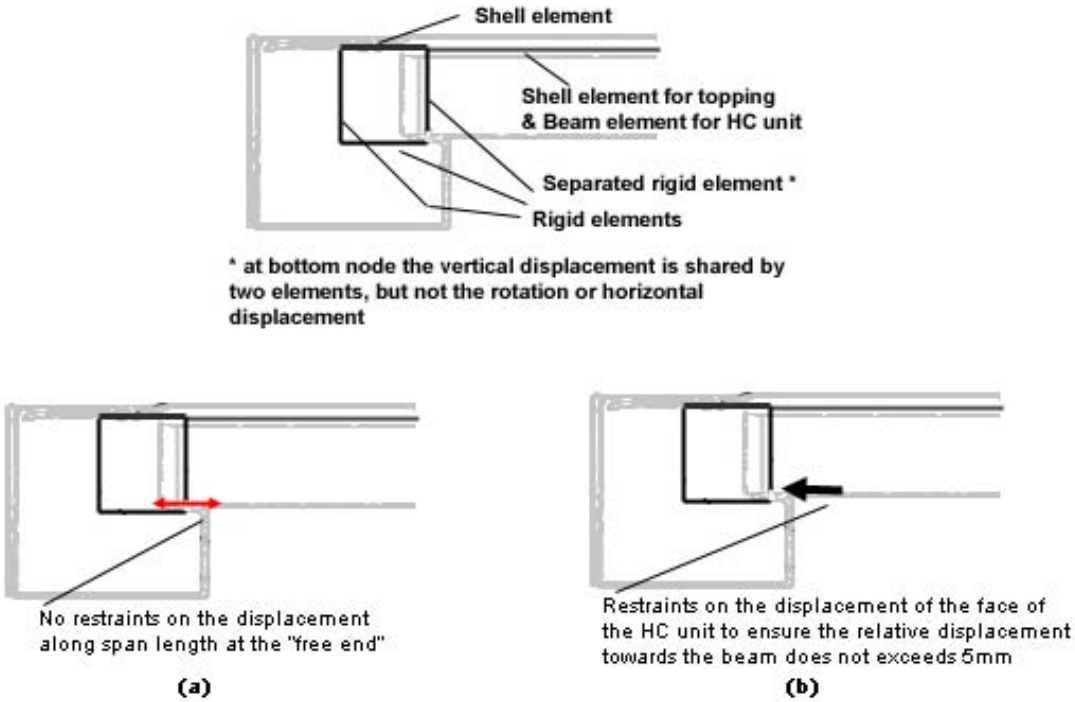

Figure 9-17 Method to simulate Lindsay's connection (a) original method (b) including restraints at the base of the face of the HC units

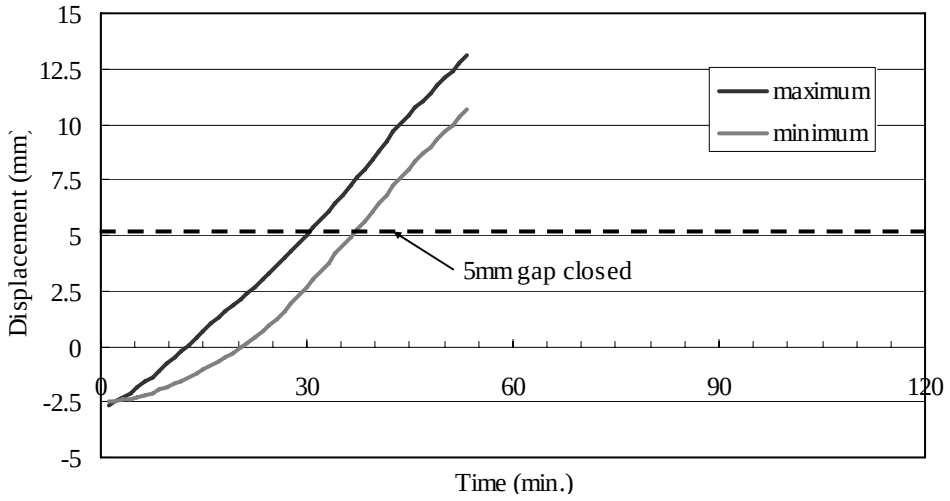

Figure 9-18 Relative movement at the bottom of the hollowcore unit and the end beam in Case C

The problem of gap closing could be resolved easily in programs that have a fictional material to allow for a limited amount of free movement, i.e. the strength and stiffness being close to zero, before the gap closed, and then a restricted movement once the gap is closed, which means the strength and stiffness suddenly become very large after the predetermined amount of strain is reached. However, SAFIR does not have such a material.

In the other hand, SAFIR allows restraints on the movement of the bottom of the end of hollowcore units to be included as shown in Figure 9-17 (b); therefore it is possible to limit the relative displacement at the end face of the hollowcore units towards the face of the end beams to only 5mm, which is the size of the gap in Lindsay's seated detail.

The following is a step by step illustration of introducing restraints on the movement of the end of hollowcore units in SAFIR. First of all, the movements at the bottom of the face of the hollowcore units without restraints are needed, and in order to obtain them the simulation was run once without restraints on the movement of the bottom of the face of the hollowcore units as in the original model shown in Figure 9-17 (a). These movements were then compared with the displacements along the span length at the end beam at the corresponding locations, and the movements were adjusted manually to ensure that the relative movement was capped at 5mm. The adjusted movements were then used as input to the new simulation model and applied as restraints to the movement at the bottom of the face of the hollowcore units as shown in Figure 9-17 (b).

There are some flaws that arise with this modelling method. The extra restraints applied onto the nodes at the bottom of the face of the hollowcore unit were considered by the program as moving external supports. These external supports are not able to transfer stresses to the other structural members, but instead they generate counter-acting reaction forces. In consequence, the end beams did not experience the lateral force which should be transferred from the slab throughout the simulation and at the instant the gap was closed no reaction at the end beams to the sudden increase in the lateral force was induced. This problem is shown in Figure 9-19, which is the bending moment along the span length shown together with the displacement at the bottom of the hollowcore units in Case C modelled with the gap closing model shown in Figure 9-17(b), both are at the centre of the end beam. It is apparent that the growth of bending moment in the new model which includes the gap closing feature is not affected by the closing of the gap. Besides, theoretically the bending moment in the new model and the original model should be the same before the gap is closed, but that is not true in the figure. This is because the applied restraints acted as external supports and did not transfer the force from the slab to the end beams.

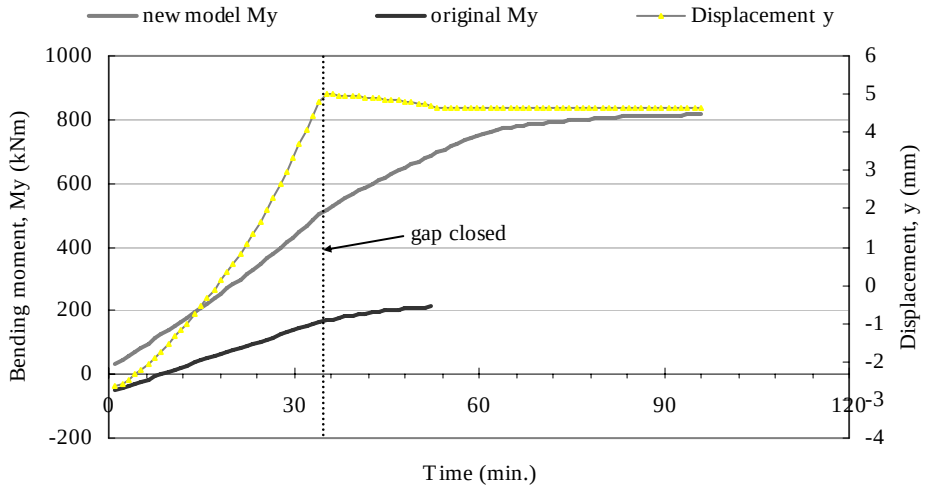

Figure 9-19 Bending moments along the span length at the centre of the end beam from the case with and without restraints on the movement at the bottom of the face of the hollowcore units

Since this modelling method would fail to capture the additional influence from the end beams after the gap closed, the results using this modelling method were deemed to be not acceptable. In the ideal situation, to model gap closing a new artificial material is required, which has a very small or no strength until reaching a certain strain and then a very high strength afterwards. This material would be used to link the end face of the hollowcore unit to the end beam. However, until now SAFIR does not allow users to define such a material. The result in this section shows that to capture the behaviour of closing gap, it is strongly suggested to have a special material as described earlier to handle this kind of problem.

9.6. Subassemblies with Different End connections

In the following set of simulations the columns were included in the model. There were four columns in the subassemblies, one at each corner of the slab. Each column was 750mm by 750mm and 3.5m high with the slab connected to its mid-height. The concrete used in columns had compressive strength of 30.2MPa and tensile strength of 2.0MPa, and the strength of reinforcing steel within the columns was 450MPa. The cross section of the column is shown in Figure 9-20. For the same reason as in the end beams, because the program cannot take account of shear failures, the shear reinforcements in the transverse direction were not included in the model for columns.

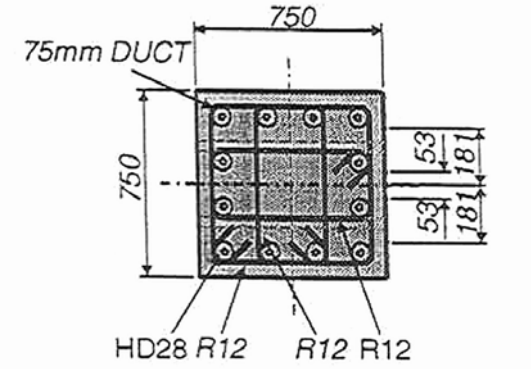

Figure 9-20 Cross section of the column [Matthews 2004]

The layout of the subassembly is shown in Figure 9-21. The side beams were not included in this set of simulations. The four end conditions studied in the previous section were used in this set of simulations, namely Matthews', Lindsay's and MacPherson's end connections as well as the rigid end connection. In the model the top and bottom of the columns have restraints on all the displacements but not on rotations.

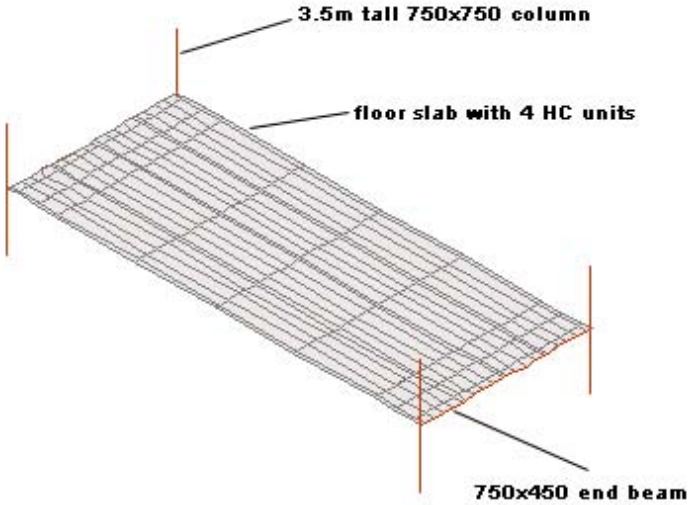

Figure 9-21 Sample subassembly model

Table 9-6 shows the simulation results of each subassembly as well as the reasons why the simulation stopped. The name of each case is shown in the table also. Compared with Tables 9-1, 9-2, 9-3 and 9-4, the results here are as expected. It is expected that the columns would provide a limited amount of restraint on both the rotations and displacements at the corners of the slab, and the behaviour and the end time of the simulation of the slab would be in between the ones from the cases shown before with ideal support conditions, i.e. Cases G, H, I, J shown in the previous

section. The subassembly with Matthews' end connection, i.e. Case K, lasted 131 minutes in fire before the simulation was terminated due to crushing of topping concrete, this time is in between those of the fix-fix and the fix-slide supported slab with the same end connection (Cases A and B), which are 69 minutes and >240 minutes respectively. Similar observation can be made in the cases with Linday's and MacPherson's end connection.

Table 9-6 Summary of the simulation results of the subassemblies with various end connections

Name	Support condition	simulation stop time	Reason
Case K	**Matthews**	131 minutes	Terminated by SAFIR: Crushing of topping near the ends
Case L	**Lindsay**	52 minutes	Terminated by SAFIR: No convergence
Case M	**MacPherson**	136 minutes	Terminated by SAFIR: Crushing of topping near the ends
Case N	**Rigid end connection**	74 minutes	Terminated by SAFIR: Crushing of topping near the supports

Figure 9-22 shows the midspan vertical displacements at the centre of the central units as well as at the edge of the slab in the subassemblies. It also shows those of the fix-fix and pin-pin supported slabs with rigid end connection (Cases I and G respectively). The deflection in all cases at the centre of the slab is greater than at the side of the slab due to the deflection of end beams. The results show that the midspan vertical displacements from the subassembly with Lindsay's connection (Case L) are similar to those from Case G, and those from the subassemblies with Matthews' or MacPherson's connections as well as from the subassembly with rigid end connection (Cases K, M and N) are all very close to each other, and they are similar to those from Case I. The results here coincide with the findings from the previous section that Lindsay's connection provides little rotational restraints along the width of the slab at the ends, therefore the overall behaviour is closer to the slab with no rotational restraints at the corners.

Figure 9-23 shows the midspan stress history of the strand at the central web of the centre unit. This figure confirms the findings before about Lindsay's connection providing less rotational restraints than the other two types of connection. It also shows that the slabs with rigid end connection and ideal supports can provide an envelope of how the subassemblies with different end connections and supporting

conditions would behave. The strand stress history from the subassembly with Lindsay's connection (Case L) was similar to that of the pin-roller supported slab with rigid end connection (Case H) but followed even more closely to the pin-pin supported slab with rigid end connection (Case G). The strand stress histories from the subassemblies with Matthews' and MacPherson's connection (Cases K and M) were almost identical to the one from the fix-slide supported slab with rigid end connection (Case J).

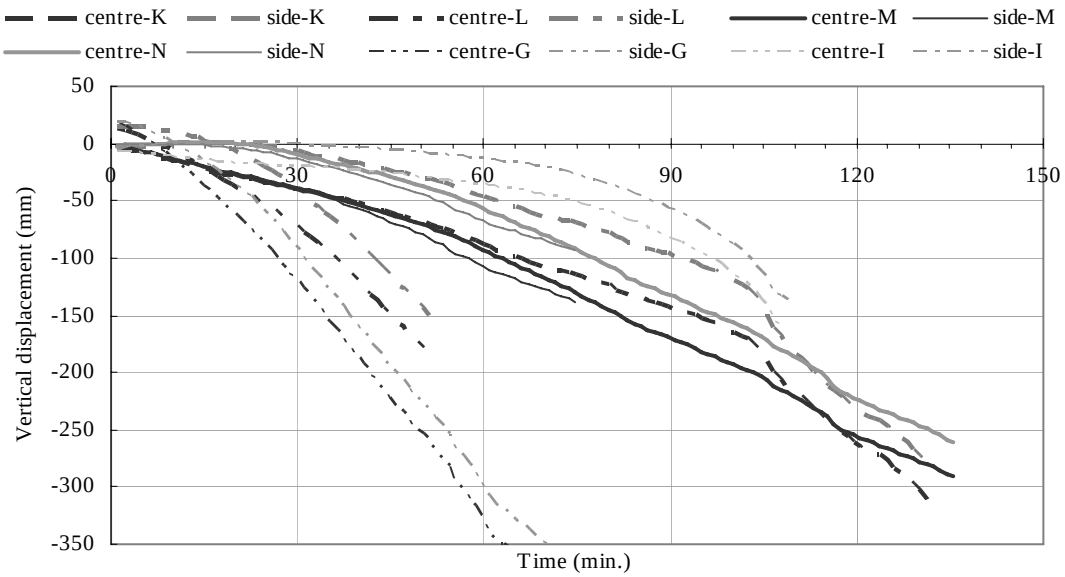

Figure 9-22 Midspan vertical displacements from the subassemblies with various end connections

Figure 9-24 shows the membrane stress distributions after 50 minutes of ISO fire exposure within the topping of the subassemblies with different end connections, and those of the slabs with rigid end connections and with pin-pin and fix-fix supports. All the graphs are to the same scale. The blue lines represent compressive forces, and the red ones mean tensile forces. The results show that Lindsay's connection would provide a stress pattern similar to that from the pin-pin supported slab with rigid end connection; Matthews' and MacPherson's connections would have a stress pattern in between the pin-pin and fix-fix supported slab with rigid end connection. The subassembly with rigid end connection and columns has a very similar stress distribution to that of fix-fix supported slab with rigid end connection at four corners. These findings agree with the findings from the plots of strand stress histories or midspan vertical displacements.

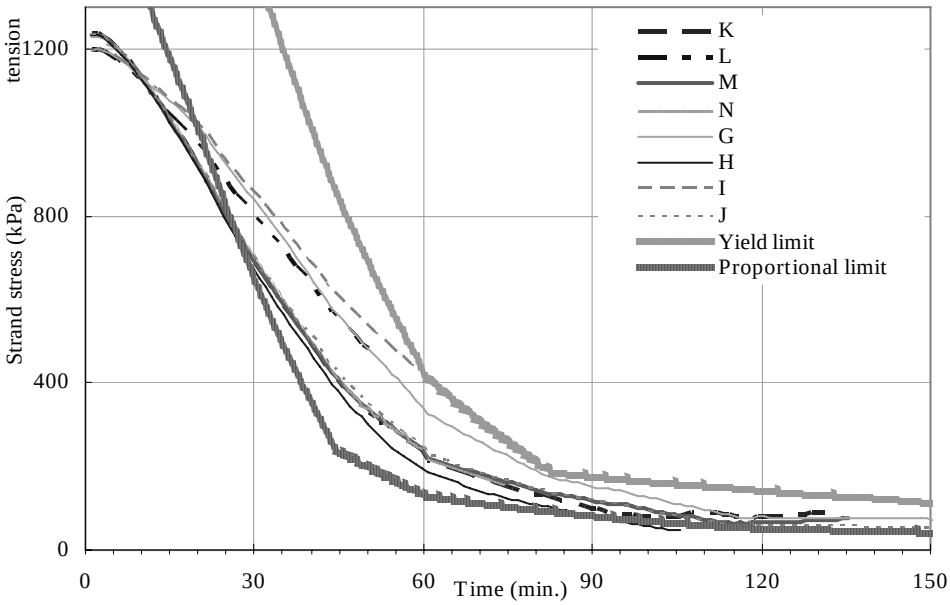

Figure 9-23 Strand stress histories of the subassemblies with various end connections

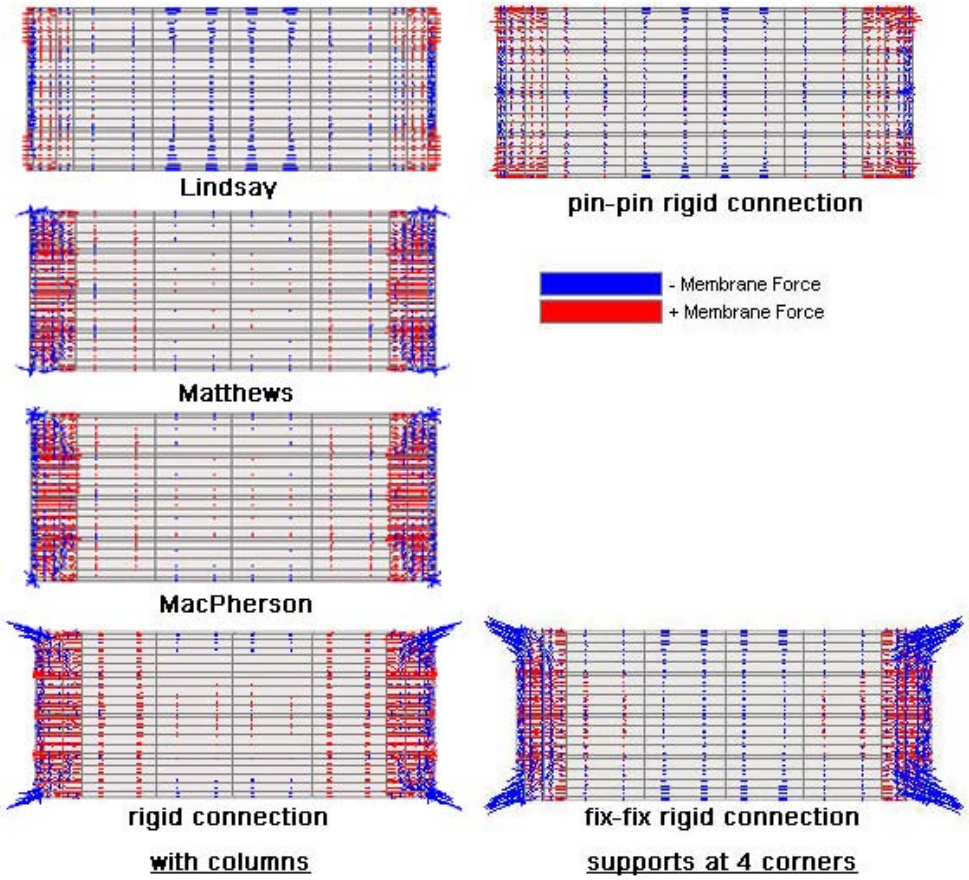

Figure 9-24 Membrane stress distributions in the topping of the subassemblies after 50 minutes of ISO fire exposure (negative: compression; positive: tension)

Figure 9-24 shows that after a period of fire exposure, the subassembly with Lindsay's connection and columns and the pin-pin supported slab with rigid end

connection at four corners had more compression near the midspan than the subassemblies with other connection types. This indicates that in the simulation the slabs with Lindsay's connection cannot have the arch action during the fire to increase the fire resistance. In a real situation, because the gap between the back of the hollowcore slab and the end beams could be closed when the deformation at the end of the slab becomes large enough, the arch action could be achieved later than in the slabs with Matthews' or MacPherson's connections rather than as in the simulation described here.

Similar to Section 9.3, judging from the results of the subassemblies with different end connection, namely the vertical displacements, the strand stress histories and the membrane stress distribution in the topping, the fire resistance of the subassembly should lie between the envelope formed by the slabs with rigid end connections and ideal support conditions, i.e. Cases G, H, I and J. The fact that the simulation of the subassembly with Lindsay's connection stopped due to failure to converge in the program also suggests that the actual fire resistance of such subassembly could be greater than what the program indicated. After considering all of these observations, the determined fire resistance of the subassemblies after the further analyses are shown in Table 9-7.

Table 9-7 Summary of the predicted fire resistance of the subassemblies with various end connections

Support condition	Predicted failure time	Reason
Matthews	131 minutes	Terminated by SAFIR: Crushing of topping near the ends
Lindsay	59 minutes	Failure: Runaway failure
MacPherson	136 minutes	Terminated by SAFIR: Crushing of topping near the ends

9.7. Summaries

The subassemblies with Matthews', Lindsay's and MacPherson's end connections were modelled using SAFIR. SAFIR could not model the closing of gap in Lindsay's connection as described in the end of Section 9.4, therefore in the simulation it was assumed that the gap would never close.

In the first part of this chapter the ideal supporting conditions were looked at and the behaviour of the slab was compared to that of the slabs with rigid end connections at the end of the slab and ideal supporting conditions at four corners as studied

previously in Section 8.4. This would provide information on the behaviour of the slab when the columns or the surrounding floor slabs are either very slender or very stiff. Table 9-8 shows the interpreted behaviour of the slab with different end connections with different column stiffness from the simulation results.

Table 9-8 Interpretation of the results from the predicted fire resistance of the slab with various end connections

Connection	Surrounding structure	Predicted fire resistance	Reason
Matthews/ MacPherson	Very stiff	69 minutes	Crushing of topping concrete near the corners
	Very slender	>240 minutes*	Designated end time of the simulation
Linsday	Very stiff	>240 minutes*	Designated end time of the simulation
	Very slender	59 minutes	**Failure:** run-away failure

The second part of the simulation attached the columns to the end of the end beams. The results were shown in Table 9-7 agreed with the finding from Table 9-8 and lied within these extreme values.

The overall results show that because Matthews' and MacPherson's end connections link the end of the slab rigidly to the end beams, they let the hollowcore floor system to have a better fire resistance comparing to Lindsay's end connection.

The results in this study also show that the Lindsay's end connection is not good for the overall structural performance of the flooring system in fire and any kind of gap between the end of the hollowcore units and the end beams decreases the fire resistance. The study cannot consider the effect of closing the gap between the hollowcore units and the end beams, therefore for a more definite conclusion to be drawn about Lindsay's end connection, a more sophisticated model which could capture the increase in strength after gap closing is needed.

In terms of model construction, to simplify the complexity in modelling the connections, the structures with all three end connections and columns can be approximated by a rigidly connected slab and beam system with ideal support conditions at four corners. The structural behaviour of the subassembly with Lindsay's end connection will lie in between those of the slab and beam systems with pin-roller and pin-pin supports at four corners. The structural behaviour of the

subassembly with Matthews' or MacPherson's end connection will lie in between those of the slab and beam systems with fix-fix and fix-slide supports at four corners. Knowing the envelope of structural behaviour can provide convenience and simplicity in the design process.

10. Effect of Membrane Action on the Fire Performance of Hollowcore Concrete Flooring Systems with Side Beams

10.1. Introduction

Membrane action in two-way supported reinforced concrete floor slabs can improve fire resistance of the floor [Lim 2004], and it varies with the width to length aspect ratio. In slabs where the width to length ratio is very big, the slab would behave closer to a one-way supported slab and lose the benefits from membrane action. In floors consisting of hollowcore units, the prestressing strands and the orientation of the webs which lies along the direction of the span, so the overall behaviour of the slab is expected to be dominated by the one-way behaviour along the direction of the span. Therefore, whether membrane action could be established and be significant enough to improve the fire resistance in hollowcore concrete flooring systems needs to be explored.

The first part of this chapter studies the effect of the side connections which are parallel to the hollowcore units. In New Zealand before the introduction of Amendment 3 of NZS3101:1995 [SNZ 2004], most hollowcore units were located right beside the parallel side beams, as shown in Figure 9-2(b), connected by the topping concrete. However, this was found to cause incompatibility between the floor slab and the side beams during earthquakes [Matthews 2004]. Amendment 3 of NZS3101:1995 requires that hollowcore units must be located a certain distance away from a parallel beam to avoid the deformation incompatibility as shown in Figures 9-4(b) and 9-5(b), with the default minimum distance being 600mm. This study will investigate whether this new requirement for more flexible side support will influence the performance of the subassembly in fire.

The second part of this chapter studies the effect of floor aspect ratio to see if membrane action can be established and be beneficial to the fire resistance of the flooring system. This section studies the behaviour of the 5.1m and 10.2m hollowcore concrete flooring system with lengths of 6.2m, 9.2m, 12.2m, 15.2m and 18.2m, and compare these results with the results on one-way supported hollowcore floor slabs shown in Chapter 8 to see the whether the membrane action has been established, and whether the fire resistance is consequently increased by the membrane action.

10.2. Floor and Beam Geometry

The floor and beam geometry follows that used in the previous chapters. The floor slabs consist of several 300 DYCORE units covered by 75mm of reinforced concrete topping. The end connections from Matthews [2004], Lindsay [2004] and MacPherson [2005] as well as the rigid connection which were used in Chapter 9 are used here again. The subassemblies simulated here are supported on square columns with cross section of 750 by 750mm; each was 3.5m high and has pin supports at the end. The columns are not exposed to fire.

All end and side beams in the subassemblies were 450 wide by 750mm deep and connected rigidly to the mid-height of the columns. The side beams in this set of simulations are assumed to be the same as the end beams and are as shown in Figure 8-38. The dimensions and mechanical properties of such beams were described in Section 8.5. The side beams used in the simulation were different from those used in seismic testing by Matthews, Lindsay or MacPherson as the purpose here is to investigate the potential benefit from a two-way supported floor slab and not to check the fire resistance of the tested specimens from the seismic studies.

The side beams are connected to the mid-height of the columns, and during the simulation they are heated on the sides and the bottom, the same as the end beams. The node lines of the side beams are modelled at the same height as the centre of the topping of the floor slab so they can share the same nodes.

The side connections between the hollowcore units and parallel beam are provided only by the concrete topping. The starter bars from the beams in all three cases lapped with the mesh in the topping only. The concrete topping was modelled using a layer of shell elements as described in Chapter 6. To model the 25mm thick non-structural timber infill used as permanent formwork by Lindsay and MacPherson and the 75mm concrete topping on top of it, the temperature curve obtained from the experimental results by Lane [2005] on thermal gradient in timbers was used in the thermal analysis to take account of the insulation provided by the timber. The strength of timber board was ignored in the structural analysis as it is assumed that the strength of the lateral connection was contributed solely by the in-situ concrete slab. Figure 10-1 is a sample simulation model which shows the different shell elements used to represent the different area of reinforced topping concrete.

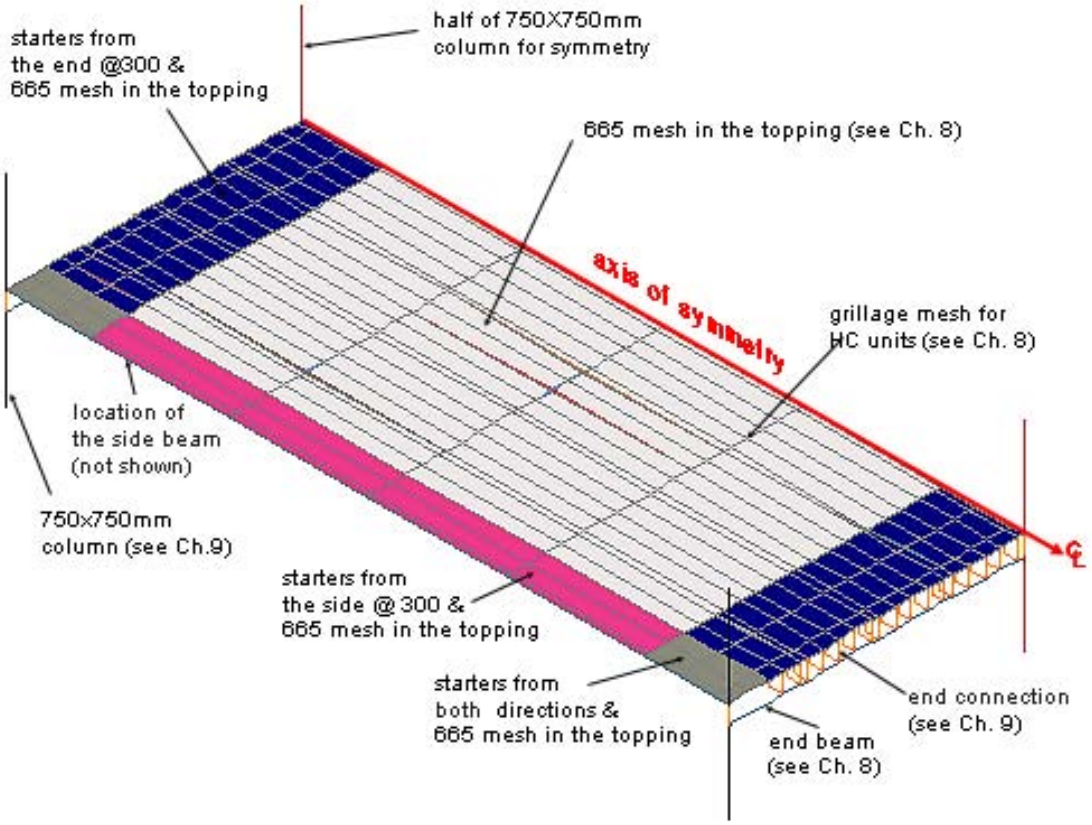

Figure 10-1 Simulation model for a 10 by 12.2m subassembly with infill slab at the side and MacPherson's end connection

10.3. Subassemblies with Side Beams 5.1m Apart and No Infill Slab

Before studying the effect of side connections, firstly the influence of the side beams was investigated. The floor slabs studied in this section are 5.1m wide and 12.2m long.

The subassemblies studied before in Section 9.5 do not have side beams. They represent one-way behaviour of a portion of a slab in a long strip as shown in the grey area in Figure 10-2, with columns supporting the ends of the end beams, but no supports at the side of the hollowcore units, as shown in Figure 10-3(a). The simulation results from Section 9.5 are reported again here in Table 10-1.

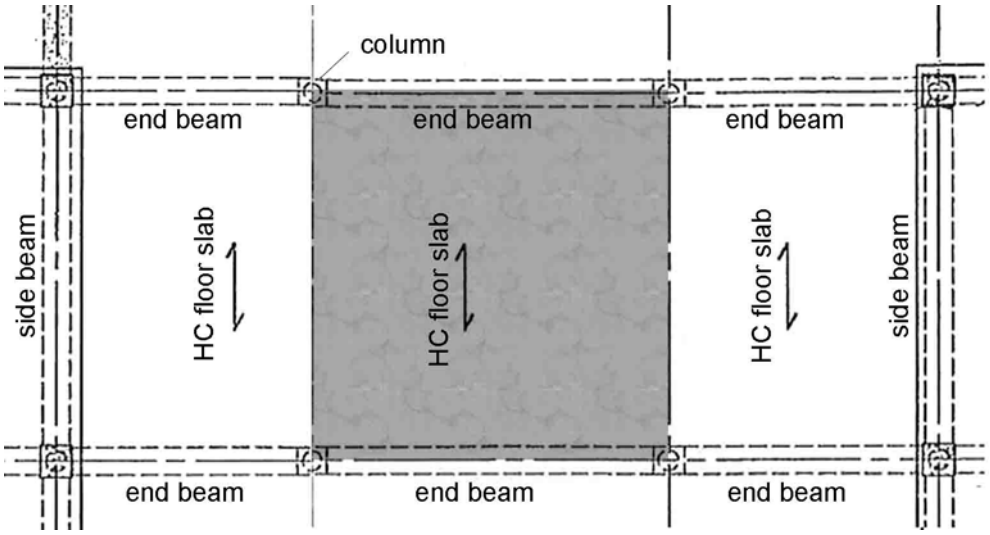

Figure 10-2 Sample floor slab

Table 10-1 Summary of the simulation results of the subassemblies with various end connections and no side beams

End connection	Simulation stop time	Reason
Rigid connection	74 minutes	Terminated by SAFIR: Crushing of topping near the supports
Matthews	131 minutes	Terminated by SAFIR: Crushing of topping near the ends
Lindsay	52 minutes	Terminated by SAFIR: No convergence
MacPherson	136 minutes	Terminated by SAFIR: Crushing of topping near the ends

The difference between the subassemblies introduced in this section and the ones used in Chapter 9 is the presence of the side beams and the reinforcement in the topping at the sides to represent the starters connecting the slab to the side beams as shown in Figure 10-3(b). This results in two-way behaviour. The slab consists of four hollowcore units and has a width of 5.1m to the centrelines of the side beams. The span length of the slab is 12.2m. The starters at the sides are 12mm bars spaced at 300mm, located at the mid-depth of the topping, extending 600mm from the face of the side beam. The starters at the end are also 12mm bars spaced at 300mm located in the mid-depth of the topping but extending 1200mm from the face of the end beam. These starters overlap with each other at the corners as shown in Figure 10-3(b).

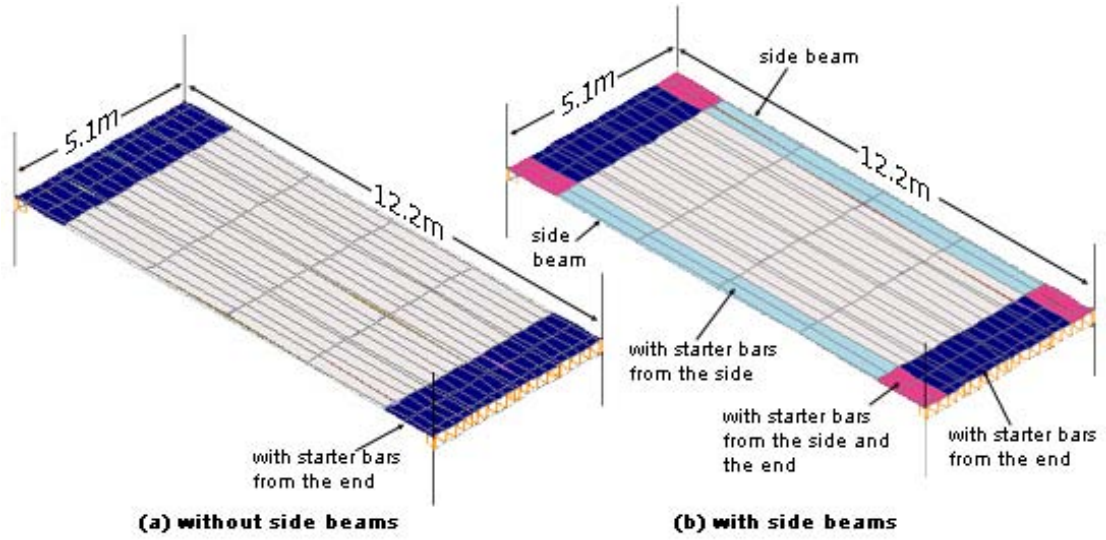

Figure 10-3 Layout of the subassemblies (a) without side beams as analysed in Chapter 9 (b) with side beams as analysed in this chapter

10.3.1. Comparisons among the subassemblies with side beams

The results of the simulation with side beams are shown in Table 10-2 to be compared with no side supports in Table 10-1. Except for MacPherson's end connection, the other three cases demonstrated that side beams give a significant increase in the fire resistance predicted by SAFIR, and all subassemblies sustained more than 2 hours of exposure to the ISO834 standard fire.

Table 10-2 Summary of the simulation results of the subassemblies with various end connections and side beams

End connection	Simulation stop time	Reason
Rigid connection	>240 minutes*	*designated end time of the simulation.
Matthews	>240 minutes*	*designated end time of the simulation
Lindsay	148 minutes	Terminated by SAFIR: stiffness matrix is not positive
MacPherson	128 minutes	Terminated by SAFIR: stiffness matrix is not positive

Figure 10-4 shows the midspan vertical displacement at the centre of the slabs. It can be seen that the displacement is greatest in the case with Lindsay's end connection because of the lack of rotational restraints provided at the ends. The displacements from the cases with Matthews' and MacPherson's end connections are almost

identical because both of these two connections link the slab rigidly to the end beams; however, at 128 minutes the displacement from the case with Matthews' end connection had a sudden increase, while the simulation stopped in the case with MacPherson's end connection. The displacement with rigid end connection initially followed very closely the trend with Matthews' and MacPherson's end connections similar to the subassemblies without side beams as shown in Figure 9-19 of, but after 90 minutes into the fire the displacement of the case with rigid end connection increased more slowly than that of the other cases.

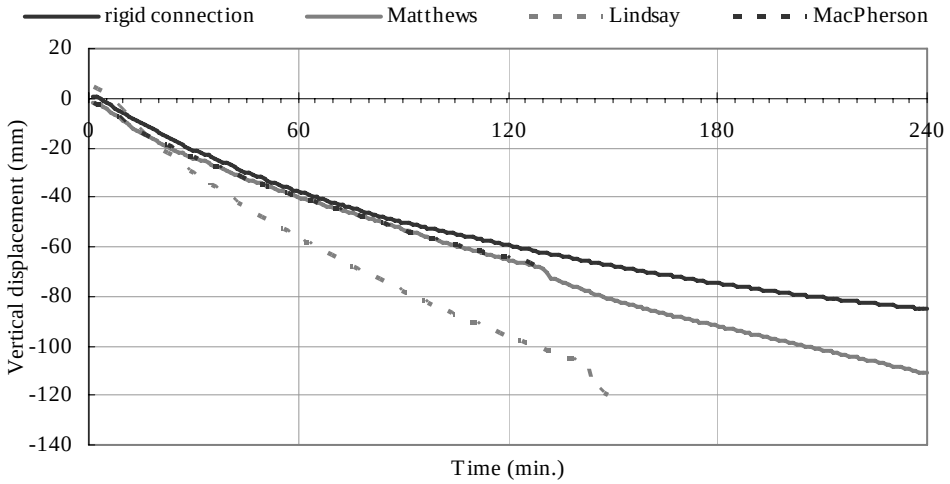

Figure 10-4 Midspan vertical displacement at the centre of the slab with side beams and different end connections

Figure 10-5 shows the axial force diagram of the subassembly with Matthews' end connection and side beams after 2 hours of ISO fire exposure. Within each section of floor slab, the total axial force is the sum of the forces within the concrete section and with the prestressing steel in the hollowcore section. The axial force diagrams of other subassemblies are similar to this one, where the highest compressive axial force within the floor slab is found near the corners, and the lowest compressive axial force or even highest tensile axial force in some cases is found near the centre of the middle units as circled in the figure.

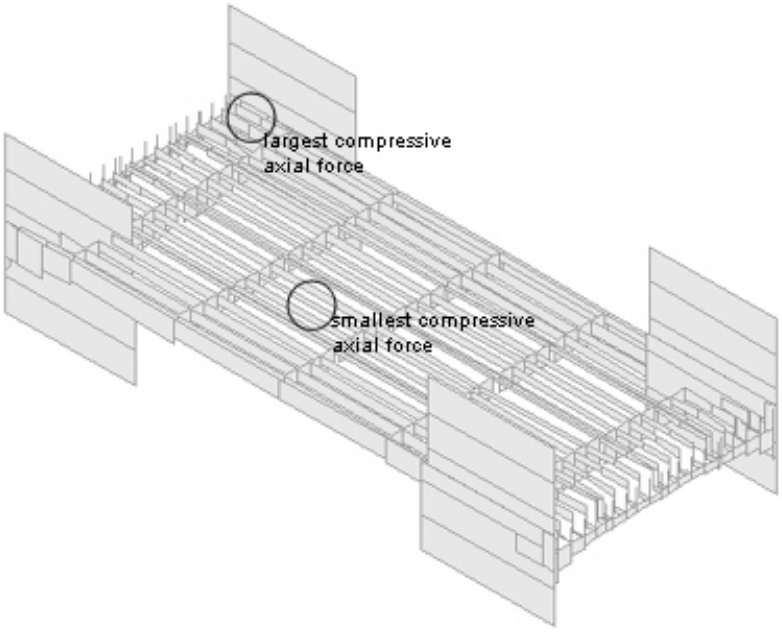

Figure 10-5 Axial force distribution within the subassembly with Matthews' end connection and side beams after 2 hours of ISO fire exposure (all in compression)

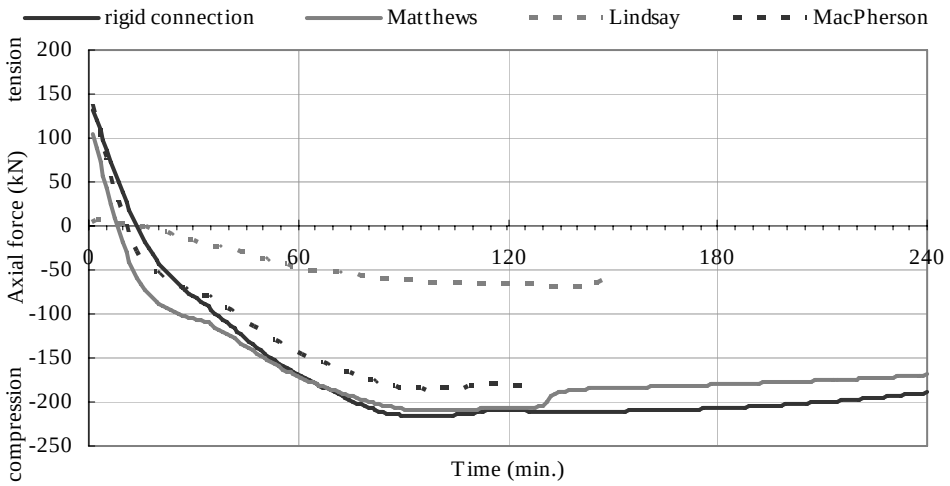

Figure 10-6 Axial force within the web at the corner of the slabs with side beams and different end connections

Figure 10-6 shows the development of axial force within the web near the end supports at the side of the hollowcore unit connected to the side beam, which is at the corner of the slab where the maximum compressive axial force occurred as shown in Figure 10-5. Figure 10-6 shows that the magnitude of the axial compressive force from the subassembly with Lindsay's end connection is smaller than that of the other cases. This is because Lindsay's end connection allows the bottom of the hollowcore units to move freely, therefore arch action cannot be developed in the way as in the assemblies with other types of end connection; consequently a significantly less

compressive force was found in the hollowcore units in the subassembly with Lindsay's end connection.

Figure 10-7 shows the stress history of the prestressing strand at the centre of the centre unit, where the compressive axial force in the cross section is the least, and the tensile axial force in the strand is the greatest, as shown in Figure 10-5. The temperature dependent yield and proportional limits of prestressing steel are also shown in the figure. Unlike in the subassemblies with no side beams shown in Chapters 8 and 9, the strand stresses from the subassemblies with side beams never reach the yield limit, and the simulation does not stop at the proportional limit like those shown in Figure 9-22, because they drop to zero or go into compression before the end of the simulations. The results shown in Figure 10-7 eliminate the possibility that the strands within the slab of any subassemblies studied herein yield in tension during heating.

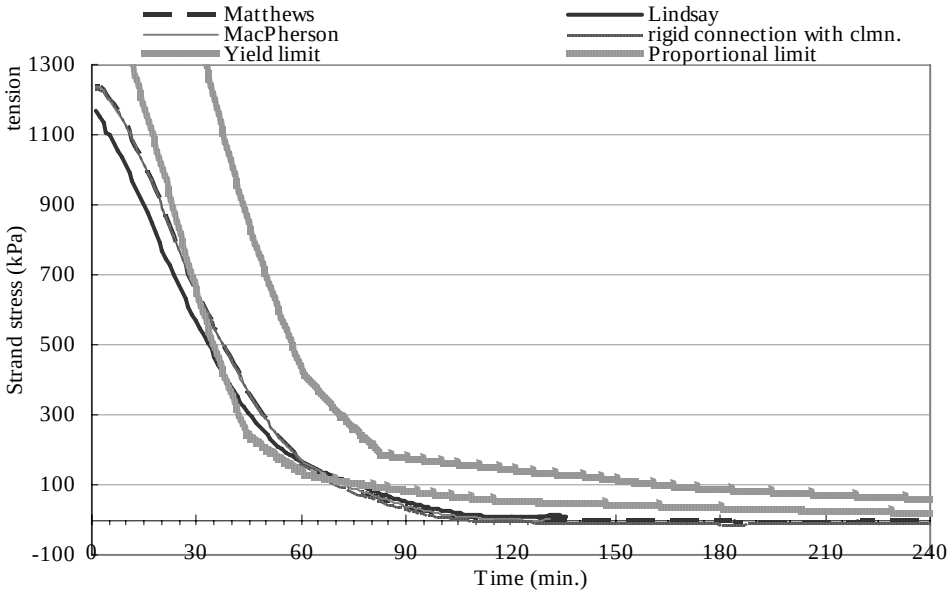

Figure 10-7 Strand stress history at the centre of the web in the centre unit of the slabs with side beams and different end connections

Figure 10-8 shows the membrane force in the topping concrete of the subassemblies with side beams and different end connections at the corner of the slabs, where the compressive membrane force is the greatest. The membrane force from the subassembly with rigid end connections is significantly higher than that of the other cases, and because the subassembly with rigid end connection did not fail during the

simulation, it can be concluded that with Lindsay's or MacPherson's connection the topping has not crushed during the simulation, and their simulations stopped because of the numerical problems in the program.

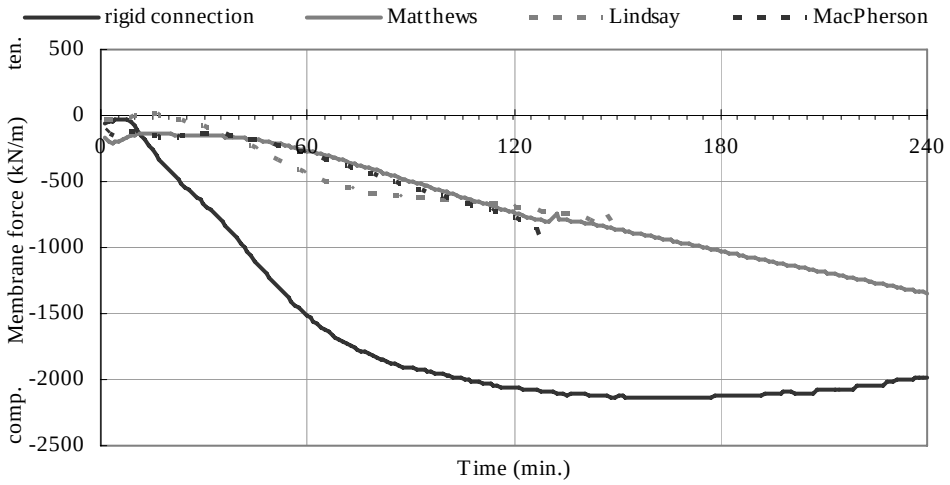

Figure 10-8 Membrane force within the topping at the corner of the slabs with side beams and different end connections

Judging from the Figures 10-4 to 10-8, it is concluded that the simulation of the subassembly with MacPherson's end connection should have lasted as long as that of the subassembly with Matthews' end connection because they showed very similar behaviour under fire. It is not known why the computation stopped due to numerical instability. Both the simulations of the subassemblies with Matthews' or Lindsay's end connection did not fail from crushing in the topping or failing of the hollowcore units, therefore the simulation with MacPherson's end connection was more likely stopped due to a numerical problem than actual failure occurring.

10.3.2. Comparisons between the subassemblies with and without side beams

Figure 10-9 shows the comparison of the maximum midspan vertical displacement in the slab of the subassemblies with and without side beams with different end connections. Even though the behaviour of the hollowcore concrete slab is dominated by the behaviour along the floor span and two-way action can be only established via the topping, the figure shows that with the presence of the side beams the deflections at the centre of the slab and at the edge are drastically reduced, and the fire resistance generally increases; therefore it is concluded that two-way action caused by side beams can increase the fire resistance of the hollowcore flooring system.

Comparing the deflection at the centre and at the side of the slab, Figure 10-9 also shows that the presence of the side beams increases the relative deflection across the slab, and this is most noticeable from the subassemblies with Lindsay's end connection. This confirms that the deflection becomes two-way when the hollowcore flooring system has side supports, and tensile membrane action could be established in such situation.

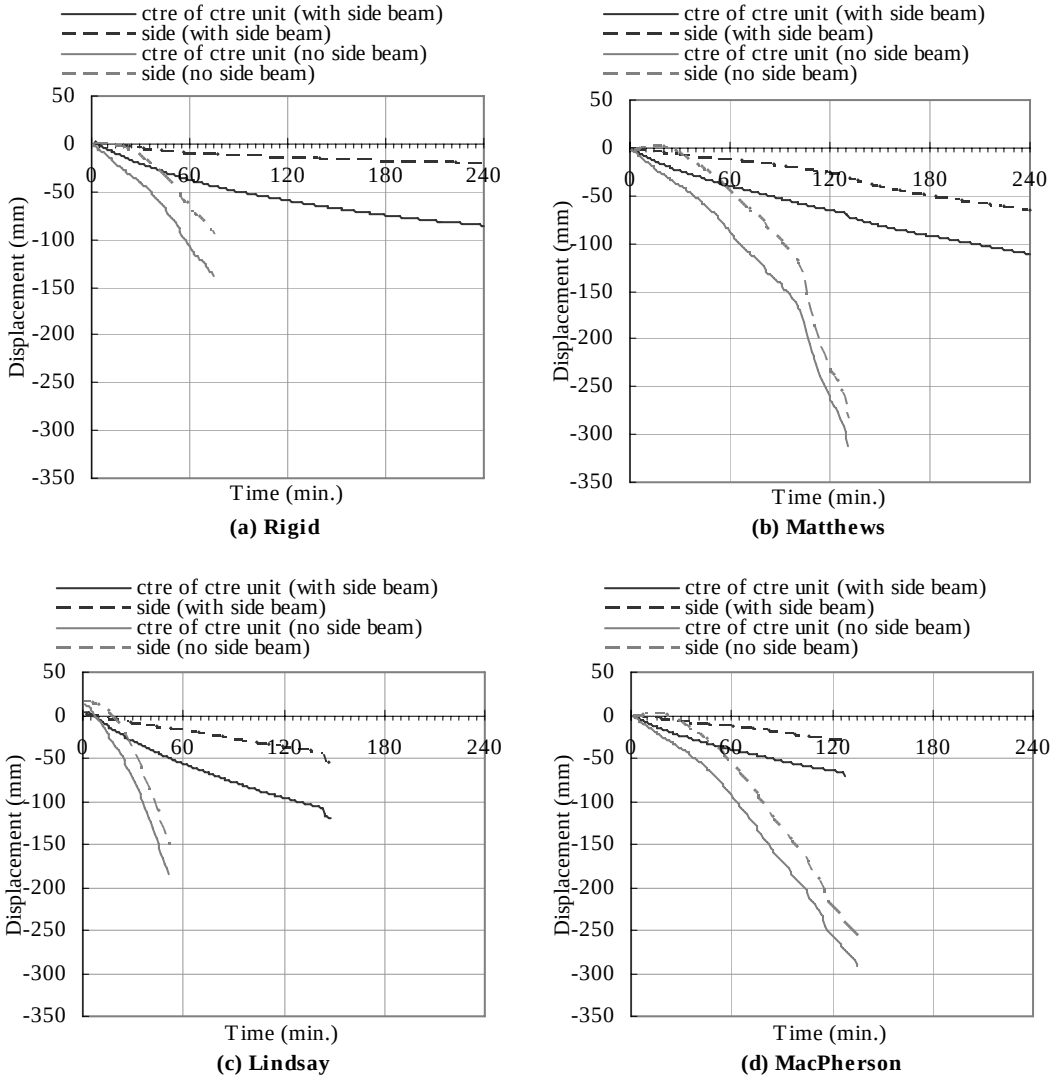

Figure 10-9 Comparison of midspan vertical displacements of the subassemblies with and without side beams and with (a) rigid end connection (b) Matthews' (c) Lindsay's (d) MacPherson's end connection

Figure 10-11 compares the axial forces of a 300mm wide strip within the web at the side of the hollowcore unit closest to the corner of the slab where the compressive axial force is the largest and at the central web at the centre unit where the compressive axial force is the smallest or tensile axial force is the largest within the

slab. The locations of these two points are shown in Figure 10-10. The axial force is the sum of forces in the cross-section of the beam element, where negative means compression.

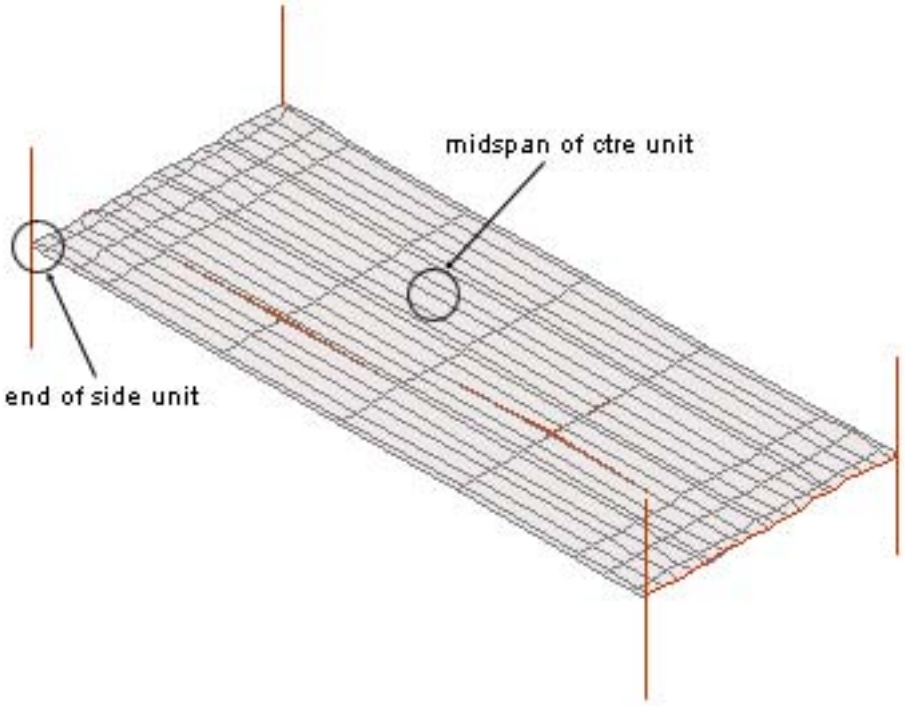

Figure 10-10 Location of the axial forces shown in Figure 10-10

Figure 10-11 shows that regardless of the type of the end connection, before 30 minutes of ISO fire exposure the axial forces found in the case with and without side beams are the same and the influence of the side beams on the axial forces happened only afterwards, and the two-way action starts to become more significant.

After 30 minutes of fire exposure, Figure 10-11 shows that the side beams reduce the compressive axial force within the hollowcore units at the ends, which means the possibility of concrete crushing at those locations was reduced. The axial force at the centre of the centre unit shows that the side beams also reduce the possibility of yielding of prestressing strands in tension, and Figure 10-7 has shown already that the prestressing strands in the subassemblies with side beams did not yield during the simulation.

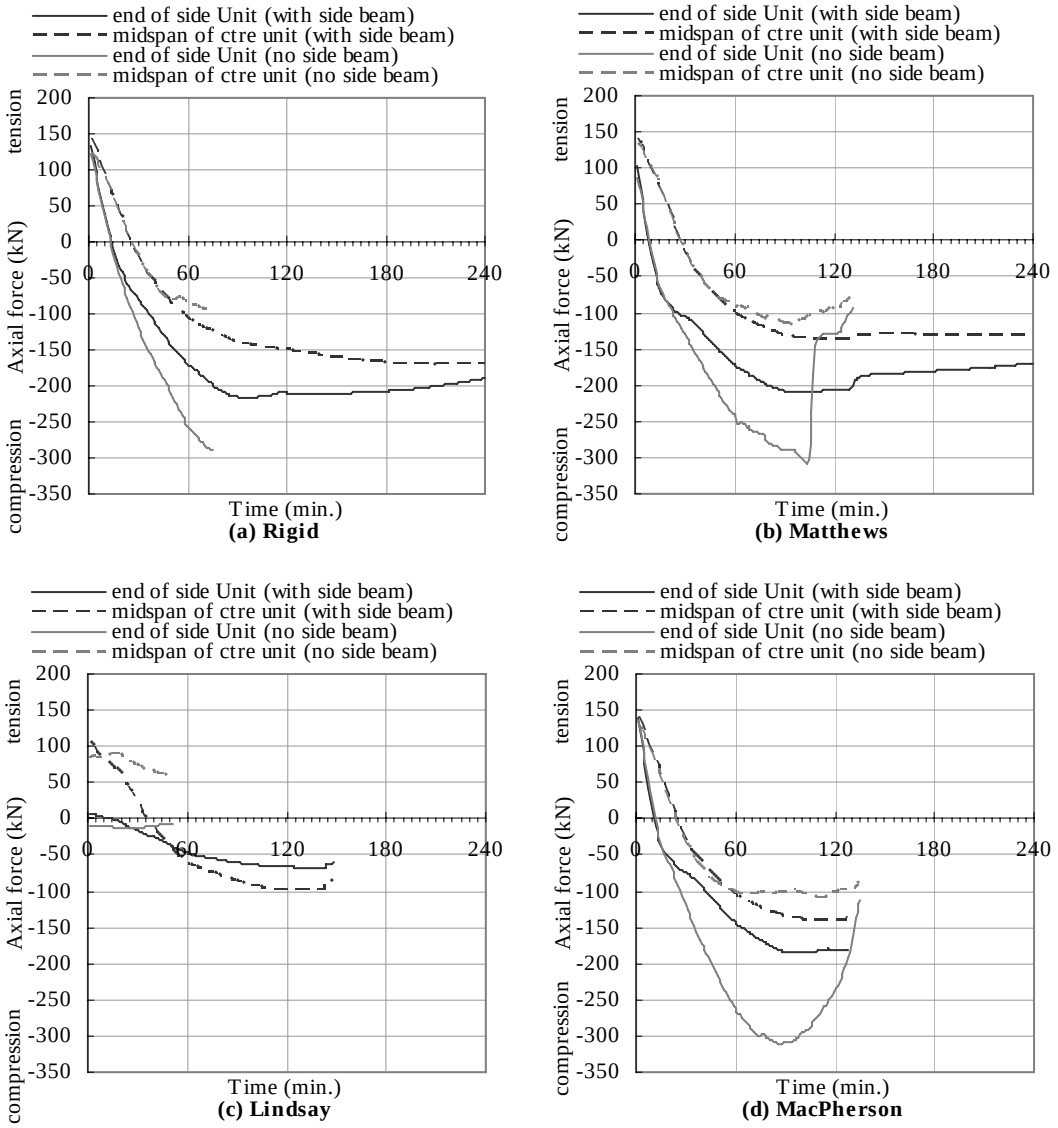

Figure 10-11 Axial force within the web at different location in the subassemblies with and without side beams with (a) rigid (b) Matthews' (c) Lindsay's (d) and MacPherson's end connection

10.3.3. Summary

The side beams provide supports at the side of the slab and establish two-way behaviour of the slab. Through the two-way behaviour and possibly tensile membrane action, the deflection of the slab reduced and the fire resistance is increased to more than twice of that of the subassemblies without side beams. The overall behaviour of the hollowcore concrete flooring system however is still dominated by the actions along the span. The most significant contribution from the side beams, however, is to provide vertical supports which limit the deflection and delay the time the simulations stop.

10.4. Subassemblies with Side Beams 10m Apart and Different Side Connections

To compare the effect of the side connections, two types of side connections are studied, the side connection with hollowcore slabs right next to the side beam will be referred to as "no-infill side connection"; and the connection with a 600mm strip and 75mm thick in-situ slab will be referred to as "infill side connection". The layouts of the two models are shown in Figure 10-12 (a) and (b) respectively. Symmetry was used in the model as in the experiment, therefore the entire floor area these models represent is 10m by 12.2m, with columns spacing 5.1m along the width of the slab.

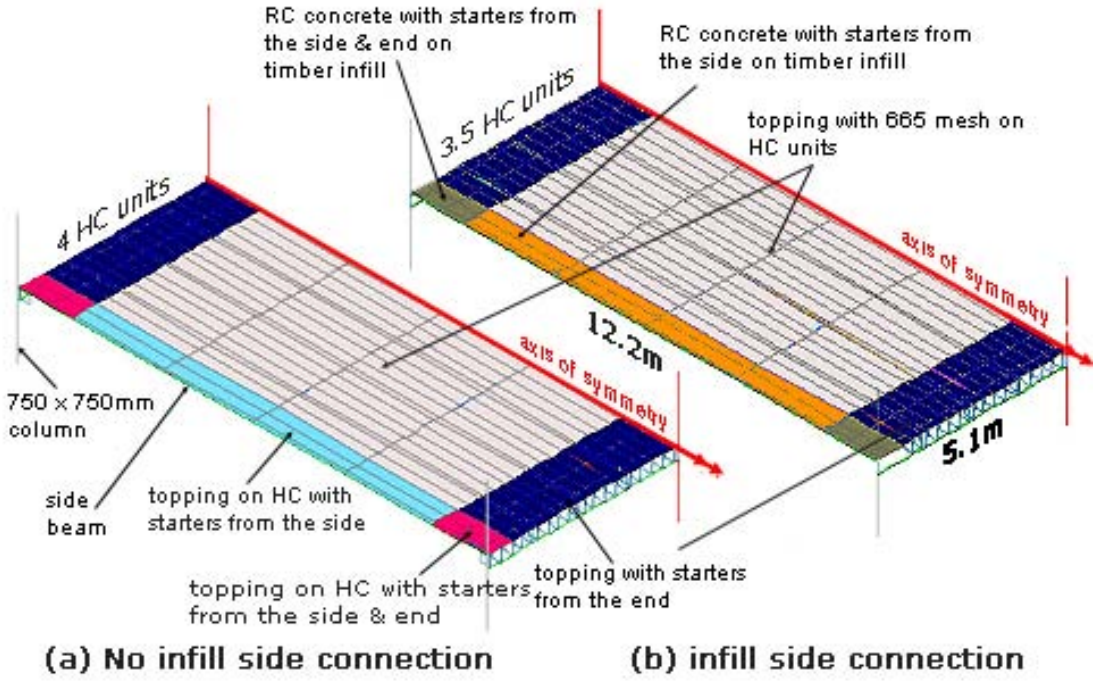

Figure 10-12 Simulation models used to study the effect of lateral connections (a) no-infill side connection (b) infill side connection

10.4.1. Subassemblies with the no-infill side connection and various end connections

Table 10-3 shows the summary of the simulation results of the subassemblies with the no-infill side connection. Notice the width of the slab is 10m in this section and the results are different from those shown in Table 10-2. Other than the subassembly with Lindsay's end connection, the subassemblies all have more than 4 hours of fire resistance. In the case with Lindsay's end connection, the simulation was terminated because of numerical problems in SAFIR and the end time does not reflect the actual

fire resistance of this subassembly.

Table 10-3 Summary of the simulation results of the subassemblies with side beams at 10m spacing various end connections and no-infill side connection

End connection	Simulation stop time	Reason
Rigid connection	>240 minutes*	*designated end time of the simulation.
Matthews	>240 minutes*	*designated end time of the simulation.
Lindsay	71 minutes	Terminated by SAFIR: no convergence after 20 iterations
MacPherson	>240 minutes*	*designated end time of the simulation.

Figure 10-14 shows the maximum midspan vertical displacement in the subassemblies with the no-infill side connection. The location of this displacement is shown in Figure 10-13. The results show the similarity between the cases with rigid end connection and Matthews' and MacPherson's end connections, while the case with Lindsay's end connection had more deflection which was due to the lack of rotational restraints at the ends.

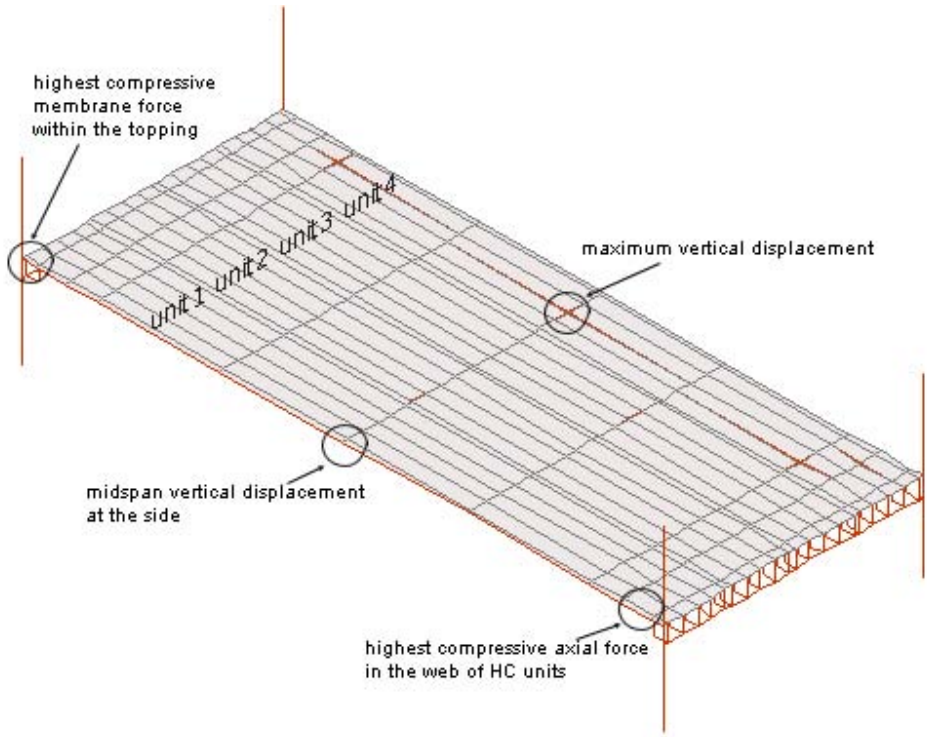

Figure 10-13 Location of the extracted data for Figures 10-14 and 10-15

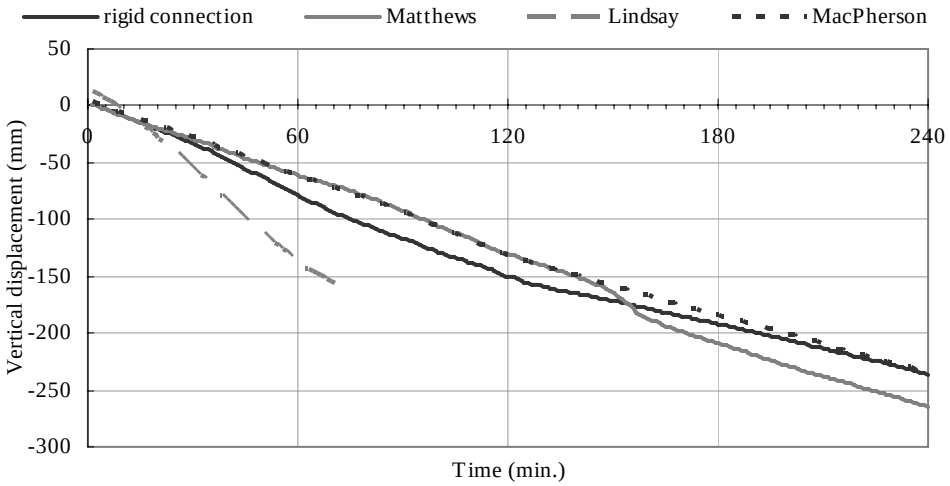

Figure 10-14 Maximum midspan vertical displacement of the 10.1m wide 12.2m long slab in the subassemblies with the no-infill side connection and different end connections

Figure 10-15 shows the axial force within the web at the corner of the slab, where negative means compression. The location of this axial force is shown in Figure 10-13, where the maximum compressive axial force often occurs. This figure shows again the similarity between all the cases except the one with Lindsay's end connection, which had much less compressive axial force during the fire because the free moving of the bottom of the hollowcore units with this type of end connection prevents the establishment of arch action in the floor slab, which is through the compressive axial force at the ends of the slab.

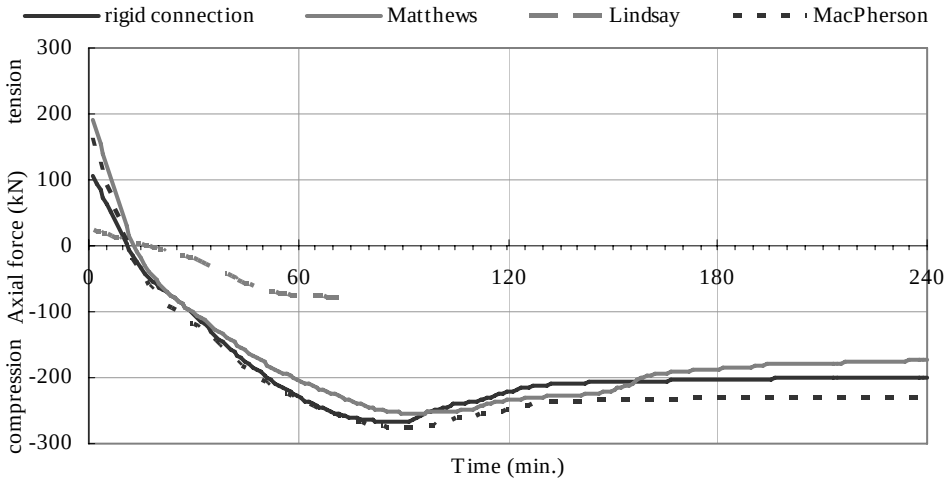

Figure 10-15 Axial force within the web at the corner of the 10.1m wide 12.2m long slab in the subassemblies with the no-infill side connection and different end connections

The results show that except the case with Lindsay's end connection, the 10:12.2m hollowcore concrete slab with the no-infill side connection has a better fire resistance than with other types of side connection. Further investigation by comparing the membrane force shows that the simulation with Lindsay's end connection stopped due to numerical problems and not structural failure. However, even by disregarding the stopping time, Figures 10-14 and 10-15 showed that the subassembly with Lindsay's end connection still behaved worse than the others.

10.4.2. Subassemblies with the infill side connection and various end connections

The schematic drawing of the subassemblies with the infill side connection is shown in Figure 10-12(b). To allow room for the in-situ infill while maintaining the same floor aspect ratio, only 3.5 hollowcore units are used in each model. Table 10-4 shows the summary of the simulation results of the subassemblies with the infill side connection. None of the simulations of these four cases showed a definite failure. Therefore the performance and fire resistance of subassemblies need to be judged from the displacement and stress within the structures.

Table 10-4 Summary of the simulation results of the subassemblies with various end connections and side beams with in-situ infill

End connection	Simulation stop time	Reason
Rigid connection	69 min.	Terminated by SAFIR: crushing of the topping concrete
Matthews	187 min.	Terminated by SAFIR: numerical problem (square root of zero)
Lindsay	60 min.	Terminated by SAFIR: no convergence after 20 iterations
MacPherson	181 min.	Terminated by SAFIR: square root of zero

Figure 10-17 shows the maximum midspan vertical displacement of the slab with the infill side connection, the location of this displacement is shown in Figure 10-16. Similar to the finding before, the deflections of the subassemblies with rigid end connection and Matthews' and MacPherson's end connections are very close to each other, while the deflection of the case with Lindsay's end connection is much bigger than the others.

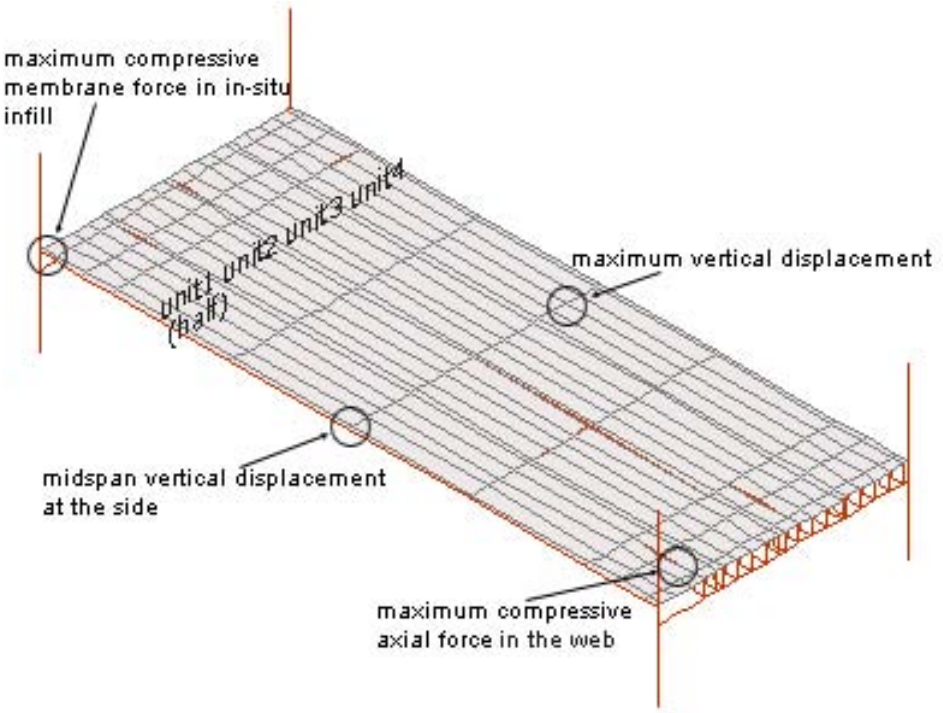

Figure 10-16 Location of the extracted data for Figures 10-17 and 10-18

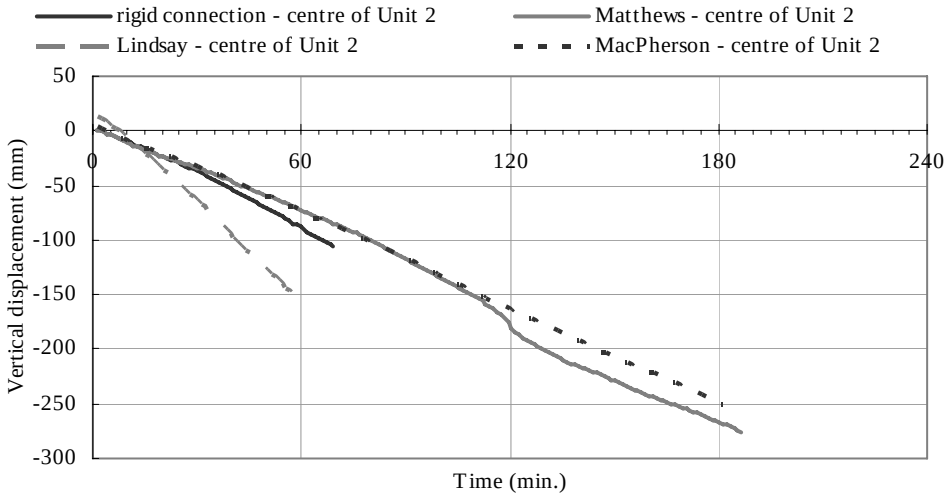

Figure 10-17 Maximum midspan vertical displacement of the slab with the infill side connection and different end connections

Because of the infill, only 3.5 hollowcore units were used in the model, and there was no hollowcore unit underneath the in-situ infill. The change of cross-section of the slab changes the location of the maximum compressive axial force within the web, and this force is now at the end of the web closest to the in-situ infill as shown in Figure 10-16. Figure 10-18 shows the axial forces at this location in the subassemblies with the infill side connection. In this scenario the cross section of the beam element

to represent the hollowcore web at that location is different when there is the core filling in the unit, therefore there is a constant difference between the axial force from the subassemblies with Matthews' end connection and that with MacPherson's end connection. Both cases with rigid end connection and MacPherson's end connection have core filling at the end of the hollowcore units, and they have similar axial force throughout the simulation. The case with Matthews' end connection has no core filling and therefore it has less concrete area to take the compressive force. The case with Lindsay's connection has very small axial force which has been observed before in other analyses.

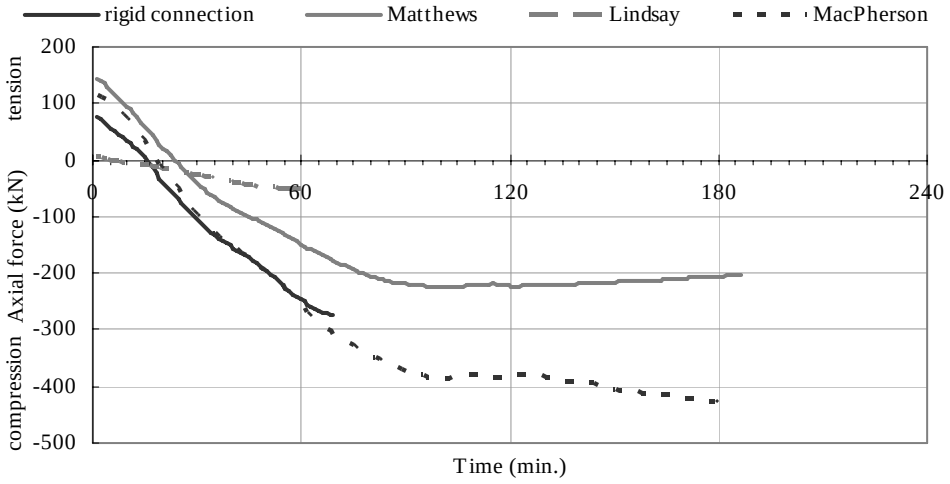

Figure 10-18 Maximum compressive axial force within the web in the subassemblies with the infill side connection and different end connections

10.4.3. Comparison of subassemblies with and without in-situ infill at the side

The simulations with the infill side connection stopped due to numerical instability. By comparing the results among themselves there is no conclusive answer to what the fire resistance of these structures might be. It requires further investigation by comparing the results between the simulations with different side connections.

Figure 10-20 shows the comparison of the midspan vertical displacement of the slab with different end and side supports. The locations of these displacements are shown in Figure 10-19. Figure 10-20 shows that the maximum deflections of the slabs with infill side connection are slightly less than those of the slabs without side beams, i.e. one-way supported only, but greater than those with the no-infill side connection.

By comparing the difference between the maximum midspan displacement and the midspan displacement at the side, Figure 10-20 shows that the relative deflection across the slab is less in the cases with no-infill side connection, i.e. B-A is smaller than D-C. This observation is further shown in Table 10-5 which compares the relative midspan displacement in the subassembly of Matthew's end connection at 120 minutes as from Figure 10-20(b). This is because with the infill side connection most of the forces are taken by the hollowcore units and smaller loads were transferred into the side beams, and it is concluded that the infill side connection reduces the influence from the side supports.

Table 10-5 Comparison of midspan displacement with different side supports of the subassembly with Matthews' end connection after 120 minutes of ISO fire exposure

Side Support Condition	Maximum Midspan Displacement	Midspan Displacement of the side beam	Difference
No side beams	265mm	-	**265mm**
Side beams with infill	176mm	24mm	**152mm**
Side beams with no-infill	130mm	44mm	**86mm**

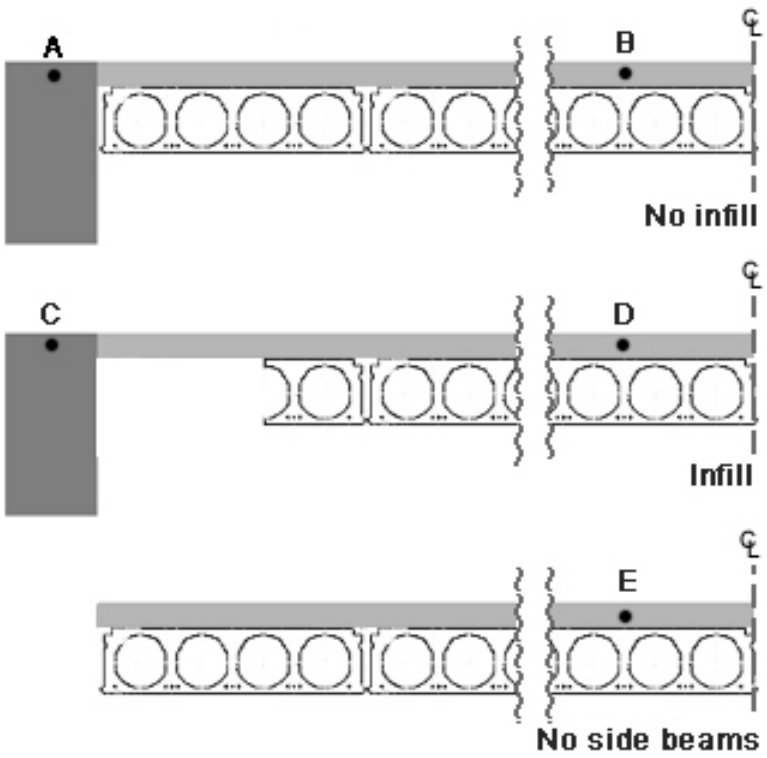

Figure 10-19 Location of the observed displacements

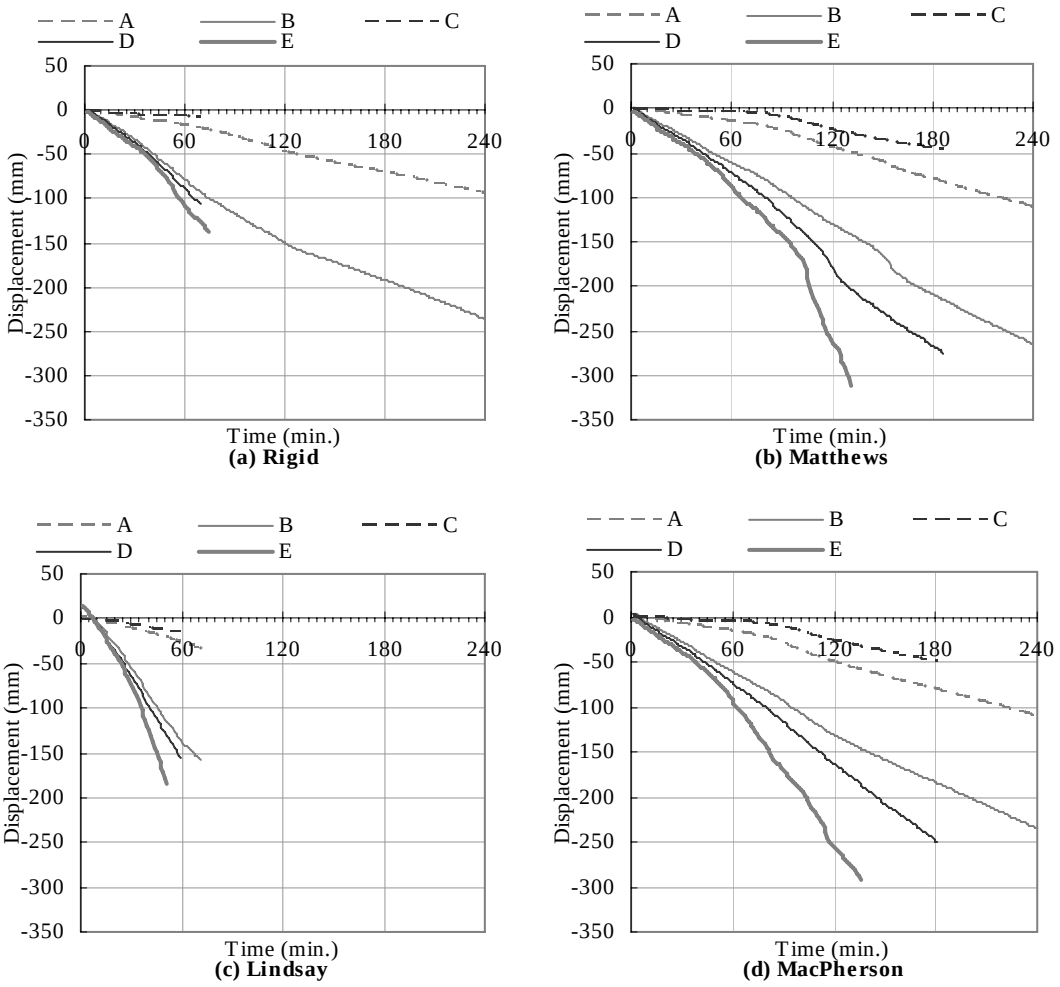

Figure 10-20 Comparison of midspan vertical displacements of the subassemblies with and without in-situ infill at the side and with (a) rigid end connection (b) Matthews' (c) Lindsay's (d) MacPherson's end connection

10.4.4. Summary

The results in this section show that with the behaviour of the slab with the infill side connection is in between that of the one-way supported slab and of the slab with the no-infill side connection. It is also found that with the no-infill side connection more forces are transferred to the side beams and more deflections can be found in the side beams. In Section 10.3 it has been shown that with the no-infill side connection the two-way action has been established in the floor, therefore this section shows that the infill side connection reduces that two-way action.

10.5. Effect of Aspect Ratio of the Floor

This section looks at the potential benefit from the supports parallel to the hollowcore units and the possibility of establishing the two-way membrane action in the hollowcore concrete flooring system. Judging from the previous results, the model for the subassemblies with Matthews' end connection is less likely to have numerical instability during the simulation than the subassemblies with other types of end connection. Therefore only such end connection is used in this section.

Figure 10-21 shows the simulated model, where W means width, and L means length of the slab, and both W and L are the variables in this section. Symmetry was used in the model to double the width of the slab. The columns are pinned at both ends and have the end beam connected to their mid-height. In all the models, the loading is 8.0kPa to be consistent to those in the previous sections. Some of the studied aspect ratios are shown in Figure 10-22.

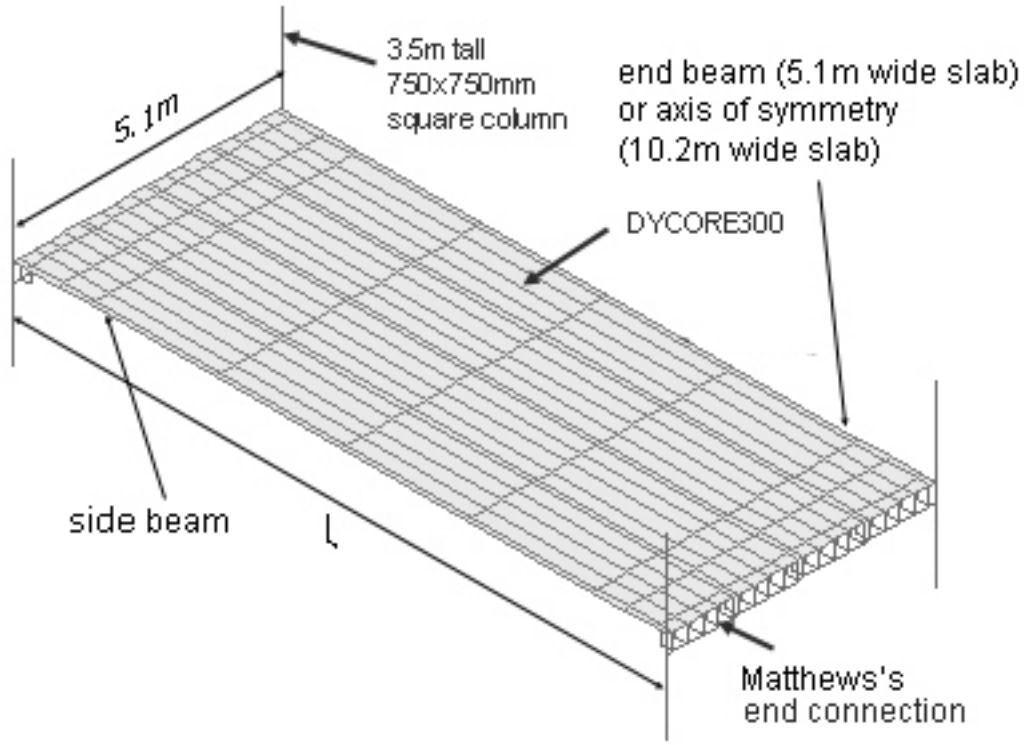

Figure 10-21 Simulated model for investigating the effect of floor aspect ratio

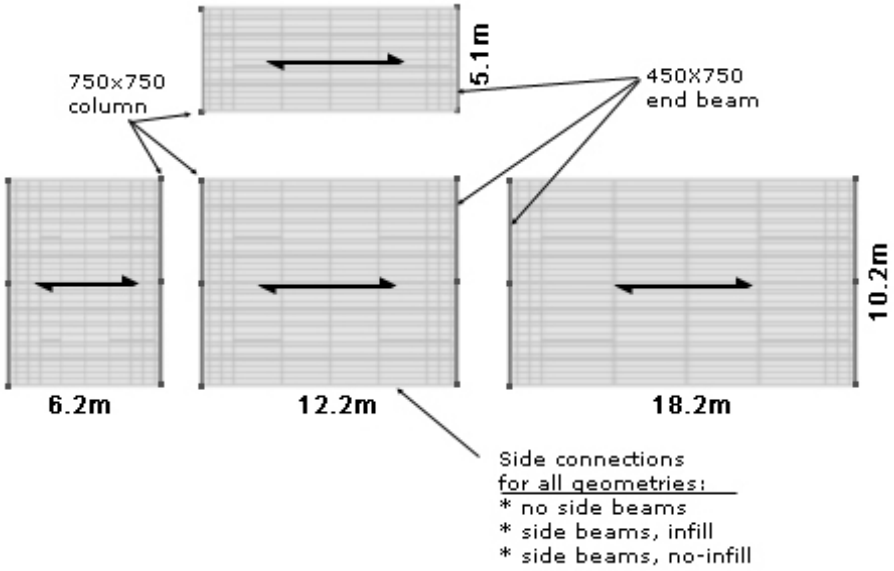

Figure 10-22 Typical floor aspect ratios investigated

10.5.1. Change of the impact from the side supports with the span length

Four different span lengths were studied, which are 9.2m, 12.2m, 15.2m and 18.2m respectively. The width of the slab was maintained constant as 10m. Three side support conditions were investigated, which are the no-infill side connection (N), infill side connection (I), and free hanging (F). The subassembly with the no-infill side connection is shown in Figure 10-12(a), and the subassembly with infill side connection is shown in Figure 10-12(b). Both the cases with or without infill side connection have side beams. The simulation results are summarised in Table 10-6. Even though from the output files most of the simulations did not have a definite failure, such as yielding of prestressing strands or cracking of the entire cross-section within the hollowcore units, the simulation results still provide an indication of an increase of fire resistance with the increasing influence from the side supports.

Table 10-6 Summary of the simulation results of 10.2m wide subassembly with various side supports and span length

L (m)	Side support	Simulation stop time	Reason
9.2	F	203min.	Terminated by SAFIR: very high compressive force in the topping near the ends
9.2	I	>240min.*	Designated end time of the simulation
9.2	N	>240min.*	Designated end time of the simulation
12.2	F	123min.	Terminated by SAFIR: very high compressive force in the topping near the ends
12.2	I	187min.	Terminated by SAFIR: numerical problem (square root of zero)
12.2	N	>240min.*	Designated end time of the simulation
15.2	F	49min.	Terminated by SAFIR: numerical problem (square root of zero)
15.2	I	98min.	Terminated by SAFIR: very high compressive force in the in-situ concrete filling
15.2	N	92min.	Terminated by SAFIR: high tension in the topping near the ends
18.2	F	28min.	Terminated by SAFIR: no convergence after 20 iterations
18.2	I	67min.	Terminated by SAFIR: numerical problem (square root of zero)
18.2	N	67min.	Terminated by SAFIR: high tension in the topping near the ends

Figure 10-23 shows the maximum displacement of the slabs with different span length and side support conditions. The maximum displacement in the slab was observed at the centre of the unit closest to the centre line at the midspan as shown in Figure 10-13. The displacements of the slabs with the no-infill side connection are the smallest throughout the fire. Other than the case with span length of 15.2m, the simulations with the no-infill side connection lasted the longest, and the simulations with no support at the sides the shortest. This indicates the benefit of having the side supports to the structural performance of the subassemblies in fire.

Figure 10-23 also shows that the displacements of the slabs with the infill side connection initially are the same as those without any support at the sides but became relatively smaller after having further exposure to the fire. Nevertheless, they are always greater than those with no-infill side connection.

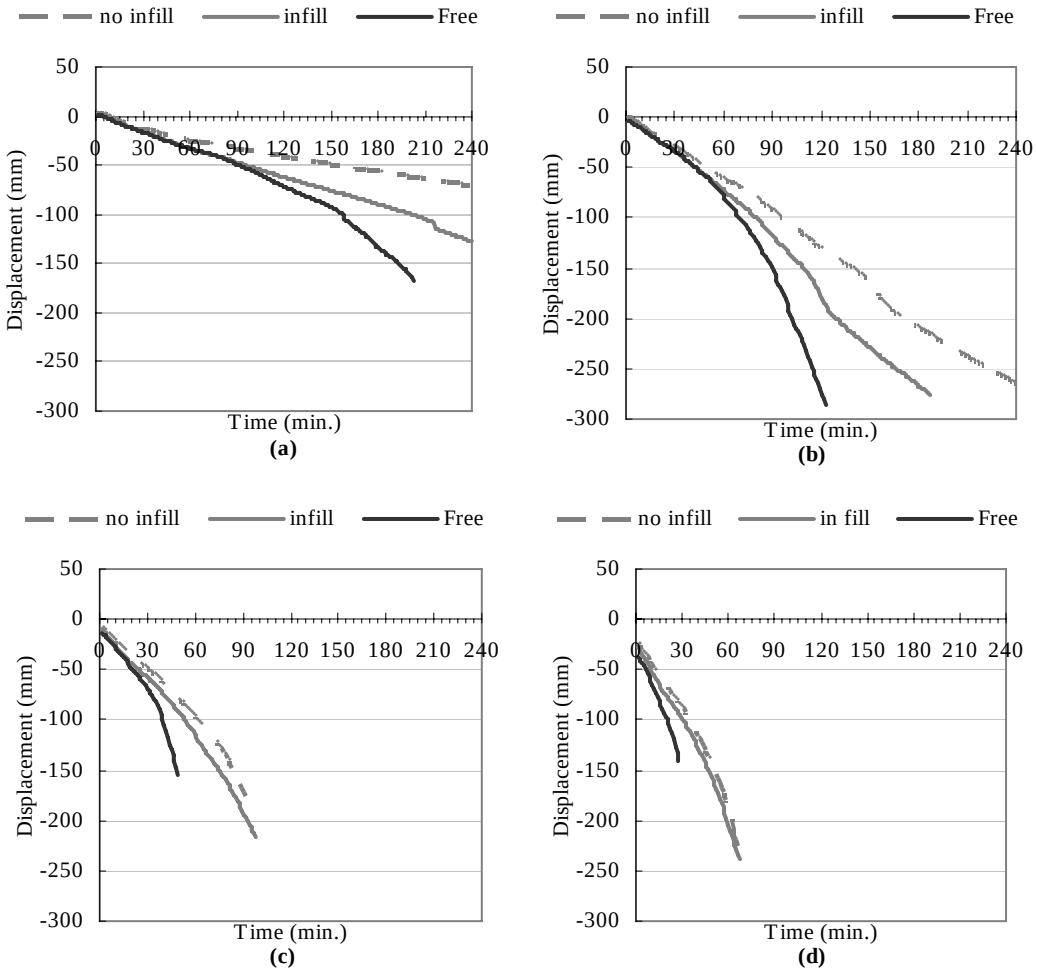

Figure 10-23 Maximum displacement at the midspan of the slab with span length of (a) 9.2m (b) 12.2m (c) 15.2m (d) 18.2m

Comparing among the charts in Figure 10-23 it shows that the difference between the displacements from the slabs with the infill side connection and those with the no-infill side connection reduces with the span length. However, these displacements are still notably smaller than those from the slab without any side beams.

In summary, the no-infill side connection could improve the structural performance of subassemblies with hollowcore concrete flooring system more than the infill side connection. However, this beneficial effect reduces with the span length.

10.5.2. Change of fire resistance with the floor aspect ratio

The subassemblies investigated in this section have Matthews' end connection and the no-infill side connection. The no-infill side connection is used in the subassemblies to fully establish the effect from the side supports. The studied floor widths are 5.1m and 10.2m; the studied span lengths are 6.2m, 9.2m, 12.2m, 15.2m

and 18.2m. The simulation results are shown in Table 10-7. Figure 10-24 shows the maximum midspan vertical displacement, the location of this displacement is shown in Figure 10-13.

Table 10-7 Summary of the simulation results of subassemblies with different floor aspect ratios

Width (m)	Length (m)	Floor aspect ratio (W:L)	Simulation stop time	Reason
5.1	6.2	0.82	>240min.*	Designated end time of the simulation
5.1	9.2	0.55	>240min.*	Designated end time of the simulation
5.1	12.2	0.42	>240min.*	Designated end time of the simulation
5.1	15.2	0.34	97min.	Terminated by SAFIR: high tension in the topping near the ends
5.1	18.2	0.28	77min.	Terminated by SAFIR: no convergence after 20 iterations
10.2	6.2	1.65	>240min.*	Designated end time of the simulation
10.2	9.2	1.11	>240min.*	Designated end time of the simulation
10.2	12.2	0.84	>240min.*	Designated end time of the simulation
10.2	15.2	0.67	92min.	Terminated by SAFIR: high tension in the topping near the ends
10.2	18.2	0.56	67min.	Terminated by SAFIR: high tension in the topping near the ends

The results in Table 10-7 indicate that reducing the spacing between the parallel beams can increase the fire resistance of the slab but not very much. In the cases with 18.2m span length, the 5.1m wide slab lasts 10 minutes longer than the 10.2m wide slab under the ISO fire, and in the cases with 15.2m span length, the difference in the simulation stopping times is 5 minutes.

However, Figure 10-24 shows that the reduced width can reduce the deflection of the slab, and this effect is more pronounced in the long spanning slabs. Figure 10-24(a) shows that the difference in the deflection between the 5.1m and 10.2m wide slab spanning 6.2m is not noticeable, but when the slab length is increased to 12.2m, the central vertical displacement in the 5.1m wide slab at 60 minutes is 70% of that in the 10.1m wide slab as shown in Figure 10-24(c), and when the slab length is increased to

18.2m, the displacement in the 5.1m wide slab at 60 minutes is only 50% of that in the 10.1m wide slab. This indicates that the side beams are more effective when the span length is long.

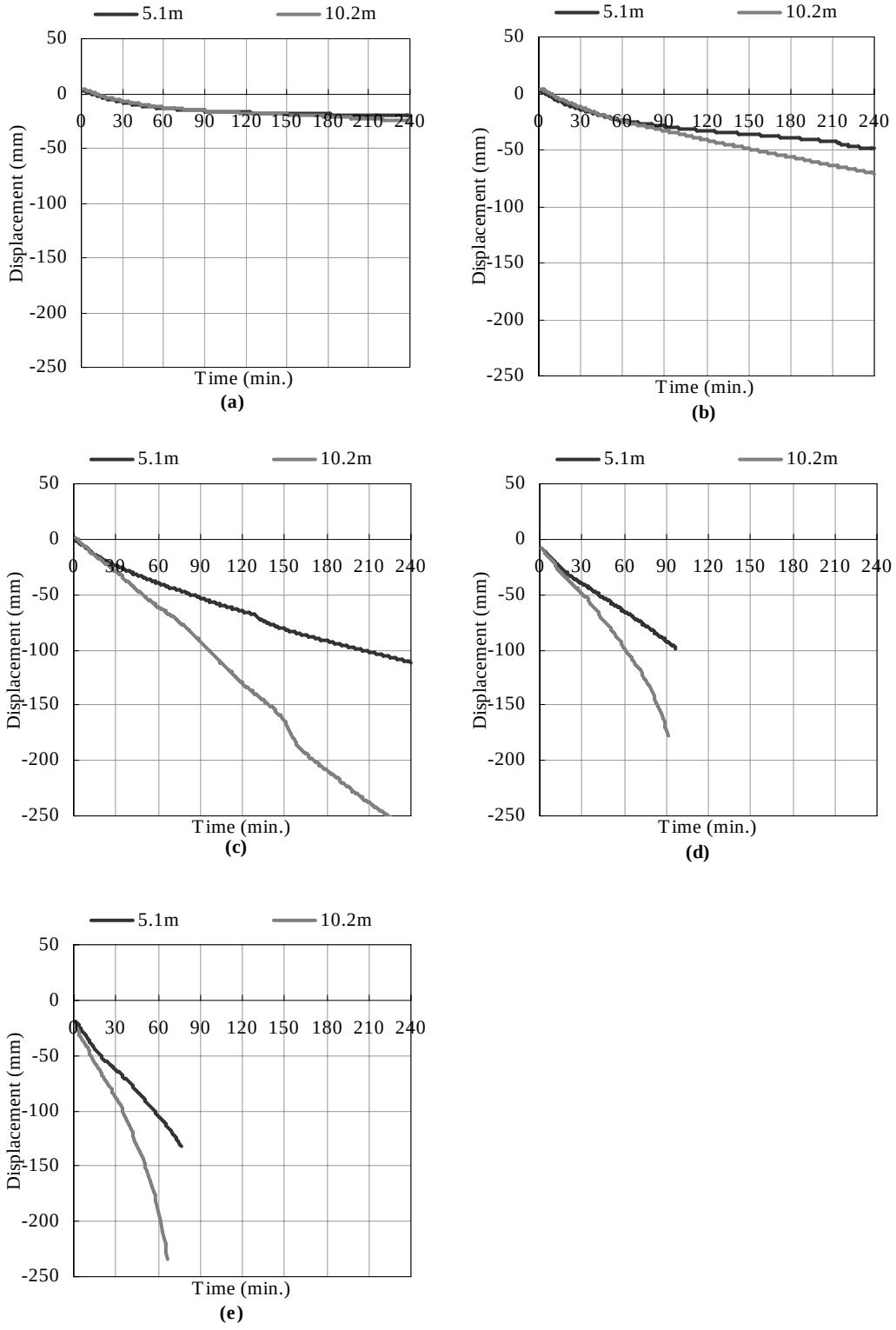

Figure 10-24 Maximum midspan vertical displacement of the slab with different span length (a) 6.2m (b) 9.2m (c) 12.2m (d) 15.2m (e) 18.2m.

In terms of floor aspect ratio, the results show that the fire resistance depends more on the length of the slab rather than the width to length ratio. The 5.1m wide and 6.2m long slab has a similar floor aspect ratio to the 10.2m wide and 12.2m long slab, and the 5.1m by 9.2m long slab has a similar floor aspect ratio to the 10.2m by 18.2m long slab, but their deflections at the centre shown in Figure 10-24 and their failure times are drastically different. Because the behaviour of the hollowcore concrete flooring systems is dominated by the behaviour parallel to the hollowcore units, this observation is as expected.

10.6. Summary

Lim [2003] showed that membrane action can be established in two-way supported slabs and increasing the fire resistance. The side connections of hollowcore flooring systems to side beams help to establish the two-way behaviour of the floor slab, and changing the aspect ratio of hollowcore flooring systems can influence the fire resistance of the structure.

10.6.1. Side connections

The first part of this chapter shows that the hollowcore concrete flooring system with the end and side connections designed prior to the introduction of the Amendment 3 of the NZS3101:1995 [SNZ 2004] performs better than those with the connections designed according to the newer standards, and the worst combination would be from the subassembly with Lindsay's end connection and the infill side connection, i.e. flexible side connection with infill concrete. This has very poor fire performance because the infill side connection cannot carry sufficient load to the side beams while the rotationally flexible end connections prevent the arch action along the span to develop.

For the connections between the hollowcore units and the parallel side beams, a rigid side connection with hollowcore units placed immediately adjacent to the side beams (the no-infill side connection), has better fire resistance than a flexible side connection with infill concrete (the infill side connection), but this effect reduces with the span length.

10.6.2. Membrane action in hollowcore concrete flooring systems

In terms of floor aspect ratio, decreasing the width of the floor bay can increase

the fire resistance of the hollowcore flooring system, but is not as effective as decreasing the length of the floor bay, as the overall structural performance is dominated by the behaviour along the span.

10.6.3. Future research

There are not many aspect ratios studied here due to the limitation of the stiffness matrix size in SAFIR 2002. Nevertheless, the results show that with a wider width the slab would behave closer to the ones without side beams studied in this research. For a wider slab the effect from the side supports would be less, therefore less likely to have two-way behaviour, and the central midspan deflection would be greater.

To study more aspect ratios, one can reduce the number of fibres in the thermal analysis or the number of elements in the structural analysis. Both methods can reduce the required size of stiffness matrix. Section 7.5 shows that the simulation results for one hollowcore unit is similar if the topping is modelled by the beam grillage and not by the shell elements. The idea of replacing shell elements with beams in the model could be pursued further, which might be able to allow modelling slabs with more hollowcore units side-by-side.

11. Fire Performance of Hollowcore Flooring Systems in Parametric Fires

11.1. Introduction

This section studies the structural behaviour of a subassembly with hollowcore concrete flooring systems exposed to parametric fires. All structural analyses in the previous chapters expose the floor slab and end beams to the ISO 834 standard fire. The aim in this section is to study the fire performance of the subassembly in parametric fires, especially during the decay phase. The simulations also show the ability of the SAFIR program to include different heating conditions in the model, which is part of the advantages of using SAFIR to investigate the fire performance of structures.

11.2. Model Description

The subassembly studied in this section has no-infill side connection to the side beams, which is the same as in Section 10.5. Both Matthews' and Lindsay's end connections are investigated. The floor is 10.2m wide and 12.2m long, and the layout of the floor is shown in Figure 11-1.

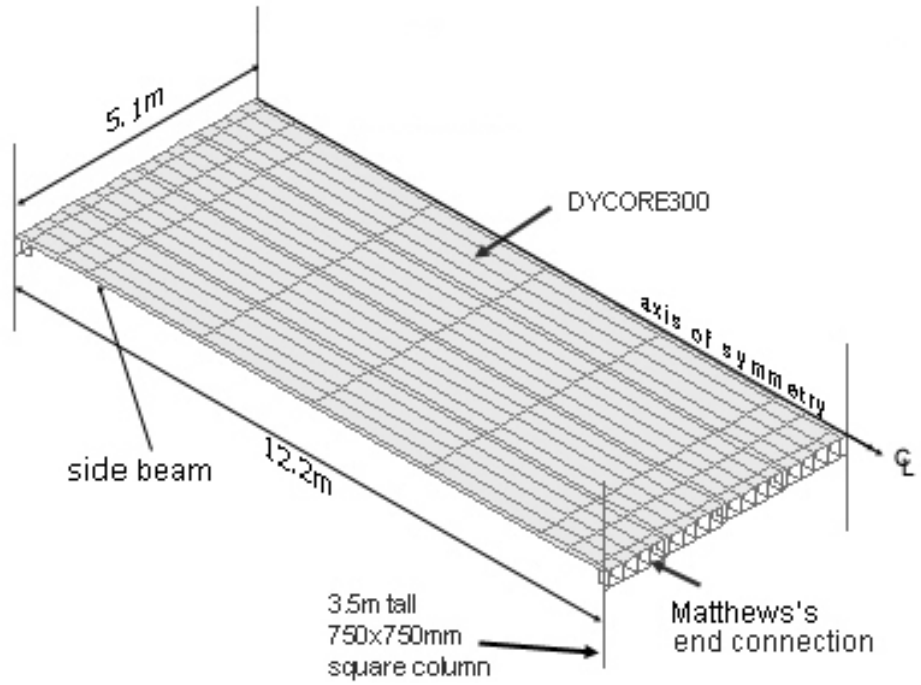

Figure 11-1 Simulated model for investigating the fire performance in parametric fires

11.3. Studied Parametric Fires

Instead of the ISO fire, the entire floor and the end beams are exposed to parametric fires. One of the studied parametric fires follows 60 minutes of the ISO fire and then enters the decay phase. To obtain the parametric fire curves, the compartment is assumed to be 3.5m high and has a floor area of 10.2m by 12.2m, which is the same as the slab area in the model. The fuel load in the compartment is assumed to be 1000MJ/m^2 per floor area.

The growth phase of the parametric fire temperatures is calculated using the following equation according to Eurocode 1 [EC1, 2001].

$$T = 1325(1 - 0.324e^{-0.2t^*} - 0.204e^{-1.7t^*} - 0.472e^{-19t^*}) \quad \text{Eq.11-1}$$

where T is the temperature in ^oC, and t^* is a fictitious time (in hours) given by

$$t^* = \Gamma t \quad \text{Eq.11-2}$$

where t is the actual time (in hours) and Γ is calculated as

$$\Gamma = \frac{(F_V / F_{ref})^2}{(b / b_{ref})^2} \quad \text{Eq.11-3}$$

where b is the square root of thermal inertia, b_{ref} is the reference value of square root of thermal inertia (1900$Ws^{0.5}/m^2K$ according to Feasey & Buchanan [2002]); F_v is the ventilation factor calculated as:

$$F_v = A_v \sqrt{H_v} / A_t \quad \text{Eq.11-4}$$

where A_t is the total internal area of the bounding surfaces, in this case 405.7m^2. H_v is the height of the window opening and assumed to be 3m. A_v is the area of the window opening. The width of the window opening is assumed to be 3.1m, therefore A_v equals 9.3m^2, and F_v is 0.04. When F_v equals F_{ref}, the reference value of the ventilation factor (0.04 from Eurocode 1 [EC1 2002]), and b equals b_{ref}, Eq. 11-1 approximates the ISO fire curve well up about 1300^oC. Therefore, in this case the growth phase of the parametric fire follows closely to the ISO fire.

Eurocode 1 [EC1 2002] provides a simple equation to calculate the duration of the burning period t_d (hours), where

$$t_d = \frac{0.00013E}{A_v \sqrt{H_v}} \quad \text{Eq.11-5}$$

where E is the total energy content of the fuel in MJ. With A_v being 9.3m^2, and H_v being 3m, the fire grows for 1 hour before entering into the decay phase.

In terms of the decay phase, Eurocode 1 uses a reference decay rate equal to 625^{o}C per hour for fires with a burning period less than half an hour, decreasing to 250^{o}C per hour for fires with a burning period greater than 2 hours. Because of the growth period of the fire is longer than 30 minutes, its decay rate is 500^{o}C per hour according to Eurocode 1. When F_v is different from F_{ref} and b from b_{ref}, i.e. the fire temperature in the burning period does not follow the ISO fire curve, Feasey & Buchanan [2002] suggests adjusting the decay phase proportionally to $\sqrt{F_v}$ and $1/\sqrt{b}$, and this decay rate is used in this study.

With the window being 3m by 3.1m wide, the fire follows closely to the ISO fire for one hour and then enters the decay phase. This fire is now referred to as the "medium fire". The short and long fires are calculated by changing only the width of the window and keeping the fuel size and the room geometry constant. The width of the window for the short fire is 6.2m, and 1.55m for the long fire. Therefore the decay rate of the short fire is 707^{o}C per hour and of the long fire is 354^{o}C per hour. The curves of these three parametric fires are shown in Figure 11-2. The window sizes for the three parametric fires and the burning periods and decay rates of the fires are summarised in Table 11-1.

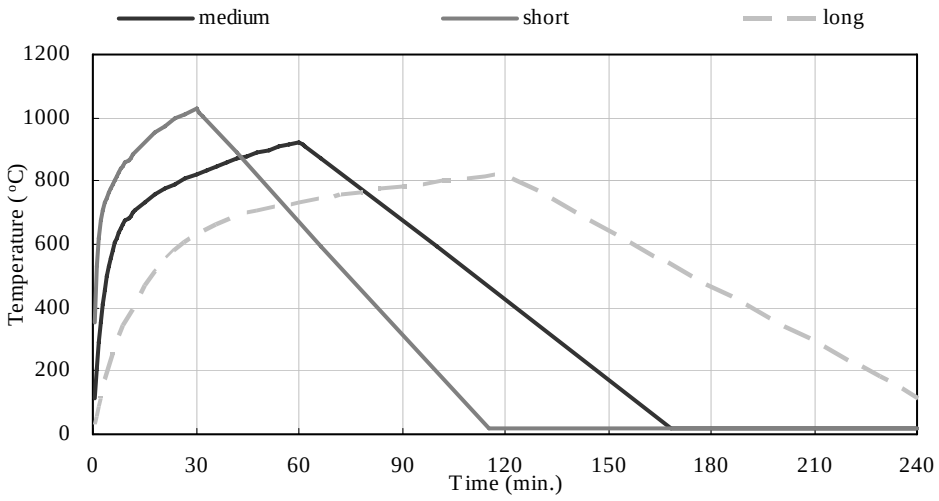

Figure 11-2 Studied parametric fires

Table 11-1 Window sizes and burning periods for fuel load of 1000MJ/m^2

	Short fire	Medium fire	Long fire
Window height	3m	3m	3m
Window width	6.2m	3.1m	1.55m
F_v	0.08	0.04	0.02
Burning period	30min.	60min.	120min.
Decay rate	707°C	500 °C	354 °C

11.4. Equivalent Fire Severity

In this study the term "fire severity" means a measure of the destructive impact of a fire on structures [Buchanan 2001], which is the thermal response of the structures to the fires, and "equivalent fire severity" relates the impact of a real fire to that of a standard fire.

11.4.1. Equivalent fire severity in Eurocode formula

Eurocode 1 [EC1 2002] provides a time equivalent formula based on the ventilation parameters of the compartment and the fuel load to calculate the equivalent fire severity, t_e (minutes), as

$$t_e = k_b w e_f \qquad \text{Eq.11-6}$$

where k_b is a parameter to account for the compartment linings, and in this case is 0.055min m^2/MJ for concrete; e_f is the fuel load and is 1000MJ/m^2 per floor area; and w is the ventilation factor calculated as

$$w = \left(\frac{6.0}{H_r}\right)^{0.3}\left[0.62 + \frac{90(0.4-\alpha_v)^4}{1+b_v\alpha_h}\right] \qquad \text{Eq.11-7}$$

where H_r is the height of the compartment and is 3.5m here; α_v is related to the area of vertical openings in the walls and is 0.150 for short fire, 0.075 for medium fire, and 0.037 for long fire; b_v is calculated based on α_v, and α_h is related to the area of horizontal openings in the roof and is 0 in the studied compartment.

The calculation shows that the equivalent fire severity calculated using the Eurocode formula is 63 minutes for the short fire, 101 minutes for the medium fire, and 138 minutes for the long fire.

11.4.2. Equivalent fire severity in maximum temperature concept

Based upon the maximum temperature concept developed by Law [1971], the equivalent fire severity is the time of exposure to the standard fire that would result in the same temperature as the maximum temperature in the structural member throughout the parametric fires.

In this case, the temperature is taken at the mid-height of the web in the hollowcore units because such location is most critical to the thermally induced mechanical strains as described in Section 4.3.1, which makes the thermally reduced mechanical strength, and consequently the temperature at this location is important.

Figure 11-3 shows the derivation of equivalent fire severity based on comparing the maximum temperature at the mid-height of the web. Because of the low conductivity in concrete, the temperature within the hollowcore units does not change as quickly as the fire temperature. Although the medium fire only grows for 60 minutes closely following the ISO fire, the equivalent fire severity is 89 minutes. It is also known that for materials with low conductivities, mild and long fires can cause greater damage than fast and short fires; therefore it is not surprising to find the equivalent fire severity of the short fire is 79 minutes and 102 minutes for the long fire. These are compared in Table 11-2.

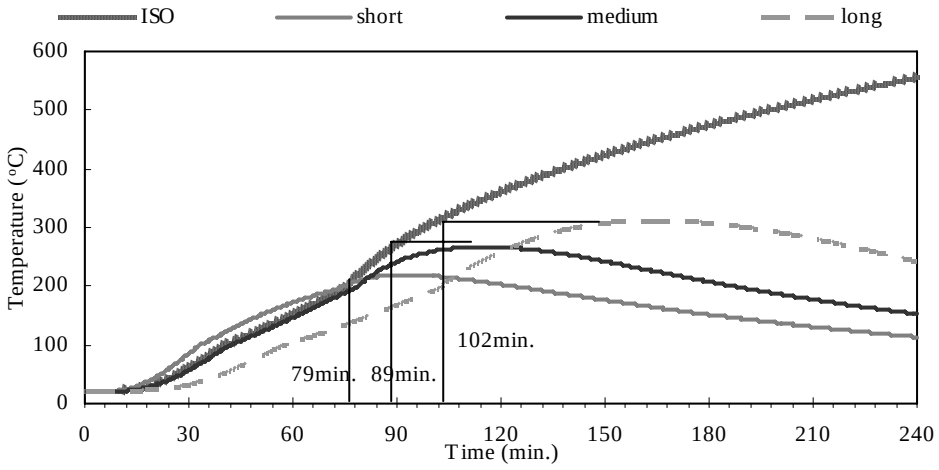

Figure 11-3 Equivalent fire severity using maximum temperature concept

11.5. Fire Performance of the Subassemblies in Parametric Fires

11.5.1. Subassembly with Matthews' end connection

In Chapter 10 it has been shown that the subassembly with Matthews' end connection can sustain more than four hours of exposure in ISO fire, and as expected the simulations here show the subassembly does not collapse under any of the three parametric fires. Figure 11-4 shows the vertical displacements at the centre of the slabs exposed to the ISO fire as well as the three parametric fires. The figure shows that the deflection at the centre of the slab recovers when the slab is cooling, but a permanent deformation has been produced during heating and can be observed at the end time of the simulation. The recovery of the deflection is caused by the regaining of the material properties and reversing of thermal expansion of concrete and prestressing steel. The permanent deformation is caused by the localised crushing and cracking of concrete within the hollowcore unit as well as by inelastic deformation in the prestressing steel. It is noteworthy that no anchorage slip is included in the model.

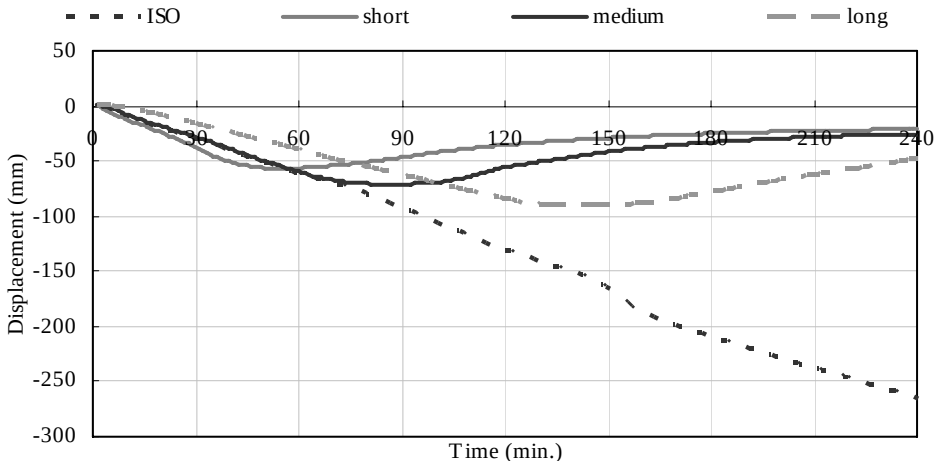

Figure 11-4 Vertical displacements at the centre of the slab with Matthews' end connection exposed to the ISO fire and parametric fires

Figure 11-4 also shows that the deflection in the medium fire, which follows one hour of the ISO fire curve, is the same as that in the ISO fire in the first 70 minutes. During the growth phase of the fire, the short fire causes the greatest rate of increase of deflection, and the long fire causes the least. However, the long duration of the long fire causes a much greater maximum deflection than the high temperature short fire. It is also interesting to notice that the equivalent fire severity shown in Section 11.4 cannot be used to predict the deflection of the slab. The time of exposure to the

ISO fire that would cause the same deflection as the maximum deflection in the long fire is 90 minutes, and in the short fire is 53 minutes.

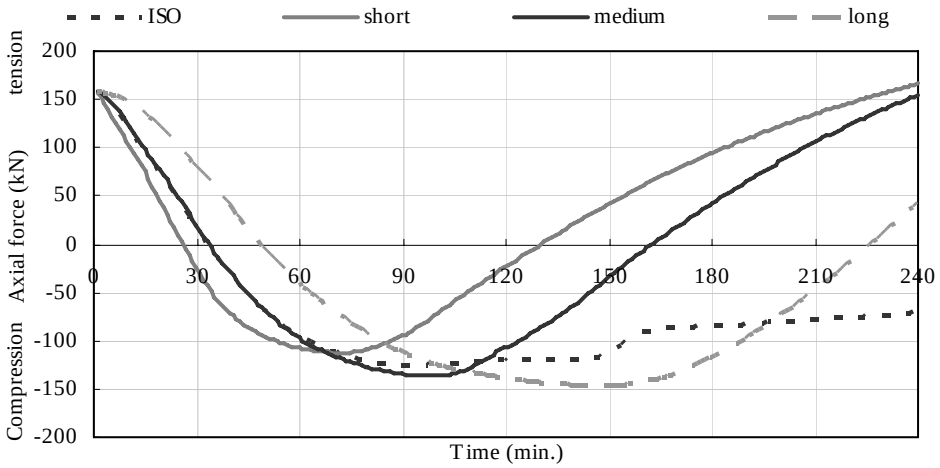

Figure 11-5 Axial force in the of the centre unit of the slab with Matthews' end connection

Figure 11-5 shows the axial forces in a 300mm wide strip at the centre of the hollowcore unit at the centre of the slab exposed to fire. The location of this web is shown in Figure 11-6. Figure 11-5 shows that under ambient conditions the axial force is in tension due to the prestressing strands, and it drops to zero and increases to compression as the temperature in the concrete increases. The high tensile force within the structure is transferred through the topping for the case with Lindsay's end connections or through all the stiff links in the case with Matthews' or MacPherson's end connections to the end beams, then it is transferred to the top and the bottom of the columns where the reaction forces come from. The magnitude of the horizontal reaction force depends on the tensile axial force in the slab and the deflection of the slab.

This thermally induced compressive force has been explained in detail in Sections 4.3.1 and 3.3.5. During the cooling phase the thermal expansion of both concrete and steel reduces and causes the recovery of deflection as shown in Figure 11-4 and creates a large tensile force becoming equal to or slightly larger than the initial prestressing level long after the fire has cooled down. In the studied cases this tensile force at the end time of the simulation is not great enough to cause the yielding of the prestressing strands, therefore no structural failure has been found in these cases. Nevertheless, designers should be aware of this potential large tensile force.

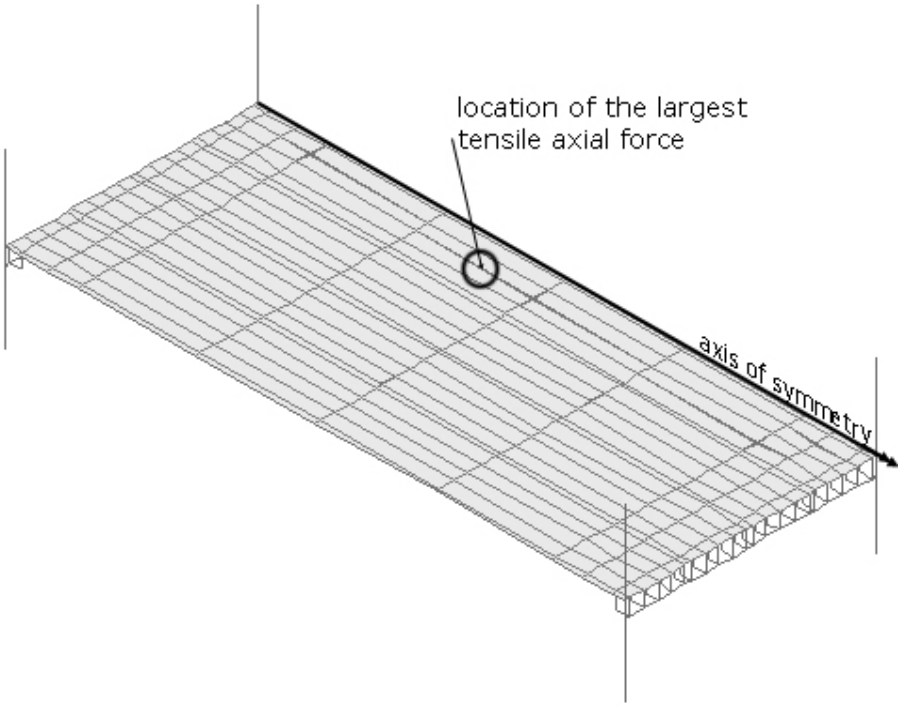

Figure 11-6 Location of the observed axial force

11.5.2. Subassembly with Lindsay's end connection

In this section the connection between the ends of the hollowcore units and the end supporting beams is following the design from Lindsay [2004]. Figure 11-7 shows the maximum displacement at the midspan of the slab. Section 10.4 showed that under the ISO fire the simulation of this subassembly stopped after 71 minutes due to numerical problems in SAFIR. The simulation of subassembly under the long parametric fire stopped after 120 minutes for the same reason. Figure 11-7 shows that the maximum displacement caused by the medium fire follows very closely to that caused by the ISO fire until 70 minutes. It is interesting to see at the end time of the simulation the midspan of the slab exposed to the short fire returns to the original height, and the deflection of the slab exposed to the medium fire is still recovering. This finding is different to the results shown in the previous section. Using linear interpolation, the time of exposure to the ISO fire that would cause the same deflection as the maximum deflection in the long fire is 80 minutes, in the medium fire is 70 minutes, and in the short fire is 55 minutes.

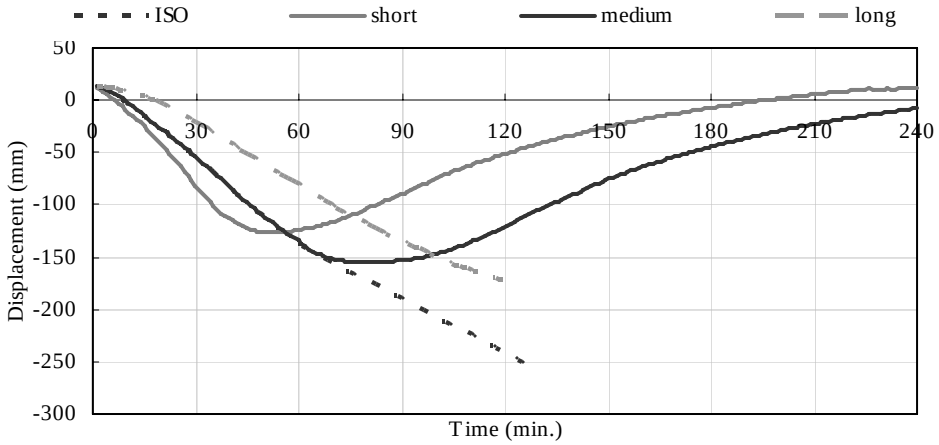

Figure 11-7 Vertical displacements at the centre of the slab with Lindsay's end connection exposed to the ISO fire and parametric fires

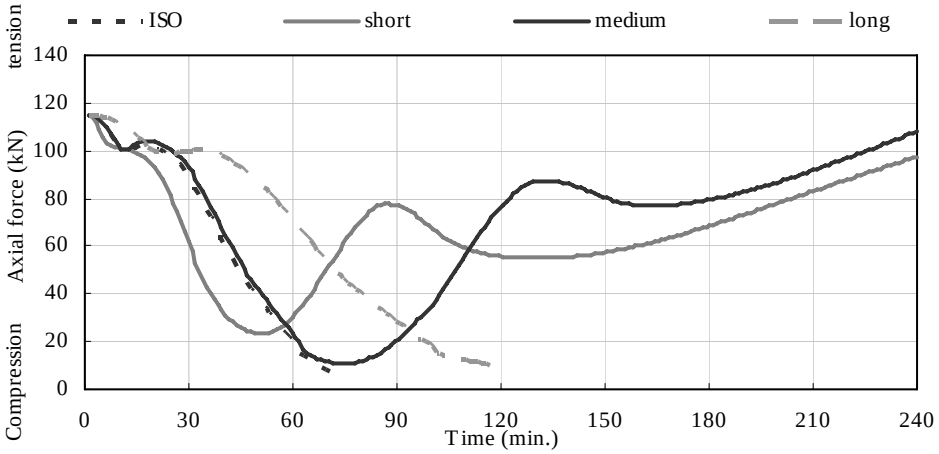

Figure 11-8 Axial force at the central web of the centre unit of the slab with Lindsay's end connection

Figure 11-8 shows the axial force in the web at the location shown in Figure 11-6. Figure 11-8 again shows that the behaviour of the slab exposed to the medium fire follows closely the behaviour of the slab exposed to the ISO fire up until 70 minutes. At the end time of the simulation the axial forces from the slab exposed to the short fire and to the medium fire are still increasing, but the magnitude of the tensile force at that time is not as large as that at the start.

11.5.3. Discussion

Slabs with different end connections in parametric fires

Matthews' end connection is rotationally rigid, and Lindsay's end connection is rotationally flexible. MacPherson's end connection is not considered in this chapter as it is also rotationally rigid like Matthews' end connection. The results show that both subassemblies are more vulnerable to the lower temperature long fire than to the

higher temperature short fire. However, it is also shown in the simulation that even though high tensile axial force is found in the slab while cooling, none of the structures collapsed due to such force during the simulation. The results also show that the slab with Lindsay's end connection has more deflection than that with Matthews' end connection, because there is less axial restraint, the compressive force is smaller in high temperatures as no arch action is developed, and the tensile force is also smaller when the fire cools down.

Comparison between simulation results and Eurocode formula for equivalent fire severity

Table 11-2 shows the equivalent fire severities obtained from the two methods as well as the times of the slab to achieve the same deflection under the ISO fire as under the parametric fires. Both the maximum temperature concept and the Eurocode formula cannot take account of the influence of the boundary conditions which is shown repeatedly throughout the research to be very important to the fire performance of the structures.

Table 11-2 Equivalent fire severities obtained using different methods

	Growth Period	**t_e (Eurocode formula)**	**Time in ISO fire to cause the same maximum temperature**	**Time in ISO fire to cause the same maximum deflection (Matthews' end connection)**	**Time in ISO fire to cause the same maximum deflection (Lindsay's end connection)**
Short	30min.	63min.	79min.	53min.	55min.
Medium	60min.	101min.	89min.	71min.	70min.
Long	120min.	138min.	102min.	90min.	80min.

Eurocode formula is based on work by Schneider et al. [1990] which is about protected steelworks, and sometimes can be applied to reinforced concrete members [Buchanan 2001]. Comparing to the equivalent fire severities calculated using maximum temperature concept, Table 11-2 shows that the Eurocode formula only crudely matches the time to maximum temperature in the hollowcore webs. It over predicts the fire severity of the medium and long fires, and underestimates the fire severity of the short fire.

Calculation using Eurocode formula shows that the medium fire will have the same effect on the structure as 101 minutes of ISO fire with no decay period.

However, with Matthews' end connection the maximum deflection caused by the medium fire is the same as that by 71 minutes of ISO fire. Table 11-2 shows that the Eurocode formula should not be used to estimate the maximum deflection of the system as it would over estimate the effect of the parametric fire.

Design methods

The three available design methods from Eurocode 2 have been described in Section 2.3.3. Table 11-3 shows the application of these three design methods when designing for hollowcore concrete flooring systems. Based upon the results in this study, it is recommended to use realistic design fires with advanced calculation method to design for hollowcore concrete flooring systems when possible.

There is no simple calculation method suggested for parametric fire exposure, because in realistic fires it is necessary to consider the recovery of the deflection during the decay phase and the extra tensile stress induced during the deflection recovery process, and the calculation of the tensile force induced during cooling is too complicated to carry out without using advanced calculation methods.

In terms of equivalent fire severity, designers can only use it if they have test results or prediction from standard fire resistance rating tests with known boundary conditions.

Table 11-3 Available design methods for hollowcore concrete flooring systems

	ISO fire	**Realistic fire (burnout)**
1	**Tabulated data** of fire resistance rating from the manufacturer	Find equivalent fire severity and use **tabulated data**
2	**Simple calculation method** – Assuming the slab is simply supported. Finding the temperature in the prestressing strand. Calculating the loss of strength	-------
3	**Advanced calculation method** – Using SAFIR and the proposed new model	**Advanced calculation method** – Using SAFIR and the proposed new model

11.6. Summaries and Conclusions

A study of exposing a subassembly to parametric fires has been carried out. The result shows that a large tensile force would be created when the structural members cool down, and this behaviour could not be observed when only exposing the structures to the ISO standard fire. Although in the simulations this large tensile force did not cause the structure to collapse, it is recommended to design the structure using not only the ISO standard fire but also a realistic design fire when possible.

The results here also show that the equivalent fire severity obtained using Eurocode formula only crudely matches the time to maximum temperature in the hollowcore webs. Designers should carry out structural analysis to get much more accurate prediction of the fire resistance of the hollowcore concrete flooring systems than using the equivalent fire severity method with published test results.

12. Conclusions and Recommendations

12.1. Introduction

This research was carried out to study the fire resistance of structures with hollowcore concrete flooring systems. The main objective of this research is to investigate the structural performance of such structures designed according to the past and current New Zealand Concrete Standard NZS3101. This research also studied the feasibility of using tensile membrane action to increase the fire resistance of two-way supported floors. The study was performed with 3D finite element analyses using SAFIR. A new method was used for simulating the structural behaviour of hollowcore concrete flooring systems to conduct the research. The fire resistance of the structures in this study is limited by flexural, tensile and compressive failure modes. Shear and anchorage failures are not considered here, so Fellinger [2004] should be consulted for details regarding those failure modes.

12.2. New Model to Simulate Buildings with Hollowcore Concrete Flooring Systems in Fire

A new model was developed to simulate the global structural behaviour of subassemblies with hollowcore concrete flooring systems under fire using the finite element analysis program SAFIR.

12.2.1. Features of the new model

- The proposed model uses shell elements for the topping reinforced concrete slab, and a grillage of 3D beam elements for each hollowcore unit.
- The longitudinal beams in the grillage enable the thermal gradient in the web to be calculated, can capture the prestressing effect, and provide the concrete stress within any point in the hollowcore units and the stress within the prestressing strands.
- Continuity between the hollowcore units can be established by the shell elements which simulate the topping concrete.
- The transverse beam elements running across the width of the hollowcore units simulate the thermal expansion and thermal bowing across each unit.

- The thermal strains and the thermally-reduced mechanical properties from Eurocode 2 are incorporated into the model. By including the thermal strains, the thermal stresses and mechanical strains induced by incompatible thermal strains are included in the structural analysis.

- The developed model was used to simulate the experiments from DIFT [Andersen et al. 1999], University of Ghent [Febe Studiecommissie SSTC 1998] and BEF [BEF 2005]. Other than not being able to predict the shear failures, the simulation results showed good agreements with the experimental results.

12.2.2. Disadvantages of the new model

- As a default of SAFIR, the prestressing is applied at the same time as the loading in the structural analysis model and this effect is also influenced by the boundary condition at the supports, hence the stress distribution within the cross section at the first time step which is at ambient temperatures may be different from the reality.

- Shear and anchorage failures, bond failures, vertical tensile stresses in the web and spalling effects are not captured in the proposed model.

- Because many simulations in SAFIR stopped due to numerical problems, much effort was needed to investigate whether the simulation stopping time represented global structural failure or some local material failure.

12.3. Structural Fire Performance of Hollowcore Concrete Flooring Systems with Various End Supports

The following are the conclusions from the simulations of hollowcore concrete floors with various support conditions at the ends and corners.

- **Stiffness of the end beams:** better fire resistance is obtained when the hollowcore floor system is supported on rigid or very stiff end beams, compared to flexible end beams.

- **Rotational restraints at the supports:** for floor slabs supported on beams and columns, it is recommended that rigid connections should be used between the slab and end beams following the recommendations from Fellinger [2004] to avoid shear and anchorage failure. For floor slabs supported on load bearing walls,

it is recommended that rotationally flexible connections to be used between the slab and the supporting walls.

- **Core filling**: filling the ends of some cores with reinforced concrete was found to increase the fire resistance of the slab system even though this finding contradicts the observations made by Fellinger [2004].

- **Axial restraints:** a supporting structure providing good axial restraints has a beneficial effect on the structural performance in fire, and good rotational restraint at the slab supports is also beneficial. Therefore, for isolated floor system exposed completely to fire, the presence of strong and stiff columns will improve the fire resistance of the floor system.

12.4. Structural Fire Performance of Hollowcore Concrete Flooring Systems Designed According to NZS3101

- **End connections:** for the prescriptive connection between the hollowcore units and the end beams, the end connection design of hollowcore flooring systems from C18.6.7(b) of NZS3101:2006, i.e. the end connection used by MacPherson [2005] is recommended.

- **End connections:** any kind of gap between the end of the hollowcore units and the end beams decreases the fire resistance. The end connection design of hollowcore flooring systems from C.18.6.7 (a) of NZS3101:2006, i.e. the end connection used by Lindsay [2004], is not good for the overall structural performance of the flooring system in fire according to the outcome of this study , which ignores the possibility of axial restraint after closure of the gap between the hollowcore units and the end beams. A more sophisticated model which could capture the increase in strength after gap closing is needed for a more definite conclusion to be drawn.

- **Side connections:** for the connections between the hollowcore units and the parallel side beams, a rigid side connection with hollowcore units placed immediately adjacent to the side beams, i.e. design before the Amendment 3 in NZS3101:1995 [SNZ 2004], has better fire resistance than a flexible side connection with infill concrete, but this effect reduces with the span length.

- Overall, the hollowcore concrete flooring systems with the end and side connections designed prior to the introduction of Amendment 3 of NZS3101:1995 [SNZ 2004] perform better than those with the connections designed according to the newer standard, and the worst combination from fire perspective would be the subassembly with Lindsay's end connection and the flexible side connection with infill concrete. This has very poor fire performance because the flexible side connection cannot transfer sufficient load to the side beams while arch action along the span fails to develop.

12.5. Membrane Action in Hollowcore Concrete Flooring Systems

Lim [2003] showed that membrane action can be established in two-way supported slabs and consequently increases the fire resistance. The side connections of hollowcore flooring systems to side beams help to establish the two-way behaviour of the floor slab. A rigid side connection is better than a flexible (infill) side connection. In terms of floor aspect ratio, decreasing the width of the floor bay can inprove the structural performance of the hollowcore concrete flooring system in fire, but not as effectively as decreasing the length of the floor bay, as the overall structural performance is dominated by the behaviour along the span.

12.6. Hollowcore Concrete Flooring Systems Exposed to Parametric Fires

The model can be used to study the performance of structures exposed to fires other than the ISO standard fire. In parametric fire during the decay phase a large tensile force is induced in the slab, this force cannot be observed when exposing the slab to only the standard fire. Therefore it is recommended to design structures using a realistic design fire when possible. The study also shows that designers should carry out structural analysis to get much more accurate prediction of the fire resistance of the hollowcore concrete flooring systems than using the equivalent fire severity method with published test results.

12.7. Recommendations to Avoid Shear and Anchorage Failure

The findings and recommendations in the previous sections are dominated by the flexural and membrane failures studied in this research. Shear and anchorage failure is

also very important in the performance of hollowcore concrete flooring systems in fire. Detailed information on the shear and anchorage behaviour is given by Fellinger [2004], with the following recommendations to avoid shear and anchorage failure:

- **Concrete mix in hollowcore units**: using a concrete mix with a high fracture energy in the hollowcore units (such as plastic or steel fibre concrete), can effectively increase the shear and anchorage capacity. It is also recommended to use concrete with low thermal expansion rather than with high thermal expansion.
- **Protecting the ends of the slab:** insulating the hollowcore slabs over the transfer length of the prestress (usually less than 1.4m) can avoid shear and anchorage failure, but insulation over only a shorter length does not improve the behaviour.
- **Core filling:** core filling near the support needs to be accompanied by adequate bond between the core filling and the hollowcore unit, of it is to be beneficial to the structural performance of hollowcore flooring systems in fire.
- **Axial restraints:** axial restraints at the supports of the hollowcore slabs are beneficial. However, the required amount of restraint to avoid shear and anchorage failures is unknown.
- **Mechanical loading:** it is recommended to reduce the shear load on hollowcore slabs in fire conditions, thus increasing the likelihood of flexural failure rather than shear or anchorage failure.

12.8. Recommendations for Future Research

The following recommendations are made for future research:

- To ensure that the idea of using shell elements and grillage system to simulate the hollowcore concrete flooring systems with reinforced concrete topping can be extended to other computer analysis programs, such as Vulcan or DIANA, and to compare the outcomes to the ones from this research.
- Develop a material model to simulate closing of the gap between the face of hollowcore slabs and the end beams during the fire, so that the effect of the end connection used by Lindsay [2004] can be simulated properly.
- Investigate the possibility of using a grillage system to capture the two-way

membrane action, so that the shell elements are not needed and simulations would stop only due to the failure within the hollowcore units and not in the topping concrete.

- Investigate the performance of the structure in realistic fires with different boundary conditions. Because in reality only a portion of the entire floor slab will be exposed to fires, investigating the effect from localised fire to the structural performance is also helpful to the designers.
- Investigate the fire performance of the structures with hollowcore units different to 300 DYCORE. The thermal strains are very important to the fire performance of the structure, and they depend on the thermal gradient which is affected by the thickness of the slab. With different thickness of the hollowcore units, the fire performance of the hollowcore concrete flooring systems might be very different.

13. References

Ali, F.A., Connolly, R. & Sullivan, P.J.E. (1996-1997), "Spalling of high strength concrete at elevated temperatures", *Journal of Applied Fire Science*, Vol.6, no.1, pp.3-14

Ali, F.A., O'Conner, D. & Abu-Tair, A. (2001) "Explosive spalling of high-strength concrete columns in fire", *Magazine of Concrete Research*, vol.53, No.3, pp. 197-204

Ali, F.A. (2002) "Is high strength concrete more susceptible to explosive spalling than normal strength concrete in fire?", *Fire and Materials*, vol.26, pp. 127-130

Anderberg, Y. (1983), *Properties of materials at High Temperatures, Steel*, Division of Building Fire Safety and Technology, Lund Institute of Technology, Sweden

Anderberg, Y. & Thelandersson, S. (1973) *Stress and Deformation Characteristics of Concrete at High Temperatures: 1. General Discussion and Critical Review of Literature. Bulletin 34*, Division of Structural Mechanics and Concrete Construction, Lund Institute of Technology, Lund, Sweden.

Anderberg, Y. & Thelandersson, S. (1976) *Stress and Deformation Characteristics of Concrete at High Temperatures: 2. Experimental Investigation and Material Behaviour Model*, *Bulletin 54*, Division of Structural Mechanics and Concrete Construction, Lund Institute of Technology, Lund, Sweden.

Andersen, N.E. & Lauridsen, D.H. (1999) *Danish Institute of Fire Technology Technical Report X 52650 Part 2 - Hollow core Concrete Slabs*, Danish Institute of Fire Technology, Denmark

ASTM (1999) *Standard Test Methods for Fire Tests of Building Construction and Materials*, E119-98, American Society for Testing and Materials, Philadelphia, USA

Bareš, R. & Massonnet, C. (1968) *Analysis of Beam Grids and Orthotropic Plates by the Guyon-Massonnet-Bareš Method*, Crosby Lockwood & Son Ltd.; London, SNTL; Prague

Batoz, J.L. & Ben Tahar, M. (1982) "Evaluation of a new quadrangular thin plate bending element", *International Journal of Numeral Method Engineering*, vol.18, pp.1655-1677

Bažant, Z.P. & Nelson, A.H (1982) *Finite Element Analysis of Reinforced Concrete*, American Society of Civil Engineers, New York

Bažant, Z.P. & Kaplan, M.F. (1996) *Concrete at High Temperatures: Material Properties and mathematical Models*, Longman Group Ltd, Essex, England

Bažant, Z.P. (1997) "Analysis of pore pressure, thermal stresses and fracture in rapidly heated concrete", *Proceeding of International Workshop on Fire Performance of High-Strength Concrete*, *NIST Special Publication 919*, National Institute of Standards and Technology, Gaithersburg, Md., pp.144-164

BEF (2003) *Hollow Core Slabs and Fire – Joint Reinforcement Guideline (fire)* (in Danish), Betonelement-Foreningen (Danish Prefab Concrete Association), Denmark

BEF (2004) Test Report, File No: PG11304, Serial No.: 9856, Betonelement-Foreningen (Danish Prefab Concrete Association), 22 Nov 2004 (http:\\betonfr.inforce.dk/graphics/betonelementforeningen/html_pdf_xls_lign_docs/PG11304_pdf.pdf)

BEF (2005) *Hollow Core Slabs and Fire – Documentation on Shear Capacity*, Birch & Krogboe A/S, Copenhagen

Bennetts, I.D. (1981), *Elevated Temperature Behaviour of Concrete and Reinforcing Steel, Report No. MRL/PS23/81/001*, BHP Melbourne Research Laboratories, Clayton, Victoria, Australia

Bernhart, D. (2004) *The effect of support conditions on the fire resistance of a reinforced concrete beam*, Fire Engineering Research Project, University of Canterbury, NZ

BIA (1992) *Building Regulations*, Building Industry Authority, Wellington

Blundell, R., Diamond C. & Browne, R.G.. (1976) *The Properties of Concrete Subjected to Elevated Temperatures*, Technical note No.9, CIRIA Underwater Engineering Group, London, UK

Bobrowski J. (ed) (1978), *Design and Detailing of Concrete Structures for Fire Resistance, Interim Guidance by a Joint Committee of the Institution of Structural Engineers and the Concrete Society*, The Institution of Structural Engineers, London

Browne R.D. (1972) "Thermal movement of concrete", *Concrete*, Vol.6, No.11, pp.51-53

Brockenbrough R.L. & Johnston, B.G. (1968), *USS Steel Design*, United States Steel Corporation, Pittsburgh PA

BSI (1980) *BS 5896:1980 Specification for High Tensile Steel Wire and Strand for the Prestressing of Concrete*, British Standards Institution, London

Buchanan, A.H (2001) *Structural Design for Fire Safety*, John Wiley & Sons, West Sussex, England

Carlson, C.C., Selvaggio S.L & Gustaferro A.H. (1965) "A review of studies of the effects of restraint on the fire resistance of prestressed concrete", *Proceedings of Symposium on Fire Resistance of Prestressed Concrete*, International Federation for Prestressing, Bauverlag GmbH, Germany. Reprinted as PCA Research Department Bulletin, 1965: 206.

Carman A, P. & Nelson, R.A. (1921) "The thermal conductivity and diffusivity of concrete", *Bulletin No.122*, University of Illinois Engineering Experiment Station, Urbana-Champaign

CEN/TC299 (2005) *Precast Concrete Products – Hollow Core Slabs*, EN1168:2005, European Committee for Standardization, Brussels

Chen, W.F. (1982) *Plasticity in Reinforced Concrete*, McGraw-Hill, New York

Connolly, R. (1995) *The Spalling of Concrete in Fires*, Thesis (PhD), University of Aston

Connolly, R. (1997) "The spalling of concrete", *Fire Engineers Journal*, v 57, n 186, p 38-40

Crisfield, M.A. (1981) "A fast incremental/iterative solution procedure that handles 'snap-through'", *Computers & Structures*, Vol.13, pp.55-62

Cruz, C.R. (1966) "Elastic properties of concrete at high temperature", *Journal of the Portland Cement Association Research and Development Laboratory (PCA Bulletin 191)*

Cruz, C.R. & Gillen, M. (1980) "Thermal expansion of Portland cement paste, mortar and concrete at high temperatures", *Fire and materials*, Vol.4, No.2, pp.66-70

Davies, G., Elliott, K.S., & Omar, W. (1990) "Horizontal diaphragm action in precast concrete floors", *The Structural Engineer*, Vol. 68, no.2, pp. 25-33

Diederichs, U., Jumppanen, U.M. & Penttala, V. (1988) "Material properties of high strength concrete at elevated temperatures", *Transactions*, 13th IABSE Congress, Helsinki, Finland, pp.489-494

Diederichs, U., Jumppanen, U.M. & Penttala, V. (1989) *Behaviour of High-Strength Concrete at High Temperatures*, *Report No. 92*, Helsinki University of Technology, Helsinki, Finland

DIFT (2004), *Test report*, *File no. PG11304*, DIFT, Denmark

Doneux, C. & Franssen, J.M. (2003) *2D Constitutive Models for the Shell Element of*

the Finite Element Software SAFIR, M&S Report 2003 (translation of Rapport Interne – SPEC/97_01), Department Mécanique des Matériaux et Structures, University of Liège, Belgium

Dotreppe, J-C. & Van Acker, A. (2002) "Shear resistance of precast prestressed hollow core slabs under fire conditions", *The First fib Congress*, Japan, pp.149-158

Dotreppe, J-C. & Franssen, J-M. (2004) "Precast hollow core slabs in fire: numerical simulations and experimental tests", *Third International Workshop "Structures in Fire"*, Ottawa, Canada, May 2004, paper S5-1

EC1 (2002) Eurocode 1: Actions on structures. PrEN 1991-1-2: Actions on structures exposed to fire, European Committee for Standardization, Brussels

EC2 (1995) Eurocode 2: Design of concrete structures. *ENV 1992: Part1-2: General rules- Structural fire design*, European Committee for Standardization, Brussels

EC2 (2002) Eurocode 2: Design of concrete structures. *prEN 1992-1-2: General rules- Structural fire design*, European Committee for Standardization, Brussels

EC3 (2002) Eurocode 3: Design of steel structures. *prEN 1993-1-2: General rules- Structural fire design*, European Committee for Standardization, Brussels

Ehm, C., Schneider, U. (1985) "The high temperature behaviour of concrete under biaxial conditions", *Cement and Concrete Research*, Vol.15, pp. 27-34

Elliott, K. & Davies, G. (1990) "Analysis of floor joints between precast concrete hollow core units in a floor diaphragm", *The Structural Engineer*, Vol.68, no.2, pp.175-187

Feasey, R. & Buchanan, A.H. (2002) "Post-flashover fires for structural design", *Fire Safety Journal*, Vol. 37, pp.83-105

FEB-CIP, 1994, "Application of high-performance concrete", *Bulletin d'Information No.222*, CEB-FIP, Paris

FeBe Studiecommissie SSTC (1998) *Résistance au Cisaillement de Dalles Alveolées Précontraintes*, Laboratorium voor Aanwending der Brandstoffen en Warmteoverdracht, Belgium

Felicetti, R. & Gambarova, P.G. (1998) "Effects of high temperature on the residual compressive strength of high-strength siliceous concretes", *ACI Materials Journal*, Vol 95, issue 4, pp.395-406

Fellinger J.H.H. (2000) *Shear and Anchorage Behaviour of Fire Exposed Hollow Core Slabs, Test report: Fire tests on bare hollow core units*, TNO report 2000-VB-R001147-TUDelft report 25.5-00-5, Delft

Fellinger J.H.H (2004) *Shear and Anchorage Behaviour of Fire Exposed Hollow Core Slabs*, DUP Science, the Netherlands

Fib (1999) *Structural Concrete, Textbook on Behaviour, Design and Performance*, fib manual, Bulletin 1, Fédération Internationale du Béton, Lausanne, Switzerland

Fib (2000) *Special Design Considerations for Precast Prestressed Hollow Core Floors – Guide to Good Practice Prepared by Fib Commission 6- Prefabrication*, Fédération Internationale du Béton, Lausanne, Switzerland

Fib (2001) *FIP Commission on Prefabrication Shear resistance of prestressed hollow core floors exposed to fire*, Fédération Internationale du Béton, Lausanne, Switzerland

FINELG (1984) *Nonlinear Finite Element Analysis Program – User's Manual Version 6.2*, MSM Department, University of Liège, Belgium

FIP (1978) FIP Commission on fire resistance of prestressed concrete structures, *FIP/CEB Report on methods of assessment of the fire resistance of concrete structural members*, Fédération Internationale de la Précontrainte by the Cement and Concrete Association, Wexham Springs

FIP (1987) *Precast Prestressed Hollow Core Floors*, Thomas Telford Ltd, London

Firth Stresscrete & Stahlton Flooring (2007), *Precast Concrete Manual 2007*, Firth Stresscrete, Porirua, NZ

Franssen, J.M. (1987) *Etude du Comportement au Feu des Structures Mixtes Acier-Béton*, Thesis (PhD), University of Liège, Belgium

Franssen, J.M (2001) *How to Go to 3D Updated by Franssen*, unpublished document last modified in 1 March 2001.

Franssen, J.M., Kodur, V.K.R. & Mason, J. (2002a) *User's Manual for SAFIR2001 Free : A Computer Program for Analysis of Structures at Elevated Temperature Conditions*, Service Ponts et Charpentes, Department Structures du Génie Civil, University of Liège, Belgium

Franssen, J.M., Kodur, V.K.R. & Mason, J. (2002b) *Elements of Theory for SAFIR2001 Free : A Computer Program for Analysis of Structures at Elevated Temperature Conditions*, Service Ponts et Charpentes, Department Structures du Génie Civil, University of Liège, Belgium

Franssen, J.M. (2004) <jm.franssen@ulg.ac.be> *Re: Hollowcore*, Private email message to Andrew Buchanan, 17 August 2004

Gustaferro, A.H. & Martin, L.D. (1989) *Design for Fire Resistance of Precast Prestressed Concrete*, 2nd Ed., Prestressed Concrete Institute, Illinois, USA

Gustaferro, A.H. (1970) "Temperature Criteria at Failure," *Fire Test Performance, ASTM STP 464*, American Society for Testing and Materials, pp. 68-84

Hambly, E.C. (1991) *Bridge Deck Behaviour*, 2nd Ed., E & FN Spon, London; New York

Harmathy, T.Z. (1970) "Thermal properties of concrete at elevated temperatures", *ASTM Journal of Materials*, Vol.5, Issue 1, pp. 47-74

Harmathy, T.Z. (1993) *Fire Safety Design of Concrete*, Longman Scientific & Technical, Essex, England

Harmathy, T.Z. & Berndt, J.E. (1966) "Hydrated Portland cement and light weight concrete at elevated temperatures", *Journal of the American Concrete Institute*, Vol.63, No.1, pp. 93-112

Harmathy, T.Z. & Stanzak, W.W. (1970) "Elevated-temperature tensile and creep properties of some structural and prestressing steels", *Fire Test Performance, ASTM STP 464*, American Society for Testing and Materials, Philadelphia, PA. pp. 186

Hertz, K. (1982) "The anchorage capacity of reinforcing bars at normal and high temperatures", *Magazine of Concrete Research*, Vol. 34, No.121, pp.213-220

Hertz, K.D. (2003) "Limits of spalling of fire-exposed concrete", *Fire Safety Journal*, vol. 38, pp. 103-116

Hietanen, T. (1992) *Fire Tests For Finnish Hollow Core Slabs*, Association of the Concrete Industry Finland, Finland (confidential)

Hietanen, T. (2005) "Actual state of the codes on fire design in Europe", *Proceedings of the Workshop Fire Design of Concrete Structures: What now? What Next?*, Milan, Italy, 2005, pp.21-24

Holmes, M. Anchor, R.D., Cook, G.M.E. & Crook, R.N. (1982) "The effects of elevated temperatures on the strength properties of reinforcing and prestressing steels", *The Structural Engineer*, Vol.60B, No.1, p.7-13

Huang, Z. Burgess, I.W. & Plank, R.J. (2006) "Behaviour of Reinforced Concrete Structures in Fire", *4th international Workshop Structures in Fire*, Aveiro, Portugal, 2006, pp. 561-572

Institution of Structural Engineers (1975) *Fire Resistance of Concrete Structures*, Report of a Joint Committee of the Institution of Structural Engineers and the Concrete Society, London

ISO 834 (1999) *Fire Resistance Test – Elements of Building Construction*, International Organization for Standardization, Geneva

Jetteur, P. (1985) *Non-Linear Shell Elements Based on Marguerre Theory: IREM Internal Report 85/5*, Swiss Federal Institute of Technology, Lausanne, Switzerland

Kani, G. N. J. (1964). "The riddle of shear failure and its solution", *ACI Journal*, Vol. 61, No. 4, pp. 441-467.

Kirby, B.R. & Preston, R.R. (1988), "High temperature properties of hot-rolled structural steels for use in fire engineering design studies", *Fire Safety Journal*, Vol. 13, pp. 27-37

Kordina, K., Ehm, C. & Schneider, U. (1985) "Effect of biaxial loading on the high temperature behaviour of concrete", *Proceedings of the first Symposium of Fire Safety Science*, Gaithersburg, 1985, pp. 281-290

Khoury, GA., Grainger, B.N. & Sullivan, P.J.E. (1985a) "Transient thermal strain of concrete: literature review, conditions within specimen and behaviour of individual constituents", *Magazine of Concrete Research*, Vol.37, No.132, pp.131-144

Khoury, GA., Grainger, B.N. & Sullivan, P.J.E. (1985b) "Strain of concrete during first heating to 600^{o}C under load", *Magazine of Concrete Research*, Vol.37, No.133, pp.195-215

Khoury, GA., Grainger, B.N. & Sullivan, P.J.E. (1986) "Strain of concrete during first cooling from 600^{o}C under load", *Magazine of Concrete Research*, Vol.38, No.134, pp.3-12

Kirby, B.R. & Preston, R.R. (1988) "High temperature properties of hot-rolled, structural steels for use in fire engineering design studies", *Fire Safety Journal*, Vol. 13, No.1, pp.27-37

Lane, W.P. (2005) *Ignition, Charring and Structural Performance of Laminated Veneer Lumber*, Fire Engineering Research Project, University of Canterbury, NZ

Law, M. (1971) “A relationship between fire grading and building design and contents”, *Fire Research Note No.877*, Fire Research station, UK

Lennon, T. (2003) “Precast Hollowcore slabs in fire”, *The Structural Engineer* Vol. 81 No. 8, pp. 30-35

Lim, L. (2003) *Membrane action in fire exposed concrete floor systems*, Thesis (PhD), University of Canterbury, New Zealand

Lim, L., Buchanan, A.H., Moss, P.J. & Franssen, J.M. (2004), “Numerical modelling of two-way reinforced concrete slabs in fire”, *Engineering Structures*, v26, pp.1081-1091

Lindsay, R. (2004), *Experiments on the Seismic Performance of Hollow-Core Floor Systems in Precast Concrete Buildings*, ME Thesis, University of Canterbury, NZ

Livesley, R.K. (1964), *Matrix Methods of Structural Analysis*, Pergamon Press Ltd, Oxford

MacPherson, C. (2005), *Seismic Performance and Forensic Analysis of a Precast Concrete Hollow-Core Floor Super-Assemblage*, ME Thesis, University of Canterbury, NZ

Maréchal, J.C. (1972) “Creep of concrete as a function of temperature”, *International Seminar on Concrete for Nuclear Reactors, ACI Special Publication* No.34, Vol.1, American Concrete Institute, Detroit, pp.547-564

Martin, L.D. & Perry, C.J. (ed.) (2004), *PCI Design Handbook - Precast and Prestressed Concrete*, 6th Ed., Precast/Prestressed Concrete Institute, Chicago

Matthews, J. (2004) *Alternative Load Paths for Floor Diaphragm Forces Following Severe Damage to the Supporting Beams*, Thesis (PhD), University of Canterbury, New Zealand

Messershmidt, F.V. (1994) *Eksplosion og afskalnign af brandpåvirket beton*, Student Report, Department of Buildings and Energy, Technical University of Denmark, Denmark

Meyer-Ottens, C., (1974a) „Verhalten von Betonbauteilen im Brandfall“, *Beton*, vol. 24, issue 4, pp. 133-136

Meyer-Ottens, C., (1974b) „Verhalten von Betonbauteilen im Brandfall“, *Beton*, vol. 24, issue 5, pp. 175-178

Micelli, F., Mariacongedo, P. & De Lorenzis, L. (2000) *Fire Resistance of Prestressed Concrete Hollow Core Panels*, internal report, Innovation Engineering Department, University of Lecce, Italy

Micelli, F., Mariacongedo, P. & De Lorenzis, L, (2005) last modified 8 July 2005, *Resistenza al fuoco di pannelli cavi in calcestruzzo precompresso*, Centro Ricerca Energia e Ambiente, Dipartimento di Ingegneria Dell'innovazione, Università degli Studi di Lecce, accessed 17 February 2006, <http://www.crea.unile.it/ricerca/progetti/progetto_04.html>

Mindess, S. & Young, J.F. (1981) *Concrete*. Prentice-Hall Inc., New Jersey. U.S.A.

Nechnech, W. (2000) *Contribution à l'Etude Numérique du Comportement du Béton et des Structures en Béton Armé Soumises à des Sollicitations Thermiques et Mécaniques Couplées : Une Approche Thermo-Elasto-Plastique Endommageable*, Thesis (PhD), L'Institut National des Sciences Appliquées de Lyon, France

Neville A.M. (1990) *Properties of concrete*, Longman scientific and technical, London

O'Brien, E.J. & Keogh, D.L.(1999), *Bridge Deck Analysis*, E & FN Spon, London

Oh, B.H., Kim, E.S. & Choi, Y.C. (2006) "Theoretical analysis of transfer lengths in pretensioned prestressed concrete members", *Journal of Engineering Mechanics*, Vol. 132, Issue 10, pp.1057-1066

Pajari, M. & Koukkari, H. (1998) “Shear resistance of PHC slabs supported on beams, Part 1, Tests”, *ASCE Journal of Structural Engineering*, pp. 1050-1061

Park, R. & Pauley, T. (1975) *Reinforced Concrete Structures*, John Wiley & Sons, USA

Petrov-Denisov, V.G., Maslennikov, LA. & Pitckob, A.M. (1972) “Heat and moisture transport during drying and first heating of heat resistant concrete” (in Russian), Бетон и Железобетон, vol.2, pp. 17-18

Phan, L. (2005) “Codes and standards for fire safety design of concrete structures in the U.S.”, *Proceedings of the Workshop Fire Design of Concrete Structures: What now? What Next?*, Milan, 2005, pp.25-34

Rostásy, F.S. & Budelmann H, (1986) “Strength and deformation of concrete with variable content of moisture at elevated temperature up to 90°C”, *Cement and Concrete Research*, Vol.16, Issue 3, pp. 353-362

Sager, H. (1985) *About the Influence of Elevated Temperature on the Bond Behaviour of Reinforcement in Concrete* (in German) Heft 68, iBMB, Braunschweig UT, Braunschweig, Germany

Salse, E.A.B. & Gustaferro, A.H. (1971) “Structural capacity of concrete beams during fires as affected by restraint and continuity”, *Proceedings of 5th CIB Congress*, Paris, France

Schneider, U. (1976) “Behaviour of concrete under thermal steady state and non-steady state conditions”, *Fire and Material*, vol.1, issue 3, pp. 103-115

Schneider, U. (1982) *Verhalten von Beton bei hohen temperaturen*, DAfStb Heft 337, Ernst & Sohn, Berlin

Schneider, U. (1985) *Properties of Materials at High Temperatures - Concrete*, RILEM Committee, 44- PHT. GhK, Kassel, Germany

Schneider, U. (1988) “Concrete at high temperatures: A general review”, *Fire Safety Journal*, 1988, vol. 13, pp. 55-68

Schneider, U., Kersken-Bradley, M., and Max, U. (1990) *Neuberechnung der Wärmeabzugsfaktoren für die DINV 18320 Teil-Baulicher Brandschutz Industribau* [in German]. Arbeitsgemeinschaft Brandsicherheit Munchen/Kassel

Shellers, H. & Pulay, P. (1984), “The adiabatic correction to molecular potential surfaces in the SCF approximation”, *Chemical Physics Letters*, vol. 103, No. 6, pp. 463-5

Simmons, W.F. & Cross, H.C.,(1955) *Elevated Temperature Properties of Carbon Steels, ASTM STP 180*, American Society for Testing Materials, Philadelphia PA.

SNZ (1991) “MP9: fire properties of building materials and elements of structure”, *Miscellaneous Publication No.9*. Standards New Zealand, Wellington, NZ

SNZ (1995) NZS 3101:1995, *The Design of Concrete Structures*, Standards New Zealand, Wellington, NZ

SNZ (2004) NZS 3101:1995, *Amendment No. 3 to 1995 Standard NZS3101*, Standards New Zealand, Wellington, NZ

SNZ (2006a) NZS 3101:Part 1:2006, *The Design of Concrete Structures*, Standards New Zealand, Wellington, NZ

SNZ(2006b) NZS3101:Part 2:2006, *Commentary on The Design of Concrete Structures*, Standards New Zealand, Wellington, NZ

Standards Australia & SNZ (2002) *AS/NZS 1170:2002 Structural Design Actions*, Standards New Zealand, Wellington

Standards Australia (2005a) *AS 1530 part 4 Methods for Fire Tests on Building Materials, Components and Structures – Fire-resistance Tests of Elements of Building Construction*, Standards Australia, Sydney, New South Wales

Standards Australia (2005b), *Concrete Structures- Draft Australian Standard to be AS3600-200x*, Committee-BD-002-Concrete Structures, Standards Australia, Sydney, New South Wales

Talamona, D. & Franssen, J.M. (2002-2003) "Nonlinear thin shell finite element for steel and concrete structures subjected to fire: theoretical development", *Journal of Applied Fire Science*, Vol.11, n.4, pp. 291-310

Talamona, D., Castagne, S. & Franssen, J.M. (2003-2004) "Nonlinear this shell finite element for steel and concrete structures subjected to fire: verification and validation", *Journal of Applied Fire Science*, Vol.12, n.1, pp.65-81

Terrin, M (1980) « Emission acoustique et comportement mécanique post-critique d'un béton sollicité en traction », *Bulletin de Liaison des Ponts et Chaussées*, no.105, pp 65-72

Thelandresson, S. (1987) "Modelling of combined thermal and mechanical action in concrete", *Journal of Engineering Mechanics*, vol113, pp. 893-906

US Army Corps of Engineers (1988) Standard CRD-C36-48. *Handbook for Concrete and Cement*, Vicksburg, Mississippi, USA

Van Acker, A. (2003) "Shear resistance of prestressed hollow core floors exposed to fire", *Structural Concrete- Journal of the fib*, vol 4, pp. 65-74

Weigler, H. & Fisher, R. (1967) „Beton bei Temperaturen von 100^{o}C bis 750^{o}C", p.87 ff., *Mehmel-Festschrift, Beton-Verlag*, GmbH, Dusseldorf

West, R.(1973a), *The Use of a Grillage Analogy for the Analysis of Slab and Pseudo-Slab Bridge Decks*, research report 21, Cement and Concrete Association, Bristol, England

West, R.(1973b), *C&CA/CIRIA Recommendations on the Use of Grillage Analysis for Slab and Pseudo-Slab Bridge Decks*, Cement and Concrete Association, London

Zoldners, N.F. (1971) “Thermal properties of concrete under sustained elevated temperatures”, *Temperature and Concrete*, *ACI Special Publication No. 25*, Paper SP 25-1. American Concrete Institute, Detroit, pp.1-31

Zhukov, V.V. (1976) “Reasons for explosive deterioration of concrete during fire”, *Concrete and Reinforced Concrete* (in Russian), Бетон и Железобетон, vol 3, pp.26-28

Appendix A SAFIR INPUT FILES

A.1. Sample Thermal Analysis Input File for Beam Elements

The sample file given below runs in SAFIR2004 to model the web in the 300DYCORE unit as shown in Figure A-1.

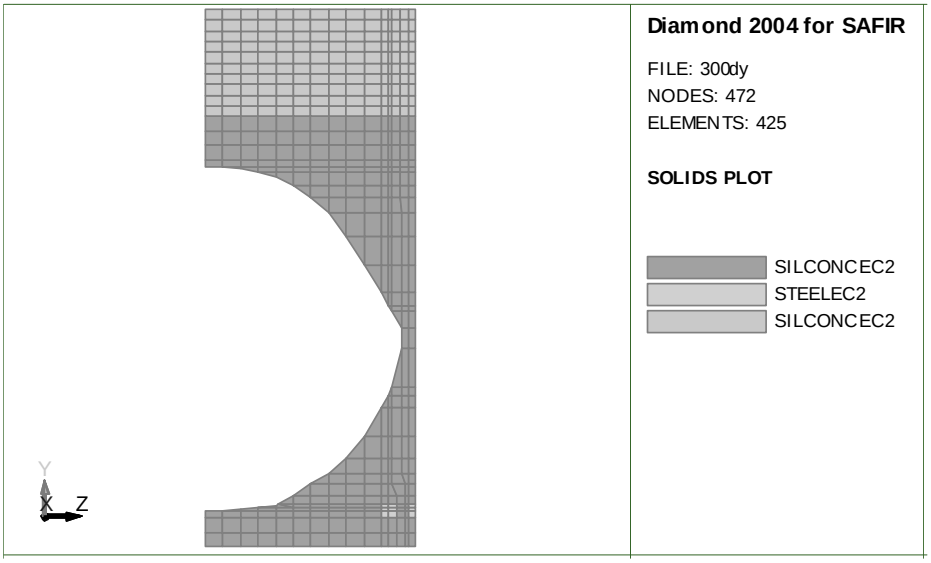

Figure A-1 Mesh of the web in 300DYCORE

```
WEB OF 300DYCORE unit

    NPTTOT          1
     NNODE  472
      NDIM    2
 NDIMMATER    1
   NDDLMAX    1
   EVERY_NODE 1
  END_NDDL
  TEMPERAT
      TETA      0.90
  TINITIAL        20
  MAKE.TEM
 LARGEUR11     7069
 LARGEUR12      1
   NORENUM
 300dyA.TEM
      NMAT    3
  ELEMENTS
     SOLID  425
        NG    2
     NVOID    1
     FRTIERVOID 28
  END_ELEM

 NODES
  NODE     1   -0.1530   0.0000
  GNODE   11   -0.1530   0.1220  1
  NODE    12   -0.1530   0.1270
  NODE    13   -0.1530   0.1320
  NODE    14   -0.1530   0.1380
  NODE    15   -0.1530   0.1410
  NODE    16   -0.1530   0.1460
  REPEAT  16    0.0100   0.0000  2
  REPEAT  16    0.0050   0.0000  1
  NODE    65   -0.1272   0.0244
  NODE    66   -0.1257   0.0366
  GNODE   73   -0.1257   0.1220  1
  NODE    74   -0.1257   0.1270
  NODE    75   -0.1257   0.1320
  NODE    76   -0.1257   0.1380
  NODE    77   -0.1257   0.1410
  NODE    78   -0.1257   0.1460
  NODE    79   -0.1242   0.0488
  NODE    80   -0.1230   0.0508
  NODE    81   -0.1230   0.0610
  GNODE   86   -0.1230   0.1220  1
  NODE    87   -0.1230   0.1270
  NODE    88   -0.1230   0.1320
  NODE    89   -0.1230   0.1380
  NODE    90   -0.1230   0.1410
  NODE    91   -0.1230   0.1460
  NODE    92   -0.1169   0.0610
  GNODE   97   -0.1169   0.1220  1
  NODE    98   -0.1169   0.1270
  NODE    99   -0.1169   0.1320
  NODE    100  -0.1169   0.1380
  NODE    101  -0.1169   0.1410
  NODE    102  -0.1169   0.1460
  NODE    103  -0.1091   0.0732
  GNODE   107  -0.1091   0.1220  1
  NODE    108  -0.1091   0.1270
  NODE    109  -0.1091   0.1290
  NODE    110  -0.1091   0.1380
  NODE    111  -0.1091   0.1410
  NODE    112  -0.1091   0.1460
```

```
NODE    113 -0.1016   0.0854
GNODE   116 -0.1016   0.1220  1
NODE    117 -0.1016   0.1270
NODE    118 -0.1016   0.1290
NODE    119 -0.1016   0.1360
NODE    120 -0.1016   0.1410
NODE    121 -0.1016   0.1460
NODE    122 -0.0913   0.0976
GNODE   124 -0.0913   0.1220  1
NODE    125 -0.0913   0.1270
NODE    126 -0.0913   0.1290
NODE    127 -0.0913   0.1360
NODE    128 -0.0913   0.1410
NODE    129 -0.0913   0.1460
NODE    130 -0.0763   0.1098
NODE    131 -0.0763   0.1220
NODE    132 -0.0763   0.1270
NODE    133 -0.0763   0.1290
NODE    134 -0.0763   0.1360
NODE    135 -0.0763   0.1410
NODE    136 -0.0763   0.1460
NODE    137 -0.0563   0.1220
NODE    138 -0.0563   0.1270
NODE    139 -0.0563   0.1290
NODE    140 -0.0563   0.1360
NODE    141 -0.0563   0.1410
NODE    142 -0.0563   0.1460
NODE    143 -0.0470   0.1270
NODE    144 -0.0470   0.1290
NODE    145 -0.0470   0.1360
NODE    146 -0.0470   0.1410
NODE    147 -0.0470   0.1460
NODE    148 -0.0420   0.1290
NODE    149 -0.0420   0.1360
NODE    150 -0.0420   0.1410
NODE    151 -0.0420   0.1460
NODE    152 -0.0150   0.1360
NODE    153 -0.0150   0.1410
NODE    154 -0.0150   0.1460
REPEAT    3  0.0150   0.0000  1
NODE    158  0.0120   0.1290
NODE    159  0.0120   0.1360
NODE    160  0.0120   0.1410
NODE    161  0.0120   0.1460
NODE    162  0.0150   0.1270
NODE    163  0.0150   0.1290
NODE    164  0.0150   0.1360
NODE    165  0.0150   0.1410
NODE    166  0.0150   0.1460
NODE    167  0.0240   0.1220
NODE    168  0.0240   0.1270
NODE    169  0.0240   0.1290
NODE    170  0.0240   0.1360
NODE    171  0.0240   0.1410
NODE    172  0.0240   0.1460
NODE    173  0.0440   0.1098
NODE    174  0.0440   0.1220
NODE    175  0.0440   0.1270
NODE    176  0.0440   0.1290
NODE    177  0.0440   0.1360
NODE    178  0.0440   0.1410
NODE    179  0.0440   0.1460
NODE    180  0.0631   0.0976
GNODE   182  0.0631   0.1220  1
NODE    183  0.0631   0.1270
NODE    184  0.0631   0.1290
```

```
  NODE     185  0.0631   0.1360
  NODE     186  0.0631   0.1410
  NODE     187  0.0631   0.1460
  NODE     188  0.0796   0.0854
  GNODE    191  0.0796   0.1220  1
  NODE     192  0.0796   0.1270
  NODE     193  0.0796   0.1290
  NODE     194  0.0796   0.1360
  NODE     195  0.0796   0.1410
  NODE     196  0.0796   0.1460
  NODE     197  0.0912   0.0732
  GNODE    201  0.0912   0.1220  1
  NODE     202  0.0912   0.1270
  NODE     203  0.0912   0.1290
  NODE     204  0.0912   0.1350
  NODE     205  0.0912   0.1410
  NODE     206  0.0912   0.1460
  NODE     207  0.0992   0.0610
  GNODE    212  0.0992   0.1220  1
  NODE     213  0.0992   0.1270
  NODE     214  0.0992   0.1290
  NODE     215  0.0992   0.1350
  NODE     216  0.0992   0.1410
  NODE     217  0.0992   0.1460
  NODE     218  0.1045   0.0488
  NODE     219  0.1083   0.0366
  GNODE    226  0.1083   0.1220  1
  NODE     227  0.1083   0.1270
  NODE     228  0.1083   0.1290
  NODE     229  0.1083   0.1350
  NODE     230  0.1083   0.1410
  NODE     231  0.1083   0.1460
  NODE     232  0.1107   0.0244
  NODE     233  0.1120   0.0000
  GNODE    243  0.1120   0.1220  1
  NODE     244  0.1120   0.1270
  NODE     245  0.1120   0.1290
  NODE     246  0.1120   0.1350
  NODE     247  0.1120   0.1410
  NODE     248  0.1120   0.1460
  REPEAT   16   0.0050   0.0000  1
  REPEAT   16   0.0100   0.0000  3
  REPEAT   16   0.0075   0.0000  10
  NODELINE       0.0000   0.1460
  YC_ZC          0.0000   0.1460

 FIXATIONS
 END_FIX

NODOFSOLID
  ELEM     1      1   2  18  17  1  0
  GELEM    15    15  16  32  31  1  0 1
  REPEAT   15    16                    2
  ELEM     46    50  51  65   0  1  0
  ELEM     47    51  52  66  65  1  0
  GELEM    59    63  64  78  77  1  0 1
  ELEM     60    66  67  79   0  1  0
  ELEM     61    67  68  80  79  1  0
  ELEM     62    80  68  81   0  1  0
  ELEM     63    68  69  82  81  1  0
  GELEM    72    77  78  91  90  1  0 1
  ELEM     73    80  81  92   0  1  0
  ELEM     74    81  82  93  92  1  0
  GELEM    83    90  91 102 101  1  0 1
  ELEM     84    92  93 103   0  1  0
  ELEM     85    93  94 104 103  1  0
```

```
GELEM   93  101 102 112 111  1  0 1
ELEM    94  103 104 113   0  1  0
ELEM    95  104 105 114 113  1  0
GELEM  102  111 112 121 120  1  0 1
ELEM   103  113 114 122   0  1  0
ELEM   104  114 115 123 122  1  0
GELEM  110  120 121 129 128  1  0 1
ELEM   111  122 123 130   0  1  0
ELEM   112  123 124 131 130  1  0
GELEM  117  128 129 136 135  1  0 1
ELEM   118  130 131 137   0  1  0
ELEM   119  131 132 138 137  1  0
GELEM  123  135 136 142 141  1  0 1
ELEM   124  137 138 143   0  1  0
ELEM   125  138 139 144 143  1  0
GELEM  128  141 142 147 146  1  0 1
ELEM   129  143 144 148   0  1  0
ELEM   130  144 145 149 148  1  0
GELEM  132  146 147 151 150  1  0 1
ELEM   133  148 149 152   0  1  0
ELEM   134  149 150 153 152  1  0
ELEM   135  150 151 154 153  1  0
ELEM   136  152 153 156 155  1  0
ELEM   137  153 154 157 156  1  0
ELEM   138  155 159 158   0  1  0
ELEM   139  155 156 160 159  1  0 1
ELEM   140  156 157 161 160  1  0
ELEM   141  158 163 162   0  1  0
ELEM   142  158 159 164 163  1  0
GELEM  144  160 161 166 165  1  0 1
ELEM   145  162 168 167   0  1  0
ELEM   146  162 163 169 168  1  0
GELEM  149  165 166 172 171  1  0 1
ELEM   150  167 174 173   0  1  0
ELEM   151  167 168 175 174  1  0
GELEM  155  171 172 179 178  1  0 1
ELEM   156  173 181 180   0  1  0
ELEM   157  173 174 182 181  1  0
GELEM  162  178 179 187 186  1  0 1
ELEM   163  180 189 188   0  1  0
ELEM   164  180 181 190 189  1  0
GELEM  170  186 187 196 195  1  0 1
ELEM   171  188 198 197   0  1  0
ELEM   172  188 189 199 198  1  0
GELEM  179  195 196 206 205  1  0 1
ELEM   180  197 208 207   0  1  0
ELEM   181  197 198 209 208  1  0
GELEM  189  205 206 217 216  1  0 1
ELEM   190  218 220 219   0  1  0
ELEM   191  218 207 221 220  1  0
ELEM   192  207 208 222 221  1  0
GELEM  201  216 217 231 230  1  0 1
ELEM   202  232 235 234   0  1  0
ELEM   203  232 219 236 235  1  0
ELEM   204  219 220 237 236  1  0
GELEM  215  230 231 248 247  1  0 1
ELEM   216  233 234 250 249  1  0
GELEM  230  247 248 264 263  1  0 1
REPEAT  15  16                   3
ELEM   276  297 298 314 313  3  0
GELEM  290  311 312 328 227  3  0 1
REPEAT  15   16                  9
NEW_MAT 41    2
NEW_MAT 42    2
NEW_MAT 55    2
NEW_MAT 56    2
```

```
 NEW_MAT 68    2
 NEW_MAT 69    2
 NEW_MAT 45    2
 NEW_MAT 59    2
 NEW_MAT 72    2



FRONTIER
   F       1       FISO   NO      NO      NO
  GF      15       FISO   NO      NO      NO     1
   F     311         NO   NO     F20      NO
  GF     425         NO   NO     F20      NO     1
END_FRONT

 VOID
         ELEM  31  3
         ELEM  46  3
         ELEM  47  3
         ELEM  60  3
         ELEM  61  3
         ELEM  73  3
         ELEM  84  3
         ELEM  94  3
         ELEM  103 3
         ELEM  111 3
         ELEM  118 3
         ELEM  124 3
         ELEM  129 3
         ELEM  133 3
         ELEM  136 4
         ELEM  138 3
         ELEM  141 3
         ELEM  145 3
         ELEM  150 3
         ELEM  156 3
         ELEM  163 3
         ELEM  171 3
         ELEM  180 3
         ELEM  191 1
         ELEM  190 3
         ELEM  203 1
         ELEM  202 3
         ELEM  216 1
 END_VOID

 SYMMETRY
   REALSYM    16 472
   SYMVOID    49 233 1
 END_SYM
PRECISION     0.001
MATERIALS
SILCONCEC2
92      25         9      0.7
  STEELEC2
25 9 0.5
SILCONCEC2
92      25         9      0.7

  TIME
               10.     3600.
               30.     14400.
  ENDTIME

  IMPRESSION
  TIMEPRINT
```

```
                30.     14400.
END_TIMEPR
```

A.2. Sample Thermal Analysis Input File for Shell Elements

The sample file given below runs in SAFIR2004 to model the 75mm reinforced concrete topping as shown in Figure A-2.

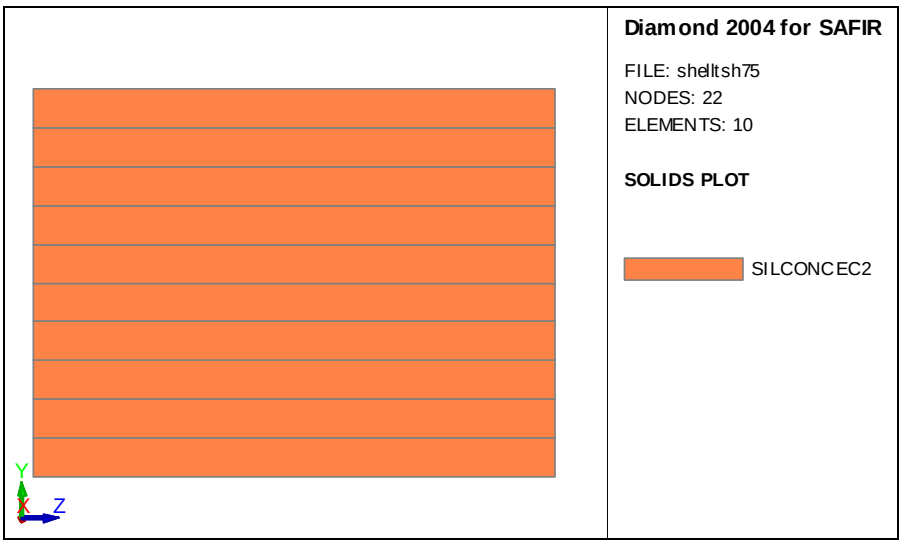

Figure A-2 Cross section of the shell element used for the 75mm topping

```
75mm RC topping on 300DYCORE

    NPTTOT   782
     NNODE   22
      NDIM    2
 NDIMMATER    1
   NDDLMAX    1
      FROM    1   TO   22 STEP    1 NDDL    1
  END_NDDL
  TEMPERAT
      TETA       0.9
  TINITIAL      20.0
  MAKE.TSH
 LARGEUR11   190
 LARGEUR12     1
   NORENUM
slab751.tsh
      NMAT    1
  ELEMENTS
     SOLID   10
        NG    2
     NVOID    0
  END_ELEM
     NODES
      NODE    1    -0.0375  -0.05
     GNODE   11     0.0375  -0.05
      NODE   12    -0.0375   0.05
     GNODE   22     0.0375   0.05
 FIXATIONS
   END_FIX
NODOFSOLID
      ELEM    1    1   12   13    2    1        0.
     GELEM   10   10   11   22   21    1        0.    1
  FRONTIER
         F         1      dy300.fct     NO          NO       NO
         F        10             NO     NO         F20       NO
 END_FRONT
  SYMMETRY
   END_SYM
 PRECISION    1.0E-3
 MATERIALS
SILCONCEC2
       92.       25.        9.      0.7
      TIME
                 30.     3600.
                 60.     14400.
   ENDTIME
   IMPRESSION
   TIMEPRINT     60.
```

A.3. Sample 3D Structural Analysis Input File

The sample file given below runs in SAFIR2002 to model the subassembly tested by MacPherson [2005] as shown in Figure A-3.

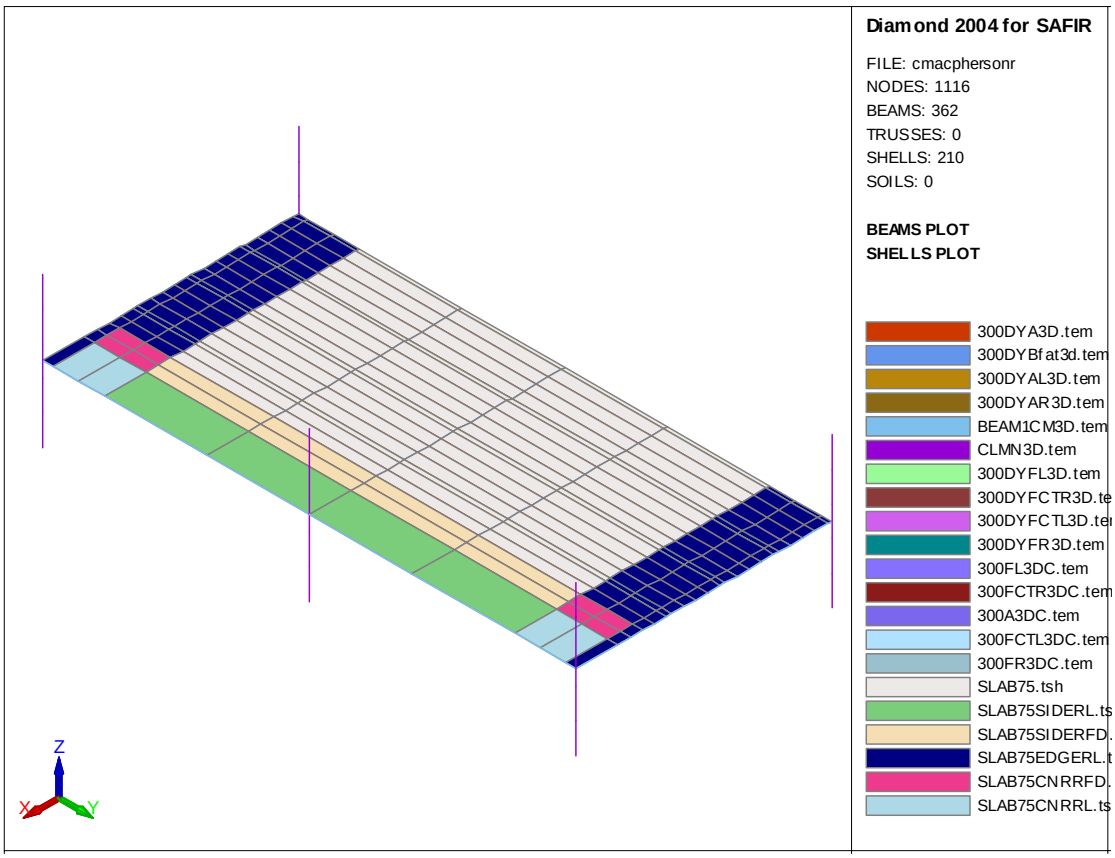

Figure A-3 Layout of the structural analysis for the subassembly from MacPherson [2005]

```
Cameron MacPherson TEST LAYOUT

    NPTTOT   421528
     NNODE   1116
      NDIM    3
 NDIMMATER    2
   NDDLMAX    7
 EVERY_NODE 0
 FROM   1    TO  17  STEP  2   NDDL  7
 FROM   2    TO  16  STEP  2   NDDL  1
 FROM   18   TO  34  STEP  2   NDDL  7
 REPEAT 18   TO  34  STEP  18  TIME  19
 FROM   19   TO  33  STEP  2   NDDL  1
 REPEAT 19   TO  33  STEP  18  TIME  19
 FROM   35   TO  377 STEP  18  NDDL  0
 FROM   378  TO  394 STEP  2   NDDL  7
 FROM   379  TO  393 STEP  2   NDDL  1
 FROM   395  TO  404 STEP  2   NDDL  7
 REPEAT  395 TO  404 STEP  10  TIME  4
 FROM   396  TO  403 STEP  2   NDDL  1
 REPEAT  396 TO  403 STEP  10  TIME  4
 FROM   404  TO  444 STEP  10  NDDL  0
 FROM   445  TO  453 STEP  2   NDDL  7
 REPEAT  445 TO  453 STEP  10  TIME  4
 FROM   446  TO  452 STEP  2   NDDL  1
 REPEAT  446 TO  452 STEP  10  TIME  4
 FROM   454  TO  494 STEP  10  TIME  0
 FROM   495  TO  503 STEP  2   NDDL  7
 REPEAT  495 TO  503 STEP  10  TIME  4
 FROM   496  TO  502 STEP  2   NDDL  1
 REPEAT  496 TO  502 STEP  10  TIME  4
 FROM   504  TO  544 STEP  10  TIME  0
 FROM   545  TO  553 STEP  2   NDDL  7
 REPEAT  545 TO  553 STEP  10  TIME  4
 FROM   546  TO  552 STEP  2   NDDL  1
 REPEAT  546 TO  552 STEP  10  TIME  4
 FROM   554  TO  594 STEP  10  TIME  0
 FROM   595  TO  596 STEP  1   NDDL  0
 FROM    597 TO  639 STEP  2 NDDL  7
 REPEAT  597 TO  639 STEP  44  TIME  1
 FROM    598 TO  638 STEP  2 NDDL  1
 REPEAT  598 TO  638 STEP  44  TIME  1
 FROM    640 TO  684 STEP  44  NDDL  0
 FROM    685 TO  724 STEP  1   NDDL  0
 FROM    725 TO  764 STEP  1   NDDL  0
 FROM    765 TO  804 STEP  1   NDDL  0
 FROM    805 TO  844 STEP  1   NDDL  0
 FROM    845 TO  884 STEP  1   NDDL  0
 FROM    885 TO  924 STEP  1   NDDL  0
 FROM    925 TO  964 STEP  1   NDDL  0
 FROM    965 TO  966 STEP  1   NDDL  0
 FROM    967 TO  975 STEP  4   NDDL  7
 REPEAT  967 TO  975 STEP  22  TIME  4
 FROM    969 TO  973 STEP  4   NDDL  1
 REPEAT  969 TO  973 STEP  22  TIME  4
 FROM    976 TO  978 STEP  2   NDDL  1
 REPEAT  976 TO  978 STEP  22  TIME  4
 FROM    977 TO  977 STEP  1   NDDL  7
 REPEAT  977 TO  977 STEP  22  TIME  4
 FROM    979 TO  987 STEP  4   NDDL  7
 REPEAT  979 TO  987 STEP  22  TIME  4
 FROM    981 TO  985 STEP  4   NDDL  1
 REPEAT  981 TO  985 STEP  22  TIME  4
 FROM    988 TO 1076 STEP  22  NDDL  0
 FROM   1077 TO 1116 STEP  1   NDDL  1
```

```
  END_NDDL
    STATIC
     NLOAD    1
   OBLIQUE    0
  COMEBACK    1E-32
NARCLENGTH
 LARGEUR11   296301
 LARGEUR12      57
  READRENUM
      NMAT    7
  ELEMENTS
      BEAM  362   15
        NG    2
    NFIBER  882
      SHELL 210   6
      NGTHICK    10
    NGAREA    2
   NREBARS    4
  END_ELEM
     NODES
  NODE  1 0.1221  -6.0000   0.0000
  REPEAT  1 0.0000  0.3000  0.000   4
  REPEAT  1 0.0000  1.2000  0.000   8
  REPEAT  1 0.0000  0.3000  0.000   4
  NODE  18  0.2288  -6.0000   0.0000
  REPEAT  1 0.0000  0.3000  0.000   4
  REPEAT  1 0.0000  1.2000  0.000   8
  REPEAT  1 0.0000  0.3000  0.000   4
  NODE  35  0.2288  -6.0000   1.0000
  REPEAT  18  0.2856  0.0000  0.000   4
  REPEAT  90  1.2500  0.0000  0.000   3
  NODE  378 6.1000  -6.0000   0.0000
  REPEAT  1 0.0000  0.3000  0.000   4
  REPEAT  1 0.0000  1.2000  0.000   8
  REPEAT  1 0.0000  0.3000  0.000   4
  NODE  395 0.2288  -4.800  0.000
  GNODE 403 1.3712  -4.800  0.000   1
  NODE  404 0.2288  -4.800  1.000
  REPEAT  10  0.0000  2.400   0.000   4
  NODE  445 1.4788  -4.800  0.000
  GNODE 453 2.6212  -4.800  0.000   1
  NODE  454 1.4788  -4.800  1.000
  REPEAT  10  0.0000  2.400   0.000   4
  NODE  495 2.7288  -4.800  0.000
  GNODE 503 3.8712  -4.800  0.000   1
  NODE  504 2.7288  -4.800  1.000
  REPEAT  10  0.0000  2.400   0.000   4
  NODE  545 3.9788  -4.800  0.000
  GNODE 553 5.1212  -4.800  0.000   1
  NODE  554 3.9788  -4.800  1.000
  REPEAT  10  0.0000  2.400   0.000   4
  NODE  595 0.0000  -6.0000   1.0000
  NODE  596 6.1000  -6.0000   1.0000

  NODE  597 0.1221  -6.2375   0.000
  NODE  598 0.1754  -6.2375   0.000
  NODE  599 0.2288  -6.2375   0.000
  GNODE 607 1.3712  -6.2375   0.000   1
  NODE  608 1.4250  -6.2375   0.000
  REPEAT  10  1.2500  0.000   0.000   2
  NODE  629 3.9788  -6.2375   0.000
  GNODE 637 5.1212  -6.2375   0.000   1
  NODE  638 5.6106  -6.2375   0.000
  NODE  639 6.1000  -6.2375   0.000
  NODE  640 6.1000  -6.2375   1.000
  REPEAT  44  0.0000  12.475  0.000   1
```

```
NODE   685 0.22880    -6.00000   -0.16875
NODE   686 0.51440    -6.00000   -0.16875
NODE   687 0.80000    -6.00000   -0.16875
NODE   688 1.08560    -6.00000   -0.16875
NODE   689 1.37120    -6.00000   -0.16875
REPEAT   5 1.25000    0.00000    0.00000    3
REPEAT   20  0.00000    12.00000   0.00000    1
REPEAT   40  0.00000    0.00000    -0.16875   1
NODE   765 0.22880    -5.50000   -0.33750
NODE   766 0.51440    -5.50000   -0.33750
NODE   767 0.80000    -5.50000   -0.33750
NODE   768 1.08560    -5.50000   -0.33750
NODE   769 1.37120    -5.50000   -0.33750
REPEAT   5 1.25000    0.00000    0.00000    3
REPEAT   20  0.00000    11.00000   0.00000    1
NODE   805 0.22880    -6.11850   -0.33750
NODE   806 0.51440    -6.11850   -0.33750
NODE   807 0.80000    -6.11850   -0.33750
NODE   808 1.08560    -6.11850   -0.33750
NODE   809 1.37120    -6.11850   -0.33750
REPEAT   5 1.25000    0.00000    0.00000    3
REPEAT   20  0.00000    12.23700   0.00000    1
NODE   845 0.22880    -6.23750   -0.33750
NODE   846 0.51440    -6.23750   -0.33750
NODE   847 0.80000    -6.23750   -0.33750
NODE   848 1.08560    -6.23750   -0.33750
NODE   849 1.37120    -6.23750   -0.33750
REPEAT   5 1.25000    0.00000    0.00000    3
REPEAT   20  0.00000    12.47500   0.00000    1
REPEAT   40  0.00000    0.00000    0.16875    1
REPEAT   40  0.00000    0.00000    -0.50625   1

NODE   965 6.10000    -6.11850    0.00000
NODE   966 6.10000     6.11850    0.00000

NODE   967 0.12210    -6.23750   -1.75000
REPEAT   1 0.00000    0.00000    0.17500    20
NODE   988 0.12210    -6.50000   -1.75000
REPEAT   22  0.00000    12.47500   0.00000    1
NODE   1011  6.10000    -6.23750   -1.75000
REPEAT   1 0.00000    0.00000    0.17500    20
NODE   1032  6.10000    -6.50000   -1.75000
REPEAT   22  0.00000    6.23750    0.00000    2

NODE   1077  0.2288   -6.1185    0.0000
NODE   1078  0.5144   -6.1185    0.0000
NODE   1079  0.8000   -6.1185    0.0000
NODE   1080  1.0856   -6.1185    0.0000
NODE   1081  1.3712   -6.1185    0.0000
NODE   1082  1.4788   -6.1185    0.0000
NODE   1083  1.7644   -6.1185    0.0000
NODE   1084  2.0500   -6.1185    0.0000
NODE   1085  2.3356   -6.1185    0.0000
NODE   1086  2.6212   -6.1185    0.0000
NODE   1087  2.7288   -6.1185    0.0000
NODE   1088  3.0144   -6.1185    0.0000
NODE   1089  3.3000   -6.1185    0.0000
NODE   1090  3.5856   -6.1185    0.0000
NODE   1091  3.8712   -6.1185    0.0000
NODE   1092  3.9788   -6.1185    0.0000
NODE   1093  4.2644   -6.1185    0.0000
NODE   1094  4.5500   -6.1185    0.0000
NODE   1095  4.8356   -6.1185    0.0000
NODE   1096  5.1212   -6.1185    0.0000
NODE   1097  0.2288   6.1185   0.0000
```

```
  NODE   1098   0.5144   6.1185   0.0000
  NODE   1099   0.8000   6.1185   0.0000
  NODE   1100   1.0856   6.1185   0.0000
  NODE   1101   1.3712   6.1185   0.0000
  NODE   1102   1.4788   6.1185   0.0000
  NODE   1103   1.7644   6.1185   0.0000
  NODE   1104   2.0500   6.1185   0.0000
  NODE   1105   2.3356   6.1185   0.0000
  NODE   1106   2.6212   6.1185   0.0000
  NODE   1107   2.7288   6.1185   0.0000
  NODE   1108   3.0144   6.1185   0.0000
  NODE   1109   3.3000   6.1185   0.0000
  NODE   1110   3.5856   6.1185   0.0000
  NODE   1111   3.8712   6.1185   0.0000
  NODE   1112   3.9788   6.1185   0.0000
  NODE   1113   4.2644   6.1185   0.0000
  NODE   1114   4.5500   6.1185   0.0000
  NODE   1115   4.8356   6.1185   0.0000
  NODE   1116   5.1212   6.1185   0.0000



FIXATIONS
  BLOCK 1    F0 NO NO NO F0 F0 NO
  BLOCK 3    F0 NO NO NO F0 F0 NO
  BLOCK 5    F0 NO NO NO F0 F0 NO
  BLOCK 7    F0 NO NO NO F0 F0 NO
  BLOCK 9    F0 NO NO NO F0 F0 NO
  BLOCK 11   F0 NO NO NO F0 F0 NO
  BLOCK 13   F0 NO NO NO F0 F0 NO
  BLOCK 15   F0 NO NO NO F0 F0 NO
  BLOCK 17   F0 NO NO NO F0 F0 NO
  BLOCK 967   F0 F0 F0 NO NO NO NO
  BLOCK 987   F0 F0 F0 NO NO NO NO
  BLOCK 989   F0 F0 F0 NO NO NO NO
  BLOCK 1009 F0 F0 F0 NO NO NO NO
  BLOCK 1011 F0 F0 F0 NO NO NO NO
  BLOCK 1031 F0 F0 F0 NO NO NO NO
  BLOCK 1033 F0 F0 F0 NO NO NO NO
  BLOCK 1053 F0 F0 F0 NO NO NO NO
  BLOCK 1055 F0 F0 F0 NO NO NO NO
  BLOCK 1075 F0 F0 F0 NO NO NO NO

  SAME   395 22   YES YES YES YES YES YES NO
  SAME   405 24   YES YES YES YES YES YES NO
  SAME   415 26   YES YES YES YES YES YES NO
  SAME   425 28   YES YES YES YES YES YES NO
  SAME   435 30   YES YES YES YES YES YES NO
  SAME   397 40   YES YES YES YES YES YES NO
  SAME   407 42   YES YES YES YES YES YES NO
  SAME   417 44   YES YES YES YES YES YES NO
  SAME   427 46   YES YES YES YES YES YES NO
  SAME   437 48   YES YES YES YES YES YES NO
  SAME   399 58   YES YES YES YES YES YES NO
  SAME   409 60   YES YES YES YES YES YES NO
  SAME   419 62   YES YES YES YES YES YES NO
  SAME   429 64   YES YES YES YES YES YES NO
  SAME   439 66   YES YES YES YES YES YES NO
  SAME   401 76   YES YES YES YES YES YES NO
  SAME   411 78   YES YES YES YES YES YES NO
  SAME   421 80   YES YES YES YES YES YES NO
  SAME   431 82   YES YES YES YES YES YES NO
  SAME   441 84   YES YES YES YES YES YES NO
  SAME   403 94   YES YES YES YES YES YES NO
  SAME   413 96   YES YES YES YES YES YES NO
  SAME   423 98   YES YES YES YES YES YES NO
```

```
SAME  433 100 YES YES YES YES YES YES NO
SAME  443 102 YES YES YES YES YES YES NO
SAME  445 112 YES YES YES YES YES YES NO
SAME  455 114 YES YES YES YES YES YES NO
SAME  465 116 YES YES YES YES YES YES NO
SAME  475 118 YES YES YES YES YES YES NO
SAME  485 120 YES YES YES YES YES YES NO
SAME  447 130 YES YES YES YES YES YES NO
SAME  457 132 YES YES YES YES YES YES NO
SAME  467 134 YES YES YES YES YES YES NO
SAME  477 136 YES YES YES YES YES YES NO
SAME  487 138 YES YES YES YES YES YES NO
SAME  449 148 YES YES YES YES YES YES NO
SAME  459 150 YES YES YES YES YES YES NO
SAME  469 152 YES YES YES YES YES YES NO
SAME  479 154 YES YES YES YES YES YES NO
SAME  489 156 YES YES YES YES YES YES NO
SAME  451 166 YES YES YES YES YES YES NO
SAME  461 168 YES YES YES YES YES YES NO
SAME  471 170 YES YES YES YES YES YES NO
SAME  481 172 YES YES YES YES YES YES NO
SAME  491 174 YES YES YES YES YES YES NO
SAME  453 184 YES YES YES YES YES YES NO
SAME  463 186 YES YES YES YES YES YES NO
SAME  473 188 YES YES YES YES YES YES NO
SAME  483 190 YES YES YES YES YES YES NO
SAME  493 192 YES YES YES YES YES YES NO
SAME  495 202 YES YES YES YES YES YES NO
SAME  505 204 YES YES YES YES YES YES NO
SAME  515 206 YES YES YES YES YES YES NO
SAME  525 208 YES YES YES YES YES YES NO
SAME  535 210 YES YES YES YES YES YES NO
SAME  497 220 YES YES YES YES YES YES NO
SAME  507 222 YES YES YES YES YES YES NO
SAME  517 224 YES YES YES YES YES YES NO
SAME  527 226 YES YES YES YES YES YES NO
SAME  537 228 YES YES YES YES YES YES NO
SAME  499 238 YES YES YES YES YES YES NO
SAME  509 240 YES YES YES YES YES YES NO
SAME  519 242 YES YES YES YES YES YES NO
SAME  529 244 YES YES YES YES YES YES NO
SAME  539 246 YES YES YES YES YES YES NO
SAME  501 256 YES YES YES YES YES YES NO
SAME  511 258 YES YES YES YES YES YES NO
SAME  521 260 YES YES YES YES YES YES NO
SAME  531 262 YES YES YES YES YES YES NO
SAME  541 264 YES YES YES YES YES YES NO
SAME  503 274 YES YES YES YES YES YES NO
SAME  513 276 YES YES YES YES YES YES NO
SAME  523 278 YES YES YES YES YES YES NO
SAME  533 280 YES YES YES YES YES YES NO
SAME  543 282 YES YES YES YES YES YES NO
SAME  545 292 YES YES YES YES YES YES NO
SAME  555 294 YES YES YES YES YES YES NO
SAME  565 296 YES YES YES YES YES YES NO
SAME  575 298 YES YES YES YES YES YES NO
SAME  585 300 YES YES YES YES YES YES NO
SAME  547 310 YES YES YES YES YES YES NO
SAME  557 312 YES YES YES YES YES YES NO
SAME  567 314 YES YES YES YES YES YES NO
SAME  577 316 YES YES YES YES YES YES NO
SAME  587 318 YES YES YES YES YES YES NO
SAME  549 328 YES YES YES YES YES YES NO
SAME  559 330 YES YES YES YES YES YES NO
SAME  569 332 YES YES YES YES YES YES NO
SAME  579 334 YES YES YES YES YES YES NO
```

```
  SAME  589 336 YES YES YES YES YES YES NO
  SAME  551 346 YES YES YES YES YES YES NO
  SAME  561 348 YES YES YES YES YES YES NO
  SAME  571 350 YES YES YES YES YES YES NO
  SAME  581 352 YES YES YES YES YES YES NO
  SAME  591 354 YES YES YES YES YES YES NO
  SAME  553 364 YES YES YES YES YES YES NO
  SAME  563 366 YES YES YES YES YES YES NO
  SAME  573 368 YES YES YES YES YES YES NO
  SAME  583 370 YES YES YES YES YES YES NO
  SAME  597 977 YES YES YES YES YES YES NO
  SAME  639 1021 YES YES YES YES YES YES NO
  SAME  641 999 YES YES YES YES YES YES NO
  SAME  386 1043 YES YES YES YES YES YES NO
  SAME  683 1065 YES YES YES YES YES YES NO
  SAME  18  599 NO  NO  NO  YES NO  NO  NO
  SAME  36  601 NO  NO  NO  YES NO  NO  NO
  SAME  54  603 NO  NO  NO  YES NO  NO  NO
  SAME  72  605 NO  NO  NO  YES NO  NO  NO
  SAME  90  607 NO  NO  NO  YES NO  NO  NO
  SAME  108 609 NO  NO  NO  YES NO  NO  NO
  SAME  126 611 NO  NO  NO  YES NO  NO  NO
  SAME  144 613 NO  NO  NO  YES NO  NO  NO
  SAME  162 615 NO  NO  NO  YES NO  NO  NO
  SAME  180 617 NO  NO  NO  YES NO  NO  NO
  SAME  198 619 NO  NO  NO  YES NO  NO  NO
  SAME  216 621 NO  NO  NO  YES NO  NO  NO
  SAME  234 623 NO  NO  NO  YES NO  NO  NO
  SAME  252 625 NO  NO  NO  YES NO  NO  NO
  SAME  270 627 NO  NO  NO  YES NO  NO  NO
  SAME  288 629 NO  NO  NO  YES NO  NO  NO
  SAME  306 631 NO  NO  NO  YES NO  NO  NO
  SAME  324 633 NO  NO  NO  YES NO  NO  NO
  SAME  342 635 NO  NO  NO  YES NO  NO  NO
  SAME  360 637 NO  NO  NO  YES NO  NO  NO
  SAME  34  643 NO  NO  NO  YES NO  NO  NO
  SAME  52  645 NO  NO  NO  YES NO  NO  NO
  SAME  70  647 NO  NO  NO  YES NO  NO  NO
  SAME  88  649 NO  NO  NO  YES NO  NO  NO
  SAME  106 651 NO  NO  NO  YES NO  NO  NO
  SAME  124 653 NO  NO  NO  YES NO  NO  NO
  SAME  142 655 NO  NO  NO  YES NO  NO  NO
  SAME  160 657 NO  NO  NO  YES NO  NO  NO
  SAME  178 659 NO  NO  NO  YES NO  NO  NO
  SAME  196 661 NO  NO  NO  YES NO  NO  NO
  SAME  214 663 NO  NO  NO  YES NO  NO  NO
  SAME  232 665 NO  NO  NO  YES NO  NO  NO
  SAME  250 667 NO  NO  NO  YES NO  NO  NO
  SAME  268 669 NO  NO  NO  YES NO  NO  NO
  SAME  286 671 NO  NO  NO  YES NO  NO  NO
  SAME  304 673 NO  NO  NO  YES NO  NO  NO
  SAME  322 675 NO  NO  NO  YES NO  NO  NO
  SAME  340 677 NO  NO  NO  YES NO  NO  NO
  SAME  358 679 NO  NO  NO  YES NO  NO  NO
  SAME  376 681 NO  NO  NO  YES NO  NO  NO



END_FIX

NODOFBEAM
```

```
300DYA3D.tem
 TRANSLATE    1    1
 TRANSLATE    2    2
 TRANSLATE    3    4
 END_TRANS
300DYBfat3d.tem
 TRANSLATE    1    1
 TRANSLATE    2    3
 TRANSLATE    3    4
 END_TRANS
300DYAL3D.tem
 TRANSLATE    1    1
 TRANSLATE    2    2
 TRANSLATE    3    4
 END_TRANS
300DYAR3D.tem
 TRANSLATE    1    1
 TRANSLATE    2    2
 TRANSLATE    3    4
 END_TRANS
BEAM1CM3D.tem
 TRANSLATE    1    7
 TRANSLATE    2    6
 END_TRANS
CLMN3D.tem
 TRANSLATE    1    7
 TRANSLATE    2    6
 END_TRANS
300DYFL3D.tem
 TRANSLATE    1    1
 TRANSLATE    2    2
 TRANSLATE    3    4
 TRANSLATE    4    6
 TRANSLATE    5    7
 END_TRANS
300DYFCTR3D.tem
 TRANSLATE    1    1
 TRANSLATE    2    2
 TRANSLATE    3    4
 TRANSLATE    4    6
 TRANSLATE    5    7
 END_TRANS
300DYFCTL3D.tem
 TRANSLATE    1    1
 TRANSLATE    2    2
 TRANSLATE    3    4
 TRANSLATE    4    6
 TRANSLATE    5    7
 END_TRANS
300DYFR3D.tem
 TRANSLATE    1    1
 TRANSLATE    2    2
 TRANSLATE    3    4
 TRANSLATE    4    6
 TRANSLATE    5    7
 END_TRANS
300FL3DC.tem
 TRANSLATE    1    1
 TRANSLATE    2    2
 TRANSLATE    3    4
 TRANSLATE    4    6
 TRANSLATE    5    7
 END_TRANS
300FCTR3DC.tem
 TRANSLATE    1    1
 TRANSLATE    2    2
```

```
 TRANSLATE    3    4
 TRANSLATE    4    6
 TRANSLATE    5    7
 END_TRANS
300A3DC.tem
 TRANSLATE    1    1
 TRANSLATE    2    2
 TRANSLATE    3    4
 END_TRANS
300FCTL3DC.tem
 TRANSLATE    1    1
 TRANSLATE    2    2
 TRANSLATE    3    4
 TRANSLATE    4    6
 TRANSLATE    5    7
 END_TRANS
300FR3DC.tem
 TRANSLATE    1    1
 TRANSLATE    2    2
 TRANSLATE    3    4
 TRANSLATE    4    6
 TRANSLATE    5    7
 END_TRANS
  ELEM  1 18  19  20  35  7
  ELEM  2 20  21  22  35  7
  ELEM  3 22  23  24  35  3
  GELEM 6 28  29  30  35  3  2
  ELEM  7 30  31  32  35  7
  ELEM  8 32  33  34  35  7
  ELEM  9 36  37  38  53  8
  ELEM  10  38  39  40  53  8
  ELEM  11  40  41  42  53  1
  GELEM 14  46  47  48  53  1  2
  ELEM  15  48  49  50  53  8
  ELEM  16  50  51  52  53  8
  ELEM  17  54  55  56  71  1
  GELEM 24  68  69  70  71  1  2
  ELEM  25  72  73  74  89  9
  ELEM  26  74  75  76  89  9
  ELEM  27  76  77  78  89  1
  GELEM 30  82  83  84  89  1  2
  ELEM  31  84  85  86  89  9
  ELEM  32  86  87  88  89  9
  ELEM  33  90  91  92  107 10
  ELEM  34  92  93  94  107 10
  ELEM  35  94  95  96  107 4
  GELEM 38  100 101 102 107 4  2
  ELEM  39  102 103 104 107 10
  ELEM  40  104 105 106 107 10
  ELEM  41  108 109 110 125 7
  ELEM  42  110 111 112 125 7
  ELEM  43  112 113 114 125 3
  GELEM 46  118 119 120 125 3 2
  ELEM  47  120 121 122 125 7
  ELEM  48  122 123 124 125 7
  ELEM  49  126 127 128 143 8
  ELEM  50  128 129 130 143 8
  ELEM  51  130 131 132 143 1
  GELEM 54  136 137 138 143 1 2
  ELEM  55  138 139 140 143 8
  ELEM  56  140 141 142 143 8
  ELEM  57  144 145 146 161 1
  GELEM 64  158 159 160 161 1 2
  ELEM  65  162 163 164 179 9
  ELEM  66  164 165 166 179 9
  ELEM  67  166 167 168 179 1
```

```
GELEM 70  172 173 174 179 1 2
ELEM  71  174 175 176 179 9
ELEM  72  176 177 178 179 9
ELEM  73  180 181 182 197 10
ELEM  74  182 183 184 197 10
ELEM  75  184 185 186 197 4
GELEM 78  190 191 192 197 4 2
ELEM  79  192 193 194 197 10
ELEM  80  194 195 196 197 10
ELEM  81  198 199 200 215 7
ELEM  82  200 201 202 215 7
ELEM  83  202 203 204 215 3
GELEM 86  208 209 210 215 3 2
ELEM  87  210 211 212 215 7
ELEM  88  212 213 214 215 7
ELEM  89  216 217 218 233 8
ELEM  90  218 219 220 233 8
ELEM  91  220 221 222 233 1
GELEM 94  226 227 228 233 1 2
ELEM  95  228 229 230 233 8
ELEM  96  230 231 232 233 8
ELEM  97  234 235 236 251 1
GELEM 104 248 249 250 251 1 2
ELEM  105 252 253 254 269 9
ELEM  106 254 255 256 269 9
ELEM  107 256 257 258 269 1
GELEM 110 262 263 264 269 1 2
ELEM  111 264 265 266 269 9
ELEM  112 266 267 268 269 9
ELEM  113 270 271 272 287 10
ELEM  114 272 273 274 287 10
ELEM  115 274 275 276 287 4
GELEM 118 280 281 282 287 4 2
ELEM  119 282 283 284 287 10
ELEM  120 284 285 286 287 10
ELEM  121 288 289 290 305 7
ELEM  122 290 291 292 305 7
ELEM  123 292 293 294 305 3
GELEM 126 298 299 300 305 3 2
ELEM  127 300 301 302 305 7
ELEM  128 302 303 304 305 7
ELEM  129 306 307 308 323 8
ELEM  130 308 309 310 323 8
ELEM  131 310 311 312 323 1
GELEM 134 316 317 318 323 1 2
ELEM  135 318 319 320 323 8
ELEM  136 320 321 322 323 8
ELEM  137 324 325 326 341 1
GELEM 144 338 339 340 341 1 2
ELEM  145 342 343 344 359 9
ELEM  146 344 345 346 359 9
ELEM  147 346 347 348 359 1
GELEM 150 352 353 354 359 1 2
ELEM  151 354 355 356 359 9
ELEM  152 356 357 358 359 9
ELEM  153 360 361 362 377 10
ELEM  154 362 363 364 377 10
ELEM  155 364 365 366 377 4
GELEM 158 370 371 372 377 4 2
ELEM  159 372 373 374 377 10
ELEM  160 374 375 376 377 10

ELEM  161 395 396 397 404 2
GELEM 164 401 402 403 404 2 2
ELEM  165 405 406 407 414 2
GELEM 168 411 412 413 414 2 2
```

```
ELEM  169 415 416 417 424 2
GELEM 172 421 422 423 424 2 2
ELEM  173 425 426 427 434 2
GELEM 176 431 432 433 434 2 2
ELEM  177 435 436 437 444 2
GELEM 180 441 442 443 444 2 2
ELEM  181 445 446 447 454 2
GELEM 184 451 452 453 454 2 2
ELEM  185 455 456 457 464 2
GELEM 188 461 462 463 464 2 2
ELEM  189 465 466 467 474 2
GELEM 192 471 472 473 474 2 2
ELEM  193 475 476 477 484 2
GELEM 196 481 482 483 484 2 2
ELEM  197 485 486 487 494 2
GELEM 200 491 492 493 494 2 2
ELEM  201 495 496 497 504 2
GELEM 204 501 502 503 504 2 2
ELEM  205 505 506 507 514 2
GELEM 208 511 512 513 514 2 2
ELEM  209 515 516 517 524 2
GELEM 212 521 522 523 524 2 2
ELEM  213 525 526 527 534 2
GELEM 216 531 532 533 534 2 2
ELEM  217 535 536 537 544 2
GELEM 220 541 542 543 544 2 2
ELEM  221 545 546 547 554 2
GELEM 224 551 552 553 554 2 2
ELEM  225 555 556 557 564 2
GELEM 228 561 562 563 564 2 2
ELEM  229 565 566 567 574 2
GELEM 232 571 572 573 574 2 2
ELEM  233 575 576 577 584 2
GELEM 236 581 582 583 584 2 2
ELEM  237 585 586 587 594 2
GELEM 240 591 592 593 594 2 2
ELEM  241 378 379 380 596 5
GELEM 248 392 393 394 596 5 2
ELEM  249 597 598 599 640 5
GELEM 269 637 638 639 640 5 2
ELEM  270 641 642 643 684 5
GELEM 290 681 682 683 684 5 2

ELEM  291 639 965 378 596 5
ELEM  292 394 966 683 596 5

ELEM  293 967 969 971 988 6
ELEM  294 971 973 975 988 6
ELEM  295 975 976 977 988 6
ELEM  296 977 978 979 988 6
ELEM  297 979 981 983 988 6
ELEM  298 983 985 987 988 6
ELEM  299 989 991 993 1010  6
ELEM  300 993 995 997 1010  6
ELEM  301 997 998 999 1010  6
ELEM  302 999 1000  1001  1010  6
ELEM  303 1001  1003  1005  1010  6
ELEM  304 1005  1007  1009  1010  6
ELEM  305 1011  1013  1015  1032  6
ELEM  306 1015  1017  1019  1032  6
ELEM  307 1019  1020  1021  1032  6
ELEM  308 1021  1022  1023  1032  6
ELEM  309 1023  1025  1027  1032  6
ELEM  310 1027  1029  1031  1032  6
ELEM  311 1033  1035  1037  1054  6
ELEM  312 1037  1039  1041  1054  6
```

```
  ELEM  313 1041  1042  1043  1054  6
  ELEM  314 1043  1044  1045  1054  6
  ELEM  315 1045  1047  1049  1054  6
  ELEM  316 1049  1051  1053  1054  6
  ELEM  317 1055  1057  1059  1076  6
  ELEM  318 1059  1061  1063  1076  6
  ELEM  319 1063  1064  1065  1076  6
  ELEM  320 1065  1066  1067  1076  6
  ELEM  321 1067  1069  1071  1076  6
  ELEM  322 1071  1073  1075  1076  6

  ELEM  323 599 1077  18  35  11
  ELEM  324 601 1078  36  53  12
  ELEM  325 603 1079  54  71  13
  ELEM  326 605 1080  72  89  14
  ELEM  327 607 1081  90  107 15
  ELEM  328 609 1082  108 125 11
  ELEM  329 611 1083  126 143 12
  ELEM  330 613 1084  144 161 13
  ELEM  331 615 1085  162 179 14
  ELEM  332 617 1086  180 197 15
  ELEM  333 619 1087  198 215 11
  ELEM  334 621 1088  216 233 12
  ELEM  335 623 1089  234 251 13
  ELEM  336 625 1090  252 269 14
  ELEM  337 627 1091  270 287 15
  ELEM  338 629 1092  288 305 11
  ELEM  339 631 1093  306 323 12
  ELEM  340 633 1094  324 341 13
  ELEM  341 635 1095  342 359 14
  ELEM  342 637 1096  360 377 15
  ELEM  343 643 1097  34  35  11
  ELEM  344 645 1098  52  53  12
  ELEM  345 647 1099  70  71  13
  ELEM  346 649 1100  88  89  14
  ELEM  347 651 1101  106 107 15
  ELEM  348 653 1102  124 125 11
  ELEM  349 655 1103  142 143 12
  ELEM  350 657 1104  160 161 13
  ELEM  351 659 1105  178 179 14
  ELEM  352 661 1106  196 197 15
  ELEM  353 663 1107  214 215 11
  ELEM  354 665 1108  232 233 12
  ELEM  355 667 1109  250 251 13
  ELEM  356 669 1110  268 269 14
  ELEM  357 671 1111  286 287 15
  ELEM  358 673 1112  304 305 11
  ELEM  359 675 1113  322 323 12
  ELEM  360 677 1114  340 341 13
  ELEM  361 679 1115  358 359 14
  ELEM  362 681 1116  376 377 15

NODOFSHELL
SLAB75.tsh
 TRANSLATE    1    5
 TRANSLATE    2    6
 END_TRANS
SLAB75SIDERL.tsh
 TRANSLATE    1    5
 TRANSLATE    2    6
 END_TRANS
SLAB75SIDERFD.tsh
 TRANSLATE    1    5
 TRANSLATE    2    6
 END_TRANS
SLAB75EDGERL.tsh
```

```
 TRANSLATE    1    5
 TRANSLATE    2    6
 END_TRANS
SLAB75CNRRFD.tsh
 TRANSLATE    1    5
 TRANSLATE    2    6
 END_TRANS
SLAB75CNRRL.tsh
 TRANSLATE    1    5
 TRANSLATE    2    6
 END_TRANS
  ELEM  1 1   3   20  18  4
  ELEM  2 3   5   22  20  4
  ELEM  3 5   7   24  22  1
  ELEM  4 7   9   26  24  1
  ELEM  5 9   11  28  26  1
  ELEM  6 11  13  30  28  1
  ELEM  7 13  15  32  30  4
  ELEM  8 15  17  34  32  4
  ELEM  9 18  20  38  36  4
  ELEM  10  20  22  40  38  4
  ELEM  11  22  24  42  40  1
  GELEM 14  28  30  48  46  1 2
  ELEM  15  30  32  50  48  4
  ELEM  16  32  34  52  50  4
  ELEM  17  36  38  56  54  4
  ELEM  18  38  40  58  56  4
  ELEM  19  40  42  60  58  1
  GELEM 22  46  48  66  64  1 2
  ELEM  23  48  50  68  66  4
  ELEM  24  50  52  70  68  4
  ELEM  25  54  56  74  72  4
  ELEM  26  56  58  76  74  4
  ELEM  27  58  60  78  76  1
  GELEM 30  64  66  84  82  1 2
  ELEM  31  66  68  86  84  4
  ELEM  32  68  70  88  86  4
  ELEM  33  72  74  92  90  4
  ELEM  34  74  76  94  92  4
  ELEM  35  76  78  96  94  1
  GELEM 38  82  84  102 100 1 2
  ELEM  39  84  86  104 102 4
  ELEM  40  86  88  106 104 4
  ELEM  41  90  92  110 108 4
  ELEM  42  92  94  112 110 4
  ELEM  43  94  96  114 112 1
  GELEM 46  100 102 120 118 1 2
  ELEM  47  102 104 122 120 4
  ELEM  48  104 106 124 122 4
  ELEM  49  108 110 128 126 4
  ELEM  50  110 112 130 128 4
  ELEM  51  112 114 132 130 1
  GELEM 54  118 120 138 136 1 2
  ELEM  55  120 122 140 138 4
  ELEM  56  122 124 142 140 4
  ELEM  57  126 128 146 144 4
  ELEM  58  128 130 148 146 4
  ELEM  59  130 132 150 148 1
  GELEM 62  136 138 156 154 1 2
  ELEM  63  138 140 158 156 4
  ELEM  64  140 142 160 158 4
  ELEM  65  144 146 164 162 4
  ELEM  66  146 148 166 164 4
  ELEM  67  148 150 168 166 1
  GELEM 70  154 156 174 172 1 2
  ELEM  71  156 158 176 174 4
```

```
ELEM  72  158 160 178 176 4
ELEM  73  162 164 182 180 4
ELEM  74  164 166 184 182 4
ELEM  75  166 168 186 184 1
GELEM 78  172 174 192 190 1 2
ELEM  79  174 176 194 192 4
ELEM  80  176 178 196 194 4
ELEM  81  180 182 200 198 4
ELEM  82  182 184 202 200 4
ELEM  83  184 186 204 202 1
GELEM 86  190 192 210 208 1 2
ELEM  87  192 194 212 210 4
ELEM  88  194 196 214 212 4
ELEM  89  198 200 218 216 4
ELEM  90  200 202 220 218 4
ELEM  91  202 204 222 220 1
GELEM 94  208 210 228 226 1 2
ELEM  95  210 212 230 228 4
ELEM  96  212 214 232 230 4
ELEM  97  216 218 236 234 4
ELEM  98  218 220 238 236 4
ELEM  99  220 222 240 238 1
GELEM 102 226 228 246 244 1 2
ELEM  103 228 230 248 246 4
ELEM  104 230 232 250 248 4
ELEM  105 234 236 254 252 4
ELEM  106 236 238 256 254 4
ELEM  107 238 240 258 256 1
GELEM 110 244 246 264 262 1 2
ELEM  111 246 248 266 264 4
ELEM  112 248 250 268 266 4
ELEM  113 252 254 272 270 4
ELEM  114 254 256 274 272 4
ELEM  115 256 258 276 274 1
GELEM 118 262 264 282 280 1 2
ELEM  119 264 266 284 282 4
ELEM  120 266 268 286 284 4
ELEM  121 270 272 290 288 4
ELEM  122 272 274 292 290 4
ELEM  123 274 276 294 292 1
GELEM 126 280 282 300 298 1 2
ELEM  127 282 284 302 300 4
ELEM  128 284 286 304 302 4
ELEM  129 288 290 308 306 4
ELEM  130 290 292 310 308 4
ELEM  131 292 294 312 310 1
GELEM 134 298 300 318 316 1 2
ELEM  135 300 302 320 318 4
ELEM  136 302 304 322 320 4
ELEM  137 306 308 326 324 4
ELEM  138 308 310 328 326 4
ELEM  139 310 312 330 328 1
GELEM 142 316 318 336 334 1 2
ELEM  143 318 320 338 336 4
ELEM  144 320 322 340 338 4
ELEM  145 324 326 344 342 5
ELEM  146 326 328 346 344 5
ELEM  147 328 330 348 346 3
GELEM 150 334 336 354 352 3 2
ELEM  151 336 338 356 354 5
ELEM  152 338 340 358 356 5
ELEM  153 342 344 362 360 5
ELEM  154 344 346 364 362 5
ELEM  155 346 348 366 364 3
GELEM 158 352 354 372 370 3 2
ELEM  159 354 356 374 372 5
```

```
  ELEM  160 356 358 376 374 5
  ELEM  161 360 362 380 378 6
  ELEM  162 362 364 382 380 6
  ELEM  163 364 366 384 382 2
  ELEM  164 366 368 386 384 2
  ELEM  165 368 370 388 386 2
  ELEM  166 370 372 390 388 2
  ELEM  167 372 374 392 390 6
  ELEM  168 374 376 394 392 6

  ELEM  169 597 599 18   1  4
  ELEM  170 599 601 36  18  4
  ELEM  171 601 603 54  36  4
  ELEM  172 603 605 72  54  4
  ELEM  173 605 607 90  72  4
  ELEM  174 607 609 108 90  4
  ELEM  175 609 611 126 108 4
  ELEM  176 611 613 144 126 4
  ELEM  177 613 615 162 144 4
  ELEM  178 615 617 180 162 4
  ELEM  179 617 619 198 180 4
  ELEM  180 619 621 216 198 4
  ELEM  181 621 623 234 216 4
  ELEM  182 623 625 252 234 4
  ELEM  183 625 627 270 252 4
  ELEM  184 627 629 288 270 4
  ELEM  185 629 631 306 288 4
  ELEM  186 631 633 324 306 4
  ELEM  187 633 635 342 324 4
  ELEM  188 635 637 360 342 4
  ELEM  189 637 639 378 360 4
  ELEM  190 641 643 34  17  4
  ELEM  191 643 645 52  34  4
  ELEM  192 645 647 70  52  4
  ELEM  193 647 649 88  70  4
  ELEM  194 649 651 106 88  4
  ELEM  195 651 653 124 106 4
  ELEM  196 653 655 142 124 4
  ELEM  197 655 657 160 142 4
  ELEM  198 657 659 178 160 4
  ELEM  199 659 661 196 178 4
  ELEM  200 661 663 214 196 4
  ELEM  201 663 665 232 214 4
  ELEM  202 665 667 250 232 4
  ELEM  203 667 669 268 250 4
  ELEM  204 669 671 286 268 4
  ELEM  205 671 673 304 286 4
  ELEM  206 673 675 322 304 4
  ELEM  207 675 677 340 322 4
  ELEM  208 677 679 358 340 4
  ELEM  209 679 681 376 358 4
  ELEM  210 681 683 394 376 4

 PRECISION     1.e-3
    LOADS
  FUNCTION     F1
   DISTRSH         9       0.0       0.0   -9200.0
  GDISTRSH       160       0.0       0.0   -9200.0    1
   DISTRSH         1       0.0       0.0   -600.0
  GDISTRSH         8       0.0       0.0   -600.0     1
   DISTRSH       161       0.0       0.0   -600.0
  GDISTRSH       168       0.0       0.0   -600.0     1
  END_LOAD

 MATERIALS
SILCONCEC2
```

```
       0.2   42E+6    2.0E+6                                1
  PSTEELA16
   210.E+9         .3   1870.E6 0 0 0 0 0
  STEELEC2
   20.5E+9         .3   42.E6
  INSULATION

SILCONC2D
       0.2   30.2E+6    2.0E+6                                 1
  STEELEC2
   210.E+9         .3   450.E6
SILCONCEC2
       0.2   30.2E+6    2.0E+6                                 1

      TIME
                  0.5      4.0
                  4.      32.0
                  8.     256.0
                  8.    1472.0
                  16.    3200.0
                  16.   14400.0
  END_TIME
LARGEDISPL
     EPSTH
IMPRESSION
 TIMEPRINT     64.0
PRINTREACT
   PRINTMN
   PRNNXSHELL
   PRNMXSHELL
```

Appendix B MATERIAL PROPERTIES

B.1. Stress-Strain Relationship of Normal Weight Concrete in Fire under Compression

Table B-1 Values for the main parameters of the stress-strain relationships of normal weight concrete with siliceous or calcareous aggregates concrete at elevated temperatures [EC2 2002]

Concrete	Siliceous aggregates			Calcareous aggregates		
temp, θ	$f_{c,\theta}/f_{ck}$	$\varepsilon_{c1,\theta}$	$\varepsilon_{cu,\theta}$	$f_{c,\theta}/f_{ck}$	$\varepsilon_{c1,\theta}$	$\varepsilon_{cu,\theta}$
[^{o}C]	[-]	[-]	[-]	[-]	[-]	[-]
20	1.00	0.0025	0.0200	1.00	0.0025	0.0200
100	1.00	0.0040	0.0225	1.00	0.0040	0.0025
200	0.95	0.0055	0.0250	0.97	0.0055	0.0250
300	0.85	0.0070	0.0275	0.91	0.0070	0.0275
400	0.75	0.0100	0.0300	0.85	0.0100	0.0300
500	0.60	0.0150	0.0325	0.74	0.0150	0.0325
600	0.45	0.0250	0.0350	0.60	0.0250	0.0350
700	0.30	0.0250	0.0375	0.43	0.0250	0.0375
800	0.15	0.0250	0.0400	0.27	0.0250	0.0400
900	0.08	0.0250	0.0425	0.15	0.0250	0.0425
1000	0.04	0.0250	0.0450	0.06	0.0250	0.0450
1100	0.01	0.0250	0.0475	0.02	0.0250	0.0475
1200	0.00	-	-	0.00	-	-

Appendix C TEST INFORMATION

C.1. DIFT [Andersen et al. 1999]

C.1.1. Hollowcore units

The prestressed hollowcore units SP18, SP22 and SP27 have the dimensions as shown in Figure C-1.

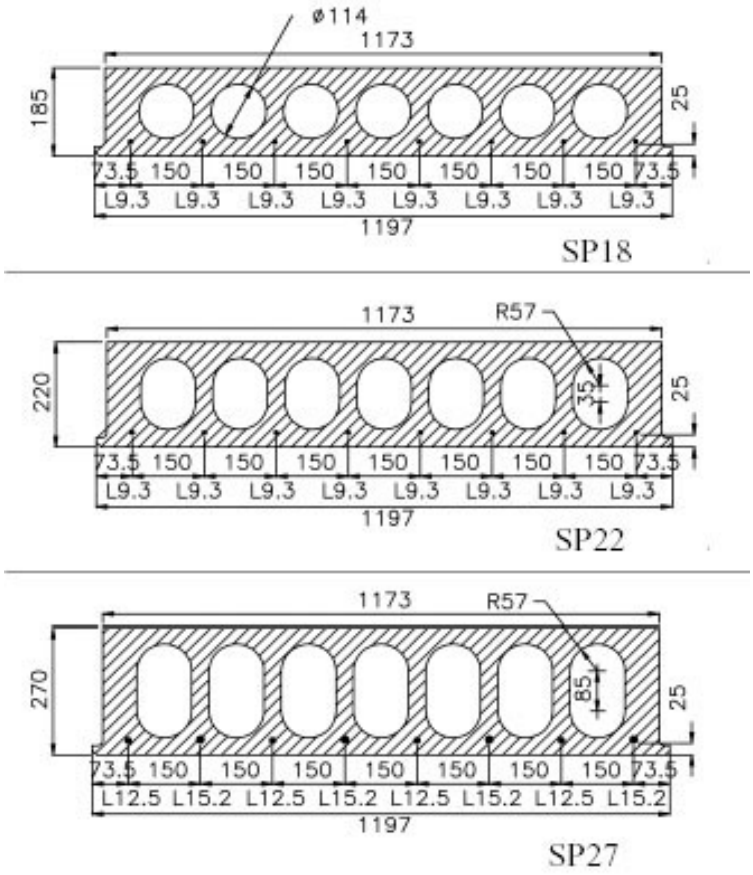

Figure C-1 Types of hollowcore concrete used in the 1998 DIFT tests

Other information:

- Concrete type: Portland cement and siliceous Danish moraine gravel
- Compressive strength of the concrete: 54MPa.
- Tensile strength of the concrete: 2MPa.
- Cover thickness to the strands: 25mm
- Self weights:

SP18:2.75kN/m^2; SP22: 3.10kN/m^2; SP27: 3.55kN/m^2

- Material properties of the strands are shown in Table C-1.

Table C-1 Material properties of the strands in the 1998 DIFT tests [Andersen et al. 1999]

Section type	**SP18**	**SP22**	**SP27**
Strands (per unit)	8 of Φ9.3mm		4 of Φ12.5mm, 4 of Φ15.2mm
Ultimate strength	1.87-1.90 kN/mm2		1.83-1.85 kN/ mm2 for Φ12.5mm, 1.82-1.84 kN/ mm2 for Φ15.2mm
Mechanical prestressing	62kN/ strand		110 kN/ strand for Φ12.5mm, 150 kN/ strand for Φ15.2mm
Modulus of elasticity	198-200 kN/mm2		198 kN/mm^2 for Φ12.5mm, 200-204 kN/mm^2 for Φ15.2mm

C.1.2. Experimental setup

- Free span length: 6.2m;
- Exposed span length: 6.0m
- Support condition: simply supported
- Loading condition: the loading conditions are shown in Figure C-2 and Table C-2.

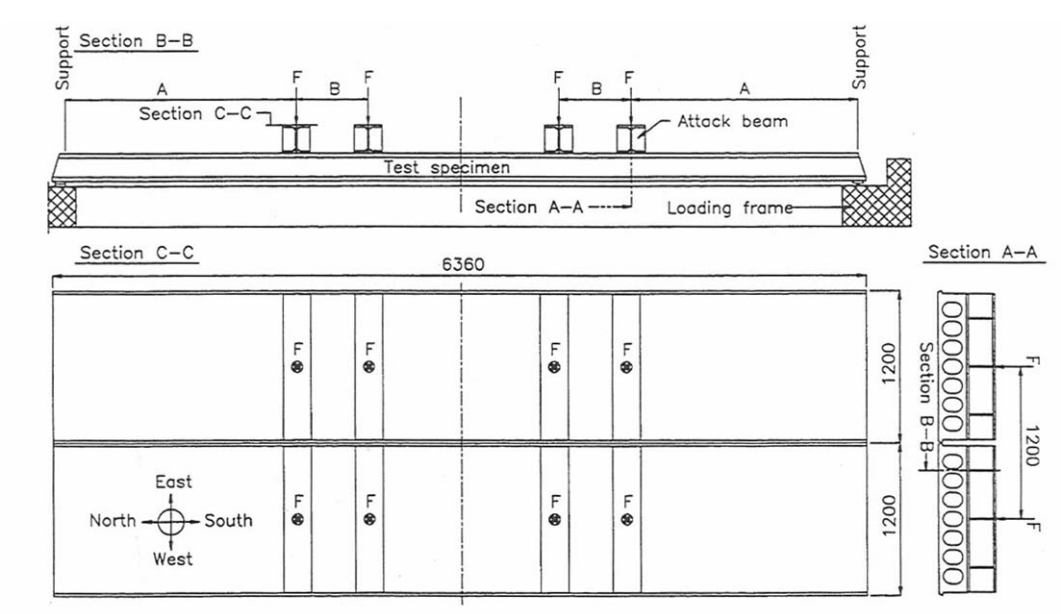

Figure C-2 Experiment set-up in the 1998 DIFT tests [Andersen 1999]

Table C-2 Magnitude and locations of the load in the 1998 DIFT tests [Andersen 1999]

Test	Total external load	F	A	B
SP18	135.4kN	16.93kN	1084mm	1200mm
SP22	135.4kN	16.93kN	1084mm	1200mm
SP27	112.1kN (for 1 slab)	28.02kN	1600mm	1000mm

C.2. University of Ghent [FeBe Studiecommissie SSTC 1998]

C.2.1. Hollowcore units

Hollowcore unit SP200 (Used in Test 1)

The prestressed hollowcore unit SP200 has the following dimensions and is as shown in Figure C-3:

- Length: 3000mm
- Width: 1196mm
- Thickness: 200mm

Other information:

- Compressive strength of the concrete: 65MPa.
- Cover thickness to the strands: 50mm
- Moisture content of the hollowcore unit: 115 litre of water/m^3.
- Prestressing strands: 7 wires with diameter of 9.5mm and with strength of 1860MPa.

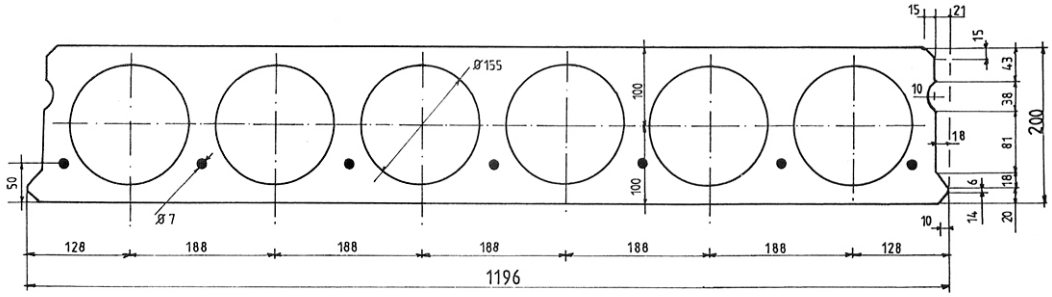

Figure C-3 Cross section of SP200 [FeBe Studiecommissie SSTC 1998]

Hollowcore unit VS20/60 (Used in Test 2 and 3)

The prestressed hollowcore unit VS20/60 has the following dimensions and is as shown in Figure C-4:

- Length: 3000mm
- Width: 597mm
- Thickness: 200mm

Other information:

- Compressive strength of the concrete: 55MPa.
- Cover thickness to the bottom strands: 45mm
- Cover thickness to the top strands: 25mm
- Moisture content of the hollowcore unit: 136 litre of water/m^3.
- Prestressing strands: 4 wires with diameter of 7mm and with strength of 1670MPa; 4 wires with diameter of 5mm and with strength of 1770MPa.

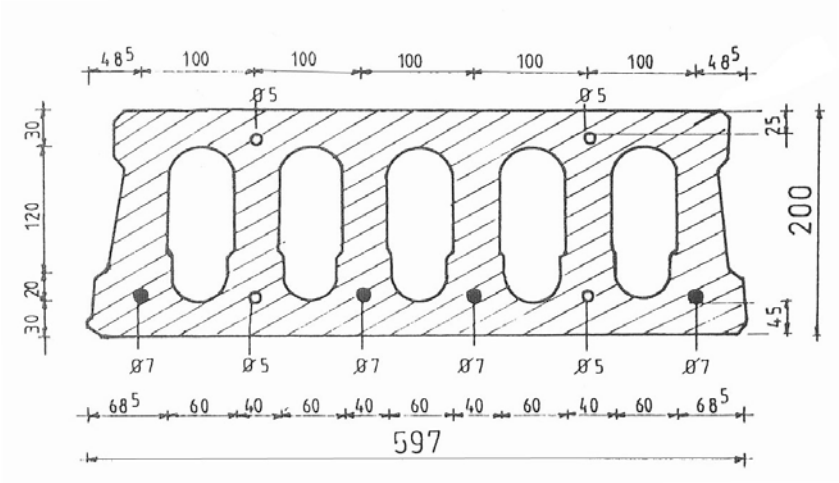

Figure C-4 Cross section of VS20/60 [FeBe Studiecommissie SSTC 1998]

Hollowcore unit SP265 (Used in Test 4)

The prestressed hollowcore unit SP265 has the following dimensions and is as shown in Figure C-5:

- Length: 3000mm
- Width: 1196mm
- Thickness: 265mm

Other information:

- Compressive strength of the concrete: 65MPa.
- Cover thickness to the strands: 49mm
- Moisture content of the hollowcore unit: 115 litre of water/m^3.
- Prestressing strands: 10 wires with diameter of 9.5mm and with strength of 1860MPa.

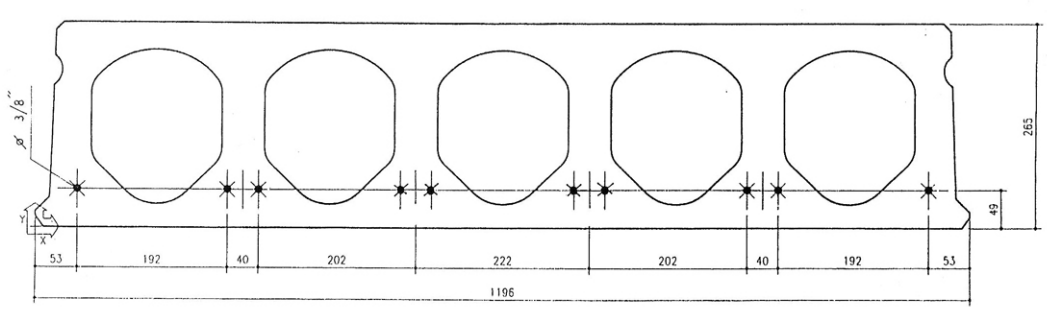

Figure C-5 Cross section of SP265 [FeBe Studiecommissie SSTC 1998]

C.2.2. Experimental set-up

Test 1

The layout of Test 1 (Experiment no.8871) was as shown in Figure C-6.

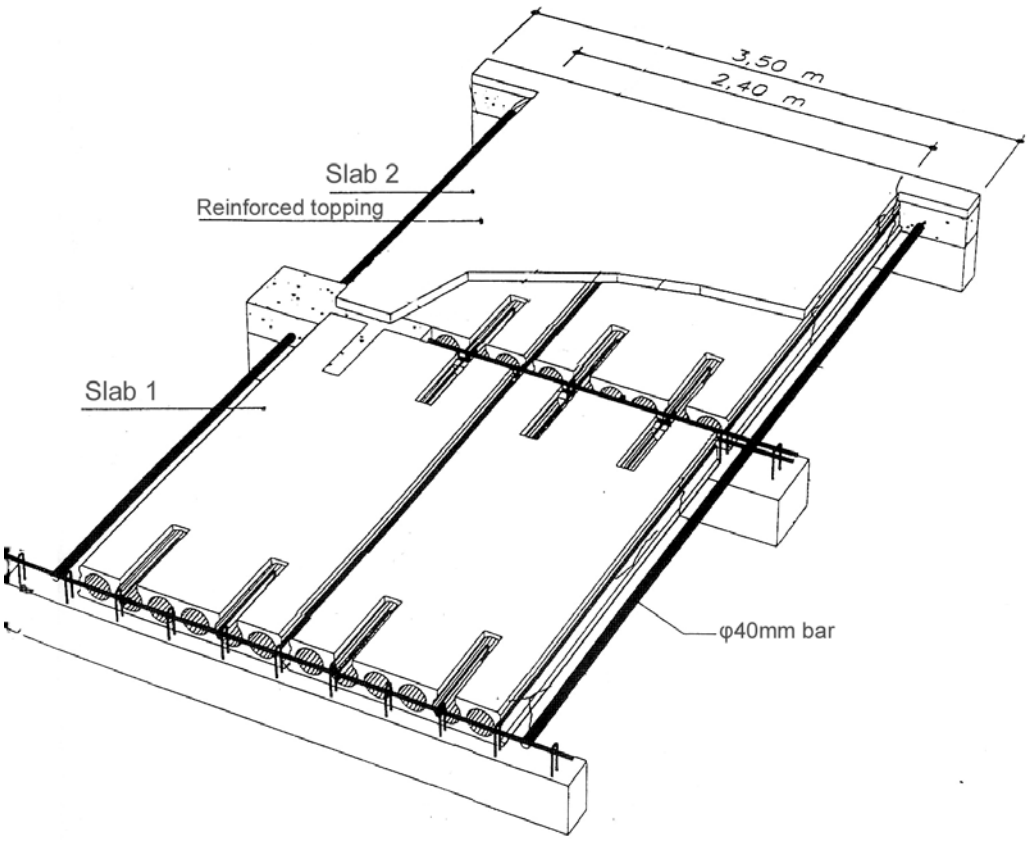

Figure C-6 Layout of Test 1 carried out at University of Ghant in 1998 [FeBe Studiecommissie SSTC 1998]

- Hollowcore unit: 4 ERGON SP200 units in total
- Reinforced concrete topping: 50mm thick of topping on Slab 2 with mesh reinforcement 150x150x5x5 in the mid-height.

Other information:

- 2 of 6 open cores in each hollowcore unit were filled by normal concrete 500mm from the ends with 12mm diameter reinforcement anchored into the end beams
- A 40mm diameter bar was placed at each side of the specimen and anchored into the supports.
- A transversal bar with 32mm diameter was placed on top of each support.
- A linear load of 100kN was applied at the midspan of each slab.

Test 2

The layout of Test 2 (Experiment no.8872) was as shown in Figure C-7.

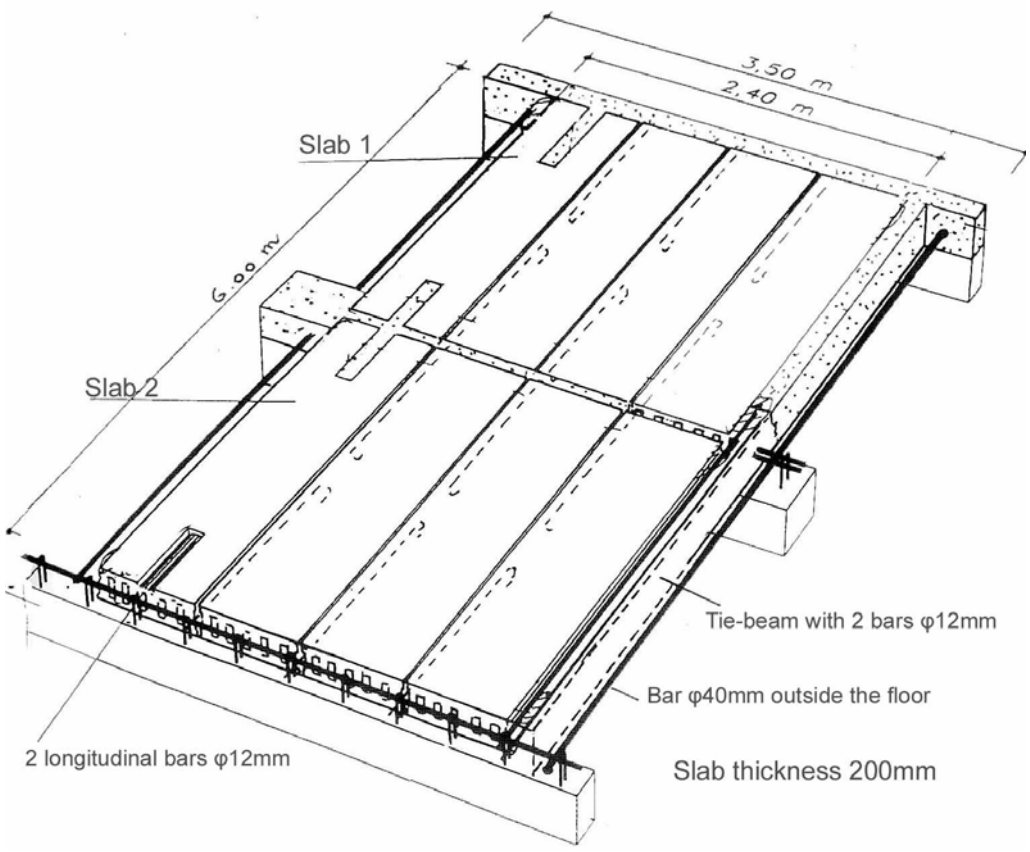

Figure C-7 Layout of Test 2 carried out at University of Ghant in 1998 [FeBe Studiecommissie SSTC 1998]

- Hollowcore unit: 8 ECHO VS20/60 units in total
- Reinforced concrete topping: none

Other information:

- 1 open cores of one unit was filled by normal concrete 500mm from the ends with 12mm diameter reinforcement anchored into the end beams
- A 40mm diameter bar was placed at each side of the specimen and anchored into the supports.
- A tie-beam with two 20mm reinforcing bars was placed at one side of the specimen.
- A 1500mm long 12mm diameter bar was placed between the side of each hollowcore units, and the gap was filled with normal concrete.
- A transversal bar with 32mm diameter was placed on top of each support.
- A linear load of 100kN was applied at the midspan of each slab.

Test 3

The layout of Test 3 (Experiment no.9157) was as shown in Figure C-8.

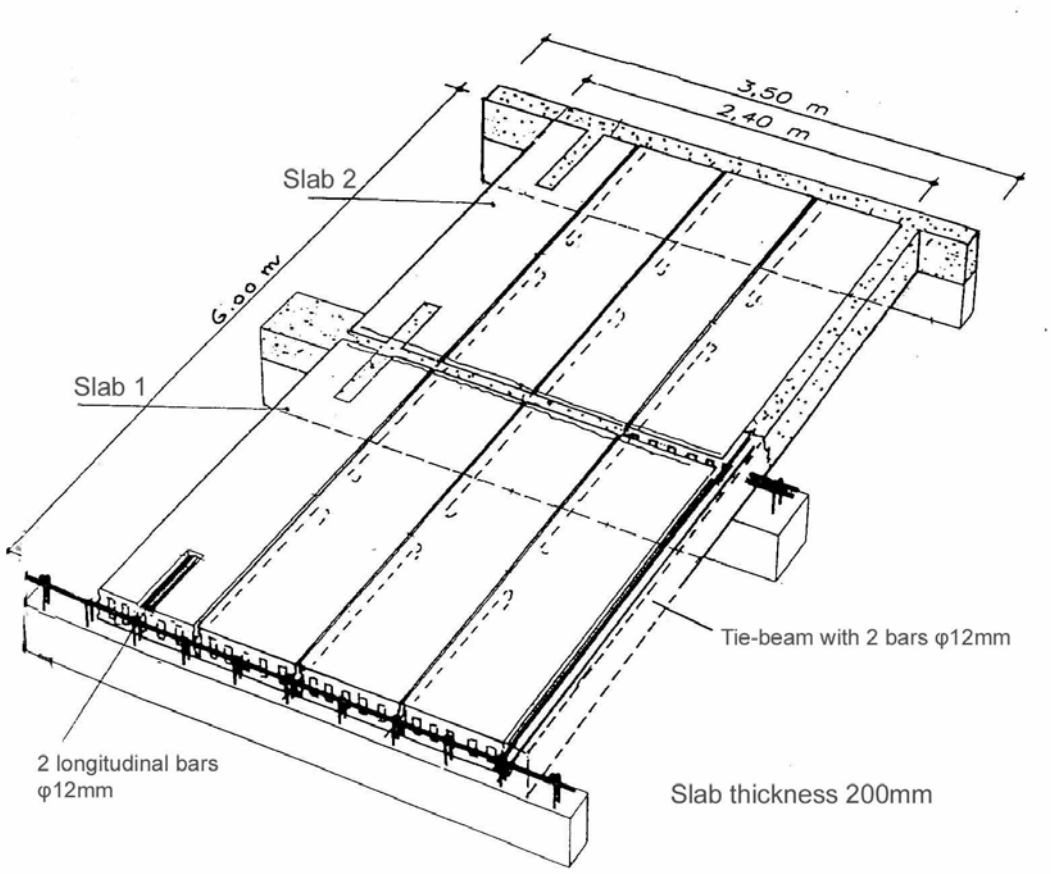

Figure C-8 Layout of Test 3 carried out at University of Ghant in 1999 [FeBe Studiecommissie SSTC 1998]

- Hollowcore unit: 8 ECHO VS20/60 units in total
- Reinforced concrete topping: none

Other information:

- 1 open cores of one unit was filled by normal concrete 500mm from the ends with 12mm diameter reinforcement anchored into the end beams
- A tie-beam with two 20mm reinforcing bars was placed at one side of the specimen.
- A 1500mm long 12mm diameter bar was placed between the side of each hollowcore units, and the gap was filled with normal concrete.
- A transversal bar with 32mm diameter was placed on top of each support.
- A linear load of 100kN was applied at the midspan of each slab.

Test 4

The layout of Test 4 (Experiment no.9158) was as shown in Figure C-8.

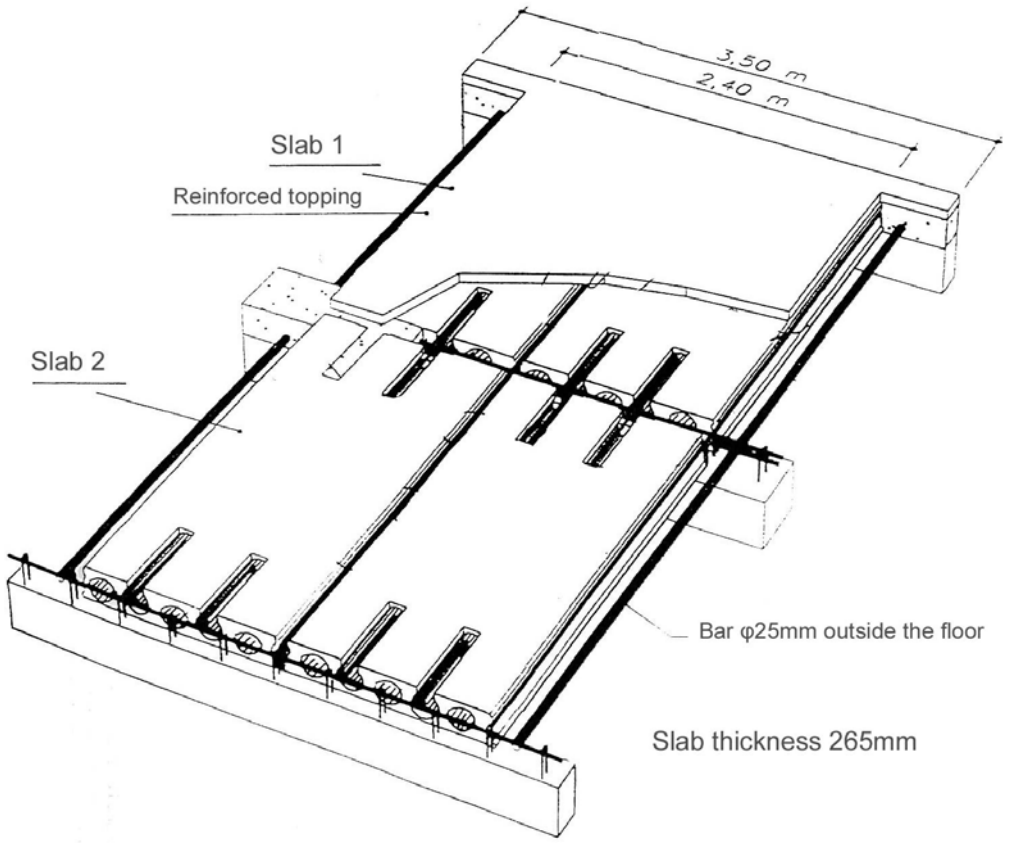

Figure C-9 Layout of Test 4 carried out at University of Ghant in 1999 [FeBe Studiecommissie SSTC 1998]

- Hollowcore unit: 4 ERGON SP265 units in total
- Reinforced concrete topping: 30mm thick of topping on Slab 2 with mesh reinforcement 150x150x5x5 in the mid-height.

Other information:

- 2 of 6 open cores in each hollowcore unit were filled by normal concrete 500mm from the ends with 12mm diameter reinforcement anchored into the end beams
- A 25mm diameter bar was placed at each side of the specimen and anchored into the supports.
- A transversal bar with 32mm diameter was placed on top of each support.
- A linear load of 100kN was applied at the midspan of each slab.

C.3. Danish Prefab Concrete Association (BEF) [BEF 2005]

C.3.1. Hollowcore units

The prestressed hollowcore unit used in the test conducted by BEF in 2005 has the dimensions as shown in Figure C-1.

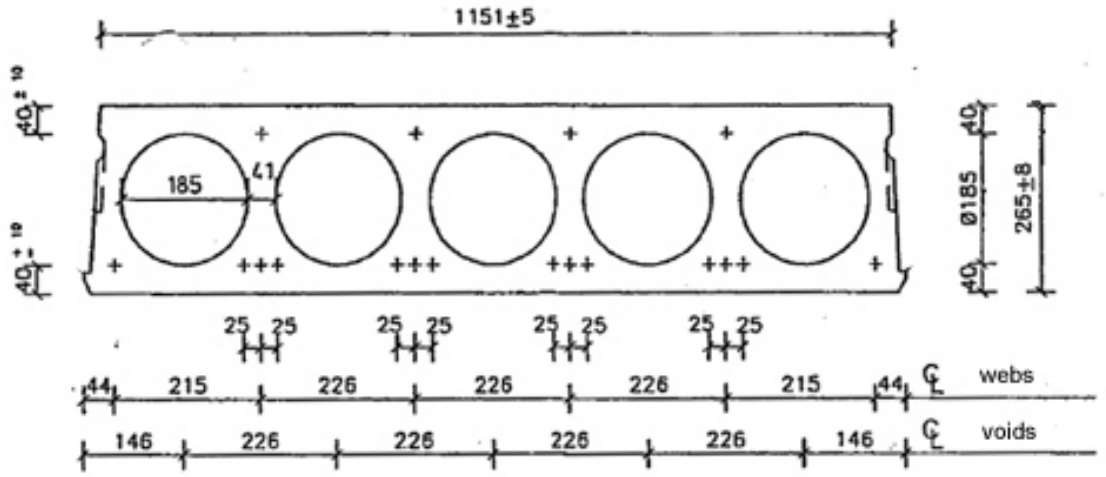

Figure C-10 Cross section of the hollowcore unit used in the BEF 2005 tests [BEF 2005]

- Length: 3000mm
- Width: 1197 ± 3mm
- Thickness: 265 ± 8mm

Other information:

- Compressive strength of the concrete: 55MPa.
- Cover thickness to the strands: 40mm
- Self-weight (including joint casting): 3.65kN/m^2
- Moisture content: 2.28% at the time of testing
- Prestressing strands: 10 of 12.5mm steel strands with the yielding strength of 1570MPa.
- Initial prestressing 1050MPa, effective prestressing 930MPa.

C.3.2. Experimental Set-up

The layout of the experiment is shown in Figure C-11. The test zone consisted of one whole and two halves of hollowcore units and was separated from the buffer zones with a longitudinal cut in the units. The two cut cores were filled with rock wool.

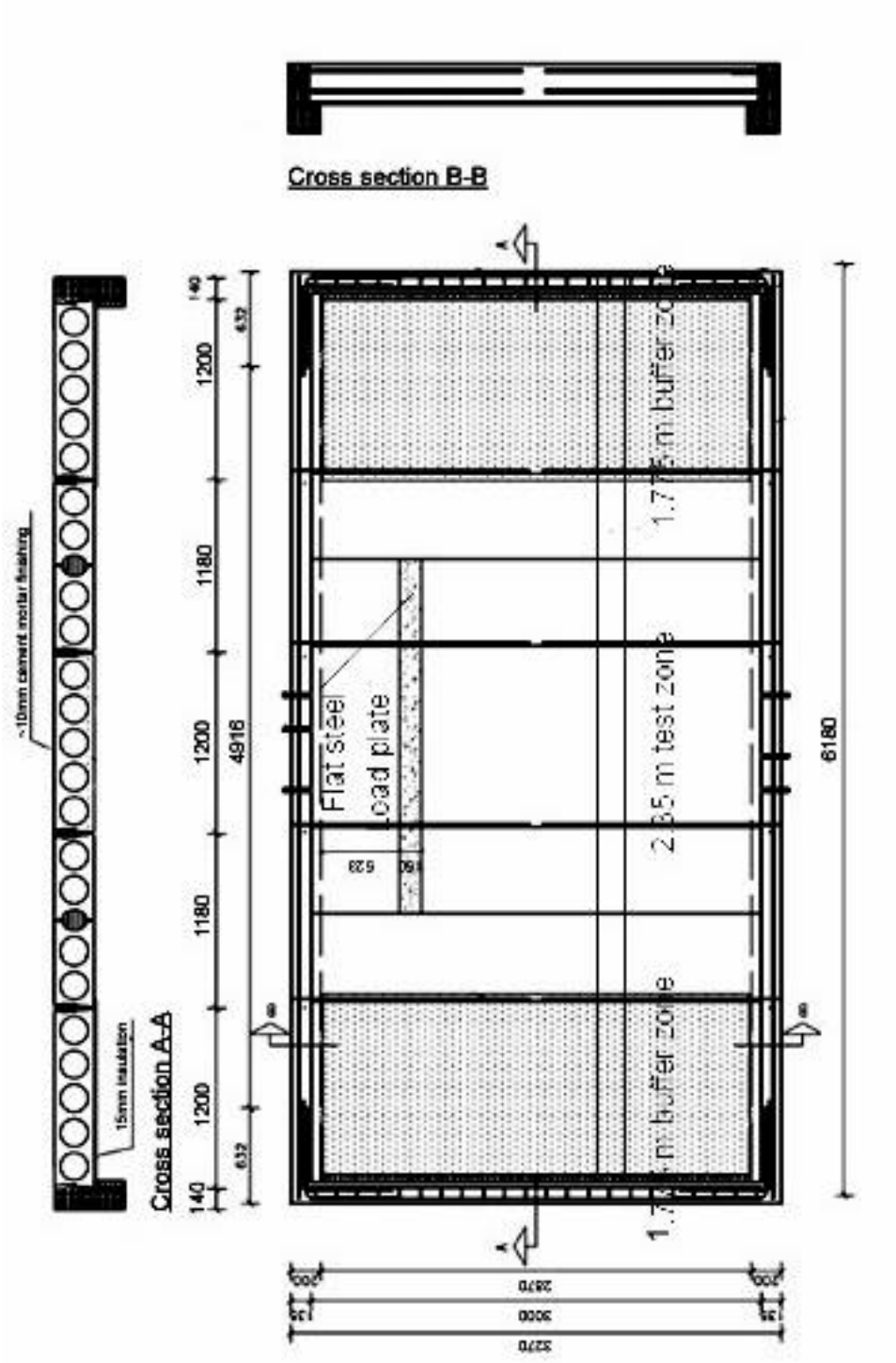

Figure C-11 Test layout in the BEF 2005 tests [modified from BEF 2005]

Loading Arrangement:

The loading arrangement is as shown in Figure C-12 with extra information shown in Table C-3. The steel plates combined weight was 0.3kN/m. The shear capacity of the slabs was 91.6kN/m determined in accordance to DS411 based on function testing with loading arrangement according to prEN1168.

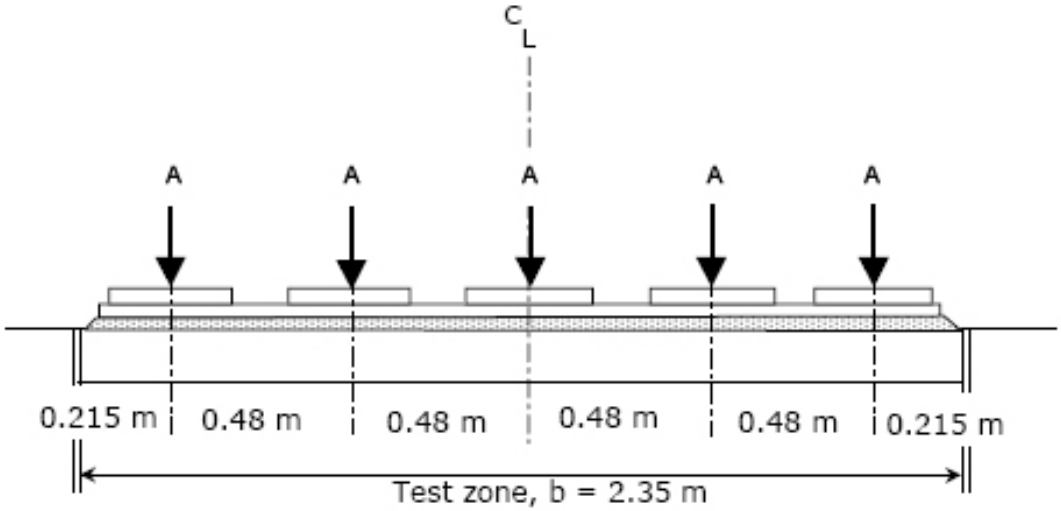

Figure C-12 Loading Arrangement on the load plate in the BEF 2005 tests [modified from BEF 2005]

Table C-3 Loading arrangements in the BEF 2005 tests

Tests	**SP-1**	**SP-2**	**SP-3**
Load Level	65% of Vud(cold)	75% of Vud(cold)	80% of Vud(cold)
Shear force into the slab	59.55kN/m	68.76kN/m	73.30kN/m
A in Figure C-12	32.3kN	37.8kN	40.5kN

Appendix D CALCULATION OF MAXIMUM UDL ON THE 100mm THICK SLAB

The reinforced concrete slab was 4.3m long, 3.3m wide and 100mm thick. It had one layer of D147 mesh, which has the properties shown in Table D-1.

Table D-1 Properties of the reinforcing steel at ambient conditions [Lim 2003]

Reinforced Steel	Bar diameter	Grid spacing	Yield stress	Steel content	Strain limit
D147 mesh	8.7mm	300mm	565MPa	198mm^2/m	2.3%

The concrete cover to the bottom bar was 25mm. The slab consisted of normal weight siliceous concrete with a compressive strength of 36.6MPa. The tensile strength of the concrete used the recommended value of $0.25\sqrt{f'c}$ by [Lim 2003] and equals 1.5MPa.

D.1. Calculation – Supported at the short side

1. Determine the failure mode (tension failure or compression failure)

$$\rho_d = \frac{0.85 f_c' \beta_1}{f_y} \frac{0.003 E_s}{0.003 E_s + f_y} \qquad \text{(Eq.4.14, Park \& Paulay 1975)}$$

where f'_c (concrete compressive strength) = 36.6MPa
β_1 (compressive area factor) = 0.85
f_y (yield strength of steel) = 565MPa
E_s (young's modulus of steel) = 210GPa
So ρ_d = 0.0247

Check against $\rho = \frac{A_s}{bd}$

where A_s (area of steel) = 198mm^2
b (width of slab) = 1m
d (effective depth) = 75mm
ρ = 0.0026 $< \rho_d$

Therefore a tension failure occurs

2. Calculate the ideal flexural strength

To calculate the flexural strength from tension failure

$$M_u = A_s f_y \left(d - 0.59 \frac{A_s f_y}{f_c' b} \right)$$ (Eq.4.6a, Park & Paulay 1975)

Mu = 8.188 kNm

3. Calculate the UDL

The slab was pin-supported. When supported at the short edge, the span length is 4.3m, using the equation

$$M = \frac{wL^2}{8}$$

where M = 8.188kNm,

L (span length) = 4.3m,

So the maximum w = 3542.9N/m on a unit width of the slab.

To avoid reaching failure under the ambient condition, a 90% of this maximum UDL is used, which equals **3188.6 N/m** every unit width of the slab (used with shell elements)

When the width of beam is 158mm, the UDL is **503.8N/m** (used with beam elements)

D.2. Calculation – Supported at the long side

Step 1 and 2 are the same as in previous calculation

3. Calculate the UDL

The slab was pin-supported. When supported at the short edge, the span length is 3.3m, using the equation

$$M = \frac{wL^2}{8}$$

where M = 8.188kNm, L (span length) = 3.3m,

So the maximum w = 6015N/m on a unit width of the slab.

To avoid reaching failure under the ambient condition, a 90% of this maximum UDL is used, which equals 5413 N/m on a unit width of the slab. This value is similar

to the value 5400N/m/m used in [Lim 2003]. In order to be consistent to the rest of the analysis, **5400 N/m** on a unit width of the slab is used for this situation.

When the width of beam is 208mm, the UDL is **1123.2N/m** (used with beam elements)